POLYPUBLIE
Polytechnique Montréal

POLYTECHNIQUE MONTRÉAL
UNIVERSITÉ D'INGÉNIERIE

Titre: Title:	Thermodynamic Optimization Of The Na2O-K2O-Al2O3-CaO-MgO-B2O3-SiO2 System
Auteur: Author:	Evgenii Nekhoroshev
Date:	2019
Type:	Mémoire ou thèse / Dissertation or Thesis
Référence: Citation:	Nekhoroshev, E. (2019). Thermodynamic Optimization Of The Na2O-K2O-Al2O3-CaO-MgO-B2O3-SiO2 System [Thèse de doctorat, Polytechnique Montréal]. PolyPublie. https://publications.polymtl.ca/4133/

Document en libre accès dans PolyPublie
Open Access document in PolyPublie

URL de PolyPublie: PolyPublie URL:	https://publications.polymtl.ca/4133/
Directeurs de recherche: Advisors:	Sergei Decterov, & Arthur Pelton
Programme: Program:	Génie métallurgique

Ce fichier a été téléchargé à partir de PolyPublie, le dépôt institutionnel de Polytechnique Montréal
This file has been downloaded from PolyPublie, the institutional repository of Polytechnique Montréal

https://publications.polymtl.ca

POLYTECHNIQUE MONTRÉAL

affiliée à l'Université de Montréal

Thermodynamic Optimization Of The Na_2O-K_2O-Al_2O_3-CaO-MgO-B_2O_3-SiO_2 System

EVGENII NEKHOROSHEV

Département de génie chimique

Thèse présentée en vue de l'obtention du diplôme de *Philosophiæ Doctor*

Génie métallurgique

Décembre 2019

© Evgenii Nekhoroshev, 2019.

POLYTECHNIQUE MONTRÉAL

affiliée à l'Université de Montréal

Cette thèse intitulée :

Thermodynamic Optimization Of The Na_2O-K_2O-Al_2O_3-CaO-MgO-B_2O_3-SiO_2 System

présentée par **Evgenii NEKHOROSHEV**

en vue de l'obtention du diplôme de *Philosophiæ Doctor*

a été dûment acceptée par le jury d'examen constitué de :

Patrice CHARTRAND, président

Sergei DECTEROV, membre et directeur de recherche

Arthur PELTON, membre et codirecteur de recherche

Jean-Philippe HARVEY, membre

Susan SCHIEFELBEIN, membre externe

ACKNOWLEDGEMENTS

I would like to express my gratitude to my research director Dr. Sergei A. Decterov for his guidance and advice during this project. His insight and rational thinking have helped me in many difficult moments of the research process. I am also grateful to him for teaching me discipline, attention and organization skills so valuable in a big research project.

I am grateful to my co-director Dr. Arthur D. Pelton; his excellent course of the thermodynamics of solutions gave me the theoretical foundation that allowed me to perform this work.

I express gratitude towards the members of the jury: Dr. Patrice Chartrand, Dr. Jean-Philippe Harvey, Dr. Susan L. Schiefelbein for their critical review and constructive comments.

I appreciate the help of my dear colleagues Evguenia Sokolenko, Eve Belisle, Dr. Jacques Melançon, Dr. Christian Robelin. Evguenia made my work much easier helping to organize and manage hundreds of articles and references. I also appreciate our friendship and small talks over a cup of coffee together. Many thanks to Eve and Jacques who were always very kind to help me with computers and software. Christian Robelin corrected the French translation of the abstract of this thesis. I appreciate his attention to details and his help in improving my written French.

I have the deepest gratitude towards my ex-supervisor Dr. Irina Uspenskaya from the Moscow State University for believing in me and giving me a chance to start a new life.

I appreciate the friendship of Vlad and Ksenia; good luck on the uneasy journey to a PhD. Many thanks to Alex for his moral support and the days we have spent together. I am thankful to my partner Jarrod for his support, love and commitment.

RÉSUMÉ

La connaissance des propriétés thermodynamiques des phases dans le système d'oxydes Na_2O-K_2O-Al_2O_3-CaO-MgO-B_2O_3-SiO_2 est importante dans plusieurs domaines, parmi lesquels on peut mentionner la production de verres, de céramiques, d'aciers ainsi que les applications en géologie. Le présent travail poursuit le développement d'une base de données thermodynamiques pour le système de sept oxydes. Le travail présenté ici se limite à l'étude des sous-systèmes incluant les oxydes de métaux alcalins. Les données expérimentales disponibles dans la littérature ont été collectées, analysées et utilisées pour une évaluation thermodynamique selon la méthode CALPHAD. Certaines approches ont été élaborées pour une meilleure description des systèmes silice-oxyde alcalin et des systèmes contenant du bore. D'habitude, les systèmes binaires et ternaires sont considérés comme les plus importants d'après la méthode CALPHAD tandis que les propriétés des systèmes ayant plusieurs composants doivent être prédites à partir des propriétés des sous-systèmes. Dans ce travail, nous avons prêté attention aux données disponibles dans les systèmes de plus de trois composants. Premièrement, il existe plusieurs solutions solides dont l'optimisation nécessite de considérer les données expérimentales dans ces systèmes. Deuxièmement, une bonne reproduction des données dans les systèmes ayant plusieurs composants est une preuve de la validité des optimisations pour les systèmes binaires et les ternaires. La modélisation des systèmes incluant les oxydes alcalins nécessite l'introduction d'espèces associées dans un modèle dont les paramètres peuvent être contraints seulement en utilisant des données des systèmes d'ordre supérieur.

Le liquide et, pour les cas rares, des solutions solides ont été modélisés à l'aide du Modèle Quasichimique Modifié. Les solutions solides ont été traitées avec le « Compound Energy Formalism ». Chaque fois que c'était possible, la construction des modèles a été accompagnée d'une explication détaillée des données de structure cristallographique. Les distorsions possibles et les transformations de la maille du réseau cristallin avec la composition et la température ont été décrites en détail.

Quelques programmes ont été créés durant ce travail pour faciliter la procédure d'optimisation. Le programme *CpFit* permet de traiter des données de capacité calorifique aussi que de capacité calorifique intégrale pour obtenir des représentations de la fonction de la capacité calorique d'une

manière fiable et uniforme. Une procédure semi-automatique d'optimisation basée sur les scripts de *MATLAB* a été développée pour modéliser des systèmes ayant besoin de plusieurs paramètres fortement corrélés.

Comme plusieurs systèmes ont une forte tendance à former des verres, la nature du verre et ses différences par rapport au liquide du point de vue des propriétés thermodynamiques ont été abordées. Ceci permet d'inclure de multiples données pour des verres en convertissant leurs propriétés en celles de liquides d'une façon physiquement fiable. Les restrictions et limitations du logiciel ainsi que les bases de données thermodynamiques existantes liées au calcul des propriétés de verres et de liquides ont été discutées.

Les optimisations effectuées sont compatibles avec la base de données d'oxydes existante déjà dans *FactSage* et peuvent être utilisées pour des prédictions de diagrammes de phases et de propriétés thermodynamiques dans des régions inconnues du système Na_2O-K_2O-Al_2O_3-CaO-MgO-B_2O_3-SiO_2.

ABSTRACT

The knowledge of thermodynamic properties of phases in the Na_2O-K_2O-Al_2O_3-CaO-MgO-B_2O_3-SiO_2 system is important in many applications, such as glass production, production of ceramics, steel-making and geology. The current work continues the efforts in constructing a full and consistent database in the seven-component system. The scope of the work is limited to the alkali-containing parts of the big system. The available data on phase relations and thermodynamic properties were collected, analysed, and used for a thermodynamic assessment using CALPHAD method. New modelling approaches had to be invented for a better description of alkali oxide-silica and boron-containing systems. Usually, CALPHAD method pays great attention to optimization of binary and ternary subsystems while the multicomponent systems are considered less important because their properties are supposed to arise from the properties of the subsystems. In this work, special attention was paid to the data on systems with a number of components greater than three. First, there are many solid solutions spreading through multicomponent systems and their optimization requires experimental data from these systems. Second, the reproduction of experimental data in multicomponent systems is a proof of correctness of optimizations in lower order systems. The modeling of alkali-containing systems requires the introduction of associate species which greatly increases the number of possible degrees of freedom in a model and which can sometimes be constrained only using data on higher order systems.

The liquid and in some rare cases solid solutions were modeled from the point of view of the Modified Quasichemical Formalism. The solid solutions are modeled using the Compound Energy Formalism. If it was possible, the model construction was accompanied by detailed explanations of the structural data. Possible distortions and lattice transformations accompanying composition and temperature changes and their influence on the choice of a model were discussed.

Custom software programs were developed during the work to facilitate the optimization procedure. *CpFit* program allows one to assess miscellaneous heat capacity and heat content data to produce reliable and uniform representations of the heat capacity. A semi-automated optimization procedure based on *MATLAB* scripts was developed to model systems requiring strongly correlated parameters.

Since many systems have strong glass-forming tendencies, the nature of glasses and their difference from liquids (from the thermodynamic point of view) was discussed. It was made possible to integrate a vast body of data on glasses into the optimizations using physically consistent recalculations of the glass properties into those of liquids. Restrictions and limitations of the existing software and the databases related to calculation of properties of glasses and liquids are discussed.

The developed optimizations are fully consistent with the existing oxide database of *FactSage* software and can be used for prediction of phase diagrams and thermodynamic properties in unexplored regions of the Na_2O-K_2O-Al_2O_3-CaO-MgO-B_2O_3-SiO_2 system.

TABLE OF CONTENTS

ACKNOWLEDGEMENTS III

RÉSUMÉ IV

ABSTRACT VI

TABLE OF CONTENTS VIII

LIST OF TABLES XVIII

LIST OF FIGURES XXIII

LIST OF SYMBOLS AND ABBREVIATIONS L

LIST OF APPENDICES LVI

CHAPTER 1 INTRODUCTION 1

1.1 Background 1

1.2 Statement of the problem 2

1.3 Scope of the work 3

1.4 Methodology 4

1.5 Organization of the thesis 5

1.6 Names of compounds and solutions 6

CHAPTER 2 CALCULATION PROCEDURES 9

2.1 Thermodynamic software 9

2.2 Processing of heat capacity and heat content data 10

2.3 Modeling of solid solutions with end-members undergoing phase transitions 16

2.4 Semi-automated optimization technique 19

2.5 Glasses and their thermodynamic properties 23

2.5.1 Glass transition phenomena 23

2.5.2 Recalculation of glass calorimetry data 26

CHAPTER 3 MODELING APPROACH TO OXIDE SYSTEMS 28

3.1 Modeling of stochiometric compounds 29

3.2 Modeling of solutions with small deviations from ideality 30

3.3 Modeling of solutions with short-range ordering 31

3.4 The Compound Energy Formalism 37

CHAPTER 4 SOLID SOLUTIONS 39

4.1 Mullite 39

4.2 Nepheline (Kalsilite) 42

4.3 Carnegieite 46

4.4 High and low-*T* (Na,K)AlO_2 47

4.5 Feldspar 48

4.6 Melilite 54

4.7 Clinopyroxene 56

4.8 Combeite 58

4.9 (2:1:3) 62

4.10 NCA2 63

4.11 C3A 64

4.12 Beta-, Beta”-alumina 65

4.13 Leucite 67

4.14 Mixed Orthosilicate 68

4.15 Pseudowollastonite and Ca-Orthosilicate 69

4.16 Milarite 69

4.17 Monoborate, Diborate and Triborate 70

CHAPTER 5 THERMODYNAMICS OF MULLITE AND MODIFICATIONS OF NON-ALKALI SYSTEMS 71

5.1 Mullite discrepancy 71

5.2 Correction of the Al_2O_3-SiO_2 system 74

5.3 Optimization results 75

5.4 Correction of the Al_2O_3-B_2O_3-SiO_2 system 75

5.5 Optimization results 76

CHAPTER 6 OPTIMIZATION OF THE Na_2O-SiO_2 SYSTEM 77

6.1 Thermodynamic modeling 77

6.2 Phase diagram 82

6.3 Calorimetry data 85

6.4 Activity data 92

6.5 Heat capacity and heat content data 99

6.6 Optimization results 105

CHAPTER 7 OPTIMIZATION OF THE Na_2O-Al_2O_3 SYSTEM 107

7.1 Phase diagram 107

7.2 Calorimetry data 109

7.3 Activity data 109

7.4 Heat capacity and heat content data 112

7.5 Optimization results 114

CHAPTER 8 OPTIMIZATION OF THE Na_2O-Al_2O_3-SiO_2 SYSTEM 116

8.1 Phase diagram 116

8.2 Calorimetry data 123

8.3 Activity data 127

8.4 Heat capacity and heat content data 135

8.5 Optimization results 141

CHAPTER 9 OPTIMIZATION OF THE K_2O-SiO_2 SYSTEM 143

9.1 Phase diagram 143

9.2 Calorimetry data 146

9.3 Activity data 151

9.4 Heat capacity and heat content data 155

9.5 Optimization results 156

CHAPTER 10 OPTIMIZATION OF THE K_2O-Al_2O_3 SYSTEM 159

10.1 Phase diagram 159

10.2 Calorimetry data 160

10.3 Activity data 161

10.4 Heat capacities and heat content data 163

10.5 Optimization results 165

CHAPTER 11 OPTIMIZATION OF THE K_2O-Al_2O_3-SiO_2 SYSTEM 166

11.1 Phase diagram 166

11.2 Calorimetry data 172

11.3 Activity data 175

11.4 Heat capacity and heat content data 177

11.5 Optimization results 181

CHAPTER 12 OPTIMIZATION OF THE K_2O-Na_2O-SiO_2 SYSTEM 183

12.1 Phase diagram 183

12.2 Calorimetry data 186

12.3 Activity data 187

12.4 Optimization results 193

CHAPTER 13 OPTIMIZATION OF THE K_2O-Na_2O-Al_2O_3-SiO_2 SYSTEM 194

13.1 Phase diagram 194

13.2 Calorimetry data 202

13.3 Activity data 207

13.4 Optimization results 213

CHAPTER 14 OPTIMIZATION OF THE CaO-Na_2O-SiO_2 SYSTEM 215

14.1 Phase diagram 215

14.2 Activity data 222

14.3 Heat capacity and heat content data 226

14.4 Optimization results 227

CHAPTER 15 OPTIMIZATION OF THE Al_2O_3-CaO-Na_2O SYSTEM 230

15.1 Phase diagram 230

15.2 Optimization results 235

CHAPTER 16 OPTIMIZATION OF THE Al_2O_3-CaO-Na_2O-SiO_2 SYSTEM 237

16.1 The Anorthite-Gehlenite-Nepheline subsystem ($CaAl_2Si_2O_8$-$Ca_2Al_2SiO_7$-$NaAlSiO_4$) 237

16.2 The Nepheline-CA subsystem ($NaAlSiO_4$-$CaAl_2O_4$) 240

16.3 The Albite-Nepheline-Wollastonite subsystem ($NaAlSi_3O_8$-$NaAlSiO_4$-$CaSiO_3$) 242

16.4 The Albite-Anorthite subsystem ($NaAlSi_3O_8$-$CaAl_2SiO_8$) 244

16.4.1 Phase diagram 244

16.4.2 Calorimetry data 245

16.4.3 Activity data 249

16.5 The Anorthite-Nepheline-Wollastonite subsystem ($CaAl_2Si_2O_8$-$NaAlSiO_4$-$CaSiO_3$) 251

16.6 The Gehlenite-Nepheline-Wollastonite subsystem ($Ca_2Al_2SiO_7$-$NaAlSiO_4$-$CaSiO_3$) 251

16.7 The Nepheline-Wollastonite-Sodium Metasilicate subsystem ($NaAlSiO_4$-$CaSiO_3$-Na_2SiO_3) 254

16.8 The Ca-Tschermak-Jadeite $CaAl_2SiO_6$-$NaAlSi_2O_6$ system 255

16.9 SiO_2-deficient part: Ca_2SiO_4-CaO-$NaAlO_2$-Al_2O_3 256

16.10 Other parts of the quaternary system 261

16.10.1 Activity data 261

16.11 Optimization results 262

CHAPTER 17 OPTIMIZATION OF THE CaO-K_2O-SiO_2 SYSTEM 264

17.1 Phase diagram 264

17.2 Calorimetry data 272

17.3 Heat capacity data 273

17.4 Optimization results 274

CHAPTER 18 OPTIMIZATION OF THE K_2O-CaO-Al_2O_3 SYSTEM 275

18.1 Phase diagram 275

18.2 Optimization results 278

CHAPTER 19 OPTIMIZATION OF THE K_2O-CaO-Al_2O_3-SiO_2 SYSTEM 280

19.1 The KC23S12-CaO-C5A3 subsystem 280

19.2 The Gehlenite-K-melilite subsystem ($Ca_2Al_2SiO_7$-$KCaAlSi_2O_7$) 280

19.3 The Anorthite-Leucite-Silica subsystem ($CaAl_2Si_2O_8$-$KAlSi_2O_6$-SiO_2) 281

19.4 Calorimetry data 283

19.5 Activity data 286

19.6 Optimization results 288

CHAPTER 20 OPTIMIZATION OF THE K_2O-Na_2O-CaO-Al_2O_3-SiO_2 SYSTEM 289

20.1 Phase diagram 289

20.2 Calorimetry data 292

20.3 Optimization results 293

CHAPTER 21 OPTIMIZATION OF THE Na_2O-MgO-SiO_2 SYSTEM 294

21.1 Phase diagram 294

21.2 Activity data 302

21.3 Optimization results 305

CHAPTER 22 OPTIMIZATION OF THE CaO-MgO-Na_2O-SiO_2 SYSTEM 306

22.1 Phase diagram 306

22.2 Activity data 310

22.3 Optimization results 313

CHAPTER 23 OPTIMIZATION OF THE MgO-Al_2O_3-Na_2O SYSTEM 314

23.1 Phase diagram 314

23.2 Optimization results 316

CHAPTER 24 OPTIMIZATION OF THE MgO-Na_2O-Al_2O_3-SiO_2 SYSTEM 317

24.1 The Forsterite-Nepheline-Silica subsystem (Mg_2SiO_4-$NaAlSiO_4$-SiO_2) 317

24.2 The Spinel-Nepheline-Silica subsystem ($MgAl_2O_4$-$NaAlSiO_4$-SiO_2) 321

24.3 The Forsterite-Albite-Cordierite subsystem (Mg_2SiO_4-$NaAlSi_3O_8$-$Mg_2Al_4Si_5O_{18}$) . 322

24.4 The Enstatite-Albite-Cordierite subsystem ($MgSiO_3$-$NaAlSi_3O_8$-$Mg_2Al_4Si_5O_{18}$) 324

24.5 The Silica-Albite-Cordierite subsystem (SiO_2-$NaAlSi_3O_8$-$Mg_2Al_4Si_5O_{18}$) 326

24.6 Other sections 328

24.7 Optimization results 328

CHAPTER 25 OPTIMIZATION OF THE MgO-CaO-Na_2O-Al_2O_3-SiO_2 SYSTEM 330

25.1 The Albite-Anorthite-Diopside subsystem ($NaAlSi_3O_8$-$CaAl_2Si_2O_8$-$CaMgSi_2O_6$) .. 330

25.2 The Albite-Anorthite-Forsterite subsystem ($NaAlSi_3O_8$-$CaAl_2Si_2O_8$-Mg_2SiO_4)..... 333

25.3 The Albite-Anorthite-Akermanite subsystem ($NaAlSi_3O_8$-$CaAl_2Si_2O_8$-$Ca_2MgSi_2O_7$)... 334

25.4 The Akermanite-Nepheline-Wollastonite subsystem ($Ca_2MgSi_2O_7$-$NaAlSiO_4$-$CaSiO_3$) 335

25.5 The Na-Melilite-Gehlenite-Akermanite subsystem ($NaCaAlSi_2O_7$-$Ca_2Al_2SiO_7$-$Ca_2MgSi_2O_7$) 339

25.6 The Akermanite-Nepheline-Diopside subsystem ($Ca_2MgSi_2O_7$-$NaAlSiO_4$-$CaMgSi_2O_6$) 341

25.7 The Diopside-Nepheline-Wollastonite subsystem ($CaMgSi_2O_6$-$NaAlSiO_4$-$CaSiO_3$)344

25.8 The Forsterite-Nepheline-Diopside subsystem (Mg_2SiO_4-$NaAlSiO_4$-$CaMgSi_2O_6$).. 345

25.9 The Anorthite-Nepheline-Diopside subsystem ($CaAl_2Si_2O_8$-$NaAlSiO_4$-$CaMgSi_2O_6$) 346

25.10 The Nepheline-Diopside-Silica subsystem ($NaAlSiO_4$-$CaMgSi_2O_6$-SiO_2) 348

25.11 The Akermanite-Albite-Diopside subsystem ($Ca_2MgSi_2O_7$-$NaAlSi_3O_8$-$CaMgSi_2O_6$).... 352

25.12 The Forsterite-Albite-Diopside subsystem (Mg_2SiO_4-$NaAlSi_3O_8$-$CaMgSi_2O_6$)..... 352

25.13 The Enstatite-Albite-Diopside subsystem ($MgSiO_3$-$NaAlSi_3O_8$-$CaMgSi_2O_6$) 353

25.14 The Wollastonite-Albite-Akermanite subsystem ($CaSiO_3$-$NaAlSi_3O_8$-$Ca_2MgSi_2O_7$) 357

25.15 The Nepheline-Albite-Akermanite subsystem ($NaAlSiO_4$-$NaAlSi_3O_8$-$Ca_2MgSi_2O_7$) 358

25.16 Other sections 359

25.17 Optimization results 359

CHAPTER 26 OPTIMIZATION OF THE K_2O-MgO-SiO_2 SYSTEM 361

26.1 Phase diagram 361

26.2 Activity data 369

26.3 Optimization results 371

CHAPTER 27 MODELING APPROACH TO BORON-CONTAINING SYSTEMS 373

27.1 Structure of boron-containing melts 373

27.2 Short-range ordering of boron-containing melts 376

27.3 Metastable miscibility gap anomaly in alkali oxide-boron oxide systems 377

27.4 Ternary miscibility gaps in M_2O-B_2O_3-SiO_2 systems 379

27.5 Liquid phase model 380

CHAPTER 28 OPTIMIZATION OF THE Na_2O-B_2O_3 SYSTEM 382

28.1 Phase diagram 382

28.2 Calorimetry data 385

28.3 Activity data 389

28.4 Species distribution data 392

28.5 Heat capacity and heat content data 394

28.6 Optimization results 396

CHAPTER 29 OPTIMIZATION OF THE Na_2O-B_2O_3-SiO_2 SYSTEM 399

29.1 Phase diagram 399

29.2 Miscibility gap 403

29.3 Calorimetry data 406

29.4 Activity data 411

29.5 Optimization results 415

CHAPTER 30 OPTIMIZATION OF THE K_2O-B_2O_3 SYSTEM 417

30.1 Phase diagram 417

30.2 Calorimetry data 420

30.3 Activity data 424

30.4 Heat capacity and heat content data 426

30.5 Optimization results 427

CHAPTER 31 OPTIMIZATION OF THE K_2O-B_2O_3-SiO_2 SYSTEM 429

31.1 Phase diagram 429

31.2 Miscibility gap 431

31.3 Calorimetry data 433

31.4 Optimization results 434

CHAPTER 32 OPTIMIZATION OF THE K_2O-Na_2O-B_2O_3 SYSTEM 436

32.1 Phase diagram 436

32.2 Calorimetry data 440

32.3 Optimization results 441

CHAPTER 33 CONCLUSION AND RECOMMENDATIONS 443

REFERENCES 446

APPENDICES 489

LIST OF TABLES

Table 1.1 Names and abbreviations of compounds in this work. Non-stoichiometric formulas are shown within quotation marks. 7

Table 1.2 Synonyms and aliases of solid solutions used in this work..... 8

Table 6.1 Regression coefficients of the calorimetric solution data for Na_2O(cr) and SiO_2(qz)... 87

Table 6.2 The enthalpies of fusion of compounds in the Na_2O-SiO_2 system. 92

Table 8.1 The enthalpies of fusion of compounds in the Na_2O-Al_2O_3-SiO_2 system..... 127

Table 9.1 Heats of solution of crystalline end-members in the K_2O-SiO_2 system in common solvents. 147

Table 9.2 Enthalpies of fusion of stoichiometric compounds in the K_2O-SiO_2 system. 151

Table 12.1 Invariant equilibria in the K_2O-Na_2O-SiO_2 system. The calculated values are shown in bold. 186

Table 14.1 Invariant points in the CaO-Na_2O-SiO_2 system. The calculated values are shown in bold. 221

Table 17.1 Invariant phase equilibria in the K_2O-CaO-SiO_2 system. The calculated values are shown in bold. 272

Table 21.1 Invariant phase equilibria in the Na_2O-MgO-SiO_2 system. The calculated values are shown in bold. 300

Table 24.1 Piercing/invariant points in the nepheline-forsterite-silica plane ($NaAlSiO_4$-Mg_2SiO_4-SiO_2) of the Na_2O-Al_2O_3-MgO-SiO_2 system. The calculated values are shown in bold. 320

Table 24.2 Piercing/invariant points in the spinel-nepheline-silica plane ($MgAl_2O_4$-$NaAlSiO_4$-SiO_2) of the Na_2O-Al_2O_3-MgO-SiO_2 system. The calculated values are shown in bold. 322

Table 24.3 Piercing/invariant points in the forsterite-albite-cordierite plane (Mg_2SiO_4-$NaAlSi_3O_8$-$Mg_2Al_4Si_5O_{18}$) of the Na_2O-Al_2O_3-MgO-SiO_2 system. The calculated values are shown in bold. 324

Table 24.4 Piercing/invariant points in the enstatite-albite-cordierite plane ($MgSiO_3$-$NaAlSi_3O_8$-$Mg_2Al_4Si_5O_{18}$) of the Na_2O-Al_2O_3-MgO-SiO_2 system. The calculated values are shown in bold. 326

Table 24.5 Piercing/invariant points in the silica-albite-cordierite plane (SiO_2-$NaAlSi_3O_8$-$Mg_2Al_4Si_5O_{18}$) of the Na_2O-Al_2O_3-MgO-SiO_2 system. The calculated values are shown in bold. 327

Table 25.1 Piercing points in the Mg_2SiO_4-$NaAlSi_3O_8$-$CaAl_2Si_2O_8$ plane (forsterite-albite-anorthite) of the CaO-MgO-Na_2O-Al_2O_3-SiO_2 system. The calculated values are shown in bold. 334

Table 25.2 Piercing points in the $Ca_2MgSi_2O_7$-$NaAlSi_3O_8$-$CaAl_2Si_2O_8$ plane (akermanite-albite-anorthite) of the CaO-MgO-Na_2O-Al_2O_3-SiO_2 system. The calculated values are shown in bold. 335

Table 25.3 Piercing points in the $Ca_2MgSi_2O_7$-$NaAlSiO_4$-$CaSiO_3$ plane (akermanite-nepheline-wollastonite) of the CaO-MgO-Na_2O-Al_2O_3-SiO_2 system. The calculated values are shown in bold. 339

Table 25.4 Piercing points in the $Ca_2MgSi_2O_7$-$NaAlSiO_4$-$CaMgSi_2O_6$ plane (akermanite-nepheline-diopside) of the CaO-MgO-Na_2O-Al_2O_3-SiO_2 system. The calculated values are shown in bold. 344

Table 25.5 Piercing points in the Mg_2SiO_4-$NaAlSiO_4$-$CaMgSi_2O_6$ plane (forsterite-nepheline-diopside) of the CaO-MgO-Na_2O-Al_2O_3-SiO_2 system. The calculated values are shown in bold. 346

Table 25.6 Piercing points in the $CaMgSi_2O_6$-$NaAlSiO_4$-$CaAl_2Si_2O_8$ plane (diopside-nepheline-anorthite) of the CaO-MgO-Na_2O-Al_2O_3-SiO_2 system. The calculated values are shown in bold. 347

Table 25.7 Piercing points in the SiO_2-$NaAlSiO_4$-$CaMgSi_2O_6$ plane (silica-nepheline-diopside) of the CaO-MgO-Na_2O-Al_2O_3-SiO_2 system. The calculated values are shown in bold. 349

Table 25.8 Piercing points in the $MgSiO_3$-$NaAlSi_3O_8$-$CaMgSi_2O_6$ plane (enstatite-albite-diopside) of the CaO-MgO-Na_2O-Al_2O_3-SiO_2 system. The calculated values are shown in bold..... 356

Table 25.9 Piercing points in the $Ca_2MgSi_2O_7$-$NaAlSi_3O_8$-$CaSiO_3$ plane (akermanite-albite-wollastonite) of the CaO-MgO-Na_2O-Al_2O_3-SiO_2 system. The calculated values are shown in bold. 357

Table 25.10 Piercing points in the $Ca_2MgSi_2O_7$-$NaAlSiO_4$-$NaAlSi_3O_8$ plane (akermanite-nepheline-albite) of the CaO-MgO-Na_2O-Al_2O_3-SiO_2 system. The calculated values are shown in bold. 358

Table 26.1 Invariant equilibria in the K_2O-MgO-SiO_2 system. The calculated values are shown in bold. 367

Table A.1 Model parameters of Mullite solid solution in the Al_2O_3-SiO_2 system. 489

Table A.2 Model parameters of Mullite solid solution in the Al_2O_3-B_2O_3-SiO_2 system. 489

Table A.3 Optimized properties of the compound phases in the Na_2O-SiO_2 system. 490

Table A.4 Gibbs energy parameters of the liquid phase in the Na_2O-SiO_2 system. 490

Table A.5 Optimized properties of the compound phases in the Na_2O-Al_2O_3 system 491

Table A.6 Gibbs energy parameters of the solution phases in the Na_2O-Al_2O_3 system..... 492

Table A.7 Optimized properties of the compound phases in the Na_2O-Al_2O_3-SiO_2 system..... 493

Table A.8 Gibbs energy parameters of the solution phases in the Na_2O-Al_2O_3-SiO_2 system..... 494

Table A.9 Optimized properties of the compound phases in the K_2O-SiO_2 system. 498

Table A.10 Gibbs energy parameters of the liquid phase in the K_2O-SiO_2 system. 498

Table A.11 Optimized properties of the compound phases in the K_2O-Al_2O_3 system. 499

Table A.12 Gibbs energy parameters of the liquid phase in the K_2O-Al_2O_3 system. 499

Table A.13 Optimized properties of the compound phases in the K_2O-Al_2O_3-SiO_2 system..... 500

Table A.14 Gibbs energy parameters of the solution phases in the K_2O-Al_2O_3-SiO_2 system..... 501

Table A.15 Gibbs energy parameters of the solution phases in the K_2O-Na_2O-Al_2O_3-SiO_2 system. 503

Table A.16 Optimized properties of the compound phases in the CaO-Na_2O-SiO_2 system. 505

Table A.17 Gibbs energy parameters of the solution phases in the $CaO-Na_2O-SiO_2$ system. 506

Table A.18 Optimized properties of the compound phases in the $CaO-Na_2O-Al_2O_3$ system. 508

Table A.19 Gibbs energy parameters of the solution phases in the $CaO-Na_2O-Al_2O_3$ system. .. 508

Table A.20 Optimized parameters of the solution phases in the $Na_2O-CaO-Al_2O_3-SiO_2$ system. 509

Table A.21 Optimized properties of the compound phases in the $CaO-K_2O-SiO_2$ system. 512

Table A.22 Gibbs energy parameters of the solution phases in the $CaO-K_2O-SiO_2$ system. 513

Table A.23 Optimized properties of the compound phases in the $CaO-K_2O-Al_2O_3$ system. 515

Table A.24 Gibbs energy parameters of the solution phases in the $CaO-K_2O-Al_2O_3$ system. 515

Table A.25 Gibbs energy parameters of the solution phases in the $Al_2O_3-CaO-K_2O-SiO_2$ system. 516

Table A.26 Optimized properties of the compound phases in the $MgO-Na_2O-SiO_2$ system. 516

Table A.27 Gibbs energy parameters of the liquid phase in the $MgO-Na_2O-SiO_2$ system. 517

Table A.28 Thermodynamic properties of the compound phases in the $MgO-Al_2O_3-Na_2O$ system. 518

Table A.29 Gibbs energy parameters of the solution phases in the $MgO-Al_2O_3-Na_2O$ system .. 518

Table A.30 Gibbs energy parameters of the liquid phase in the $Na_2O-Al_2O_3-MgO-SiO_2$ system. 519

Table A.31 Gibbs energy parameters of the solution phases in the $Al_2O_3-CaO-MgO-Na_2O-SiO_2$ system. 519

Table A.32 Optimized properties of the compound phases in the $K_2O-MgO-SiO_2$ system. 520

Table A.33 Gibbs energy parameters of the solution phases in the $K_2O-MgO-SiO_2$ system. 520

Table A.34 Optimized properties of the compound phases in the $Na_2O-B_2O_3$ system. 522

Table A.35 Gibbs energy parameters of the liquid phase in the $Na_2O-B_2O_3$ system. 523

Table A.36 Optimized properties of the compound phases in the $Na_2O-B_2O_3-SiO_2$ system. 524

Table A.37 Gibbs energy parameters of the liquid phase in the Na_2O-B_2O_3-SiO_2 system. 524

Table A.38 Optimized properties of the compound phases in the K_2O-B_2O_3 system..... 525

Table A.39 Gibbs energy parameters of the liquid phase in the K_2O-B_2O_3 system..... 526

Table A.40 Optimized properties of the compound phases in the K_2O-B_2O_3-SiO_2 system. 527

Table A.41 Gibbs energy parameters of the liquid phase in the K_2O-B_2O_3-SiO_2 system. 527

Table A.42 Gibbs energy parameters of the solution phases in the K_2O-Na_2O-B_2O_3 system..... 528

LIST OF FIGURES

Figure 2.1 Fitting (***a***) and Splitting (***b***) interfaces of *CpFit* program. 14

Figure 2.2 The Na_2O-Al_2O_3 phase diagram (given for illustrative purposes). 15

Figure 2.3 The heat capacities of Na_2O and Al_2O_3 as in the current *FToxid* database together with the extrapolated values (*CpFit* program). The $NaAlO_2$ heat capacity is calculated using Neumann's rule from the *FToxid* (colored lines) and extrapolated heat capacities (black lines) of Na_2O and Al_2O_3, correspondingly. 16

Figure 2.4 The specific enthalpy (***a***) and the entropy (***b***) of low-$NaAlSi_3O_8$, high-$NaAlSi_3O_8$ and the generic end-member of Feldspar solution (the values correspond to the $NaAlSi_3O_8$ formula unit). 18

Figure 2.5 The dataflow for automation of the optimization procedure. 20

Figure 2.6 The heat capacity of crystal and liquid/glass B_2O_3. The image is taken from Decterov et al. [15]. 23

Figure 2.7 The heat capacities of liquids of Na_2O, SiO_2 and $(Na_2O)_{0.5}(SiO_2)_{0.5}$ compositions. The dotted vertical lines indicate the glass transition and the liquidus temperature at $(Na_2O)_{0.5}(SiO_2)_{0.5}$ composition. The solid lines show the heat capacities in the oxide database. The dashed lines are physically consistent extrapolations of the heat capacity of the liquids. 25

Figure 3.1 Phase diagram as a projection of the Gibbs energy of the system [25]. 28

Figure 3.2 The molar enthalpy and the entropy of mixing for a system A-B calculated at 1000°C with $Z_A = Z_B = 2$ from the quasichemical model for short-range ordering with Δg_{AB} = constant = 0, -21, -42, and -84 kJ. The image is taken from Pelton et al. [27]. 33

Figure 3.3 Geometrical extrapolation models: Kohler (***a***), Toop (***b***), Muggianu (***c***). 35

Figure 4.1 The sillimanite structure. The Al polyhedra are shown in red and green, the Si tetrahedra are blue. 40

Figure 4.2 The mullite structure (crystallographic data are taken from Angel and Prewitt [31]). Only T sites are shown in (***a***) while (***b***) features both T and T* sites. 41

Figure 4.3 $Al_4B_2O_9$ structure from Fischer et al. [32]. The view dimensions: $0.2 < a < 0.8$, $0.2 < b < 1.4$, $0 < c < 0.55$ 42

Figure 4.4 Slightly different view angles along the *c* axis of unit cells of the crystal structures of nepheline ($Na_{0.75}K_{0.25}AlSiO_4$ composition) (***a***, ***b***, ***c***) [34] and kalsilite (***d***, ***e***, ***f***) [35]. The structure of their common parent, tridymite, is also shown (***g***, ***h***, ***i***) [36]. The structures were shifted and multiplied correspondingly to better represent the topological similarity. Violet spheres are K atoms, Na is shown in orange. AlO_4 tetrahedra are shown in blue, SiO_4 in grey. 43

Figure 4.5 Compositions of natural nephelines in the $NaAlSiO_4$-$KAlSiO_4$-SiO_2 plane, projected from the $Ca_{0.5}AlSiO_4$ corner. The image is taken from Dollase and Thomas [38]. 44

Figure 4.6 Crystal structure of carnegieite at different view angles along the *c* axis (***a***, ***b***, ***c***). Na is shown in orange, AlO_4 tetrahedra are blue, SiO_4 are grey. 46

Figure 4.7 The monoalbite (***a***, ***b***, ***c***) and low albite (***d***, ***e***, ***f***) crystal structures [58]. The monoalbite structure: T1 tetrahedra are shown in green, T2 are shown in blue [59]. The low albite structure: T1 tetrahedra are shown in light green, T2 in dark green, T3 in light blue, T4 in dark blue. Alkali atoms are shown in orange. Two alkali pairs on the left and on the right in (***a***) and (***c***) are shared between two adjacent cells, the corresponding atoms in (***d***) and (***f***) completely belong to one cell. 49

Figure 4.8 $C\bar{1}$ anorthite crystal structure [58] along *a*, *b* and *c* axes (***a***, ***b***, ***c*** correspondingly). T1 tetrahedra are shown in light green, T2 in dark green, T3 in light blue, T4 in dark blue. Violet and light blue spheres indicate Na/Ca sites with ½ occupancy. 50

Figure 4.9 A metastable phase diagram obtained by a rapid cooling in the $NaAlSi_3O_8$-$KAlSi_3O_8$ system. Only the displacive transformation between the monoclinic high sanidine and the triclinic anorthoclase is observed (supposedly second order). No Al/Si ordering occurs (both solid phases are disordered high modifications). The image is taken from Smith [67]. 51

Figure 4.10 A metastable phase diagram obtained with an average rate of cooling in the $NaAlSi_3O_8$-$KAlSi_3O_8$ system. The Al/Si ordering occurs only partially in the K-end (low sanidine forms), anorthoclase does not yet transform to low albite. The image is taken from Smith [67]. 52

Figure 4.11 The stable phase diagram obtained by a slow cooling in the $NaAlSi_3O_8$-$KAlSi_3O_8$ system. Formation of the low ordered phases is observed (low albite, orthoclase, microcline). The image is taken from Smith [67]. 52

Figure 4.12 The phase diagram of plagioclases $NaAlSi_3O_8$-$CaAl_2Si_2O_8$ [68]; s.s. stands for solid solution. 53

Figure 4.13 The gehlenite structure, a view along the *c* axis slightly tilted to the left with (***a***) and without (***b***) coordination polyhedra of cations. The structural data are taken from Smith [70]. ... 54

Figure 4.14 The clinopyroxene structure, a view along the *a* axis with (***a***) and without (***b***) coordination polyhedra of cations. The structural data are taken from Okamura et al. [76]. 57

Figure 4.15 The metasilicate section in the Na_2O-CaO-SiO_2 system (schematic). The phase diagram features α-$CaSiO_3$, combeite and (2:1:3) solid solutions. The image is taken from Moir and Glaser [87]. 59

Figure 4.16 The metasilicate section in the Na_2O-SrO-SiO_2 system. The phase diagram features α-$SrSiO_3$, combeite and (2:1:3) solid solutions. The image is taken from Moir and Glaser [88]. 60

Figure 4.17 The high-combeite structure, viewed along the *a* axis. The image features six-membered silicon tetrahedra rings and four types of cations: M1 (orange), M2 (light grey), M3 (light blue) and M4 (navy). Based on the data by Ohsato et al. [90]. 61

Figure 4.18 Comparison of the leucite (***a***) and jadeite structures (***b***). The crystallographic data are taken from Mazzi et al. [110] and Prewitt and Burnham [84], correspondingly. 68

Figure 5.1 Primary phase fields in the Na_2O-Al_2O_3-SiO_2 (***a***), K_2O-Al_2O_3-SiO_2 (***b***), CaO-Al_2O_3-SiO_2 (***c***), MgO-Al_2O_3-SiO_2 (***d***) and PbO-Al_2O_3-SiO_2 (***e***) systems. Primary phase data [55] (***a***), [119] (***b***), [120] (***c***), [121] (***d***), [122] (***e***) and calculated univariant lines. 72

Figure 5.2 Primary phase fields in the CaO-Al_2O_3-SiO_2 (***a***) and the MgO-Al_2O_3-SiO_2 (***b***) systems with the current (black lines) and a modified optimization of the Al_2O_3-SiO_2 binary system (blue lines). Primary phase data [120] (***a***), [121] (***b***) and calculated univariant lines. 73

Figure 5.3 Phase diagram of the Al_2O_3-SiO_2 system. Experimental points [119, 124-138] and calculated lines: the optimization from Eriksson and Pelton [123] in red, the current optimization in black. 75

Figure 5.4 Liquidus projection in the SiO_2-B_2O_3-Al_2O_3 system, isotherms in the range of 1200-1450°C (***a***) and of 1500-1750°C (***b***). Experimental points [139, 140], the original optimization from Swamy et al. [16] in gray and the optimization with the new Mullite solution in rainbow colors (isotherms) and black (univariant lines). 76

Figure 6.1 Optimized phase diagrams from the works of Wu et al. [17] (***a***) and Lambotte and Chartrand [141] (***b***). 77

Figure 6.2 The optimized phase diagram of the Li_2O-SiO_2 system from Konar et al. [142]. 78

Figure 6.3 Silica liquidi for alkali oxide and alkali-earth oxide-silica binary systems alongside with the theoretical prediction of the liquidus slope in case of one- and two-particle second component (see the text for the details). Experimental points [143-152] and calculated lines. 79

Figure 6.4 The caging effect upon addition of an alkali oxide to a silica network. 81

Figure 6.5 Distribution of the ordinary and dimer Na_2O end-members with the silica molar fraction at two different temperatures. 82

Figure 6.6 Phase diagram of the Na_2O-SiO_2 system. Experimental points [145, 146, 153, 154, 159-161, 163, 164, 166-170] and calculated lines. 84

Figure 6.7 Metastable miscibility gap of the Na_2O-SiO_2 system. Experimental points [171-179] and calculated lines. 85

Figure 6.8 The enthalpy of solution of quartz in 20 wt% HF vs temperature (***a***) [158, 181-183, 187]; the enthalpy of solution of quartz at 298K vs HF concentration (***b***) [180, 185, 196]; the enthalpy of solution of Na_2O(cr) at 299.5K vs HF concentration (***c***) [180, 183]; the enthalpy of solution of quartz in 2PbO-B_2O_3 vs temperature (***d***) [190-194]. Experimental points and regression lines. 88

Figure 6.9 The enthalpy of mixing of liquid in the Na_2O-SiO_2 system. Experimental points [158, 183-185, 188, 189, 197-204] and calculated lines. 89

Figure 6.10 The partial enthalpy of SiO_2 in Na_2O-SiO_2 melts; the reference state is the pure liquid SiO_2. Experimental points [205] and calculated lines. 90

Figure 6.11 The enthalpies of formation of solid compounds from oxides per mole of components. Experimental points [158, 180, 183-185, 188, 189, 202, 203, 206, 207] and calculated lines..... 91

Figure 6.12 Na_2O activity over solid mixtures of Na_2O-SiO_2 compounds. The reference state of Na_2O is β-Na_2O ($Na_2O(s_2)$). Experimental points [211, 215] and calculated lines. 93

Figure 6.13 The concentration dependence of Na_2O activity in the Na_2O-SiO_2 system. The reference state is the pure liquid Na_2O (properties taken from *FactSage*). Experimental points [210, 213-225] and calculated lines..... 94

Figure 6.14 Na_2O activity in glasses at low temperatures. The reference state is the pure liquid Na_2O. Experimental data points [226] and calculated lines. 95

Figure 6.15 Temperature dependence of Na_2O activity in the Na_2O-SiO_2 system at low temperatures, $X(Na_2O) = 0.105$-0.255. The reference state is the pure liquid Na_2O. Experimental points [210, 211, 216, 219, 225, 227-231] and calculated lines. 96

Figure 6.16 Temperature dependence of Na_2O activity in the Na_2O-SiO_2 system, $X(Na_2O) = 0.275$-0.390. The reference state is the pure liquid Na_2O. Experimental data points [210, 211, 216, 219, 225, 227-230, 232, 233] and calculated lines. 97

Figure 6.17 Temperature dependence of Na_2O activity in the Na_2O-SiO_2 system, $X(Na_2O) = 0.395$-0.650. The reference state is the pure liquid Na_2O. Experimental data points [210-212, 216, 219, 225, 227-230, 232] and calculated lines. 98

Figure 6.18 The low temperature heat capacities of crystalline solids in the Na_2O-SiO_2 system. Experimental data points [234, 235] and calculated lines. 99

Figure 6.19 The heat content of liquid and crystalline Na_2SiO_3. Experimental data points [209, 237] and calculated lines..... 100

Figure 6.20 The heat content of the vitreous and liquid $Na_2Si_2O_5$. The heat content was calculated using *FactSage* heat capacities of the end-members and the real heat capacities extrapolated below

the corresponding melting points. Experimental data points [203, 209, 236-238] and calculated lines. 101

Figure 6.21 The heat contents of liquids (***a***) and glasses (***b***). The reference temperature for liquids is 500°C and for glasses is 100°C. The heat content of liquids was calculated in *FactSage* (dashed lines) and predicted using constant heat capacities of Na_2O(liq) and SiO_2(liq) (solid lines). Experimental points [203, 236-238] and calculated lines. 104

Figure 6.22 The heat capacities of glasses and liquids vs composition. Glass heat capacities are shown as filled symbols, heat capacities of liquids as empty symbols. Experimental points [203, 209, 237, 241-245] and calculated lines. 104

Figure 7.1 Phase diagram of the Na_2O-Al_2O_3 system. Experimental points [55, 104, 246, 248-252] and calculated lines. 108

Figure 7.2 Na_2O activity in two-phase fields of the Na_2O-Al_2O_3 system. The reference state is β-Na_2O ($Na_2O(s_2)$). Experimental points [263-272, 275, 277, 278, 280-282] and calculated lines. 111

Figure 7.3 The heat capacity data for $NaAlO_2$. Experimental data points [283] and calculated lines. 112

Figure 7.4 The mean heat capacity of $NaAlO_2$. Experimental data points [249] and calculated lines. 113

Figure 7.5 The heat capacity of $NaAl_9O_{14}$ (β-Al_2O_3). Experimental data points [284, 285] and calculated lines. 114

Figure 8.1 Liquidus projection in the Na_2O-Al_2O_3-SiO_2 system in the temperature range of 750-1200°C. Experimental points [55] and calculated lines. 117

Figure 8.2 Liquidus projection in the Na_2O-Al_2O_3-SiO_2 system in the temperature range of 1250-1700°C. Experimental points [55] and calculated lines. 118

Figure 8.3 Phase diagram in the $NaAlO_2$-SiO_2 section of the Na_2O-Al_2O_3-SiO_2 system. Experimental data [104, 291] and calculated lines. 119

Figure 8.4 Phase diagrams in the sections through the Na_2O-Al_2O_3-SiO_2 system: $Na_2Si_2O_5$-$NaAlSi_3O_8$ (***a***), $NaAlSi_3O_8$-Al_2O_3 (***b***), $Na_2Si_2O_5$-$NaAlSiO_4$ (***c***), $Na_2Si_2O_5$-Al_2O_3 (***d***), Na_2SiO_3-$NaAlSiO_4$ (***e***), Na_2SiO_3-$NaAlO_2$ (***f***). Experimental points [49, 55, 292, 293] and calculated lines. 120

Figure 8.5 Isothermal sections in the Na_2O-Al_2O_3-SiO_2 system at different temperatures (***a***-***d***). Experimental points [288] and calculated lines. Colors in the markers correspond to the forming phases. If a marker has two colors, the corresponding two phases are present together..... 121

Figure 8.6 The enthalpy of mixing in the $NaAlO_2$-SiO_2 section. Experimental points [301, 302, 304] and calculated lines..... 124

Figure 8.7 The enthalpy of formation from oxides of compounds in the $NaAlO_2$-SiO_2 section. Experimental points [187, 295, 296, 305-312] and calculated lines. For clarity, the values of the enthalpy of formation per mol of XO_2 where also shown as horizontal lines. 125

Figure 8.8 The enthalpy of mixing of Nepheline solution in the $NaAlSiO_4$-Si_2O_4 section. Pure nepheline of $NaAlSiO_4$ composition and quartz were used as the end-members for calculation. Experimental points [313] and calculated lines. 126

Figure 8.9 Compositions for which Na_2O activity was measured in the Na_2O-Al_2O_3-SiO_2 system [164, 222, 228, 318, 319] and the sections drawn through them. 128

Figure 8.10 Na_2O activity in the Na_2O-Al_2O_3-SiO_2 system along the sections with a constant SiO_2 content and temperature. The reference state is the pure liquid Na_2O. Experimental points [222, 319], points, interpolated and extrapolated from the experimental data [164, 228] and calculated lines..... 129

Figure 8.11 Na_2O activity in the Na_2O-Al_2O_3-SiO_2 system along the section with $0.75SiO_2$ at 400°C. The reference state is the pure liquid Na_2O. Points interpolated from experimental data [318] and calculated lines. EMF reference compositions: ref1 is $Na_2O{\cdot}3SiO_2$, ref2 is $x(Na_2O){\cdot}6SiO_2$..... 130

Figure 8.12 Na_2O activity in the $(Na_2O)_{0.25}(SiO_2)_{0.75}$-$(Al_2O_3)_{0.50}(SiO_2)_{0.50}$ section of the Na_2O-Al_2O_3-SiO_2 system at 400°C. The reference state is the pure liquid Na_2O. Points interpolated from the experimental data [318] and calculated lines. EMF reference composition is $Na_2O{\cdot}3SiO_2$.. 131

Figure 8.13 Sample compositions from the work of Rys [164]. Thick black lines show possible composition shifts. 132

Figure 8.14 Na_2O activities in the Na_2O-Al_2O_3-SiO_2 system at the compositions indicated in Figure 8.13. The reference state is the pure liquid Na_2O. The activity data measured by mass spectrometry were taken from the original source [164] without further recalculations. The data marked with empty symbols were recalculated from the raw *P*(Na) data using *FactSage* properties of Na_2O. 133

Figure 8.15 Isothermal Na_2O activities along the Na_2O depletion directions for the samples from Rys [164]. The reference state is the pure liquid Na_2O. 134

Figure 8.16 The heat capacity of carnegieite. Experimental data [47] and calculated lines. 136

Figure 8.17 The heat capacity of nepheline. Experimental points [47, 48, 294, 320] and calculated lines. 136

Figure 8.18 The mean heat capacity of nepheline, carnegieite and non-crystalline $NaAlSiO_4$. Experimental points [47, 48, 314, 321] and calculated lines. 137

Figure 8.19 The heat capacity of crystalline and vitreous jadeite. Experimental points [26, 48, 322] and calculated lines. 138

Figure 8.20 The mean heat capacity of crystalline and vitreous jadeite. Experimental points [314] and calculated lines. 139

Figure 8.21 The heat capacity of low, high and vitreous albite. Experimental points [48, 323-328] and calculated lines. 140

Figure 8.22 The mean heat capacity of crystalline and vitreous albite. Experimental points [314, 329, 330] and calculated lines. 141

Figure 9.1 Phase diagram of the K_2O-SiO_2 system. Experimental points [147-149, 331, 334, 335, 337-339] and calculated lines. 145

Figure 9.2 Metastable miscibility gap in the K_2O-SiO_2 system. Experimental data [174, 340] and the calculated line. 146

Figure 9.3 The enthalpy of mixing of the liquid phase in the K_2O-SiO_2 system. Experimental points [158, 200, 305] and calculated lines. 148

Figure 9.4 The enthalpy of formation from oxides of crystalline solids in the K_2O-SiO_2 system. Experimental points [158, 305, 338] and the calculated line. 149

Figure 9.5 The partial enthalpy of mixing of SiO_2 in the K_2O-SiO_2 system. Experimental points [205, 343] and calculated lines. 150

Figure 9.6 Isothermal K_2O activities in the liquid phase of the K_2O-SiO_2 system. The reference state is the pure liquid K_2O. Experimental points [220, 226, 231, 232, 337, 346, 349, 350] (mass spectrometry, EMF and evaporation studies) and calculated lines. 153

Figure 9.7 K_2O activity in the liquid phase in the K_2O-SiO_2 system as a function of the temperature at constant compositions. The reference state is the pure liquid K_2O. Experimental points [220, 226, 231, 232, 345, 346, 350-352] and calculated lines. 155

Figure 9.8 The heat capacity of crystalline and vitreous K_2SiO_3 and $K_2Si_2O_5$ compounds. Experimental points [235, 353, 354] and calculated lines. 155

Figure 9.9 The mean heat capacity of crystals, glasses and liquids of mono-, di- and tetrasilicate compositions. Experimental points [203, 236, 329, 338] and calculated lines. 156

Figure 9.10 Distribution of the ordinary and dimer K_2O end-members with silica molar fraction at two different temperatures. 157

Figure 10.1 Phase diagram of the K_2O-Al_2O_3 system. Experimental points [46, 254, 360] and calculated lines. 160

Figure 10.2 K_2O activity in biphasic regions of the K_2O-Al_2O_3 system. The reference state is the pure solid K_2O. Experimental points [280, 350, 362, 363] and calculated lines. 162

Figure 10.3 The heat capacity of potassium aluminate $KAlO_2$. Experimental data points [365] and calculated lines. 164

Figure 10.4 The mean heat capacity of potassium aluminate $KAlO_2$. Experimental data points [365] and calculated lines. 165

Figure 11.1 The ordering scheme for $KAlSi_3O_8$. The columns of numbers show relative Al occupancy of four (Al, Si) sites in the structure. One of the intermediate potassium feldspars, studied in the source article, is also shown. The image is taken from Barth [381]..... 167

Figure 11.2 Liquidus projection in the K_2O-Al_2O_3-SiO_2 system; isotherms from 700° to 1000°C. Experimental points [119] and calculated lines. 168

Figure 11.3 Liquidus projection in the K_2O-Al_2O_3-SiO_2 system; isotherms from 1050° to 1350°C. Experimental points [119] and calculated lines. 168

Figure 11.4 Liquidus projection in the K_2O-Al_2O_3-SiO_2 system; isotherms from 1400° to 1700°C. Experimental points [119] and calculated lines. 169

Figure 11.5 Phase diagram in the $KAlO_2$-SiO_2 section of the K_2O-Al_2O_3-SiO_2 system. Experimental points [108, 119, 370, 371, 378] and calculated lines. Marker shapes correspond to the studies; colors correspond to phases. If a marker has two colors, the two corresponding phases are present. 170

Figure 11.6 Phase diagrams in sections through the K_2O-Al_2O_3-SiO_2 system. Experimental points [119] and calculated lines. 172

Figure 11.7 The enthalpy of mixing of the liquid phase in the $KAlO_2$-SiO_2 join of the K_2O-Al_2O_3-SiO_2 system. Experimental points [302] and the calculated line. 173

Figure 11.8 The partial enthalpy of Al_2O_3 in $(K_2O)_{0.25}(SiO_2)_{0.75}$ solvent at 1490°C. Experimental points [343] and the calculated line..... 174

Figure 11.9 The enthalpy of mixing of Nepheline solution in the $KAlSiO_4$-Si_2O_4 section. Pure kalsilite of $KAlSiO_4$ composition and quartz were used as the end-members for calculation. Experimental points [313] and calculated lines. 175

Figure 11.10 K_2O activities of fixed compositions versus temperature; the compositions are indicated in the compositional triangle. The calculation includes solid phases. Experimental points [319, 349] and calculated lines..... 176

Figure 11.11 The heat capacity of kalsilite $KAlSiO_4$. Experimental data points [48, 385] and calculated lines. 177

Figure 11.12 The heat capacity of leucite $KAlSi_2O_6$. Experimental data points [385-387] and calculated lines. 178

Figure 11.13 The mean heat capacity of kalsilite $KAlSiO_4$ and leucite $KAlSi_2O_6$. Experimental data points [388] and calculated lines. 179

Figure 11.14 The heat capacity of potassium feldspar $KAlSi_3O_8$. Experimental data points [323, 324, 326] and calculated lines. 180

Figure 11.15 The mean heat capacity of $KAlSi_3O_8$. Experimental data points [389] and calculated lines. 181

Figure 12.1 Liquidus projection in the Na_2O-K_2O-SiO_2 system. Isotherms from 600° to 900°C. Experimental points [390] and calculated lines. 184

Figure 12.2 Liquidus projection in the Na_2O-K_2O-SiO_2 system. Isotherms from 950° to 1300°C. Experimental points [390] and calculated lines. 184

Figure 12.3 Phase diagrams in the disilicate (***a***) and metasilicate (***b***) sections of the K_2O-Na_2O-SiO_2 system. Experimental points [390] and calculated lines. 185

Figure 12.4 The enthalpy of mixing at 500°C for sections with a constant silica content of the K_2O-Na_2O-SiO_2 system. Experimental points [393, 394] and calculated lines. 187

Figure 12.5 Isothermal activity ratio of alkali oxides in the K_2O-Na_2O-SiO_2 system. Experimental points measured by mass spectrometry [336] and calculated lines. 189

Figure 12.6 Alkali oxide activity ratios at fixed composition versus the inverse temperature in the series $XSiO_2 + (1-X)[(1-x)Na_2O + xK_2O]$. Experimental points measured by mass spectrometry [336] and calculated lines. 192

Figure 13.1 Liquidus projection in the SiO_2-$NaAlSiO_4$-$KAlSiO_4$ section of the Na_2O-K_2O-Al_2O_3-SiO_2 system. Experimental [396] (thick curves) and calculated isotherms and univariant lines. 195

Figure 13.2 Phase diagram of the $NaAlSiO_4$-$KAlSiO_4$ section in the Na_2O-K_2O-Al_2O_3-SiO_2 system. Experimental points [39, 41, 43, 50] and calculated lines. 197

Figure 13.3 Nepheline miscibility gap in $NaAlSiO_4$-$KAlSiO_4$ series with different amounts of excess silica: 3.34 mol% (***a***), 9.87 mol% (***b***), 22.22 mol% (***c***), 22.85 mol% (***d***). Experimental points [40, 44] and calculated lines. 198

Figure 13.4 Phase diagram of the $NaAlSi_3O_8$-$KAlSi_3O_8$ section in the Na_2O-K_2O-Al_2O_3-SiO_2 system. Experimental data [395-403, 405] and calculated lines. 200

Figure 13.5 Phase diagram of the $NaAlSi_3O_8$-$KAlSi_2O_6$ section in the Na_2O-K_2O-Al_2O_3-SiO_2 system. Experimental data [109] and calculated lines. 201

Figure 13.6 Isothermal section of the $NaAlO_2$-$KAlO_2$-SiO_2 plane of the Na_2O-K_2O-Al_2O_3-SiO_2 system at 1200°C showing the coexisting phases. The blue line indicates the $NaAlSi_3O_8$-$KAlSi_2O_6$ section. 202

Figure 13.7 The enthalpy of mixing of the liquid in the $NaAlSi_2O_6$-$KAlSi_2O_6$ section. Experimental points [410] and calculated lines. 203

Figure 13.8 The enthalpy of mixing of nepheline solid solution with different amounts of excess silica. Experimental points [44, 411] and calculated lines. 204

Figure 13.9 The enthalpy of mixing in the $NaAlSi_3O_8$-$KAlSi_3O_8$ section of crystalline feldspars and the liquid. Experimental points [297, 298, 307, 407, 409, 412-416] and calculated lines.... 206

Figure 13.10 Logarithm of the activity ratio of the nepheline end-members as a function of the composition. Experimental points [45, 417, 419, 420] and calculated lines. 208

Figure 13.11 Logarithm of the activity ratio of the nepheline end-members as a function of the composition in nepheline solutions with a fixed excess silica content $X(SiO_2)$. Experimental points [418, 419] and calculated lines. 209

Figure 13.12 Logarithm of the activity ratio of the feldspar end-members as a function of the composition. Experimental data [417-421] and calculated lines. 211

Figure 13.13 Compositions used for activity measurements in the K_2O-Na_2O-Al_2O_3-SiO_2 system [164]. 212

Figure 13.14 Na_2O and K_2O activities as a function of the inverse temperature in a few compositions of the Na_2O-K_2O-Al_2O_3-SiO_2 system. The reference states are the pure liquid Na_2O and K_2O. Experimental data [164] and calculated lines. 213

Figure 14.1 Liquidus projection in the CaO-Na_2O-SiO_2 system; isotherms from 750° to 1150°C. Experimental points [86, 425] and calculated lines. 218

Figure 14.2 Liquidus projection in the CaO-Na_2O-SiO_2 system; isotherms from 1200° to 1600°C. Experimental points [86, 425] and calculated lines. 218

Figure 14.3 Phase diagram in the metasilicate section Na_2SiO_3-$CaSiO_3$ of the Na_2O-CaO-SiO_2 system. Experimental points [87, 423, 424] and calculated lines. 219

Figure 14.4 Phase diagrams in the sections drawn through the Na_2O-CaO-SiO_2 system. Experimental points [86, 117, 425, 434] and calculated lines. 220

Figure 14.5 Isoactivity lines in the Na_2O-CaO-SiO_2 system at 1250°C (***a***) and 1400°C (***b***). The reference state is the pure liquid Na_2O. Experimental points [435, 436] and calculated lines. ... 223

Figure 14.6 Compositions in the Na_2O-CaO-SiO_2 system for which Na_2O activity was measured [214, 229, 319, 437]. 223

Figure 14.7 Na_2O activity over joins $(Na_2O)_x(SiO_2)_{(1-x)}$-CaO. The reference state is the pure liquid Na_2O. Experimental points [229, 319] and calculated lines. 225

Figure 14.8 Na_2O activity over joins with a constant Na_2O content. The reference state is the pure liquid Na_2O. Experimental points [214, 437] and calculated lines. 226

Figure 14.9 The mean heat capacity of Na_2CaSiO_4, $Na_2Ca_2Si_2O_7$ compounds and "$Na_2Ca_2Si_3O_9$" (Combeite) and "$Na_4CaSi_3O_9$" (2:1:3) solid solutions. Experimental points [431] and calculated lines. 227

Figure 15.1 Liquidus projection in the Al_2O_3-CaO-Na_2O system. 232

Figure 15.2 Subsolidus relations in the Al_2O_3-CaO-Na_2O system at 1200°C (***a***) and 1400°C (***b***). Experimental triangulation [96, 441, 442] and calculated lines. 232

Figure 15.3 Phase diagrams in sections through the CaO-Na_2O-Al_2O_3 system. Experimental points [97, 443] and calculated lines. 233

Figure 16.1 Phase diagram of the $Ca_2Al_2SiO_7$-$NaAlSiO_4$ section of the Na_2O-CaO-Al_2O_3-SiO_2 system. Experimental points [447] and calculated lines. 237

Figure 16.2 Phase diagram of the $CaAl_2Si_2O_8$-$NaAlSiO_4$ section of the Na_2O-CaO-Al_2O_3-SiO_2 system. Experimental points [52] and calculated lines. 238

Figure 16.3 Liquidus projection in the $Ca_2Al_2SiO_7$-$CaAl_2Si_2O_8$-$NaAlSiO_4$ plane of the Na_2O-CaO-Al_2O_3-SiO_2 system. Experimental points [449] and calculated lines. 240

Figure 16.4 Phase diagram of the $CaAl_2O_4$-$NaAlSiO_4$ section of the Na_2O-CaO-Al_2O_3-SiO_2 system. Experimental points [51] and calculated lines. 241

Figure 16.5 Phase diagram of the $CaSiO_3$-$NaAlSi_3O_8$ section of the Na_2O-CaO-Al_2O_3-SiO_2 system. Experimental points [73] and calculated lines. 243

Figure 16.6 Phase diagram of the $CaSiO_3$-$NaAlSiO_4$ section of the Na_2O-CaO-Al_2O_3-SiO_2 system. Experimental points [73] and calculated lines. 243

Figure 16.7 Liquidus projection of the $NaAlSi_3O_8$-$CaSiO_3$-$NaAlSiO_4$ plane of the Na_2O-CaO-Al_2O_3-SiO_2 system. Experimental points [73] and calculated lines. 244

Figure 16.8 Phase diagram of the $NaAlSi_3O_8$-$CaAl_2Si_2O_8$ section of the Na_2O-CaO-Al_2O_3-SiO_2 system. Experimental points [286, 377], the compiled phase diagram by Smith [68] and the calculated lines. 245

Figure 16.9 The enthalpy of mixing in the $NaAlSi_3O_8$-$CaAl_2Si_2O_8$ section for the liquid and feldspar. Experimental points [297, 299, 315, 450, 452] and calculated lines. 247

Figure 16.10 The heat content in the albite-anorthite ($NaAlSi_3O_8$-$CaAl_2Si_2O_8$) section. Experimental points [453] and calculated lines. 248

Figure 16.11 Activities of $NaAlSi_3O_8$ and $CaAl_2Si_2O_8$ in plagioclase feldspars at different temperatures. Experimental points [299, 454-456] and calculated lines. 250

Figure 16.12 Liquidus projection in the $CaAl_2Si_2O_8$-$CaSiO_3$-$NaAlSiO_4$ plane of the Na_2O-CaO-Al_2O_3-SiO_2 system. Experimental points [448] and calculated lines. 251

Figure 16.13 Liquidus projection in the $Ca_2Al_2SiO_7$-$CaSiO_3$-$NaAlSiO_4$ plane of the Na_2O-CaO-Al_2O_3-SiO_2 system. Experimental points [72] and calculated lines. 252

Figure 16.14 Phase diagram of the $Ca_2Al_2SiO_7$-$NaCaAlSi_2O_7$ section of the Na_2O-CaO-Al_2O_3-SiO_2 system. Experimental points [459, 461] and calculated lines. 253

Figure 16.15 Liquidus projection in the $Ca_2Al_2SiO_7$-$CaSiO_3$-$NaAlSiO_4$ + 10 wt% $CaAl_2Si_2O_8$ plane of the Na_2O-CaO-Al_2O_3-SiO_2 system. Experimental points [462] and calculated lines.... 254

Figure 16.16 Liquidus projection in the $NaAlSiO_4$-$CaSiO_3$-Na_2SiO_3 plane of the Na_2O-CaO-Al_2O_3-SiO_2 system. Experimental points [463] and calculated lines. 255

Figure 16.17 The enthalpy of mixing of $CaAl_2SiO_6$-$NaAlSi_2O_6$ clinopyroxenes. Data calculated from equilibria [464] (the points are from a digitized curve) and the calculated line..... 256

Figure 16.18 Liquidus projection in the Ca_2SiO_4-$Na_2Al_{12}O_{19}$-CaO plane of the Na_2O-CaO-Al_2O_3-SiO_2 system. Experimental points [443] and calculated lines. 257

Figure 16.19 Tie-lines of the miscibility gap appearing in the liquidus projection of the Ca_2SiO_4-$Na_2Al_{12}O_{19}$-CaO plane at 1200°C without any solid phases selected. The binary systems with strong negative interactions are shown in blue, the binary systems with ideal or near-ideal interactions are shown in red. 258

Figure 16.20 Phase diagram of the Ca_2SiO_4-$Na_2Al_{12}O_{19}$ section of the Na_2O-CaO-Al_2O_3-SiO_2 system. Experimental points [443] and calculated lines..... 259

Figure 16.21 Liquidus projection in the Ca_2SiO_4-$Na_2Al_6O_{10}$-CaO plane of the Na_2O-CaO-Al_2O_3-SiO_2 system. Experimental points [443] and calculated lines. 259

Figure 16.22 Liquidus projection in the Ca_2SiO_4-$Na_2Al_2O_4$-CaO plane of the Na_2O-CaO-Al_2O_3-SiO_2 system. Experimental points [443] and calculated lines. 260

Figure 16.23 Phase diagram of the $NaAlO_2$-Ca_2SiO_4 section of the Na_2O-CaO-Al_2O_3-SiO_2 system. Experimental points [466, 471] and calculated lines..... 261

Figure 16.24 Isoactivity plots in the SiO_2-Na_2O-$(CaO)_{0.8}(Al_2O_3)_{0.2}$ (***a***) and SiO_2-Na_2O-$(CaO)_{0.5}(Al_2O_3)_{0.5}$ (***b***) sections of the Al_2O_3-CaO-Na_2O-SiO_2 system at 1400°C. The reference state is the pure liquid Na_2O. Points recalculated from the published data [436] and calculated lines. 262

Figure 17.1 Liquidus projection in the $CaO-K_2O-SiO_2$ system; isotherms from 750° to 1000°C. Experimental points [92, 474] and calculated lines. 267

Figure 17.2 Liquidus projection in the $CaO-K_2O-SiO_2$ system; isotherms from 1050° to 1300°C. Experimental points [92, 474] and calculated lines. 267

Figure 17.3 Liquidus projection in the $CaO-K_2O-SiO_2$ system; isotherms from 1350° to 1650°C. Experimental points [92, 474] and calculated lines. 268

Figure 17.4 Phase diagrams in sections through the $K_2O-CaO-SiO_2$ system. Experimental points [92] and calculated lines. 271

Figure 17.5 The partial enthalpy of SiO_2 in $CaO-K_2O-SiO_2$ melts ($K_2O/(K_2O+CaO) = 0.8$). Experimental points [343] and the calculated line. 273

Figure 18.1 Liquidus projection in the $K_2O-CaO-Al_2O_3$ system. 276

Figure 18.2 Isothermal section in the $K_2O-CaO-Al_2O_3$ system at 1100°C. Experimental triangulation [480] and calculated lines. 276

Figure 18.3 Phase diagrams in sections through the $K_2O-CaO-Al_2O_3$ system. Experimental points [479] and calculated lines. "C5A3" phase is a hydrate which does not exist in the anhydrous system. 278

Figure 19.1 Liquidus projection in the KC23S12-CaO-C5A3 plane of the $CaO-K_2O-Al_2O_3-SiO_2$ system. Experimental points [118] and calculated lines. 280

Figure 19.2 Phase diagram in the $Ca_2Al_2SiO_7-KCaAlSi_2O_7$ section of the $CaO-K_2O-Al_2O_3-SiO_2$ system. Experimental points [481] and calculated lines. 281

Figure 19.3 Liquidus projection in the $SiO_2-KAlSi_2O_6-CaAl_2Si_2O_8$ plane of the $CaO-K_2O-Al_2O_3-SiO_2$ system in different temperature intervals (***a-b***). Experimental points [483] and calculated lines. 282

Figure 19.4 Phase diagram in the $CaAl_2Si_2O_8-KAlSi_2O_6$ section of the $CaO-K_2O-Al_2O_3-SiO_2$ system. Experimental data [483] and calculated lines. 282

Figure 19.5 Phase diagram in the $CaAl_2Si_2O_8-KAlSi_3O_8$ section in the $CaO-K_2O-Al_2O_3-SiO_2$ system. Experimental data [69, 483] and calculated lines. 283

Figure 19.6 The enthalpy of mixing of metastable $KAlSi_3O_8$-$CaAl_2Si_2O_8$ feldspars. Experimental points [450] and the calculated line. 284

Figure 19.7 The partial enthalpy of Al_2O_3 in $K_2O{\cdot}CaO{\cdot}6SiO_2$ melts. Experimental points [343] and the calculated line. 285

Figure 19.8 K_2O activity at 1430°C as a function of K_2O content at several base CaO-Al_2O_3-SiO_2 compositions. Experimental points [486] and calculated lines. 287

Figure 20.1 Liquidus projection in the $CaAl_2Si_2O_8$-$NaAlSi_3O_8$-$KAlSi_2O_6$ plane of the Na_2O-K_2O-CaO-Al_2O_3-SiO_2 system. Experimental data [109] and calculated lines. 289

Figure 20.2 Liquidus projection in the $CaAl_2Si_2O_8$-$NaAlSiO_4$-$KAlSi_2O_6$ plane of the Na_2O-K_2O-CaO-Al_2O_3-SiO_2 system with (***a***) and without (***b***) Corundum phase included into calculation. Experimental data [484] and calculated lines. 290

Figure 20.3 Liquidus projection in the $CaAl_2Si_2O_8$-$NaAlSi_3O_8$-$KAlSi_3O_8$ plane of the Na_2O-K_2O-CaO-Al_2O_3-SiO_2 system. Experimental data [488] and calculated lines. 291

Figure 20.4 Feldspar miscilibity gap at 500°C (***a***), 650°C (***b***), 700°C (***c***), 750°C (***d***), 825°C (***e***), 900°C (***f***). Experimental points [457, 489-491] and calculated lines. 292

Figure 20.5 The enthalpy of mixing of ternary $NaAlSi_3O_8$-$KAlSi_3O_8$-$CaAl_2Si_2O_8$ feldspars. Experimental points [494] and the calculated line. 293

Figure 21.1 Stoichiometric compounds and the investigated sections in the Na_2O-MgO-SiO_2 system. 295

Figure 21.2 Phase diagram in the Na_2SiO_3-$MgSiO_3$ section of the Na_2O-MgO-SiO_2 system. Experimental points [424] and calculated lines. 296

Figure 21.3 Primary fields in the Na_2O-MgO-SiO_2 system. Experimental univariant lines [391, 497] and the calculated phase diagram. The phase labels correspond to the calculated phase diagram and mostly coincide with the fields by Schairer et al. [391]; the field labels by Botvinkin et al. [497] are marked in brown. 298

Figure 21.4 Isotherms in the Na_2O-MgO-SiO_2 system. Experimental isotherms (thick lines) [497] and the calculated phase diagram. 298

Figure 21.5 Phase diagram in the $Na_2Si_2O_5$-$Na_2Mg_5Si_{12}O_{30}$ section of the Na_2O-MgO-SiO_2 system (the disilicate section). Experimental points [495] and calculated lines. 299

Figure 21.6 Phase diagram in the $Na_2Si_2O_5$-$Na_4Mg_3Si_5O_{15}$ section of the Na_2O-MgO-SiO_2 system. Experimental points [495] and calculated lines. 300

Figure 21.7 Isoactivity lines in the Na_2O-MgO-SiO_2 system at 1250°C (***a***) and 1400°C (***b***). The reference state is the pure liquid Na_2O. Experimental points [435, 436] and calculated lines. ... 303

Figure 21.8 Temperature dependence of Na_2O activity of the liquid phase at compositions in the trisilicate section. The reference state is the pure liquid Na_2O. Experimental points [226] and calculated lines. 304

Figure 21.9 Na_2O activity of the liquid phase along the trisilicate section at 500°C. The reference state is the pure liquid Na_2O. Experimental points [226] and the calculated line. 305

Figure 22.1 Liquidus projection in the 5 wt% MgO plane of the CaO-MgO-Na_2O-SiO_2 system. Isotherms from 750° to 1050°C (***a***) and 1100° to 1350°C (***b***). Experimental points [504] and calculated lines. 306

Figure 22.2 Liquidus projection in the 10 wt% MgO plane of the CaO-MgO-Na_2O-SiO_2 system. Isotherms from 950° to 1200°C (***a***) and 1250° to 1450°C (***b***). Experimental points [504] and calculated lines. 307

Figure 22.3 Liquidus projection in the SiO_2-Na_2O-$Ca_{0.5}Mg_{0.5}O$ plane of the CaO-MgO-Na_2O-SiO_2 system. Experimental points [505] and calculated lines. 307

Figure 22.4 Base compositions of the sections studied in the CaO-MgO-Na_2O-SiO_2 system [506-511]. Sections have either CaO replaced by MgO or MgO was added to a base composition. .. 308

Figure 22.5 Phase diagrams in sections obtained by a gradual addition of MgO to fixed Na_2O-CaO-SiO_2 compositions. Experimental points [508, 509] and calculated lines. 309

Figure 22.6 Phase diagrams of sections obtained by a gradual replacement of CaO for MgO to fixed Na_2O-CaO-SiO_2 compositions. Experimental points [508, 510, 511] and calculated lines. 310

Figure 22.7 Na_2O isoactivity plots in the SiO_2-Na_2O-$Ca_{0.2}Mg_{0.8}O$ section of the CaO-MgO-Na_2O-SiO_2 system at 1250°C (***a***) and 1400°C (***b***). Points recalculated from the published data [512] and calculated lines. 311

Figure 22.8 Na_2O isoactivity plots in the SiO_2-Na_2O-$Ca_{0.5}Mg_{0.5}O$ section of the CaO-MgO-Na_2O-SiO_2 system at 1250°C (***a***) and 1400°C (***b***). Points recalculated from the published data [512] and calculated lines. 311

Figure 22.9 Na_2O isoactivity plots in the SiO_2-Na_2O-$Ca_{0.8}Mg_{0.2}O$ section of the CaO-MgO-Na_2O-SiO_2 system at 1250°C (***a***) and 1400°C (***b***). The reference state is the pure liquid Na_2O. Points recalculated from the published data [512] and calculated lines. 312

Figure 22.10 Activity of Na_2O as a function of the inverse temperature for a fixed composition in the CaO-MgO-Na_2O-SiO_2 system. The reference state is the pure liquid Na_2O. Experimental points [513] and the calculated line. 313

Figure 23.1 An isothermal section of the Na_2O-MgO-Al_2O_3 phase diagram at 1700°C. Experimental data [104] and calculated lines. 315

Figure 23.2 Liquidus projection in the MgO-Al_2O_3-Na_2O system. 315

Figure 24.1 Liquidus projection in the Mg_2SiO_4-$NaAlSiO_4$-SiO_2 plane of the MgO-Na_2O-Al_2O_3-SiO_2 system. Experimental points and isotherms (thick lines) [516, 518] and calculated lines. . 318

Figure 24.2 Phase diagram in the $NaAlSi_3O_8$-Mg_2SiO_4 section of the MgO-Na_2O-Al_2O_3-SiO_2 system. Experimental points [516] and calculated lines. 319

Figure 24.3 Phase diagram in the $NaAlSi_2O_6$-Mg_2SiO_4 section of the MgO-Na_2O-Al_2O_3-SiO_2 system. Experimental points [520] and calculated lines. 320

Figure 24.4 Liquidus projection in the SiO_2-$NaAlSiO_4$-$MgAl_2O_4$ plane of the MgO-Na_2O-Al_2O_3-SiO_2 system. Experimental points [521] and calculated lines. 321

Figure 24.5 Liquidus projection in the Mg_2SiO_4-$NaAlSi_3O_8$-$Mg_2Al_4Si_5O_{18}$ plane of the MgO-Na_2O-Al_2O_3-SiO_2 system. Experimental points and isotherms (thick lines) [522] and calculated lines. 323

Figure 24.6 Liquidus projection in the $MgSiO_3$-$NaAlSi_3O_8$-$Mg_2Al_4Si_5O_{18}$ plane of the MgO-Na_2O-Al_2O_3-SiO_2 system. Experimental points and isotherms (thick lines) [522] and calculated lines. 325

Figure 24.7 Phase diagram of the MgO-SiO_2 system featuring the binary miscibility gap (***a***) and an isothermal section $NaAlO_2$-MgO-SiO_2 (only liquid phase) at 1200°C showing the propagation of the binary miscibility gap into the quaternary system (***b***). 325

Figure 24.8 Liquidus projection in the SiO_2-$NaAlSi_3O_8$-$Mg_2Al_4Si_5O_{18}$ plane of the MgO-Na_2O-Al_2O_3-SiO_2 system. Experimental points and isotherms (thick lines) [522] and calculated lines. 327

Figure 24.9 Isoactivity plots in the SiO_2-Na_2O-$(MgO)_{0.8}(Al_2O_3)_{0.2}$ (***a***) and SiO_2-Na_2O-$(MgO)_{0.5}(Al_2O_3)_{0.5}$ (***b***) sections of the Al_2O_3-MgO-Na_2O-SiO_2 system at 1400°C. The reference state is the pure liquid Na_2O. Points recalculated from the published data [436] and calculated lines. 328

Figure 25.1 Phase diagram in the $CaMgSi_2O_6$-$NaAlSi_3O_8$ section of the CaO-MgO-Al_2O_3-Na_2O-SiO_2 system. Experimental points [523, 524] and calculated lines. 330

Figure 25.2 Liquidus projection in the $CaMgSi_2O_6$-$NaAlSi_3O_8$-$CaAl_2Si_2O_8$ plane of the CaO-MgO-Na_2O-Al_2O_3-SiO_2 system. Experimental points and isotherms (thick lines) [523, 529] and calculated lines. 331

Figure 25.3 The enthalpy of mixing of liquid in the $NaAlSi_3O_8$-$CaMgSi_2O_6$ section of the CaO-MgO-Al_2O_3-Na_2O-SiO_2 system recalculated from glass calorimetry data. Experimental points [315] and calculated lines. 332

Figure 25.4 Liquidus projection in the Mg_2SiO_4-$NaAlSi_3O_8$-$CaAl_2Si_2O_8$ plane of the CaO-MgO-Na_2O-Al_2O_3-SiO_2 system. Experimental points and isotherms (thick lines) [531] and calculated lines. 333

Figure 25.5 Isotherms of the Mg_2SiO_4-$NaAlSi_3O_8$-$CaAl_2Si_2O_8$ plane of the CaO-MgO-Na_2O-Al_2O_3-SiO_2 system at 1280°C (***a***) and 1300°C (***b***). Experimental [531] and calculated tie-lines. 334

Figure 25.6 Liquidus projection in the $Ca_2MgSi_2O_7$-$NaAlSi_3O_8$-$CaAl_2Si_2O_8$ plane of the CaO-MgO-Na_2O-Al_2O_3-SiO_2 system. Experimental points and isotherms (thick lines) [532] and calculated lines. 335

Figure 25.7 Phase diagram in the $Ca_2MgSi_2O_7$-$NaCaAlSi_2O_7$ section of the CaO-MgO-Al_2O_3-Na_2O-SiO_2 system. Experimental points [459, 461, 534, 535, 542] and calculated lines. 337

Figure 25.8 Phase diagram in the $Ca_2MgSi_2O_7$-$NaAlSiO_4$ section of the CaO-MgO-Al_2O_3-Na_2O-SiO_2 system. Experimental points [541] and calculated lines. 338

Figure 25.9 Liquidus projection in the $Ca_2MgSi_2O_7$-$NaAlSiO_4$-$CaSiO_3$ plane of the CaO-MgO-Na_2O-Al_2O_3-SiO_2 system. Experimental points [540] and calculated lines. 338

Figure 25.10 Liquidus projection in the $Ca_2MgSi_2O_7$-$NaCaAlSi_2O_7$-$Ca_2Al_2SiO_7$ plane of the CaO-MgO-Na_2O-Al_2O_3-SiO_2 system. Experimental points and isotherms (thick lines) [459] and calculated lines. 339

Figure 25.11 Isothermal sections in the $Ca_2MgSi_2O_7$-$NaCaAlSi_2O_7$-$Ca_2Al_2SiO_7$ plane (akermanite-soda melilite-gehlenite) of the CaO-MgO-Na_2O-Al_2O_3-SiO_2 system: 1120°C (***a***), 1150°C (***b***), 1200°C (***c***), 1250°C (***d***). Experimental points [71] and calculated lines. 340

Figure 25.12 Phase diagram in the $CaMgSi_2O_6$-$NaAlSiO_4$ section of the CaO-MgO-Al_2O_3-Na_2O-SiO_2 system. Experimental points [544, 545] and calculated lines. 342

Figure 25.13 Liquidus projection in the $Ca_2MgSi_2O_7$-$NaAlSiO_4$-$CaMgSi_2O_6$ plane of the CaO-MgO-Na_2O-Al_2O_3-SiO_2 system. Experimental points [540] and calculated lines. 343

Figure 25.14 Phase diagram in the $Ca_2MgSi_2O_7$-$CaMgSi_2O_6$ section of the CaO-MgO-SiO_2 system taken from the original optimization by Jung et al. [546]. 344

Figure 25.15 Liquidus projection in the $CaMgSi_2O_6$-$NaAlSiO_4$-$CaSiO_3$ of the CaO-MgO-Na_2O-Al_2O_3-SiO_2 system. Experimental points [540] and calculated lines. 345

Figure 25.16 Liquidus projection in the Mg_2SiO_4-$NaAlSiO_4$-$CaMgSi_2O_6$ plane of the CaO-MgO-Na_2O-Al_2O_3-SiO_2 system. Experimental points [547] and calculated lines. 346

Figure 25.17 Liquidus projection in the $CaMgSi_2O_6$-$NaAlSiO_4$-$CaAl_2Si_2O_8$ plane of the CaO-MgO-Na_2O-Al_2O_3-SiO_2 system. Experimental points [548] and calculated lines. 347

Figure 25.18 Phase diagram of the $CaMgSi_2O_6$-$NaAlSi_2O_6$ section of the CaO-MgO-Al_2O_3-Na_2O-SiO_2 system. Experimental points [81, 524] and calculated lines. 348

Figure 25.19 Liquidus projection in the SiO_2-$NaAlSiO_4$-$CaMgSi_2O_6$ plane of the CaO-MgO-Na_2O-Al_2O_3-SiO_2 system. Experimental points [524] and calculated lines. 349

Figure 25.20 The enthalpy of mixing of Clinopyroxene solid solution along the diopside-jadeite join ($CaMgSi_2O_6$-$NaAlSi_2O_6$). Experimental points [78, 79] and the calculated line. 350

Figure 25.21 End-member activities in Clinopyroxene $NaAlSi_2O_6$-$CaMgSi_2O_6$ solid solution at different temperatures. Experimental points [80, 551, 553] and calculated lines. 351

Figure 25.22 Liquidus projection in the $Ca_2MgSi_2O_7$-$NaAlSi_3O_8$-$CaMgSi_2O_6$ plane of the CaO-MgO-Na_2O-Al_2O_3-SiO_2 system. Experimental points [540] and calculated lines. 352

Figure 25.23 Liquidus projection in the Mg_2SiO_4-$NaAlSi_3O_8$-$CaMgSi_2O_6$ plane (olivine-albite-diopside) in the CaO-MgO-Na_2O-Al_2O_3-SiO_2 system. Experimental points [521] and calculated lines. 353

Figure 25.24 Liquidus projection in the $MgSiO_3$-$NaAlSi_3O_8$-$CaMgSi_2O_6$ plane of the CaO-MgO-Na_2O-Al_2O_3-SiO_2 system. Experimental points and isotherms (thick lines) [554] and calculated lines. 354

Figure 25.25 Isothermal sections of the $MgSiO_3$-$NaAlSi_3O_8$-$CaMgSi_2O_6$ plane in the CaO-MgO-Na_2O-Al_2O_3-SiO_2 system at 1150°C (***a***), 1200°C (***b***), 1250°C (***c***), 1300°C (***d***), and 1350°C (***e***). Experimental points [554] and calculated lines. 355

Figure 25.26 Phase diagram of the $MgSiO_3$-$CaMgSi_2O_6$ boundary from the optimization by Jung et al. [546]. 356

Figure 25.27 Liquidus projection in the $Ca_2MgSi_2O_7$-$NaAlSi_3O_8$-$CaSiO_3$ plane of the CaO-MgO-Na_2O-Al_2O_3-SiO_2 system. Experimental points [540] and calculated lines. 357

Figure 25.28 Liquidus projection in the $Ca_2MgSi_2O_7$-$NaAlSiO_4$-$NaAlSi_3O_8$ plane of the CaO-MgO-Na_2O-Al_2O_3-SiO_2 system. Experimental points [540] and calculated lines. 358

Figure 25.29 Isoactivity plots in the $(SiO_2)_{0.95}(Al_2O_3)_{0.05}$-$Na_2O$-$(Ca_{0.5}Mg_{0.5}O)_{0.95}(Al_2O_3)_{0.05}$ (***a***) and $(SiO_2)_{0.95}(Al_2O_3)_{0.05}$-$Na_2O$-$(Ca_{0.8}Mg_{0.2}O)_{0.95}(Al_2O_3)_{0.05}$ (***b***) sections of the Al_2O_3-CaO-MgO-Na_2O-

SiO_2 system at 1400°C. The reference state is the pure liquid Na_2O. Points recalculated from the published data [436] and calculated lines. 359

Figure 26.1 Liquidus projection in the K_2O-MgO-SiO_2 system; isotherms from 700 to 1000°C. Experimental points [114, 115] and calculated lines. 362

Figure 26.2 Liquidus projection in the K_2O-MgO-SiO_2 system; isotherms from 1050° to 1300°C. Experimental points [114, 115] and calculated lines. 362

Figure 26.3 Liquidus projection in the K_2O-MgO-SiO_2 system; isotherms from 1350° to 1600°C. Experimental points [114, 115] and calculated lines. 363

Figure 26.4 Sections through the K_2O-MgO-SiO_2 system [46, 114]. 364

Figure 26.5 Phase diagram of the $K(Mg_{0.5}Si_{0.5})O_2$-SiO_2 section of the K_2O-MgO-SiO_2 system. Experimental points [46, 114] and calculated lines. 364

Figure 26.6 Phase diagrams in different sections through the K_2O-MgO-SiO_2 system: $MgSiO_3$-$K_2Si_7O_{15}$ (***a***), $K_2MgSi_5O_{12}$-$K_2Mg_5Si_{12}O_{30}$ (***b***), $K_2MgSi_5O_{12}$-Mg_2SiO_4 (***c***), $K_2MgSi_3O_8$-Mg_2SiO_4 (***d***), $K_2Si_4O_9$-$K_2MgSi_5O_{12}$ (***e***), $K_2Si_2O_5$-$K_2MgSi_5O_{12}$ (***f***), $K_2Si_2O_5$-K_2MgSiO_4 (***g***), K_2SiO_3-K_2MgSiO_4 (***h***). Digitized lines from the source (shown as points) [114] and calculated lines. 367

Figure 26.7 Temperature dependence of K_2O activity of the liquid phase at compositions in the trisilicate section. The reference state is the pure liquid K_2O. Experimental points [226] and calculated lines. 370

Figure 26.8 K_2O activity of the liquid phase along the trisilicate section at 500°C. The reference state is the pure liquid K_2O. Experimental points [226] and the calculated line. 371

Figure 27.1 The schematic representation of the B_2O_3 glass structure. The image is taken from Krogh-Moe [559]. 374

Figure 27.2 Specific volume of vitreous and liquid B_2O_3 (***a***) and the apparent activation energy of viscous flow for B_2O_3 (***b***). The images are taken from Krogh-Moe [559]. 374

Figure 27.3 The concentration of boroxol rings in pure B_2O_3 as a function of temperature (***a***) and the ratio of the number of boron atoms in boroxol groups to the number of other boron atoms in

Na_2O-B_2O_3 mixtures at 298K (***b***). The images are taken from Vedishcheva and Shakhmatkin (modified) [562] and Jellison and Bray [561], correspondingly. 375

Figure 27.4 The main structural units present in Li_2O-B_2O_3 glasses: boroxol unit (***a***), pentaborate unit (***b***), triborate unit (***c***), diborate unit (***d***), metaborate unit (***e***), pyroborate unit (***f***), orthoborate unit (***g***), loose BO_4 unit (***h***). The image is taken from Bray and Lui [563]. 376

Figure 27.5 Tetraborate group present in Na_2O-B_2O_3 melts. The image is taken from Bray and Lui [563]..... 376

Figure 27.6 Miscibility gaps in the MO-SiO_2 systems, where M = Mg, Ca, Sr, Ba, calculated based on the existing optimizations in the *FToxid* database. 378

Figure 27.7 Metastable miscibility gaps in Na_2O-B_2O_3 (***a***), K_2O-B_2O_3 (***b***), Rb_2O-B_2O_3 (***c***) systems. The images are taken from Shaw and Uhlmann [571]. 378

Figure 27.8 Metastable miscibility gap in the Na_2O-B_2O_3-SiO_2 system. The image is taken from Haller et al. [575]..... 379

Figure 28.1 Phase diagram of the Na_2O-B_2O_3 system. Experimental points [334, 576-578, 581, 582, 589, 598-608] and calculated lines. 384

Figure 28.2 Metastable miscibility gap in the Na_2O-B_2O_3 system. Experimental points [571, 609]. 385

Figure 28.3 The enthalpy of mixing of the liquid phase in the Na_2O-B_2O_3 system. Experimental points [197, 201, 610, 614, 616-619, 623] and calculated lines. 387

Figure 28.4 The enthalpy of formation from oxides of crystalline compounds in the Na_2O-B_2O_3 system. Experimental points [615, 620-622, 624, 625] and the calculated line. 388

Figure 28.5 The partial enthalpy of B_2O_3 in the Na_2O-B_2O_3 system. Experimental points [564] and the calculated line. 389

Figure 28.6 Na_2O activity in the liquid phase in the Na_2O-B_2O_3 system. The reference state is the pure liquid Na_2O. Experimental points [565-570] and calculated lines. 391

Figure 28.7 Distribution of the four-coordinated boron in Na_2O-B_2O_3 glasses and melts. Experimental points [561, 609, 632-639] and calculated lines. 393

Figure 28.8 The heat capacity of sodium metaborate $NaBO_2$. Experimental points [640, 641] and the calculated line. 394

Figure 28.9 The heat capacity of sodium diborate $Na_2B_4O_7$. Experimental points [642] and the calculated line. 395

Figure 28.10 The heat content of four compounds in the Na_2O-B_2O_3 system. Experimental points [620, 643] and calculated lines. 396

Figure 29.1 Liquidus projection in the Na_2O-B_2O_3-SiO_2 system. Experimental points [645] and calculated lines. 401

Figure 29.2 Phase diagram of the $NaBO_2$-SiO_2 section of the Na_2O-B_2O_3-SiO_2 system. Experimental points [645, 647] and calculated lines. 402

Figure 29.3 Phase diagrams of sections through the Na_2O-B_2O_3-SiO_2 system: $Na_2B_4O_7$-SiO_2 (***a***), $Na_2B_8O_{13}$-SiO_2 (***b***), Na_3BO_3-SiO_2 (***c***), Na_2SiO_3-$NaBO_2$ (***d***). Experimental points [644-647, 649] and calculated lines. 403

Figure 29.4 Isothermal projections of the metastable miscibility gap in the Na_2O-B_2O_3-SiO_2 system. Experimental points [573, 651, 653, 654, 656] and calculated lines. 404

Figure 29.5 Polythermal sections through the metastable miscibility gap in the Na_2O-B_2O_3-SiO_2 system. Experimental points [574, 575, 655, 658] and calculated lines. 405

Figure 29.6 The enthalpy of mixing in the $NaBO_2$-SiO_2 section of the Na_2O-B_2O_3-SiO_2 system at different temperatures. Experimental points [303, 661, 664] and calculated lines. 407

Figure 29.7 The partial enthalpy of SiO_2 in the $NaBO_2$-SiO_2 section of the Na_2O-B_2O_3-SiO_2 system at 1121°C. Experimental points [661] and calculated lines. 408

Figure 29.8 The enthalpy of mixing in the Na_3BO_3-SiO_2 section of the Na_2O-B_2O_3-SiO_2 system. Experimental points [664] and calculated lines. 409

Figure 29.9 The enthalpy of mixing in the $Na_2B_8O_{13}$-SiO_2 section of the Na_2O-B_2O_3-SiO_2 system. Experimental points [664] and calculated lines. 410

Figure 29.10 The enthalpy of mixing at 20 mol% Na_2O of the Na_2O-B_2O_3-SiO_2 system at different temperatures. Experimental points [201] and calculated lines. 411

Figure 29.11 Compositions in the Na_2O-B_2O_3-SiO_2 system at which Na_2O activities were studied [222, 233, 665] and the isothermal sections plotted through them in this work. 412

Figure 29.12 Na_2O activity at 900°C along the $NaBO_2$-SiO_2 section. Experimental points [233], points interpolated from experimental data [665] and the calculated line. 413

Figure 29.13 Na_2O activity at 900°C in sections with a constant Na_2O content. The reference state is the pure liquid Na_2O. Points interpolated from experimental data [665] and calculated lines. 414

Figure 29.14 Na_2O activity at 1027°C in sections with a constant B_2O_3 content. The reference state is the pure liquid Na_2O. Experimental points [222] and calculated lines. 415

Figure 30.1 Phase diagram of the K_2O-B_2O_3 system. Experimental data [334, 598, 666-669, 672, 677] and calculated lines. Stable equilibria are shown in black, the metastable in magenta. 419

Figure 30.2 Metastable miscibility gap in the K_2O-B_2O_3 system. Experimental points [571]. ... 420

Figure 30.3 The enthalpy of mixing of the liquid phase in the K_2O-B_2O_3 system. Experimental points [342, 614, 617-619, 683] and calculated lines. 422

Figure 30.4 The enthalpy of formation of crystalline solids from oxides in the K_2O-B_2O_3 system. Experimental points [614, 616-619, 683] and the calculated line. 423

Figure 30.5 The partial enthalpy of B_2O_3 in the K_2O-B_2O_3 melts. Experimental points [564] and the calculated line. 424

Figure 30.6 K_2O activity of the liquid phase in the K_2O-B_2O_3 system. The reference state is the pure liquid K_2O. Experimental points [566, 570, 630] and calculated lines. 425

Figure 30.7 The heat capacity of potassium metaborate KBO_2. Experimental points [684] and the calculated line. 426

Figure 30.8 The mean heat capacity of potassium borates. Experimental points [683] and calculated lines. 427

Figure 31.1 Liquidus projection in the K_2O-B_2O_3-SiO_2 system. Experimental points [685] and calculated lines. 430

Figure 31.2 Phase diagram in the KBO_2-SiO_2 section of the K_2O-B_2O_3-SiO_2 system. Experimental points [677, 685] and calculated lines. 430

Figure 31.3 Phase diagrams in sections through the K_2O-B_2O_3-SiO_2 system: K_2SiO_3-KBO_2 (***a***), $K_2B_4O_7$-$KBSi_2O_6$ (***b***), $K_2B_8O_{13}$-SiO_2 (***c***). Experimental points [677, 685] and calculated lines. 431

Figure 31.4 Isothermal projections of the metastable miscibility gap in the K_2O-B_2O_3-SiO_2 system. Experimental points [653, 688] and calculated lines. 432

Figure 31.5 Polythermal sections through the metastable miscibility gap in the K_2O-B_2O_3-SiO_2 system. Experimental points [653, 685, 688] and calculated lines. 433

Figure 31.6 The enthalpy of mixing in the K_2O-B_2O_3-SiO_2 system at 20 mol% K_2O. Experimental points [342] and calculated lines. 434

Figure 32.1 Phase diagram of the monoborate $NaBO_2$-KBO_2 section of the Na_2O-K_2O-B_2O_3 system. Experimental points [582, 607, 689-691] and calculated lines. 437

Figure 32.2 Phase diagram of the diborate $Na_2B_4O_7$-$K_2B_4O_7$ section of the Na_2O-K_2O-B_2O_3 system. Experimental points [582, 694] and calculated lines. 438

Figure 32.3 Phase diagram of the triborate NaB_3O_5-KB_3O_5 section of the Na_2O-K_2O-B_2O_3 system. Experimental points [695] and calculated lines. 439

Figure 32.4 Phase diagrams of the diborate-monoborate cross-sections: $K_2B_4O_7$-$NaBO_2$ (***a***) and $Na_2B_4O_7$-KBO_2 (***b***). Experimental points [582] and calculated lines. 439

Figure 32.5 The enthalpy of mixing of the liquid phase in the triborate section NaB_3O_5-KB_3O_5 at 25°C. Experimental points [696] and the calculated line. 440

Figure 32.6 The enthalpy of mixing of the liquid phase in the section with 80 mol% (***a***) and 86 mol% (***b***) B_2O_3 at 25°C. Experimental points [682] and calculated lines. 441

LIST OF SYMBOLS AND ABBREVIATIONS

Symbols:

a Activity

a, b, c Crystallographic axes

C_{En} Einstein heat capacity function

C_P Molar heat capacity

E Electromotive force

G(compound) Gibbs energy of an existing compound

g°(EM) Gibbs energy expression of EM end-member in a solution model

$G°_A$, $g°$(A) Gibbs energy of an end-member

G^{add} Added Gibbs energy term

$g^{ij}_{A,B}$ Term in a series expansion of a Quasichemical Gibbs energy of pair interaction in the pair fraction basis

H Enthalpy

I Ion current intensity

${}^{i}L_{A,B}$ Redlich-Kister term of interaction in the site fraction basis, $I \geq 0$

n_A Amount of A

n_{AB} Amount of AB pairs

O Octahedral site

P Pressure

$q^{ij}_{A,B}$ Term in a series expansion of a Quasichemical Gibbs energy of pair interaction in the equivalent fraction basis

$q^{ijk}_{A,B(C)}$ Coefficient of a ternary A-B(C) Quasichemical interaction

R Gas constant

s.s.	Solid solution
$S°_{298}$	Standard entropy at 298K
T	Temperature
T	Tetrahedral site
T_{glass}, T_{gl}	Glass transition temperature
T_{misc}	Miscibility temperature
T_{ref}	Reference temperature (in drop calorimetry)
$\overline{x}$	Composition vector
x_A, X_A	Molar fraction of A
X_{AB}	Molar fraction of AB pairs
Y_A	Equivalent molar fraction of A
Z_A	Coordination number of A
$Z^A{}_{AB}$	Coordination number of A when surrounded by B
$\Delta_{A,B//X,Y}$	Reciprocal interaction parameter
$\Delta_f H$	Enthalpy of formation (from elements or oxides)
$\Delta_{fus} H$	Enthalpy of fusion
$\Delta g_{A,B}$	Gibbs energy of quasichemical pair interaction
ΔG^{ex}	Excess Gibbs energy of mixing
$\Delta_{mix} H$	Enthalpy of mixing of a phase
$\Delta_r G°$	Standard Gibbs energy of reaction
ΔS^{config}	Configurational entropy of mixing
ΔS^{id}	Ideal entropy of mixing
$\Delta_{soln} H$	Enthalpy of solution
$\Delta_{tr} H$, $\Delta_{trans} H$	Enthalpy of transition

θ Characteristic Einstein temperature

$\omega^{ij}_{A,B}$ Term in a series expansion of a Bragg-Williams Gibbs energy of pair interaction in the equivalent fraction basis

Abbreviations:

Ab Albite

Adu Adularia

Aker Akermanite

An Anorthite

And Andalusite

Beta β-alumina, Beta-alumina

Beta'' β''-alumina, Beta''-alumina

BM Beginning of Melting

calc calculated

CALPHAD CALculation of PHAse Diagrams

Ca-Tsch Ca-Tschermak pyroxene

CEF Compound Energy Formalism

Cg Carnegieite

Cor Corundum

Cord Cordierite

cPyr clinopyroxene

cr crystal

CRCT Centre for Research in Computational Thermochemistry

Cri Cristobalite

Dev Devitrite

Di	Diopside
DSC	Differential Scanning Calorimetry
DTA	Differential Thermal Analysis
EMF	ElectroMotive Force
En	Enstatite
exp	experimental
Fds	Feldspar
Fors	Forsterite
g	gas
Geh	Gehlenite
gl	glass
Gro	Grossularite
IR	Infra-Red
Jd	Jadeite
Ks	Kalsilite
Kyan	Kyanite
Lc	Leucite
Leu	Leucite
liq	liquid
Liq	Liquid
mAb	monoAlbite
Mel	Melilite
Mer	Merwinite
misc	miscibility

Mono	Monoxide
MQM	Modified Quasichemical Model
MS	Mass Spectrometry
Mull	Mullite
Ne	Nepheline
NLLS	Non-Linear Least Squares
NMR	Nuclear Magnetic Resonance
Oliv	Olivine
oPyr	orthopyroxene
Or	Orthoclase
Orth	Orthosilicate
pEn	protoEnstatite
pPyr	protoPyroxene
Prp	Pyrope
pWo	pseudoWollastonite
Qz, qz	Quartz
ref	reference
Roed	Roedderite
s	solid
s_1, s_2, s_3	compound polymorths in a *FactSage* database
San	Sanidine
Sap	Sapphirine
SAXS	Small-Angle X-ray Scattering
SEM	Scanning Electron Microscope

Sill	Sillimanite
Sp	Spinel
SRO	Short-Range Ordering
Tri	Tridymite
Wo	Wollastonite
XRD	X-Ray Diffraction

LIST OF APPENDICES

APPENDIX A OPTIMIZED PARAMETERS 489

CHAPTER 1 INTRODUCTION

1.1 Background

The Na_2O-K_2O-Al_2O_3-CaO-MgO-B_2O_3-SiO_2 system studied in this work includes materials made and used in glass making, cement production, steelmaking and non-ferrous metal production (slags, fluxes and refractories). It is also important in the process of coal combustion and geology: this system includes the majority of rocks and minerals on Earth.

Alkali-containing systems play an important role in glass making. Alkali oxides are used as fluxing modifiers in the production of glass: the addition of alkali oxides to silica allows a decrease in the liquidus temperature. The most common glass compositions belong to the CaO-Na_2O-SiO_2 system. To produce glasses with specific properties such as a high refractive index, low thermal expansion, or a high mechanical and chemical resistance, other elements are added. For example, potassium is important in the production of the chemically strengthened glasses used in tablets and smartphones [1]. Boron oxide is another important component of glasses with special properties. It is used in the production of mechanically resistant fibres [2]. High-quality optical fibre and so-called “E-glass” with extra low electric conductivity contain boron oxide [3]. Boron-containing glasses are indispensable in the production of chemically and thermally resistant laboratory equipment, cookware and solar panels [4]. To increase the chemical resistance and to slow the aging process alumina is added. It is also a component of glasses used for the entrainment of nuclear waste. Information on the phase stability in these glasses would allow to increase the possible time of nuclear waste storage [5].

Knowledge of the properties of alkali containing slags is important in coal combustion. Traces of alkalies in coal (mostly potassium) become volatile during combustion and the resulting alkali vapor reacts with refractory materials, with consequent vitrification, which can cause clogging and sudden rupture of the top layer of refractory bricks [6, 7].

Alkali oxides are an essential part of some geologically important groups of minerals (feldspars, nepheline, kalsilite, leucite) and can potentially dissolve in others (melilite, clinopyroxene).

Alkali oxides dissolve in hydraulically active phases ($Ca_3Al_2O_6$) of cement powders modifying their hydration abilities and parameters [8, 9].

A layered structure of β- and β”-alumina makes them very good ionic conductors with mobile sodium or potassium cations. They find applications in fuel cell and battery technology [10].

1.2 Statement of the problem

The optimization of the alkali-containing part of the Na_2O-K_2O-CaO-MgO-Al_2O_3-B_2O_3-SiO_2 system is challenging in several ways. First, there is the difficulty of identifying a correct modeling approach that reproduces the essential features of the investigated systems in a natural and physically consistent way. Secondly, there is the challenge of the organization, classification and analysis of the available experimental data.

The binary systems Na_2O-SiO_2, K_2O-SiO_2, Na_2O-B_2O_3 and K_2O-B_2O_3 are systems with the most negative enthalpies of mixing among binary oxide systems. Such strong deviations from ideality require accounting for the short-range ordering that appears. A steep silica liquidus together with the metastable miscibility gap present a weak point of the previous optimizations of the Na_2O-SiO_2 and the K_2O-SiO_2 systems. The ternary systems Na_2O-Al_2O_3-SiO_2 and K_2O-Al_2O_3-SiO_2 feature the “charge compensation effect” [11]: aluminium ions entering the silica network keep nearby an immobilized alkali ion forming $NaAl^{4+}$ and KAl^{4+} associates, correspondingly.

Unlike silicon, boron is able to change its coordination number in mixtures with alkalies. Three- and four-coordination boron cations form complex clusters whose concentration depends on the composition: boroxol, pentaborate, tetraborate, diborate, metaborate, etc. Alkali-boron oxide systems are sometimes said to have medium-range order due to the presence of multiple clusters [12]. According to the behaviour of thermodynamic properties, alkali borate systems exhibit double compositions of maximum short-range ordering: the main one located at $x(B_2O_3) = 0.25$ and the secondary one at $x(B_2O_3) = 0.8$. Another unique feature of binary alkali borate systems is the presence of a metastable miscibility gap with the critical temperature essentially the same among systems with different alkali cations; the majority of systems with miscibility gaps show a clear correlation of the critical temperature and the cationic radius. The miscibility gap is located approximately at the composition of the secondary maximum short-range ordering which also makes it unique and challenging from the modeling point of view.

The alkali-poor parts of the Na_2O-B_2O_3-SiO_2 and K_2O-B_2O_3-SiO_2 systems feature a ternary metastable miscibility gap which plays an important role in the production of B_2O_3-containing glasses with special purposes.

The amount of experimental data on the system in the literature is substantial because of the importance in various areas of interest and applications. For example, there is a significant body of phase diagram data on the quinary Na_2O-CaO-MgO-Al_2O_3-SiO_2 system which contains many geologically important compositions. The data on this multicomponent system were analysed along with the data on binary and ternary systems. They are required for optimization of multicomponent solid solutions and serve to evaluate the quality of optimizations of the binary and ternary subsystems.

1.3 Scope of the work

This thesis deals with the thermodynamic optimization of the Na_2O-K_2O-CaO-MgO-Al_2O_3-B_2O_3-SiO_2 system. The non-alkali part of the system has been optimized previously [13-16]. Compatible optimizations of the subsystems in the Na_2O-K_2O-Al_2O_3-SiO_2, Na_2O-Al_2O_3-MgO-SiO_2, K_2O-Al_2O_3-MgO-SiO_2 and CaO-K_2O-Al_2O_3-SiO_2 already exist [11, 17-20]; however, we reoptimized them because of the new optimization approach based on the dimer Na_2 and K_2 species in the Na_2O-SiO_2 and K_2O-SiO_2 systems.

Within this research, all alkali-containing systems in the Na_2O-K_2O-Al_2O_3-CaO-MgO-SiO_2 system, all binary and ternary alkali boron subsystems and a few alkali boron subsystems with the number of components more than three were optimized. The results of this work have been communicated to the Glass Consortium who financed the project. Due to the overwhelming amount of data on the whole seven-component system only some of the optimizations were included in this thesis - specifically the complete Na_2O-K_2O-CaO-Al_2O_3-SiO_2 and Na_2O-CaO-MgO-Al_2O_3-SiO_2 subsystems, the ternary K_2O-MgO-SiO_2 system and the binary and ternary subsystems in the Na_2O-K_2O-B_2O_3-SiO_2 system.

1.4 Methodology

In a thermodynamic optimization each phase is described based on its Gibbs energy function. The choice of the Gibbs energy for modeling is explained as it is a characteristic function: all other thermodynamic properties can be expressed as functions of the Gibbs energy and/or its derivatives. The natural variables of the Gibbs energy are temperature, pressure and composition. There are different thermodynamic models and formalisms available, each with a different applicability and limitations. A thermodynamic model for a phase must be chosen based on its composition span, structure, the nature and the strength of the interactions.

Thermodynamic models define the functional form of the Gibbs energy with parameters whose values need to be constrained during the optimization procedure. In this work, the generally accepted approach of CALPHAD ("CALculation of PHAse Diagrams") was used. In this approach, in order to obtain a set of parameters for all phases in a system, all available phase diagram and thermodynamic data are evaluated simultaneously. The derived parameter sets are compiled together with the model descriptions into electronic thermodynamic databases which are later used to calculate thermodynamic properties and phase diagrams using thermodynamic software, such as *FactSage*. A fundamental difference between a thermodynamic optimization and a simple parameter fitting is that the optimization is based on a sound physical model of the Gibbs energy, which unites all thermodynamic properties together and sets thermodynamic constraints upon them. For example, activity data can be used together with phase diagram data to find experimental discrepancies based on other data sets.

The described methodology can be represented in the following steps:

- The literature is reviewed to collect all available data that can be useful for thermodynamic optimization: phase diagrams, site occupancies, activity measurements, calorimetry, etc.
- Stoichiometric compounds and solution phases are identified with the consideration of the possible solubility and exchange mechanisms. This information is used to choose the specific model for each phase.

- The optimization of a multicomponent system begins with the optimization of its subsystems, which recursively leads to the optimization of the ternary, binary and unary systems. Sometimes, however, subsystems need to be optimized with regard to the data in the supersystem. It is often the case that an optimization is based on a set of previously optimized subsystems. This work used previous optimizations for all unary systems as well as the non-alkali parts of the Na_2O-K_2O-CaO-MgO-Al_2O_3-B_2O_3-SiO_2 system.
- The model parameters for a given system are estimated for stoichiometric compounds and subsequently for the solid and liquid solutions. Areas lacking in experimental data to fix the parameters are identified. Sometimes optimizations are coupled with experiments; however, in this work no experiments were made due to the vast scope and the significant time such experiments require. Areas remaining unexplored in the Na_2O-K_2O-CaO-MgO-Al_2O_3-B_2O_3-SiO_2 system usually present significant experimental challenges and resolving them requires substantial effort and experience.

1.5 Organization of the thesis

The thesis begins with an overview of the calculation procedures and methods used in this work (Chapter 2). The thermodynamic software *FactSage* is discussed in Section 2.1 with the general principles of the Gibbs energy minimization and an overview of the phase diagram tracing algorithms. Sections 2.2-2.4 discuss innovative methods of data processing which were utilized in this work. These sections also introduce the proprietary software developed during the research.

Section 2.5 describes glass thermodynamics and the nature of the glass transition considering the differences in thermodynamic properties between glasses and liquids of the same composition. Methods to recalculate these properties into the properties of the corresponding liquids are proposed.

Chapter 3 describes the thermodynamic models employed within this work for stoichiometric compounds, solutions close to ideality, solutions with short-range ordering and solid solutions with multiple sublattices.

Chapter 4 details solid solution models developed and/or extended in this work. Wherever possible, the crystallochemical structures of solid solutions are presented and discussed. Thermodynamic models of these solutions were developed based on the structural similarities, equivalency of atom positions and substitution mechanisms.

Chapter 5 introduces corrections to the existing optimizations of the Al_2O_3-SiO_2 and Al_2O_3-B_2O_3-SiO_2 systems caused by the new Mullite model. However, full reoptimization of these systems is beyond the scope of the current work.

Chapter 6 through Chapter 26 and Chapter 28 through Chapter 32 present uniform and consistent optimizations of different systems described herein. All experimental data are reviewed in the corresponding sections: primarily, phase diagram, calorimetry, activity, heat capacity and heat content data with an optimization chapter terminating in a section on the optimization results, our assumptions and the choice of specific optimization parameters. The listing of the properties of the stoichiometric compounds and solution phases in each system appears in Appendix A.

Due to a high complexity, the modeling approach to alkali-boron-containing systems is discussed separately from the corresponding optimizations (see Chapter 27).

1.6 Names of compounds and solutions

The following abbreviations of complex oxides with long formulas are accepted: a compound is written in the basis of simple oxides denoted with the corresponding capital letters: A for Al_2O_3, N for Na_2O, S for SiO_2, etc. For example, the $Na_2Ca_3Si_6O_{16}$ compound is written as NC3S6 with the coefficients denoted without subscript. Common names of compounds that are generally accepted in the literature are used. For instance, the low-temperature form of $CaSiO_3$ is called wollastonite while the high-temperature modification is generally referred to as pseudowollastonite. Table 1.1 is comprised of compound names accepted within this work. Both stoichiometric and non-stoichiometric compounds with their formulas within quotation marks are listed.

Table 1.1 Names and abbreviations of compounds in this work. Non-stoichiometric formulas are shown within quotation marks.

Name	**System**	**Chemical formula**	**Abbreviation**	**Part of a solid solution in this work**
corundum	Al_2O_3	Al_2O_3	Cor	Corundum
cristobalite	SiO_2	SiO_2	Cri	–
tridymite	SiO_2	SiO_2	Tri	–
quartz	SiO_2	SiO_2	Qz	–
wollastonite	CaO-SiO_2	$CaSiO_3$	Wo	Wollastonite
pseudowollastonite	CaO-SiO_2	$CaSiO_3$	pWo	Pseudowollastonite
rankinite	CaO-SiO_2	$Ca_3Si_2O_7$	–	–
hatrurite	CaO-SiO_2	Ca_3SiO_5	–	Ca3SiO5
forsterite	MgO-SiO_2	Mg_2SiO_4	Fors	Olivine
enstatite	MgO-SiO_2	$MgSiO_3$	Ens	Protopyroxene
mullite	Al_2O_3-SiO_2	“A3S2”	Mull	Mullite
sillimanite	Al_2O_3-SiO_2	Al_2SiO_5	Sill	–
andalusite	Al_2O_3-SiO_2	Al_2SiO_5	And	–
kyanite	Al_2O_3-SiO_2	Al_2SiO_5	Kyan	–
β-alumina, β-Al_2O_3	Al_2O_3-Na_2O, Al_2O_3-K_2O	“$NaAl_9O_{14}$”, “KAl_9O_{14}”	Beta	Beta-alumina
β”-alumina, β”-Al_2O_3	Al_2O_3-Na_2O, Al_2O_3-K_2O	“$Na_2Al_{12}O_{19}$”, “$K_2Al_{12}O_{19}$”	Beta”	Beta”-alumina
nepheline	Al_2O_3-Na_2O-SiO_2	$NaAlSiO_4$	Ne	Nepheline
carnegieite	Al_2O_3-Na_2O-SiO_2	$NaAlSiO_4$	Cg	Carnegieite
jadeite	Al_2O_3-Na_2O-SiO_2	$NaAlSi_2O_6$	Jd	Clinopyroxene
albite	Al_2O_3-Na_2O-SiO_2	$NaAlSi_3O_8$	Ab	Feldspar
monalbite	Al_2O_3-Na_2O-SiO_2	$NaAlSi_3O_8$	mAb	Feldspar
analbite	Al_2O_3-Na_2O-SiO_2	$NaAlSi_3O_8$	aAb	Feldspar
kalsilite	Al_2O_3-K_2O-SiO_2	$KAlSiO_4$	Ks	Nepheline
leucite	Al_2O_3-K_2O-SiO_2	$KAlSi_2O_6$	Lc, Leu	Leucite
orthoclase	Al_2O_3-K_2O-SiO_2	$KAlSi_3O_8$	Or	Feldspar
sanidine	Al_2O_3-K_2O-SiO_2	$KAlSi_3O_8$	San	Feldspar
adularia	Al_2O_3-K_2O-SiO_2	$KAlSi_3O_8$	Adu	Feldspar
devitrite	CaO-Na_2O-SiO_2	$Na_2Ca_3Si_6O_{16}$	Dev	–
combeite	CaO-Na_2O-SiO_2	“NC2S3”	–	Combeite
gehlenite	Al_2O_3-CaO-SiO_2	$Ca_2Al_2SiO_7$	Geh	Melilite
anorthite	Al_2O_3-CaO-SiO_2	$CaAl_2Si_2O_8$	An	Feldspar
Ca-Tschermak	Al_2O_3-CaO-SiO_2	$CaAl_2SiO_6$	Ca-Tsch	Clinopyroxene
grossularite	Al_2O_3-CaO-SiO_2	$Ca_3Al_2Si_3O_{12}$	Gro	Garnet
cordierite	Al_2O_3-MgO-SiO_2	$Mg_2Al_4Si_5O_{18}$	Cord	Cordierite
sapphirine	Al_2O_3-MgO-SiO_2	$Mg_4Al_{10}Si_2O_{23}$	Sap	–
pyrope	Al_2O_3-MgO-SiO_2	$Mg_3Al_2Si_3O_{12}$	Prp	–

Name	**System**	**Chemical formula**	**Abbreviation**	**Part of a solid solution in this work**
diopside	CaO-MgO-SiO_2	$CaMgSi_2O_6$	Di	Clinopyroxene
akermanite	CaO-MgO-SiO_2	$Ca_2MgSi_2O_7$	Aker	Melilite
merwinite	CaO-MgO-SiO_2	$Ca_3MgSi_2O_8$	Mer	Merwinite
roedderite	K_2O-MgO-SiO_2	$K_2Mg_5Si_{12}O_{30}$	Roed	Roedderite

A distinction is made between the names of minerals and the names of solution models. Usually, the names of solution models begin with a capital letter. For example, nepheline is a mineral with a variable composition, Nepheline is a solution model that describes nepheline and kalsilite minerals (see Section 4.2 for more details). The aliases for solid solutions used in this work are listed in Table 1.2.

Table 1.2 Synonyms and aliases of solid solutions used in this work.

Solid solution	**Aliases**
Mullite	Mull
Nepheline	Ne
Carnegieite	Cg
Leucite	Leu, Lc
Beta-, Beta”-Alumina	Beta, Beta”
Feldspar	Fds
Melilite	Mel
Pseudowollastonite	pWo
Wollastonite	Wo
Ca-Orthosilicate	C2S
Mixed Orthosilicate	Orth
Clinopyroxene	cPyr
Protopyroxene	pPyr
Orthopyroxene	oPyr
Monoborate	MonoB
Diborate	DiB
Triborate	TriB

CHAPTER 2 CALCULATION PROCEDURES

2.1 Thermodynamic software

All thermodynamic calculations in this work were performed using the *FactSage* software package. *FactSage* consists of several modules grouped according to their functions: database management, calculations and post-calculation treatment.

Internally, *FactSage* uses a Gibbs energy minimization algorithm (SOLGASMIX) to calculate the compositions of the coexisting phases at equilibrium. The total Gibbs energy of the system is minimized as a function of the system variables (usually, phase amounts and phase compositions) with given constraints such as temperature, pressure and amounts of system components.

Equilib module is a flexible tool for calculation of data presented in a tabular form. Both ordinary and target calculations are supported, and the calculated data can be exported to a number of formats for consequent treatment outside of *FactSage*.

PhaseDiagram module allows to calculate phase diagrams with different variables as axes. The module uses the Zero Phase Fraction line (ZPF) method to plot the areas with different stable phases [21]. First, the algorithm scans the axes for changes in phase assemblages and then traces along the lines at which a certain phase starts to exist (activity is equal to one, the phase amount is equal to zero). If any other phase changes occur at certain points of the traced lines, they are also traced. One of the drawbacks of the ZPF technique is that isolated phase boundary lines cannot be captured. For example, in the Na_2O-B_2O_3-SiO_2 system, the metastable miscibility gap forms an ellipsoid at ternary compositions without touching the axes. In this particular case, the phase boundary had to be calculated in *Equilib* and plotted manually. There are methods which do not have the same drawback, such as the convex hull method [22]. This method allows to plot a binary or a ternary diagram very fast including isolated phase boundaries, but it is not very efficient in the case of sections through multicomponent systems. One of the requirements of the convex hull method is that the Gibbs energy should be calculated over the whole compositional region while the ZPF along with Gibbs energy minimization does not have this requirement.

Experimental data used in this work are usually presented graphically in the form of phase diagrams or charts where experimental points are compared to lines calculated in *FactSage*. Visual

estimation of the quality of optimization is preferred over statistical methods. Model parameters are reported in the same form as in the database files without rounding. Usually, in thermodynamic models, all parameters have significant correlation which leads to non-diagonal values of the dispersion matrix. Removing "insignificant" digits in parameter values in the rounding procedure, however, is done using only the diagonal values of the dispersion matrix. No parameter rounding was done in order to avoid accuracy losses.

2.2 Processing of heat capacity and heat content data

Thermodynamic software such as *FactSage* requires compounds and solution end-members to have their C_P data expressed in a fixed polynomial form:

$$C_P(T) = a + bT + cT^{-2} + dT^2 + \sum_{i=1}^{4} e_i T^{k_i} \tag{1}$$

where k_i is a real number.

This approach is quite common for representing thermodynamic data and implies that the whole temperature range of interest is split into one or more intervals with a separate C_P equation in form (1). This common approach, however, has a few drawbacks.

From the physical point of view, a heat capacity curve of a non-metallic compound without phase transitions arises due to consequent excitations of complex oscillation modes in the crystal. Upon heating a crystal from around 0K, first collective lattice vibrations with low energy take place and soon reach saturation. Next, individual bond vibrations with higher excitation energy start to occur. Different physical models were developed to capture this behaviour, assuming excitation of certain vibrational states. For example, the Debye model derives the heat capacity at low temperatures based on a uniform continuous spectrum of low frequency vibrations. The Einstein model assumes that the heat capacity is derived from a single frequency vibrational mode. The essential properties of any heat capacity curve (without phase transitions) are a monotonous growth starting from zero at 0K up to a limiting value which is reached asymptotically (the law of Dulong-Petit).

However, the polynomial equation (1) is not derived from any feasible physical model and is usually chosen because of its good fitting properties. Therefore, the C_P values predicted outside the

defined temperature range are not reliable. They can decrease with growing temperature, reach negative or infinite values. This equation can be used only for interpolation purposes.

Strictly speaking, if a few temperature intervals are used, the values of the polynomials and their first derivatives at the joint ends of the intervals must be the same. From the practical point of view, however, one just needs to be sure that the values of the polynomials are close enough, so the difference does not affect any calculations.

In the optimization practice, it is important to extend the heat capacity of a compound over a vast temperature interval while the experimental data are only available in a rather small temperature range. It is impossible to do so with polynomials like (1). This would require an extrapolation procedure with a set of equations chosen due to their physical consistency and not only fitting flexibility.

The approach used in the current work is based on representation of a non-anomalous heat capacity curve as a sum of Einstein functions [23]:

$$C_P(T) = \sum_{i=1}^{k} C_{En}\left(\frac{\theta_i}{T}\right) \tag{2}$$

where

$$C_{En}\left(\frac{\theta}{T}\right) = 3R\left(\frac{\theta}{T}\right)^2 \frac{\exp\left(\frac{\theta}{T}\right)}{\left[\exp\left(\frac{\theta}{T}\right)-1\right]^2} \tag{3}$$

A set of equations (2) has good extrapolation properties because they are derived from the Einstein model. In its pure form, the Einstein model is rarely used to fit experimental heat capacity data. However, if several Einstein functions are used, the reproduction of experimental results is much better. Although Voronin and Kutsenok [23] argue that their model has flaws because, strictly speaking, the Einstein model is developed using the assumption of a constant volume and not a constant pressure, the approach still gives excellent results because of a good guess of the class of fitting functions [23]. The original article discusses the applicability of Einstein functions for fitting of heat capacities at a constant pressure in detail.

Using the model, the heat capacity can be interpreted as a result of the vibrational excitation of a few most relevant vibrational modes. Low-energy Debye contribution is important only for temperatures close to 0K and makes up only a fine adjustment to the compound entropy according to:

$$S^{\circ}_{298} = \int_{0K}^{298K} \frac{C_P(T)}{T} dT \tag{4}$$

There are three main types of experimental data concerning the heat capacity available in the literature: adiabatic calorimetry, differential scanning calorimetry, and drop calorimetry

Adiabatic calorimetry is a high accuracy technique allowing to measure the heat capacity starting from the liquid helium temperatures up to the room temperatures. Due to technical difficulties, the measurement temperatures seldom exceed 300-350K. Adiabatic calorimetry allows to calculate the standard entropy of compounds, but its drawbacks are a high cost and relatively long measurements times.

Differential Scanning Calorimetry (DSC) is a cheaper and faster technique but the existing technologies set the lower temperature limit down to the liquid nitrogen region although the upper limit can be as high as several hundred degrees. DSC is generally considered a less accurate technique due to the dynamic nature of measurements.

Drop calorimetry does not measure the heat capacity directly but rather its integrated form, called the heat content:

$$H(T) - H(T_{ref}) = \int_{T_{ref}}^{T} C_P(T) dT \tag{5}$$

where T_{ref} is generally close to the room temperature.

It is rare that for a given compound all three types of data are available. For instance, it is desirable to be able to derive the high temperature C_P if only adiabatic calorimetry data are available. It is sometimes also required to estimate the entropy based on DSC data or even heat content. Using the method described above, it becomes possible.

In this work, a software tool was developed which allows to extrapolate heat capacities beyond a measured temperature interval in a consistent manner based on the method described by Voronin and Kutsenok [23].

CpFit program is a hybrid application with a graphical interface written in *Java* programming language and a backend (calculation routines) provided by *MATLAB* package. Its graphical interface consists of two windows called *Fitting* and *Splitting* interfaces (Figure 2.1).

Experimental data are stored in ordinary *Excel* files for greater convenience of users who are not familiar with the intricacies of *MATLAB* software. The application is loaded from inside the *MATLAB* environment. It allows to export the fitted functions into the *MATLAB* workspace automatically for further advanced handling, if needed.

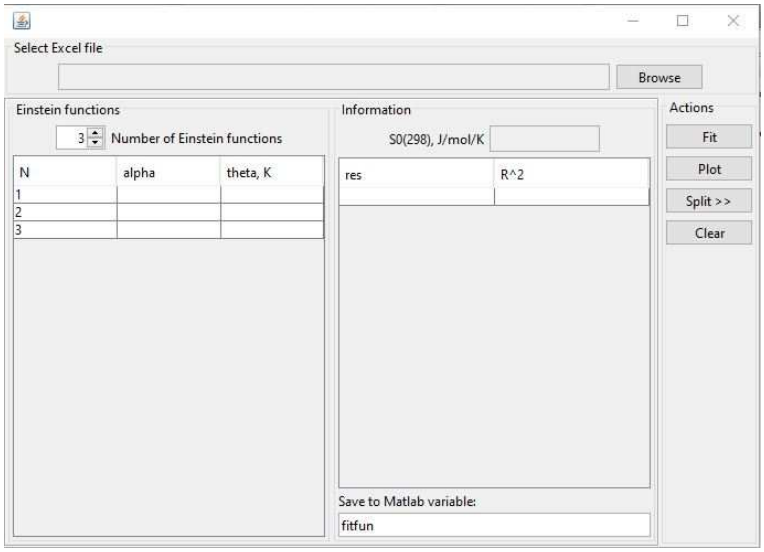

(***a***)

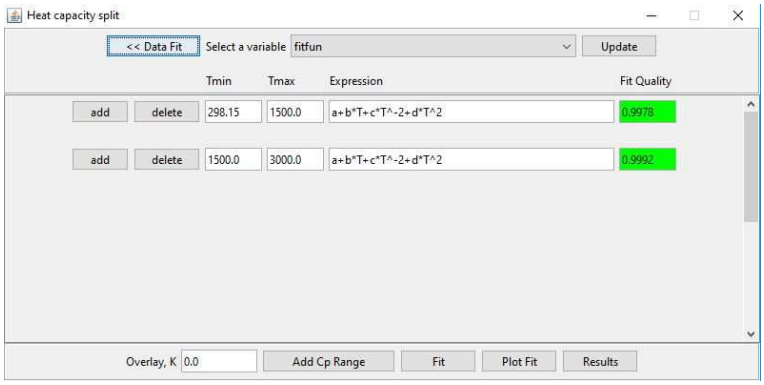

(***b***)

Figure 2.1 Fitting (***a***) and Splitting (***b***) interfaces of *CpFit* program.

Experimental data (the heat capacity and the heat content) are loaded from an *Excel* file and then fitted with Einstein functions whose number can vary. Generally, 4 or 5 functions are enough if there are low-*T* heat capacity data in a dataset. Datasets with only heat content data are recommended to fit only with one function to avoid overfitting.

The quality of a fit is controlled with the values of residuals and the correlation coefficient as well as visually plotting the data together with the prediction curves. The standard entropy is automatically calculated for each fit. Usually, its value is in a good agreement with the values calculated in the literature based on adiabatic calorimetry and it can also be a good estimation if DSC data are used starting from the liquid nitrogen region.

The obtained function provides a good extrapolation to non-investigated temperatures and even temperatures beyond the decomposition or melting point of the compound. However, the optimized coefficients cannot be directly inserted into a compound database and need to be converted to the form accepted by *FactSage*. The *Splitting* interface was designed to transform Einstein-sum fits into polynomials accepted by *FactSage Compound* module.

The number of temperature intervals and their limits are freely chosen. In this work, fitting was generally performed inside a single interval 298-3000K in the form:

$$C_P(T)=a+bT+cT^{-2}+dT^2+eT^n \quad (6)$$

It was empirically found that values of n of -1, 0.5 and -0.5 usually work the best.

CpFit program proved to be useful even if there are no experimental data available for a compound. For illustrative purposes, let us assume we want to estimate the heat capacity of $NaAlO_2$ compound based only on heat capacities of simple oxides (although there are C_P data for it). If we were to estimate its heat capacity with Neumann's rule, the following equation would be used:

$$C_P(NaAlO_2)(T)=0.5C_P(Na_2O)(T)+0.5C_P(Al_2O_3)(T) \quad (7)$$

Unfortunately, the development of the *FToxid* database began a long time ago and the C_P functions for many simple compounds resemble those for Na_2O and Al_2O_3 in Figure 2.3. These functions represent the heat capacity of the most stable phase at a given temperature including phase transitions. However, they are assigned only to the solid phase. Looking at the Na_2O-Al_2O_3 phase diagram (Figure 2.2), it can be realized that in order to estimate the C_P function of $NaAlO_2$ around its melting point we would need to extrapolate the C_P function of Na_2O to it, although Na_2O itself melts at a much lower temperature.

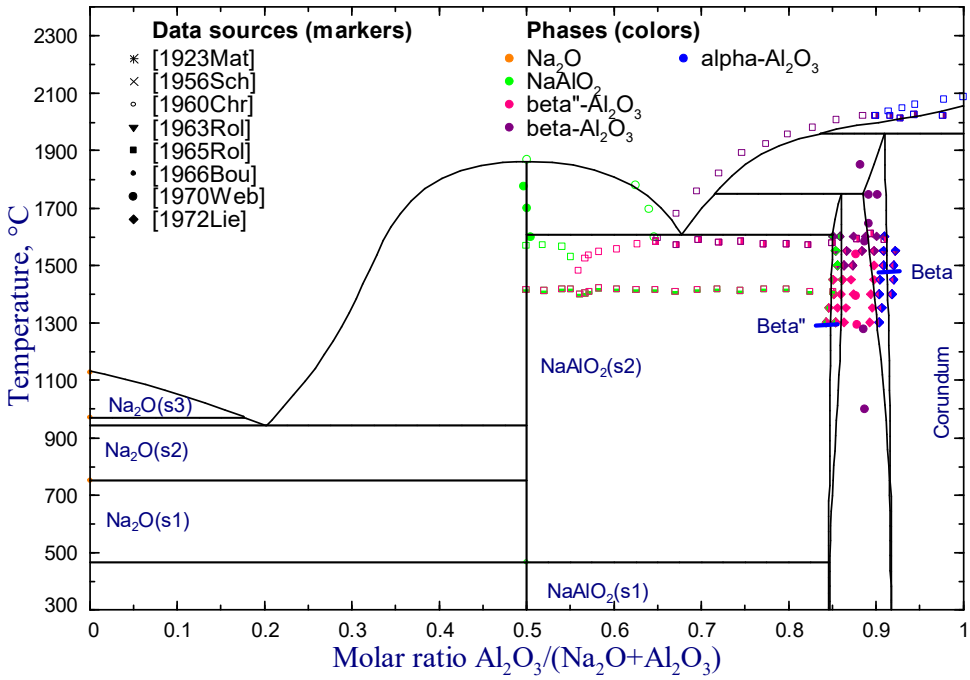

Figure 2.2 The Na_2O-Al_2O_3 phase diagram (given for illustrative purposes).

If the heat capacities of Na_2O and Al_2O_3 are taken directly from the *FToxid* database, the resulting curve for $NaAlO_2$ looks like in Figure 2.3 (the green solid curve). It has two jumps derived from the melting transitions of Na_2O and Al_2O_3 although it is obvious that $NaAlO_2$ should not have them.

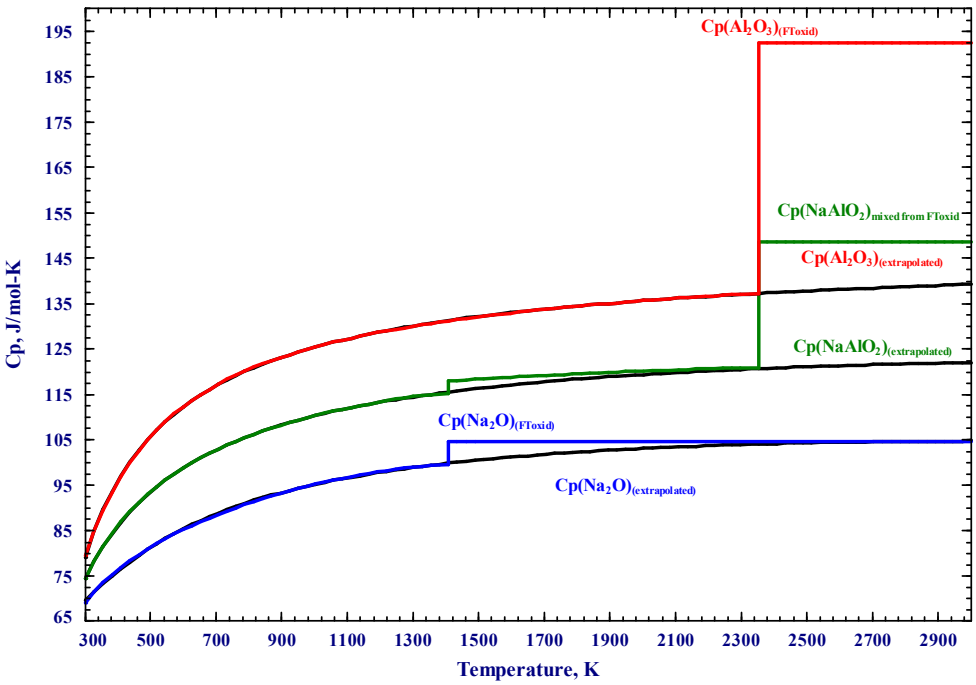

Figure 2.3 The heat capacities of Na_2O and Al_2O_3 as in the current *FToxid* database together with the extrapolated values (*CpFit* program). The $NaAlO_2$ heat capacity is calculated using Neumann's rule from the *FToxid* (colored lines) and extrapolated heat capacities (black lines) of Na_2O and Al_2O_3, correspondingly.

If, however, we take the lower smooth parts of Na_2O and Al_2O_3 heat capacities and extrapolate them using *CpFit* program to a certain high temperature (in this work, 3000K) and then use these smoothed C_P curves (shown as black lines in Figure 2.3), we would obtain a smooth heat capacity for $NaAlO_2$ without artifacts. It was not feasible to change the C_P functions for Na_2O, Al_2O_3 and some other simple compounds as this would require to reoptimize the whole *FToxid* database. However, we tried to include smoothed extrapolated C_P functions for the compounds included in this work whenever it was possible.

2.3 Modeling of solid solutions with end-members undergoing phase transitions

It is often the case that stoichiometric compounds present in oxide systems have several polymorphs with different structures which are stable at different temperatures and pressures. Most

of them differ only in the overall symmetry of the crystal. As a rule, the symmetry grows with the temperature. The symmetry changes are generally caused by relatively small distortions of the crystal lattice without bond rearrangements and with the network topology preserved. Therefore, such distortions have a low activation energy and occur fast. From the thermochemical point of view, symmetry transitions have a low transition enthalpy, on the order of a few $kJ \cdot mol^{-1}$.

Strictly speaking, a solid solution can be formed only among end-members with the same symmetry because from the definition of a solution, all its properties must change smoothly with the composition. To optimize model parameters for two similar solid solutions with different symmetry, their areas of stability need to be known at intermediate compositions. The situation can also be complicated by the fact that some solid solutions with mixed compositions start to exhibit an additional splitting of the symmetry sites at lower temperatures forming another solid solution whose pure end-members are not stable by itself. Omphacites, intermediate ordered compositions in the $CaMgSi_2O_6$-$NaAlSi_2O_6$ clinopyroxenes are such an example.

It is quite common that phase transition data are available only for pure end-members while lacking for intermediate compositions. If we want to model each solid solution separately, in most cases it would be impossible to fix their model parameters. However, for practical applications, it is not important which polymorph exactly forms and they can be merged together into a single solid solution.

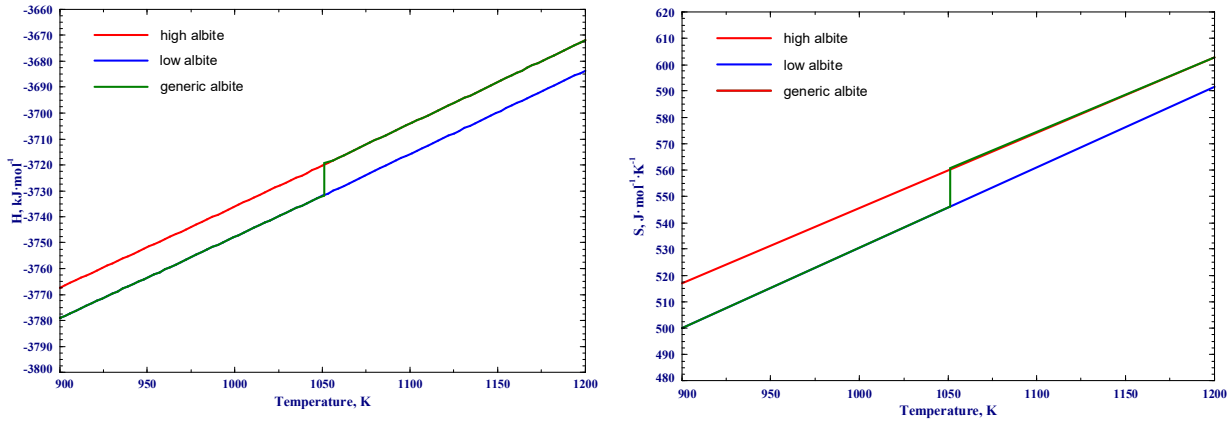

(***a***) (***b***)

Figure 2.4 The specific enthalpy (***a***) and the entropy (***b***) of low-$NaAlSi_3O_8$, high-$NaAlSi_3O_8$ and the generic end-member of Feldspar solution (the values correspond to the $NaAlSi_3O_8$ formula unit).

This work proposed a simplification while constructing models of solid solutions. For end-members with a low phase transition enthalpy and lacking phase stability for intermediate compositions, the regions of different symmetry are treated as a single solid solution. Figure 2.4 gives an example of two end-members with different symmetries. For the single solid solution, we introduce so-called generic end-members which are stable in the whole temperature range and whose Gibbs energy at a given temperature is equal to the Gibbs energy of the most stable polymorph at the same temperature. These generic end-members are present only in the solution database. With the full species selection in *FactSage*, the calculated equilibrium will represent either the true end-members if no solution forms in the system or the generic solid solution if it is present. Figure 2.4 presents an example of the two modifications of albite which were merged into a generic end-member of Feldspar solution.

The enthalpy of transition between two polymorphs is not always small. For example, the transition between nepheline and carnegieite results in a deep topological rearrangement of aluminosilicate chains. The transition enthalpy exceeds a few $kJ \cdot mol^{-1}$ and is around 10 $kJ \cdot mol^{-1}$ per XO_2 unit or 20 $kJ \cdot mol^{-1}$ per $NaAlSiO_4$ formula unit. Therefore, nepheline and carnegieite have to be modeled as two different solid solutions.

2.4 Semi-automated optimization technique

Thermodynamic optimization implies defining a physically sound model for every phase in a system and finding an optimal set of model parameters so that all available thermodynamic data are reproduced in a consistent manner.

FactSage software provides *OptiSage* module which is supposed to serve the optimization purpose. However, it is rarely used because of convergence problems. Usually, model parameters are found manually. In many cases, this is possible because model parameters have different limited ranges of influence on the phase diagram and, therefore, can be set independently with iterative corrections.

However, the scope of the current work includes systems whose optimization requires to include complex species (for example, the Na_2O-Al_2O_3-SiO_2 and Na_2O-B_2O_3-SiO_2 systems). In these systems, the variable separation does not occur, and to find a good solution point manually would be very time consuming. Introduction of complex species also increased the number of independent model parameters.

It was decided to create an automated optimization tool to cope with these problems.

Such a tool would consist of logical parts performing the following tasks:

- the optimization itself, a routine returning an optimal parameter set when provided a residual vector
- storing/retrieving of experimental data with adjustment of data weights and a possibility of switching datasets on and off
- reading/writing to *FactSage* databases (solution databases in a text format and compound databases in a binary format)
- running *FactSage* calculations in a batch from a script without a graphical interface
- reading and interpreting of calculation results saved by *Equilib*

The calculations need to be stored in form of *Equilib* Equi*.DAT files.

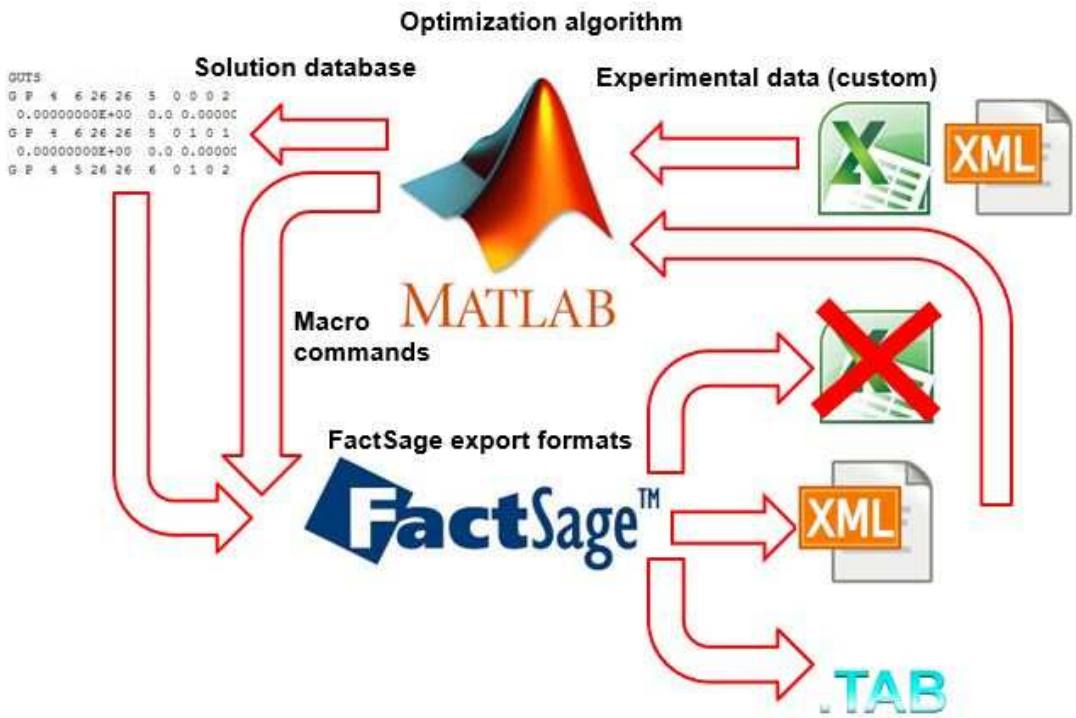

Figure 2.5 The dataflow for automation of the optimization procedure.

The logical parts described above are shown in Figure 2.5. The process is run as a *MATLAB* script using one of the optimization functions of *Optimization* toolbox. The experimental data are stored in *Excel* files or in XML format; a part of the *MATLAB* script reads them. For now, only solution databases in the text format can be accessed. Writing and reading are carried out at indicated positions in a database. Database parsing (recognition) is not performed because it would require a significant time investment. In principle, it is possible to make a routine to access the binary compound format but it was not done because significant time investments are required. Macro processing in *FactSage* allows to execute calculations without the graphical interface. A macro file itself is a text file with *.MAC extension which is composed by a corresponding *MATLAB* code. The calculated results in *FactSage* can be stored in *Excel* files or as XML or a tabulated text format. It was found that if *Excel* output is chosen, it takes unacceptably long times to run. The tabulated format (TAB) is preferred because of its simplicity and flexibility. A stored vector of experimental values and a newly formed vector of calculated values are fed to the optimization algorithm on each iteration together with the data weights.

There are certain requirements to the optimization algorithm: it should be able to deal with non-linear problems, correctly respond to NaN (not-a-number) values resulting from possible calculation failures of *FactSage*, use possibly small number of function evaluations as *FactSage* calculations can be time-consuming, not use direct search or genetic algorithms where parameter values can change unpredictably and cause convergence problems of *FactSage*. *MATLAB* package provides a vast arsenal of optimization algorithms of different types. Empirically it was found that non-linear least squares with Levenberg-Marquardt algorithm worked best for these practical purposes (*lqsnonlin* function). However, a few modifications need to be introduced to the default settings of the algorithm. First, the parameter step for calculation of finite differences must be set to a value around 0.1-1. The default step is too small and does not reflect on the phase equilibria. Secondly, model parameters of different kinds need to be scaled depending on their typical values.

Experimental data are typically stored in *Excel* spreadsheets or in XML files obtained by conversion of the *Excel* spreadsheets. Possible target variables cover all the variables which can be extracted from *FactSage* by one of the output formats. The weighting of datasets of different kinds (liquidus temperature and enthalpies of mixing) is a complex problem by itself and in this work weights were selected according to relative contributions to the residual vector.

There is an *Equilib* file corresponding to every type of the experimental data, which can produce the corresponding calculated values for the optimization algorithm. An optimization set includes several *Equilib* files with the corresponding experimental data and the auxiliary information such as data weights.

The following program workflow is followed each time an optimization is run:

1. The program reads the experimental data from a corresponding storage file;
2. The program sets the initial approximation and the custom settings to the non-linear least squares algorithm (NLLS);
3. The NLLS algorithm repeats function evaluations until one of the stopping criteria is met.

A function evaluation consists of:

1. The parameters are saved to the text database;

2. A macro file is created based on the optimization configuration, including the *Equilib* files to calculate;
3. Command-line instructions are passed to run *FactSage* in the batch mode using the name of the macro file as an input;
4. The calculated values are read from the corresponding output files;
5. A difference vector $\left(\overline{Y}^{\text{calc}} - \overline{Y}^{\text{exp}}\right) \cdot \overline{w}$ is calculated and returned.

There are certain limitations a researcher should be aware of for efficient use of the optimization tool.

Requirements to experimental data quality:

- The optimization tool is not able to have a critical judgement of the quality of the experimental data. It is up to a researcher to verify the data correctness and analyse the way they were measured and also possible uncertainties and errors;
- If there is a noticeable scatter between the data from different sources, it is recommended to define manually how the function should behave and use it for the optimization;
- For miscellaneous data types (liquidus temperatures, activities, enthalpies) the researcher should provide a reasonable weighting scheme. It is recommended to set data type weights according to relative contributions to the residual vector.

Choice of the model parameters:

- It is the researcher's responsibility to define a set of model parameters to optimize. Although one can optimize all possible parameters, it is not recommended as the resulting optimizations tend to have inferior extrapolating properties.
- It should be verified that the parameters used for optimization act in areas sufficiently constrained with available experimental data. Otherwise, an unreasonable parameter value can be obtained.

Choice of a good initial point:

- The target function should not return undefined values at the initial evaluation (although they can be tolerated for the next iterations).
- In case an associate is used, its concentration should be noticeable at the initial evaluation. Otherwise, the parameters related to the associate will not be used.

2.5 Glasses and their thermodynamic properties

2.5.1 Glass transition phenomena

Glasses are amorphous bodies with very high relaxation times compared to liquids. Usually, glasses form upon cooling of viscous liquids. The transition temperature between liquid and glass is called the glass transition temperature. It is not a true thermodynamic transition of either first or higher-order type. Glass transition depends on liquid viscosity and occurs at viscosity values around 10^{13} Ps [24]. Below the glass transition temperature, the properties resemble those of a crystalline body (Figure 2.6).

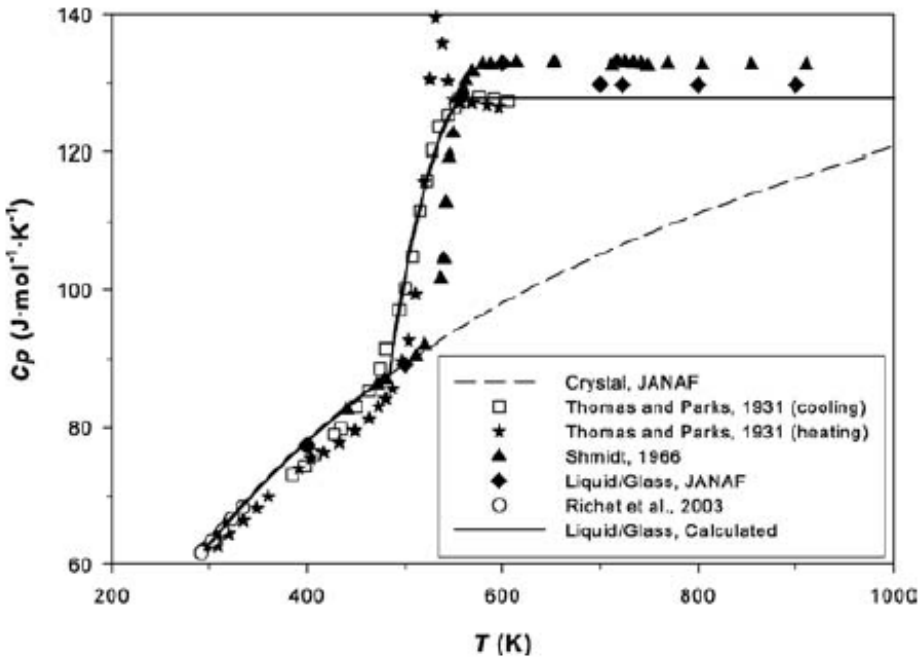

Figure 2.6 The heat capacity of crystal and liquid/glass B_2O_3. The image is taken from Decterov et al. [15].

The heat capacity of a liquid usually does not depend on the temperature. The heat capacity of a glass is temperature-dependent and can be approximated with the heat capacity of a crystalline solid with the same composition. Noticeable deviations between them can be observed only at temperatures near 0K [24].

To avoid a negative value of the entropy of liquid, it is required that at a temperature, low enough, the heat capacity of a liquid drops and becomes zero at the absolute zero. In other words, there is a thermodynamic requirement for any liquid to either crystallize or undergo a glass transition when cooled deep enough. For some liquids, such as molten SiO_2 or B_2O_3, the glass transition can be observed experimentally, for others, such as molten Al_2O_3, Na_2O, CaO, it is purely hypothetical.

The glass transition temperature of liquids with variable composition changes non-linearly with the composition. Usually, in systems of the network former-network modifier type (Na_2O-SiO_2, Na_2O-B_2O_3) the highest T_{glass} corresponds to the composition of the pure network former and drops if a network modifier is added.

It is possible to find the glass transition temperature of oxide melts in *FactSage* using its *Viscosity* module but the Gibbs energy minimization modules (*Equilib* and *Phase Diagram*) do not support calculation involving glasses.

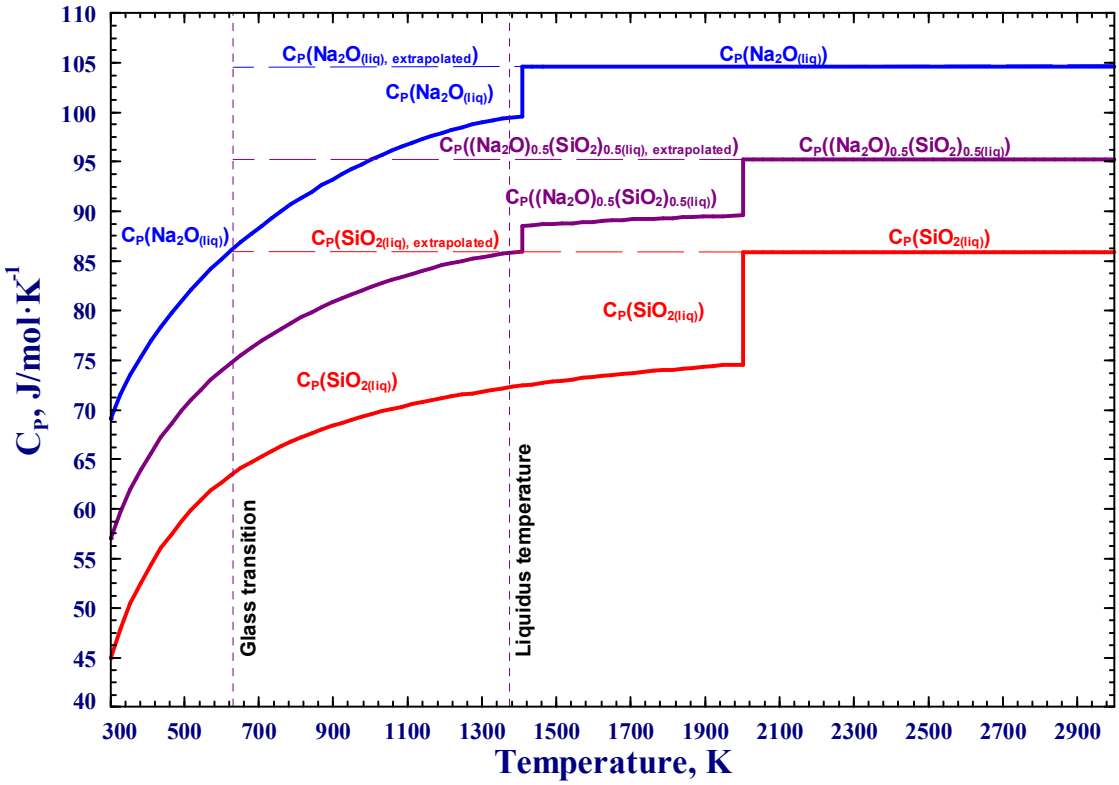

Figure 2.7 The heat capacities of liquids of Na_2O, SiO_2 and $(Na_2O)_{0.5}(SiO_2)_{0.5}$ compositions. The dotted vertical lines indicate the glass transition and the liquidus temperature at $(Na_2O)_{0.5}(SiO_2)_{0.5}$ composition. The solid lines show the heat capacities in the oxide database. The dashed lines are physically consistent extrapolations of the heat capacity of the liquids.

For systems with a wide liquidus range (such as the Na_2O-SiO_2 system), it is important to have a good extrapolation of liquid properties at different temperatures. The experimental heat capacity of liquid with an intermediate composition in Figure 2.7 is constant down to the glass transition temperature for this composition. This heat capacity can be approximated as a weighted sum of the extrapolated constant heat capacities of liquid Na_2O and SiO_2. The heat capacity curves of pure end-members in *FactSage* databases include the phase transitions and actually represent the heat capacity of solids below the melting temperatures. As a result, the calculated heat capacity runs lower than the actual value. This drawback cannot be easily overcome as changes in the solution end-members would require a complete reoptimization of the whole set of systems.

Obviously, liquid heat contents are underestimated with the current oxide database. However, incorrect heat capacities are not important for the functions of mixing. To illustrate that, let us take

the enthalpy of mixing of Na_2O-SiO_2 at T_1, where T_1 is a temperature below the melting points of both Na_2O and SiO_2. Let us recalculate it to T_2, where T_2 is a temperature above the melting points of both end-members assuming there is no excess heat capacity.

$$\Delta_{mix}H\left(\left(Na_2O\right)_{1-x}\left(SiO_2\right)_x,T_1\right)=H\left(\left(Na_2O\right)_{1-x}\left(SiO_2\right)_x,T_1\right)-\left(1-x\right)H\left(Na_2O,T_1\right)-xH\left(SiO_2,T_1\right) \tag{8}$$

$$\Delta_{mix}H\left(\left(Na_2O\right)_{1-x}\left(SiO_2\right)_x,T_2\right)=\Delta_{mix}H\left(\left(Na_2O\right)_{1-x}\left(SiO_2\right)_x,T_1\right)+\int_{T_1}^{T_2}\Delta_{mix}C_P\left(\left(Na_2O\right)_{1-x}\left(SiO_2\right)_x,T\right)dT \tag{9}$$

The integral in (9) is equal to zero without the excess heat capacity and does not depend on the heat capacity of the end-members. Therefore, even if we want to recalculate experimental mixing properties using proper heat capacities of liquid, this would not change anything.

2.5.2 Recalculation of glass calorimetry data

Calorimetry data are important for optimization purposes because they allow to constrain the enthalpy of solutions and compounds. For glass-forming systems, there is an abundance of experimental data on solution calorimetry of glasses (usually at room temperature). The problem is that glass properties cannot be directly reproduced in *FactSage*; therefore, the glass data need to be recalculated to be compared with calculated values.

To be able to use solution enthalpy data for glasses, a correction has to be made to convert these data to those corresponding to the liquid phase. Usually, the experimental data are reported in the form of $\Delta_f H$(glass) from crystalline oxides. The enthalpy of glass can be recalculated using equation (10), the enthalpies of pure liquid end-members are obtained using equation (11). The enthalpy of glass transition is equal to zero; combining them together, we get the enthalpy of mixing of liquid (12) with *n* end-members.

$$H\left(liq,T_1\right)=H\left(glass,T_1\right)+\int_{T_1}^{T_{glass}}C_P\left(glass,T\right)dT+\int_{T_{glass}}^{T_1}C_P\left(liq,T\right)dT \tag{10}$$

$$H_i\left(liq,T_1\right)=H_i\left(solid,T_1\right)+\int_{T_1}^{T_{fus}} C_{P,i}\left(solid,T\right)dT+\Delta_{fus}H_i+\int_{T_{fus}}^{T_1} C_{P,i}\left(liq,T\right)dT \tag{11}$$

$$\Delta_{mix}H\left(liq,T_1\right)=H\left(liq,T_1\right)-\sum_{i=1}^{n}x_iH_i\left(liq,T_1\right) \tag{12}$$

$$\sum_{i=1}^{n}x_i=1 \tag{13}$$

The heat capacities of glasses are approximated as a weighted sum of the heat capacities of pure crystalline end-members. The heat capacities of liquid need to be the same in (10) and (11) in order to make the compensation as in (12).

CHAPTER 3 MODELING APPROACH TO OXIDE SYSTEMS

To characterize thermodynamic properties of a phase, one needs to define its Gibbs energy as a function of the temperature, pressure and composition. The reason why the Gibbs energy is so special for modeling purposes is that it is a so-called characteristic function of a system. In the thermodynamics, a function is called characteristic, if all other thermodynamic properties can be derived from it and its derivatives (first and higher order, if necessary). Any thermodynamic bounds and restrictions (such as the Gibbs-Duhem equation, the Gibbs phase rule) are fulfilled automatically. So, modeling the Gibbs energy is fundamental for optimization.

The pure thermodynamics does not give us any way to predict the Gibbs energy of an arbitrary system. It can be either calculated based on first principles or assessed using experimental data on phase equilibria and thermochemical data. Assessing Gibbs energy functions using available experimental data was chosen in the current work.

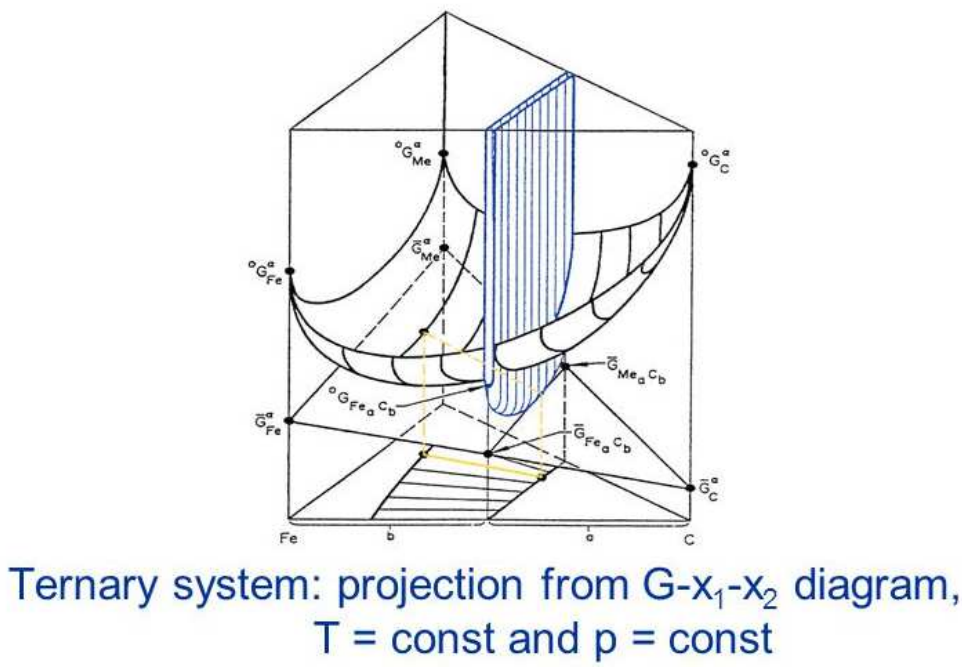

Figure 3.1 Phase diagram as a projection of the Gibbs energy of the system [25].

Strictly speaking, to get a **unique** Gibbs energy function without any prior knowledge is impossible; there is no one-to-one correspondence between the Gibbs energy and the experimental data. A typical example is the assessment of the Gibbs energy from phase diagram data. Figure 3.1

illustrates that a phase diagram of an isothermal section is constructed as a projection of the Gibbs energy to the composition plane. Obviously, the backward transformation is not possible as there are many possible functions with the same projection. Generally, other data are required to reconstruct the Gibbs energy. In terms of projections, we would require a projection to another plane, for example, *G-x*.

There is no direct way to measure the integral Gibbs energy of a phase, but the following relation can be used:

$$G(T,P,\bar{x}) = H(T,P,\bar{x}) - TS(T,P,\bar{x}) \tag{14}$$

In this work, we do not model phase properties as a function of pressure and can, therefore, omit pressure dependency from the model used.

The enthalpy is a function that can be measured experimentally, but to perform the transformation to the Gibbs energy, the entropy of a phase is needed as well. The vibrational part of the entropy can usually be obtained from experimental data or estimated, but its configurational part can be derived only based on physical assumptions. So, a sound model is required to predict the configurational entropy correctly.

A key to a successful optimization is two factors: presence of miscellaneous data and physically sound models for each phase.

3.1 Modeling of stochiometric compounds

The Gibbs energy of stochiometric compounds can be expressed as a function of the temperature in the following manner:

$$G(T) = H - TS = H^{\circ}_{298} + \int_{298}^{T} C_P(T)\,dT - TS^{\circ}_{298} - T\int_{298}^{T} \frac{C_P(T)}{T}\,dT \tag{15}$$

The absolute value of the standard enthalpy H°_{298} cannot be known and a reference state is required. *FactSage* chooses the standard state as the state of pure elements at 298.15 K and 1 atm in their most stable polymorphic modifications. It is possible to calculate the absolute value of the standard entropy S°_{298} as:

$$S^{\circ}_{298} = \int_{0}^{298} \frac{C_P(T)}{T} dT \tag{16}$$

The heat capacity is measured experimentally; in case of lack of data, it can be estimated as an additive function of composition.

The heat capacity depends on the vibrational spectrum of the crystal lattice of a compound. At low temperatures, only low energy vibrations with long wavelengths are present in a crystal. These vibrations depend on the medium and long-range structure configuration. The heat capacity at higher temperatures is mostly contributed to by vibrations of high energy, dependent on the interatomic bonds. The high-temperature heat capacity for an oxide compound is approximately an additive function of the heat capacities of the simple oxides forming the compound [26]:

$$A_xO + B_yO = 2A_{\frac{x}{2}}B_{\frac{y}{2}}O \tag{17}$$

The number of A-O and B-O bonds does not change and, therefore, the heat capacity is an additive function.

The value of the standard entropy also depends on the low temperature heat capacity which is not an additive function of composition. However, its relative contribution is small and in absence of experimental data the entropy can be estimated using an additive scheme (in case there is no configurational contribution).

Unfortunately, the additive schemes do not apply to the standard enthalpy of formation.

3.2 Modeling of solutions with small deviations from ideality

One of the simplest solution models is the random mixing solution model. Let us consider a binary phase consisting of A and B species. At a given temperature and pressure, its Gibbs energy can be written as:

$$G(\bar{x}) = x_A G^{\circ}_A + x_B G^{\circ}_B + RT\left(x_A \ln x_A + x_B \ln x_B\right) \tag{18}$$

The configurational entropy of randomly distributed species is called the ideal entropy. The ideal entropy of mixing is:

$$\Delta S^{id}\left(\overline{x}\right) = -R\left(x_A \ln x_A + x_B \ln x_B\right) \tag{19}$$

The enthalpy of mixing in the ideal model is zero; to account for a nonideality, the excess terms are introduced:

$$\Delta G^{ex}\left(\overline{x}\right) = x_A x_B \alpha\left(\overline{x}\right) \tag{20}$$

The model can describe solutions with a low to medium interaction energy. In this work, it was mostly used to model some simple solid solutions with one sublattice (NCA2, C3A, Pseudowollastonite, Ca-Orthosilicate, Milarite, Monoborate, Diborate and Triborate).

The ideal configurational entropy is the theoretical limit of the configurational entropy possible for a solution phase. Strong interactions reduce the configurational entropy. The total entropy (configurational + vibrational) can only slightly exceed the ideal limit due to the vibrational component. The ideal entropy can be used as a limiting value to estimate the soundness of an optimization.

3.3 Modeling of solutions with short-range ordering

It is quite common in the modeling practice to deal with solutions with significant negative interactions between species. In this case, models with the ideal entropy of mixing do not work well. If A and B have a large interaction energy, the species prefer to be surrounded by the species of the other kind to minimize the total Gibbs energy of the phase. This deviation from randomness leads to a lower entropy of mixing.

The Quasichemical Model accounts for the non-random distribution of species using the assumption of a random distribution of species pairs.

The Gibbs energy of a binary solution with short-range ordering is:

$$G = \left(n_A g_A^{\circ} + n_B g_B^{\circ}\right) - T\Delta S^{config} + \left(n_{AB}/2\right)\Delta g_{AB} \tag{21}$$

where the configurational entropy ΔS^{config} is:

$$\Delta S^{config} = -R\left(n_A \ln X_A + n_B \ln X_B\right) - R\left[n_{AA}\ln\left(\frac{X_{AA}}{Y_A^2}\right) + n_{BB}\ln\left(\frac{X_{BB}}{Y_B^2}\right) + n_{AB}\ln\left(\frac{X_{AB}}{2Y_A Y_B}\right)\right] \tag{22}$$

Y_i 's are "coordination-equivalent" fractions:

$$Y_A = Z_A X_A / \left(Z_A X_A + Z_B X_B \right) \tag{23}$$

And X_{ij} 's are molar fractions of pairs AA, BB and AB.

The ratio of the coordination numbers allows to set a maximum short-range ordering composition. An example of the enthalpy and the entropy of mixing for binary solutions with different degrees of ordering is shown in Figure 3.2.

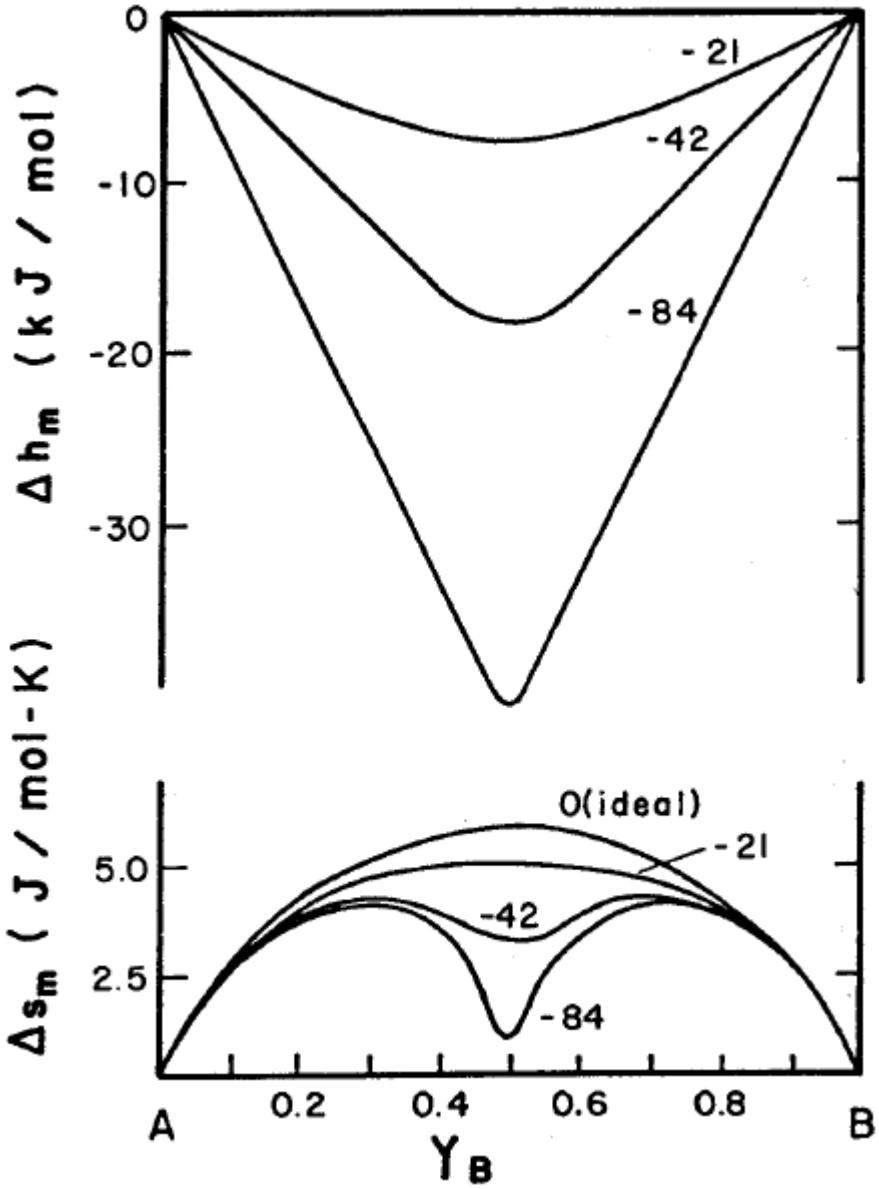

Figure 3.2 The molar enthalpy and the entropy of mixing for a system A-B calculated at 1000°C with $Z_A = Z_B = 2$ from the quasichemical model for short-range ordering with Δg_{AB} = constant = 0, -21, -42, and -84 kJ. The image is taken from Pelton et al. [27].

The Gibbs energy of pair interaction Δg°_{AB} can be expanded as a series in the basis of the coordination-equivalent fractions Y_i (quasichemical parameters, (24)) or in the basis of pair fractions (GUTS parameters, (25)).

$$\Delta g_{A,B} = \Delta g^{\circ}_{A,B} + \sum_{i+j\geq 1} q^{ij}_{A,B} Y^i_A Y^j_B \tag{24}$$

$$\Delta g_{A,B} = \Delta g^{\circ}_{A,B} + \sum_{i\geq 1} g^{i0}_{A,B} X^i_{AA} + \sum_{j\geq 1} g^{0j}_{A,B} X^j_{BB} \tag{25}$$

It is shown that the pair-fraction expansion produces model parameters which are more localized with the composition [27].

If the pair interaction is small, the quasichemical model is reduced to the ordinary Bragg-Williams model with an ideal entropy of mixing, making the two models compatible with each other.

If the pair interaction is strong, the composition of short-range ordering splits the whole composition range of A-B into two independent subsystems with different properties. This behavior reflects phenomena occurring in many real systems with strong interactions. Thermodynamic properties exhibit very significant changes over the composition of the maximum short-range ordering.

The coordination numbers of species are usually expressed as linear functions of composition:

$$\frac{1}{Z_A} = \frac{1}{Z^A_{AA}}\left(\frac{2n_{AA}}{2n_{AA}+n_{AB}}\right) + \frac{1}{Z^A_{AB}}\left(\frac{n_{AB}}{2n_{AA}+n_{AB}}\right) \tag{26}$$

$$\frac{1}{Z_B} = \frac{1}{Z^B_{BB}}\left(\frac{2n_{BB}}{2n_{BB}+n_{AB}}\right) + \frac{1}{Z^B_{BA}}\left(\frac{n_{AB}}{2n_{BB}+n_{AB}}\right) \tag{27}$$

For a ternary system A-B-C, it allows to set the short-range ordering compositions in the binary subsystems independently of each other.

In multicomponent solutions, the Gibbs energy is constructed based on the Gibbs energy in the subsystems. There are several conventional ways to do so and they are geometrically expressed in Figure 3.3.

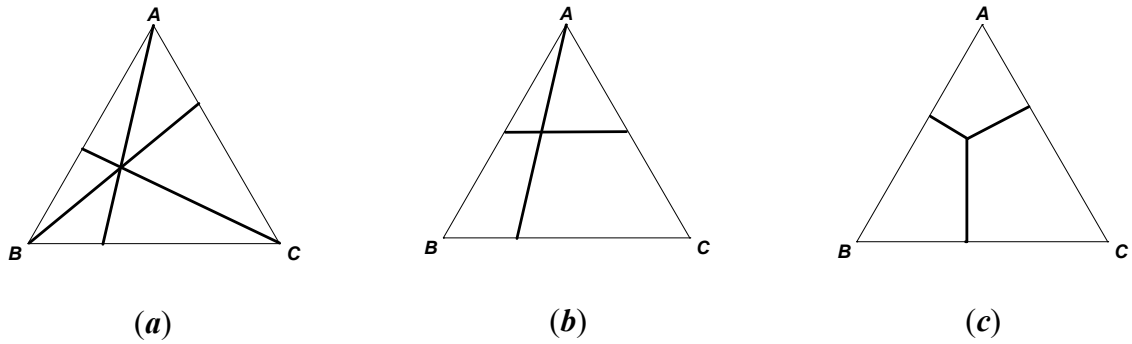

Figure 3.3 Geometrical extrapolation models: Kohler (***a***), Toop (***b***), Muggianu (***c***).

The meaning of the geometrical models is the following: the Gibbs energy of a point in a ternary solution A-B-C is evaluated based on the Gibbs energies of the binary solutions plus the ternary terms, if applicable. The lines in Figure 3.3 show the binary compositions at which the Gibbs energies are evaluated. In the symmetrical Kohler model, it is assumed that the best approximation of the A-B interaction in a ternary solution is the interaction in the binary with the same A/(A+B) ratio as in the ternary. The lines in Figure 3.3, (***a***) show the compositions with a constant ratio of component pairs. The Gibbs energy of A-B interaction at a ternary composition is written in terms of equivalent fractions as follows [28]:

$$\Delta g_{\mathrm{A,B}} = \left(\Delta g^{\circ}_{\mathrm{A,B}} + \sum_{(i+j)\geq 1} q^{ij}_{\mathrm{A,B}} \left(\frac{Y_{\mathrm{A}}}{Y_{\mathrm{A}} + Y_{\mathrm{B}}} \right)^{i} \left(\frac{Y_{\mathrm{B}}}{Y_{\mathrm{A}} + Y_{\mathrm{B}}} \right)^{j} \right) + \sum_{\substack{k\geq 1 \\ i\geq 0 \\ j\geq 0}} q^{ijk}_{\mathrm{A,B(C)}} \left(\frac{Y_{\mathrm{A}}}{Y_{\mathrm{A}} + Y_{\mathrm{B}}} \right)^{i} \left(\frac{Y_{\mathrm{B}}}{Y_{\mathrm{A}} + Y_{\mathrm{B}}} \right)^{j} Y_{\mathrm{C}}^{k} \quad (28)$$

A similar expression can be written for an interaction in terms of pair fractions:

$$\begin{aligned} \Delta g_{\mathrm{A,B}} = & \left(\Delta g^{\circ}_{\mathrm{A,B}} + \sum_{(i+j)\geq 1} g^{ij}_{\mathrm{A,B}} \left(\frac{X_{\mathrm{AA}}}{X_{\mathrm{AA}} + X_{\mathrm{AB}} + X_{\mathrm{BB}}} \right)^{i} \left(\frac{X_{\mathrm{BB}}}{X_{\mathrm{AA}} + X_{\mathrm{AB}} + X_{\mathrm{BB}}} \right)^{j} \right) \\ & + \sum_{\substack{k\geq 1 \\ i\geq 0 \\ j\geq 0}} g^{ijk}_{\mathrm{A,B(C)}} \left(\frac{X_{\mathrm{AA}}}{X_{\mathrm{AA}} + X_{\mathrm{AB}} + X_{\mathrm{BB}}} \right)^{i} \left(\frac{X_{\mathrm{BB}}}{X_{\mathrm{AA}} + X_{\mathrm{AB}} + X_{\mathrm{BB}}} \right)^{j} Y_{\mathrm{C}}^{k} \end{aligned} \quad (29)$$

The asymmetrical Toop model (Figure 3.3, (***b***)) implies that the B-C interaction is evaluated as in the Kohler model but for the interactions A-B and A-C the binary compositions with a constant content of A are taken. The Gibbs energy of A-B interaction at a ternary composition is written in terms of equivalent fractions as follows [28]:

$$\Delta g_{\mathrm{A,B}} = \left(\Delta g^{\circ}_{\mathrm{A,B}} + \sum_{(i+j)\geq 1} q^{ij}_{\mathrm{A,B}} Y_{\mathrm{A}}{}^{i} \left(1 - Y_{\mathrm{A}}\right)^{j} \right) + \sum_{\substack{k\geq 1 \\ i\geq 0 \\ j\geq 0}} q^{ijk}_{\mathrm{A,B(C)}} Y_{\mathrm{A}}{}^{i} \left(1 - Y_{\mathrm{A}}\right)^{j} \left(\frac{Y_{\mathrm{C}}}{Y_{\mathrm{B}} + Y_{\mathrm{C}}} \right)^{k} \tag{30}$$

In the Muggianu model the binary compositions found using perpendicular lines from a ternary composition are used for the extrapolation. This model was criticized by Pelton and Chartrand [28] because of its physical inconsistency. So, if a B-C solution with only traces of A is taken, its Gibbs energy should be approximated based on pure B + traces of A and pure C + traces of A binary compositions rather than binary A-B and A-C compositions with a high A content resulting from this extrapolation.

The details of how the Gibbs energy is extrapolated in multicomponent solutions based on ternary extrapolations are given in the paper by Pelton and Chartrand [28].

Generally, if in a ternary system all three components are chemically alike (mathematically it is equivalent to the same order of magnitude of interaction in all binary systems), the Kohler model is preferred. If two components are alike and the third one is different, an asymmetric model is preferred. A wrong choice of the geometrical model can lead to spurious miscibility gaps [29]. In oxide systems, components are usually divided into groups according to their acidity or basicity. For example, Na_2O and CaO are basic oxides while SiO_2 is an acidic oxide, in the CaO-Na_2O-SiO_2 system the appropriate extrapolation is asymmetrical Toop with SiO_2 as the special oxide. This classification, however, is well correlated to the order of magnitude of the parameters of interaction: there are strong negative interactions in the Na_2O-SiO_2 and CaO-SiO_2 subsystems while the Na_2O-CaO system is modeled as ideal.

In a multicomponent system, the number of ternary subsystems grows very fast with each new component added. In order to facilitate the task of assigning the geometrical extrapolations, a concept of grouping was introduced. The components of a solutions are divided into a few groups according to their properties. For example, in the oxide database, alkali and alkali-earth oxides are in one group and silica and boron oxide are in another. This division is explained by the obvious distinction between network formers (SiO_2, B_2O_3) and network modifiers (Na_2O, K_2O, CaO, MgO). If in a ternary system all components are from the same group, the symmetrical Kohler model is used. If two are from the same group and the third one is from another, the model is

asymmetrical. If all three species are in different groups, the model is symmetrical. However, sometimes it is required to make an exception from the general rule given by the groups. In this case, a *group exception* is added to the database. For example, CaO, MgO and Al_2O_3 might be in the same group but in the specific case of the CaO-MgO-Al_2O_3 subsystem we would want to make a Toop extrapolation on Al_2O_3 (Al_2O_3 apart).

3.4 The Compound Energy Formalism

Hillert [30] has developed a formalism allowing to model solid solutions with several sublattices. The model is based on the idea that in many solid solutions the ions do not mix all together, but rather certain groups of ions mix only on specific sublattices each. Ions and vacancies can occupy different crystallochemical sites and certain foreign ions would only enter specific sites according to their size and preferred coordination.

The compound energy formalism treats a solution as consisting of several sublattices. Although there can be many of them (*FactSage* supports up to five), we consider a two-sublattice solution $(A,B)_k(C,D)_l$ for clarity. Usually, A, B, C, D are charged ions. The end-members of this solution are all possible combinations: A_kC_l, B_kC_l, A_kD_l, B_kD_l. If the charges of ions on the same sublattice are different, some end-members can be charged. The concentrations of species on each sublattice are determined using site fractions:

$$x_{\mathrm{A}} = \frac{n_{\mathrm{A}}}{n_{\mathrm{A}} + n_{\mathrm{B}}}, x_{\mathrm{B}} = \frac{n_{\mathrm{B}}}{n_{\mathrm{A}} + n_{\mathrm{B}}}, x_{\mathrm{C}} = \frac{n_{\mathrm{C}}}{n_{\mathrm{C}} + n_{\mathrm{D}}}, x_{\mathrm{D}} = \frac{n_{\mathrm{D}}}{n_{\mathrm{C}} + n_{\mathrm{D}}}, \tag{31}$$

The Gibbs energy for the solution is written as:

$$G = G^{ref} + G^{conf} + G^{ex} \tag{32}$$

The reference Gibbs energy G^{ref} is a weighted sum of the Gibbs energies of the end-members:

$$G^{ref} = x_{\mathrm{A}} x_{\mathrm{C}} G^{\circ}_{\mathrm{A_k C_l}} + x_{\mathrm{A}} x_{\mathrm{D}} G^{\circ}_{\mathrm{A_k D_l}} + x_{\mathrm{B}} x_{\mathrm{C}} G^{\circ}_{\mathrm{B_k C_l}} + x_{\mathrm{B}} x_{\mathrm{D}} G^{\circ}_{\mathrm{B_k D_l}} \tag{33}$$

The configurational Gibbs energy is calculated from an assumption of random distribution of species on every sublattice:

$$G^{conf} = RT\left[k\left(x_A \ln x_A + x_B \ln x_B\right) + l\left(x_C \ln x_C + x_D \ln x_D\right)\right] \tag{34}$$

The excess Gibbs energy is a sum of one-sublattice and reciprocal interactions. For example, a one sublattice interaction is an interaction between A and B on the first sublattice while the second is filled with ions of one kind: A,B//C, A,B//D. It is generally assumed that the type of ions on other sublattices does not affect much the interaction parameter. The parameters of A,B//C interaction are supposed to be the same as for A,B//D interaction. Reciprocal interactions are written in the form A,B//C,D.

The excess Gibbs energy is defined as:

$$G^{ex} = \sum_{a}\sum_{b\neq a}\sum_{c} Y_a^i Y_b^j Y_c L_{a,b//c}^{ij} + \sum_{a}\sum_{c}\sum_{d\neq c} Y_a Y_c^i Y_d^j L_{a//c,d}^{ij} + \sum_{a}\sum_{b\neq a}\sum_{c}\sum_{d\neq c} Y_a^i Y_b^j Y_c^k Y_d^l L_{a,b//c,d}^{ijkl} \qquad (35)$$

The first term in (35) is the sum of all interactions on the first sublattice, the second is the sum of interactions on the second sublattice and the last term is the sum of all reciprocal interactions.

The main complication of the Compound Energy Formalism is that in case of many sublattices there are too many end-members whose properties need to be defined. For charged end-members, there is no independent way to define their properties. Reasonable combinations between the end-members in the form of reactions are given with model assumptions about the Gibbs energies of these reactions. Usually, the Gibbs energies of these reactions serve as model parameters. Together with the charge balance equations they allow to express the Gibbs energies of the end-members using a smaller number of independent model parameters.

CHAPTER 4 SOLID SOLUTIONS

The Na_2O-K_2O-CaO-MgO-Al_2O_3-B_2O_3-SiO_2 system features many complex solid solutions with different types of substitution mechanisms. The current chapter covers the solid solution models used in this work. Some of them were introduced for the first time (Mullite, Nepheline, Carnegieite, Combeite, (2:1:3), Leucite, Milarite, Monoborate, Diborate and Triborate) while others are extensions of already existing models (high and low-*T* (Na,K)AlO2, NCA2, C3A, Feldspar, Melilite, Clinopyroxene, Beta- and Beta”-Alumina, Pseudowollastonite and Ca-Orthosilicate). The published models are referenced in the corresponding sections. Some models were developed internally at Center for Research in Computational Chemistry and were available in form of private communications.

4.1 Mullite

Mullite is the only solid solution in the Al_2O_3-SiO_2 system and has great importance in the production of ceramics. Its composition range is 58-64 mol% Al_2O_3. Along with the limited non-stoichiometry in the Al_2O_3-SiO_2 system, it is also able to dissolve significant amounts of boron oxide as well as Fe_2O_3 and Cr_2O_3. Due to a non-isomorphous substitution mechanism the structure of mullite is abundant with vacant oxygen positions. This fact might be able to explain mullite's low density which favours its formation under low pressures. The combination of a high temperature and a low pressure is seldom fulfilled in the nature; therefore, mullite is a quite unusual component of mineral assemblages although it is extremely important in industrial applications. Instead, Al_2SiO_5 polymorphs are common minerals whose formation is favoured under high pressures. Mullite is the only intermediate phase in the system Al_2O_3-SiO_2 stable at high temperatures and under low pressures.

In order to establish a physically consistent thermodynamic model of Mullite solid solution and account for all possible substitution mechanisms, the crystal structure of mullite was analyzed. The structure of mullite can be considered as derived from the sillimanite structure (Al_2SiO_5 polymorph) somewhat distorted due to the presence of a considerable number of vacancies. All the major features of sillimanite's structure (Figure 4.1) are preserved in mullite.

Aluminium in sillimanite can take either a six-fold or a four-fold coordinated position (see Figure 4.1). Columns of edge-sharing AlO_6 octahedra are linked with alternating Al- and Si-tetrahedra. The columns define the highly anisotropic properties of mullite crystals (such as the bulk modulus and preferential growth in acicular habit). There are two types of tetrahedral sites, filled with Al and Si, correspondingly.

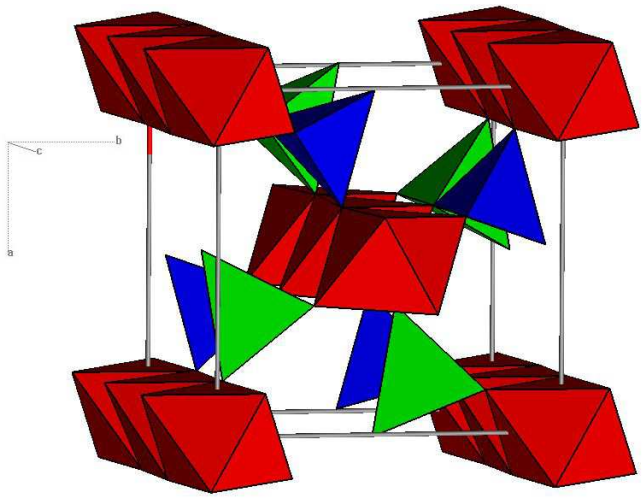

Figure 4.1 The sillimanite structure. The Al polyhedra are shown in red and green, the Si tetrahedra are blue.

The derived mullite structure is shown in Figure 4.2 for comparison (the mullite's unit cell parameter *c* is two times shorter, so, two periods along the *c* axis are shown).

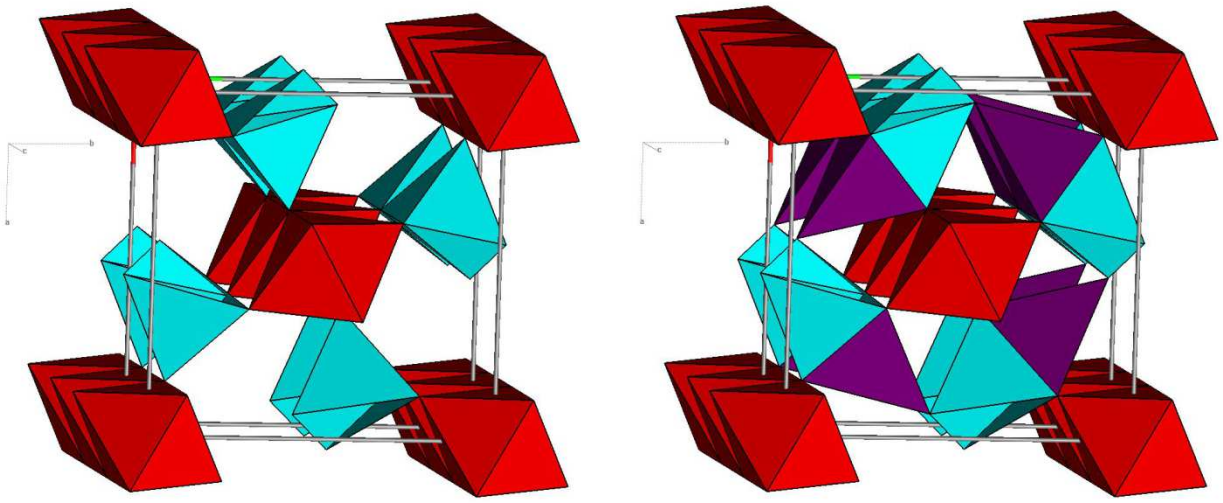

(***a***) (***b***)

Figure 4.2 The mullite structure (crystallographic data are taken from Angel and Prewitt [31]). Only T sites are shown in (***a***) while (***b***) features both T and T* sites.

Two neighbour tetrahedra chains share some oxygens. This type of oxygen is designated as Oc and it is the only oxygen to be replaced by vacancies during a substitution of Si with Al [31]. If there is a vacant Oc site, the two adjacent tetrahedral cations are displaced from T to T* sites in order to compensate the coordination deficiency. This positional change incurs an additional shift of an adjacent oxygen at an Oc position leaving the symmetry center and occupying an Oc* site.

In order to develop a thermodynamic model, one should consider the fact that oxygen atoms in the mullite structure are non-equivalent to each other and only those placed at Oc site are capable of being replaced by vacancies. The original structure of sillimanite features alternating Al and Si cations and the data of NMR analysis show that a significant degree of ordering between Al and Si in T sites of mullite still persists. Therefore, the T sites can be thought of as residual Al^{IV} sites alternated with Si^{IV} sites which can be replaced with Al. T* sites are derived from T sites next to vacant Oc positions and in the present model they will not be distinguished from the ordinary T sites. To sum up, the proposed model is written as follows:

$$(Al^{3+})^{O}(Al^{3+})^{T}[Al^{3+},Si^{4+}]^{T}[O^{2-},Va][O^{2-}]_4 \quad (36)$$

A non-isomorphous substitution in mullite gives rise to an incommensurate structure with modulated properties [31]. The structure fitted based on an X-ray analysis reflects the averaged properties.

In order to get a fuller insight of the possible substitution mechanisms occurring in mullite, structural data on different substituted mullites have been analysed.

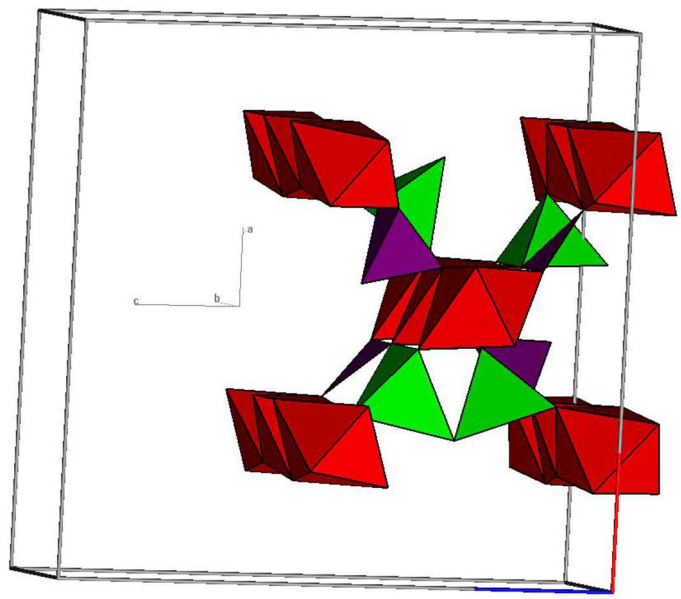

Figure 4.3 $Al_4B_2O_9$ structure from Fischer et al. [32]. The view dimensions: $0.2 < a < 0.8$, $0.2 < b < 1.4$, $0 < c < 0.55$.

The octahedral sites of $Al_4B_2O_9$ (Figure 4.3) are occupied only by Al atoms. The tetrahedral sites are occupied by Al and the triangles are boron sites. According to the model (36), $Al_4B_2O_9$ formula will be expressed as:

$$(Al^{3+})^{O}(Al^{3+})^{T}[B^{3+}]^{T}[O^{2-}_{0.5},Va_{0.5}][O^{2-}]_4 \quad (37)$$

Mullite can dissolve noticeable amounts of Fe_2O_3 and Cr_2O_3. Due to a strong preference of Fe^{3+} and Cr^{3+} for an octahedral coordination, these cations occupy the octahedral sites.

Finally, considering the possible substitution mechanisms in mullite, the general solution model can be written as:

$$(Al^{3+},Fe^{3+},Cr^{3+})^{O}(Al^{3+})^{T}[B^{3+},Al^{3+},Si^{4+}]^{T}[O^{2-},Va][O^{2-}]_4 \quad (38)$$

4.2 Nepheline (Kalsilite)

Nepheline belongs to the feldspathoid group of minerals. This group also includes kalsilite, leucite, melilite, sodalite and some others. They have geological properties similar to those of feldspars but form in phase assemblies poor in silica [33]. Nepheline is a tectosilicate with the formula (Na,

K)$AlSiO_4$. It mainly contains sodium and potassium but can also contain noticeable amounts of calcium and iron.

The nepheline structure belongs to a series of structures topologically derived from tridymite. As it can be seen from Figure 4.4, a tridymite-like network is regularly distorted forming two types of cationic sites of different size in proportion of one larger site to three smaller sites. The larger sites fit potassium cations very well; the smaller cavities are most suited for sodium.

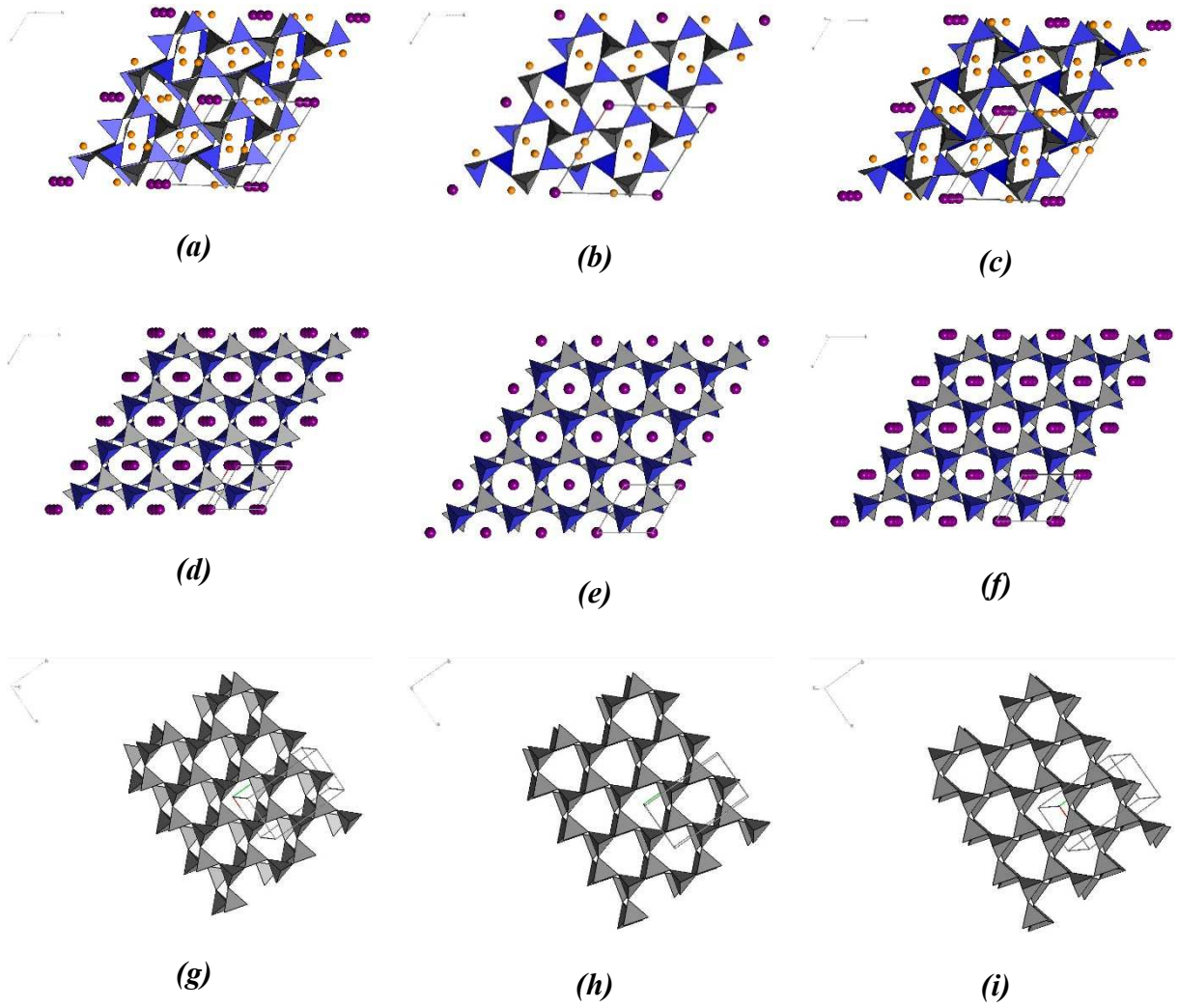

Figure 4.4 Slightly different view angles along the *c* axis of unit cells of the crystal structures of nepheline ($Na_{0.75}K_{0.25}AlSiO_4$ composition) (***a***, ***b***, ***c***) [34] and kalsilite (***d***, ***e***, ***f***) [35]. The structure of their common parent, tridymite, is also shown (***g***, ***h***, ***i***) [36]. The structures were shifted and

multiplied correspondingly to better represent the topological similarity. Violet spheres are K atoms, Na is shown in orange. AlO_4 tetrahedra are shown in blue, SiO_4 in grey.

The compositions of naturally occurring nephelines are plotted in Figure 4.5. There is a clear tendency towards the line $0.75NaAlSiO_4 \cdot 0.25KAlSiO_4$-$0.60NaAlSiO_4 \cdot 0.40SiO_2$. Apparently, the excess silica enters the nepheline structure according to the substitution:

$$Na^{+}(K^{+})+Al^{3+} \leftrightarrow Va+Si^{4+} \tag{39}$$

Vacancies occupy the larger sites. Indeed, if we recalculate the $0.60NaAlSiO_4 \cdot 0.40SiO_2$. composition, it becomes $0.75NaAlSiO_4 \cdot 0.25VaSi_2O_4$. According to Hovis et al. [37], K and Va have almost the same affinity for the larger sites.

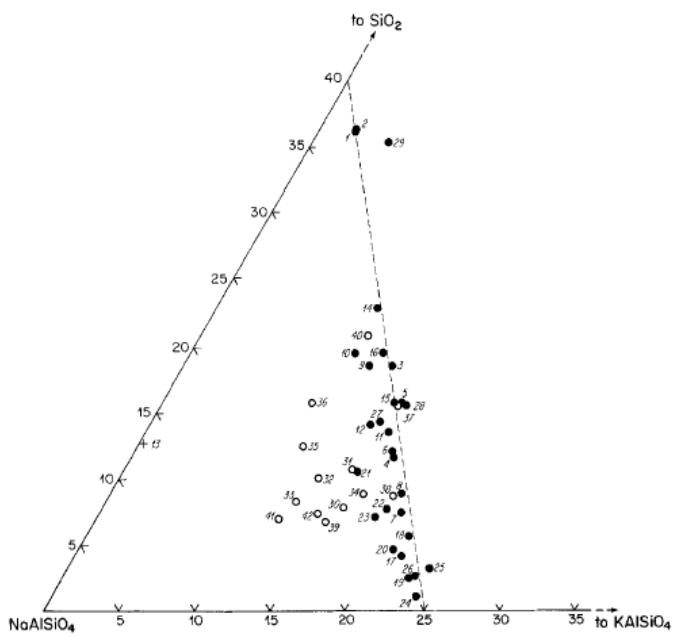

Figure 4.5 Compositions of natural nephelines in the $NaAlSiO_4$-$KAlSiO_4$-SiO_2 plane, projected from the $Ca_{0.5}AlSiO_4$ corner. The image is taken from Dollase and Thomas [38].

Sodium, however, is not energetically favored in the larger sites. It is asymmetrically placed there and even causes a structural collapse at lower temperatures in the pure $NaAlSiO_4$ [39]. In fact, the low-temperature modifications of $NaAlSiO_4$ appear due to a reversible collective collapse of the network and these modifications quickly become destabilized upon a substitution with excess silica or kalsilite.

The smaller sites are also able to host calcium ions always present in noticeable amounts in natural nephelines [40].

In the $NaAlSiO_4$-$KAlSiO_4$ series, the substitution of sodium for potassium happens very easily up to $Na_{0.75}K_{0.25}AlSiO_4$ composition; almost no structural strain appears. However, starting from the $Na_{0.75}K_{0.25}AlSiO_4$ composition, it becomes harder for potassium cations to fit into the remaining smaller sites. This is reflected by the existence of a subsolidus miscibility gap between $Na_{0.75}K_{0.25}AlSiO_4$ and $KAlSiO_4$ [41], as well as the enthalpy of mixing of $NaAlSiO_4$-$KAlSiO_4$ solid solutions [42]. The enthalpies of mixing between the sodium and potassium end-members increase with SiO_2 content (mostly on the sodium side). It can be explained by a higher stability of the pure sodium end-member with increasing amount of silica.

Strictly speaking, kalsilite $KAlSiO_4$ has a crystal symmetry different from nepheline: for example, it has only one type of cationic site, suitable for potassium. Because of that, the ability to dissolve excess silica for this compound is very moderate. Sodium substitution in kalsilite quickly leads to formation of intermediate phases, such as tetrakalsilite [43]. Tetrakalsilite has three types of cationic sites: one kalsilite-like and two nepheline-like [42, 44]. In fact, tetrakalsilite is a complex structure combining nepheline and kalsilite blocks together [45]. The kalsilite structure can be derived from the nepheline structure by distortion as shown in Figure 4.4. In this work it was decided to treat nepheline and kalsilite as one solution phase.

Compositions of geologically important nephelines are usually expressed in the basis of Ne ($NaAlSiO_4$), Ks ($KAlSiO_4$), 2Qz ($[]Si_2O_4$), and 0.5An ($[]_{0.5}Ca_{0.5}AlSiO_4$), although pure Qz and An compositions are never reached [44].

The data by Roth [46] indicate that $K_2MgSi_3O_8$ compound is isomorphous with kalsilite and, therefore, belongs to Nepheline solution. Apparently, Mg^{2+} and Si^{4+} are couple substituted for $2Al^{3+}$ in the $KAlSiO_4$-KMS3 join.

Considering all possible substitution mechanisms, the following model of nepheline using the Compound Energy Formalism was derived:

$$[VaSi_2^{8+},NaAlSi^{8+},KAlSi^{8+},CaAl_2^{8+},0.5Na_2MgSi_3^{16+},0.5K_2MgSi_3^{16+}]_2$$

$$[NaAlSi^{8+},KAlSi^{8+},CaAl_2^{8+},0.5Na_2MgSi_3^{16+},0.5K_2MgSi_3^{16+}]_6\{O^{2-}\}_{32} \qquad (40)$$

The model has two non-trivial sublattices and one trivial (filled only with oxygen anions).

The model was written in such a way that any charged end-members can be avoided to reduce the total number of end-members. For subsystems with the same Al/Si ratio, the ideal Gibbs energy expressions can be simplified to the same form both in case of a model with charged and a model with neutral end-members (the $NaAlSiO_4$-$KAlSiO_4$ subsystem). The expressions of the ideal Gibbs energy in case $NaAlSiO_4$-$CaAl_2O_4$, (an example where Al/Si ratio changes), are different; however, no problems were encountered during optimization of properties of calcium-containing nephelines.

4.3 Carnegieite

Carnegieite is a mineral with the $NaAlSiO_4$ formula. Although it has the same stoichiometry as nepheline, its crystal structure is quite different (Figure 4.6). In fact, its structure bears a significant resemblance with the cristobalite structure where part of silicon tetrahedra have been replaced with $NaAlO_2$ tetrahedra.

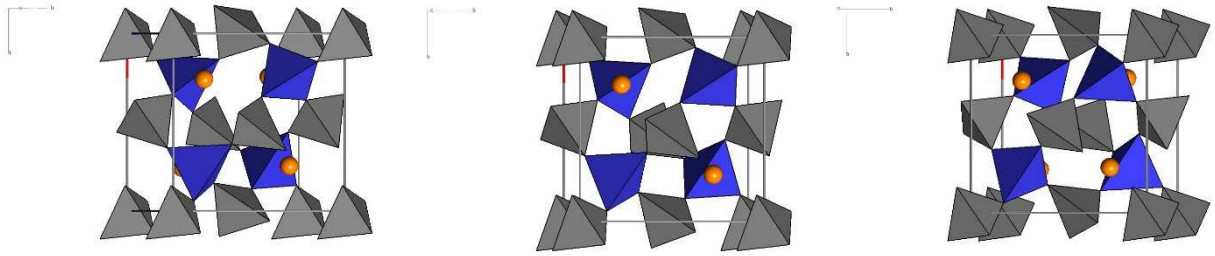

(a) ***(b)*** ***(c)***

Figure 4.6 Crystal structure of carnegieite at different view angles along the *c* axis (***a***, ***b***, ***c***). Na is shown in orange, AlO_4 tetrahedra are blue, SiO_4 are grey.

The transformation carnegieite/nepheline requires a significant amount of network reorganization in the crystal structure which causes a slow kinetics of this transformation. In fact, although carnegieite is stable at temperatures above 1256°C, its properties can be studied at room temperatures [47, 48].

While the nepheline structure has two different cationic sites, the carnegieite structure is simpler and contains only one cationic site. Carnegieite can dissolve excess silica [49], potassium [50] and calcium [51, 52]. Compared to nepheline, their solubility in carnegieite is smaller.

The following substitution mechanisms allow these types of solubility:

$$Na^{+} \leftrightarrow K^{+} \tag{41}$$

$$Na^{+}+Al^{3+} \leftrightarrow Va+Si^{4+} \tag{42}$$

$$Na^{+}+Si^{4+} \leftrightarrow Ca^{2+}+Al^{3+} \tag{43}$$

However, only $NaAlSiO_4$ can exist as a pure stable end-member and "Si_2O_4", $KAlSiO_4$, $CaAl_2O_4$ do not form corresponding stable polymorphs.

The following model has been proposed for Carnegieite solid solution based on the substitution mechanisms (41)-(43):

$$(NaAlSi^{8+},VaSi_2^{8+},KAlSi^{8+},CaAl_2^{8+})_4\{O\}_{16} \tag{44}$$

The end-members in this model are charge neutral and in many cases their properties can be approximated based on the properties of existing compounds and phase diagram data.

4.4 High and low-*T* (Na,K)AlO_2

Alkali aluminates $NaAlO_2$ and $KAlO_2$ both have a low and a high modification with corresponding structures. There are some other similar compounds sharing the same structure type: $NaFeO_2$, $KFeO_2$ [53, 54] which form solid solutions among each other.

There are some less obvious substitution types that can occur in the aluminate structure. Sodium and potassium aluminates form extensive solid solutions with silica [55]. So, the high aluminate modification is isomorphous with cristobalite and the low modification with tridymite. The substitution between aluminate and silica occurs with a charge compensation mechanism:

$$Na^{+}+Al^{3+} \leftrightarrow Va+Si^{4+} \tag{45}$$

K_2MgSiO_4 compound is isomorphous with $KAlO_2$ and also can dissolve considerable amounts of silica [46]:

$$2K^{+}+Mg^{2+} \leftrightarrow Va+Si^{4+} \tag{46}$$

It is important to note that extra cations appearing for charge compensation are locally bound to the substitution sites and do not contribute to the configurational entropy. For example, from the modeling point of view, Na^{+} and Al^{3+} form an effective particle together and should be written as $NaAl^{4+}$. The same applies to K_2Mg^{4+}. Plus, as there is no K_2MgO_2 end-member or a composition poorer in silica than K_2MgSiO_4, it means that Mg must be alternated with Si (Mg-Mg avoidance principle) and the effective particle for this end-member would be $0.5K_2MgSi^{8+}$. Keeping all that in mind, the following model was proposed:

$$(NaAl^{4+},KAl^{4+},VaSi^{4+},0.5Na_2MgSi^{8+},0.5K_2MgSi^{8+})\{O^{2-}\}_2 \quad (47)$$

There is no stable Na_2MgSiO_4 with the aluminate structure, but it was included as an end-member in the model. Its properties can be estimated based on the solubility limit given by Berezhnoi et al. [56].

The model produces only neutral end-members whose thermodynamic properties have an actual meaning. It also reduces the number of end-members. If an end-member actually exists as a compound, its Gibbs energy is equal to the Gibbs energy of the compound. If not, as in case of $VaSiO_2$ and $0.5Na_2MgSiO_4$, the Gibbs energy of actual compounds with different structures are taken and a term of added Gibbs energy is included.

4.5 Feldspar

The most general feldspar formula is $A_{(1-x-y)}B_xVa_yT^{I}_{(1+x-y)}T^{II}_{(3-x+y)}O_8$. A is an alkali cation, B is an alkali-earth cation, T^{I} and T^{II} are cations with tetrahedral coordination. Some of the end-members of the solid solutions are very abundant in nature and make up around 41 wt% of the Earth's continental crust. According to Kroll [57], feldspars with the following cations are known:

A = Na^{+}, $(NH_4)^{+}$, K^{+}, Tl^{+}, Rb^{+}

B = Ca^{2+}, Sr^{2+}, Ba^{2+}, Pb^{2+}

T^{I} = B^{3+}, Al^{3+}, Ga^{3+}, Fe^{3+}

T^{II} = Si^{4+}, Ge^{4+}

The most relevant end-members of the feldspar series are $NaAlSi_3O_8$ (albite, monalbite), $KAlSi_3O_8$ (microcline, orthoclase, adularia, sanidine) and $CaAl_2Si_2O_8$ (anorthite) and only they were considered in this work.

Felspars can exist in a triclinic (low-temperature) and a monoclinic (high-temperature) modification. The transformation between them is fast and it requires only a slight shift in atom positions (Figure 4.7). This transformation in feldspars is called the displacive transformation and it cannot be quenched.

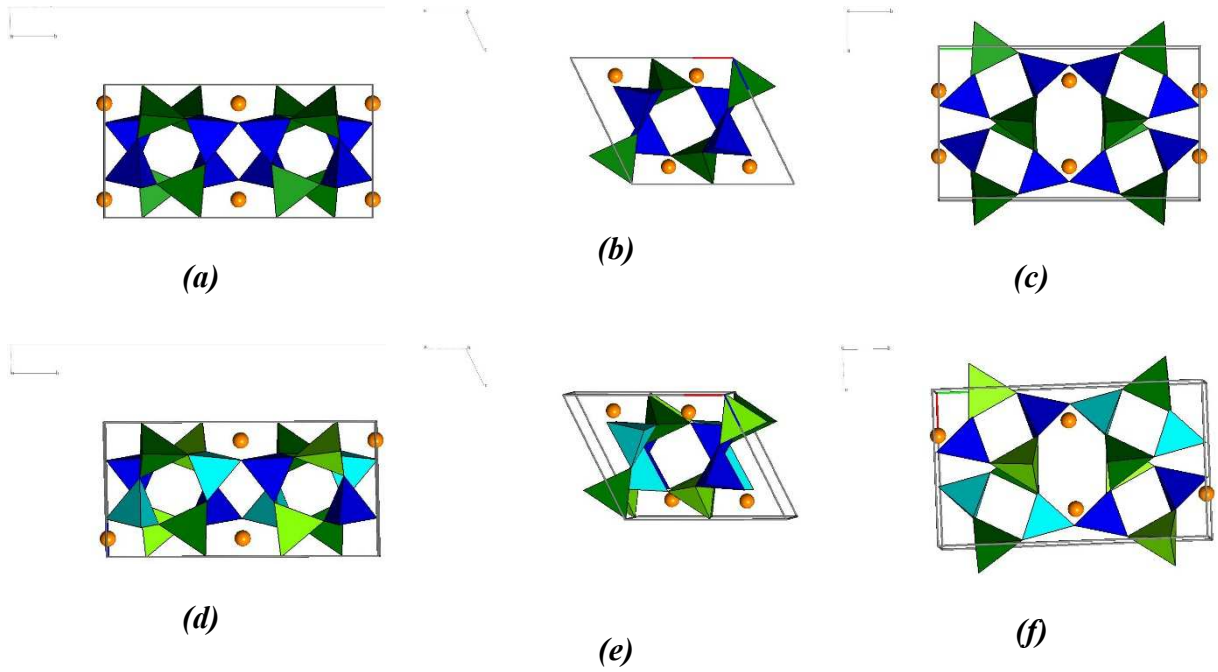

Figure 4.7 The monoalbite (***a***, ***b***, ***c***) and low albite (***d***, ***e***, ***f***) crystal structures [58]. The monoalbite structure: T1 tetrahedra are shown in green, T2 are shown in blue [59]. The low albite structure: T1 tetrahedra are shown in light green, T2 in dark green, T3 in light blue, T4 in dark blue. Alkali atoms are shown in orange. Two alkali pairs on the left and on the right in (***a***) and (***c***) are shared between two adjacent cells, the corresponding atoms in (***d***) and (***f***) completely belong to one cell.

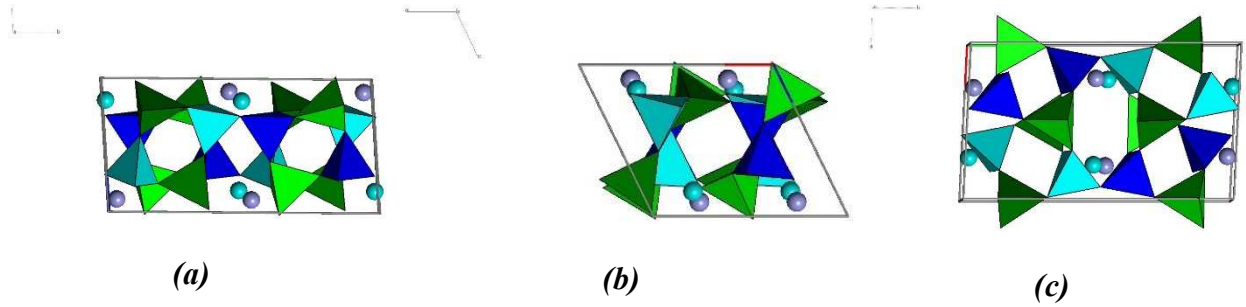

Figure 4.8 $C\bar{1}$ anorthite crystal structure [58] along *a*, *b* and *c* axes (***a***, ***b***, ***c*** correspondingly). T1 tetrahedra are shown in light green, T2 in dark green, T3 in light blue, T4 in dark blue. Violet and light blue spheres indicate Na/Ca sites with ½ occupancy.

Figure 4.7-Figure 4.8 show the crystal structures of albite and anorthite. In the monoclinic modifications, there are two types of Al/Si tetrahedral sites which each split into two in the triclinic structure. The Al/Si distribution between these sites is described by a degree of ordering. The process of Al/Si ordering/disordering is very slow and is called the diffusive transformation. The disordering happens upon heating of feldspars, the ordering can be observed only on a geological timescale or under hydrothermal conditions. The $CaAl_2Si_2O_8$ end-member is always ordered due to the alumina avoidance rule [57]. In solid solutions, alkali cation ordering can also be present, but it is not as sluggish as the Al/Si ordering. It also appears to be strongly correlated with the Al/Si ordering. The Al/Si distribution in feldspars can be derived from the unit cell parameters obtained from X-ray powder data [60, 61]. Al/Si ordering is a continuous transition of an order higher than one in both albite and potassium feldspar [62-64]. In this work, low and high albites were treated as separate modifications.

Let us consider an example of the alkali feldspars $NaAlSi_3O_8$-$KAlSi_3O_8$ to observe the role of the displacive and the diffusive transformations on the phase diagram.

Depending on the cooling rate, different metastable phase diagrams can be observed for the alkali feldspar section. For the case of a rapid cooling, no Al/Si ordering occurs, the only two solid solutions are triclinic anorthoclase (sodic part) and high sanidine (potassic part), with a transition of second order [65, 66] (Figure 4.9).

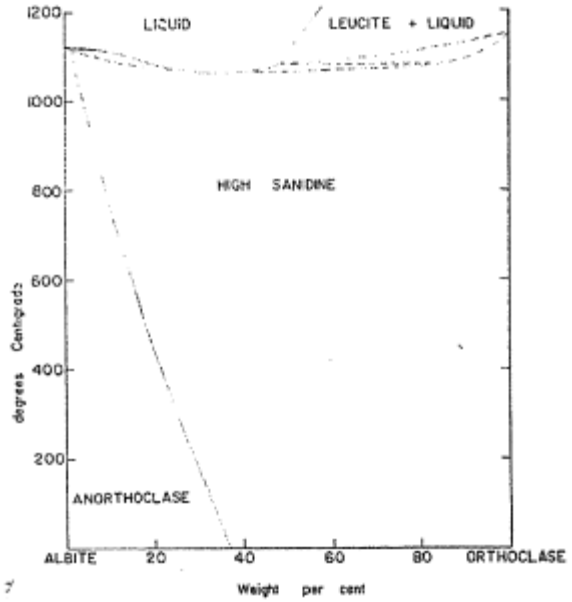

Figure 4.9 A metastable phase diagram obtained by a rapid cooling in the $NaAlSi_3O_8$-$KAlSi_3O_8$ system. Only the displacive transformation between the monoclinic high sanidine and the triclinic anorthoclase is observed (supposedly second order). No Al/Si ordering occurs (both solid phases are disordered high modifications). The image is taken from Smith [67].

As the cooling rates slow down, a partial Al/Si ordering develops in the solid phases. For example, low sanidine can be observed (Figure 4.10) and an immiscibility gap is observed, too.

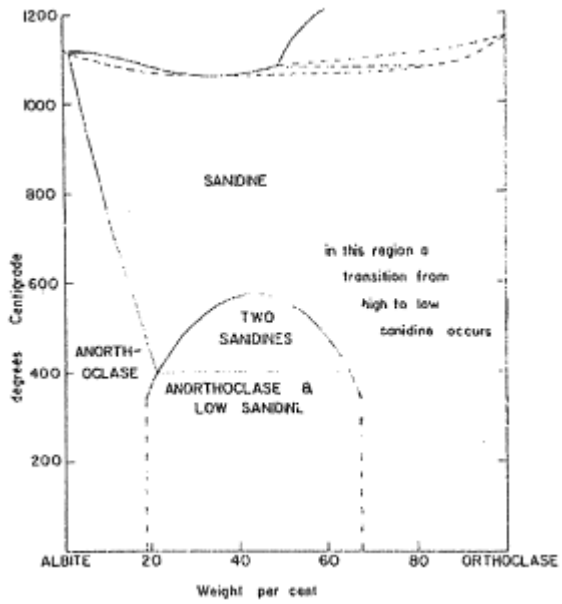

Figure 4.10 A metastable phase diagram obtained with an average rate of cooling in the $NaAlSi_3O_8$-$KAlSi_3O_8$ system. The Al/Si ordering occurs only partially in the K-end (low sanidine forms), anorthoclase does not yet transform to low albite. The image is taken from Smith [67].

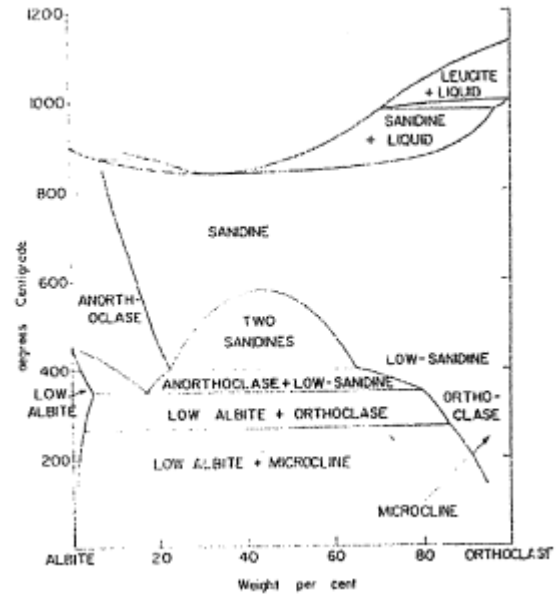

Figure 4.11 The stable phase diagram obtained by a slow cooling in the $NaAlSi_3O_8$-$KAlSi_3O_8$ system. Formation of the low ordered phases is observed (low albite, orthoclase, microcline). The image is taken from Smith [67].

Slow cooling, found in nature, leads to development of separate phases with a substantial degree of ordering (low albite, orthoclase and microcline). The equilibrium phase diagram is believed to be close to the one depicted in Figure 4.11 [67].

Pure anorthite $CaAl_2Si_2O_8$ has a body-centered lattice ($C\bar{1}$) and can be disordered upon heating above 1000°C. Cooled below 250°C, the anorthite structure undergoes local distortions around small Ca^{2+} cations and transforms into a $P\bar{1}$ structure. Ca ions form large long-order domains whose textures depend on the thermal history and the extent of chemical substitutions.

Sodium-calcium feldspars are often referred to as plagioclases in the literature. Considering the transitions occurring in the pure end-members, the phase field of plagioclase must be intersected by two lines: monoalbite/high albite and high-albite/body-centered anorthite. The last transition is a first-order transition. At low temperatures, there is a miscibility gap between albite and anorthite (Figure 4.12).

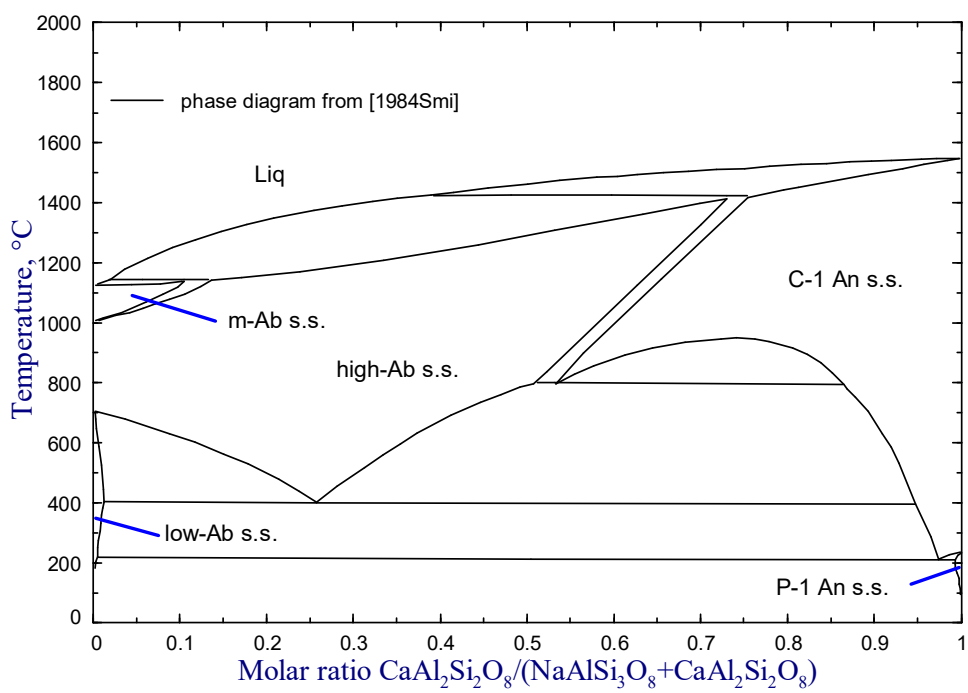

Figure 4.12 The phase diagram of plagioclases $NaAlSi_3O_8$-$CaAl_2Si_2O_8$ [68]; s.s. stands for solid solution.

$KAlSi_3O_8$ and $CaAl_2Si_2O_8$ end-members have a very small mutual solubility which increases only under high pressures [69].

Following the approach described in section 2.3, all feldspars were described using the same Feldspar solid solution. A simple model of Feldspar solid solution with a possible short-range ordering (although it might not be necessary) was developed:

$$(NaAlSi^{8+},KAlSi^{8+},CaAl_2^{8+})\{Si_2O_8^{8-}\} \quad (48)$$

The end-members in the model are neutrally charged and their properties correspond to the properties of the pure compounds.

4.6 Melilite

Melilites is a vast group of minerals with the general formula of $M^I{}_2M^{II}T_2O_7$, where $M^I = Ca^{2+}$, Sr^{2+}, Ba^{2+}, Pb^{2+}, Na^+, K^+, $M^{II} = Mg^{2+}$, Al^{3+}, B^{3+}, Fe^{2+}, Fe^{3+}, Zn^{2+}, $T = Al^{3+}$, B^{3+}, Si^{4+}, Fe^{3+}. The most important melilite minerals are gehlenite $Ca_2AlAlSiO_7$ and akermanite $Ca_2MgSi_2O_7$. There is a series of other rare minerals belonging to the melilite group: alumoakermanite $(Ca,Na)_2(Al,Mg,Fe^{2+})Si_2O_7$, okayamalite Ca_2BBSiO_7, etc.

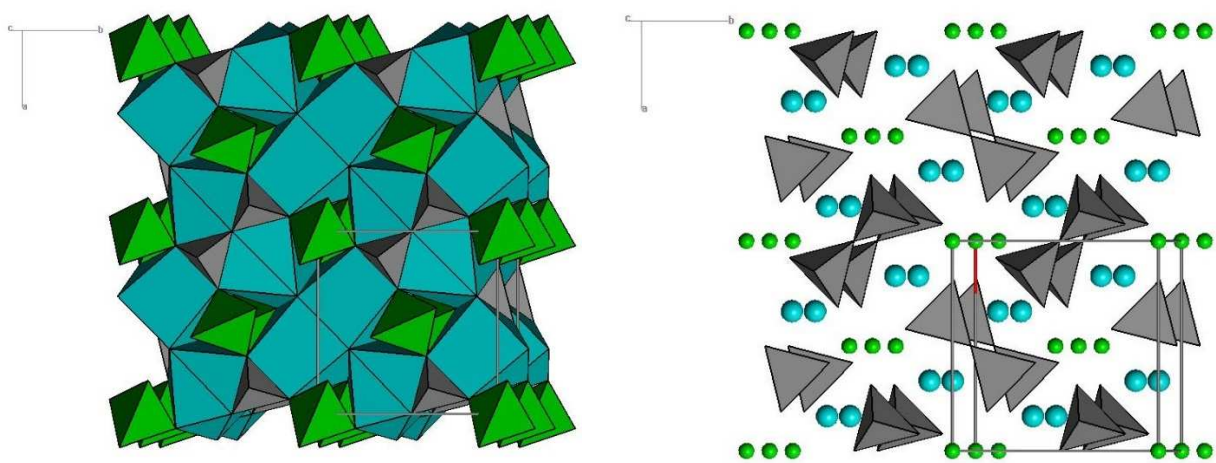

(***a***) (***b***)

Figure 4.13 The gehlenite structure, a view along the *c* axis slightly tilted to the left with (***a***) and without (***b***) coordination polyhedra of cations. The structural data are taken from Smith [70].

Melilites belong to the sorosilicate group of silicates, i.e. silicon tetrahedra are coupled (Figure 4.13). The rest of the cations are divided between the small tetrahedral M^{II} sites and the big

distorted octahedral M^I sites. The site preference of cations depends on their relative size and the affinity for the octahedral and tetrahedral coordination.

The following melilites are important in the Na_2O-K_2O-Al_2O_3-CaO-MgO-SiO_2-B_2O_3 system: gehlenite $Ca_2AlAlSiO_7$, akermanite $Ca_2MgSi_2O_7$, Na-melilite $NaCaAlSi_2O_7$, K-melilite $KCaAlSi_2O_7$. There are possible boron-containing end-members but, unfortunately, no data concerning them in the literature were found. Schairer et al. [71] has shown that the pure $NaCaAlSi_2O_7$ end-member cannot be obtained under the normal pressure and becomes stabilized only under moderate pressures. Under 1 atm, synthesized crystals break down into nepheline $NaAlSiO_4$ and wollastonite $CaSiO_3$. Studies of the $NaAlSiO_4$-$CaSiO_3$ system (which contains the $CaNaAlSi_2O_7$ composition) also confirm the absence of any stable compounds in the $NaAlSiO_4$-$CaSiO_3$ boundary [72, 73]. According to the studies of the $Ca_2Al_2SiO_7$-$CaNaAlSi_2O_7$ system, the content of Na-Mel in the solid solution does not exceed 52 wt% [71]. Na-melilite can be synthesized under high pressures.

In this work, sodium and potassium were added to the Melilite model developed earlier within the framework of the CEF [74]:

$$(Ca^{2+},Na^{+},K^{+})_2{}^{O}[Mg^{2+},Al^{3+},B^{3+}]^{T}\{Al^{3+},B^{3+},Si^{4+}\}_2\{O^{2-}\}_7 \quad (49)$$

According to model (49), there are 27 end-members in the system and one of them is charge neutral (akermanite $Ca_2MgSi_2O_7$). Gehlenite, Na- and K-melilite are in fact solid solutions and not true end-members. The Gibbs energies of fictive end-members need to be derived from the Gibbs energies of akermanite, gehlenite, Na- and K-melilites.

The Gibbs energies of the sodium-containing end-members were set according to the following equations:

$$G_{NaMel} = 0.5G_{CAS}+0.5G_{NAS}+2RT\ln(0.5) \quad (50)$$

$$\Delta_{CN//A//AS} = G_{CAA}+G_{NAS}-G_{CAS}-G_{NAA} \quad (51)$$

where G_{NaMel} is the Gibbs energy of Na-melilite $NaCaAlSi_2O_7$, G_{CAS}, G_{NAS}, G_{CAA}, G_{NAA} are the Gibbs energies of $Ca_2AlSi_2O_7^{+}$, $Na_2AlSi_2O_7^{-}$, $Ca_2AlAl_2O_7^{-}$ and $Na_2AlAl_2O_7^{3-}$ end-members, correspondingly. $\Delta_{CN//A//AS}$ is an exchange parameter.

As the true thermodynamic properties of Na-melilite are not known, its Gibbs energy was represented in the following way:

$$G_{\mathrm{NaMel}} = G(\mathrm{Ca_2Al_2SiO_7})+G(\mathrm{NaAlSi_3O_8})-G(\mathrm{CaAl_2Si_2O_8})+G^{add} \quad (52)$$

G^{add} and $\Delta_{\mathrm{CN//A//AS}}$ are independent model parameters which were adjusted in order to reproduce the experimental data in the CaO-Na_2O-Al_2O_3-SiO_2 system. For the remaining end-members, the Gibbs energy expressions are derived as follows:

$$G_{\mathrm{NAS}} = 2G_{\mathrm{NaMel}}-G_{\mathrm{CAS}}-4RT\ln(0.5) \quad (53)$$

$$G_{\mathrm{NAA}} = G_{\mathrm{CAA}}-3G_{\mathrm{CAS}}+2G_{\mathrm{NaMel}}-4RT\ln(0.5)-\Delta_{\mathrm{CN//A//AS}} \quad (54)$$

Two other exchange parameters allow us to introduce the sodium/magnesium-containing end-members:

$$\Delta_{\mathrm{CN//AM//S}} = G_{\mathrm{CMS}}+G_{\mathrm{NAS}}-G_{\mathrm{CAS}}-G_{\mathrm{NMS}} \quad (55)$$

$$\Delta_{\mathrm{N//MA//AS}} = G_{\mathrm{NMS}}+G_{\mathrm{NAA}}-G_{\mathrm{NMA}}-G_{\mathrm{NAS}} \quad (56)$$

The missing Gibbs energies are expressed as follows:

$$G_{\mathrm{NMS}} = G_{\mathrm{CMS}}-2G_{\mathrm{CAS}}+2G_{\mathrm{NaMel}}-4RT\ln(0.5)-\Delta_{\mathrm{N//MA//AS}} \quad (57)$$

$$G_{\mathrm{NMA}} = G_{\mathrm{CMS}}-4G_{\mathrm{CAS}}+2G_{\mathrm{NaMel}}-4RT\ln(0.5)+G_{\mathrm{CAA}}-\Delta_{\mathrm{N//AM//AS}}-\Delta_{\mathrm{CN//A//AS}} \quad (58)$$

Addition of the potassium-containing end-members to the solution is done in the same manner as for the sodium-containing end-members.

4.7 Clinopyroxene

Structurally, there are four types of pyroxenes: clino-, low clino-, ortho- and proto-pyroxene. Based on relative sizes of cations these structural types can have different ranges of temperature and composition stability. The clinopyroxene group includes a wide number of minerals. Their general chemical formula is $M^{I}M^{II}T^{I}T^{II}O_6$, where $M^{I} = Mg^{2+}$, Fe^{2+}, Mn^{2+}, Na^{+}, Li^{+}, Fe^{3+}, Al^{3+}, Cr^{3+}, Ti^{3+}, $M^{II} = Ca^{2+}$, Mg^{2+}, Fe^{2+}, Mn^{2+}, Na^{+}, Li^{+}, $T^{I} = Si^{4+}$, Al^{3+}, Cr^{3+}, Ti^{3+}, and $T^{II} = Si^{4+}$ [75].

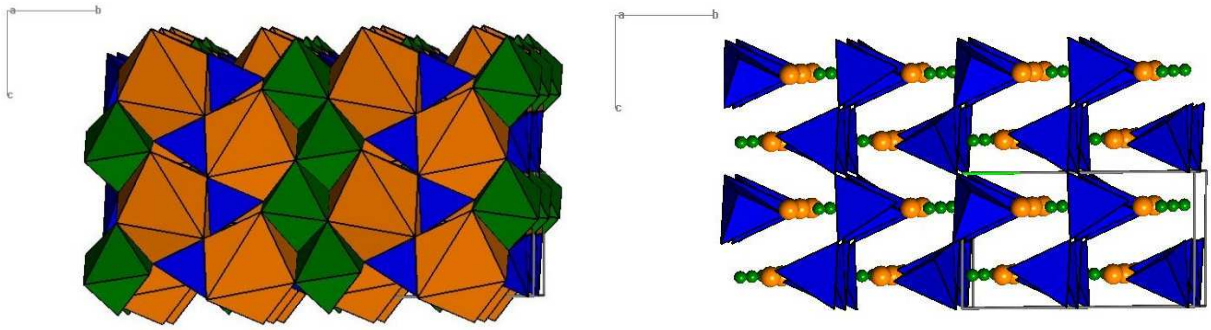

(***a***) (***b***)

Figure 4.14 The clinopyroxene structure, a view along the *a* axis with (***a***) and without (***b***) coordination polyhedra of cations. The structural data are taken from Okamura et al. [76].

The clinopyroxene structure is composed of alternating tetrahedra and octahedra layers (Figure 4.14). Tetrahedra are connected into infinite chains. There are two types of tetrahedral sites: one that is always occupied by silicon and the other which can exchange its silicon for other cations with a preference for tetrahedral coordination. M^{I} is a regular octahedral site while M^{II} is bigger in size and can change its coordination according to the type of cation it hosts.

In the Na_2O-K_2O-Al_2O_3-CaO-MgO-SiO_2 system, there are a few compounds which belong to the clinopyroxenes: Tschermak's pyroxene $CaAlAlSiO_6$, diopside $CaMgSi_2O_6$ and jadeite $NaAlSi_2O_6$. There is no stable K-analogue of jadeite because $KAlSi_2O_6$ has a completely different structure [77]; therefore, the solubility of potassium in clinopyroxene must be negligibly small and it was not modeled

Under higher pressures, there is a solid solution between diopside and jadeite [78-80]. However, under ambient pressures, sodium solubility in diopside is quite small [81].

Three end-members of Clinopyroxene solid solution belong to the quaternary system: Ca-Tschermak $CaAl_2SiO_6$, jadeite $NaAlSi_2O_6$ and Ca-Eskola $Ca_{0.5}AlSi_2O_6$. The last one is usually introduced to account for the solubility of excess silica in the solid solution. $NaAlSi_2O_6$-$CaAl_2SiO_6$ clinopyroxenes can dissolve up to 7.5-8.0 wt% silica [82, 83].

There are no data on alkali solubilities in other pyroxene solutions. In this work, only Clinopyroxene solution was modified as jadeite belongs to the clinopyroxene group [84]. The

current Clinopyroxene model was adopted after Jung [85]. The model is built using the Compound Energy Formalism and includes three non-trivial sublattices:

$$[Ca^{2+},Mg^{2+},Na^{+}]^{MII}[Mg^{2+},Al^{2+}]^{MI}(Si^{4+},Al^{3+})^{TI}\{Si^{4+}\}^{TII}\{O^{2-}\}_{6} \quad (59)$$

Sodium occupies exclusively the bigger M^{II} sites.

According to model (59), there are 12 end-members in total and only four of them are charge neutral. The properties of the charge neutral end-members can be evaluated from experimental data while the properties of the charged end-members need to be derived.

4.8 Combeite

Combeite is an important solid phase occurring in the CaO-Na_2O-SiO_2 system. Early works on the system note an unusually flat liquidus of the phase. A possible explanation included formation of a solid solution [86]. The phase was believed to have an approximately 1:2:3 stoichiometry ($Na_2Ca_2Si_3O_9$), thus being a mixed metasilicate. A more detailed research by Moir and Glasser [87] confirmed that the phase is a solid solution and its composition ranges between 28.5 to 53.5 mol% Na_2SiO_3 (Figure 4.15). Combeite solution exists in a low and a high form, the transition between them is detectable by DTA. The transformation rates are different for $CaSiO_3$- and Na_2SiO_3-rich solutions. Moir and Glasser [87] did not investigate the substitution mechanism in combeite. Low and high combeites were modeled with one Combeite solution (see section 2.3).

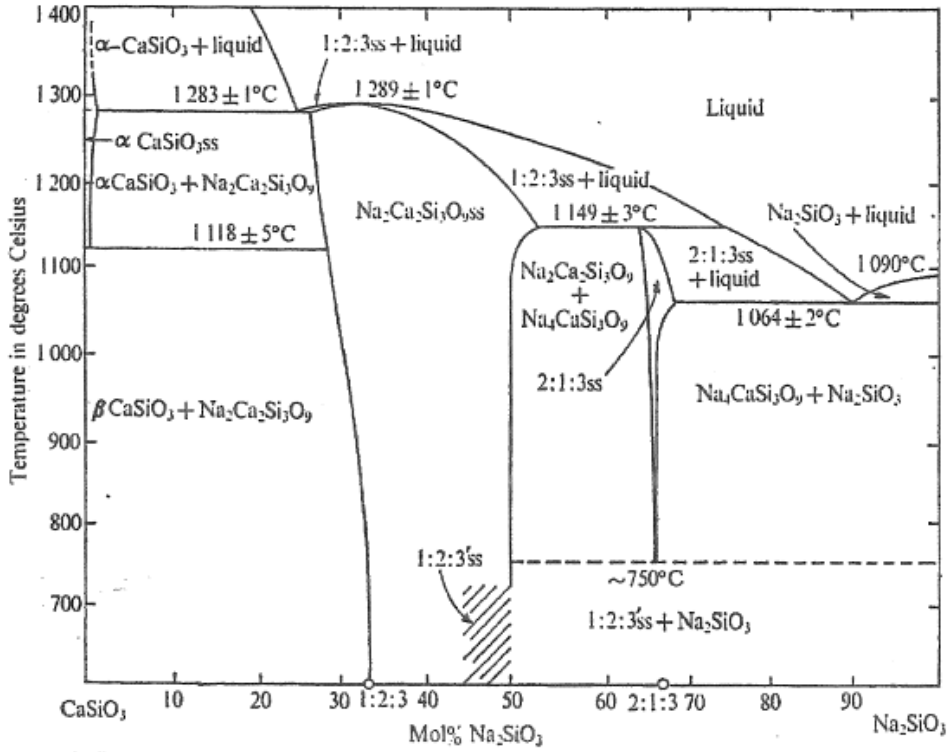

Figure 4.15 The metasilicate section in the Na_2O-CaO-SiO_2 system (schematic). The phase diagram features α-$CaSiO_3$, combeite and (2:1:3) solid solutions. The image is taken from Moir and Glaser [87].

In the K_2O-CaO-SiO_2 system, no phase equivalent to combeite was found. However, in the Na_2O-SrO-SiO_2 system, it also exists although has a narrower non-stoichiometry range (Figure 4.16). There are also phase equilibrium data on a mixed Ca/Sr-combeite in the Na_2O-CaO-SrO-SiO_2 system [88].

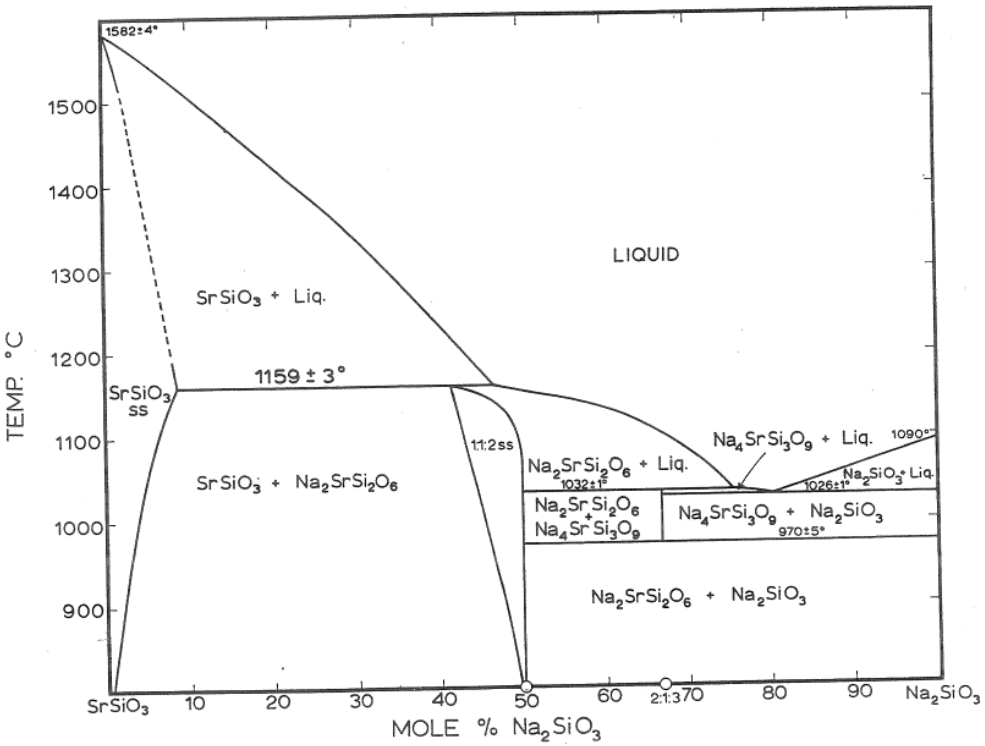

Figure 4.16 The metasilicate section in the Na_2O-SrO-SiO_2 system. The phase diagram features α-$SrSiO_3$, combeite and (2:1:3) solid solutions. The image is taken from Moir and Glaser [88].

A structural study of combeite was carried out by Ohsato et al. [89, 90] (the site notation was adopted after the original study). The high modification has four cationic sites in the structure (occupied by either sodium or calcium) with different preferences for calcium and sodium. At low temperatures, these sites split into symmetrically non-equivalent subsites. Both modifications have a trigonal symmetry. According to the charge neutrality equation, a calcium cation needs to be exchanged with two sodium cations, one of them taking the same site and another going to a previously vacant site.

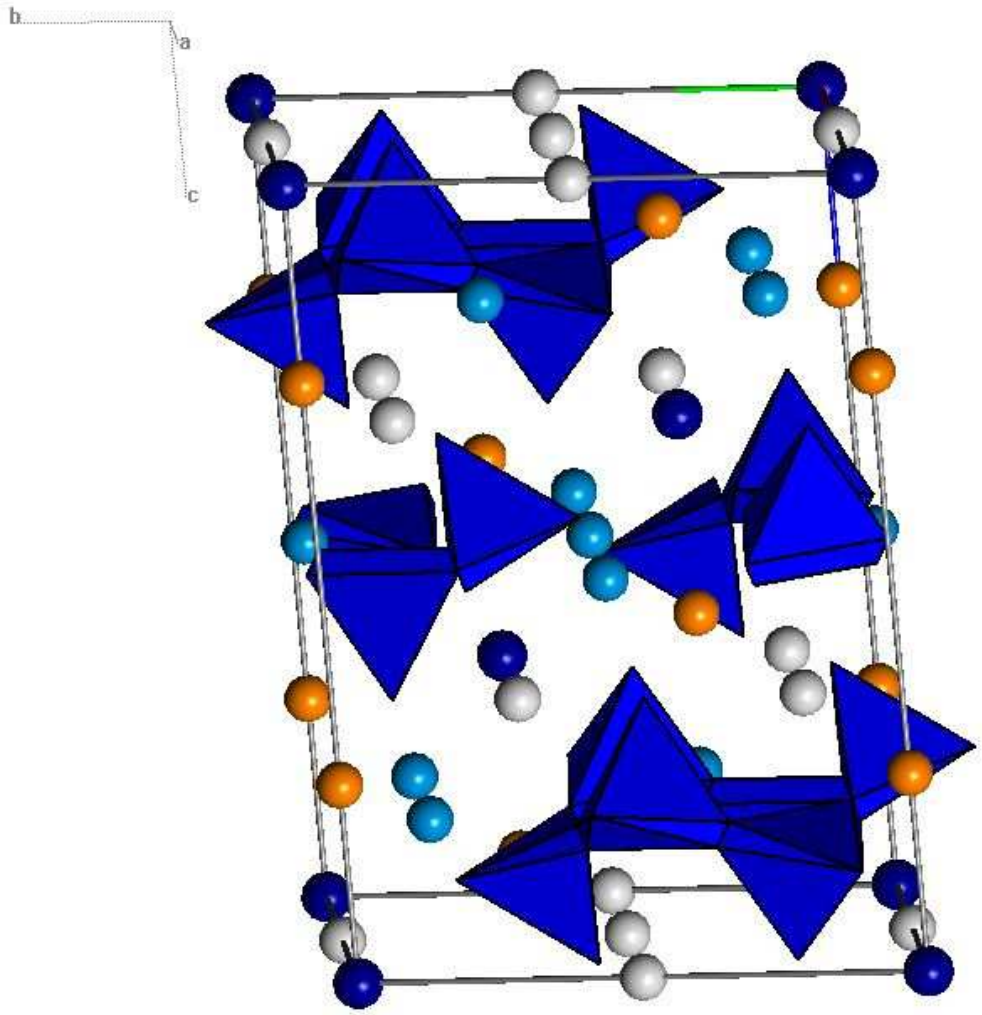

Figure 4.17 The high-combeite structure, viewed along the *a* axis. The image features six-membered silicon tetrahedra rings and four types of cations: M1 (orange), M2 (light grey), M3 (light blue) and M4 (navy). Based on the data by Ohsato et al. [90].

The structure of combeite is presented in Figure 4.17. Due to the stoichiometry, metasilicates have their silicon tetrahedra arranged either as infinite chains without branching or form closed tetrahedra rings. In the case of combeite, silicon tetrahedra form six-membered rings, two of them are completely visible in Figure 4.17.

Combeite phase is mostly encountered in artificial phase assemblages although sometimes it occurs naturally. The composition of a natural specimen is $Na_{2.4}Ca_{1.5}(Fe, Mn, Mg, Zn)_{0.3}Si_3O_9$ [89].

As already mentioned, there are four cationic sites in the structure. M4 is occupied exclusively by calcium which cannot be exchanged with sodium. M1 and M3 are occupied by both sodium and calcium and M2 corresponds to the vacant site occupied with excess sodium according to the substitution mechanism:

$$Ca^{2+} \leftrightarrow 2Na^{+} \tag{60}$$

Keeping in mind the given structure, the following model was proposed for combeite:

$$(Na_2^{2+},Ca^{2+},Sr^{2+})_2(Ca^{2+},Na_2^{2+},Sr^{2+})_3(Ca^{2+},Sr^{2+})_1\{Si_6O_{18}^{12-}\} \tag{61}$$

The model includes strontium as well, although it goes beyond the scope of the current work. The first two sublattices correspond to M1 and M3 sites, the third sublattice accounts for the calcium and strontium in M4. There is no sublattice corresponding to M2 site, as the excess sodium ions present there are locally bound and do not contribute to the configurational entropy. These ions are coupled and present as Na2 pairs in the model.

The proposed model assumes that the solid solution consists of neutral end-members. It reduces the model complexity compared to models with charged end-members.

4.9 (2:1:3)

Moir and Glasser [87] have found that N2CS3 or (2:1:3) compound in the CaO-Na_2O-SiO_2 system has a small non-stoichiometry range. Their phase diagram of the Na_2SiO_3-$CaSiO_3$ join is presented in Figure 4.15. It has a cubic structure [91]. There is an equivalent compound in the CaO-K_2O-SiO_2 system [92, 93]. An analogous compound with the same structure has also been found in the Na_2O-SrO-SiO_2 system [88]. However, no non-stoichiometry has been reported in the K_2O-CaO-SiO_2 and Na_2O-SrO-SiO_2 systems. It is either negligibly small or has not been studied in detail. Although no data on the K_2O-SrO-SiO_2 system were found, it is possible that this system also contains the same compound. It can be assumed that all these compounds are end-members in a solid solution extending throughout the Na_2O-K_2O-CaO-SrO-SiO_2 system. A compound of (2:1:3) stoichiometry was found in the K_2O-BaO-SiO_2 system [94] but not in the Na_2O-BaO-SiO_2 [95].

Ion exchange mechanisms involved in formation of the solid solution among $Na_4CaSi_3O_9$-$K_4CaSi_3O_9$-$Na_4SrSi_3O_9$-$K_4SrSi_3O_9$ are straightforward:

$$Na^{+} \leftrightarrow K^{+} \quad (62)$$

$$Ca^{2+} \leftrightarrow Sr^{2+} \quad (63)$$

However, to explain the non-stoichiometry of $Na_4CaSi_3O_9$ along the Na_2SiO_3-$CaSiO_3$ metasilicate join, the following ion exchange scheme is required:

$$Ca^{2+} \leftrightarrow 2Na^{+} \quad (64)$$

Scheme (64) implies that one sodium ion (or potassium) goes into the site previously occupied by Ca^{2+} and the second one, required for change balance, goes somewhere else, probably into a site which is usually vacant.

According to the crystallographic data by Fischer and Tillmanns [91], a unit cell in the cubic structure of $Na_4CaSi_3O_9$ contains 16 formula units:

$$(Na/Ca1)_8(Na/Ca2)_8(Na/Ca3)_8(Na1)_{24}(Na2)_{24}(Ca1)_4(Ca2)_4(Si1)_{24}(Si2)_{24}O_{144} \quad (65)$$

Keeping in mind the total stoichiometry, the sites Na/Ca1, Na/Ca2, Na/Ca3 must contain in total 8 ions of calcium and 16 ions of sodium. The third site has the highest sodium content and is supposed to be the site for charge-compensating sodium cations. The Na1 and Na2 sites can be merged together for the model's simplicity as well as Ca1 and Ca2.

The following model with neutral end-members was proposed:

$$(Ca^{2+},Sr^{2+},Na_2^{2+},K_2^{2+})_1(Ca^{2+},Sr^{2+},Na_2^{2+},K_2^{2+})_1(Na+,K+)_6(Ca^{2+},Sr^{2+})_1\{Si_6O_{18}^{12-}\} \quad (66)$$

Although there are no data on the structure of mixed crystals, it is assumed that potassium can enter any sites where sodium goes as well as strontium can enter the calcium-containing sites. The first and second sublattices correspond to Na/Ca1 and Na/Ca2 sites, Na/Ca3 site is omitted as sodium in it is locally bound to substitution sites and does not contribute to the total configurational entropy. The third sublattice represents Na1 and Na2 sites merged together and the fourth is Ca1 + Ca2.

4.10 NCA2

NCA2 is a solid solution between $Na_2CaAl_4O_8$ compound and $NaAlO_2$ reported by Verweij and Saris [96]. There are no crystallographic data on how the ion substitution occurs but apparently, as

in many other solutions including both sodium and calcium, calcium is substituted for sodium because their sizes are close and the second sodium required for the charge compensation enters a vacant position in the crystallographic structure. However, this second sodium is not configurationally free and is locally bound to the substitution site. It does not contribute to the configurational entropy and both sodium cations effectively act as one particle Na_2. Based on that, the following model was developed for this solution:

$$(Na_2^{2+}, Ca^{2+})\{Na_2Al_4O_8^{2-}\} \quad (67)$$

Model (67) implies two neutral end-members.

4.11 C3A

Tricalcium aluminate is an important phase in the cement production and the fact that it dissolves a few percent of alkali oxides plays an important role.

Apparently, the substitution of calcium for sodium or potassium is accompanied by introduction of a second sodium (or potassium) in a vacant site for the charge balance. Apparently, the second cation is bound to the site to maintain the local charge neutrality of the structure and does not contribute to the configurational entropy of the solution; two cations can be treated as one particle. The corresponding solid solutions were investigated by Brownmiller and Bogue [97], Conwicke and Day [98], Shin and Glasser [99], Nishi and Takeuchi [100]. The solution can change symmetry at different alkali oxide contents [98]. The maximum solubility reaches NC8A3 composition. The solid solution $Ca_{8.5}NaAl_6O_{18}$ studied by Nishi and Takeuchi [100] is orthorhombic. It contains Al_6O_{18} rings made of AlO_4 tetrahedra sharing corners. There are altogether 36 available locations for the 34 Ca atoms in the unit cell. The excess locations are preferably distributed in the set of Ca(5) positions to accommodate two of the four Na's per cell. The remaining two Na's are located at the centers of the tetrahedral rings (occupancy of 0.5).

The following model was proposed:

$$(Na_2^{2+}, K_2^{2+}, Ca^{2+})\{Ca_8Al_6O_{18}^{2-}\} \quad (68)$$

4.12 Beta-, Beta”-alumina

Al_2O_3-rich areas of the Na_2O-Al_2O_3 and K_2O-Al_2O_3 systems feature two compounds with layered spinel structure which were originally thought to be polymorphic modifications of pure alumina (β- and β”-alumina), until it was later proved that their formation requires the presence of alkali oxides [101, 102]. The compounds have approximate compositions of $NaAl_9O_{14}$ (β-alumina) [103] and $Na_2Al_{12}O_{19}$ (β”-alumina) [104]. The compounds are of high practical interest because of their high alkali ion conductivity which makes them useful as solid electrolytes for battery applications [10]. The high ion mobility is explained by the layered structure of the compounds, where spinel-like alumina blocks are separated by conduction planes consisting of oxygen, alkali cations and vacancies and where the alkali ions can hop into vacant sites with a low activation energy. The structure of β- and β”-alumina can be stabilized by Mg or Li [105, 106] which can lead to lower alkali pressures and higher degradation resistance.

Both β- and β”-alumina can exchange their alkalies for a wide variety of single and double charged cations [105]. In the Na_2O-Al_2O_3 and K_2O-Al_2O_3 binaries, they exhibit deviations from the stoichiometry of 2-3 mol% alkali oxide [18].

The solution models for β- and β”-alumina were taken from the work of Kim [18]. The models are identical, different properties are achieved by choice of different model parameters. They developed the model for potassium and magnesium containing solutions, in this work it was extended to include sodium as well.

The model by Kim [18] is formulated in the following way:

$$[Na^+,K^+,Va]_1^{BR}[Na^+,K^+,Va]_1^{aBR}[Al^{3+},Mg^{2+}]_2^{T}[O^{2-},Va]_1^{mO}Al_9^{other}O_{17} \quad (69)$$

The first, second and forth sublattices in (69) refer to the conduction planes: Beever-Ross and anti-Beever-Ross sites for alkali cations and the anionic sublattice for oxygen, compensating charge of the alkali cations. Those aluminium cations in the spinel blocks which occupy tetrahedral sites, can exchange for magnesium cations. The rest of the aluminium cations cannot be exchanged.

The modeling approach and the model parameters are described in detail in the work by Kim [18]. It is reproduced in this work.

The model by Kim [18] is based on the Gibbs energies of pure compounds whose stoichiometries were considered to be $KAl_{11}O_{17}$ for β-alumina and $K_4Al_{22}O_{25}$ for β”-alumina. In this work, different stoichiometries were accepted: $(Na,K)Al_9O_{14}$ for β-alumina and $(Na,K)_2Al_{12}O_{19}$ for β”-alumina. The potassium part of the solid solutions remained untouched but for the sodium compounds a conversion was made using the ratio of molar masses $NaAl_{11}O_{17}/NaAl_9O_{14}$ and $Na_4Al_{22}O_{25}/Na_2Al_{12}O_{19}$. The Gibbs energies of binary end-members are expressed as follows (potassium is left for example purposes):

Binary β-alumina

$$G_{\mathrm{KVAV}} = G^{\circ}(\mathrm{KAl_{11}O_{17}}) \tag{70}$$

$$G_{\mathrm{KKAO}} = G_{\mathrm{KKAV}} = 0.5[G^{\circ}(\mathrm{K_4Al_{22}O_{35}})+\Delta S^{conf}+G^{add(1)}] \tag{71}$$

Binary β”-alumina

$$G_{\mathrm{KVAV}} = G^{\circ}(\mathrm{KAl_{11}O_{17}})+G^{add(2)} \tag{72}$$

$$G_{\mathrm{KKAO}} = G_{\mathrm{KKAV}} = 0.5(G^{\circ}(\mathrm{K_4Al_{22}O_{35}})+\Delta S^{conf}) \tag{73}$$

Independent model parameters are introduced so the Gibbs energies of the remaining end-members can be expressed with them:

$$\Delta^2 = G_{\mathrm{KVAO}}+G_{\mathrm{KKAV}}-G_{\mathrm{KKAO}}-G_{\mathrm{KKAV}} \tag{74}$$

$$I^1 = G_{\mathrm{VKAV}}-G_{\mathrm{KVAV}} \tag{75}$$

$$\Delta^5 = G_{\mathrm{KVAV}}+G_{\mathrm{VKAV}}-G_{\mathrm{KKAV}}-G_{\mathrm{VVAV}} \tag{76}$$

$$I^2 = G_{\mathrm{VKAO}}-G_{\mathrm{KVAO}} \tag{77}$$

$$\Delta^8 = G_{\mathrm{VVAV}}+G_{\mathrm{VKAO}}-G_{\mathrm{VKAV}}-G_{\mathrm{VVAO}} \tag{78}$$

Mg-containing end-members add more parameters to the model:

$$G_{\mathrm{KKMV}} = G_{\mathrm{KVAV}}+G^{add(\mathrm{K\text{-}Mg})} \tag{79}$$

$$G_{\mathrm{KVMV}} = G_{\mathrm{KVAV}}+G^{add(\mathrm{Va\text{-}Mg})} \tag{80}$$

$$\Delta^1 = G_{\mathrm{KVMO}}+G_{\mathrm{KVAV}}-G_{\mathrm{KVAO}}-G_{\mathrm{KVMV}} \tag{81}$$

$$\Delta^3 = G_{\mathrm{KKAO}}+G_{\mathrm{KKMV}}-G_{\mathrm{KKMO}}-G_{\mathrm{KKAV}} \tag{82}$$

$$\Delta^4 = G_{KVMV}+G_{VVAV}-G_{KVAV}-G_{VVMV} \quad (83)$$

$$\Delta^6 = G_{KKAV}+G_{VKMV}-G_{VKMV}-G_{VKAV} \quad (84)$$

$$\Delta^7 = G_{VVMV}+G_{VVAO}-G_{VVAV}-G_{VVMO} \quad (85)$$

$$\Delta^9 = G_{VKAV}+G_{VKMO}-G_{VKMV}-G_{VKAO} \quad (86)$$

The derived expressions of the Gibbs energy for each end-member can be found in the original work [18].

4.13 Leucite

Leucite is a compound in the K_2O-Al_2O_3-SiO_2 system with $KAlSi_2O_6$ formula. It is structurally distinct from jadeite $NaAlSi_2O_6$ with the same stoichiometry but different coordination numbers of cations. While leucite is a stable phase forming a primary crystallization field, jadeite is stable only at high pressures [107]. So, Al in jadeite is six-coordinated while in leucite it occupies the same positions as Si (Figure 4.18). Apparently, leucite can have different degrees of Al/Si ordering [108]. Sodium ions are too small to stabilize a leucite-like structure. Based on these considerations, it can be assumed that the substitution of potassium for sodium in leucite is not significant. In fact, Gupta and Edgar [109] found that the maximum solubility of sodium end-member in leucite does not exceed 5 mol%.

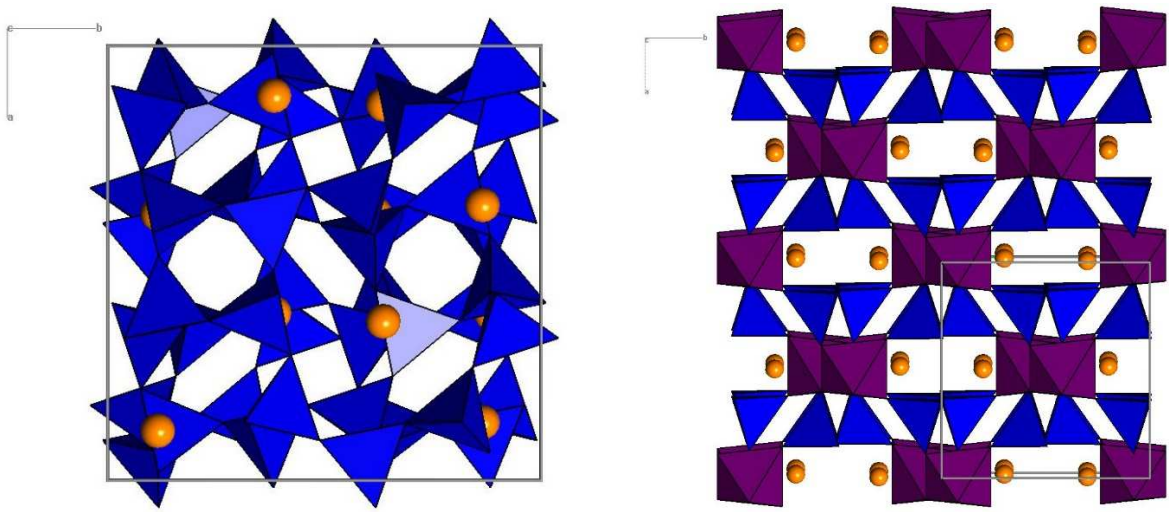

(***a***) (***b***)

Figure 4.18 Comparison of the leucite (***a***) and jadeite structures (***b***). The crystallographic data are taken from Mazzi et al. [110] and Prewitt and Burnham [84], correspondingly.

There are several other compounds which are reported to have a leucite-like structure. For example, $KBSi_2O_6$ compound, boroleucite, is one of them [111, 112]. It forms a complete solid solution with $KAlSi_2O_6$ [113]. The substitution mechanism which leads to the formation of the solid solution can be expressed as:

$$Al^{3+} \leftrightarrow B^{3+} \tag{87}$$

Some compounds in the K_2O-MgO-SiO_2 system are structurally similar to the compounds in the K_2O-Al_2O_3-SiO_2 system. So, $K_2MgSi_5O_{12}$ bears a close resemblance to leucite and there is a solid solution between them [114-116]. The substitution mechanism can be written as follows:

$$2Al^{3+} \leftrightarrow Mg^{2+} + Si^{4+} \tag{88}$$

In this work, a Leucite model was created that would allow for substitution mechanisms discussed above as well as partial substitution of potassium for sodium.

Keeping both substitution mechanisms in mind, a two-sublattice CEF model for the solid solution of leucite was proposed:

$$(K^+,Na^+)[Al^{3+},B^{3+},Mg^{2+}Si^{4+}]Si_2O_6 \tag{89}$$

The properties of the neutral end-members are evaluated based on the data of the corresponding compounds.

4.14 Mixed Orthosilicate

Compounds with (1:1:1) stoichiometry exist in almost all alkali oxide-alkali-earth oxide-silica systems: Na_2CaSiO_4, K_2CaSiO_4, Na_2MgSiO_4, K_2MgSiO_4, Na_2SrSiO_4, K_2SrSiO_4. As a rule, they have the same cubic structure and a solid solution is possible among the end-members [56]. The only exception is K_2MgSiO_4 which is isostructural with $KAlO_2$ [46]. Based on the data by Berezhnoi et al. [56] these solutions are close to ideality.

The following model was proposed:

$$(Na,K)_2[Ca,Mg,Sr]SiO_4 \tag{90}$$

The properties of the neutral end-members are evaluated based on the data of the corresponding compounds; in case of K_2MgSiO_4, a stability parameter is required to account for the structure change.

4.15 Pseudowollastonite and Ca-Orthosilicate

Pseudowollastonite is a high-temperature modification of $CaSiO_3$. $SrSO_3$ also has modifications analogous to wollastonite and pseudowollastonite. Pseudowollastonite is able to dissolve a few percent of Na_2SiO_3 or K_2SiO_3; the low-temperature modification (wollastonite), however, does not show any noticeable solubility [87]. It has been proposed that a sodium cation substitutes for Ca^{2+} while the second Na^+ enters a vacant site in the structure for charge balance. The following model was proposed:

$$(Ca^{2+},Sr^{2+},Na_2^{2+},K_2^{2+})SiO_3 \tag{91}$$

The second sodium cation entering the structure is locally bound to the first one and does not contribute to the configurational entropy. Therefore, Na_2^{2+} and K_2^{2+} are designed as single particles. The properties of the neutral end-members are evaluated based on the properties of the stoichiometric compounds. Na_2SiO_3 and K_2SiO_3 end-members require stability parameters to account for the structure change.

Two forms of calcium orthosilicate, α- and α'-Ca_2SiO_4, are able to dissolve some amounts of sodium [117] and potassium [118]. Apparently, the solution mechanism is similar to the one in pseudowollastonite solution. K_4SiO_4 solubility in calcium orthosilicate has been modeled by Kim [18] who added K_4SiO_4 end-member to existing one-sublattice models of α- and α'-Ca_2SiO_4. In this work, Na_4SiO_4 end-member was added:

$$(0.5Ca_2SiO_4,0.5Mg_2SiO_4,0.5Na_4SiO_4,0.5K_4SiO_4)_2 \tag{92}$$

4.16 Milarite

Milarite is a solid solution between $Na_2Mg_5Si_{12}O_{30}$ and $K_2Mg_5Si_{12}O_{30}$ compounds. It is known that the compounds have the same structure, but the properties of the solid solutions are unknown. A model based on the CEF was proposed:

$$(Na^+,K^+)_2\{Mg_5Si_{12}O_{30}^{2-}\} \tag{93}$$

The properties of the neutral end-members are evaluated based on the data of the corresponding compounds.

4.17 Monoborate, Diborate and Triborate

In the Na_2O-K_2O-B_2O_3 system, the corresponding mono-, di- and triborate end-members form complete solid solutions. They were modeled within the framework of CEF with two sublattices: one for cation mixing and a trivial second sublattice:

$$(Na^+,K^+)\{BO_2\} \tag{94}$$

$$(Na^+,K^+)_2\{B_4O_7^{2-}\} \tag{95}$$

$$(Na^+,K^+)\{B_3O_5^-\} \tag{96}$$

CHAPTER 5 THERMODYNAMICS OF MULLITE AND MODIFICATIONS OF NON-ALKALI SYSTEMS

5.1 Mullite discrepancy

Mullite is the main solid solution in the Al_2O_3-SiO_2 system (see Section 4.1). The primary crystallization field of Mullite propagates from the Al_2O_3-SiO_2 side in ternary systems with an alkali or alkali earth oxide third component. During this work, it was noticed that a series of ternary systems, such as CaO-Al_2O_3-SiO_2, MgO-Al_2O_3-SiO_2, PbO-Al_2O_3-SiO_2, Na_2O-Al_2O_3-SiO_2, K_2O-Al_2O_3-SiO_2 and some others show the same deviation from the experimental data: Mullite primary field is consistently larger than it is supposed to be and the Mullite/Corundum boundary descends in the ternary system at a wrong angle (see Figure 5.1). The experimental points in Figure 5.1 are given for illustrative purposes; an exhaustive search for experimental data in the systems was beyond the scope of the current work (Section 1.3).

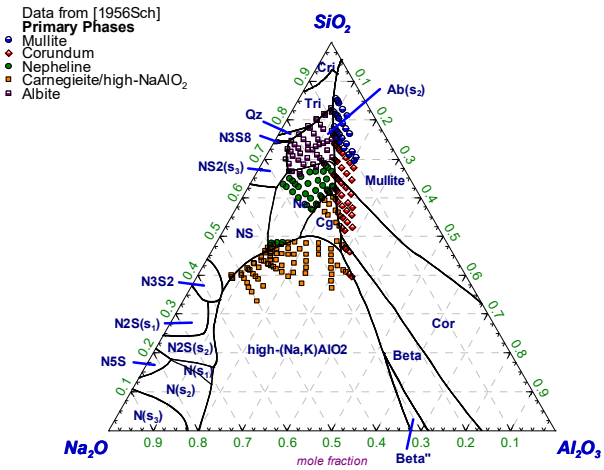

(*a*)

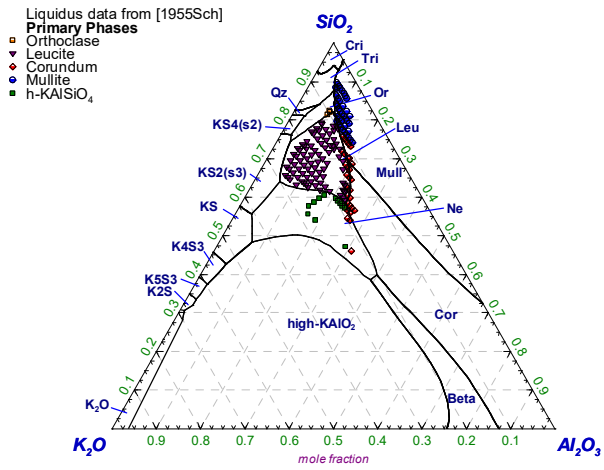

(*b*)

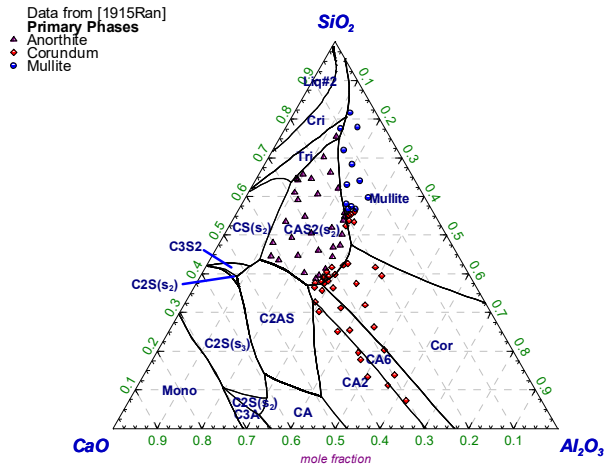

(*c*)

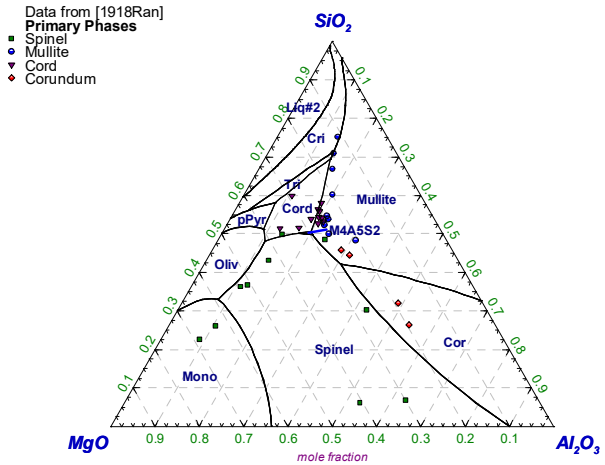

(*d*)

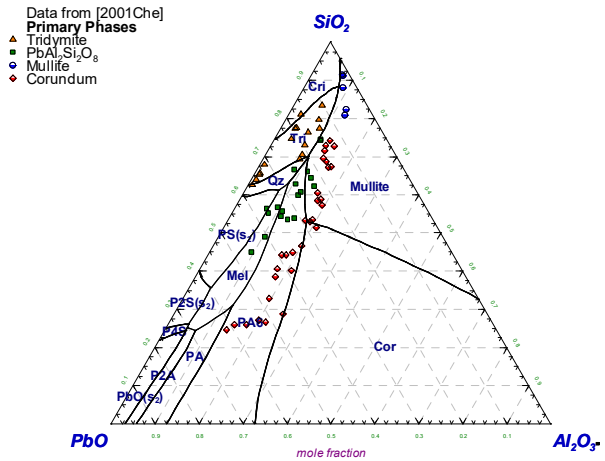

(*e*)

Figure 5.1 Primary phase fields in the Na_2O-Al_2O_3-SiO_2 (***a***), K_2O-Al_2O_3-SiO_2 (***b***), CaO-Al_2O_3-SiO_2 (***c***), MgO-Al_2O_3-SiO_2 (***d***) and PbO-Al_2O_3-SiO_2 (***e***) systems. Primary phase data [55] (***a***), [119] (***b***), [120] (***c***), [121] (***d***), [122] (***e***) and calculated univariant lines.

Based on the optimization experience, it is known that the position of the Mullite/Corundum binary is not affected by ternary parameters in the Na_2O-Al_2O_3-SiO_2 and K_2O-Al_2O_3-SiO_2 systems. Supposedly, it is also the case in all other systems although they are beyond the scope of the current work. As Mullite and Corundum are made up only of alumina and silica components, it is logical to assume that their relative stability is mainly defined by the interaction parameters in the Al_2O_3-SiO_2 binary system and is not affected much by the presence of a third component. The

optimization of the Al_2O_3-SiO_2 system currently accepted in the oxide database of *FactSage* was performed by Eriksson and Pelton [123]. Their review of the literature data shows that mostly phase diagram data are available while calorimetry data are lacking. Usually, systems lacking stability data on at least one of the phases in equilibrium should be treated with care. Almost identical phase diagrams can be obtained in optimizations with more stable liquid/more stable solid and less stable liquid/less stable solid pairs. Usually, these kinds of systems can be assessed reliably only if they feature large phase fields of phases with known properties. However, the majority of the liquidus field in the Al_2O_3-SiO_2 system is occupied by Mullite while fields of Al_2O_3 and SiO_2 whose properties are known are small. Wrong stability of a solid phase and the liquid in a binary system might not matter in the binary system itself but the difference becomes important when other components are added (ternary and multicomponent systems).

To prove the hypothesis, a trial optimization with a more stable Mullite and liquid was done in the Al_2O_3-SiO_2 system. Figure 5.2 shows phase fields in the CaO-Al_2O_3-SiO_2 and MgO-Al_2O_3-SiO_2 systems with the current Al_2O_3-SiO_2 optimization and an optimization with a more stable Mullite and liquid. It can be seen that the discrepancy present in Figure 5.1 disappears.

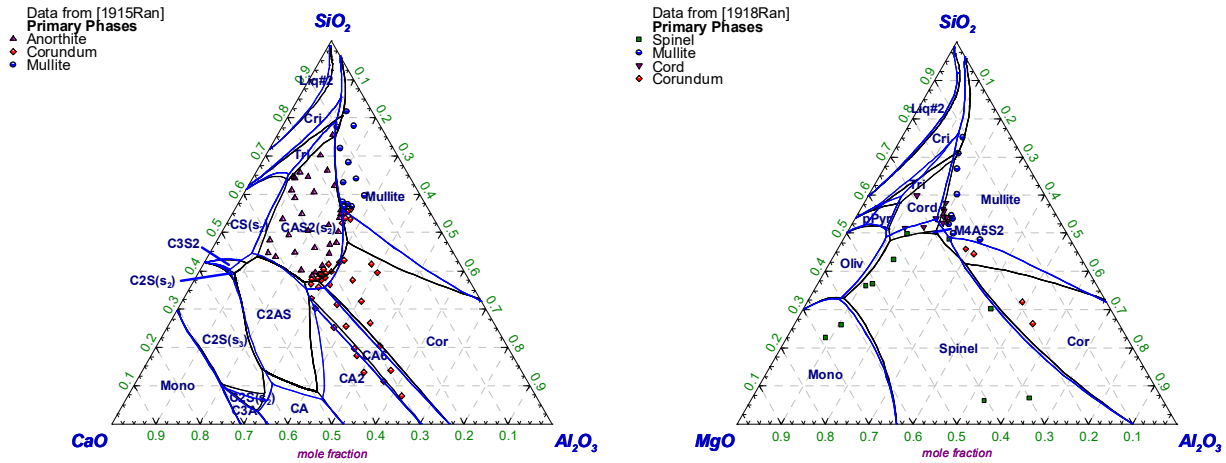

(***a***) (***b***)

Figure 5.2 Primary phase fields in the CaO-Al_2O_3-SiO_2 (***a***) and the MgO-Al_2O_3-SiO_2 (***b***) systems with the current (black lines) and a modified optimization of the Al_2O_3-SiO_2 binary system (blue lines). Primary phase data [120] (***a***), [121] (***b***) and calculated univariant lines.

It seems logical that phase stabilities in the Al_2O_3-SiO_2 system should be increased compared to the old optimization by Eriksson and Pelton [123]. However, the Al_2O_3-SiO_2 system is a cornerstone of the current oxide database of *FactSage* which comprises many more components than the Na_2O-K_2O-CaO-MgO-Al_2O_3-B_2O_3-SiO_2 system studied in this work. A reoptimization of the Al_2O_3-SiO_2 would render it incompatible with the rest of the oxide database and was not feasible within the framework of the current research project.

5.2 Correction of the Al_2O_3-SiO_2 system

The original optimization of the Al_2O_3-SiO_2 system was published by Eriksson and Pelton [123]. The need of a partial reoptimization of the system was caused by the introduction of a new Mullite model. The old model miscounted the number of octahedral sites per formula unit. Although there are much more data on phase equilibria available in the literature than those sources used for the optimization, a full reoptimization of this binary system would require a consequent reoptimization of many systems than are not part of the current research project. The purpose of this correction is to reproduce the old optimization of the binary system as closely as possible but using the new Mullite model (Figure 5.3). The parameters of the liquid phase remained unchanged to keep the compatibility with the optimized systems which include the Al_2O_3-SiO_2 system as a subsystem.

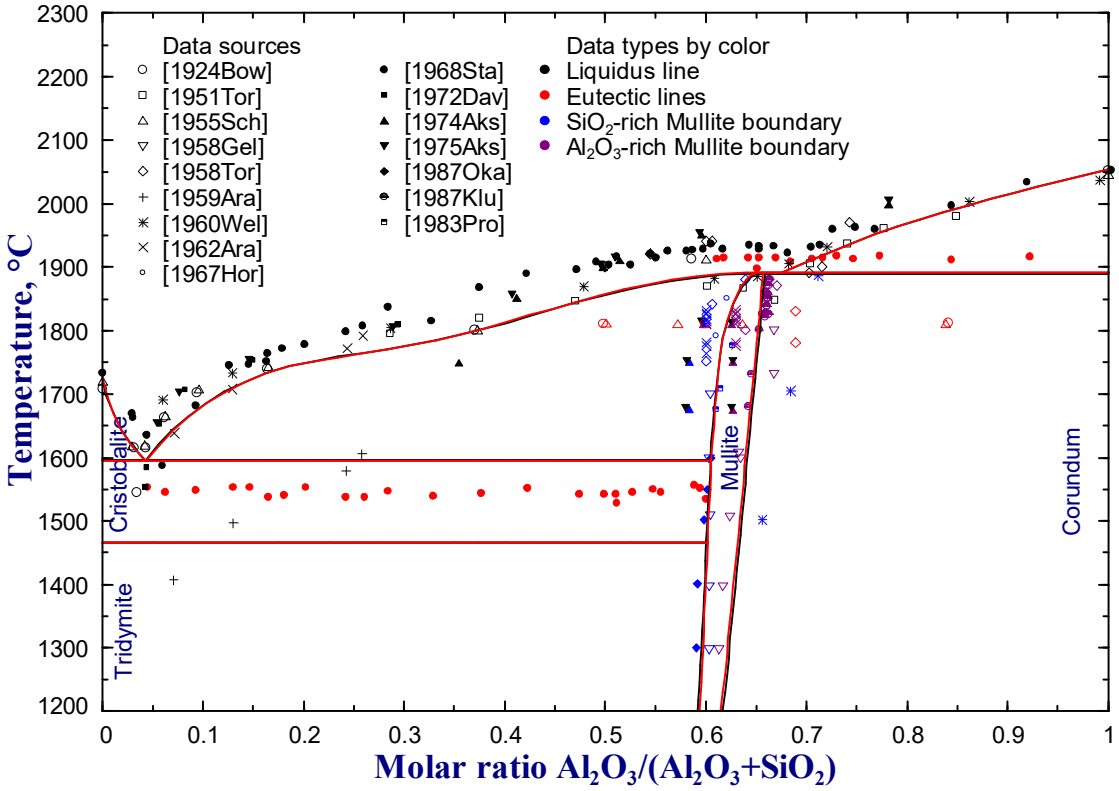

Figure 5.3 Phase diagram of the Al_2O_3-SiO_2 system. Experimental points [119, 124-138] and calculated lines: the optimization from Eriksson and Pelton [123] in red, the current optimization in black.

5.3 Optimization results

The model parameters of Mullite are given in Table A.1.

5.4 Correction of the Al_2O_3-B_2O_3-SiO_2 system

The original optimization of the Al_2O_3-B_2O_3-SiO_2 system was published by Swamy et al. [16]. The original Mullite model was replaced with the new one and the model parameters were chosen to reproduce the data used in the original optimization as closely as possible.

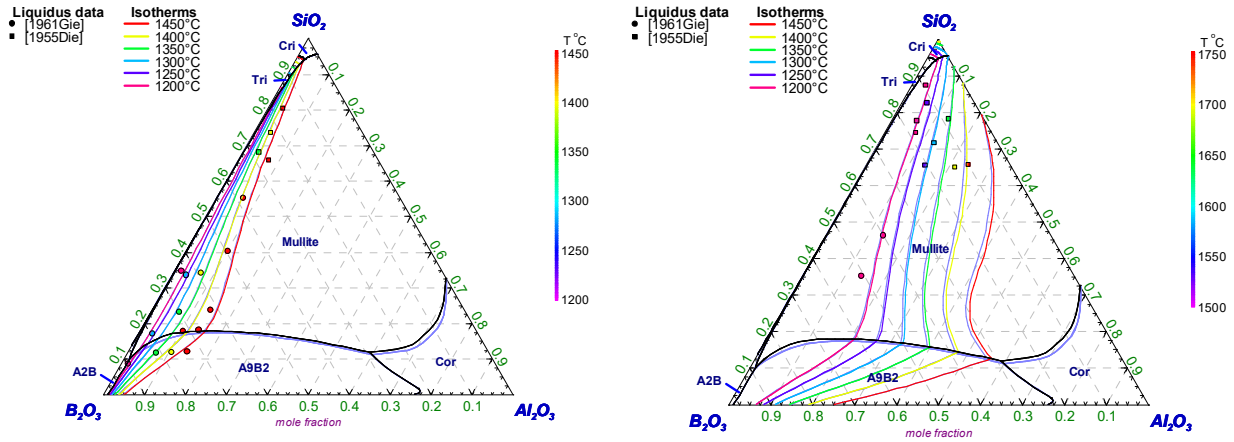

(***a***) (***b***)

Figure 5.4 Liquidus projection in the SiO_2-B_2O_3-Al_2O_3 system, isotherms in the range of 1200-1450°C (***a***) and of 1500-1750°C (***b***). Experimental points [139, 140], the original optimization from Swamy et al. [16] in gray and the optimization with the new Mullite solution in rainbow colors (isotherms) and black (univariant lines).

Liquidus projections in the ternary system for different temperature intervals are presented in Figure 5.4.

5.5 Optimization results

The model parameters of the boron-containing mullite are given in Table A.2.

CHAPTER 6 OPTIMIZATION OF THE Na_2O-SiO_2 SYSTEM

6.1 Thermodynamic modeling

The previous optimizations of the Na_2O-SiO_2 system usually encountered problems with the high-SiO_2 region including the cristobalite liquidus [17, 141]. Generally, the predicted liquidus is lower than the corresponding experimental points (Figure 6.1).

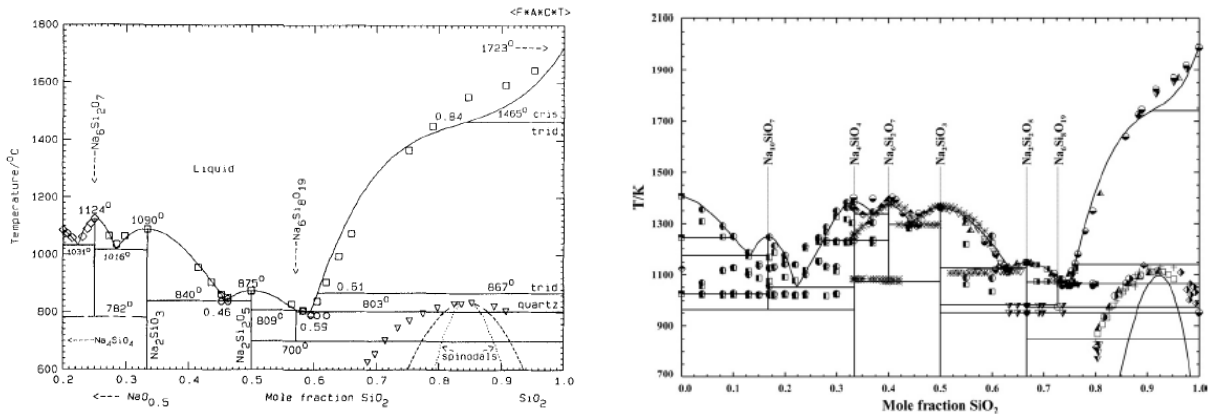

(***a***) (***b***)

Figure 6.1 Optimized phase diagrams from the works of Wu et al. [17] (***a***) and Lambotte and Chartrand [141] (***b***).

A recent optimization of the Li_2O-SiO_2 system by Konar et al. [142] shows a poor reproduction of the cristobalite liquidus (Figure 6.2), the same as in the Na_2O-SiO_2 optimizations. This makes us conclude that the problem is not in the experimental data which are from different independent sources but in the modeling approach.

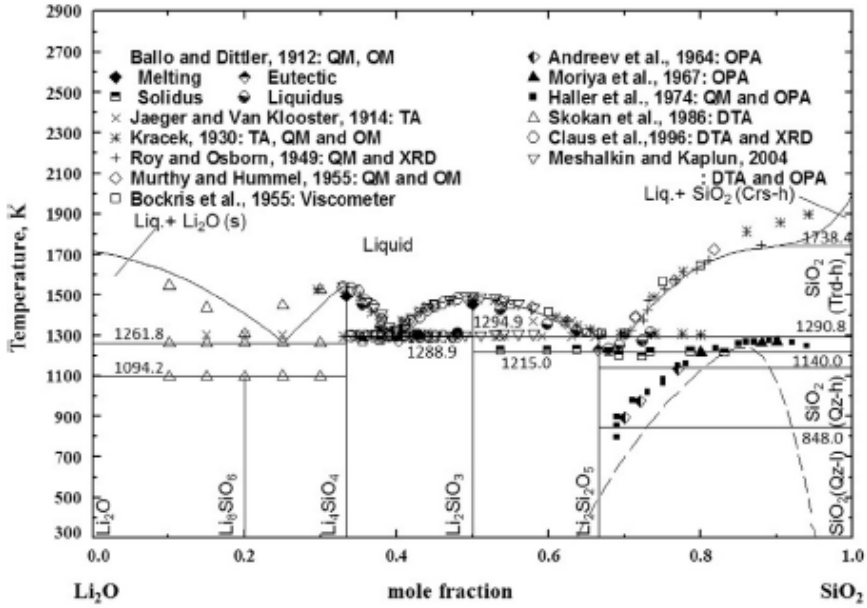

Figure 6.2 The optimized phase diagram of the Li_2O-SiO_2 system from Konar et al. [142].

Trying to reproduce the optimizations, it can be noticed that the cristobalite liquidus does not change much even if excess parameters of a high order are used. This gave us the idea that this discrepancy is rather related to the limiting mixing properties of the liquid phase. To eliminate the possibility of an experimental error, cristobalite liquidus data were systematically gathered for the alkali and alkali-earth silicate systems.

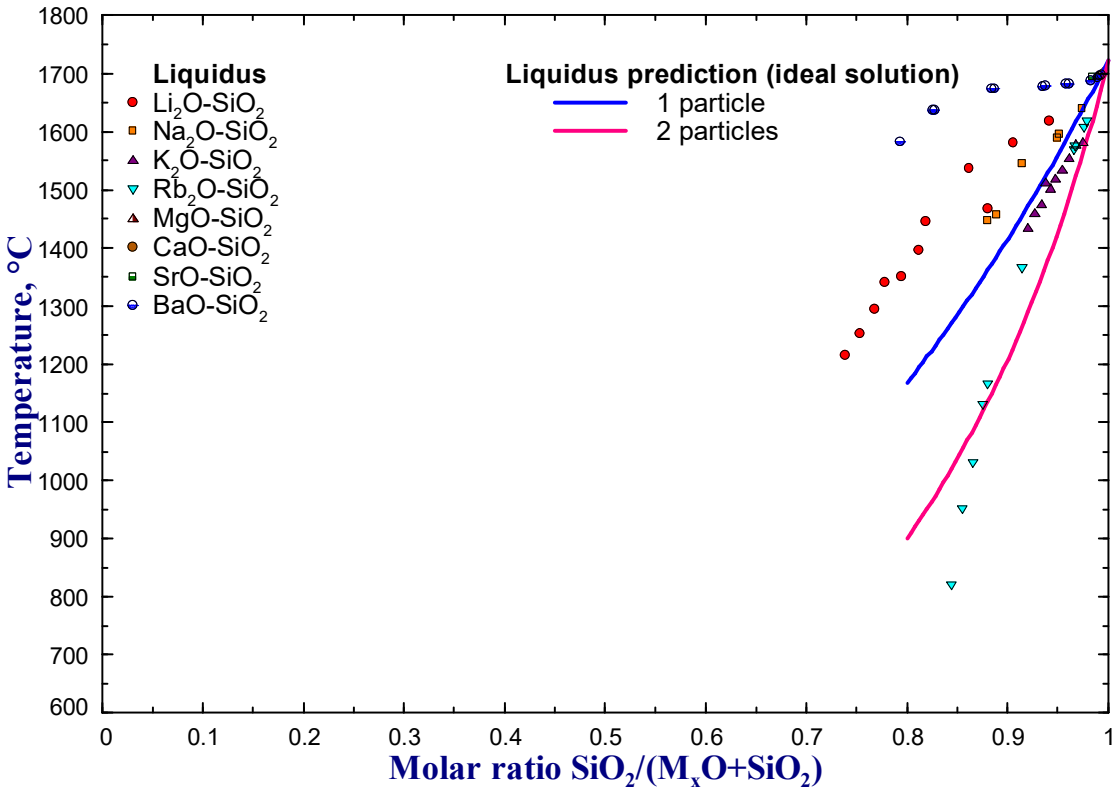

Figure 6.3 Silica liquidi for alkali oxide and alkali-earth oxide-silica binary systems alongside with the theoretical prediction of the liquidus slope in case of one- and two-particle second component (see the text for the details). Experimental points [143-152] and calculated lines.

The experimental points on the cristobalite liquidus in the systems Li_2O-SiO_2, Na_2O-SiO_2, K_2O-SiO_2 and Rb_2O-SiO_2 are summarized in Figure 6.3. The liquidus points for alkali-earth oxide systems are plotted alongside. As the previous optimizations failed to reproduce the limiting slope of the cristobalite liquidus, we suspected that the model entropy is somehow wrong close to the pure silica composition. As the limiting entropy does not depend on excess parameters, an assumption of an ideal infinitely diluted solution was made. Figure 6.3 also shows the liquidus curves derived from the LeChatelier-Shreder equation in assumption that the activity coefficient of silica is equal to one. This assumption is supposed to be valid given that the concentration of the second component is small enough.

Integration of the LeChatelier-Shreder equation:

$$\frac{d\ln a\left(\mathrm{SiO_2}\right)}{dT}=\frac{\Delta_{fus}H\left(\mathrm{SiO_2}\right)}{RT^2} \tag{97}$$

leads to the following expression:

$$\ln x\left(\mathrm{SiO_2}\right)\approx\ln a\left(\mathrm{SiO_2}\right)=\frac{\Delta_{fus}H\left(\mathrm{SiO_2}\right)}{R}\left(\frac{1}{T_0}-\frac{1}{T}\right) \tag{98}$$

where the liquidus temperature can be expressed as the following function of silica molar fraction:

$$T=\frac{1}{\left(\frac{1}{T_0}-\frac{R}{\Delta_{fus}H\left(\mathrm{SiO_2}\right)}\ln x\left(\mathrm{SiO_2}\right)\right)} \tag{99}$$

The temperature and the enthalpy of fusion of cristobalite were taken from the *FactSage* compound database and are equal to 1995.99 K and 9581.4 $J\cdot mol^{-1}\cdot K^{-1}$.

Two calculated curves are plotted in Figure 6.3: for the case where the second component produces one particle on the cationic sublattice per mole of the added component, and in case when it produces two particles. The alkali-earth oxide systems have limiting liquidus slopes approaching the “1 particle curve” which is logical as an alkali-earth oxide would produce 1 cation. We could expect that an alkali oxide liquidus slope would be approximated with the “2 particles curve” but the experimental points for lithium and sodium oxide rather tend to the “1 particle curve” and the points for potassium and rubidium oxides lie in between the two theoretical curves.

To explain the phenomenon, we introduced a “caging” hypothesis. This hypothesis is based solely on phase equilibria data and it does not yet have a direct structural confirmation. Let us suppose that sodium oxide just starts to enter the silica three-dimensional network. Its concentration is not yet high enough to depolymerize the network and the resulting sodium cations are stuck together at the place where a Si-O-Si bond has been broken.

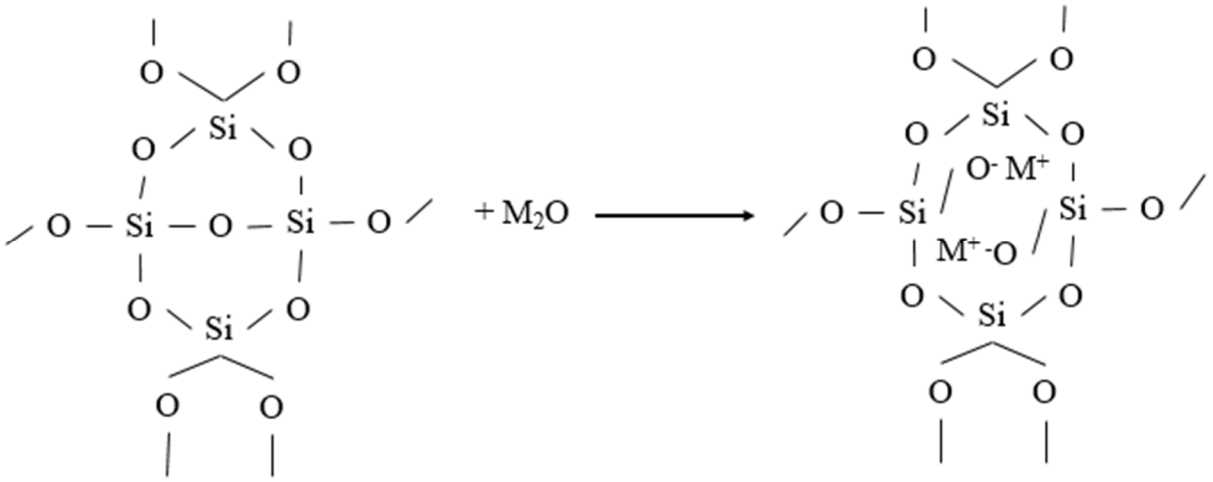

Figure 6.4 The caging effect upon addition of an alkali oxide to a silica network.

The resulting sodium cations are forced to stay together and from the thermodynamic point of view, behave as a single particle. They give the same contribution to the configurational entropy as an alkali-earth cation does. Only upon further addition of the alkali oxide, the silica network becomes depolymerized enough for two adjacent alkali cations to split apart and become configurationally independent.

From the point of view of the thermodynamic modeling, the described effect can be reproduced using an additional dimer species on the cationic sublattice. Therefore, the current liquid model contains Na^{+}, Si^{4+}, $(Na_2)^{2+}$ species on the cationic sublattice and O^{2-} species on the anionic sublattice. Addition of the dimer end-member to the model is quite straightforward. In the pure liquid Na_2O, there are negligible amounts of the dimer end-member as it exists only in the presence of the silica network. The thermodynamic properties of the dimer end-member can be assumed to be the same as those of the ordinary Na_2O end-member plus a positive stability parameter. In the high-silica region, sodium almost exclusively exists in the form of the dimer end-member. This can be achieved by using a negative dimer-silica interaction parameter.

The caging effect in case of the K_2O-SiO_2 and the Rb_2O-SiO_2 systems does not seem to be as profound as for the Li_2O-SiO_2 and the Na_2O-SiO_2 systems. This could be explained by the bigger sizes of potassium and rubidium cations, it is more difficult for them to fit a cage.

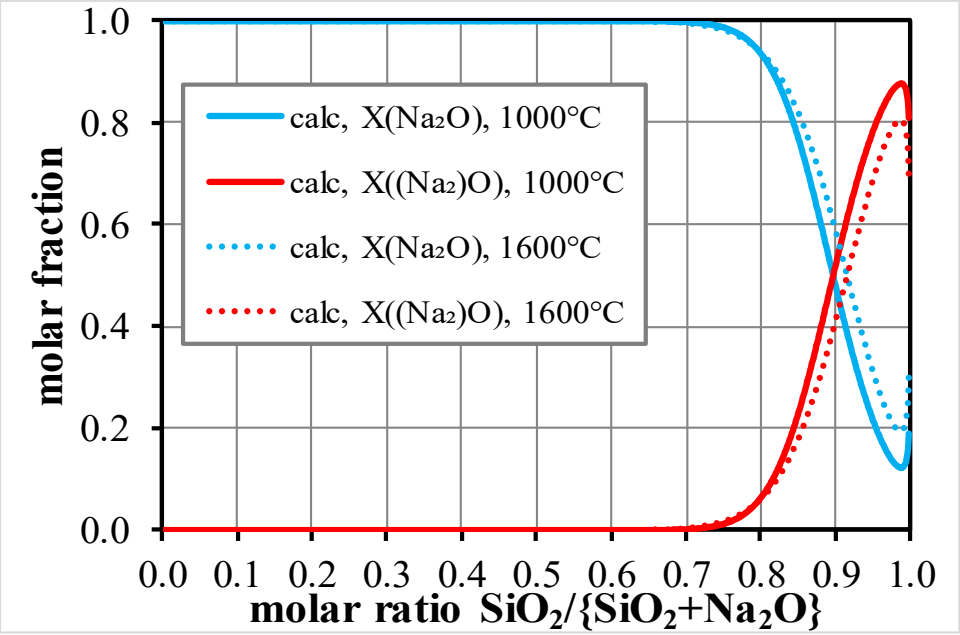

Figure 6.5 Distribution of the ordinary and dimer Na_2O end-members with the silica molar fraction at two different temperatures.

The theoretical distribution of sodium between the monomer and the dimer forms is given in Figure 6.5 at two different temperatures. As the silica network does not depolymerize in a significant way upon heating, it was assumed that there should not be a strong temperature dependence of the dimer content.

6.2 Phase diagram

There are quite a lot of studies devoted to Na_2O-SiO_2 phase relations but they are mostly limited by the range of compositions from the pure silica to sodium metasilicate. The study of the Na_2O-rich area of the phase diagram is complicated due to the high volatility of Na_2O and incomplete decomposition of Na_2CO_3 used as the most common source of the alkali oxide. It was shown that at 960°C Na_2CO_3 completely reacts with silica to form sodium metasilicate [146], while Na_4SiO_4 cannot be obtained in a pure state from SiO_2 and Na_2CO_3 [145]. The region of the phase diagram between Na_2SiO_3 and Na_4SiO_4 compositions can be investigated using silica and NaOH as precursors. In that case, Na_4SiO_4 was crystallized first and its mixtures with Na_2SiO_3 were used to prepare samples [153]. The study of compositions richer in Na_2O than Na_4SiO_4 needs the pure Na_2O as the precursor. Special attention must be paid to the conditions of experiments as the melts

are highly corrosive and lose Na_2O via volatilization [153]. Another experimental difficulty was posed by the region around $Na_2Si_2O_5$-quartz eutectic where the crystallization of samples is problematic because of the high melt viscosity. However, cristobalite and tridymite, forming at higher temperatures, proved to crystallize easily [146].

Among the binary compounds in the Na_2O-SiO_2 system, Na_2SiO_3 (metasilicate) and $Na_2Si_2O_5$ (disilicate) have been very well established as congruently melting compounds in the first works on the system [145]. No phase transitions of Na_2SiO_3 compound are mentioned in the literature.

According to Kracek [154], $Na_2Si_2O_5$ shows two thermal arrests at 678° and 707°C, with the corresponding heats of transition of about 1523 and 760 $J \cdot mol^{-1}$. The work of Willgallis and Range [155] has confirmed the existence of three $Na_2Si_2O_5$ modifications named α, β, γ. Williamson and Glaser [156] have shown the existence of three modifications having reversible transition temperatures identical to those from [154] and have also found other modifications, apparently metastable. The work by Boivin et al. [157] says that there are no phase transformations of $Na_2Si_2O_5$ except for the one at 840°C, not observed by other authors, with $\Delta_{tr}H = 14.4$ $kJ \cdot mol^{-1}$. Apparently, the authors made a mistake in assigning the effect to an unknown phase transformation, since the enthalpy of transition is very large. It seems reasonable to assume that the observed effect is in fact the $Na_2Si_2O_5$-Na_2SiO_3 eutectic (confirmed by the phase diagram), because the sample was not entirely pure. The low rate of the true transformations didn't allow them to be detected using a differential calorimetric analysis. The heats of transformation can also be found in the work of Morey [158] on the solution calorimetry of $Na_2Si_2O_5$ modifications.

The first works on phase equilibria in the Na_2O-SiO_2 system do not indicate a presence of any compounds, richer in silica than $Na_2Si_2O_5$, but Matveev [159] has found a trisilicate compound $Na_2Si_3O_7$ whose formula was later rectified as $Na_6Si_8O_{19}$ [160, 161]. The compound has an upper and lower stability temperature decomposing into quartz + liquid at 808°C and β-$Na_2Si_2O_5$ + quartz at 700°C, correspondingly. The formation of $Na_6Si_8O_{19}$ is difficult to observe due to kinetic reasons and the earlier studies must have overlooked it [160].

The orthosilicate was described by Kracek [145] as an incongruently melting compound with the decomposition temperature of 1118°C, although the authors admit that the sample was not completely free of Na_2CO_3. The portion Na_4SiO_4-Na_2SiO_3 of the phase diagram was studied by

D'Ans and Löffler [153]. A thermal arrest at 960°C was found and described as a phase transformation temperature because it didn't shift upon addition of NaCl in the system (which would be the case for an eutectic temperature). The melting point of Na_4SiO_4 was 1083°C. Löffler [162] considers the conclusion about the incongruent melting of Na_4SiO_4 by Kracek [145] to be erroneous since it implies a decomposition into Na_2O and liquid. The pure Na_2O at this temperature is already liquid (m.p. 925°C).

The pyrosilicate compound $Na_6Si_2O_7$ was first mentioned in the work of D'Ans and Löffler [153] and later confirmed in the works of Meshalkin and Kaplun [163] and Rys [164]. Meshalkin and Kaplun indicate that it has a lower stability limit while Rys considers it to be stable at the room temperature. Also, Rys described $Na_{10}SiO_7$ compound. Apparently, $Na_{10}SiO_7$ can be obtained only starting from Na_2O as the experiments with NaOH didn't show any other compounds beyond the orthosilicate composition [165]. $Na_{10}SiO_7$ melts congruently and has a lower stability limit.

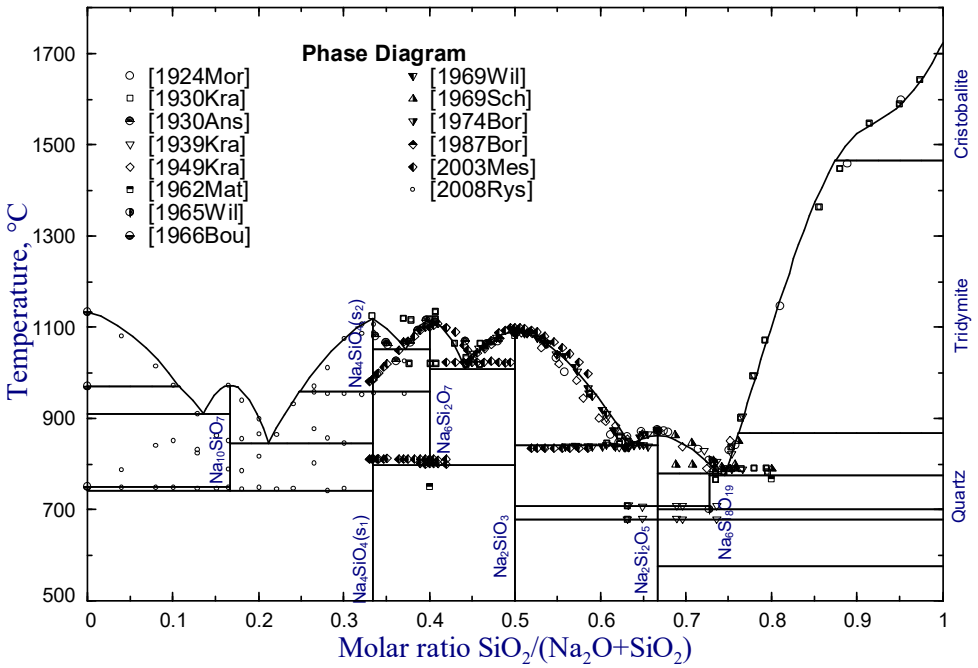

Figure 6.6 Phase diagram of the Na_2O-SiO_2 system. Experimental points [145, 146, 153, 154, 159-161, 163, 164, 166-170] and calculated lines.

The phase equilibria in the Na_2O-SiO_2 are summarized in Figure 6.6.

Glasses in the Na_2O-SiO_2 show a tendency to demixing and the system features a metastable miscibility gap. A number of works [171-179] was devoted to study its position and their results can be considered as reliable although some inconsistency remains at low temperatures. The metastable miscibility gap is shown in Figure 6.7.

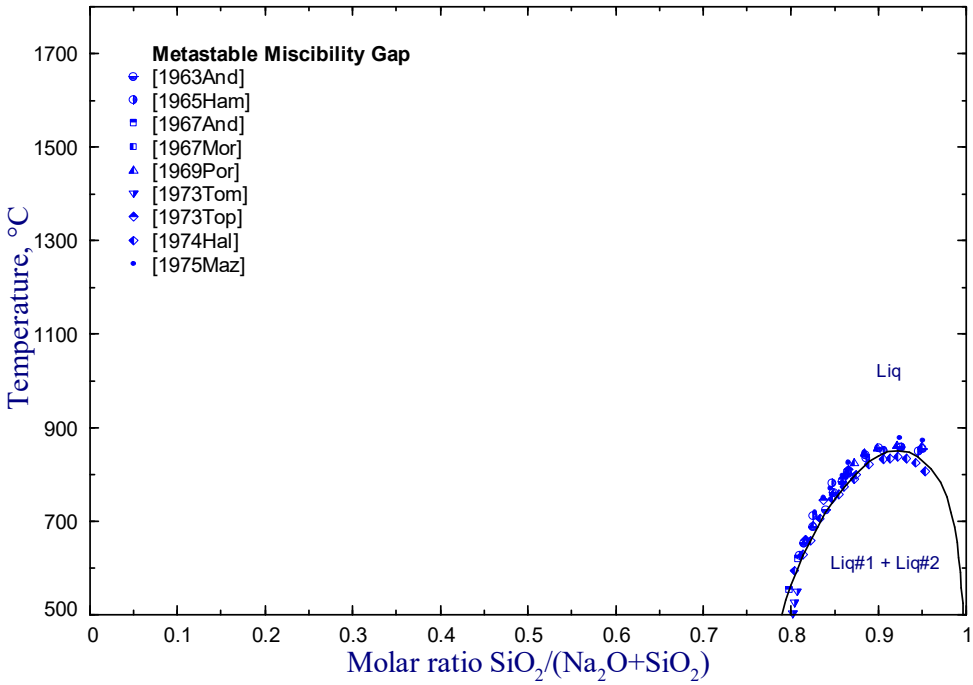

Figure 6.7 Metastable miscibility gap of the Na_2O-SiO_2 system. Experimental points [171-179] and calculated lines.

6.3 Calorimetry data

The solution calorimetry was widely used to determine thermochemical properties of compounds, liquids and glasses in the Na_2O-SiO_2 system. Usually, Na_2O-SiO_2 samples do not present difficulties during dissolution and different solvents can be utilized. Two the most common are hydrofluoric acid (temperature range about 20-50°C) of various concentrations and boron oxide-based solvents $2PbO$-B_2O_3 and $9PbO$-$3CdO$-$4B_2O_3$ (operating temperatures about 700°C). The solution calorimetry data serve to calculate the enthalpies of formation from oxides given that the enthalpies of solution of pure oxides are also known. Although the solution calorimetry is prevalent, some other methods can also be found in the literature.

First, the calorimetric data on the pure Na_2O and SiO_2 were collected. Even if the solvent is of the same type, to compare the data from different sources, the temperature and concentration of solvent must be considered.

There are quite a lot of data concerning dissolution of both vitreous and crystalline silica in hydrofluoric acid. It was preferred to use quartz dissolution data, as different thermal histories of silica glass can introduce uncertainties into the experimental values. The enthalpy of solution of quartz in HF under different conditions can be found in the works of Stevens and Turkdogan [180], King [181], Torgeson and Sahama [182], Troitsch (taken from Stevens and Turkdogan [180]), Hummel and Schwiete [183, 184], Morey [158], Takahashi and Yoshio [185], Hovis [186] and Hemingway and Robie [187].

Despite the technical difficulties of direct measurements of the solution enthalpy of Na_2O, several indirect determinations are available in the literature. The only direct measurement was performed by Stevens and Turkdogan [180] and gave the value of -381.41 $kJ \cdot mol^{-1}$ for 19% HF at 298K. Other works determined the heat of solution of Na_2CO_3, recalculated into the heat of solution of Na_2O: Hummel and Schwiete [183, 184], Roth and Troitzsh [188], Kroger and Kreitlow [189] measured the heat of dissolution of Na_2CO_3 in 20% 4.8HF+1HCl acid mixture, but apparently, their values agree with the rest of works using the same concentration of HF acid without HCl. Morey [158] determined $\Delta_{soln}H(Na_2O)$ using sulfate and chloride cycles.

The $2PbO\text{-}B_2O_3$ is one of the most common solvents in the silicate calorimetry because of its good dissolving properties and a low crystallization temperature. Quartz solution calorimetry was reported in the works of Charlu et al. [190], Hlabse and Kleppa [191], Shearer and Kleppa [192], Petrovic et al. [193] and Kiseleva et al. [194]. As for Na_2O, its heat of solution in $2PbO\text{-}B_2O_3$ was reported in the study of Petrovic et al. [193] and originated from the work of Zygan et al. [195] who carried out the dissolution of Na_2CO_3 and $NaAlO_2$ and found a very good agreement between these two independently derived values (the value of -172.21 $kJ \cdot mol^{-1}$ at 975K was accepted).

For each end-member and solvent, measurements performed at different temperatures (and solvent concentrations, in case of HF), were collected and described by an empirical linear dependence. For further recalculations, the enthalpies of solution were calculated using those dependencies.

Equations (100) and (101) were used for HF solution measurements and $2PbO\text{-}B_2O_3$ measurements, correspondingly:

$$\Delta_{soln}H(\text{kJ}\cdot\text{mol}^{-1}) = p_{00}+p_{10}\cdot\text{wt\%HF}+p_{01}\cdot T(\text{K}) \quad (100)$$

$$\Delta_{soln}H(\text{kJ}\cdot\text{mol}^{-1}) = p_1\cdot T(\text{K})+p_2 \quad (101)$$

The coefficients in equations (100) and (101) are summarized in Table 6.1 and the empirical dependencies are plotted in Figure 6.8.

Table 6.1 Regression coefficients of the calorimetric solution data for Na_2O(cr) and SiO_2(qz).

End-member	**Solvent**	**Coefficients**
SiO_2(qz)	HF	$p_{00} = -108$ $p_{10} = -0.351$ $p_{01} = -0.0723$
Na_2O(cr)	HF	$p_{00} = -441.6$ $p_{10} = -2.022$ $p_{01} = 0.3117$
SiO_2(qz)	$2PbO\text{-}B_2O_3$	$p_1 = 0.04321$ $p_2 = -46.38$
Na_2O(cr)	$2PbO\text{-}B_2O_3$	The enthalpy of solution was considered constant as only data at 973 and 975K are available

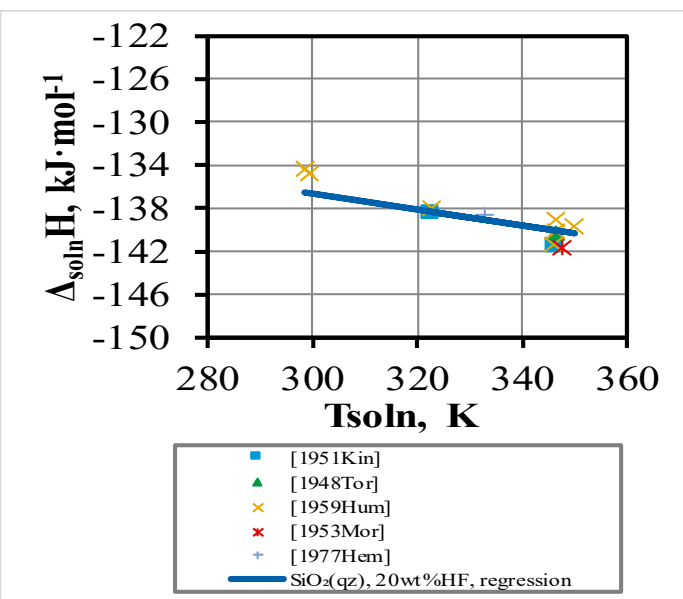

(*a*)

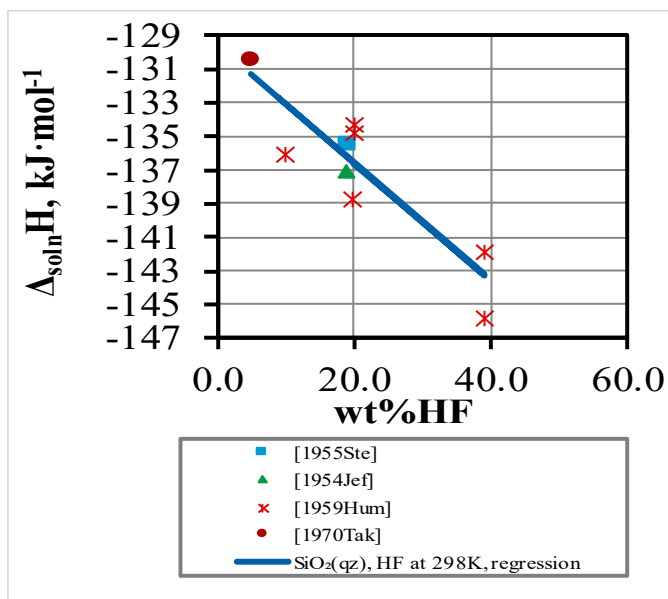

(*b*)

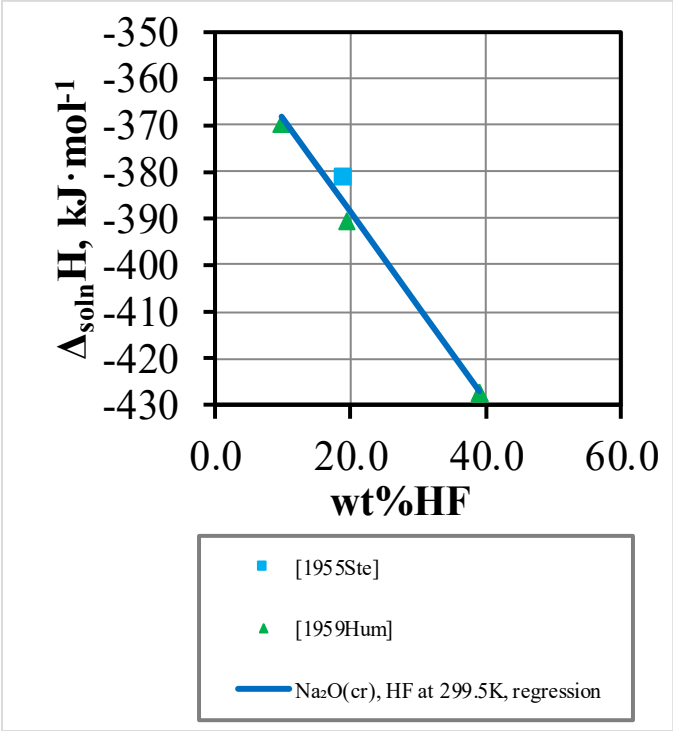

(*c*)

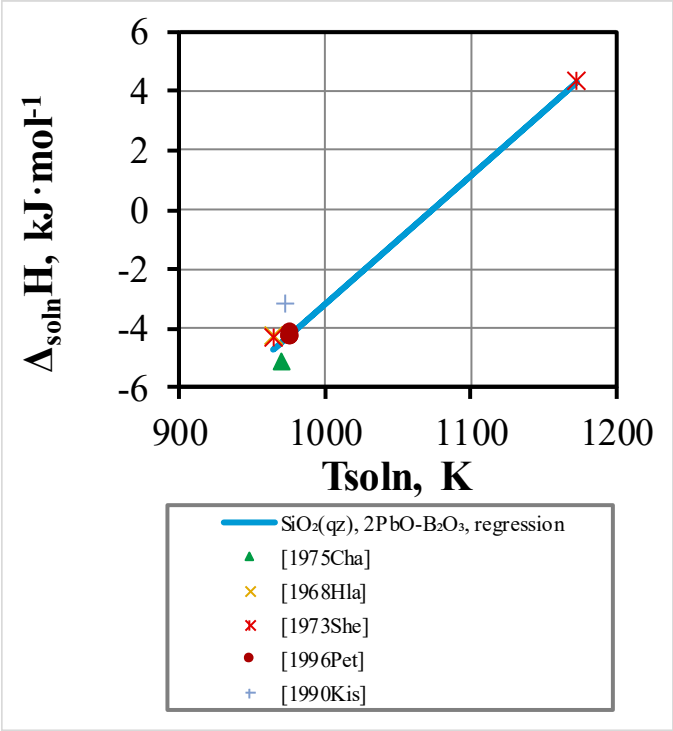

(*d*)

Figure 6.8 The enthalpy of solution of quartz in 20 wt% HF vs temperature (***a***) [158, 181-183, 187]; the enthalpy of solution of quartz at 298K vs HF concentration (***b***) [180, 185, 196]; the enthalpy of solution of Na_2O(cr) at 299.5K vs HF concentration (***c***) [180, 183]; the enthalpy of solution of quartz in 2PbO-B_2O_3 vs temperature (***d***) [190-194]. Experimental points and regression lines.

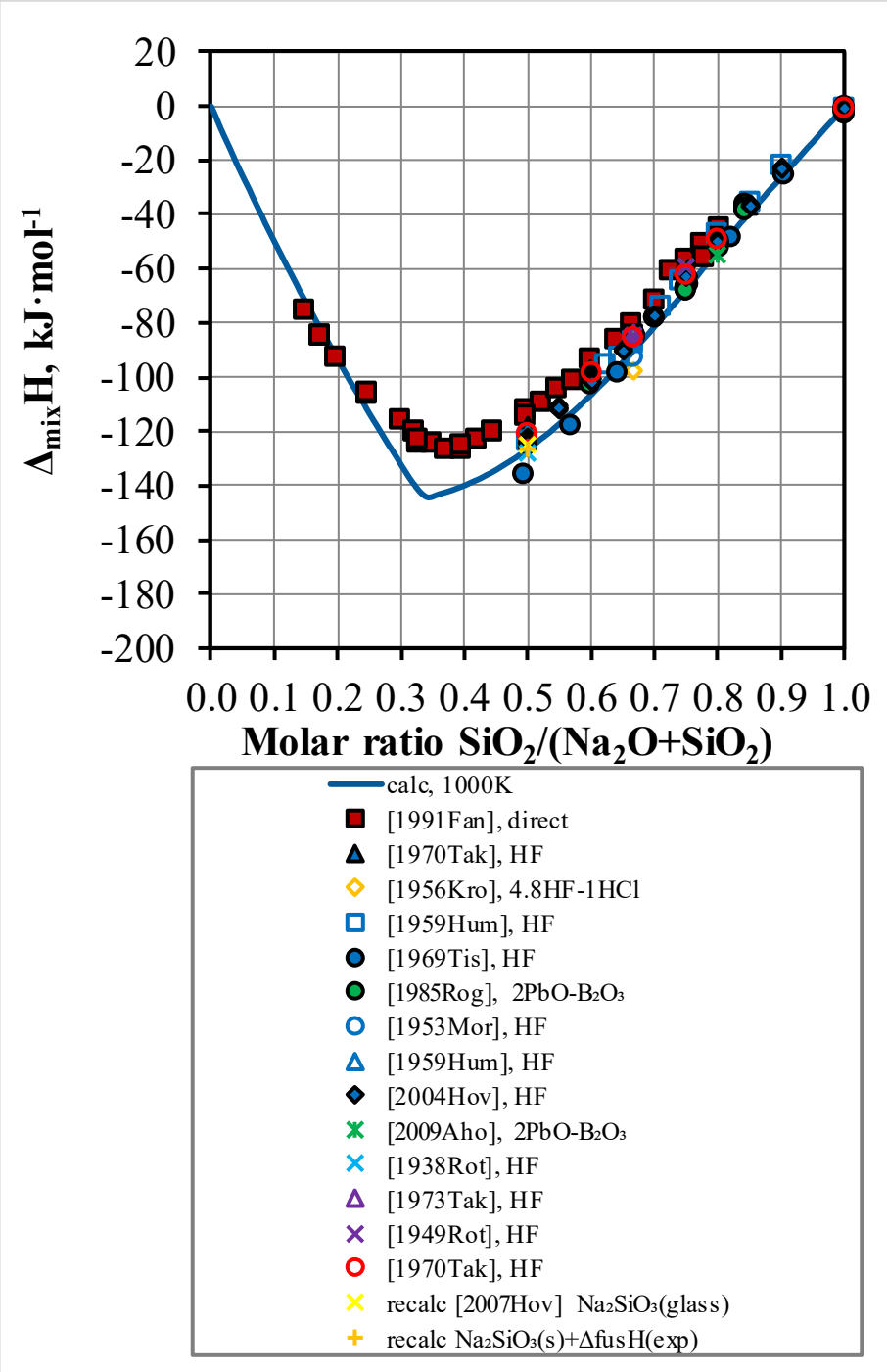

Figure 6.9 The enthalpy of mixing of liquid in the Na_2O-SiO_2 system. Experimental points [158, 183-185, 188, 189, 197-204] and calculated lines.

Fan [197] prepared solid mixtures of Na_2O and SiO_2 and directly measured the enthalpies of reaction by drop calorimetry. They are generally considered to be less negative than the true values due to the slow rate of reaction at its final stages.

The heat of solution of Na_2O-SiO_2 glasses in HF was measured in the works of Takahashi and Yoshio [185, 203], Hummel and Schwiete [183, 184], Tischer [198], Morey [158], Hovis et al. [199], Roth and Richter [202], Roth and Troitzsch [188]. One point for dissolution of a disilicate glass is given by Kroger and Kreitlow [189] in 20% (4.8HF+1HCl) media, the auxiliary information (the enthalpies of dissolution of Na_2O(cr) and SiO_2(qz)) can be derived from the data given in their study and does not differ much from the enthalpies of solution in 20% HF at the same temperature. Na_2O-SiO_2 glasses and liquids were also dissolved in $2PbO$-B_2O_3 by Rogez and Mathieu [200] and Ahoussou et al. [201].

All experimental data in Figure 6.9 were recalculated using the procedure described in Section 2.5.2.

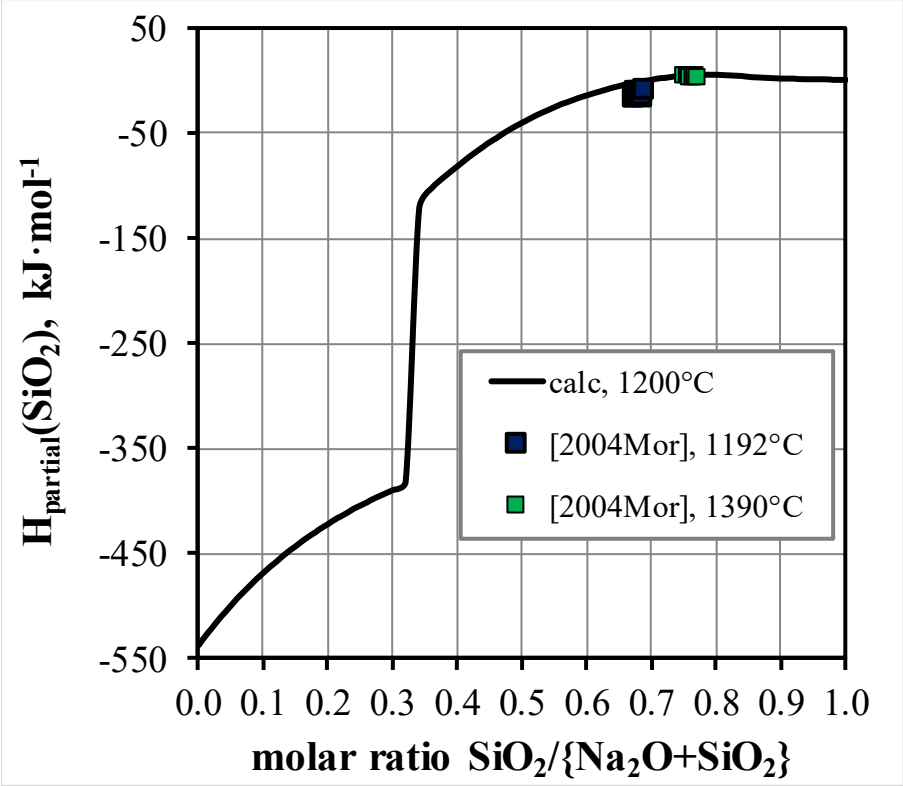

Figure 6.10 The partial enthalpy of SiO_2 in Na_2O-SiO_2 melts; the reference state is the pure liquid SiO_2. Experimental points [205] and calculated lines.

Morishita et al. [205] carried out measurements of the partial molar enthalpy of SiO_2 in Na_2O-SiO_2 melts (see Figure 6.10).

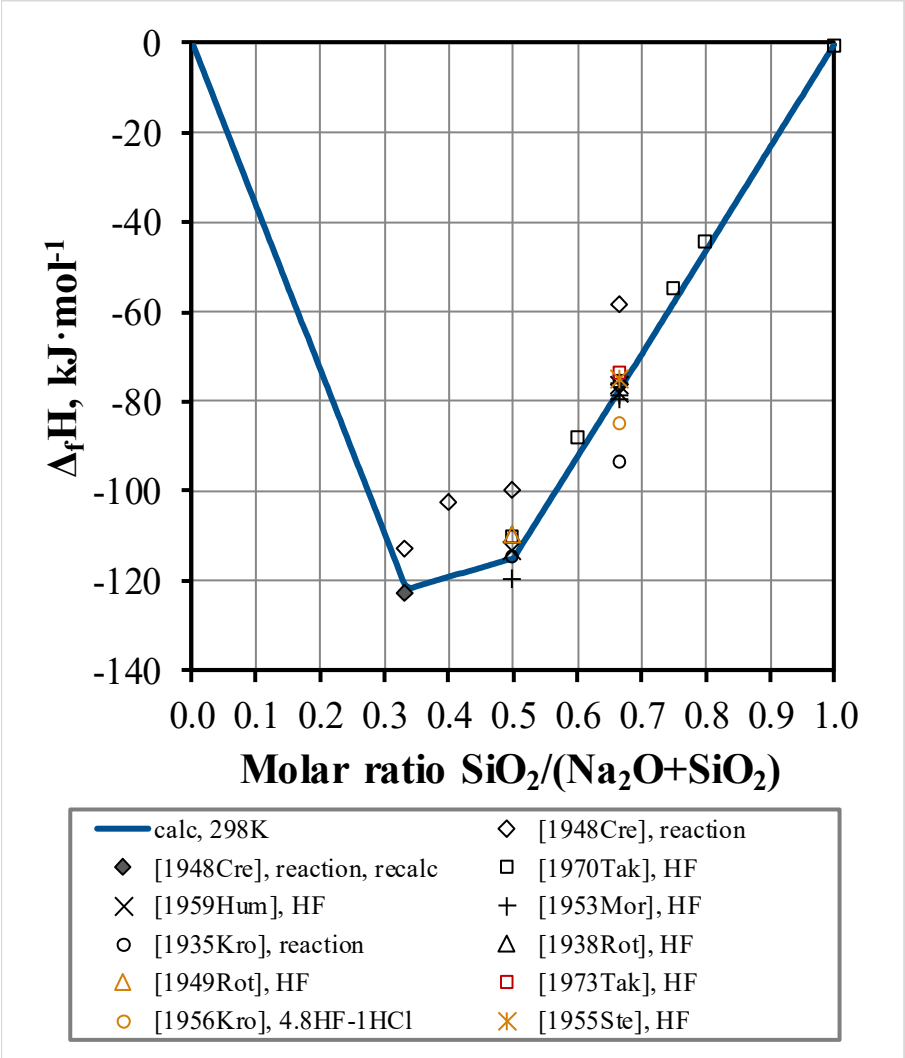

Figure 6.11 The enthalpies of formation of solid compounds from oxides per mole of components. Experimental points [158, 180, 183-185, 188, 189, 202, 203, 206, 207] and calculated lines.

Figure 6.11 summarizes the data on the enthalpy of formation of the stoichiometric compounds. McCready [206] gives a review of enthalpy data obtained by indirect methods on $Na_2Si_2O_5$, Na_2SiO_3, $Na_6Si_2O_7$ and Na_4SiO_4. Kroger [207] gives enthalpy data calculated from partial pressures of CO_2 in silicate/carbonate mixtures. A number of calorimetric studies with HF-based solvents are also available [158, 180, 183-185, 188, 189, 202, 203].

Available data on the enthalpies of fusion of Na_2SiO_3 and $Na_2Si_2O_5$ are summarized in Table 6.2. Adams and Cohen [208] calculated the heats of fusion of compounds based on the curvature of the liquidi. Richet and Bottinga [24] and Naylor [209] measured the heat of fusion of Na_2SiO_3 directly by drop calorimetry. Boivin et al. [157] derived the heats of fusion from DSC curves.

Table 6.2 The enthalpies of fusion of compounds in the Na_2O-SiO_2 system.

Compound	**$\Delta_{fus}H$(calc), kJ·mol^{-1}**	**$\Delta_{fus}H$(exp), kJ·mol^{-1}**
Na_2SiO_3	53.28 (1092°C)	52.304 [208]
		52.00 [24]
		52.20 [209]
$Na_2Si_2O_5$	45.22 (859°C)	36.814 [208]
		34 [157]
SiO_2 (for comparison)	9.582 (1723°C)	7.542 [208]

The enthalpy of fusion of Na_2SiO_3 is in a good agreement with the experimental data. The enthalpy of fusion of $Na_2Si_2O_5$, however, shows certain deviation from the experimental data. It can be explained using excess parameters with a strong temperature dependence in the liquid phase (see Table A.4). In turn, they are required to reproduce SiO_2 liquidus in a very wide range of temperatures. *T*-dependent terms of the interaction parameters deviate the entropy of mixing in the composition range from around disilicate to tridymite liquidus. Supposedly, if a correct extrapolation of the heat capacity of liquid SiO_2 end-member were used, these measures could have been avoided and the enthalpy of fusion of $Na_2Si_2O_5$ would be reproduced better. For a detailed explanation on the heat capacity of the liquid end-members, see Section 2.2.

6.4 Activity data

Na_2O activity in the Na_2O-SiO_2 system has been investigated using different methods. Measurements of EMF between a sample and a reference melt of a fixed composition allow to derive the activity of Na_2O relative to the activity in the reference [210]. Another popular method is Knudsen cell mass spectrometry [211, 212]. Upon vaporization, Na_2O almost completely decomposes into Na(g) and O_2(g). Measurements of the partial pressure of sodium allows to calculate Na_2O activity in the melt upon the assumption that $P(O_2) = 0.25P(Na)$. A few examples of the equilibration technique can be found in the literature: Tsukihashi and Sano [213] equilibrated

Na_2O-SiO_2 melts with Pb-Na alloys and Rego et al. [214] measured Na(g) partial pressures over mixtures with carbon.

If it was possible, the reference activities and partial pressures were calculated using *FactSage*; in rare cases (equilibration with a Pb-Na alloy) the auxiliary data of the authors were used.

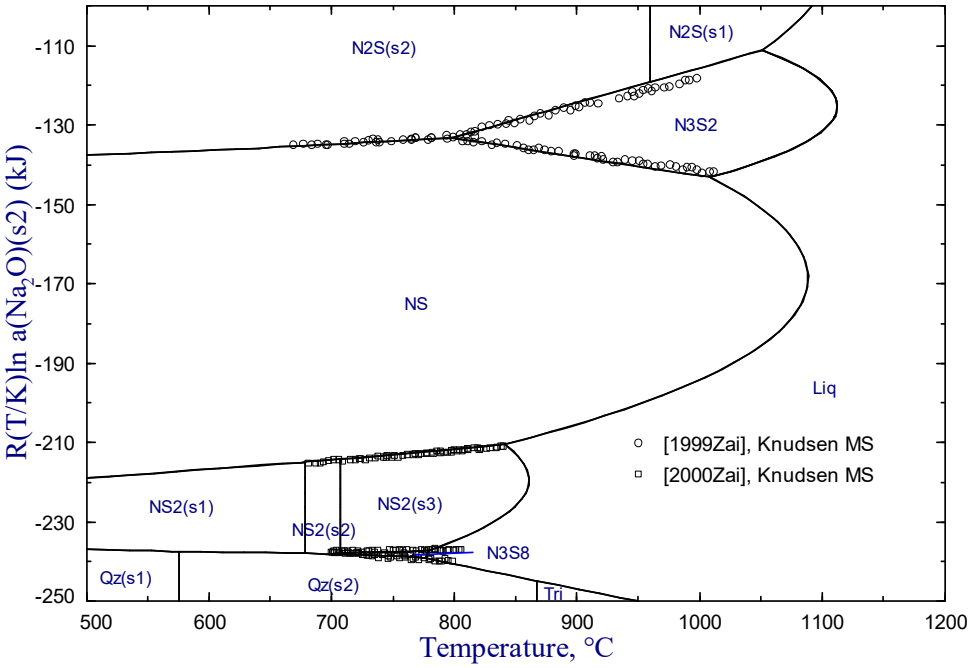

Figure 6.12 Na_2O activity over solid mixtures of Na_2O-SiO_2 compounds. The reference state of Na_2O is β-Na_2O ($Na_2O(s_2)$). Experimental points [211, 215] and calculated lines.

Figure 6.12 presents Na_2O activity data in two-phase regions of the phase diagram at subliquidus temperatures. The samples were prepared from Na_2CO_3 and SiO_2 but as the reaction was performed in vacuum (Knudsen cell conditions), the data on equilibria of $Na_6Si_2O_7$ and Na_4SiO_4 can be considered reliable.

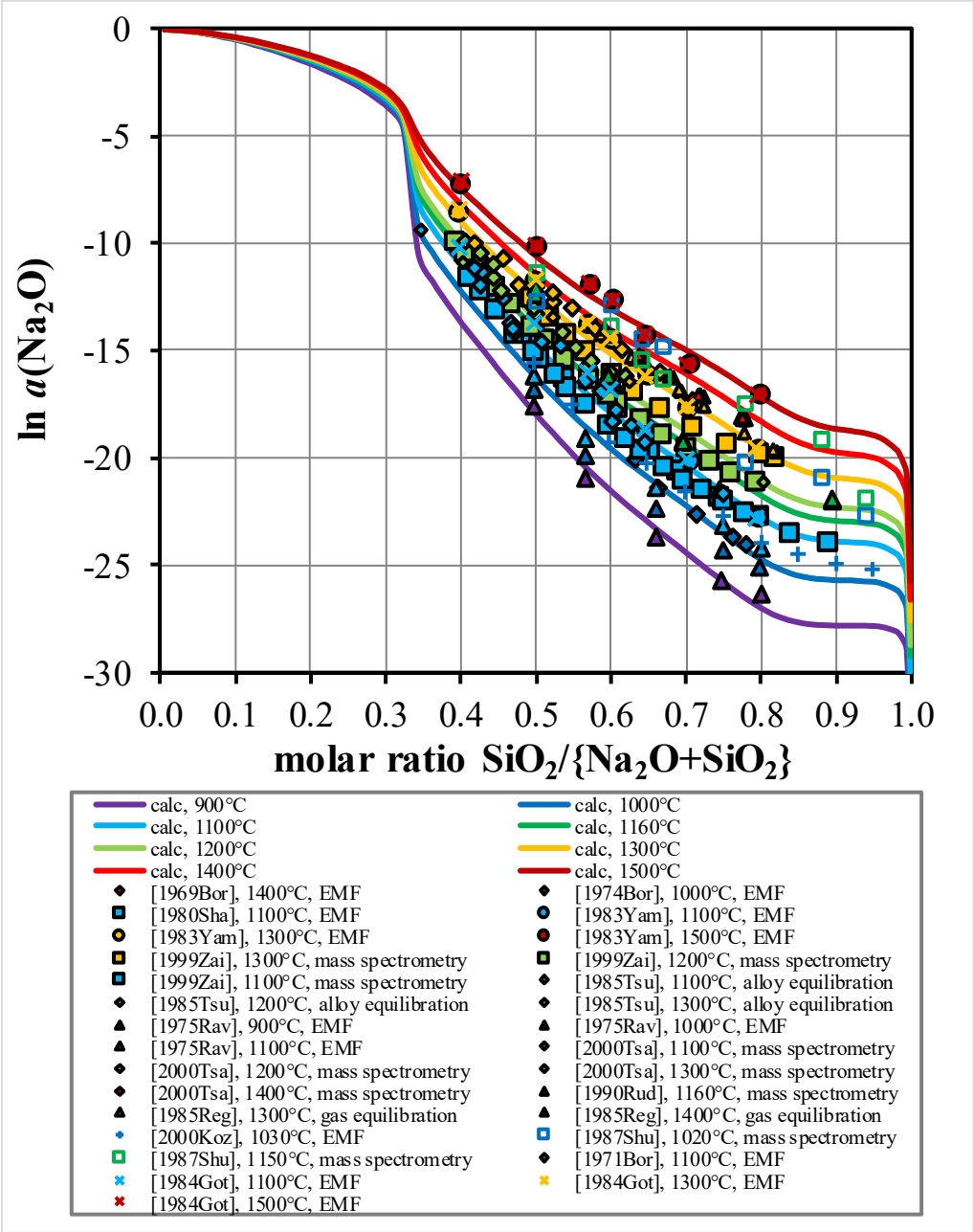

Figure 6.13 The concentration dependence of Na_2O activity in the Na_2O-SiO_2 system. The reference state is the pure liquid Na_2O (properties taken from *FactSage*). Experimental points [210, 213-225] and calculated lines.

Figure 6.13 presents isothermal Na_2O activities with the pure liquid Na_2O as the standard state. It is often the case that original sources publish raw experimental data (EMF, for example) as well as the calculated Na_2O activities. In fact, different authors calculate them using different Na_2O(liq)

properties. There are noticeable discrepancies of properties of the liquid Na_2O in the literature because they cannot be measured directly and are usually estimated. To assure the coherence between the experimental points and the calculated values, the properties of Na_2O(liq) were taken from *FactSage* for all the experimental sources. Wherever it was possible, the raw measured data (EMF, for example) were recalculated in this work.

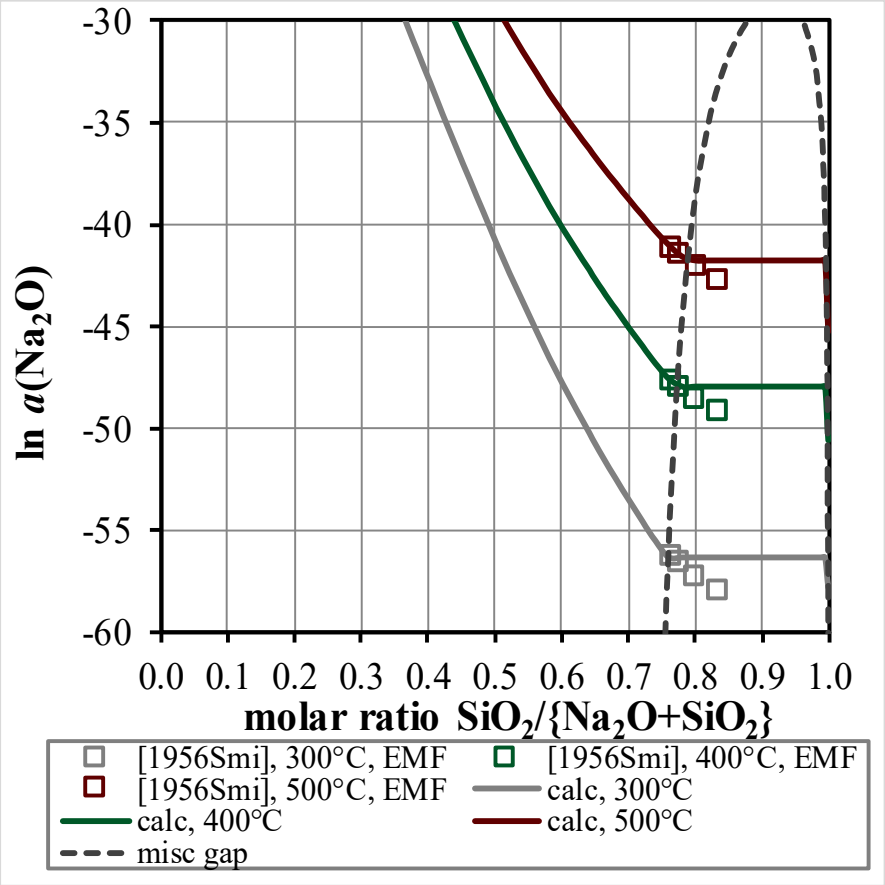

Figure 6.14 Na_2O activity in glasses at low temperatures. The reference state is the pure liquid Na_2O. Experimental data points [226] and calculated lines.

Figure 6.14 indicates that the model adequately predicts the activity data even in the glass region far below the liquidus temperature. The horizontal plateaus in the calculated activities reveal the presence of the metastable miscibility gap. However, the experimental points do not show any unmixing tendencies. This behaviour can be explained by the metastable nature of glass samples which did not decompose into two phases due to kinetic reasons.

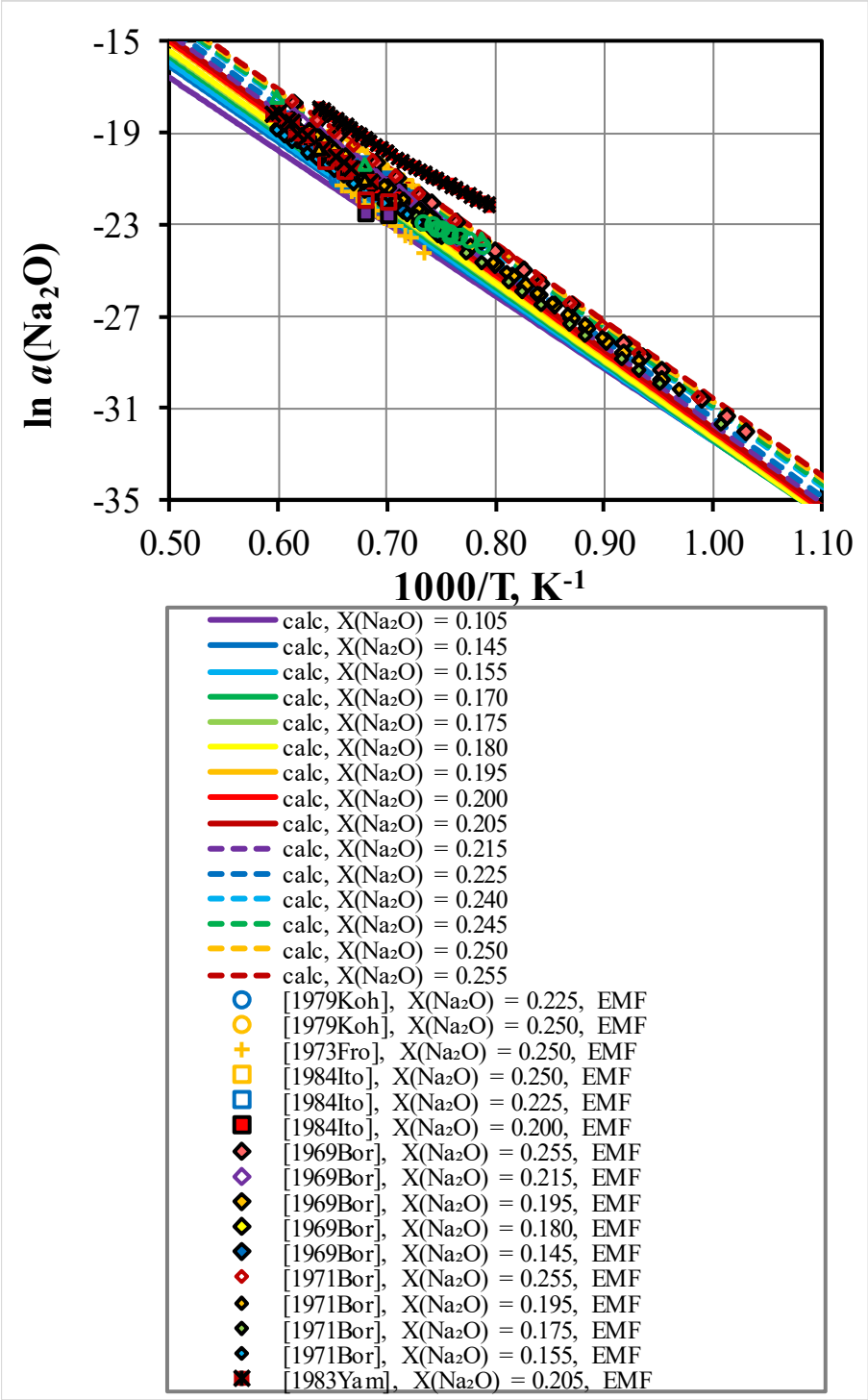

Figure 6.15 Temperature dependence of Na_2O activity in the Na_2O-SiO_2 system at low temperatures, X(Na_2O) = 0.105-0.255. The reference state is the pure liquid Na_2O. Experimental points [210, 211, 216, 219, 225, 227-231] and calculated lines.

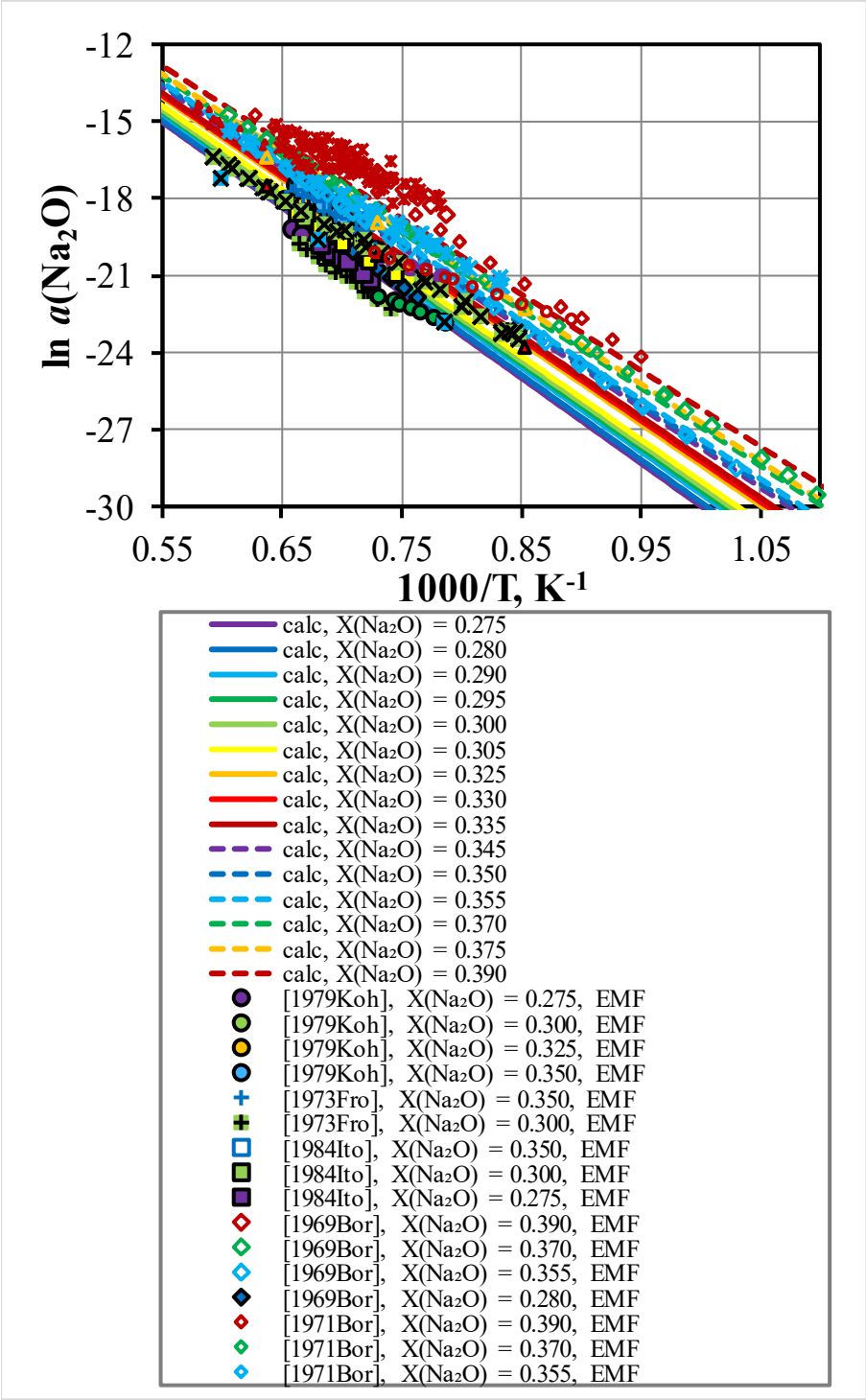

Figure 6.16 Temperature dependence of Na_2O activity in the Na_2O-SiO_2 system, X(Na_2O) = 0.275-0.390. The reference state is the pure liquid Na_2O. Experimental data points [210, 211, 216, 219, 225, 227-230, 232, 233] and calculated lines.

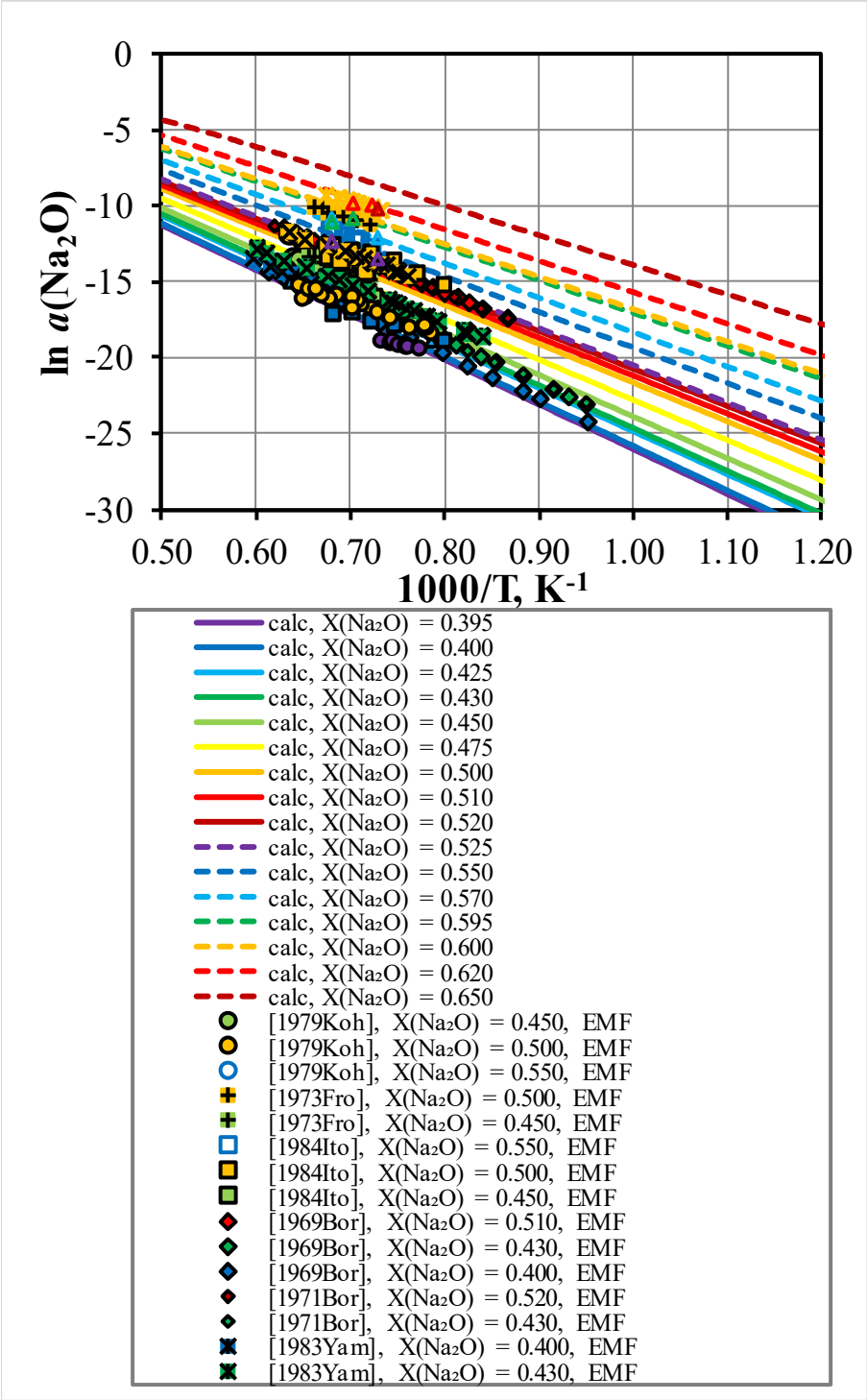

Figure 6.17 Temperature dependence of Na_2O activity in the Na_2O-SiO_2 system, $X(Na_2O)$ = 0.395-0.650. The reference state is the pure liquid Na_2O. Experimental data points [210-212, 216, 219, 225, 227-230, 232] and calculated lines.

Figure 6.15-Figure 6.17 show the temperature dependence of Na_2O activity for fixed compositions.

6.5 Heat capacity and heat content data

Low temperature heat capacity data for crystalline compounds are available in the work of Kelley [234] for Na_4SiO_4 and Na_2SiO_3 and in the work of Labban et al. [235] for $Na_2Si_2O_5$. The optimized heat capacity curves along with the experimental data are shown in Figure 6.18. It should be noted that the optimized heat capacities do not cover the temperature range below 298K although the experimental data in this range were used for extrapolation (Section 2.2).

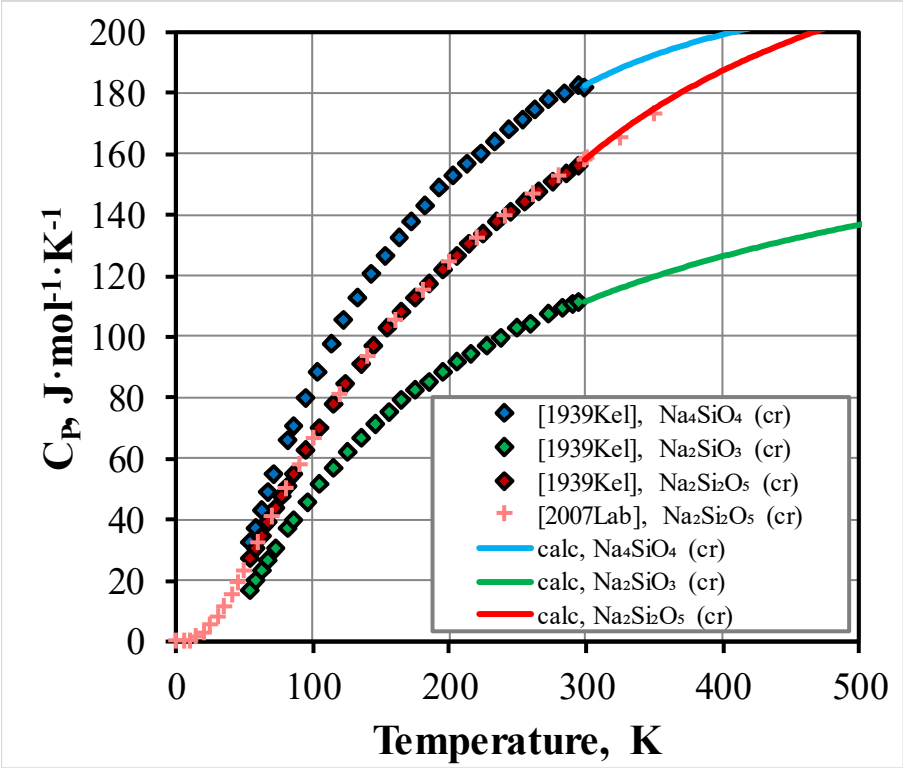

Figure 6.18 The low temperature heat capacities of crystalline solids in the Na_2O-SiO_2 system. Experimental data points [234, 235] and calculated lines.

Naylor [209] carried out drop calorimetry experiments on crystalline, liquid and vitreous samples of Na_2SiO_3 and $Na_2Si_2O_5$. Crystalline $Na_2Si_2O_5$ samples were studied by Takahashi and Yoshio [203], vitreous and liquid Na_2SiO_3 by Tashiro [236].

Na_2SiO_3 liquid samples crystallize much easier than $Na_2Si_2O_5$; therefore, upon cooling they transform to a crystalline state while $Na_2Si_2O_5$ remains vitreous.

The heat content of the crystalline and liquid Na_2SiO_3 is shown in Figure 6.19. The curve jump corresponding to the enthalpy of fusion of the compound is clearly seen.

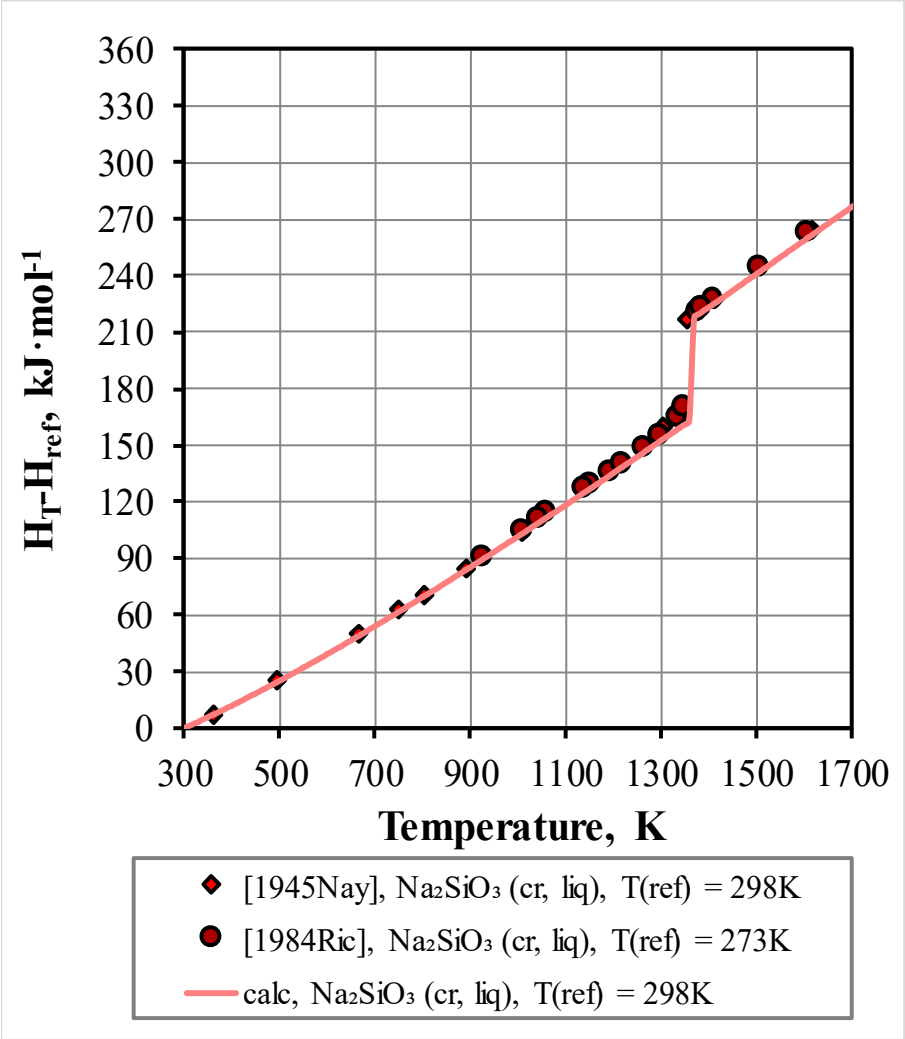

Figure 6.19 The heat content of liquid and crystalline Na_2SiO_3. Experimental data points [209, 237] and calculated lines.

Figure 6.20 summarized the drop calorimetry data on crystalline, vitreous and liquid forms of $Na_2Si_2O_5$ compound. As liquid samples could not crystallize during drop trials, no heat content step corresponding to the enthalpy of fusion is seen.

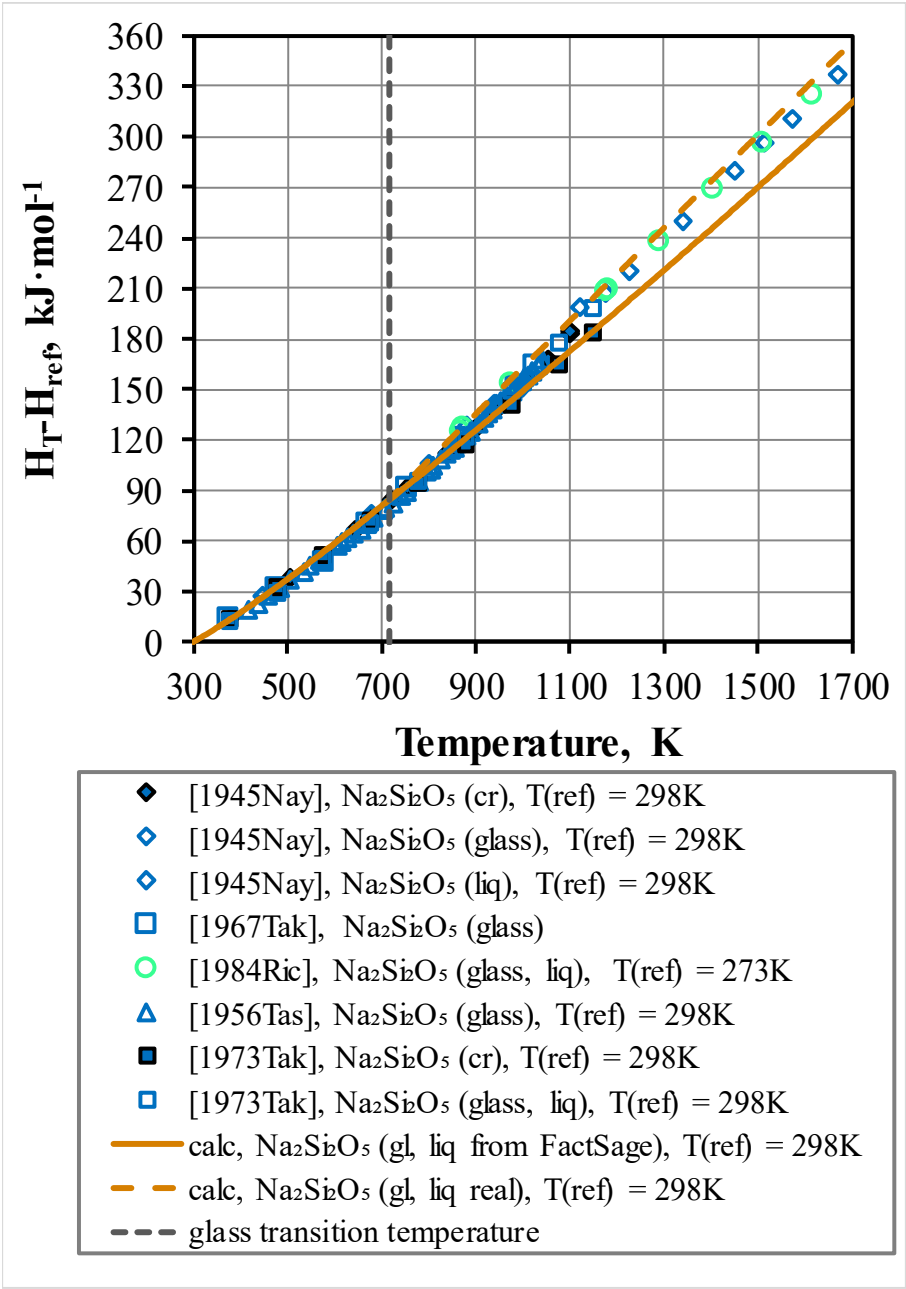

Figure 6.20 The heat content of the vitreous and liquid $Na_2Si_2O_5$. The heat content was calculated using *FactSage* heat capacities of the end-members and the real heat capacities extrapolated below the corresponding melting points. Experimental data points [203, 209, 236-238] and calculated lines.

Since the liquid heat capacities are temperature-dependent in *FactSage* and are lower than the real values, the experimental values on the liquid heat content are better predicted manually using

constant C_P values for Na_2O(liq) and SiO_2(liq) and using the additive rule. However, the heat capacities of glasses are in a good match with the heat capacity of the crystalline compound [239]. Richet [240] states that entropies and heat capacities starting from ambient temperatures usually can be approximated as a linear combination of the corresponding properties of the pure end-members. The heat capacity of silicate glasses above the room temperature is an additive function of composition within ±1% (Figure 6.21). The same applies to the liquids (Figure 6.22).

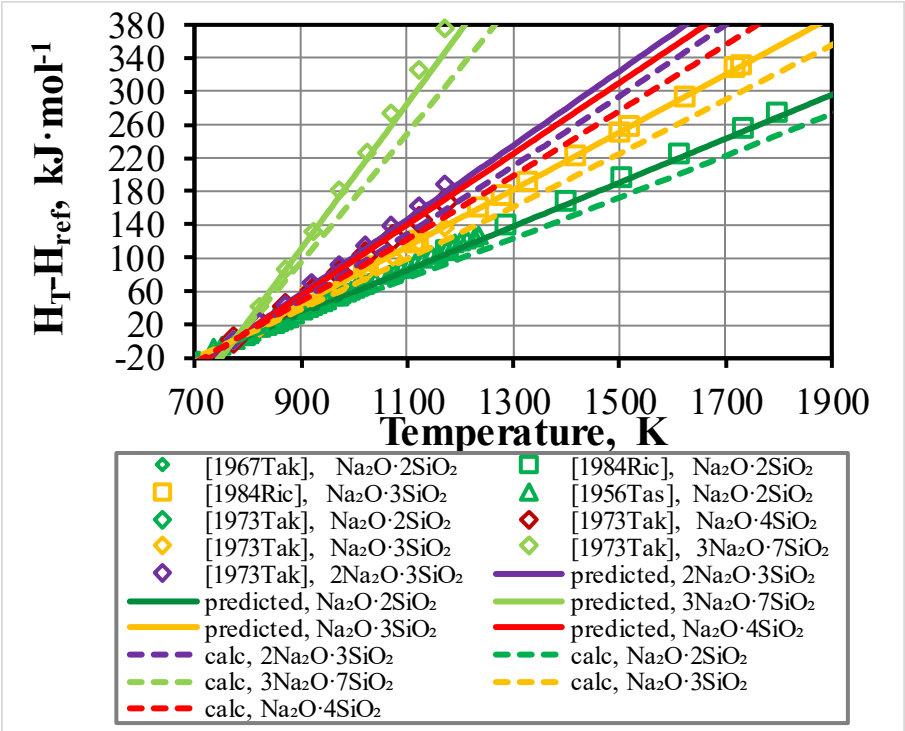
H_T-H_{ref}, kJ·mol^{-1}
380
340
300
260
220
180
140
100
60
20
-20
700
900
1100
1300
1500
1700
1900
Temperature, K
[1967Tak], $Na_2O·2SiO_2$
[1984Ric], $Na_2O·2SiO_2$
[1984Ric], $Na_2O·3SiO_2$
[1956Tas], $Na_2O·2SiO_2$
[1973Tak], $Na_2O·2SiO_2$
[1973Tak], $Na_2O·4SiO_2$
[1973Tak], $Na_2O·3SiO_2$
[1973Tak], $3Na_2O·7SiO_2$
[1973Tak], $2Na_2O·3SiO_2$
predicted, $2Na_2O·3SiO_2$
predicted, $Na_2O·2SiO_2$
predicted, $3Na_2O·7SiO_2$
predicted, $Na_2O·3SiO_2$
predicted, $Na_2O·4SiO_2$
calc, $2Na_2O·3SiO_2$
calc, $Na_2O·2SiO_2$
calc, $3Na_2O·7SiO_2$
calc, $Na_2O·3SiO_2$
calc, $Na_2O·4SiO_2$

(*a*)

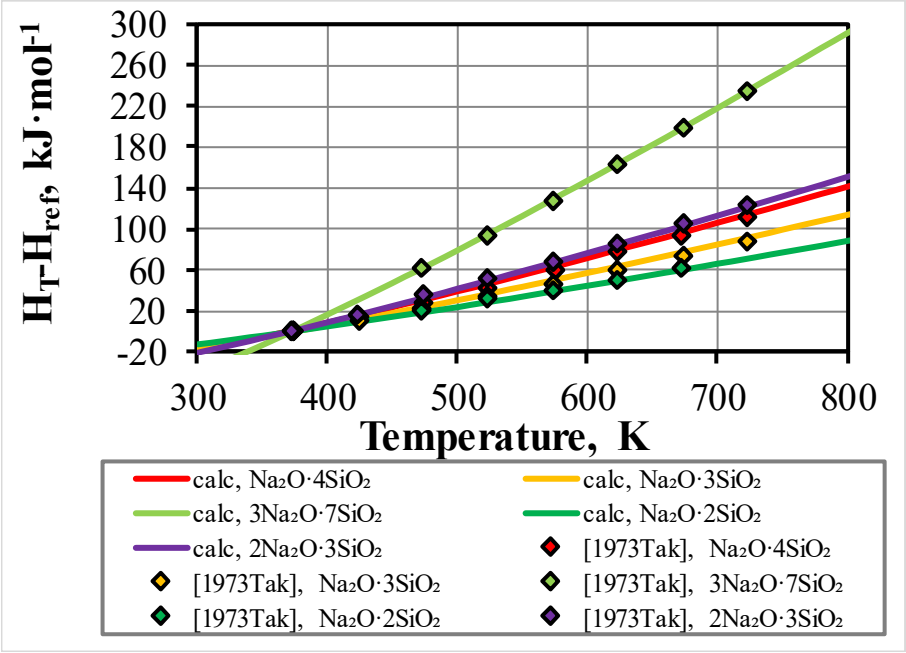
H_T-H_{ref}, kJ·mol^{-1}
300
260
220
180
140
100
60
20
-20
300
400
500
600
700
800
Temperature, K
calc, $Na_2O·4SiO_2$
calc, $Na_2O·3SiO_2$
calc, $3Na_2O·7SiO_2$
calc, $Na_2O·2SiO_2$
calc, $2Na_2O·3SiO_2$
[1973Tak], $Na_2O·4SiO_2$
[1973Tak], $Na_2O·3SiO_2$
[1973Tak], $3Na_2O·7SiO_2$
[1973Tak], $Na_2O·2SiO_2$
[1973Tak], $2Na_2O·3SiO_2$

(*b*)

Figure 6.21 The heat contents of liquids (***a***) and glasses (***b***). The reference temperature for liquids is 500°C and for glasses is 100°C. The heat content of liquids was calculated in *FactSage* (dashed lines) and predicted using constant heat capacities of Na_2O(liq) and SiO_2(liq) (solid lines). Experimental points [203, 236-238] and calculated lines.

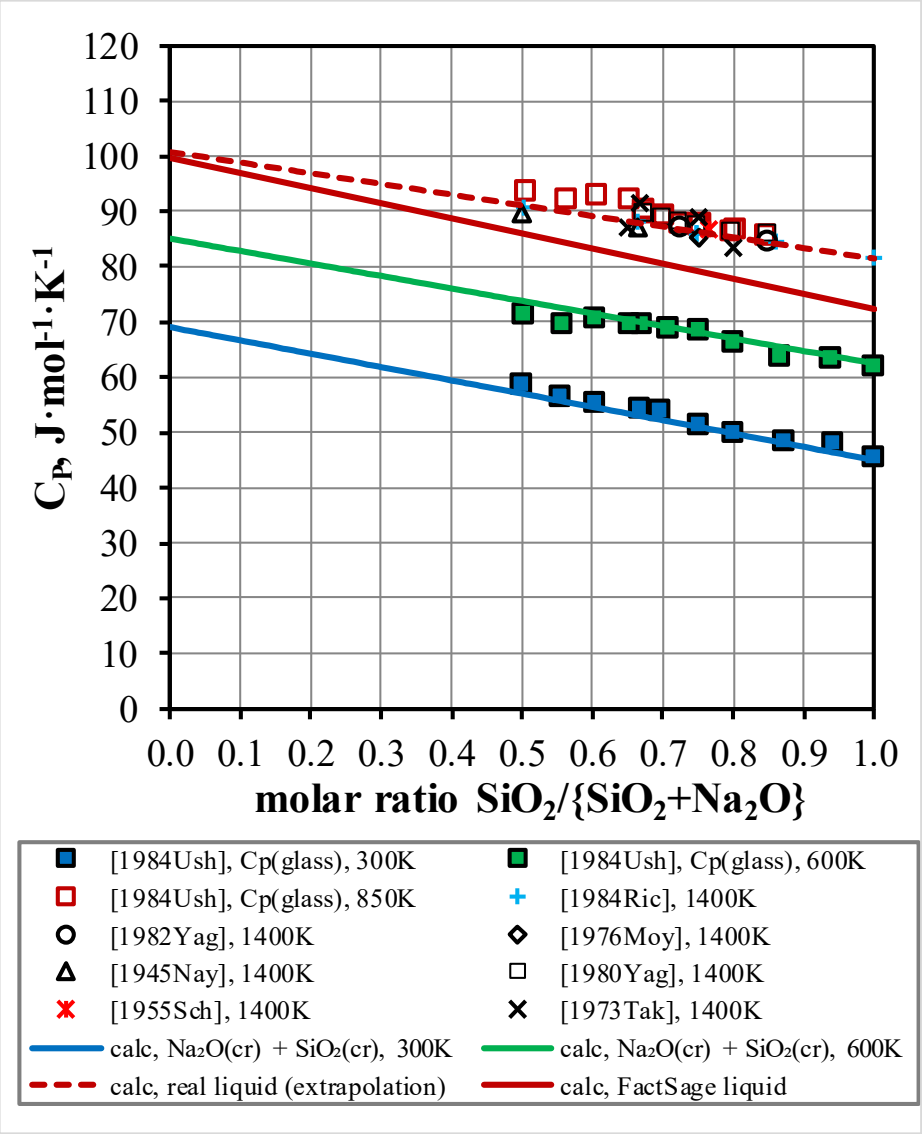

Figure 6.22 The heat capacities of glasses and liquids vs composition. Glass heat capacities are shown as filled symbols, heat capacities of liquids as empty symbols. Experimental points [203, 209, 237, 241-245] and calculated lines.

Strictly speaking, the current database is capable of an accurate prediction of the heat capacity and the heat content of only crystalline and vitreous compositions. The predicted values for liquids are

systematically lower than the experimental points (Figure 6.20, Figure 6.21). This is explained by the fact that the Na_2O(liq) and SiO_2(liq) heat capacities were historically chosen to be equal to the heat capacities of pure compositions in their most stable state and it is currently unfeasible to change that (Section 2.5.1). However, this inaccuracy concerns only the heat capacities and the heat contents but not the mixing properties (see section 2.5.1). For example, the calculated enthalpy of mixing would adequately represent the measured values because the inaccuracies would cancel each other.

6.6 Optimization results

The optimized parameters for the compounds and the liquid phase are given in Table A.3 and Table A.4, correspondingly. The properties of the end-members, Na_2O and SiO_2 were taken unchanged from the work of Wu et al. [17]. The entropies at 298K of Na_4SiO_4, Na_2SiO_3 and $Na_2Si_2O_5$ were calculated based on the low temperature heat capacities summarized in Figure 6.18. The heat capacities of solids were derived from the whole set of heat capacity and heat content data, if applicable.

The enthalpies of formation of Na_4SiO_4, Na_2SiO_3 and $Na_2Si_2O_5$ were chosen as the middle values among the data presented in Figure 6.11. Slight adjustments were introduced for a better fitting of the Na_2O activity data in two-phase solid mixtures from Figure 6.12.

The properties of three compounds, $Na_{10}SiO_7$, $Na_6Si_2O_7$, $Na_6Si_8O_{19}$ were not investigated in the literature. In this case, the heat capacities were estimated as weighted sums of the heat capacities of compounds with known properties. The enthalpies of formation and entropies of $Na_6Si_2O_7$ and $Na_6Si_8O_{19}$ can be fixed using both Na_2O activity data in solids and the phase diagram (Figure 6.12 and Figure 6.6). The properties of $Na_{10}SiO_7$ were assessed to reproduce the data by Rys [164].

The temperatures and enthalpies of the phase transformations of $Na_2Si_2O_5$ were set according to the data of Kracek [154]. The enthalpy of transformation of Na_4SiO_4 could not be found in literature and was estimated.

The liquid interaction parameters listed in Table A.4 were set using the automated optimization procedure. The properties of the dimer end-member $(Na_2)O$ were chosen in such a way that it would not affect the properties of the pure liquid Na_2O. It remains the prevailing sodium species in the

silica content range of 0.9-1.0 and its concentration does not change significantly with temperature. To do so, a positive stability parameter was chosen for the pure end-member and a strong negative interaction with silica ($g^{01}_{\mathrm{Na_2,Si}}$). To raise the cristobalite liquidus, a positive interaction with the dimer of higher order was required ($g^{05}_{\mathrm{Na_2,Si}}$). This interaction should be noticeable but not stronger than $g^{01}_{\mathrm{Na_2,Si}}$ to avoid decomposition. The interaction parameter $g^{06}_{\mathrm{Na_2,Si}}$ was used for fine tuning of the phase diagram.

A temperature dependence of $\Delta g^{\circ}_{\mathrm{Na,Si}}$ is required to adequately reproduce the sharp melting behaviour of Na_4SiO_4 (the composition of short-range ordering) as well as the minimum value of the enthalpy of mixing. Temperature dependencies of the high-order parameters are needed to reproduce both the steep silica liquidus and the metastable miscibility gap.

Compared with the previous Na_2O-SiO_2 optimization accepted in the *FToxid* database of *FactSage* (Wu et al. [17]), the optimization including $(Na_2)O$ dimer gives much better results in the high-silica area, both for the liquidus and the metastable miscibility gap.

CHAPTER 7 OPTIMIZATION OF THE Na_2O-Al_2O_3 SYSTEM

7.1 Phase diagram

The Na_2O-Al_2O_3 system has a few binary compounds; the liquidus temperatures are very high. The studies of the system are mostly limited to the $NaAlO_2$-Al_2O_3 part where samples can be prepared from alumina and Na_2CO_3. Besides the experimental difficulties related to high liquidus temperatures, the studies are complicated by the Na_2O volatilization.

Rolin and Thanh [246] determined the phase diagram of the Na_2O-Al_2O_3 system in the range of compositions between $NaAlO_2$ and Al_2O_3. In their experiments, the volatilization of Na_2O was not suppressed (unsealed crucibles were used) although it was mentioned that below 70 wt% of $NaAlO_2$ no condensation products were observed. The phase diagram by Weber and Venero [104] was investigated using sealed crucibles. There is a limited number of works concerning the Na_2O-$NaAlO_2$ part of the phase diagram. Bunzel and Kohlmeyer [247] describe Na_5AlO_4 compound with peritectic melting at 980°C and eutectic temperature of 720°C between Na_2O and Na_5AlO_4. On the contrary, Rys [164] did not find any compounds between Na_2O and $NaAlO_2$, only a simple eutectic. The optimized phase diagram is shown in Figure 7.1.

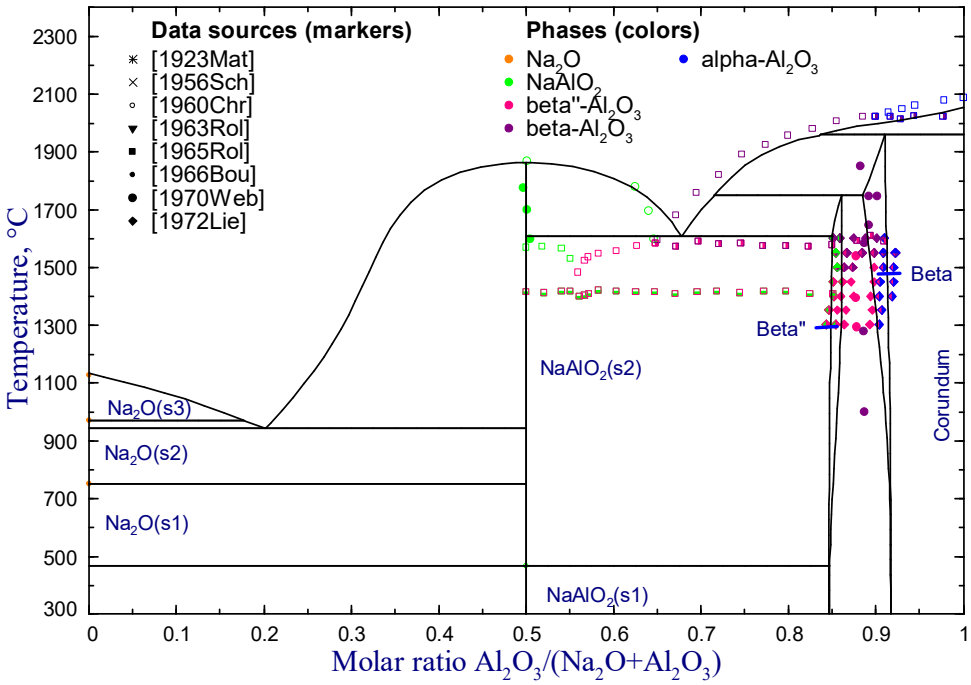

Figure 7.1 Phase diagram of the Na_2O-Al_2O_3 system. Experimental points [55, 104, 246, 248-252] and calculated lines.

The melting point of sodium aluminate $NaAlO_2$ is somewhat difficult to determine because of possible Na_2O losses. Matignon [248] reported a melting point of 1650°C for $NaAlO_2$, while Weber and Venero [104] give the value of 1867°C (in sealed crucibles). The extrapolation of the liquidus temperatures for carnegieite solid solutions in the system $NaAlO_2$-$NaAlSiO_4$ by Schairer and Bowen [55] gives the value of 1850°C, which is a fairly close match to the value determined directly by Weber and Venero [104]. Two different modifications of $NaAlO_2$ were found by Théry and Briançon [53], Ampian [253] and Otsubo [254]. The orthorhombic structure, stable at room temperature undergoes a phase transformation to a tetragonal modification. Théry et al. predict a high temperature cubic modification, stable above 1100°C [255]. Rys [164] observed a structural change at about 1430°C and Weber and Venero [104] report a transition at 1410°C.

β-Al_2O_3 was discovered by Rankin and Merlin [101] and first it was considered an allotropic modification of α-Al_2O_3. Only later it was shown that soda plays an essential role in the structure stabilization [102]. Two more structurally related phases were reported in the literature, β'-Al_2O_3 and β"-Al_2O_3 [256], but only the existence of β"-Al_2O_3 has been confirmed. Both β- and β"-Al_2O_3 have a spinel-like structure and can form solid solutions with a number of mono-, di-, and tri-valent

cations [53, 257, 258]. The difference between them is the periodicity along the *c* axis, sometimes they are also called 2- and 3-block β-phases. Due to a high cationic conductivity, β-Al_2O_3 materials find application as solid electrolytes [252], mostly stabilized with MgO and Li_2O to prevent Na_2O losses [106]. In the work of Duncan and West [259], solid solutions of β"-Al_2O_3 with Li_2O and MgO were studied and $NaAl_5O_8$ is proposed as an ideal sodium end-member, although the ideal composition is never reached. Apparently, its formula unit can be described as $Na_2Al_{12}O_{19}$ [104]. For β-Al_2O_3, the formula of $Na_2O \cdot 11Al_2O_3$ can be seen in literature but, according to Choudhury [103], this composition is in fact a mixture of α-Al_2O_3 and $NaAl_9O_{14}$.

According to literature sources, it is extremely difficult to determine the true stability ranges of β-aluminas as the energetic gain of their formation is very small and there are certain kinetic limitations to their formation. So, β-Al_2O_3 starts to form only above 1480°C [104], but does not decompose below this temperature. Although use of inert NaF solvent [252] can facilitate the formation of β-Al_2O_3, β"-Al_2O_3 does not transform into β-Al_2O_3 at the same conditions.

7.2 Calorimetry data

Calorimetry measurements are available only for the $NaAlO_2$ compound. Hemingway [187] performed HF solution calorimetry, and Coughlin [260] carried out HCl solution calorimetry. Their values of the enthalpy of formation from oxides are -89.22±1.26 and -87.40±3.26 $kJ \cdot mol^{-1}$, correspondingly. Koehler [261] reviewed the work of Hemingway [262] and gives the value of -87.65±2.3 $kJ \cdot mol^{-1}$. The revaluated value from Coughlin [260] is -88.83±1.40 kJ/mol.

7.3 Activity data

Mono- and two-phase regions of the Na_2O-Al_2O_3 phase diagram were investigated by many authors with EMF technique. The general schema of an electrochemical cell is:

$$\mathrm{Na}(a_1)||\text{solid electrolyte}||\text{sample, } \mathrm{O_2}(a_2) \tag{102}$$

where Na_2O activity in the sample can be calculated using the following equation:

$$\ln a(\mathrm{Na_2O}) = (-2FE - \Delta_r G^\circ)/RT + 2\ln a(\mathrm{Na}) + 0.5\ln a(\mathrm{O_2}) \tag{103}$$

Various mixtures can be used as a source of sodium: Na(liq) [263-266], Pb-Na alloys [267], Au+Au_2Na [268], W+WS_2+Na_2S [266, 269], Na_2CO_3 [270-272], Ni+NiF_2+NaF [273], $NaFeO_2$+Fe_2O_3+O_2 [274]. Various compositions are used as well as an oxygen source: air [268, 274], Cu+Cu_2O [265, 273, 275], In+In_2O_3 [270], Fe + "FeO" [267], Ni+NiO [275]. To improve the reliability of EMF measurements, it is desirable to lower the total potential difference between the cathode and the anode and avoid very low partial pressures of oxygen in the system to exclude the p-conductivity mechanism. The pairs sodium source/oxygen source need to be selected accordingly depending on the studied samples.

Concentration cells were used as well to investigate the Na_2O-Al_2O_3 system. EMF is generated by migration of Na_2O from the electrode with a higher Na_2O activity to that with a lower activity. The schema of this kind of cells can be written in the following way:

$$Na_2O(a_1)||\text{solid electrolyte}||\text{sample}, Na_2O(a_2) \quad (104)$$

In that case, the activity of Na_2O in the right part can be calculated according to the following expression:

$$\ln a(Na_2O) = -2FE/RT + \ln a(Na_2O, ref) \quad (105)$$

Concentration cells were employed by Rog et al. [276, 277], Rog and Kozlowska-Rog [278, 279] and Kummer [105]. One of the reference materials was Na_2O deposited on NASICON matrix [276-279]. Na_2O was obtained during calcination of Na_2CO_3-embedded NASICON and supposedly has the activity equal one. It remains unclear how Na_2O could be obtained as Na_2CO_3 does not form it upon heating or why it has the activity equal one if it is stabilized by the matrix (stabilization would lower the chemical potential and the activity).

If possible, the raw EMF data were recalculated using *FactSage* databases for auxiliary compounds. In some cases, however, the original activities were taken (cells with Au+Au_2Na, W+WS_2+Na_2S, Ni+NiF_2+NaF) because the data on these systems are absent in *FactSage*.

Na_2O activities in different regions of the Na_2O-Al_2O_3 phase diagram are summarized in Figure 7.2.

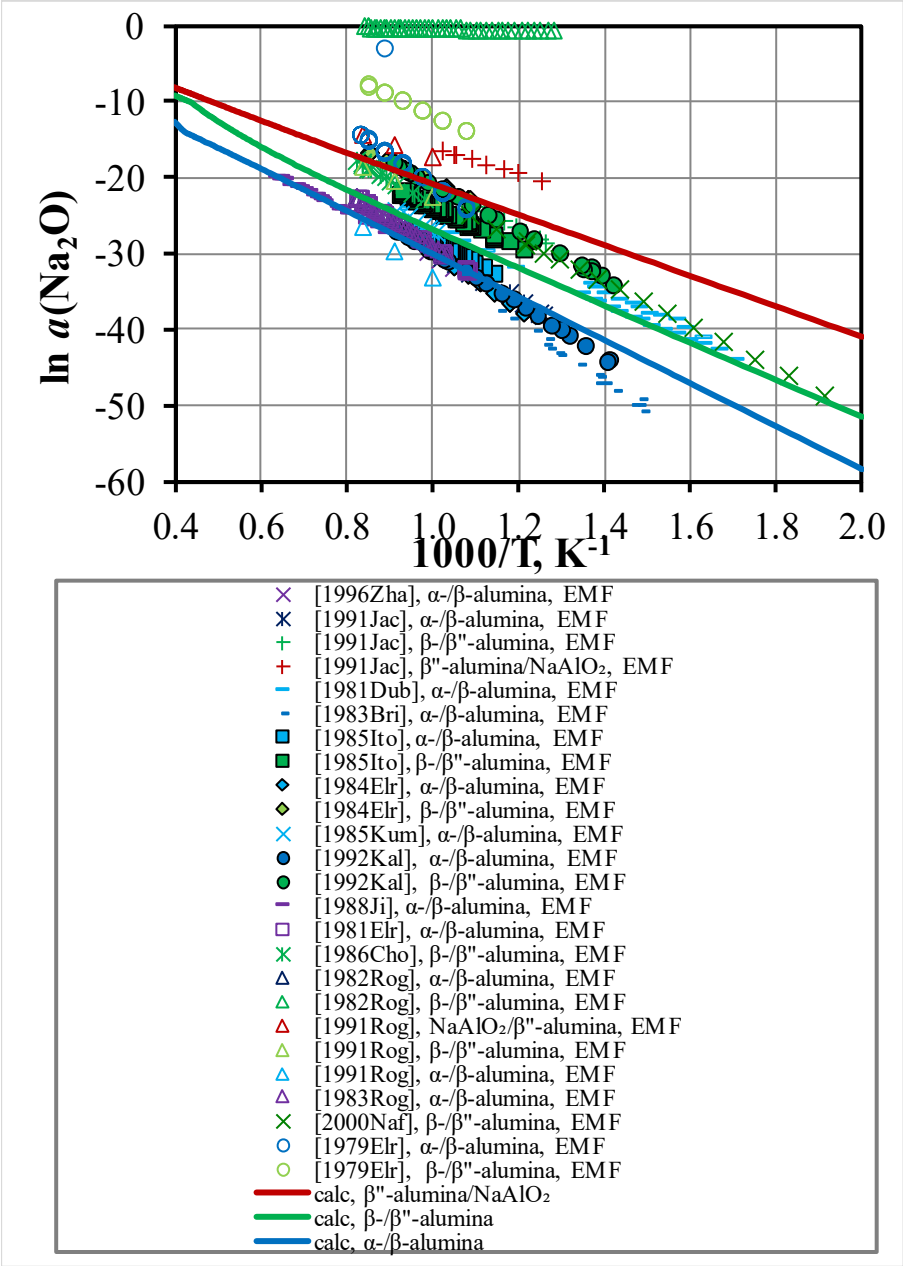

Figure 7.2 Na_2O activity in two-phase fields of the Na_2O-Al_2O_3 system. The reference state is β-Na_2O ($Na_2O(s_2)$). Experimental points [263-272, 275, 277, 278, 280-282] and calculated lines.

There is a lot of disagreement among the experimental data (Figure 7.2) as there are certain experimental difficulties related to the reproducibility and reversibility in the experiments.

7.4 Heat capacity and heat content data

The heat capacity and the heat content of $NaAlO_2$ were measured by King [283] and Christensen et al. [249]. According to the data by Christensen et al. [249], the phase transformation at 467°C is accompanied by a heat effect of 1.20 kJ·mol^{-1} (Figure 7.4).

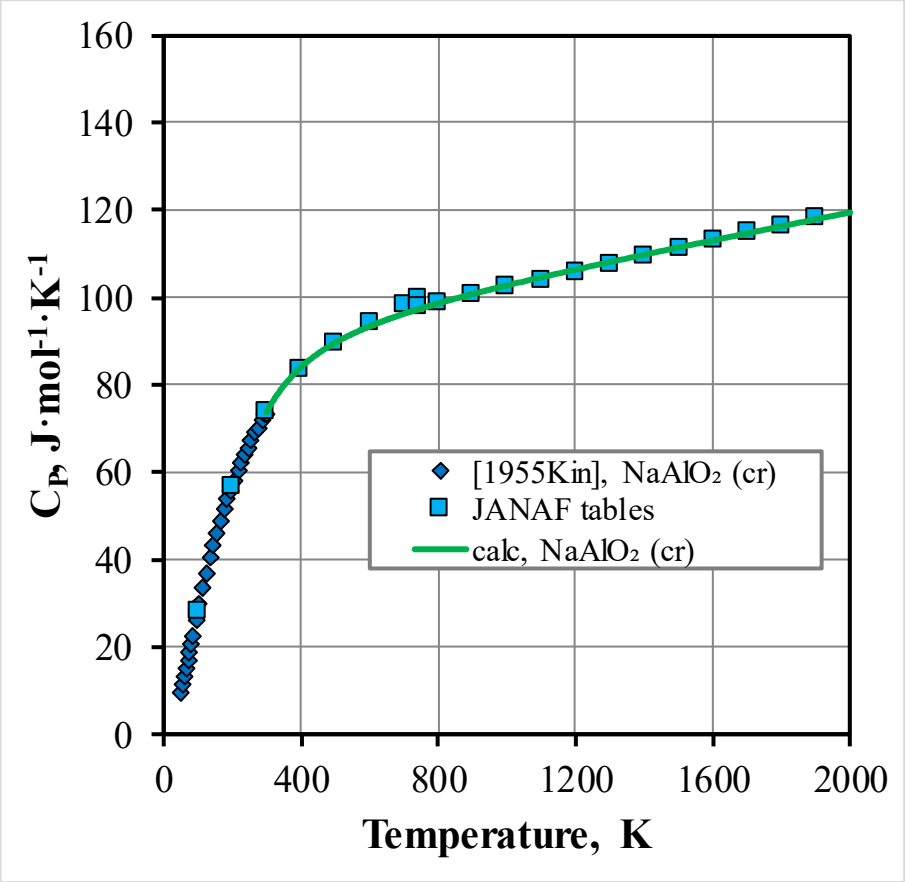

Figure 7.3 The heat capacity data for $NaAlO_2$. Experimental data points [283] and calculated lines.

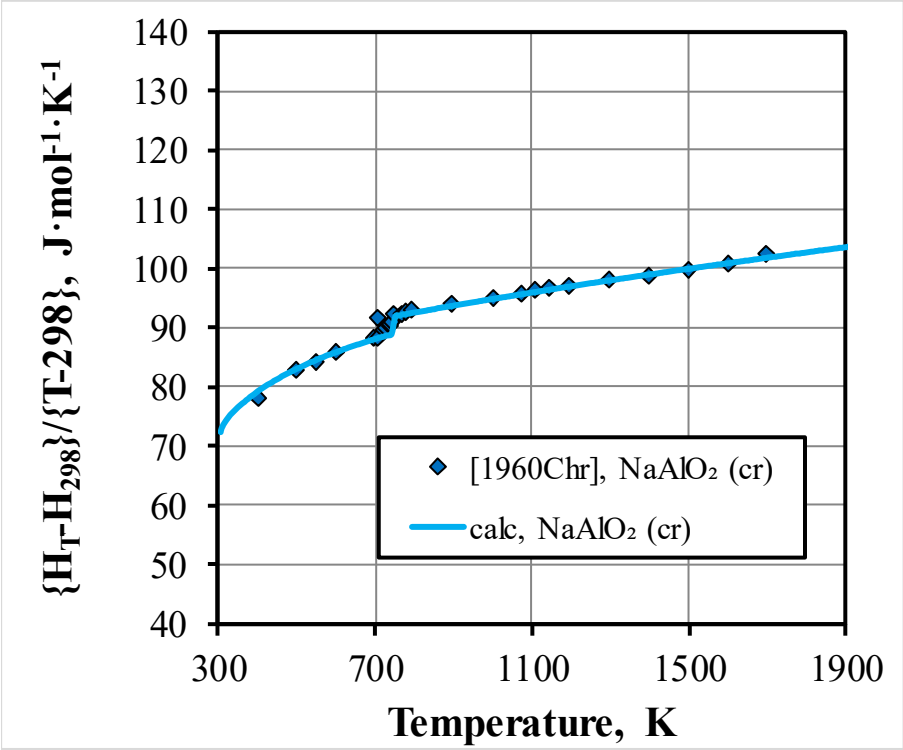

Figure 7.4 The mean heat capacity of $NaAlO_2$. Experimental data points [249] and calculated lines.

The heat capacity of β-Al_2O_3 in the range of 1-40K was reported by McWhan et al. [284] and the values at higher temperatures were recalculated from the data of Bjorkstam et al. [285].

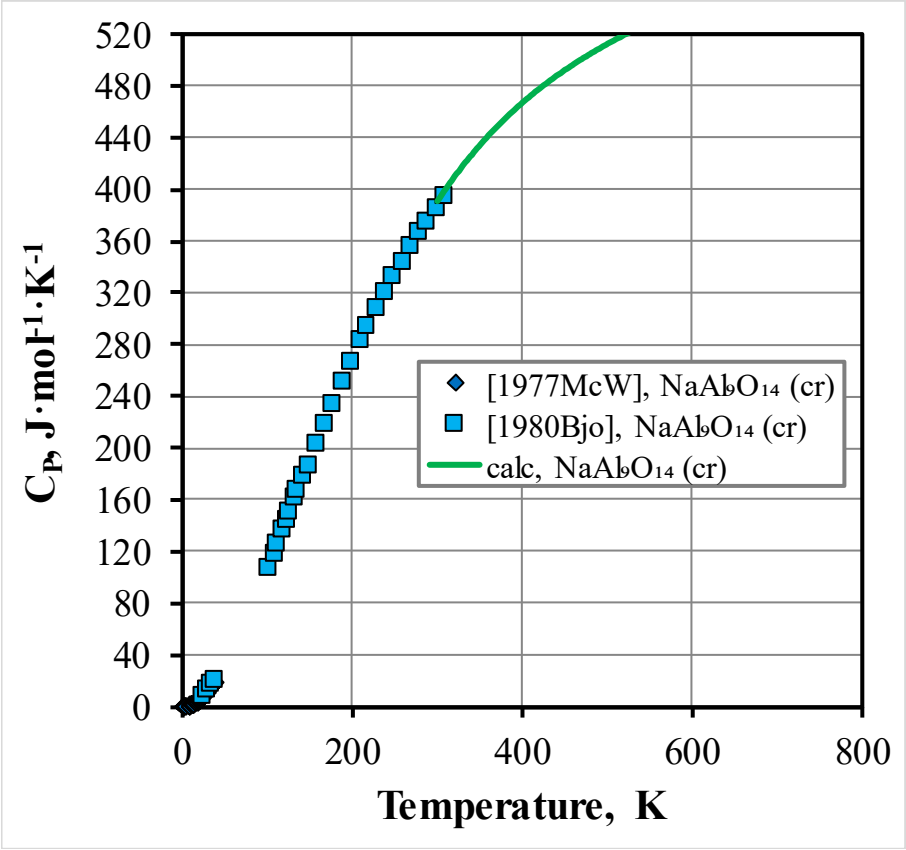

Figure 7.5 The heat capacity of $NaAl_9O_{14}$ (β-Al_2O_3). Experimental data points [284, 285] and calculated lines.

7.5 Optimization results

$NaAlO_2$ was treated as a stoichiometric compound with two modifications. Its enthalpy of formation, the entropy and the heat capacity were evaluated based on the available experimental calorimetry data.

Two other compounds, β- and β”-aluminas were treated as solid solutions according to the model described in section 4.12. Their stabilities were adjusted to reproduce the phase diagram.

The liquid phase model includes an associate species $NaAlO_2$ required for an adequate reproduction of the Na_2O-Al_2O_3-SiO_2 system. Its Gibbs energy is a sum of the Gibbs energies of the other two end-members plus a temperature-dependent stability parameter. This stability parameter lowers the liquidus around $NaAlO_2$ compound whose properties are fixed. A similar

effect is achieved by the $\Delta g^{\circ}_{\mathrm{Na,Al}}$ parameter; there is an ambiguity between the extent of the interaction and the stability of the associate. The binary system was optimized as a part of multicomponent systems; it appears that a stable associate is required to reproduce some of the multicomponent sections, for example, the $CaSiO_3$ liquidus in the $NaAlSiO_4$-$CaSiO_3$ and $NaAlSi_3O_8$-$CaSiO_3$ sections. It seems that the associate stability plays an important role until a certain value is reached; after this, a more stable associate does not change the multicomponent systems much.

The temperature dependence of the associate stability parameter is another ambiguous parameter which can only be resolved in the higher-order systems. So, in the $NaAlSiO_4$-SiO_2 section of the Na_2O-Al_2O_3-SiO_2 system, the curvature of the carnegieite liquidus depends on the *T*-term of the associate stability parameter and also on the *T*-term of the $\Delta g^{\circ}_{\mathrm{NaAl,Si}}$ interaction parameter (the same curvature is obtained for the same sum of the terms). However, given that the carnegieite properties and the enthalpy of mixing in the liquid phase are known, there is only one way to distribute weights between the terms. The *T*-term of the $\Delta g^{\circ}_{\mathrm{Na,Al}}$ interaction parameter is used to get a good curvature of $NaAlO_2$ liquidus in the Na_2O-Al_2O_3 phase diagram, the $\Delta g^{\circ}_{\mathrm{Al,NaAl}}$ and $g^{30}_{\mathrm{Al,NaAl}}$ parameters fit the eutectics in the $NaAlO_2$-Al_2O_3 area. Based on the optimization of the Na_2O-Al_2O_3-SiO_2 system, a negative $\Delta q^{\circ}_{\mathrm{Na,NaAl}}$ parameter is required to avoid a false miscibility gap close to the Na_2O-$NaAlO_2$ boundary.

The optimization approach in regard of Beta and Beta" solutions is reproduced after Kim [18]. Their stabilities were adjusted to reproduce the invariant equilibria.

The optimized parameters are shown in Table A.5 and Table A.6.

CHAPTER 8 OPTIMIZATION OF THE Na_2O-Al_2O_3-SiO_2 SYSTEM

8.1 Phase diagram

A few ternary compounds and end-members of solid solutions are known in the Na_2O-Al_2O_3-SiO_2 system. All ternary compounds are located in the $NaAlO_2$-SiO_2 section. The $NaAlSiO_4$ composition corresponds to two structures, nepheline and carnegieite. Nepheline is a part of minerals occurring naturally and is usually found as a solid solution with an excess of silica and the potassium end-member. Carnegieite is an artificial phase forming upon heating of nepheline. Two other compounds, albite $NaAlSi_3O_8$ and jadeite $NaAlSi_2O_6$ occur in nature as end-members of feldspar and clinopyroxene solid solutions.

The phase equilibria in the ternary system were investigated by a number of researchers. Bowen [286] determined the melting point of albite, 1100°C. According to Bowen [52], the melting point of carnegieite is 1526°C, and the nepheline/carnegieite inversion takes place at 1248°C. Due to the sluggishness of the nepheline/carnegieite transition, the high temperature modification of carnegieite can undergo a rapid transformation into a twinned structure with a lower symmetry at about 690°C [287]. The study of Greig and Barth [49] confirmed the melting point of carnegieite and corrected the melting point of albite to 1118°C. They also stated that jadeite is metastable under the atmospheric pressure and decomposes to nepheline and glass. The liquidus and invariant points in the ternary system were investigated by Schairer and Bowen [55]. The authors proposed that there is a solid solution between $NaAlO_2$ and carnegieite. The data by Schairer and Bowen are plotted in Figure 8.1-Figure 8.2 in different temperature intervals. The authors did not make a distinction between carnegieite and the high-*T* aluminate phase. The phase, marked as "Na_4SiO_4?", according to the authors, is probably a solid solution between $NaAlO_2$ and Na_4SiO_4. In the $NaAlSiO_4$-Al_2O_3 section the formation of β-Al_2O_3 was observed which was considered as metastable because it further disappeared. As no special attention was paid to avoid possible Na_2O losses before, De Pablo-Galan and Foster [288] analysed β-Al_2O_3 primary crystallization field trying to minimize Na_2O evaporation.

It is very difficult to measure the exact melting temperature of albite because of the overheating, slow kinetics of melting and long relaxation times of molten albite close to the melting point [289].

According to Navrotsky et al. [290], it can be explained by formation of a solid solution of $NaAlSi_3O_8$ with $NaAlSiO_4$ with an approximate compositional range of $NaAlO_2$ between 0.245-0.265. The idea of a solid solution between albite and nepheline was proposed by Greig and Barth [49] but it was difficult to prove. Boettcher et al. [291] investigated phase relations in the system $NaAlSi_3O_8$-SiO_2 under normal and high pressures. Although the runs at high pressures were reversible, the reversibility was not reached under 1 atm.

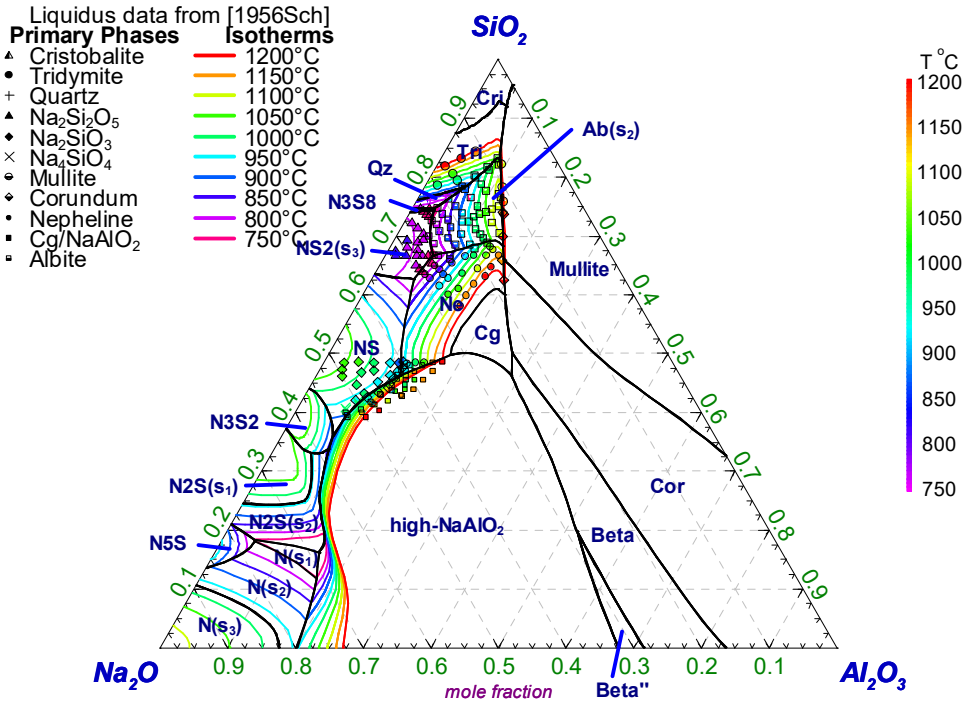

Figure 8.1 Liquidus projection in the Na_2O-Al_2O_3-SiO_2 system in the temperature range of 750-1200°C. Experimental points [55] and calculated lines.

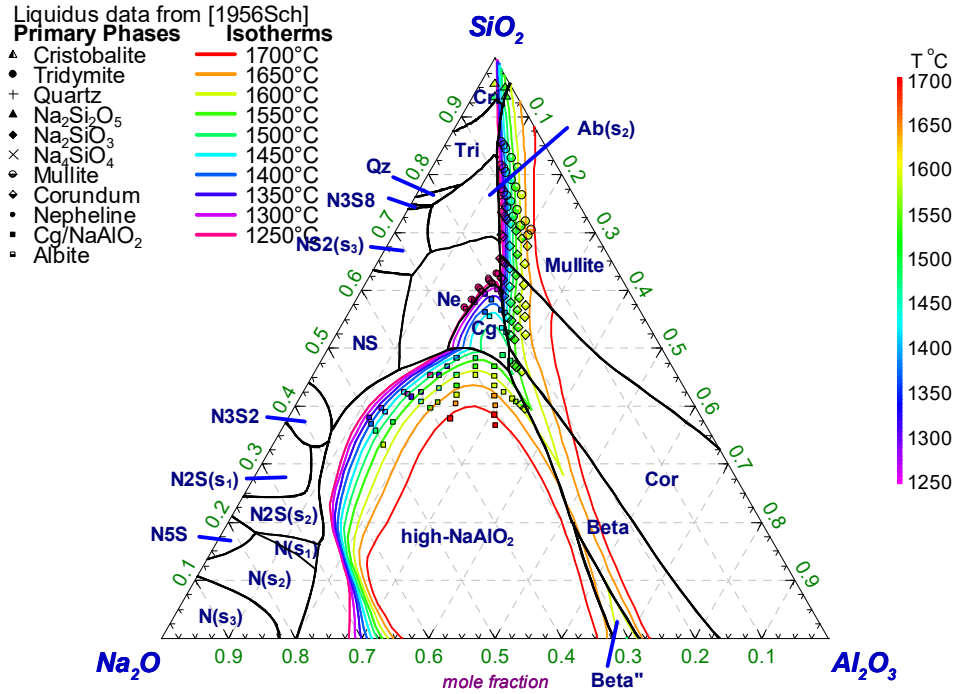

Figure 8.2 Liquidus projection in the Na_2O-Al_2O_3-SiO_2 system in the temperature range of 1250-1700°C. Experimental points [55] and calculated lines.

The liquidus projection data in Figure 8.1-Figure 8.2 are well reproduced apart from the position of the Mullite/Corundum boundary curve. The reason why the calculated Mullite field is larger than it is supposed to be according to the experimental data is discussed in detail in Section 5.1.

Polythermal sections through the ternary system are presented in Figure 8.3-Figure 8.4.

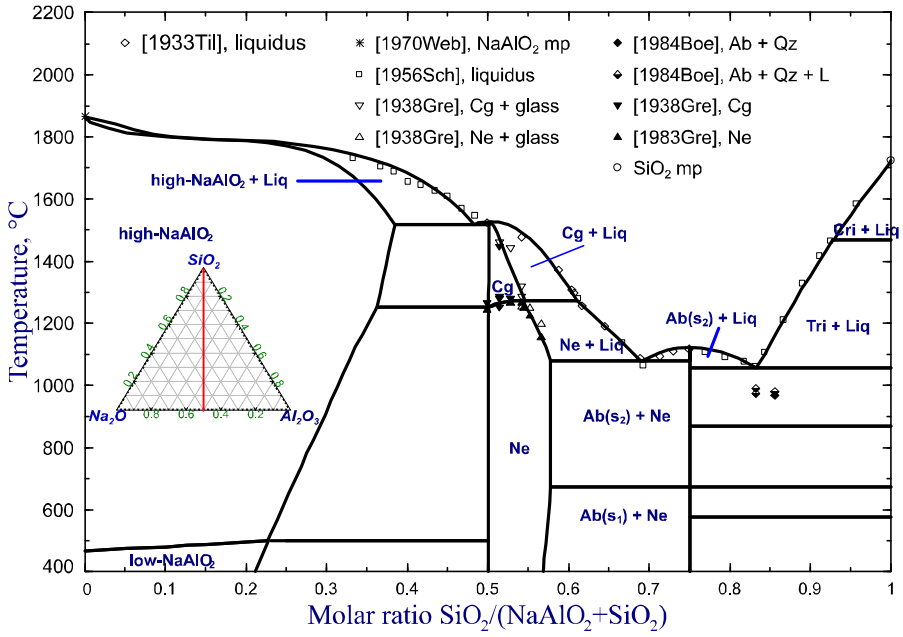

Figure 8.3 Phase diagram in the $NaAlO_2$-SiO_2 section of the Na_2O-Al_2O_3-SiO_2 system. Experimental data [104, 291] and calculated lines.

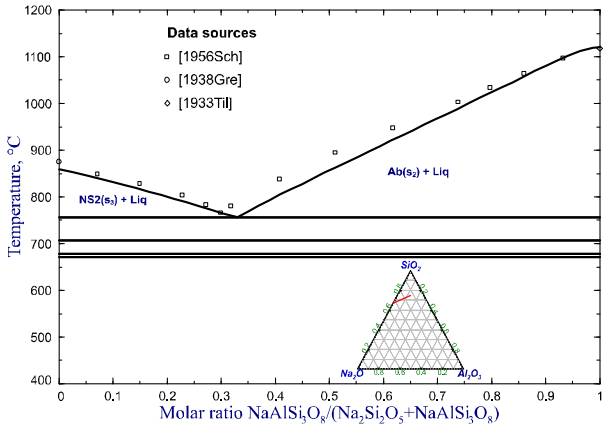

(*a*)

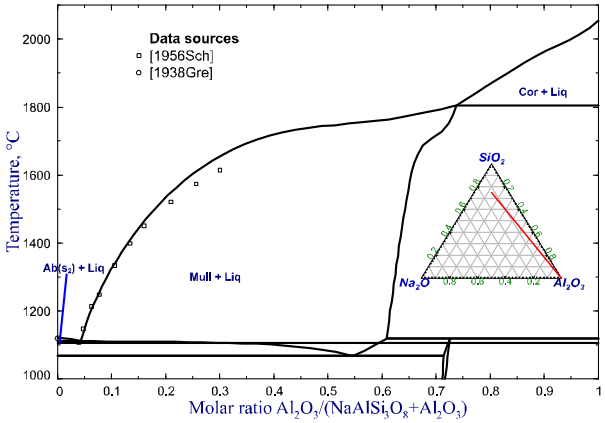

(*b*)

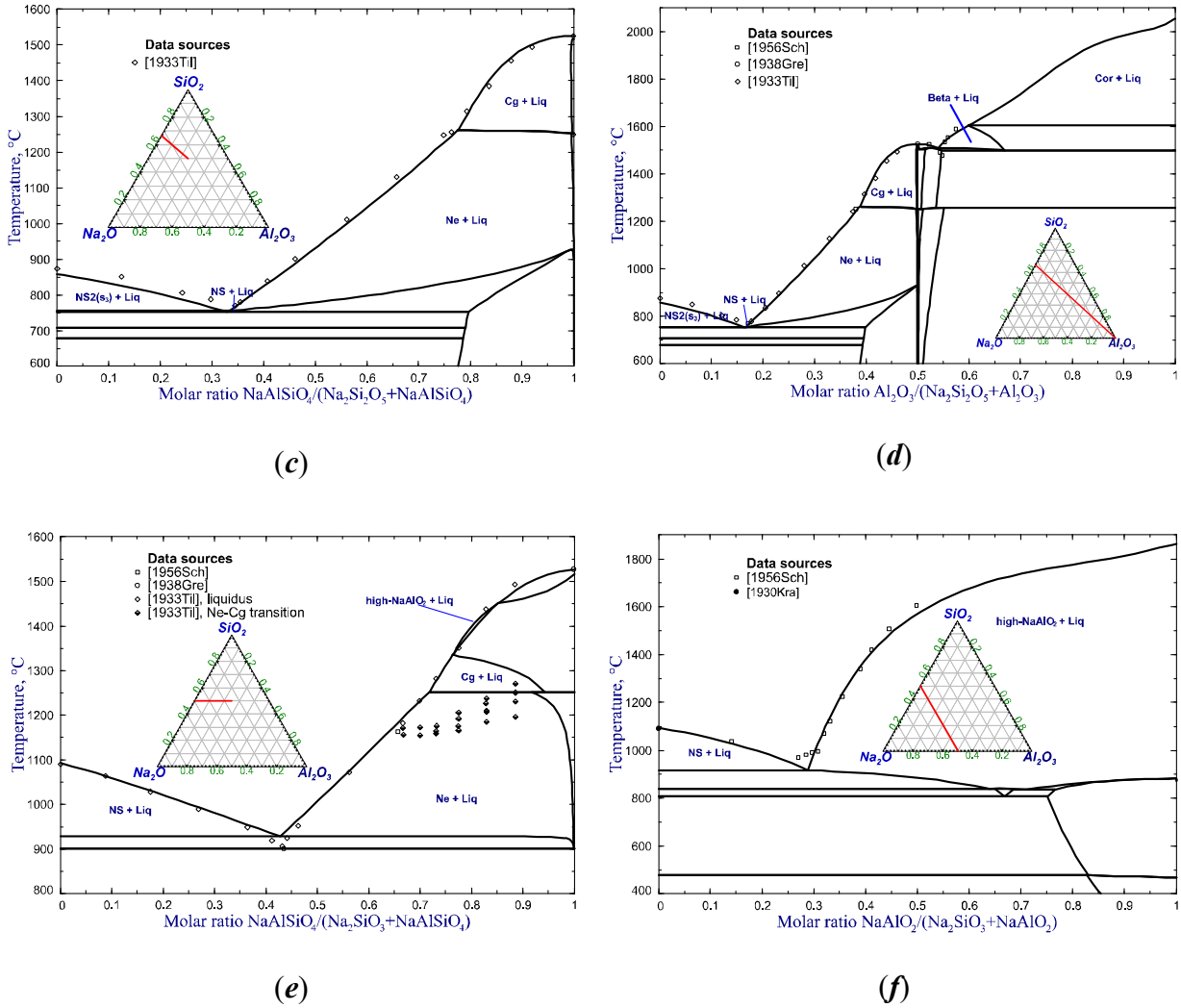

Figure 8.4 Phase diagrams in the sections through the Na_2O-Al_2O_3-SiO_2 system: $Na_2Si_2O_5$-$NaAlSi_3O_8$ (***a***), $NaAlSi_3O_8$-Al_2O_3 (***b***), $Na_2Si_2O_5$-$NaAlSiO_4$ (***c***), $Na_2Si_2O_5$-Al_2O_3 (***d***), Na_2SiO_3-$NaAlSiO_4$ (***e***), Na_2SiO_3-$NaAlO_2$ (***f***). Experimental points [49, 55, 292, 293] and calculated lines.

The isothermal data by De Pablo-Galan and Foster [288] is summarized in Figure 8.5.

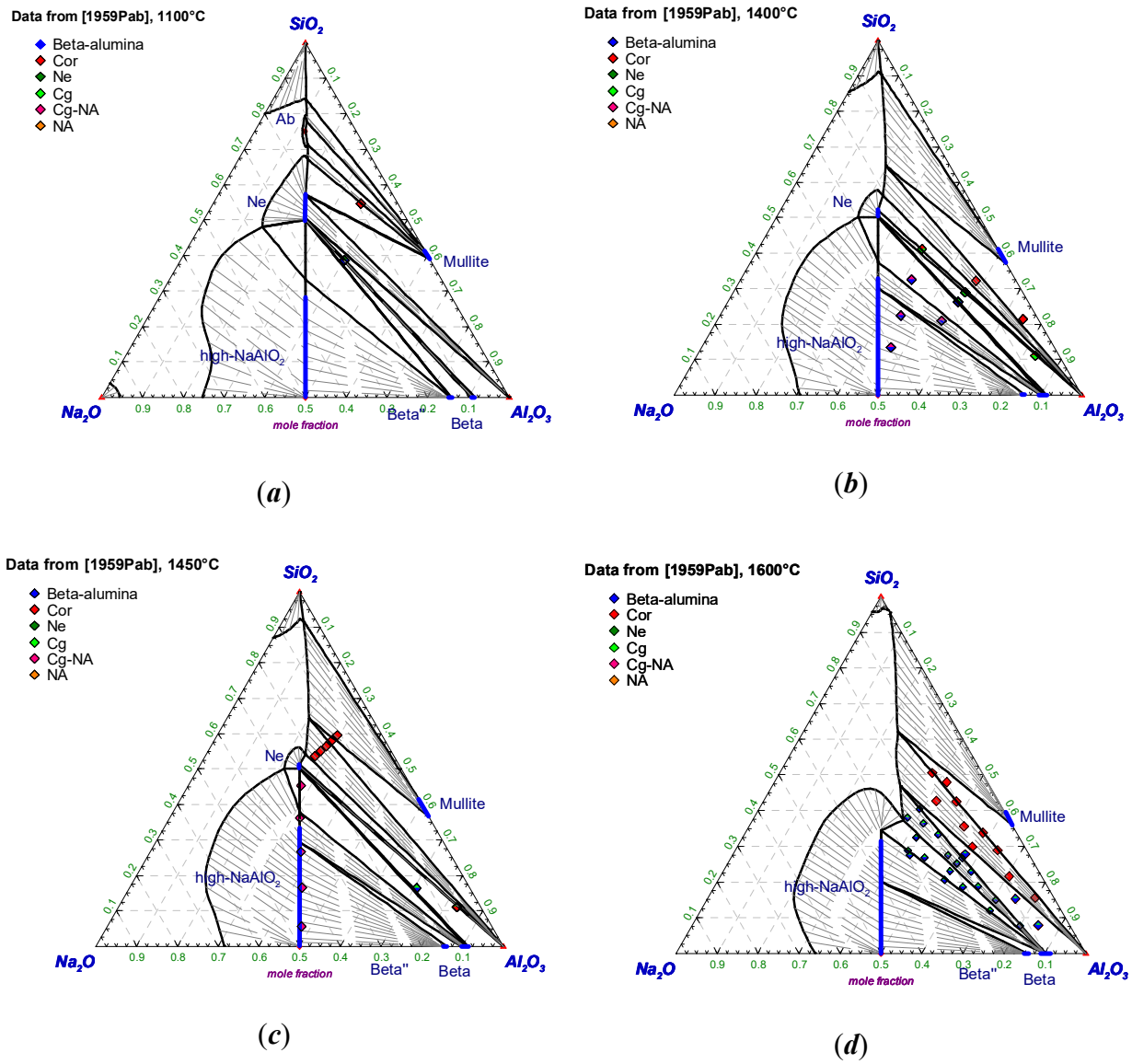

Figure 8.5 Isothermal sections in the Na_2O-Al_2O_3-SiO_2 system at different temperatures (***a-d***). Experimental points [288] and calculated lines. Colors in the markers correspond to the forming phases. If a marker has two colors, the corresponding two phases are present together.

Although they have the same stoichiometry, nepheline and carnegieite are very different from the structural point of view. Carnegieite is often seen as a derivative of the cristobalite structure where part of the silica tetrahedra were replaced with $NaAlO_2$ tetrahedra. The high-temperature modification of carnegieite is cubic. The nepheline structure has a lower symmetry and is rhombohedral. It is considered as a derivative from the tridymite structure and has two non-

equivalent cationic sites of different sizes. The nepheline/carnegieite transition requires to rebuild the network topology and is kinetically slow. Carnegieite exists at room temperature in a metastable state and its properties can be studied. According to Richet et al. [47], high-*T* α-carnegieite transforms into β-carnegieite at 693°C metastably with the enthalpy of transition of 8.1±0.3 $kJ \cdot mol^{-1}$.

DSC investigations of nepheline by Henderson and Thompson [294] reveal that the compound undergoes two phase transitions with temperature. Low-*T* δ-nepheline transforms into β-nepheline at 190°C ($\Delta_{trans}H$ = 1291 $J \cdot mol^{-1}$) which in its turn transforms into high-*T* γ-nepheline at 875°C ($\Delta_{trans}H$ = 390 $kJ \cdot mol^{-1}$). These transitions disappear upon addition of the potassium end-member and are most likely explained by a collective network collapse around the big cation sites in the nepheline structure. The enthalpic effects of the transitions are seen in Figure 8.18.

The phase transitions within the nepheline and carnegieite series are fast and accompanied by overall network distortions rather than by a change in topology.

Albite can have a triclinic and monoclinic structure (at high temperatures); its transitions are complicated by the presence of Al/Si ordering of different degree. From the crystallochemical point of view, Al and Si occupy different types of tetrahedral sites. At high temperatures, there are only two types of sites in the monoclinic modification: T1 and T2. Upon cooling, a fast displacive transformation leads to structure distortion and the symmetry becomes triclinic. Al/Si sites split into two subsites each, denoted T1(0), T1(m), T2(0) and T2(m).

A slow diffusive transformation governs the Al/Si distribution over the monoclinic and triclinic sites. In general, for feldspars with different chemical formulas, both triclinic and monoclinic modifications can be in an ordered or disordered state. However, in the particular case of albite $NaAlSi_3O_8$, the stable monoclinic modification is always disordered and is called monalbite. If quenched, it forms crystals of the triclinic modification with multiple twinning. An ordered triclinic albite is called low albite and its disordered form high albite.

Some authors [295] think that the low/high albite transition is a first order transition, i.e. it has a fixed temperature and the corresponding enthalpy of transition. Others suppose that it is rather a higher-order transition with a smoothly changing parameter of ordering [62, 63].

The enthalpy of disordering of albite was measured in a series of works [295-299]. As albite ordering is very sluggish, only natural mineral samples can be used for measurements. However, natural albites are almost never fully ordered. The degree of ordering of the starting albite sample is important. According to the data by Holm and Kleppa [295], the low/high transformation occurs in two steps. At heating temperature of 1045°C, the first step, energetically equivalent to 10.04 $kJ \cdot mol^{-1}$, completes within 3 days. The second step of 4.2 $kJ \cdot mol^{-1}$ lasts over three weeks.

8.2 Calorimetry data

The enthalpies of mixing and formation of crystalline and vitreous samples in the Na_2O-Al_2O_3-SiO_2 can be derived based on the solution calorimetry data. The main solvents used are HF (ambient temperatures) and $2PbO \cdot B_2O_3$ melt (around 700°C).

The enthalpies of solution of simple oxides and end-members in the lead borate were taken from Petrovic and Navrotsky [300] and Zygan et al. [195] for Na_2O and $NaAlO_2$. A series of works report data for α-Al_2O_3 [190, 192-194] and for SiO_2(qz) [190-194].

Calculation of the enthalpies of formation based on HF calorimetry data is complicated due to insolubility of corundum. To overcome this, the enthalpy of solution of gibbsite γ-$Al(OH)_3$ was measured by Hemingway and Robie [187]. Another indirect cycle, based on the heat of solution of metallic Al, was performed by Morey [158]. Enthalpies of solution of simple oxides and end-members in case of HF calorimetry were compiled for SiO_2(qz) [158, 180-183, 185-187, 196], for Na_2O[158, 188], for α-Al_2O_3 [158, 187], for $NaAlO_2$ [187].

Glasses along the $NaAlO_2$-SiO_2 join were studied by HF calorimetry [301] and lead borate solution calorimetry [302, 303].

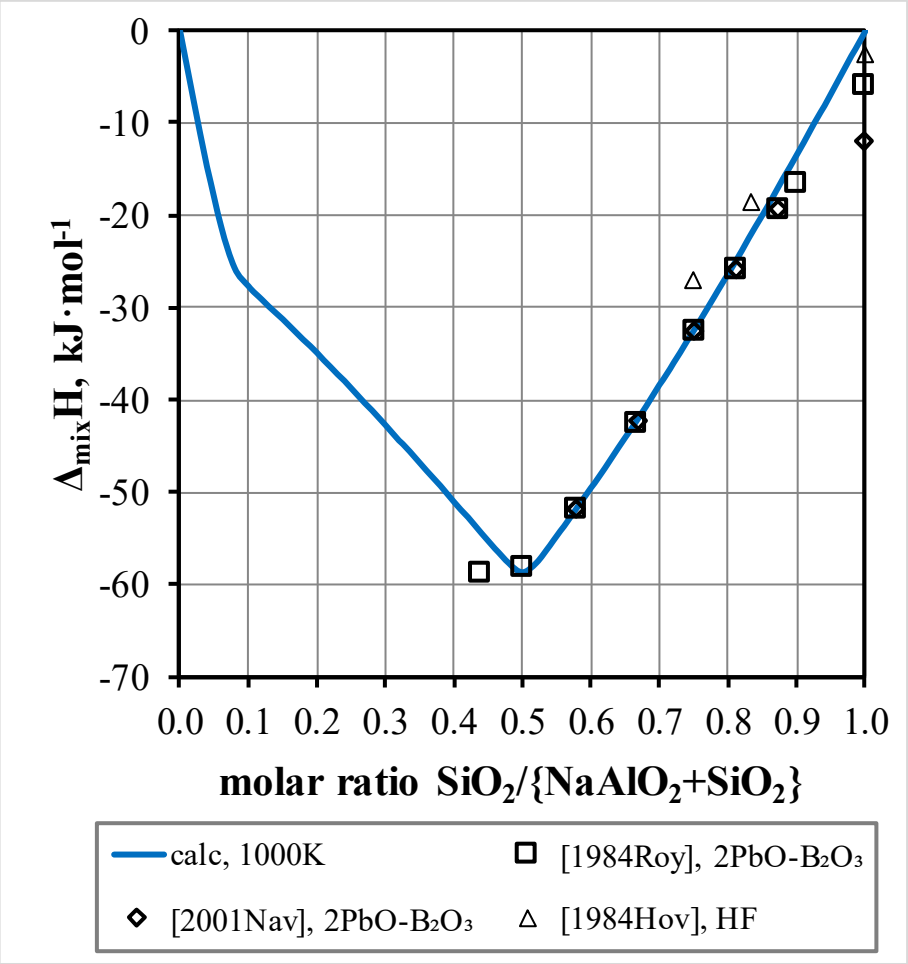

Figure 8.6 The enthalpy of mixing in the $NaAlO_2$-SiO_2 section. Experimental points [301, 302, 304] and calculated lines.

The solution calorimetry data for crystalline solids were recalculated into the enthalpy of formation from oxides (Figure 8.7).

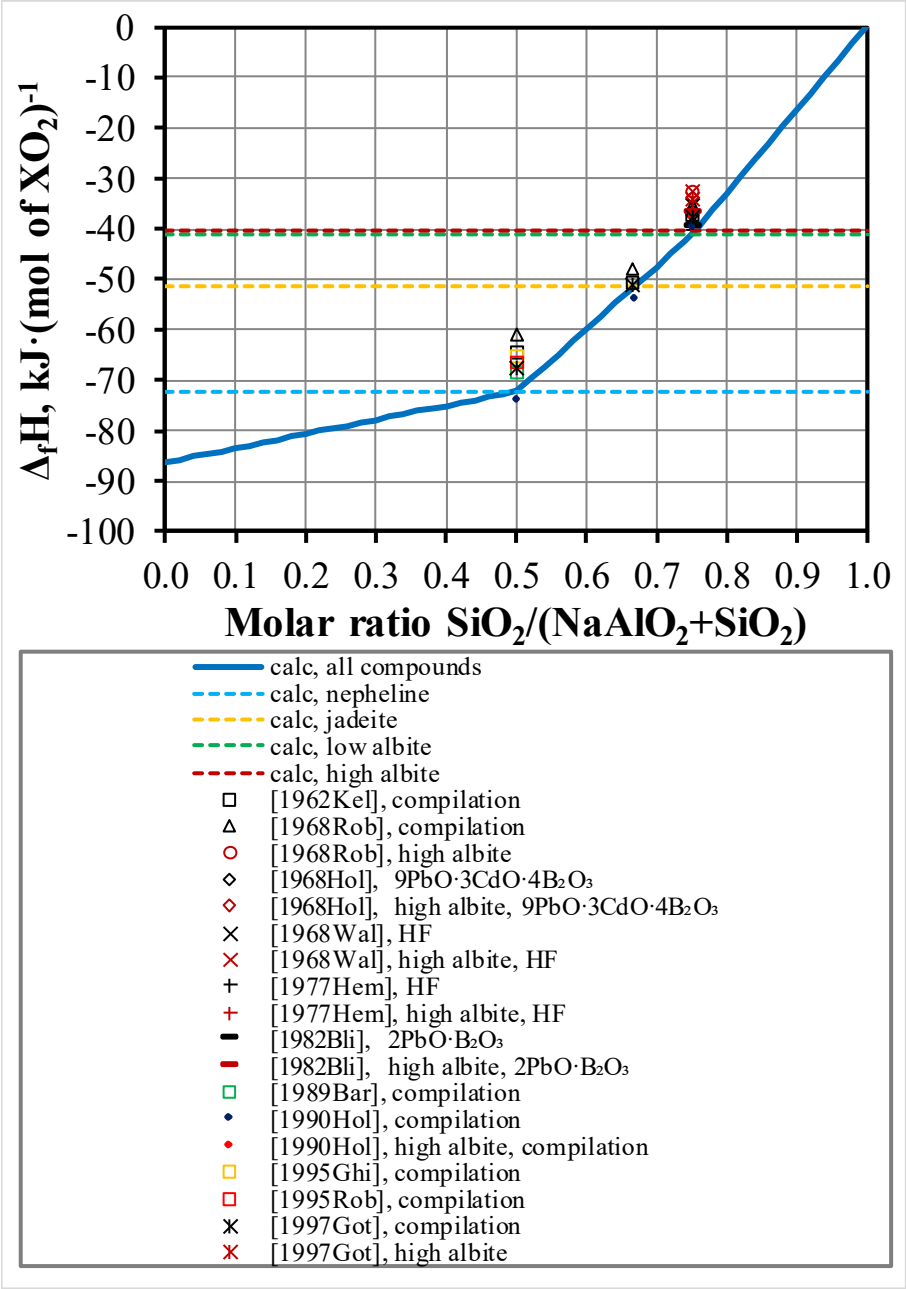

Figure 8.7 The enthalpy of formation from oxides of compounds in the $NaAlO_2$-SiO_2 section. Experimental points [187, 295, 296, 305-312] and calculated lines. For clarity, the values of the enthalpy of formation per mol of XO_2 where also shown as horizontal lines.

Jadeite $NaAlSi_2O_6$ is unstable under normal pressures and has a metastable melting point at 800°C [107]. Attempts to crystallize the compound from a melt of the same composition were unsuccessful [49]. HF calorimetry of jadeite samples was performed by Kracek et al. [107]. The

authors claim that according to their calorimetric results, jadeite could possibly form at 25°C from nepheline and albite given there are no kinetic hurdles. Jadeite stability has also been investigated by means of lead borate solution calorimetry by Hlabse and Kleppa [191].

The enthalpy of formation of albite was recalculated by Hemingway and Haselton [262] based on calorimetry data from elsewhere.

Besides the calorimetric data on a pure synthetic nepheline (Figure 8.7), Hovis and Roux [313] performed HF calorimetry of samples of synthetic nepheline with a different content of excess silica. These points were recalculated into the enthalpy of mixing using pure $NaAlSiO_4$ nepheline and quartz as the end-members (Figure 8.8).

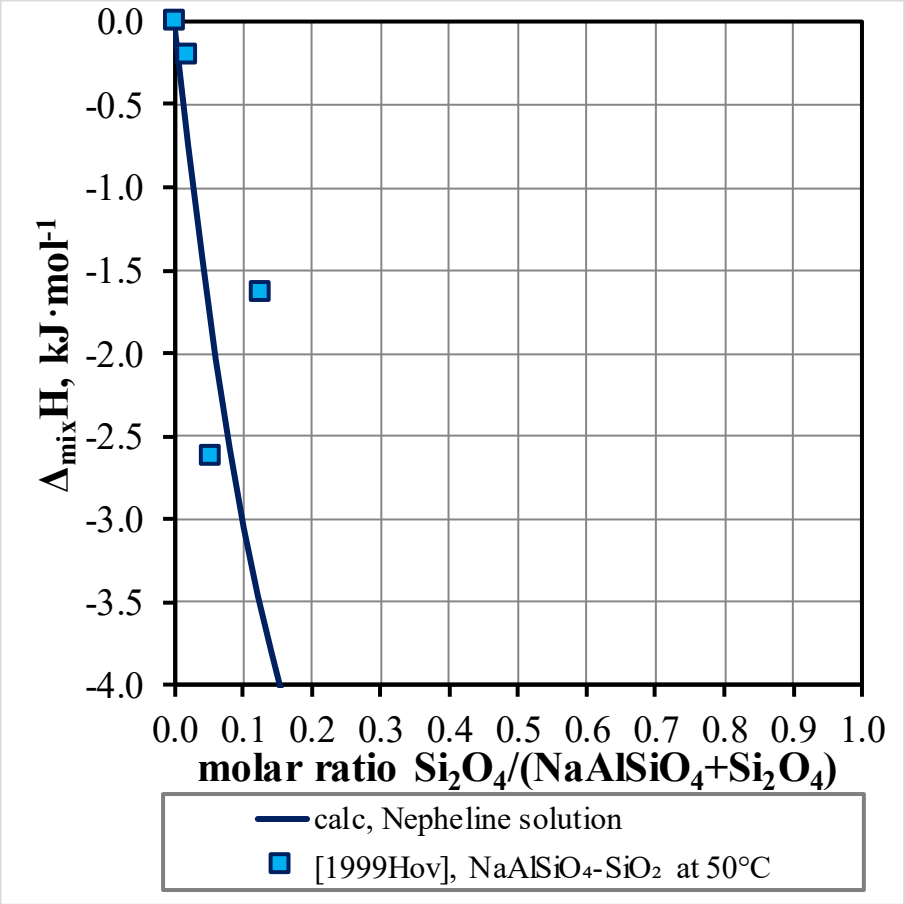

Figure 8.8 The enthalpy of mixing of Nepheline solution in the $NaAlSiO_4$-Si_2O_4 section. Pure nepheline of $NaAlSiO_4$ composition and quartz were used as the end-members for calculation. Experimental points [313] and calculated lines.

Richet et al. [47] measured the enthalpy of fusion of carnegieite using drop calorimetry. Richet and Bottinga [314] calculated the enthalpy of fusion of albite by extrapolating the enthalpy of devitrification to the melting temperature using the heat capacities they determined for the crystalline, glassy and liquid phases. Similar calculations were made based on the data by Navrotsky et al. [315]. The enthalpies of fusion are summarized in Table 8.1.

Table 8.1 The enthalpies of fusion of compounds in the Na_2O-Al_2O_3-SiO_2 system.

Compound	**$\Delta_{fus}H$(calc), kJ·mol^{-1}**	**$\Delta_{fus}H$(exp), kJ·mol^{-1}**
$NaAlSiO_4$ (carnegieite)	42.56 (per mole $NaAlSiO_4$) at 1520°C	43.4±6 at 1526°C [47]
$NaAlSiO_4$ (nepheline)	55.42 (per mole $NaAlSiO_4$) at 1414°C	46.3±2 [315]
$NaAlSi_2O_6$ (jadeite)	44.93 at 498°C (metastable)	59.3±3 [315]
$NaAlSi_3O_8$ (high albite)	57.94 (per mole $NaAlSi_3O_8$) at 1120°C	64.9±1.2 [315]
		64.5±3 [314]

8.3 Activity data

Na_2O activities in ternary liquids and melts are measured in the literature by either EMF or in vapor pressure experiments in a Knudsen cell. Usually, experimental data are presented in the form of temperature dependence for a series of fixed compositions, as it is the most convenient way to perform measurements.

For EMF measurements, a reference melt, usually a binary low-melting composition in the Na_2O-SiO_2 system is employed [222, 228, 316-318]. The main drawback of the method is inability to measure Na_2O activities directly; they need to be recalculated with an assumption that Na_2O activities in the reference melt are known. It is important to recalculate the raw EMF data from the sources using our database and not rely on the activity recalculations performed in the original works.

Vapor pressure measurements with a Knudsen cell and mass-spectrometric registration of particles is an alternative method to measure Na_2O activity [164, 319]. To calculate Na_2O activities with the pure liquid Na_2O as the reference state, the vapor pressure over the reference state needs to be

known. If it was possible (authors published the raw data), activities were recalculated using Na_2O(liq)/(g) properties from *FactSage*.

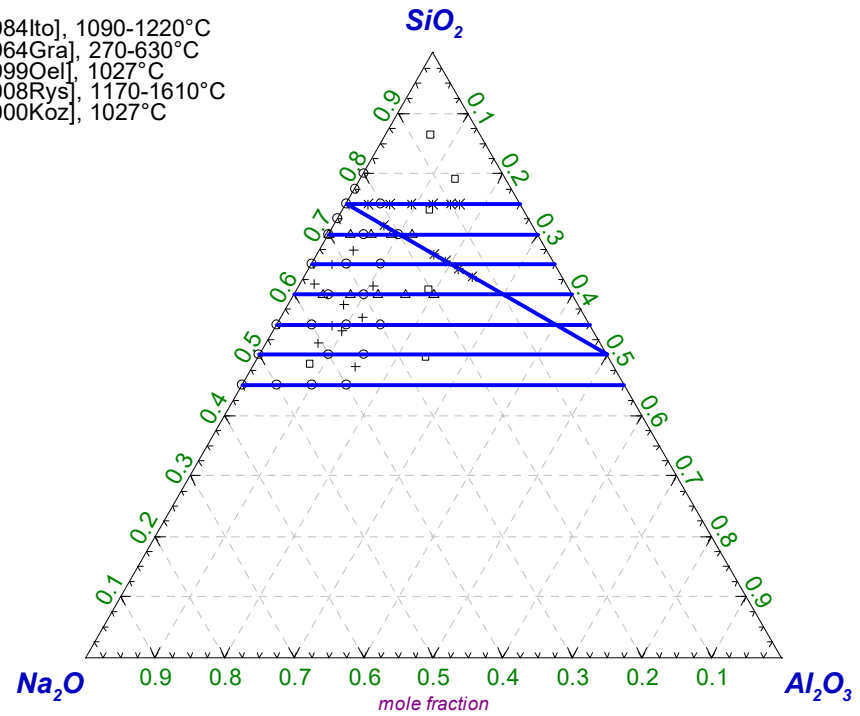

Figure 8.9 Compositions for which Na_2O activity was measured in the Na_2O-Al_2O_3-SiO_2 system [164, 222, 228, 318, 319] and the sections drawn through them.

All compositions for which Na_2O activity was measured are summarized in Figure 8.9. Isothermal activities along different directions in the system are shown in Figure 8.10-Figure 8.12.

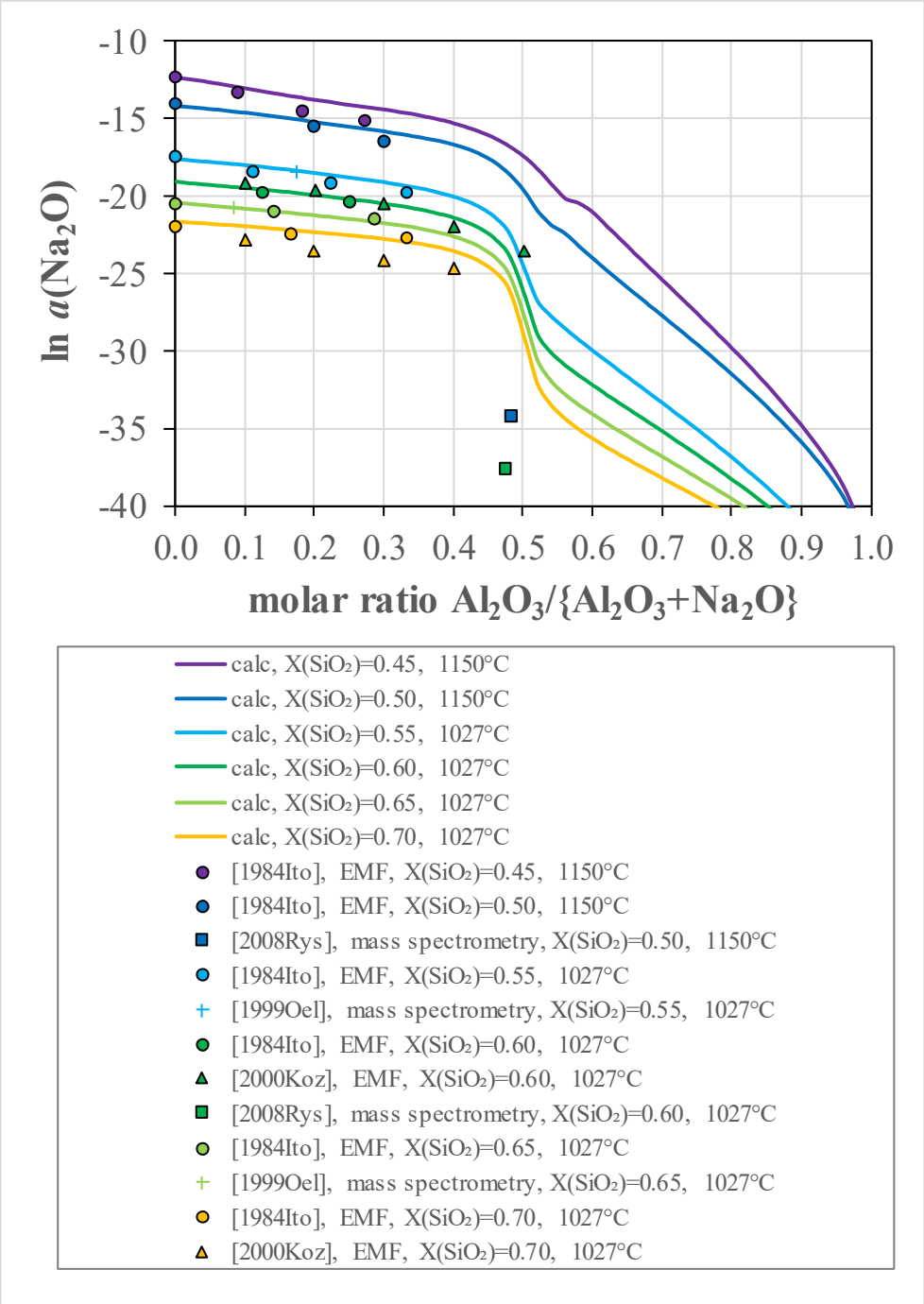

Figure 8.10 Na_2O activity in the Na_2O-Al_2O_3-SiO_2 system along the sections with a constant SiO_2 content and temperature. The reference state is the pure liquid Na_2O. Experimental points [222, 319], points, interpolated and extrapolated from the experimental data [164, 228] and calculated lines.

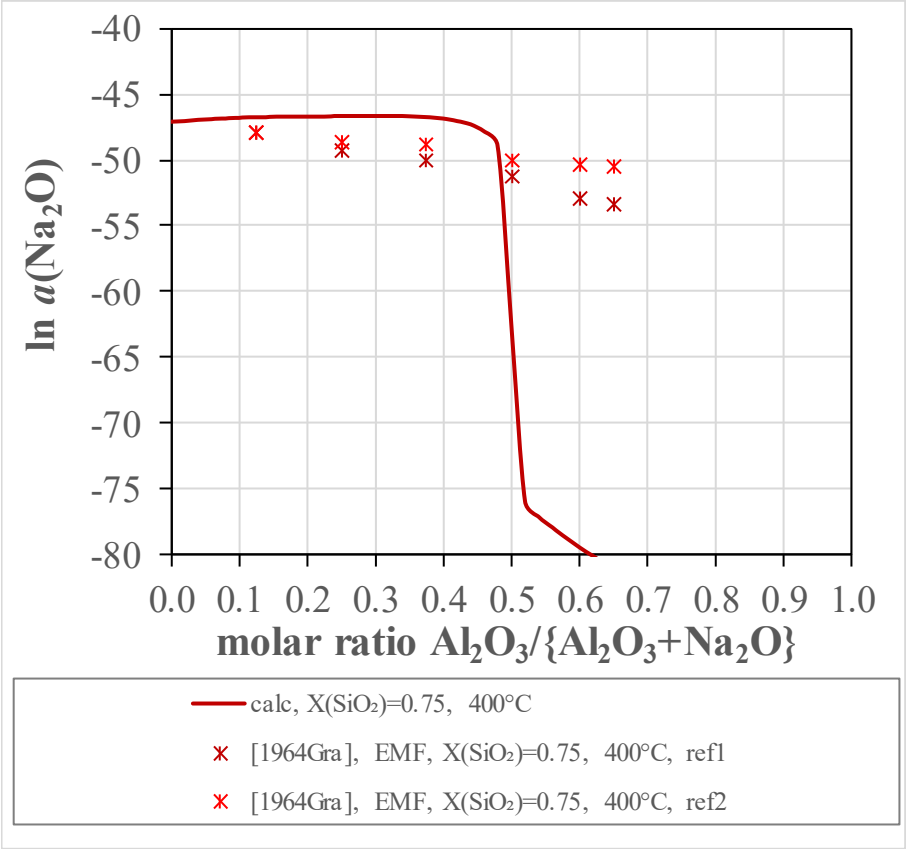

Figure 8.11 Na_2O activity in the Na_2O-Al_2O_3-SiO_2 system along the section with $0.75SiO_2$ at 400°C. The reference state is the pure liquid Na_2O. Points interpolated from experimental data [318] and calculated lines. EMF reference compositions: ref1 is $Na_2O{\cdot}3SiO_2$, ref2 is $x(Na_2O){\cdot}6SiO_2$.

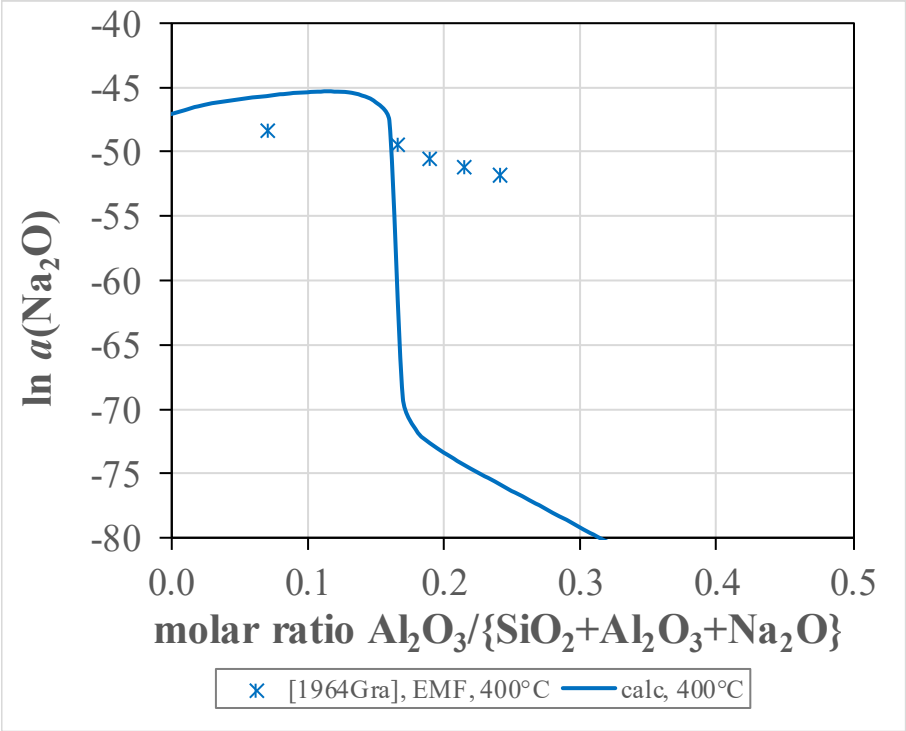

Figure 8.12 Na_2O activity in the $(Na_2O)_{0.25}(SiO_2)_{0.75}$-$(Al_2O_3)_{0.50}(SiO_2)_{0.50}$ section of the Na_2O-Al_2O_3-SiO_2 system at 400°C. The reference state is the pure liquid Na_2O. Points interpolated from the experimental data [318] and calculated lines. EMF reference composition is $Na_2O{\cdot}3SiO_2$.

The composition series in Figure 8.10-Figure 8.12 pass through Na_2O/Al_2O_3 ratio equal to one. Due to the presence of a stable $NaAlO_2$ associate, we can assume that at the silica content of the samples the equilibrium of the reaction $Na_2O+Al_2O_3 = NaAlO_2$ is strongly shifted to the right. That would inevitably cause a significant difference in Na_2O activity in compositions with Na_2O/Al_2O_3 ratio higher and lower than one. The activity drop is clearly seen in Figure 8.10. However, the experimental data by Graham and Rindone [318] fail to show it although the drop must be even more evident at the temperatures they performed the measurements at. The data by Graham and Rindone were considered unreliable and were not used in the optimization.

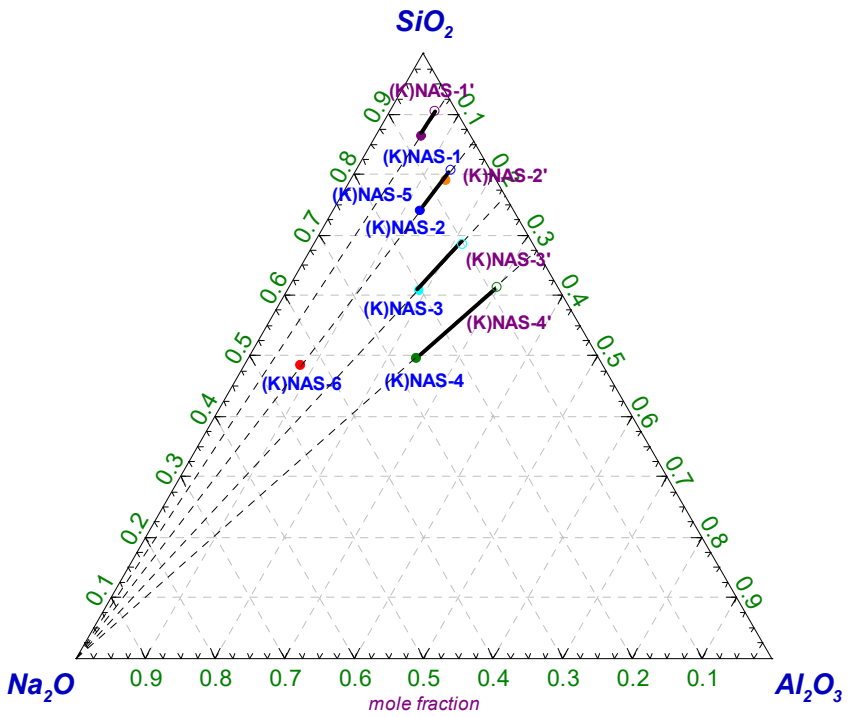

Figure 8.13 Sample compositions from the work of Rys [164]. Thick black lines show possible composition shifts.

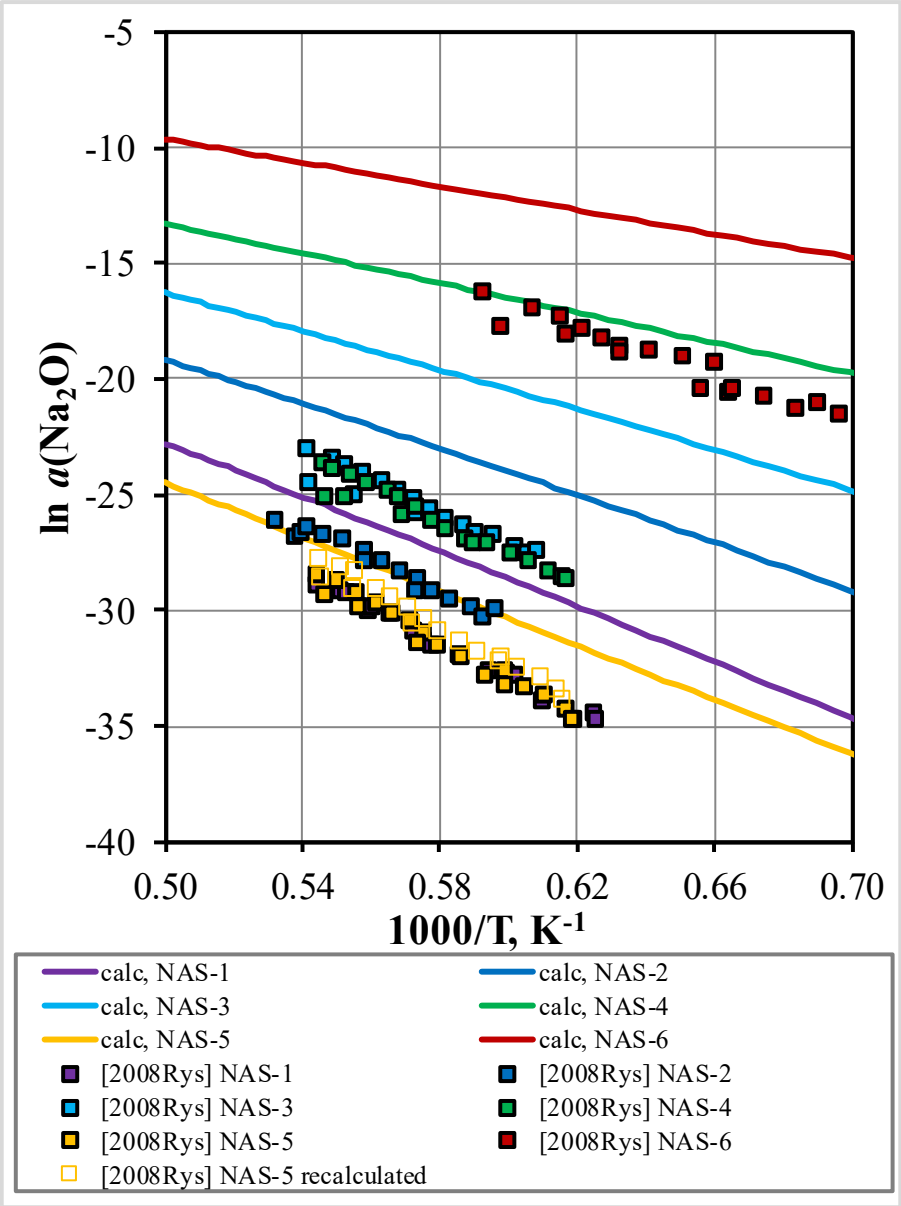

Figure 8.14 Na_2O activities in the Na_2O-Al_2O_3-SiO_2 system at the compositions indicated in Figure 8.13. The reference state is the pure liquid Na_2O. The activity data measured by mass spectrometry were taken from the original source [164] without further recalculations. The data marked with empty symbols were recalculated from the raw *P*(Na) data using *FactSage* properties of Na_2O.

Figure 8.13 shows compositions investigated in the work of Rys [164] (vapor pressure measurements). The corresponding activities are shown in Figure 8.14. Only values at NAS-5 composition (to the right from the $NaAlO_2$-SiO_2 section in Figure 8.13) are adequately predicted.

For the rest of the compositions located in the $NaAlO_2$-SiO_2 section, there is a significant difference between the calculated and measured activities. The influence of the choice of thermodynamic data of Na_2O(liq) is seen from the comparison of the recalculated values at NAS-5 with the original ones (unfortunately, Na pressures were published only for this composition). It is noticeable, but not significant. However, there are enough data in the ternary system, both phase equilibria and the enthalpy of mixing, to fix the properties of the liquid phase. The controversy of the data by Rys is also seen in Figure 8.10.

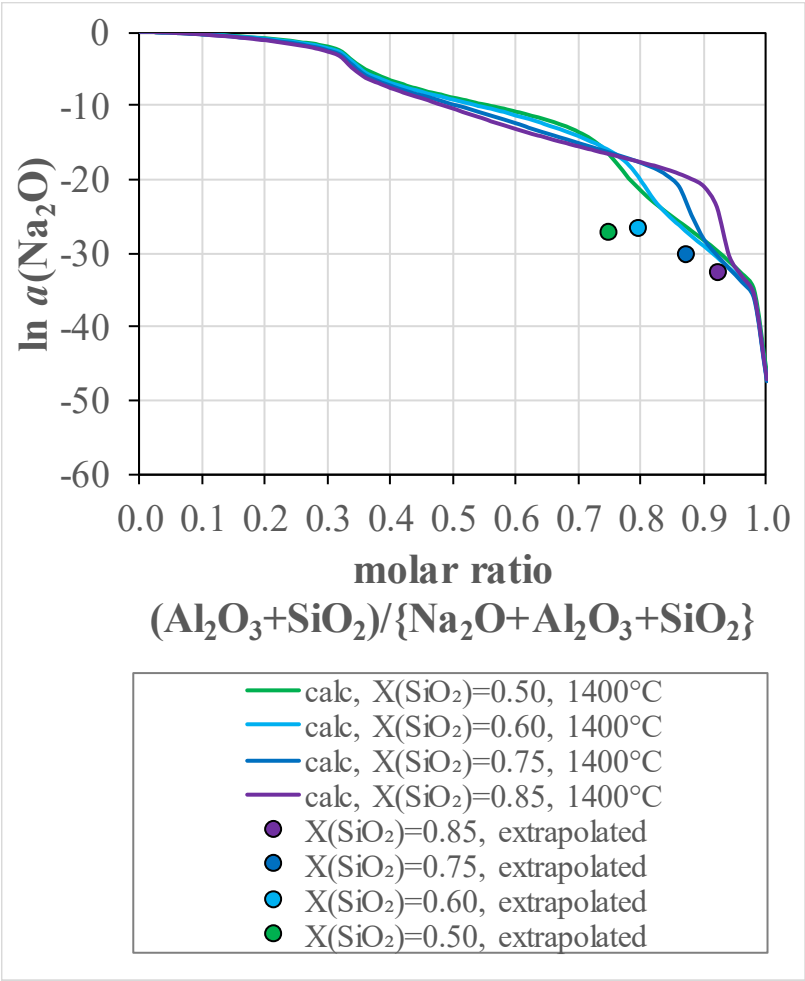

Figure 8.15 Isothermal Na_2O activities along the Na_2O depletion directions for the samples from Rys [164]. The reference state is the pure liquid Na_2O.

A reasonable explanation to the poor fit seems to be a commonly known phenomenon in vaporization studies. If viscous liquids are investigated, the measured vapor pressure does not

correspond to the bulk composition of the sample. Due to diffusion problems the superficial layer of the liquid quickly becomes depleted in the volatile component. This effect is magnified by the short-range ordering occurring across the $NaAlO_2$-SiO_2 section. The prevalent Na_2O-$NaAlO_2$-SiO_2 species assembly transforms into $NaAlO_2$-SiO_2-Al_2O_3 which is accompanied by a Na_2O activity drop. So, relatively small shifts in Na_2O content would cause significant deviations in Na_2O activity (see Figure 8.15).

In the first approximation, Na_2O activities in the left part of the composition plane (Na_2O-$NaAlO_2$-SiO_2 species assembly) are mostly defined by the concentration of free Na_2O not bound into $NaAlO_2$ associate and does not depend on $NaAlO_2$ stability. However, in the right part of the composition plane ($NaAlO_2$-SiO_2-Al_2O_3 species assembly), the Na_2O activity depends only on associate stability. The good fit of NAS-5 activity data shows that $NaAlO_2$ associate properties are well reproduced by the current model.

8.4 Heat capacity and heat content data

Heat capacities of crystalline and vitreous compounds are generally measured by either adiabatic calorimetry (high precision, working range from liquid helium temperatures up to room temperature) or differential scanning calorimetry DSC (lower precision, working range from liquid nitrogen temperatures up to several hundred K). Adiabatic C_P data are especially valuable for calculation of standard entropies, while DSC is required to derive C_P equations at high temperatures. Heat content measurements mostly performed by means of drop calorimetry are also used to derive C_P equations of compounds and ascertain enthalpies of phase transitions.

According to Richet and Bottinga [24], heat capacities of glasses at ambient and high temperatures are almost identical to heat capacities of crystalline solids with the same composition. Glass data were also used wherever it was possible to estimate compound properties.

Adiabatic calorimetry of synthetic carnegieite samples along with glassy $NaAlSiO_4$ was carried out by Richet et al. [47]

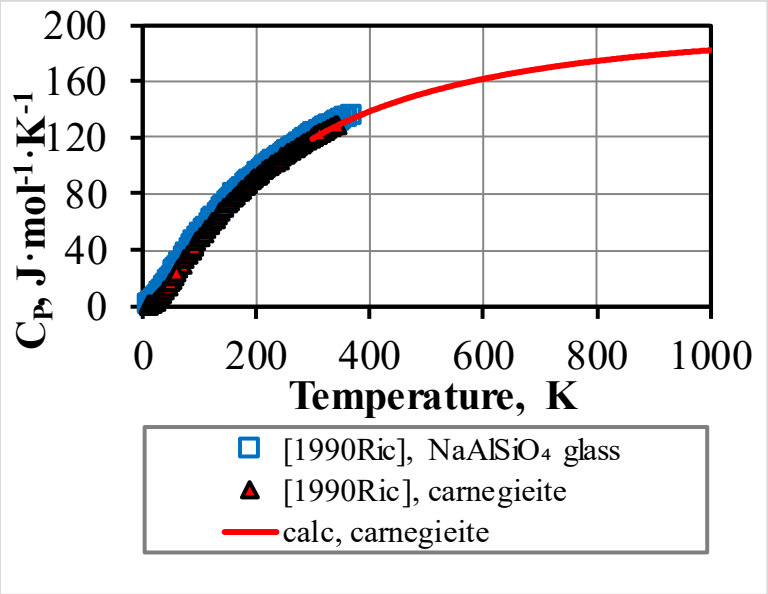

Figure 8.16 The heat capacity of carnegieite. Experimental data [47] and calculated lines.

Adiabatic calorimetry of synthetic nepheline samples was performed by de Ligny [320], Kelley et al. [48]; Henderson and Thomson carried out DSC experiments [294].

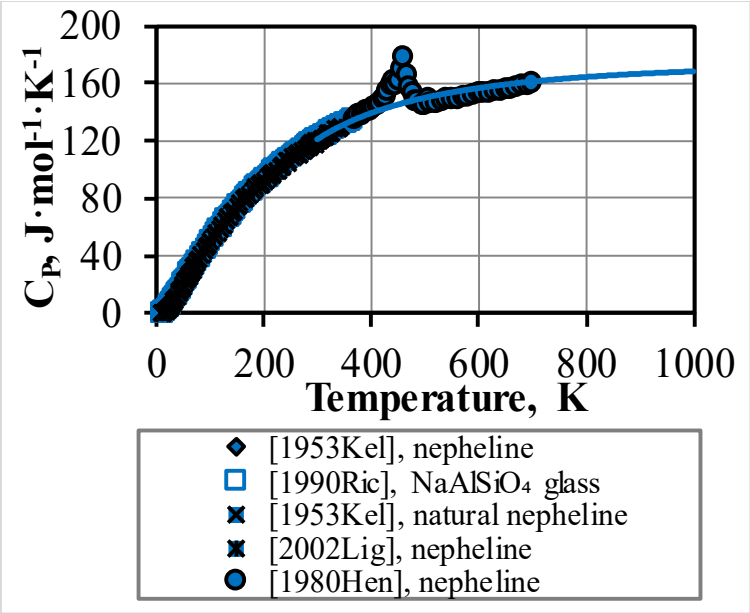

Figure 8.17 The heat capacity of nepheline. Experimental points [47, 48, 294, 320] and calculated lines.

Drop calorimetry of glassy and crystalline carnegieite $NaAlSiO_4$ was performed by Richet and Bottinga [314]. Their data on the crystalline samples indicate a phase transition between the low and high modifications of carnegieite. Similarly, the data by Kelley et al. [48] indicates the phase transitions in nepheline and carnegieite. Stebbins et al. [321] and Richet et al. [47] measured the heat content of glassy and liquid $NaAlSiO_4$.

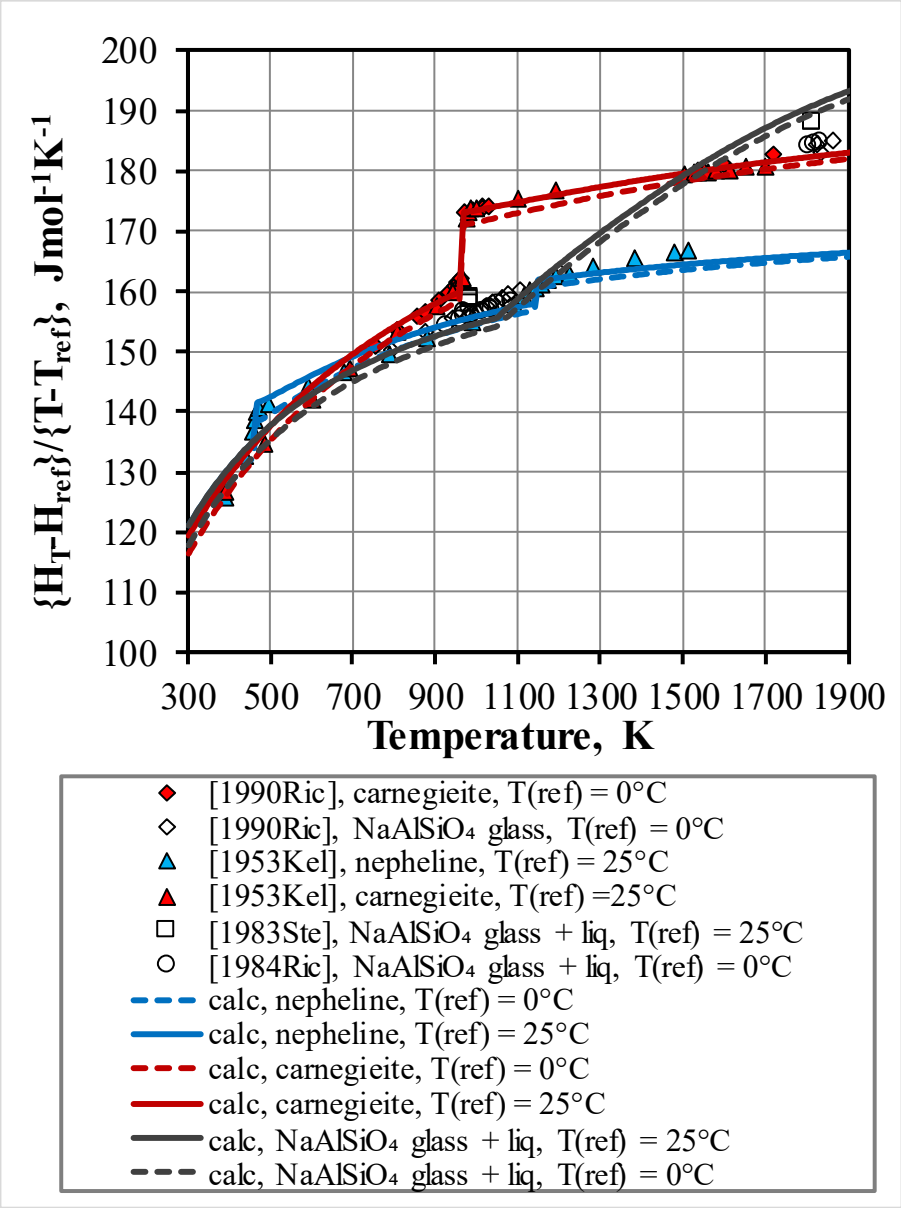

Figure 8.18 The mean heat capacity of nepheline, carnegieite and non-crystalline $NaAlSiO_4$. Experimental points [47, 48, 314, 321] and calculated lines.

Adiabatic calorimetry of crystalline jadeite $NaAlSi_2O_6$ and a glass with the same composition was performed by Richet et al. [26], Hemingway et al. [322], Kelley et al. [48]. There are no anomalies in the heat capacity curve for this compound (Figure 8.19).

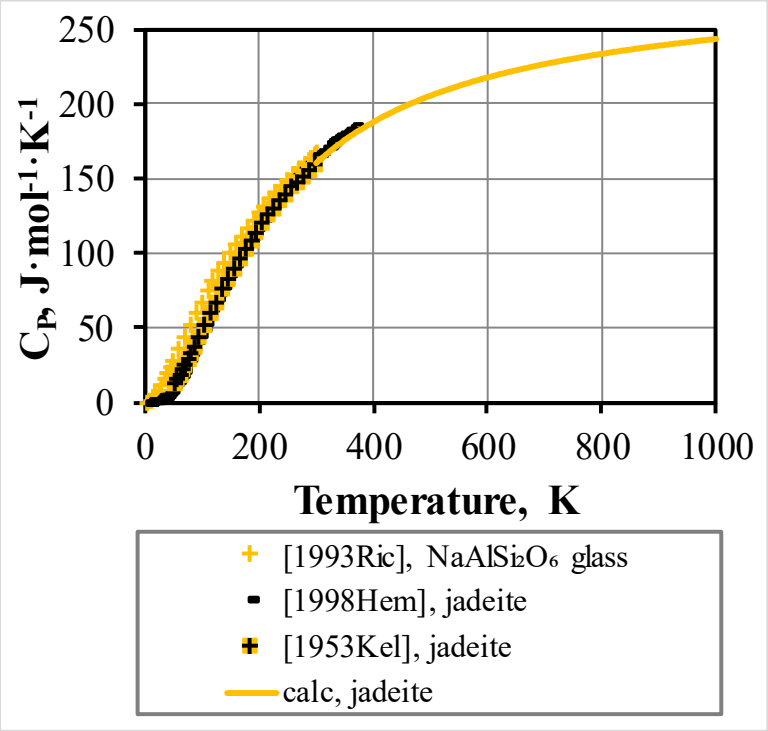

Figure 8.19 The heat capacity of crystalline and vitreous jadeite. Experimental points [26, 48, 322] and calculated lines.

The calculated curves of the mean heat content for crystalline jadeite and a glass of the same composition are shown in Figure 8.20 together with the data by Richet and Bottinga on vitreous $NaAlSi_2O_6$. [314]. Up to the glass transition point, the calculated curves are identical and after the glass transition point, the curves start to diverge due to a higher heat capacity of the liquid. The heat capacity of the liquid was taken from *FactSage*.

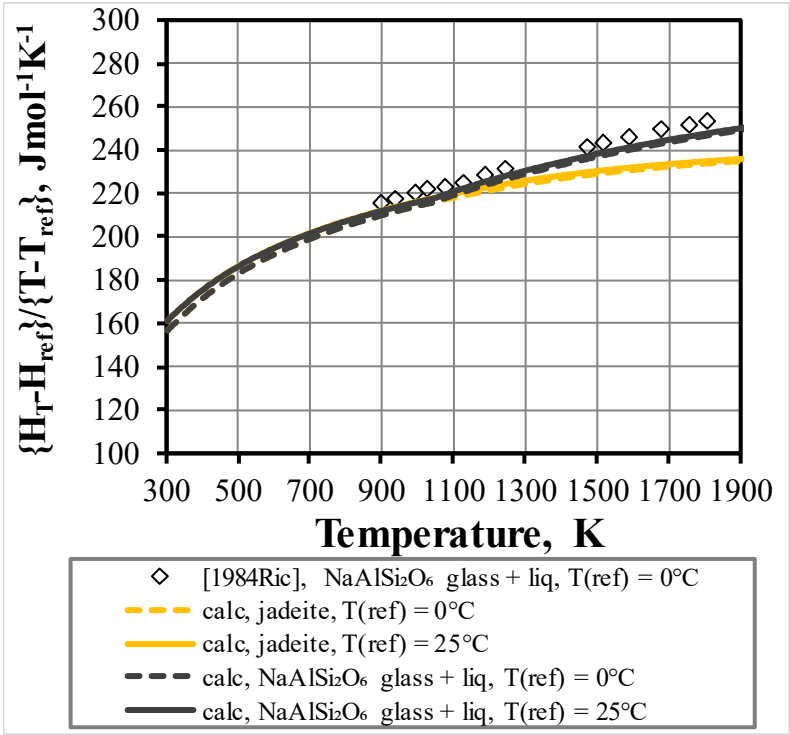

Figure 8.20 The mean heat capacity of crystalline and vitreous jadeite. Experimental points [314] and calculated lines.

Adiabatic calorimetry of albite was carried out by Openshaw et al. [323], Kelley et al. [48], Haselton et al. [324]. DSC experiments on albite were performed by Salje et al. [325], Hemingway et al. [326], Krupka et al. [327]. Adiabatic calorimetry of albite glasses was performed by Robie et al. [328]. All these data are summarized in Figure 8.21; the data do not show any anomalies in the heat capacity curve.

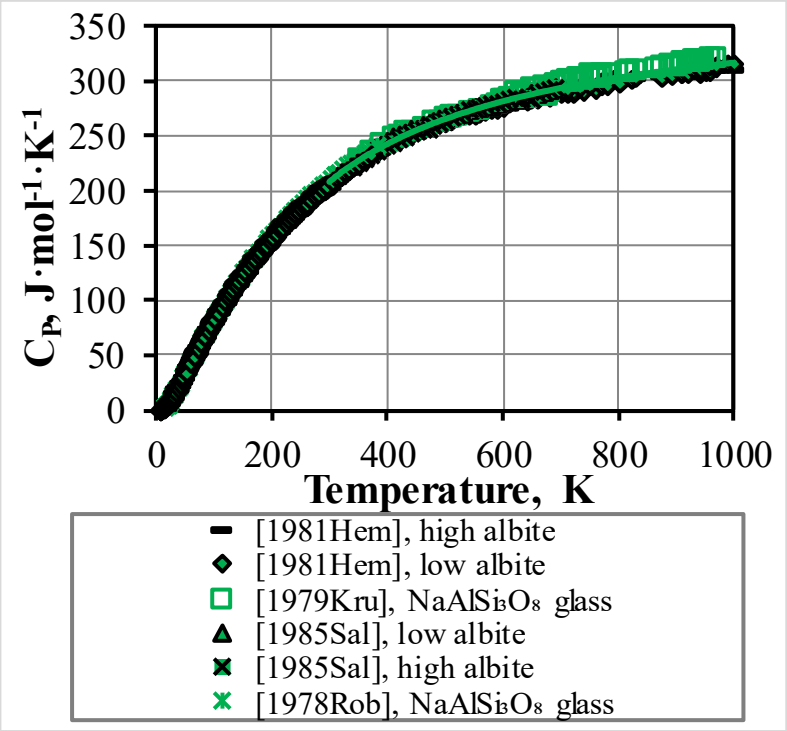

Figure 8.21 The heat capacity of low, high and vitreous albite. Experimental points [48, 323-328] and calculated lines.

Mean heat content data on vitreous/liquid samples of $NaAlSi_3O_8$ are shown in Figure 8.22 [314, 329, 330]. The calculated curves for the crystalline albite and glass/liquid are shown alongside. The calculated curves start to diverge at the glass transition point, because the heat capacity of glass is approximated as the heat capacity of a crystalline solid of the same composition and the heat capacities of liquid are generally higher.

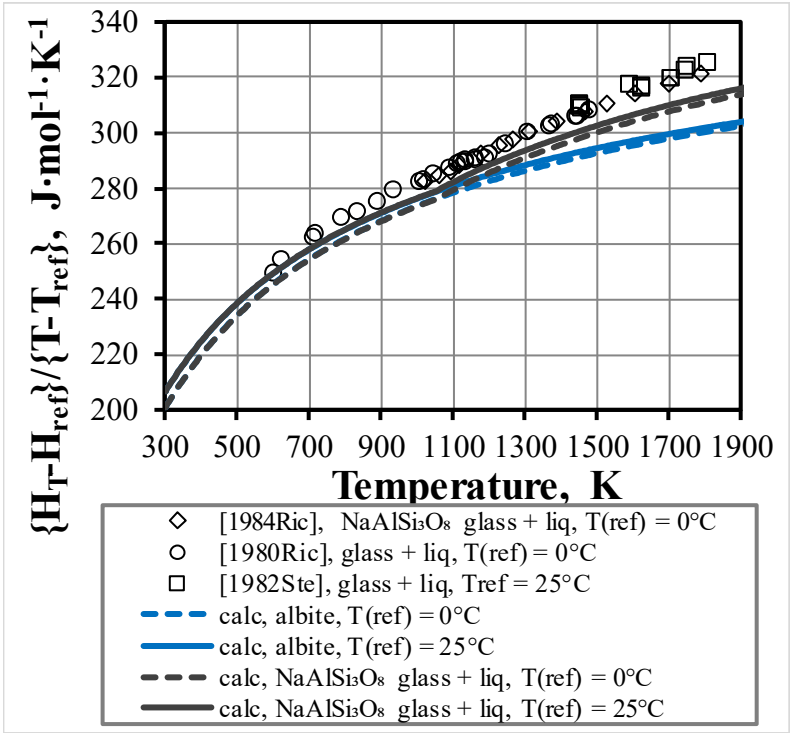

Figure 8.22 The mean heat capacity of crystalline and vitreous albite. Experimental points [314, 329, 330] and calculated lines.

8.5 Optimization results

The Na_2O-SiO_2 and Na_2O-Al_2O_3 binary subsystems were optimized in this work (Chapter 6 and Chapter 7, correspondingly); an optimization of the Al_2O_3-SiO_2 system by Eriksson and Pelton [123] was adopted with a change of Mullite model.

The way the Na_2O-Al_2O_3-SiO_2 system was optimized was influenced not only by the data in the ternary system but also by higher order systems, in particular, the Na_2O-CaO-Al_2O_3-SiO_2 system. Different exception rules for species grouping can lead to similar fits in the ternary but behave differently in the quaternary system. By trial and error, it was found that the exceptions listed in Table A.8 are the most suited. The enthalpies of formation of nepheline and feldspar were chosen to be more negative than the average experimental values (but still within the range of the experimental data) as it gives a better description of the higher order systems.

The presence of an associate species turns the ternary system into a quaternary from the point of view of interactions. Given the assumption that $NaAlO_2$ associate is quite stable, the whole

composition region can be roughly divided into parts of prevalent content of the following species: Na-NaAl-Si//O region ($X(SiO_2 > 50$ mol%, $Na_2O/Al_2O_3 > 1$)), NaAl-Al-Si//O region ($X(SiO_2 > 50$ mol% , $Na_2O/Al_2O_3 < 1$)) and the mixed Na-NaAl-Al-Si//O in the SiO_2-poor area. This can serve as an indicator to what kind of excess parameters to use in order to reproduce the data in the corresponding regions. $\Delta q^{\circ}_{\mathrm{NaAl,Si}}$ interaction and its extensions are used to fit the data along the $NaAlO_2$-SiO_2 join, including the liquidus and the enthalpy of mixing. Ternary interactions among Na-NaAl-Si and Al-NaAl-Si serve to reproduce the liquidus data to the left and to the right from the $NaAlO_2$-SiO_2 join (see Figure 8.1-Figure 8.2). Two parameters of Na-Al-Si interaction act mostly at $X(SiO_2) < 50$ mol% and influence the sodium aluminate liquidus.

Carnegieite and Nepheline parameters were set according to the solubility and calorimetry data in the $NaAlO_2$-SiO_2 system. For sodium aluminate solid solutions only the liquidus data in the $NaAlO_2$-SiO_2 and the Na_2SiO_3-$NaAlO_2$ sections are available. It was assumed that the interaction parameters in the low and high modifications would not differ much and as there are no data on the dependence of the transition temperature vs the composition, these were assumed equal.

The optimized parameters are summarized in Table A.7 and Table A.8.

CHAPTER 9 OPTIMIZATION OF THE K_2O-SiO_2 SYSTEM

9.1 Phase diagram

The available phase diagram data in the K_2O-SiO_2 are limited to the compositions with more than 50 mol% of SiO_2. The most available source of potassium oxide for the sample preparation is potassium carbonate. It is known that in the Na_2O-SiO_2 system, the compositions richer in Na_2O than Na_2SiO_3 need either NaOH (from Na_2SiO_3 to $Na_6Si_2O_7$) or the pure Na_2O as a source of alkali oxide to form truly binary compositions. From the chemical point of view, K_2O is an even stronger basic oxide than Na_2O. It means that K_2O has a higher affinity for CO_2 and it is harder to decompose K_2CO_3 than Na_2CO_3. If silica can substitute CO_2 from Na_2CO_3 only up to the metasilicate level and no Na_4SiO_4 forms (Section 6.2), K_2CO_3 and silica do not form orthosilicate either.

and silica can substitute CO_2 from K_2CO_3 only up to the metasilicate level and is not strong enough to form the orthosilicate by substituting CO_2 from K_2CO_3.

An early work on phase relations in the K_2O-SiO_2 system is a study by Kracek [147]. They reported three main potassium silicates: metasilicate K_2SiO_3, disilicate $K_2Si_2O_5$ and tetrasilicate $K_2Si_4O_9$. The liquidus was studied by quenching. To prevent an early crystallization of samples between K_2SiO_3 and $K_2Si_2O_5$ compositions, they had to be quenched in mercury; the use of mercury is explained by its high thermal conductivity and very fast cooling rates However, the crystallization properties change drastically with the composition and tetrasilicate melts required preliminary seeding to form crystals. Disilicate $K_2Si_2O_5$ undergoes a reversible transition at 590-596°C. Later, the same authors measured the same system to introduce corrections to their previous work, especially in the area of $K_2Si_2O_5$ [149]. The $K_2Si_2O_5$ inversion was confirmed, the new value of the transition temperature is 592°C with the heat of inversion of 1.07±0.27 $kJ \cdot mol^{-1}$.

DTA of crystalline disilicate samples was performed by Boivin et al. [157], the reported melting point of $K_2Si_2O_5$ is 1038°C, the enthalpy of fusion is 31.3±3 $kJ \cdot mol^{-1}$. The inversion was not observed but it can be probably explained by its slow kinetics.

The work by Goranson and Kracek [331] was specifically aimed at investigation of $K_2Si_4O_9$ phase relations under normal and elevated pressures. The melting point under the normal pressure is 765°C with the heat of melting of 48.93±9.6 $kJ \cdot mol^{-1}$. The compound undergoes an inversion at

592°C with the heat of inversion of 3.2±0.43 kJ·mol^{-1}. The inversion of tetrasilicate was also confirmed by Kracek et al. [149].

The only authors who used the pure potassium oxide as a precursor in sample preparation instead of K_2CO_3, are Bon and Gleitzer [332]. However, they performed only a phase analysis of the samples and no phase diagram points are available. They observed $K_6Si_2O_7$ compound. The same compound was obtained and characterized by means of single-crystal X-ray analysis by Schartau and Hoppe [333].

Bockris et al. [148] performed viscosity measurements in the binary system but they also report liquidus points. It remains unclear if they were measured in the work or were taken from elsewhere.

The phase diagram equilibria at compositions with less than 50 mol% SiO_2 are reported by Meshalkin and Kaplun [334]. However, the method of sample preparation and the initial reagents were not described. The liquidus was measured by oscillation method combined with thermal analysis. The melting points and liquidus are reported for the following compounds: K_4SiO_4, $K_{10}Si_3O_{11}$, $K_6Si_2O_7$, $K_8Si_3O_{10}$, K_2SiO_3. The melting point of K_2SiO_3 coincides with that measured in other sources but the liquidus is too steep.

Stypula et al. [335] reported melting points for several compounds in the K_2O-SiO_2 system but there is no mention of the source of the data. Especially it concerns K_4SiO_4 compound as there is lack of reliable data on it.

A few liquidus points can be derived from the slope breaks of K pressure over melts measured with Knudsen cell mass spectrometry by Chastel and Rogez [336].

Kim [18] reported DTA measurements of the eutectic K_4SiO_4-K_2SiO_3; however, the procedure of sample preparation does not allow to assume that a true binary composition was obtained. The samples were prepared using K_2CO_3 and heated in air. A calculation made with the published thermodynamic properties of K_4SiO_4 confirms that orthosilicate does not form under the described conditions; in fact, we believe that the measured eutectic belonged to the K_2SiO_3-K_2CO_3 system.

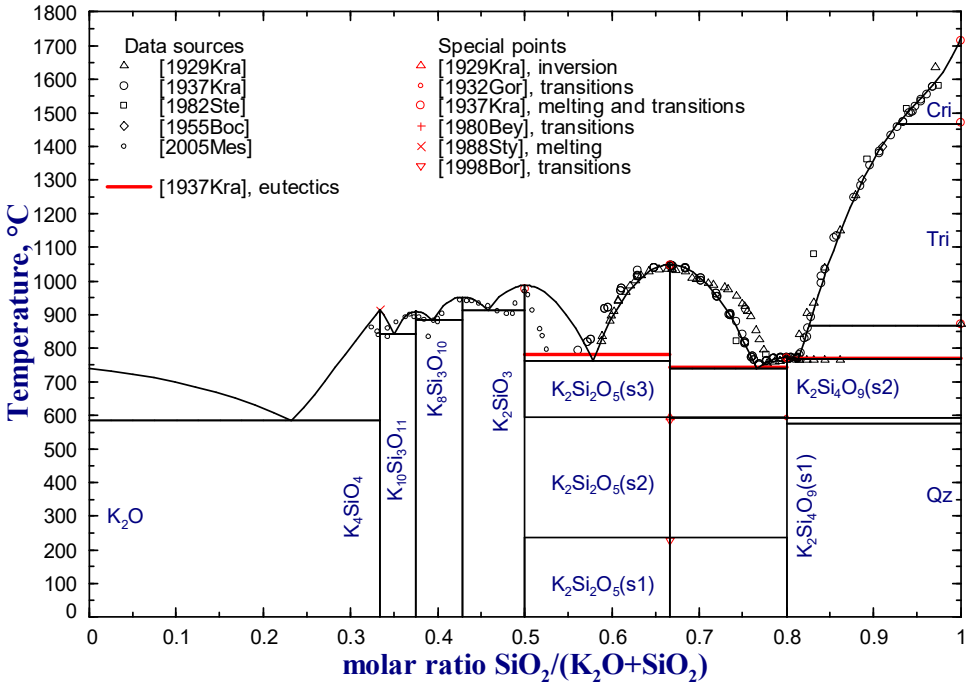

Figure 9.1 Phase diagram of the K_2O-SiO_2 system. Experimental points [147-149, 331, 334, 335, 337-339] and calculated lines.

The available experimental data on phase equilibria in the K_2O-SiO_2 are summarized in Figure 9.1.

There is a metastable miscibility gap in the SiO_2-rich area of the K_2O-SiO_2 system, following the trend of the Li_2O-SiO_2 and Na_2O-SiO_2 systems. However, it is situated below the glass transition temperature and is very hard to measure. In the work of Moriya et al. [174], the miscibility gap in the K_2O-SiO_2 binary system was extrapolated from the data on mixed alkali systems. Kawamoto and Tomozawa [340] predicted the position of the miscibility gap based on the data in the Na_2O-SiO_2 system and critical temperatures of a few ternary compositions. There is a significant discrepancy between the two sources (Figure 9.2).

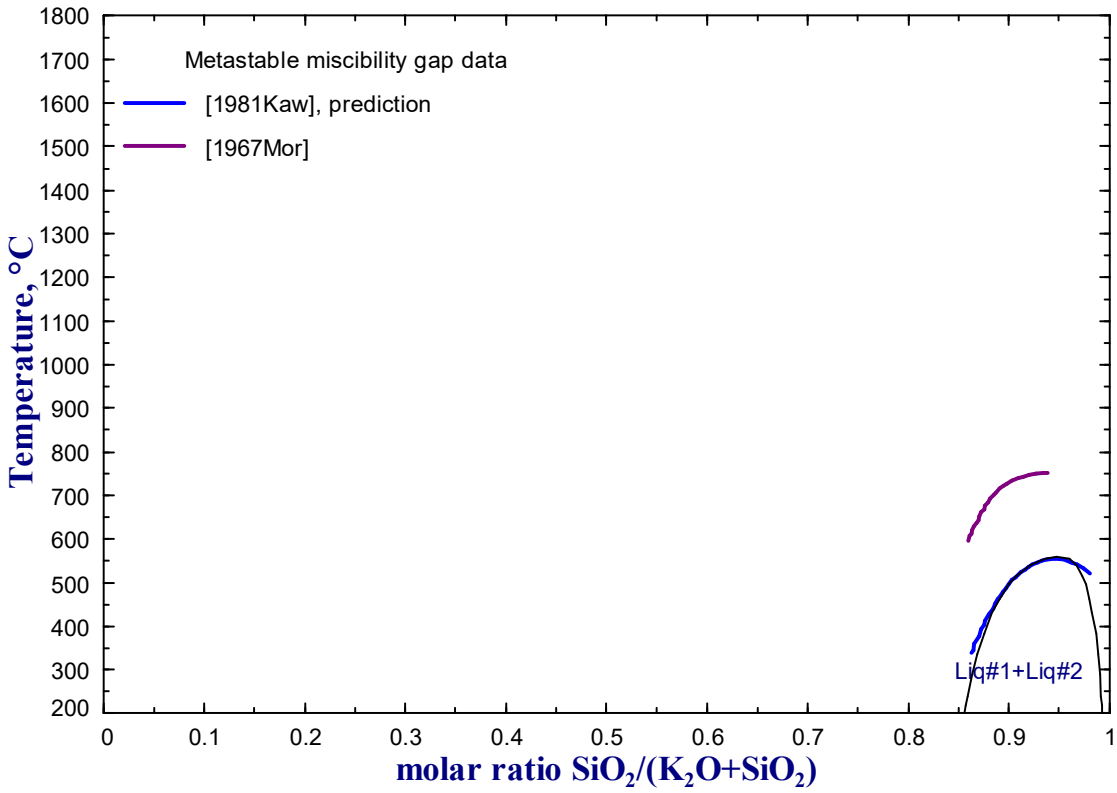

Figure 9.2 Metastable miscibility gap in the K_2O-SiO_2 system. Experimental data [174, 340] and the calculated line.

9.2 Calorimetry data

Heats of solution of K_2O-SiO_2 glasses and solids were determined in 5% HF [185], in 39% HF [198] (both at room temperature), and in 20% HF at 74.7°C [158]. Morey [158] gives the heats of solution of pure crystalline Li_2O, Na_2O, K_2O calculated indirectly using chloride and sulfate schemes.

Heats of solution of glasses in 2PbO-B_2O_3 solvent at 603°C were determined by Rogez and Mathieu [200]. All the samples were liquid at the experimental temperature, the dissolution kinetics was slowed down by aggregation of fine glass particles upon heating. No recrystallization was observed for potassium silicate samples. The uncertainty of the measurements was estimated to be ±1 kJ/mol. Heats of solution of crystalline $K_2Si_2O_5$ and $K_2Si_4O_9$ were measured under the same conditions. Heats of solution of crystalline and glassy $K_2Si_4O_9$ in 2PbO-B_2O_3 at 700°C measured by Geisinger et al. [341] allowed to establish the heat of fusion of tetrasilicate equal to 42.9 kJ·mol^{-}

[1]. One point belonging to the K_2O-SiO_2 system was measured by Ahoussou and Rogez [342] who measured the enthalpy of solution of $(K_2O)_{0.2}(B_2O_3\text{-}SiO_2)_{0.8}$ glasses in $2PbO\text{-}B_2O_3$ melt at 700°C.

The information used in this work to recalculate the enthalpy of solution data into the enthalpy of mixing/the enthalpy of formation is summarized in Table 9.1.

Table 9.1 Heats of solution of crystalline end-members in the K_2O-SiO_2 system in common solvents.

End-member	**Solvent**	**$\Delta_{soln}H$, kJ·mol^{-1}**
SiO_2(qz)	20% HF, 74.7°C	-139.33 [158]
SiO_2(qz)	$2PbO\cdot B_2O_3$, 603°C	-8.53, recalculated from the data on glassy SiO_2 from [200]
K_2O(cr)	20% HF, 74.7°C	-461.79 [158]
K_2O(cr)	$2PbO\cdot B_2O_3$, 603°C	-266.23 [195]

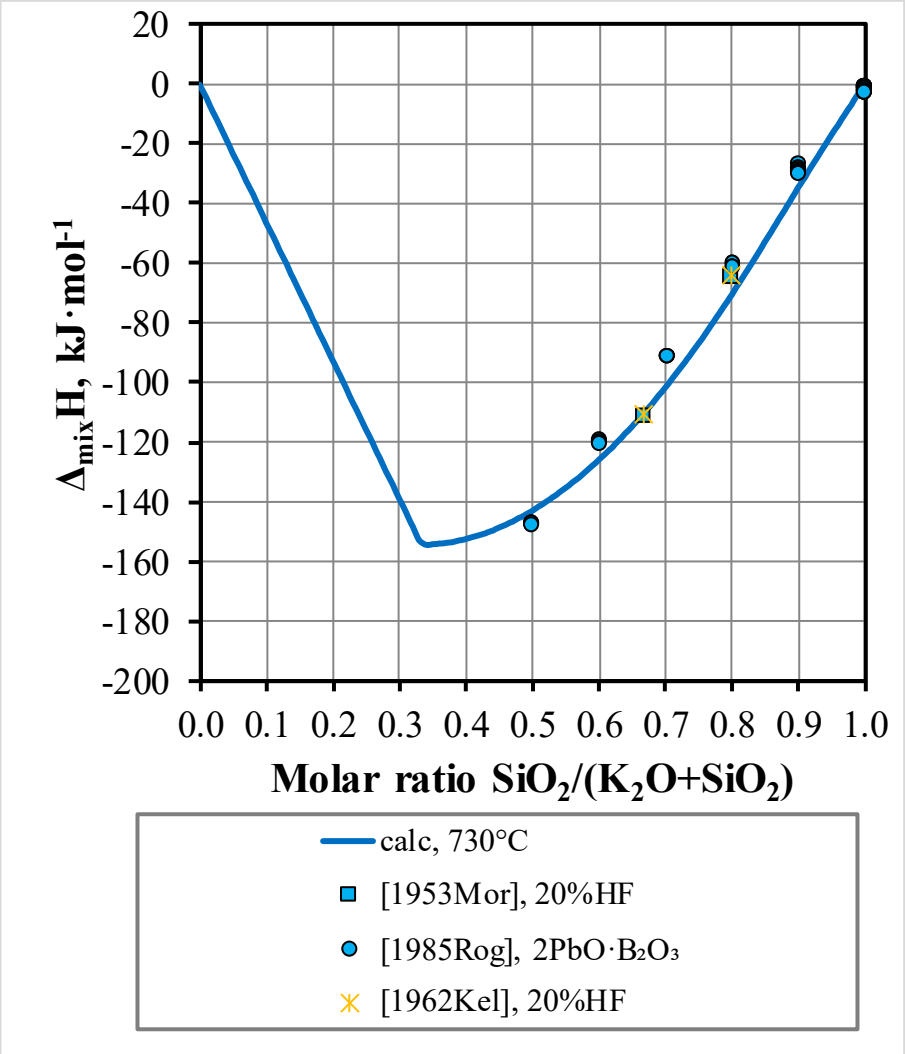

Figure 9.3 The enthalpy of mixing of the liquid phase in the K_2O-SiO_2 system. Experimental points [158, 200, 305] and calculated lines.

The data on the enthalpy of mixing of the liquid recalculated from the solution calorimetry data using the auxiliary data in Table 9.1 are presented in Figure 9.3.

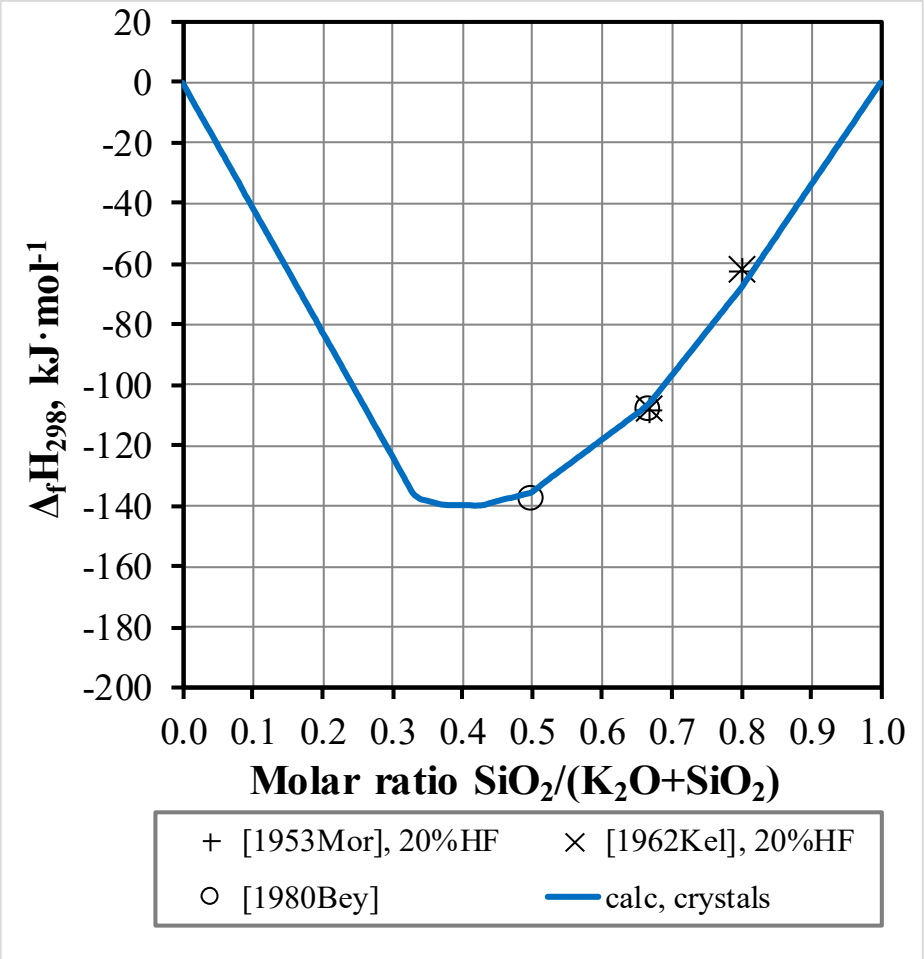

Figure 9.4 The enthalpy of formation from oxides of crystalline solids in the K_2O-SiO_2 system. Experimental points [158, 305, 338] and the calculated line.

The solution calorimetry data for crystalline solids were recalculated into the enthalpy of formation from oxides (see Figure 9.4).

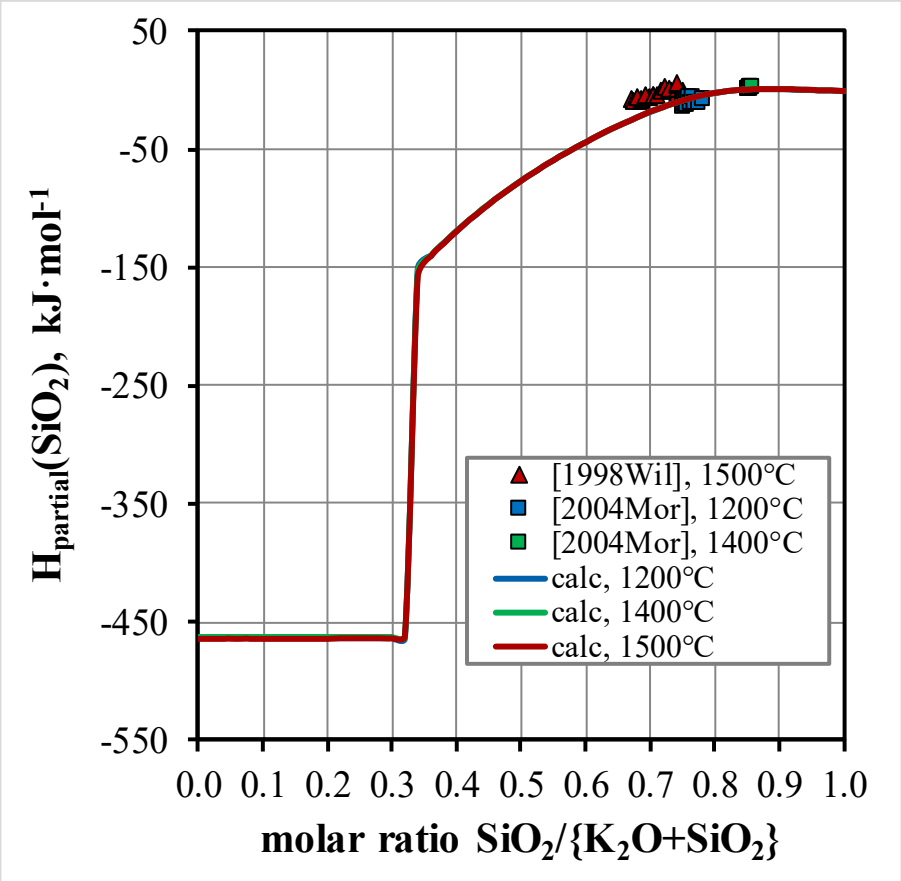

Figure 9.5 The partial enthalpy of mixing of SiO_2 in the K_2O-SiO_2 system. Experimental points [205, 343] and calculated lines.

Partial molar enthalpies of SiO_2 were directly measured for K_2O-SiO_2 melts at 1200° and 1400°C by drop-solution calorimetry (as well as for other alkali systems) by Morishita et al. [205]. The samples were taken at room temperature and dropped into a preheated melt. The total heat effect comprises the heat content, the enthalpy of fusion and the partial enthalpy of dissolution. The total errors in the drop enthalpy were 3% and 5% for 1200° and 1400°C. Partial molar enthalpies of SiO_2 at 1500°C were measured by Wilding and Navrotsky [343]. To recalculate the raw data, the values of the heat content of quartz and the heat of fusion of SiO_2 of 105.6±5.4 kJ·mol^{-1} and 16.07 kJ·mol^{-1} were taken from *FactSage*, correspondingly. The experimental data on the partial enthalpy of SiO_2 are summarized in Figure 9.5.

The enthalpies of fusion were calculated from the drop calorimetry data by Richet and Bottinga [24] for $K_2Si_2O_5$ and K_2SiO_3 (see Table 9.2). Boivin et al. performed DSC of potassium disilicate

and measured the heat of melting by integration of heating curves [157]; the same was done for tetrasilicate by Goranson and Kracek [331]. The enthalpy of fusion of $K_2Si_4O_9$ was extrapolated from the solution data by Geisinger et al. [341]. Spencer [344] gives a compilation of thermodynamic data on silicates.

Table 9.2 Enthalpies of fusion of stoichiometric compounds in the K_2O-SiO_2 system.

Compound	**$\Delta_{fus}H°$, kJ·mol^{-1}, experimental**	**$\Delta_{fus}H°$, kJ·mol^{-1}, calculated**
K_2SiO_3	19.6±4.0 [24] 48.1 [344]	28.22
$K_2Si_2O_5$	31.3±3 [157] 32.0±4.0 [24] 41.0 [344]	47.30
$K_2Si_4O_9$	48.93±9.6 [331] 42.9 [341]	58.17

The value of the enthalpy of fusion of K_2SiO_3 is well within the range of the values reported in the literature. The calculated values of the enthalpy of fusion of $K_2Si_2O_5$ and $K_2Si_4O_9$ are higher then the experimental values. We explain it using excess parameters with a strong temperature dependence in the liquid phase (see section 6.6). In turn, they are required to reproduce SiO_2 liquidus in a very wide range of temperatures. *T*-dependent terms of the interaction parameters deviate the entropy of mixing in the composition range from around disilicate to tridymite liquidus. We suppose that if a correct extrapolation of the heat capacity of liquid SiO_2 end-member were used, these measures could have been avoided and the enthalpy of fusion of $K_2Si_2O_5$ and $K_2Si_4O_9$ would be reproduced better. For a detailed explanation on the heat capacity of the liquid end-members, see section 2.2.

9.3 Activity data

A series of works was dedicated to measuring activities of K_2O in potassium silicate samples. A large group of studies deals with EMF measurements between glasses of different compositions. The details of each EMF experiment differ, but the idea is to measure the difference of the chemical potential of K_2O between the investigated sample and a reference sample. As a reference, a fixed composition in the same system is used, preferably with a lowest possible melting point. In order to use the data, the activities of K_2O in the reference sample need to be known. EMF was measured by Frohberg et al. [232] ($0.214K_2O·0.786SiO_2$ used as the reference), Kozhina [345]

($0.127K_2O \cdot 0.873SiO_2$ as the reference), Ravaine et al. [220] and Smith and Rindone [226] ($0.25K_2O \cdot 0.75SiO_2$ as the reference).

Another large group of studies is related to Knudsen effusion method with a coupled mass spectrometer. It has been shown [346] that only K_2O oxide evaporates from melts. In the presence of an inert crucible material, such as platinum, K_2O predominantly decomposes in the gas phase according to the reaction:

$$K_2O(\text{silicate, liq}) \leftrightarrow 2K(g) + 0.5O_2(g) \tag{106}$$

Activities of K_2O in liquid silicate melt can be calculated using the following relation:

$$a(K_2O) = a(K_2O)_{ref} \frac{(P_K)^2 (P_{O_2})^{1/2}}{(P_K^{ref})^2 (P_{O_2}^{ref})^{1/2}} \tag{107}$$

However, a more careful study of the gaseous species present over K_2O-SiO_2 melts by Zaitsev et al. [347] has shown that a noticeable amount of K_2O as well as other alkali oxides can decompose according to the mechanism:

$$2K_2O(\text{silicate, liq}) \leftrightarrow 3K(g) + KO_2(g) \tag{108}$$

This can introduce uncertainly to the interpretation of MS experimental data.

In the case where a non-inert crucible material is employed (Nb, Ta, Mo, Ni, Al), volatile metal oxides form and contribute to the total pressure [347]:

$$n\text{K2O(silicate,liq)} + \text{M(cr)} \leftrightarrow \text{MO}_n(g) + 2n\text{K}(g) \tag{109}$$

There is a series of works related to weight loss measurements in K_2O-SiO_2 melts. Although weight loss is a kinetic measure of the system, Callow [348] states that all other conditions being equal, the initial rate of weight loss is directly proportional to the vapor pressure.

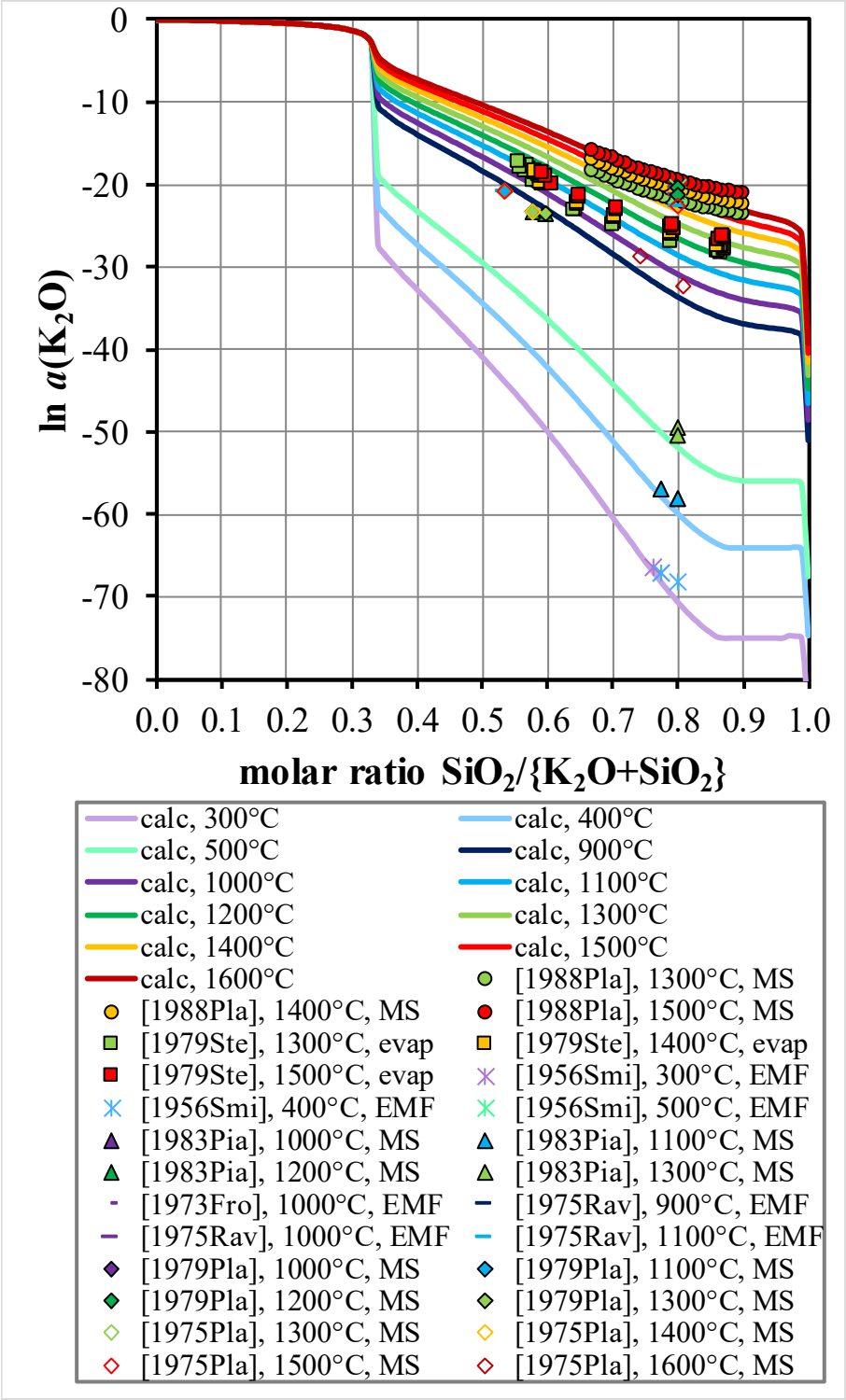

Figure 9.6 Isothermal K_2O activities in the liquid phase of the K_2O-SiO_2 system. The reference state is the pure liquid K_2O. Experimental points [220, 226, 231, 232, 337, 346, 349, 350] (mass spectrometry, EMF and evaporation studies) and calculated lines.

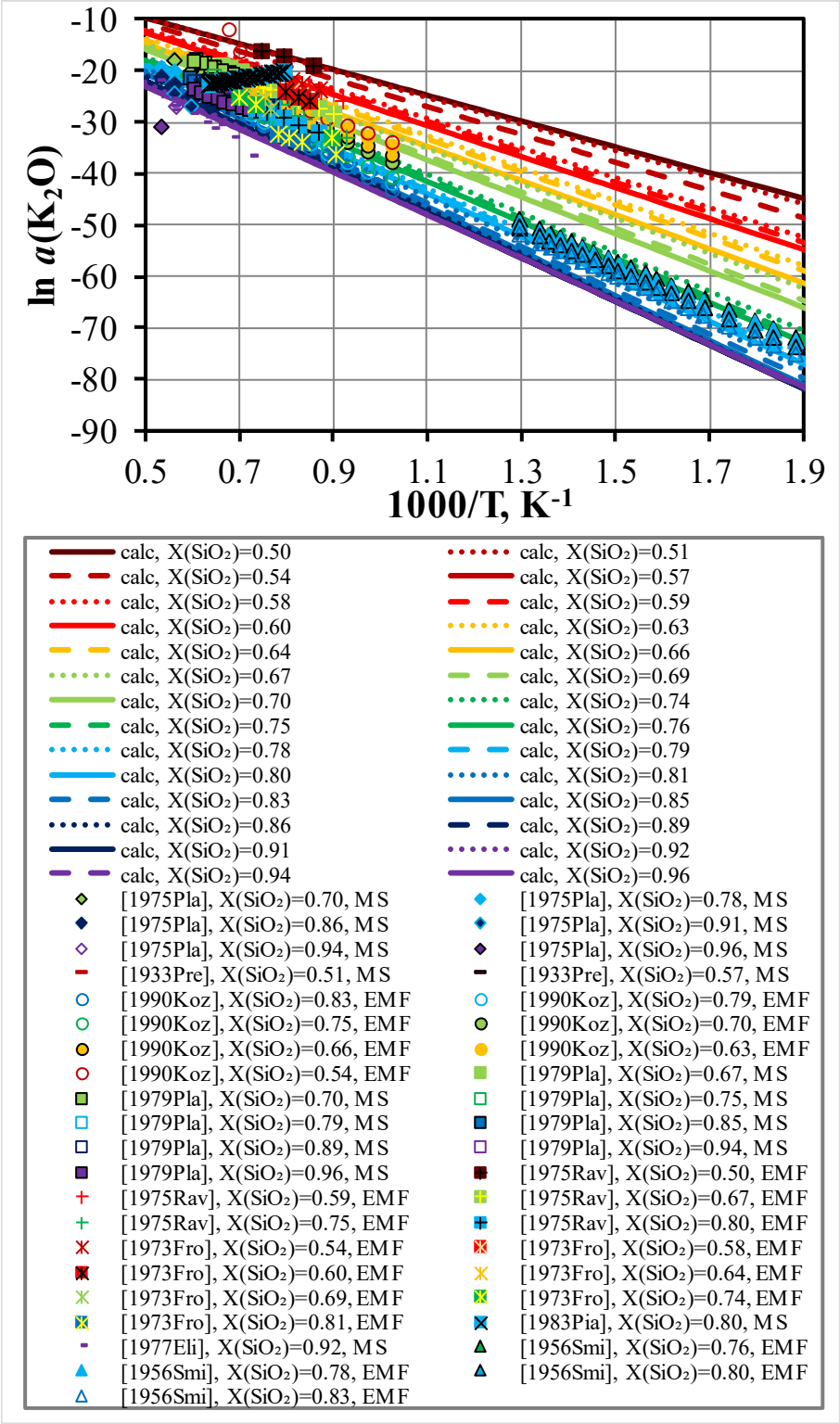
-10
-20
-30
-40
-50
-60
-70
-80
-90
ln a(K2O)
0.5
0.7
0.9
1.1
1.3
1.5
1.7
1.9
1000/T, K-1
calc, X(SiO2)=0.50
calc, X(SiO2)=0.51
calc, X(SiO2)=0.54
calc, X(SiO2)=0.57
calc, X(SiO2)=0.58
calc, X(SiO2)=0.59
calc, X(SiO2)=0.60
calc, X(SiO2)=0.63
calc, X(SiO2)=0.64
calc, X(SiO2)=0.66
calc, X(SiO2)=0.67
calc, X(SiO2)=0.69
calc, X(SiO2)=0.70
calc, X(SiO2)=0.74
calc, X(SiO2)=0.75
calc, X(SiO2)=0.76
calc, X(SiO2)=0.78
calc, X(SiO2)=0.79
calc, X(SiO2)=0.80
calc, X(SiO2)=0.81
calc, X(SiO2)=0.83
calc, X(SiO2)=0.85
calc, X(SiO2)=0.86
calc, X(SiO2)=0.89
calc, X(SiO2)=0.91
calc, X(SiO2)=0.92
calc, X(SiO2)=0.94
calc, X(SiO2)=0.96
[1975Pla], X(SiO2)=0.70, MS
[1975Pla], X(SiO2)=0.78, MS
[1975Pla], X(SiO2)=0.86, MS
[1975Pla], X(SiO2)=0.91, MS
[1975Pla], X(SiO2)=0.94, MS
[1975Pla], X(SiO2)=0.96, MS
[1933Pre], X(SiO2)=0.51, MS
[1933Pre], X(SiO2)=0.57, MS
[1990Koz], X(SiO2)=0.83, EMF
[1990Koz], X(SiO2)=0.79, EMF
[1990Koz], X(SiO2)=0.75, EMF
[1990Koz], X(SiO2)=0.70, EMF
[1990Koz], X(SiO2)=0.66, EMF
[1990Koz], X(SiO2)=0.63, EMF
[1990Koz], X(SiO2)=0.54, EMF
[1979Pla], X(SiO2)=0.67, MS
[1979Pla], X(SiO2)=0.70, MS
[1979Pla], X(SiO2)=0.75, MS
[1979Pla], X(SiO2)=0.79, MS
[1979Pla], X(SiO2)=0.85, MS
[1979Pla], X(SiO2)=0.89, MS
[1979Pla], X(SiO2)=0.94, MS
[1979Pla], X(SiO2)=0.96, MS
[1975Rav], X(SiO2)=0.50, EMF
[1975Rav], X(SiO2)=0.59, EMF
[1975Rav], X(SiO2)=0.67, EMF
[1975Rav], X(SiO2)=0.75, EMF
[1975Rav], X(SiO2)=0.80, EMF
[1973Fro], X(SiO2)=0.54, EMF
[1973Fro], X(SiO2)=0.58, EMF
[1973Fro], X(SiO2)=0.60, EMF
[1973Fro], X(SiO2)=0.64, EMF
[1973Fro], X(SiO2)=0.69, EMF
[1973Fro], X(SiO2)=0.74, EMF
[1973Fro], X(SiO2)=0.81, EMF
[1983Pia], X(SiO2)=0.80, MS
[1977Eli], X(SiO2)=0.92, MS
[1956Smi], X(SiO2)=0.76, EMF
[1956Smi], X(SiO2)=0.78, EMF
[1956Smi], X(SiO2)=0.80, EMF
[1956Smi], X(SiO2)=0.83, EMF

Figure 9.7 K_2O activity in the liquid phase in the K_2O-SiO_2 system as a function of the temperature at constant compositions. The reference state is the pure liquid K_2O. Experimental points [220, 226, 231, 232, 345, 346, 350-352] and calculated lines.

9.4 Heat capacity and heat content data

Stull et al. [353] measured C_P of K_2SiO_3 in an adiabatic calorimeter. Labban et al. [235] performed adiabatic calorimetry of vitreous and crystalline $K_2Si_2O_5$.

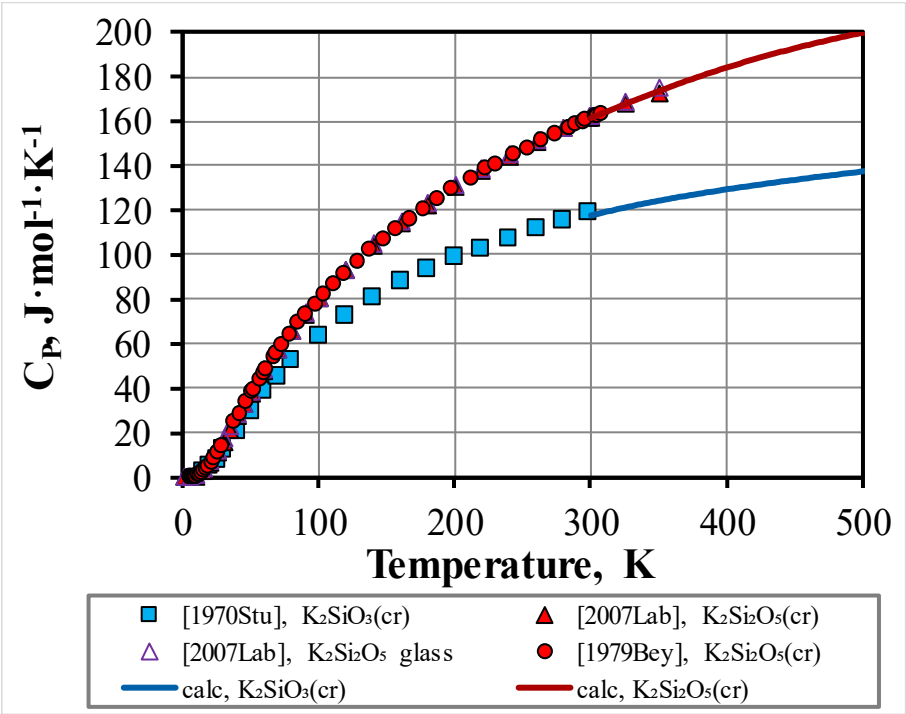

Figure 9.8 The heat capacity of crystalline and vitreous K_2SiO_3 and $K_2Si_2O_5$ compounds. Experimental points [235, 353, 354] and calculated lines.

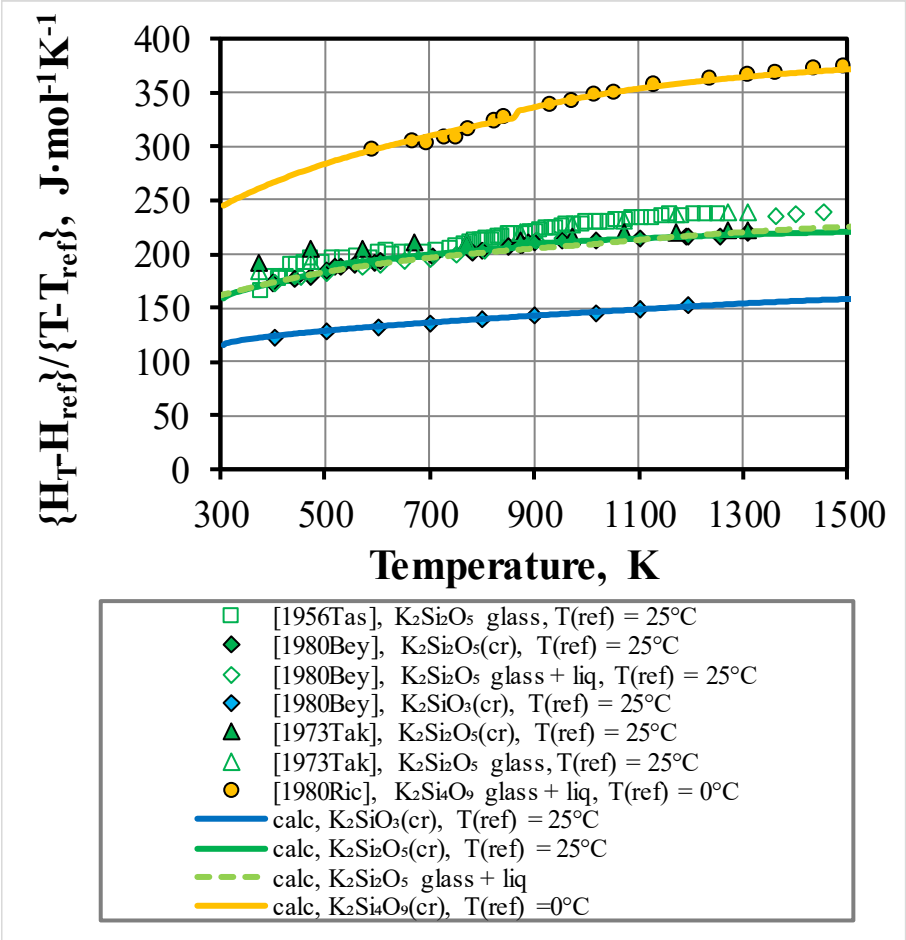

Figure 9.9 The mean heat capacity of crystals, glasses and liquids of mono-, di- and tetrasilicate compositions. Experimental points [203, 236, 329, 338] and calculated lines.

The heat content of glasses of various compositions was measured [203, 236, 238, 245, 329, 338]. The heat content of crystalline compounds was measured for K_2SiO_3 [338] and for $K_2Si_2O_5$ [203, 338]. The low-temperature heat capacities were measured for K_2SiO_3 [353] and for $K_2Si_2O_5$ [235, 354]. All the data are summarized in Figure 9.9.

9.5 Optimization results

Thermodynamic properties of the stoichiometric compounds in the K_2O-SiO_2 system are given in Table A.9. The compound properties were taken from the work of Kim [18] with slight modifications; two compounds not present in that work, $K_{10}Si_3O_{11}$ and $K_8Si_3O_{10}$, were evaluated;

the C_P curves and the standard entropies were obtained as weighted sums of heat capacities of K_4SiO_4 and K_2SiO_3, the enthalpies of formation were adjusted to fit the liquidus.

The logic behind the optimization of the K_2O-SiO_2 system closely follows the one for the Na_2O-SiO_2 system. The optimization of the Na_2O-SiO_2 system required a dimer species to be introduced into the model in order to reproduce cristobalite liquidus (see Chapter 6). It was predicted that the caging effect is very important in the Li_2O-SiO_2 and Na_2O-SiO_2 systems; however, the liquidus in the K_2O-, Rb_2O-, and Cs_2O-SiO_2 systems indicate that less dimer would be required (section 6.1). It is probably explained by the growing size of the cations in the series Li→Na→K→Rb→Cs.

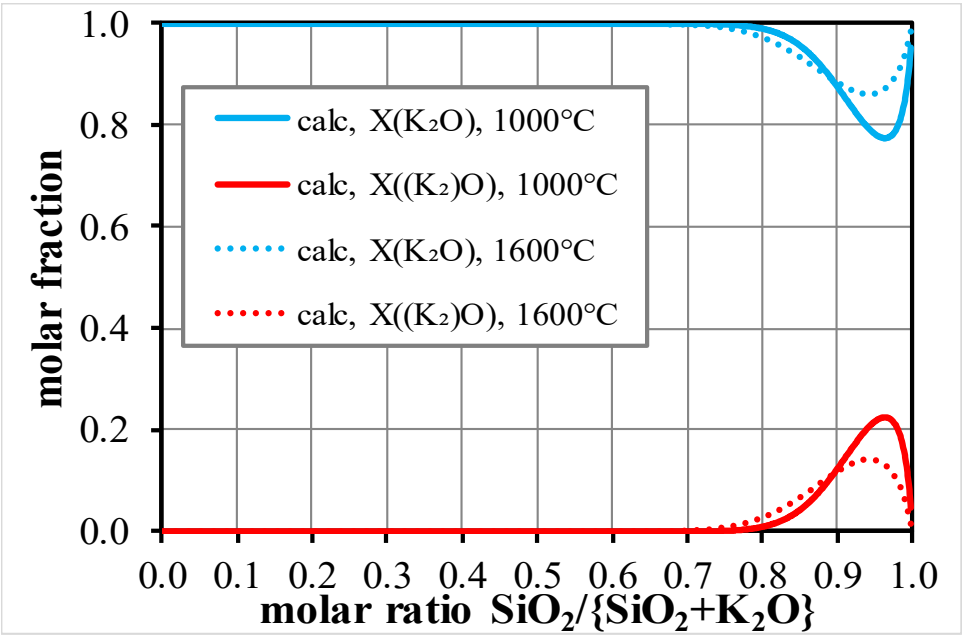

Figure 9.10 Distribution of the ordinary and dimer K_2O end-members with silica molar fraction at two different temperatures.

The Gibbs energy of $(K_2)O$ end-member is equal to the Gibbs energy of K_2O plus a positive stability parameter so its concentration in the pure liquid K_2O would be negligible. It also helps to avoid any changes in the previously optimized systems. $(K_2)O$ does not affect a system unless a strong negative interaction parameter with it is present. A negative $g^{01}_{K_2,Si}$ makes the dimer appear in the SiO_2-rich region and a positive $g^{06}_{K_2,Si}$ raises SiO_2 liquidus. The temperature-dependent parameters in the SiO_2-rich region are required to describe simultaneously the steep SiO_2 liquidus

and the metastable miscibility gap. The short-range ordering appears at K_4SiO_4 composition. The optimized parameters are summarized in Table A.9 and Table A.10.

CHAPTER 10 OPTIMIZATION OF THE K_2O-Al_2O_3 SYSTEM

10.1 Phase diagram

The phase diagram of the system was investigated by Moya et al. [355] between $KAlO_2$ and Al_2O_3 compositions. K_2CO_3 and Al_2O_3 were used as the precursors; the reaction products were highly hydroscopic. The main problem in investigation of this system, besides the hygroscopicity, is the volatility of K_2O from samples at the temperatures of interest (1200-1700°C). K-β-alumina phase was reported with a homogeneity range of 83-91 mol% Al_2O_3. Apparently, it is a solid solution isostructural with Na-β-alumina. The eutectic between $KAlO_2$ and K-β-alumina was observed at 1450°C and 62 mol% Al_2O_3.

Roth [46] studied the $KAlO_2$-Al_2O_3 system as a part of the K_2O-MgO-Al_2O_3-Fe_2O_3-SiO_2 system. The homogeneity limits of K-β-alumina solid solution were found at 85-90 mol% Al_2O_3 which is within the interval given by Moya et al. [355]. Also, Roth tried to measure the melting point of $KAlO_2$ compound in a sealed iridium crucible. The results indicate that the melting point is greater than 2100°C and the value of 2150±100°C is the best estimate. The rupture pressure of K_2O vapor in a Mo sealed crucible was achieved at around 2260°C. Also, an eutectic (apparently, between $KAlO_2$ and K-β-Al_2O_3) was observed at 1910°C with an unknown composition. However, this value significantly deviates from the eutectic temperature by Moya et al. at 1450°C.

Later, Roth et al. [356] continued the study of the system. Both β-alumina and β”-alumina could not be found below 1000°C but between 1000° and 1200°C they can coexist. The eutectic temperature of 1450°C by Moya et al. [355] was not confirmed, no signs of melting were observed below 1900°C. K-β”-alumina was considered metastable but it can be stabilized by addition of, for example, MgO.

Schaefer et al. [357] summarized the available data in the literature and also conducted their own experiments to construct a consistent phase diagram of the system. According to their phase diagram, the composition range of 83-91 mol% by Moya et al. [355] is in fact shared between K-β”- and K-β-aluminas. K-β”-alumina decomposes peritectically into $KAlO_2$ and K-β-alumina at 1700°C, there is a $KAlO_2$-K-β-alumina eutectic at 1780°C and 62 mol% Al_2O_3; K-β-alumina decomposes peritectically into liquid and corundum at 1920°C.

K^+ ions in K-β- and K-β”-aluminas have a high mobility which makes these materials interesting in solid electrolyte applications [355]. K-β”-alumina has a higher conductivity but easily loses K_2O and transforms into K-β-alumina and corundum [357]. Strictly speaking, both K-β- and K-β”-alumina are narrow solid solutions but, for simplicity sake, they are sometimes considered as stoichiometric compounds. The recommended K_2O:Al_2O_3 ratios are 1:9 and 1:6 for K-β- and K-β”-alumina, correspondingly [358].

$KAlO_2$ is structurally similar to $NaAlO_2$, $LiAlO_2$ and some other aluminates [359]. Different modifications of the compound and their crystal structures were studied by de Kroon et al. [360]. So, a high-temperature δ-$KAlO_2$ has a cubic structure and transforms into a tetragonal γ-$KAlO_2$ at 1350°C which in its turn transforms into an orthorhombic β-$KAlO_2$ at 600°C.

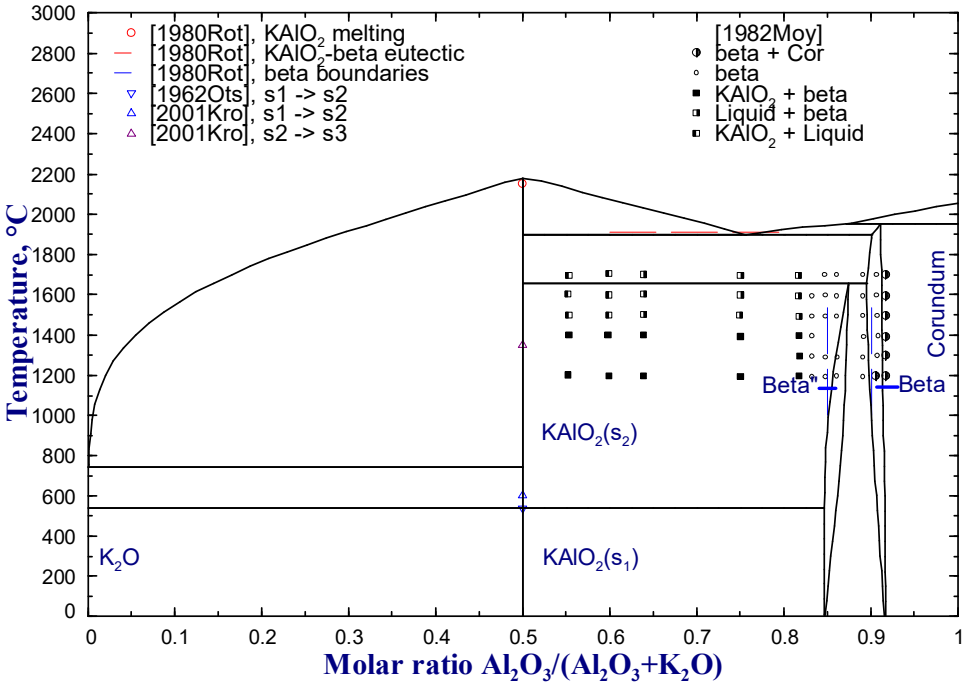

Figure 10.1 Phase diagram of the K_2O-Al_2O_3 system. Experimental points [46, 254, 360] and calculated lines.

10.2 Calorimetry data

The enthalpy of formation of $KAlO_2$ was determined by HF calorimetry by Bennington and Daut [361]. The acid media was 20.0 wt% HF+5.0 wt% HCl, the obtained value was

−1140.56±5.98 kJ·mol^{-1}. The value was calculated using a chloride cycle. Zygan et al. [195] performed $2PbO{\cdot}B_2O_3$ calorimetry of $KAlO_2$ and their value of the enthalpy of formation is −1135.54±1.67 kJ·mol^{-1}.

10.3 Activity data

K_2O activity in the two-phase regions was determined by EMF and Knudsen effusion methods.

Kumar and Kay [280] employed an oxygen concentration cell of the following type:

$$Pt,Ag+Ag_2S+K_2S+Al_2O_3+\beta\text{-alumina}|(CaO)ZrO_2|Air,Pt \quad (110)$$

giving rise to the following electrochemical reaction:

$$K(K_2S+Ag+Ag_2S)+0.5O_2(air)\rightarrow K_2O(\beta\text{-alumina}) \quad (111)$$

Itoh and Kozuka [362] determined K_2O activity in the K-β-alumina/Al_2O_3 region using the following electrochemical cell:

$$Pt,O_2,(Al_2O_3+\beta\text{-alumina})|\beta\text{-alumina}|K_2SO_4,SO_2+SO_3+O_2,Pt \quad (112)$$

the total reaction in cell (112) is:

$$K_2O(Al_2O_3+\beta\text{-alumina})+SO_3\rightarrow K_2SO_4 \quad (113)$$

Kale and Jacob [363] constructed an electrochemical cell of the following type:

$$Ta,Bi\text{-}5mol\%\ K|Al_2O_3+\beta\text{-alumina}|In+In_2O_3 \quad (114)$$

The reaction in cell (114) results in:

$$2K(Bi\text{-}5mol\%\ K)+0.5O_2(In+In_2O_3)\rightarrow K_2O(\beta\text{-alumina}) \quad (115)$$

Plante et al. [350] measured K pressures over $KAlO_2$/K-β”-alumina and K-β-alumina/Al_2O_3 mixtures. K_2O was assumed to decompose completely into K(g) and O_2. The same phase assemblages were investigated by Marinkovic et al. [364].

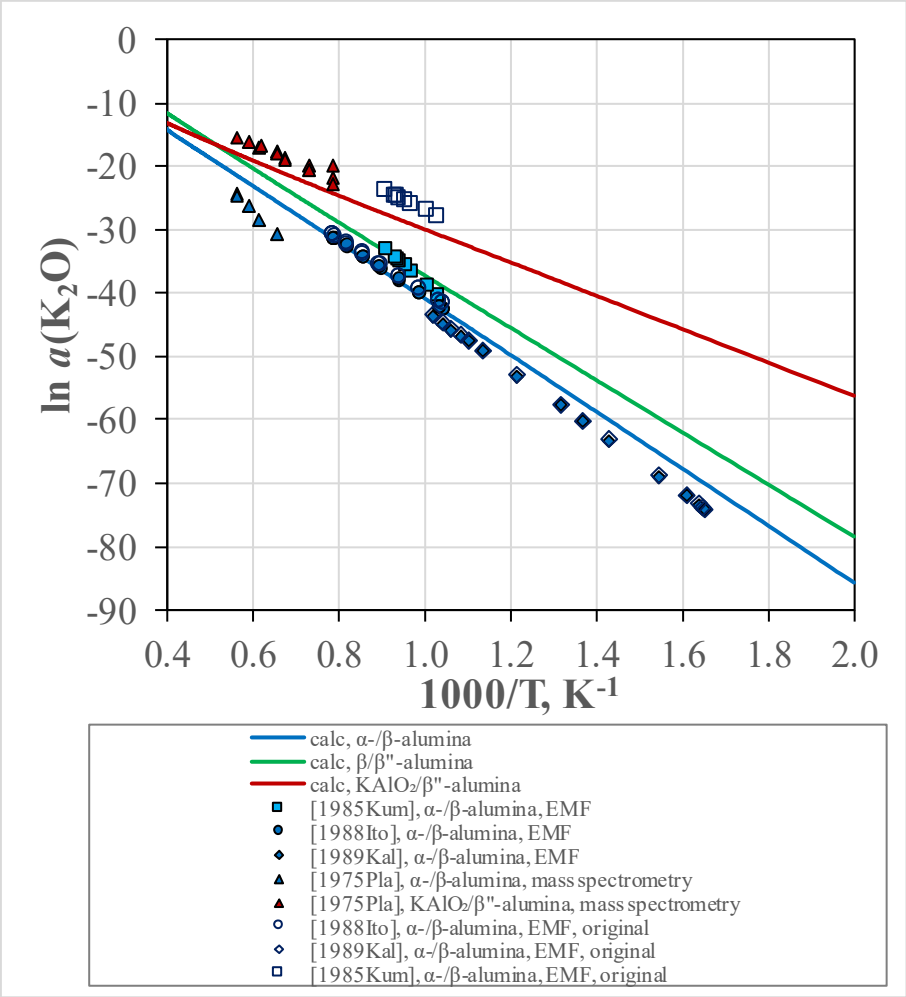

Figure 10.2 K_2O activity in biphasic regions of the K_2O-Al_2O_3 system. The reference state is the pure solid K_2O. Experimental points [280, 350, 362, 363] and calculated lines.

The resulting K_2O activity values (the pure solid K_2O is used as a reference state) are summarized in Figure 10.2. If it was possible, the original activity data from the sources are plotted alongside with the values calculated from the raw experimental data using thermodynamic properties of the auxiliary materials from *FactSage*. The properties of the Ta-Bi-K alloy [363], however, were used unchanged as they are absent in *FactSage* databases. The recalculated data on α/β-alumina equilibrium are more or less consistent for several authors; however, the recalculated values from Kumar and Kay [280] significantly deviate from the original ln $a(K_2O)$ vs T dependence proposed by the authors. It is hardly possible to explain the difference of the thermodynamic properties from *FactSage* and those used by Kumar and Kay (the extent of this uncertainly can be seen from the

comparison of the original and recalculated activity by Kale and Jacob [363] and Itoh and Kozuka [362]). We tend to think that a misprint or a numerical error was in the article by Kumar and Kay.

10.4 Heat capacities and heat content data

The low-temperature heat capacity of $KAlO_2$ was measured from 5 to 303K by adiabatic calorimetry by Beyer et al. [365] as well as the heat content by copper-block calorimetry. A reversible transition at 537°C with the enthalpy of transition of 1295 $J \cdot mol^{-1}$ was found. Otsubo et al. [254] found a reversible transition at 535°C, Arakelyan [366] at 522°C, Cook [367] at 540°C.

The heat capacity of K-β-alumina was measured by Anthony and Anderson [368] at ultra-low temperatures (less than 1K). McWhan et al. [284] measured heat capacity of K-β-alumina at temperatures up to 40K.

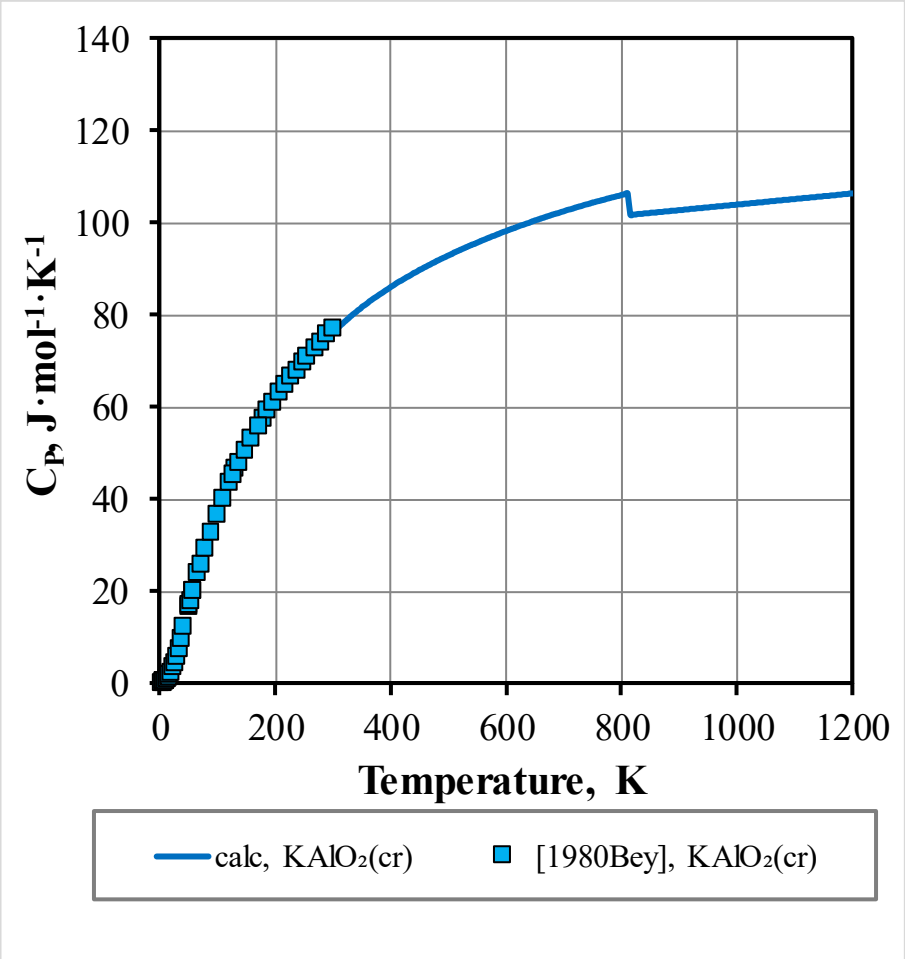

Figure 10.3 The heat capacity of potassium aluminate $KAlO_2$. Experimental data points [365] and calculated lines.

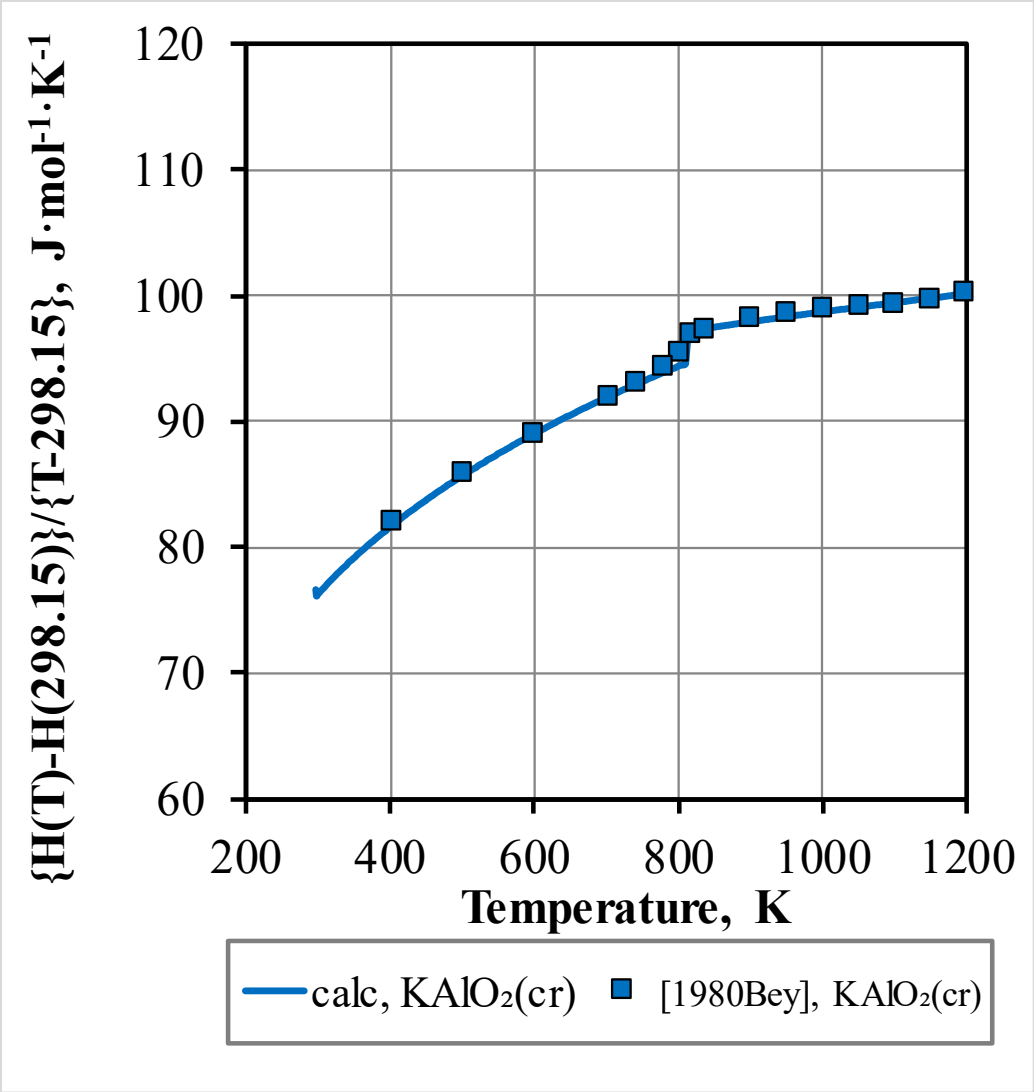

Figure 10.4 The mean heat capacity of potassium aluminate $KAlO_2$. Experimental data points [365] and calculated lines.

10.5 Optimization results

The current optimization of the K_2O-Al_2O_3 system is mostly based on the optimization by Kim [18]. The properties of $KAlO_2$ compound and the Beta, Beta" solid solutions in the system were adopted without changes. The liquid phase, however, was modified in order to better reproduce the enthalpy of mixing in the $KAlO_2$-SiO_2 section of the K_2O-Al_2O_3-SiO_2 system. The optimized parameters are shown in Table A.11-Table A.12.

CHAPTER 11 OPTIMIZATION OF THE K_2O-Al_2O_3-SiO_2 SYSTEM

11.1 Phase diagram

One of the earliest works on the K_2O-Al_2O_3-SiO_2 system was performed by Schairer and Bowen [369]. Phase relations were studied using a quenching technique and an optical investigation of crystalline phases. Unfortunately, they could not publish the detailed data, only the invariant points are available. The following binary systems were found: $KAlSi_2O_6$-SiO_2, $KAlSi_2O_6$-Al_2O_3, $K_2Si_2O_5$-$KAlSi_2O_6$, $KAlSiO_4$-$KAlSi_2O_6$, $K_2Si_2O_5$-$KAlSiO_4$, $KAlSiO_4$-Al_2O_3, $K_2Si_4O_9$-$KAlSi_3O_8$ (partially binary). The detailed data from Schairer and Bowen [369] were published later [119].

The $KAlO_2$-SiO_2 section was studied in a series of works [46, 370, 371]. An extensive solid solution of SiO_2 in $KAlO_2$ was reported. With a progressive substitution with SiO_2, the transition temperature between the low-*T* orthorhombic and high-*T* cubic modifications lowers. The cubic solution extends to about 0.235 SiO_2 [372]. Roth [46] and Husheer et al. [370] report incongruent melting of $KAlSiO_4$.

Orthorhombic $KAlSiO_4$ transforms to another orthorhombic phase on heating above 1450-1485°C with a larger unit cell [371]. Also, $KAlSiO_4$ can dissolve moderate amounts of silica in its structure.

$KAlSiO_4$ has several polymorphs, but only two were encountered [369]. At 1540°C, the hexagonal form transforms into an orthorhombic modification which is stable up to the congruent melting point. The melting point was not located exactly and is somewhat above 1750°C. According to Cook et al. [371] the transformation between the modifications occurs between 1450° and 1485°C.

A tetragonal phase $K_{1+x}Al_{1+x}Si_{1-x}O_4$ (x is about 0.1) was reported [46, 370, 371]. It exists in the temperature range of 1400-1600°C [371]. However, Li et al. [372] did not confirm its stability.

Leucite $KAlSi_2O_6$ melts congruently at 1686±5°C and shows an inversion somewhat above 600°C. $KAlSi_3O_8$ melts incongruently at 1150±20°C decomposing into leucite and liquid. A tetragonal/cubic transition in leucite is reported at 665°C [77, 108, 373-376].

The incongruent melting behaviour of $KAlSi_3O_8$ was investigated in detail [291, 377, 378]. According to different authors, its melting point is 1170°C [378], 1150±20°C [369], 1055±5°C [291]. The compound was found to melt very sluggishly with significant overheating and a large

determination error of the melting point [377, 378]. According to Boettcher et al. [291], the melting behaviour of $KAlSi_3O_8$ becomes congruent under high pressures. $KAlSi_3O_8$ compound belongs to the feldspar family of minerals and plays a very important role in geology. It exists in several forms depending on the degree of Al/Si ordering and the symmetry of the crystal lattice. The completely ordered form is called microcline (triclinic), and the completely disordered is called sanidine (monoclinic). There are also forms with intermediate ordering. The ordering scheme in $KAlSi_3O_8$ is shown in Figure 11.1. The temperature of the triclinic/monoclinic transition in $KAlSi_3O_8$ is 451±47°C [379], 500±50°C [380].

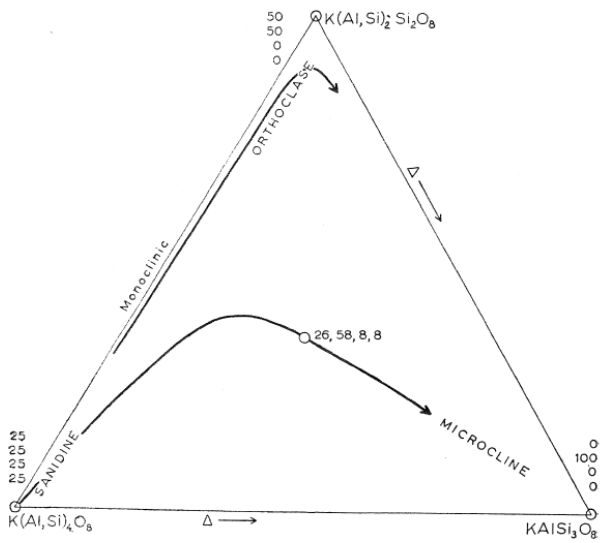

Figure 11.1 The ordering scheme for $KAlSi_3O_8$. The columns of numbers show relative Al occupancy of four (Al, Si) sites in the structure. One of the intermediate potassium feldspars, studied in the source article, is also shown. The image is taken from Barth [381].

Liquidus projections in the K_2O-Al_2O_3-SiO_2 system in different temperature intervals are given in Figure 11.2-Figure 11.4.

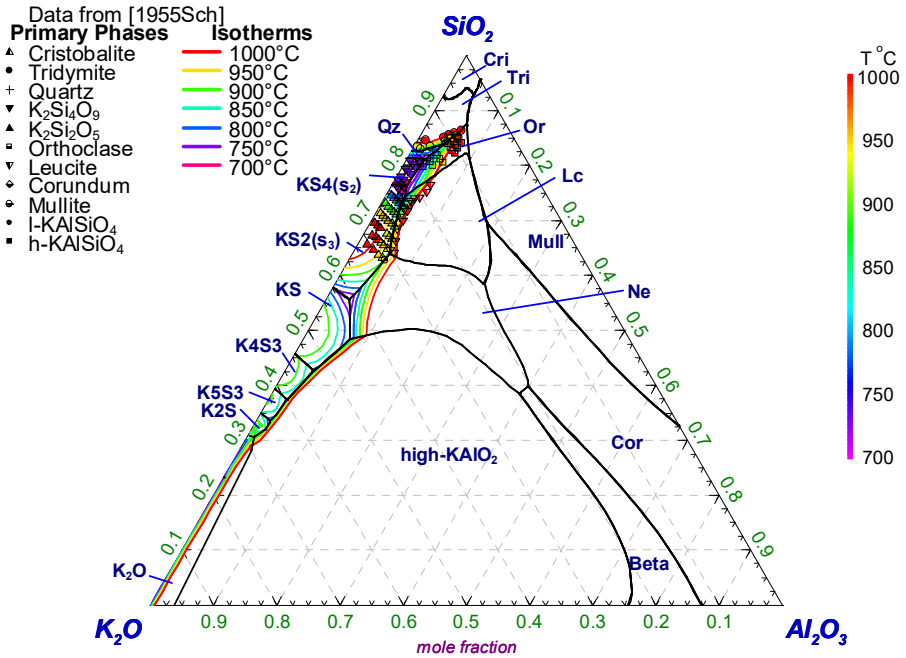

Figure 11.2 Liquidus projection in the K_2O-Al_2O_3-SiO_2 system; isotherms from 700° to 1000°C. Experimental points [119] and calculated lines.

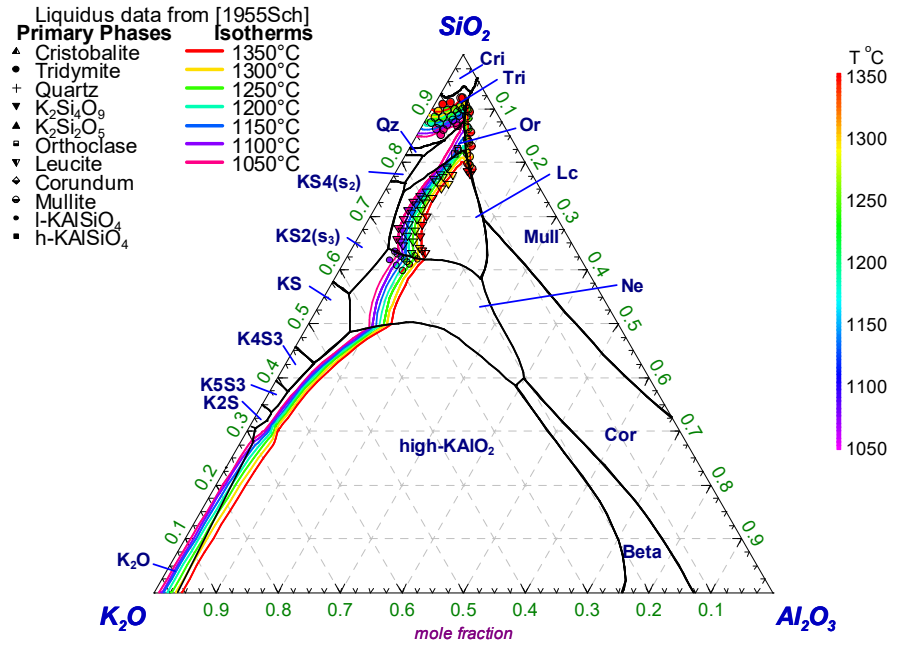

Figure 11.3 Liquidus projection in the K_2O-Al_2O_3-SiO_2 system; isotherms from 1050° to 1350°C. Experimental points [119] and calculated lines.

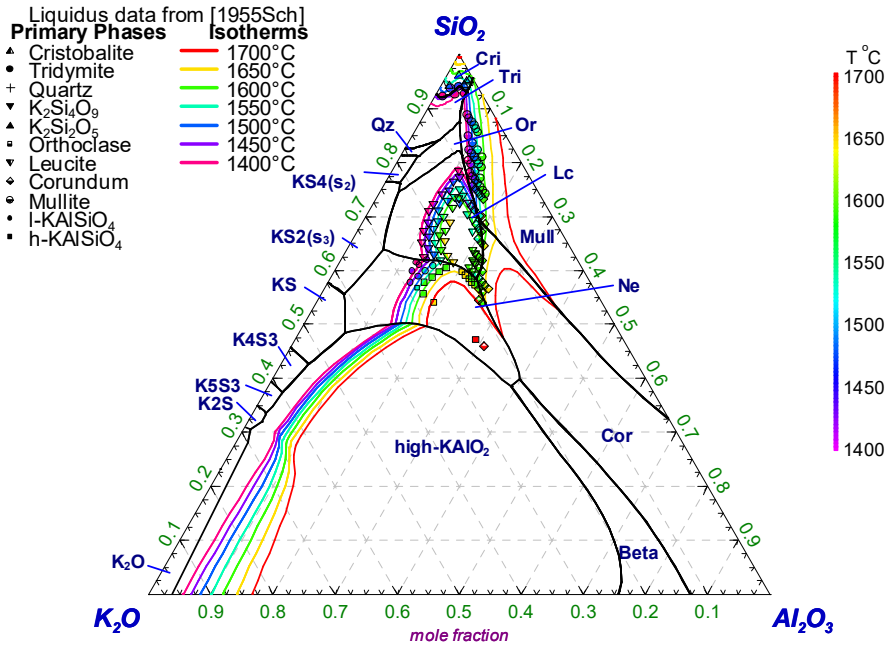

Figure 11.4 Liquidus projection in the K_2O-Al_2O_3-SiO_2 system; isotherms from 1400° to 1700°C. Experimental points [119] and calculated lines.

The position of the Mullite/Corundum boundary in the liquidus projection is shifted down (Figure 11.4). The reason why it happens is discussed in detail in Section 5.1.

The central $KAlO_2$-SiO_2 section of the ternary system is shown in Figure 11.5.

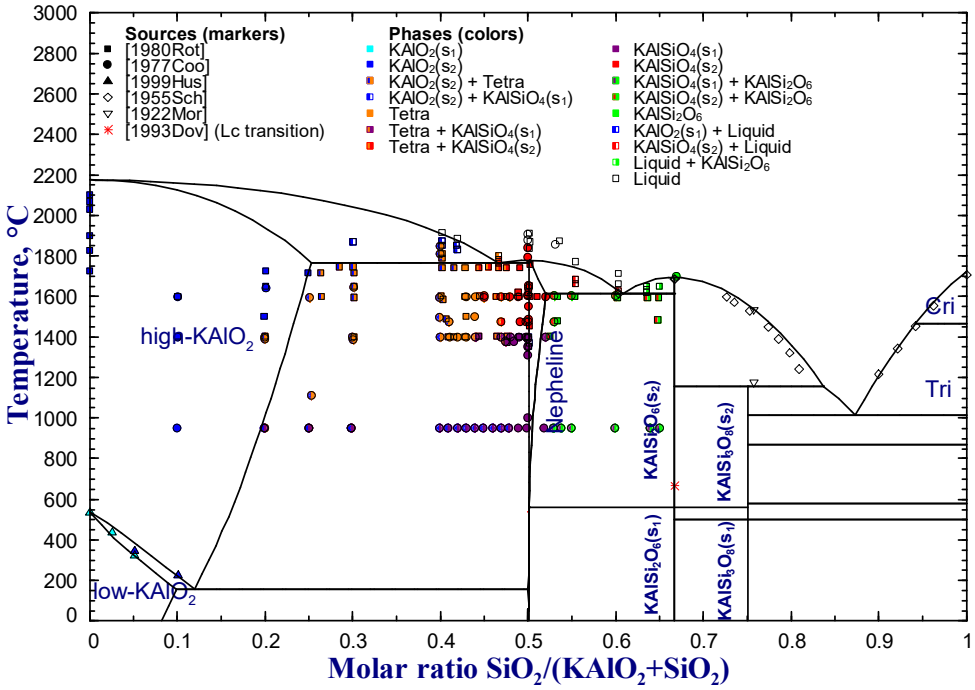

Figure 11.5 Phase diagram in the $KAlO_2$-SiO_2 section of the K_2O-Al_2O_3-SiO_2 system. Experimental points [108, 119, 370, 371, 378] and calculated lines. Marker shapes correspond to the studies; colors correspond to phases. If a marker has two colors, the two corresponding phases are present.

Different sections of the $(K_2O)_{(1-x)}(SiO_2)_x$-Al_2O_3 type can be made through the dataset by Schairer and Bowen [119]; they are summarized in Figure 11.6.

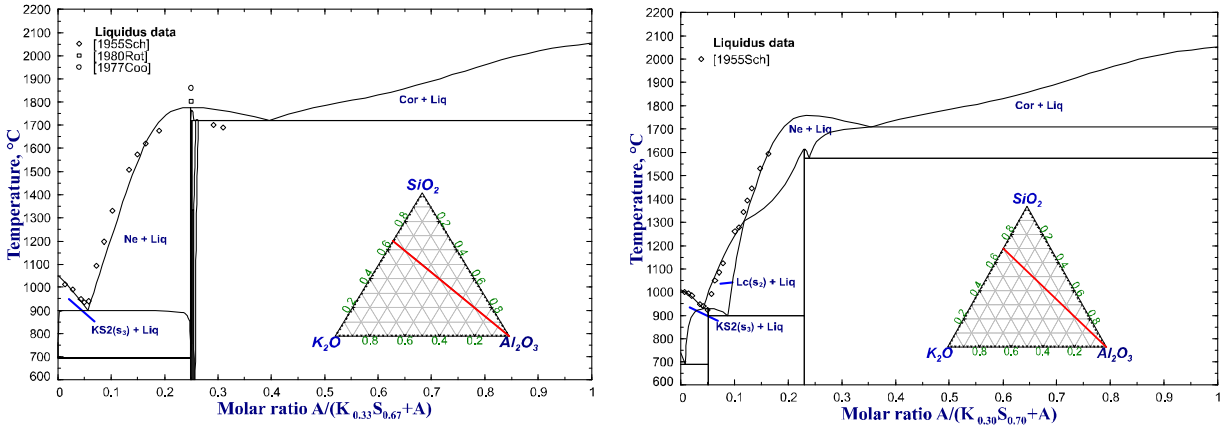

(*a*) (*b*)

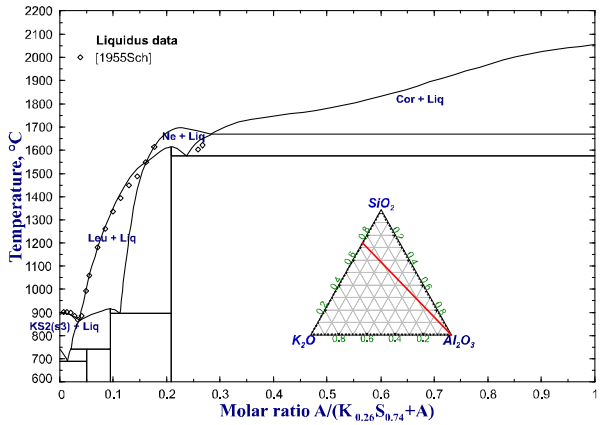
Liquidus data
[1955Sch]
Cor + Liq
Ne + Liq
Leu + Liq
KS2(s3) + Liq
Temperature, °C
Molar ratio A/(K 0.26S0.74+A)
SiO2
K2O
Al2O3

(*c*)

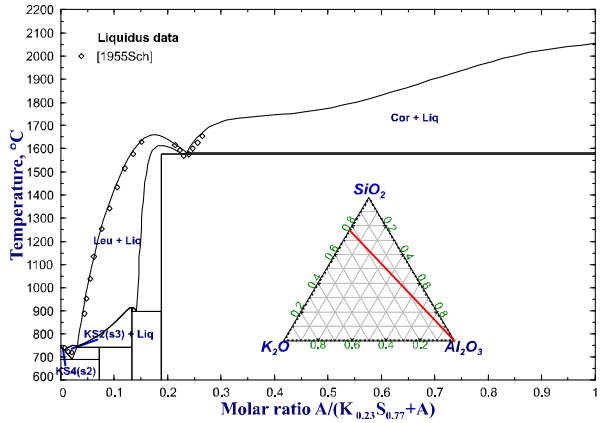
Liquidus data
[1955Sch]
Cor + Liq
Leu + Liq
KS2(s3) + Liq
KS4(s2)
Temperature, °C
Molar ratio A/(K 0.23S0.77+A)
SiO2
K2O
Al2O3

(*d*)

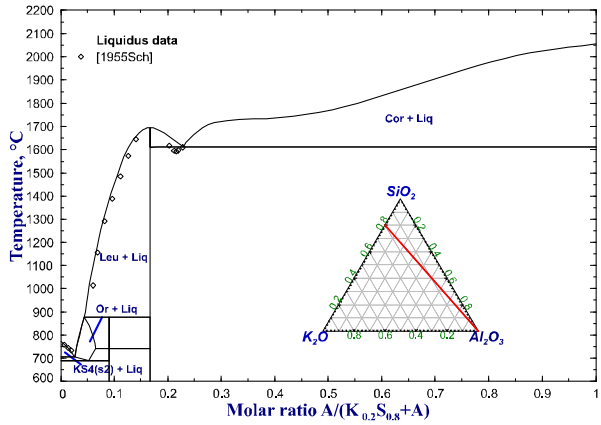
Liquidus data
[1955Sch]
Cor + Liq
Leu + Liq
Or + Liq
KS4(s2) + Liq
Temperature, °C
Molar ratio A/(K 0.2S0.8+A)
SiO2
K2O
Al2O3

(*e*)

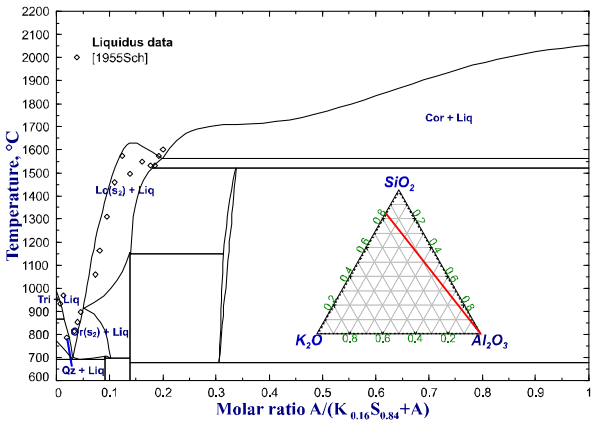
Liquidus data
[1955Sch]
Cor + Liq
Lc(s2) + Liq
Tri + Liq
Or(s2) + Liq
Qz + Liq
Temperature, °C
Molar ratio A/(K 0.16S0.84+A)
SiO2
K2O
Al2O3

(*f*)

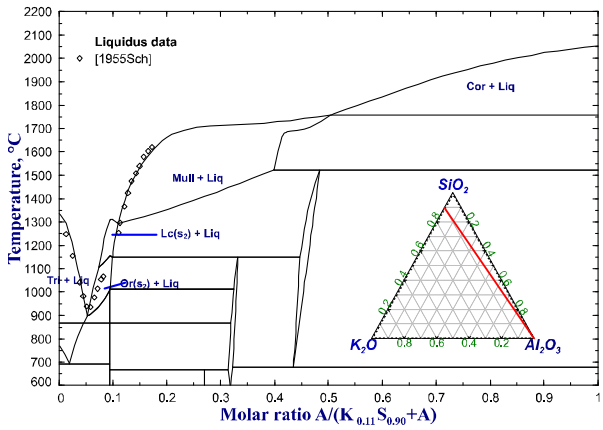
Liquidus data
[1955Sch]
Cor + Liq
Mull + Liq
Lc(s2) + Liq
Tri + Liq
Or(s2) + Liq
Temperature, °C
Molar ratio A/(K 0.11S0.90+A)
SiO2
K2O
Al2O3

(*g*)

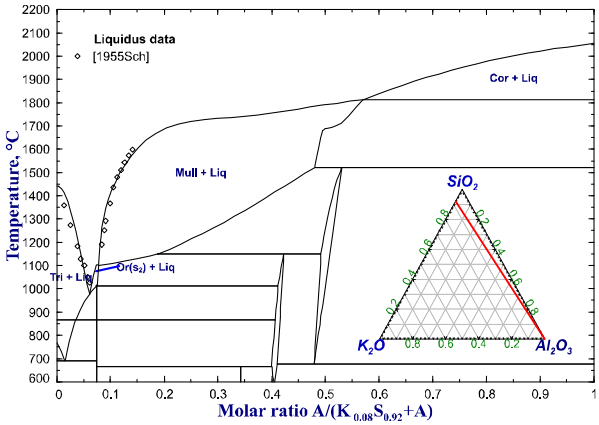
Liquidus data
[1955Sch]
Cor + Liq
Mull + Liq
Or(s2) + Liq
Tri + Liq
Temperature, °C
Molar ratio A/(K 0.08S0.92+A)
SiO2
K2O
Al2O3

(*h*)

Figure 11.6 Phase diagrams in sections through the K_2O-Al_2O_3-SiO_2 system. Experimental points [119] and calculated lines.

11.2 Calorimetry data

A few compilations of thermodynamic data on compounds, including the compounds in the K_2O-Al_2O_3-SiO_2 system, exist [305, 306, 308-312, 382]. Heats of solution of monoclinic feldspars as a function of their Al/Si ordering were measured by HF calorimetry by Hovis [383]. The enthalpy of solution was found to depend significantly on the degree of ordering. The heat of transition between microcline and sanidine as well as the heat of crystallization of $KAlSi_3O_8$ glass were measured by Waldbaum [307]. Hovis [186, 262] corrects the previously published results of the enthalpy of formation of adularia [187, 384] because of an error found in determination of the enthalpy of solution of corundum in HF.

Lead borate solution calorimetry of microcline was performed by Kiseleva et al. [194]. Their obtained value of -3979.26 ± 3.62 kJ·mol^{-1} is somewhat different from the value by Robie et al. [384] of -3967.69 ± 3.37 kJ·mol^{-1}. The enthalpy of solution of glasses in the $KAlO_2$-SiO_2 join were measured by lead borate solution calorimetry by Roy and Navrotsky [302]. The calculated enthalpy of mixing in the $KAlO_2$-SiO_2 join is shown in Figure 11.7.

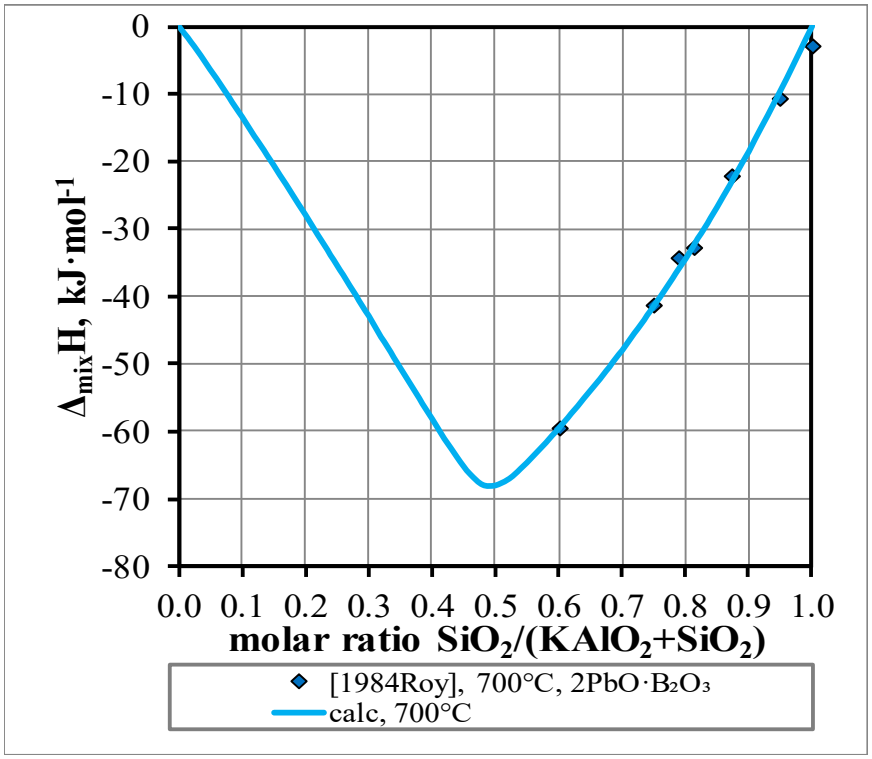

Figure 11.7 The enthalpy of mixing of the liquid phase in the $KAlO_2$-SiO_2 join of the K_2O-Al_2O_3-SiO_2 system. Experimental points [302] and the calculated line.

The partial enthalpy of corundum was measured in $K_2O \cdot 3SiO_2$ solvent by Wilding and Navrotsky [343] (see Figure 11.8).

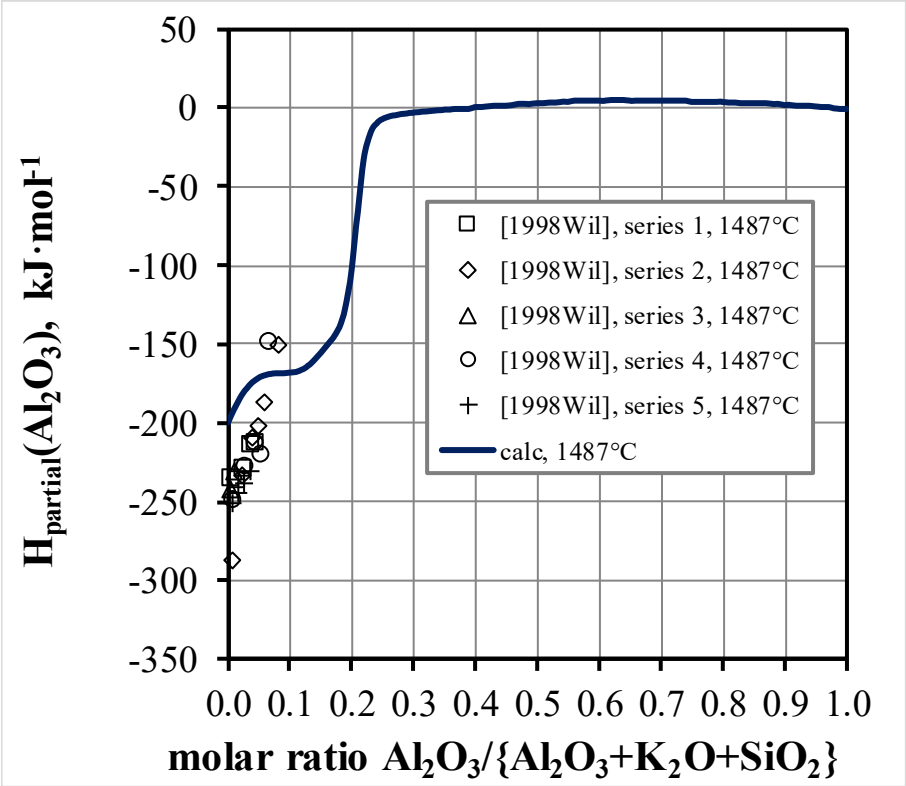

Figure 11.8 The partial enthalpy of Al_2O_3 in $(K_2O)_{0.25}(SiO_2)_{0.75}$ solvent at 1490°C. Experimental points [343] and the calculated line.

Hovis and Roux [313] performed HF calorimetry of samples of synthetic nepheline/kalsilite with different content of excess silica. These points were recalculated into the enthalpy of mixing using pure $KAlSiO_4$ kalsilite and quartz as the end-members (Figure 11.9).

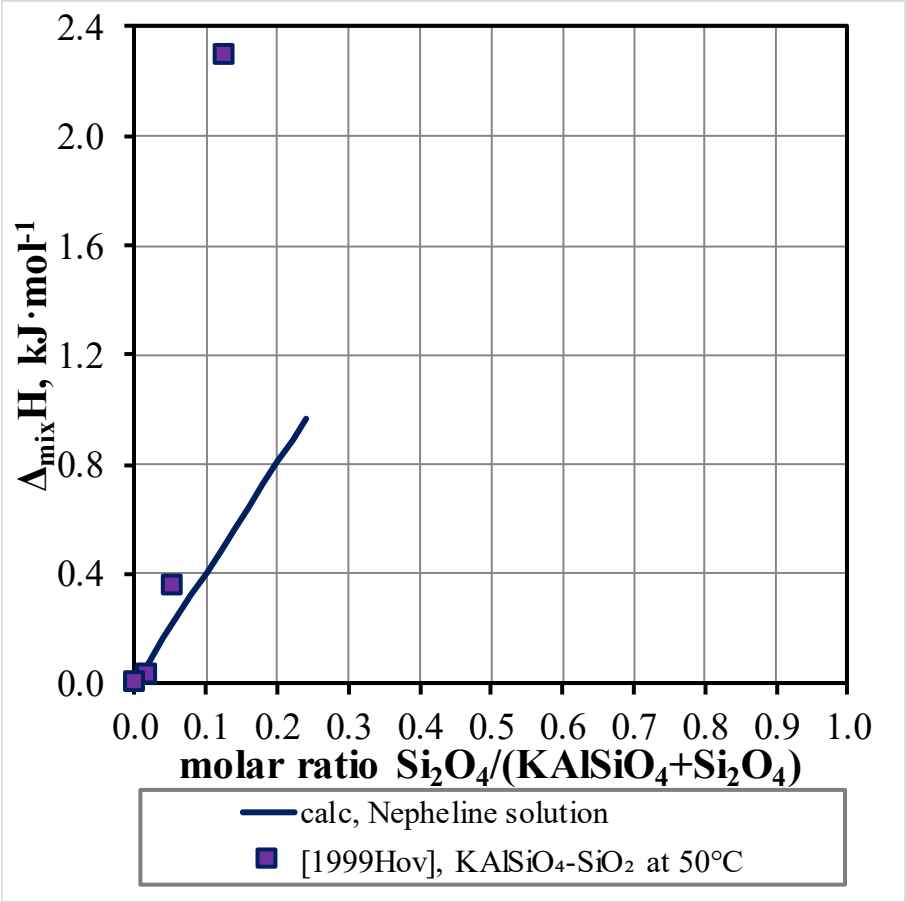

Figure 11.9 The enthalpy of mixing of Nepheline solution in the $KAlSiO_4$-Si_2O_4 section. Pure kalsilite of $KAlSiO_4$ composition and quartz were used as the end-members for calculation. Experimental points [313] and calculated lines.

11.3 Activity data

Oeltjen [319] performed Knudsen cell mass spectrometry of a few potassium-containing slags; one composition belongs to the K_2O-Al_2O_3-SiO_2 system. Plante et al. [349] carried out similar experiments with another composition in the system.

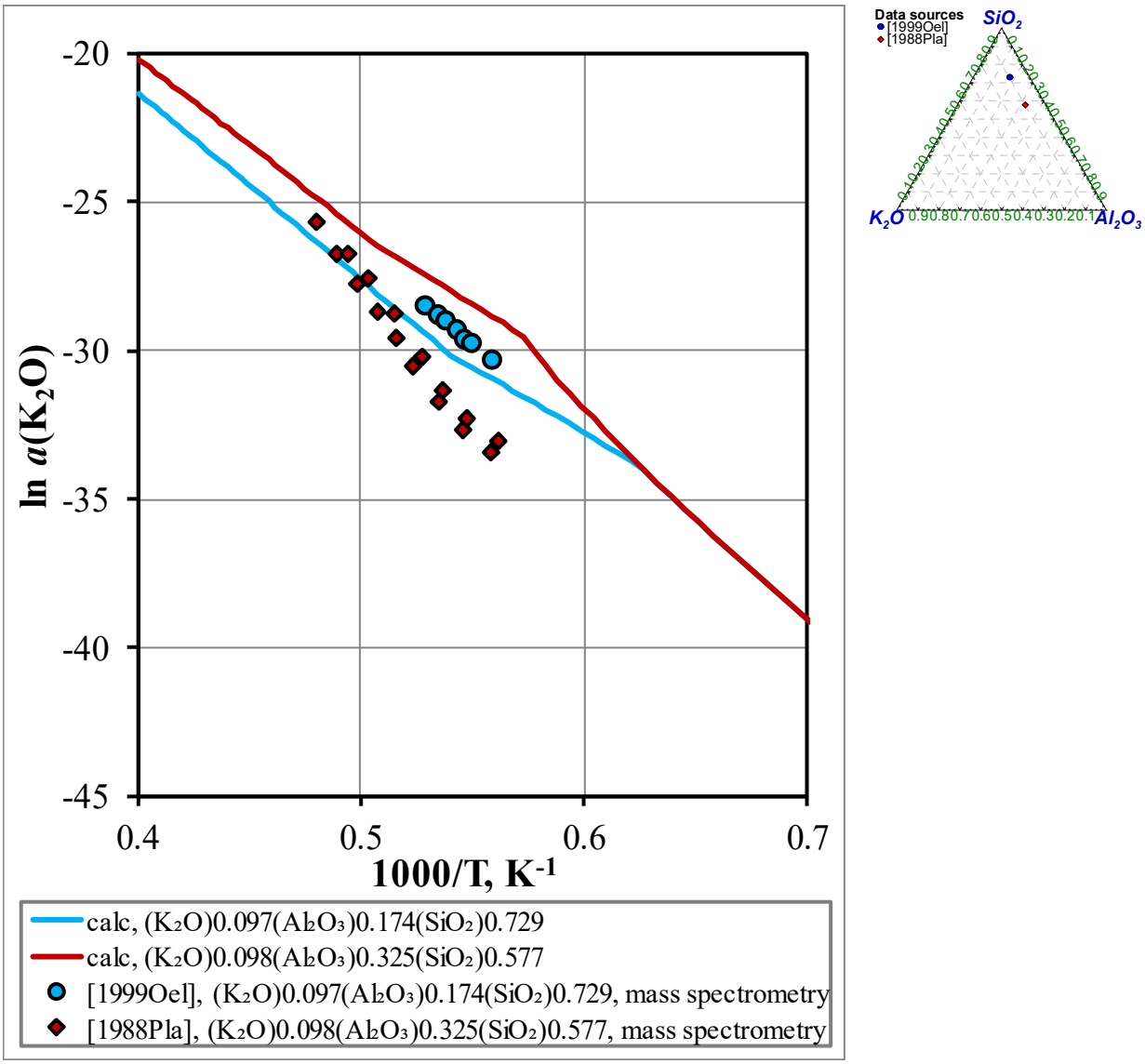

Figure 11.10 K_2O activities of fixed compositions versus temperature; the compositions are indicated in the compositional triangle. The calculation includes solid phases. Experimental points [319, 349] and calculated lines.

The lines in Figure 11.10 were calculated based on the observation that the temperatures of the experiments correspond to a liquid coexisting with solid(s) according to the phase diagram and the prediction is much better if the solid phases are included in the calculation.

11.4 Heat capacity and heat content data

Low-temperature heat capacities of adularia $KAlSi_3O_8$, leucite $KAlSi_2O_6$ and kalsilite $KAlSiO_4$ were measured by Kelley et al. [48]. DSC of crystalline $KAlSiO_4$ and $KAlSi_2O_6$ was carried out by Lange et al. [385], and two anomalies in the C_P curve were reported for kalsilite indicating phase transitions.

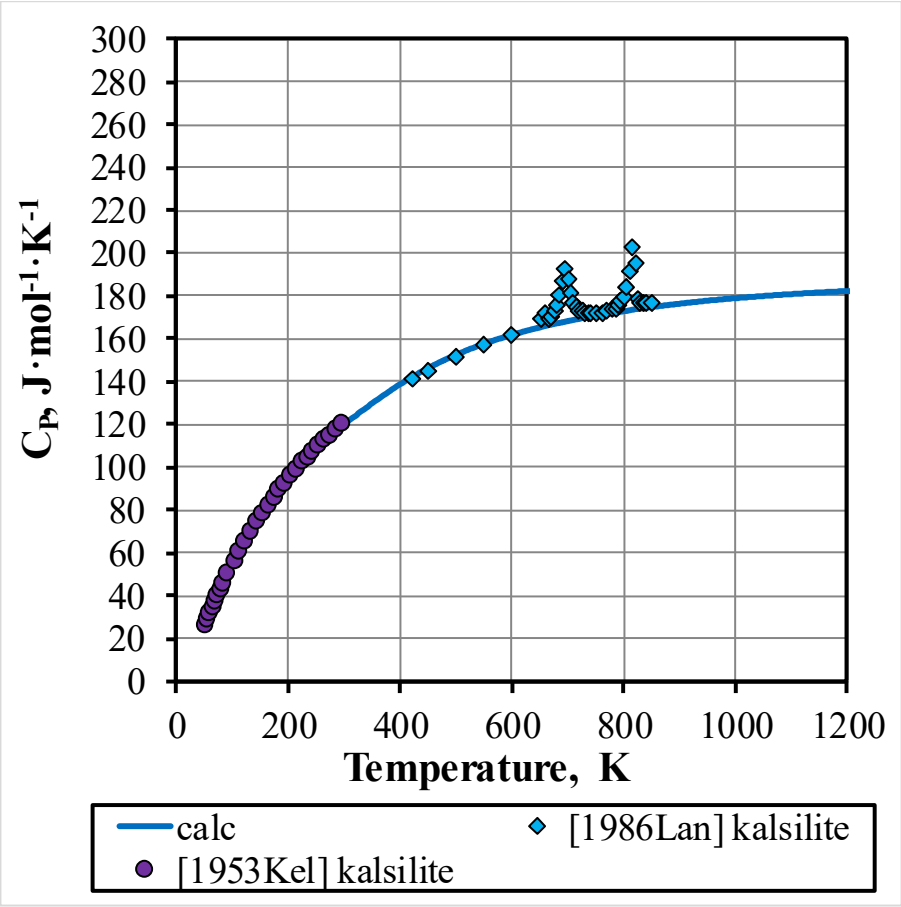

Figure 11.11 The heat capacity of kalsilite $KAlSiO_4$. Experimental data points [48, 385] and calculated lines.

Low temperature heat capacities of leucite were measured by different authors [385-387]. The measured temperature interval begins at 77K [387]; adiabatic calorimetry of leucite was carried out by Paukov et al. [386] in the temperature range 5.9-310K. No anomalies were detected. Hirao and Soga [387] performed adiabatic calorimetry up to 300K. The C_P data were extrapolated to

calculate the standard entropy. Integration of the data by Paukov et al. [386] gives the value of $S°_{298}$ = 180.0±1.0 J·mol^{-1}·K^{-1} while the data by Hirao and Soga [387] give only 166.5±2.0 J·mol^{-1}·K^{-1}. This discrepancy is explained by low quality of the data of Hirao and Soga multiplying the extrapolation error. Hirao and Soga [387] also made measurements at higher temperatures with DSC. Although the DSC points are not given, it was found that leucite undergoes a phase transformation at 833K.

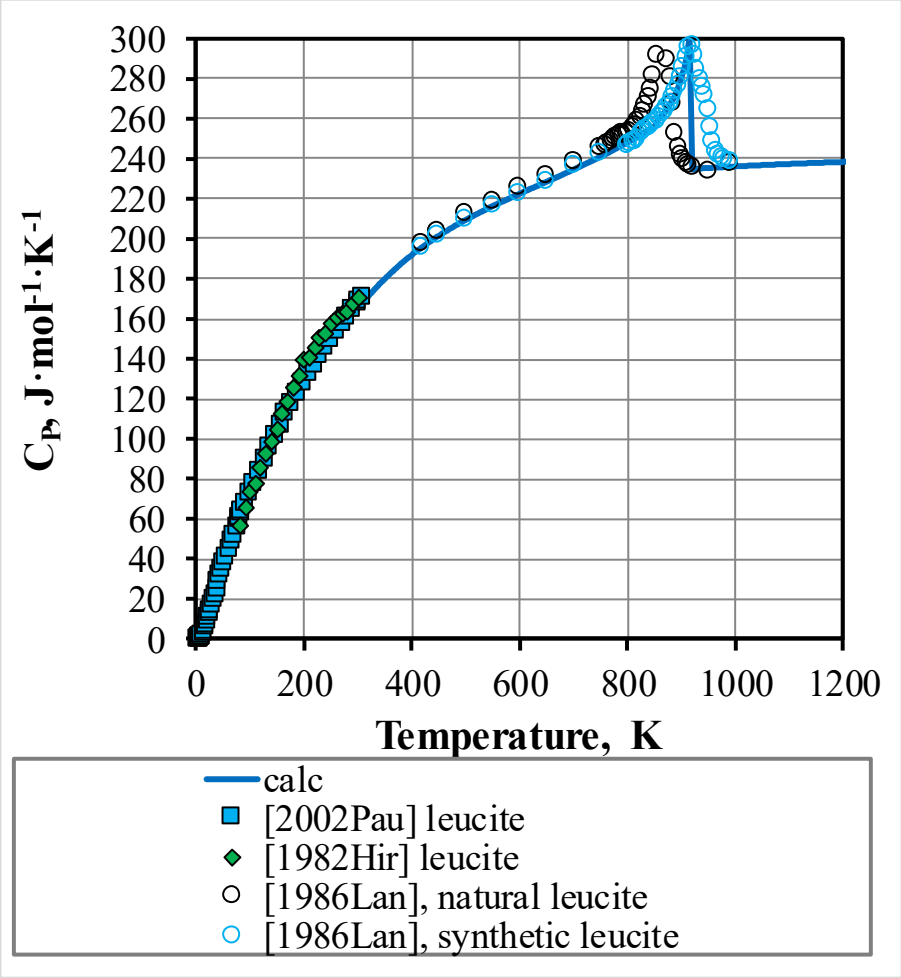

Figure 11.12 The heat capacity of leucite $KAlSi_2O_6$. Experimental data points [385-387] and calculated lines.

Heat content measurements for kaliophilite $KAlSiO_4$ and leucite $KAlSi_2O_6$ were performed by Pankratz [388].

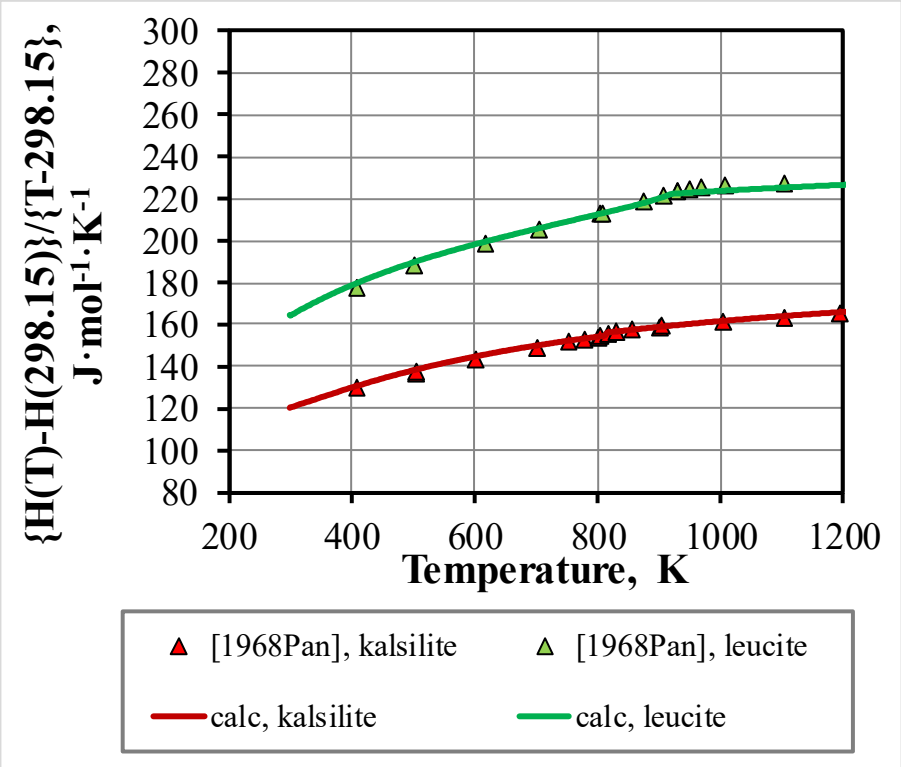

Figure 11.13 The mean heat capacity of kalsilite $KAlSiO_4$ and leucite $KAlSi_2O_6$. Experimental data points [388] and calculated lines.

Low-temperature heat capacities of potassium feldspar in its different structural forms were measured by Openshaw et al. [323], Haselton et al. [324] (adiabatic calorimetry) and by Hemingway et al. [326], Krupka et al. [327] (DSC). Robie et al. [328] measured C_P of $KAlSi_3O_8$ glass. There are no anomalies in the heat capacity curves, and the heat capacities of microcline and sanidine differ only slightly (Figure 11.14).

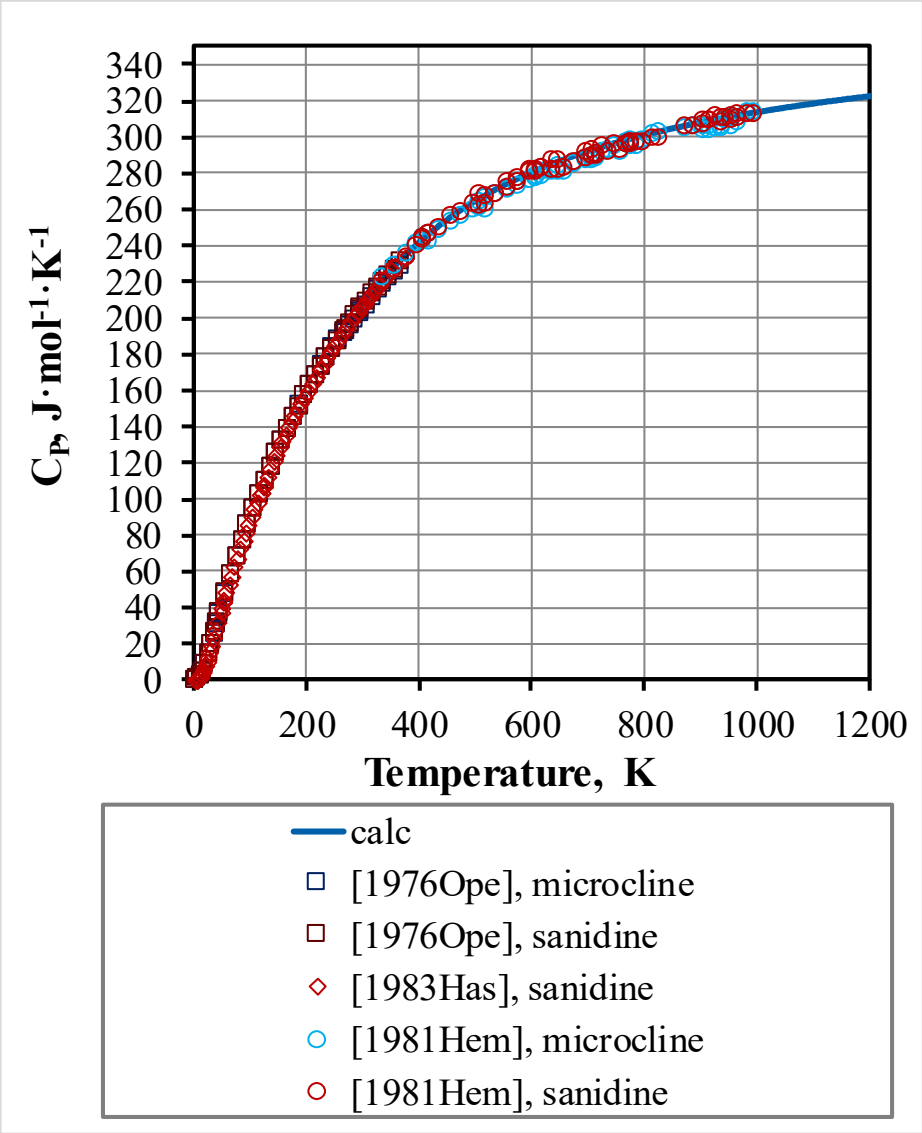

Figure 11.14 The heat capacity of potassium feldspar $KAlSi_3O_8$. Experimental data points [323, 324, 326] and calculated lines.

Heat contents of crystalline and vitreous $KAlSi_3O_8$ were measured by Richet and Bottinga [314], Stebbins et al. [321]. The tabulated heat content for microcline is taken from the compilation of Kelley [389] (Figure 11.15).

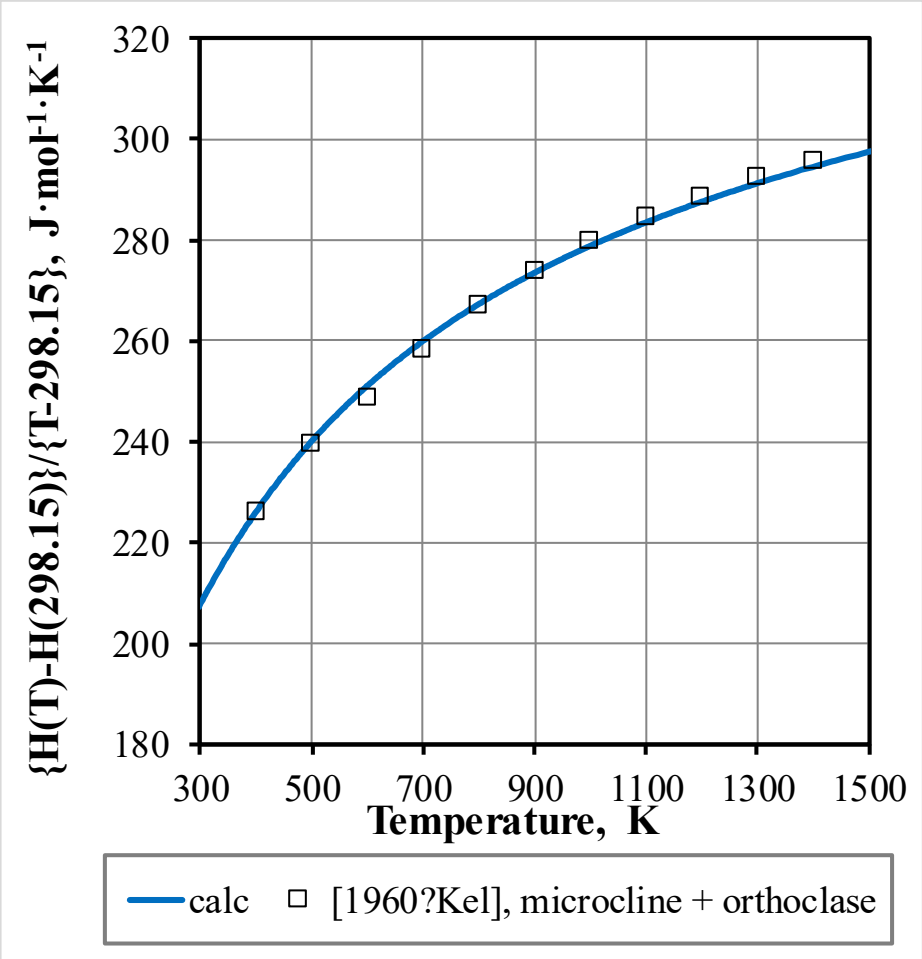

Figure 11.15 The mean heat capacity of $KAlSi_3O_8$. Experimental data points [389] and calculated lines.

11.5 Optimization results

The K_2O-SiO_2 and K_2O-Al_2O_3 binary subsystems were optimized in this work; an optimization of the Al_2O_3-SiO_2 system by Eriksson and Pelton [123] was adopted with a change of Mullite model.

The properties of compounds were adopted from the work by Kim [18] with some changes. Low leucite and microcline modifications were introduced. The transition temperature of leucite is 560°C according to the heat capacity curve (Figure 11.12). The enthalpy of transition is calculated based on the transition temperature and assuming that the entropy of transition is essentially only the configurational contribution due to Al/Si disordering (15.87 $J \cdot mol^{-1} \cdot K^{-1}$). The temperature of

microcline/sanidine transition of 500°C was accepted with the enthalpy of transition of 7.91 $kJ \cdot mol^{-1}$ based on the calorimetric measurements by Waldbaum [307].

The optimization logic in the K_2O-Al_2O_3-SiO_2 system closely follows the one in the Na_2O-Al_2O_3-SiO_2 system. Different types of parameters have corresponding composition areas of influence. The parameters of KAl-Si interaction influence the liquidus in the $KAlO_2$-SiO_2 area. The compositions with K_2O/Al_2O_3 ratio more than one are governed by K-Si(KAl) interactions. If K_2O/Al_2O_3 ratio is less that one (mullite and corundum liquidus), Al-Si(KAl) and KAl-Si(Al) interactions are used.

Excess parameters in high-(Na,K)AlO_2, low-(Na,K)AlO_2 and Nepheline solutions are chosen to reproduce the solubility limits in the $KAlO_2$-SiO_2 section. Unlike the $NaAlO_2$-SiO_2 section, the temperature dependence of the low/high inversion in aluminates is available which allows to chose parameters in high-(Na,K)AlO_2 and low-(Na,K)AlO_2 independently. The optimized parameters are summarized in Table A.13 and Table A.14.

CHAPTER 12 OPTIMIZATION OF THE K_2O-Na_2O-SiO_2 SYSTEM

12.1 Phase diagram

The phase diagram of the Na_2O-K_2O-SiO_2 system was studied in an early work of Kracek [390]. Liquidus temperatures were measured by the quenching method, possible alkali losses were controlled. Compositions from metasilicate to disilicate can be easily crystallized; however, specimens with SiO_2 content larger than in disilicates are hard to crystallize. The $Na_2Si_2O_5$-$K_2Si_2O_5$-SiO_2 eutectic was especially hard to observe. Kracek did not report any ternary compounds. There are three binary systems within the ternary system: Na_2SiO_3-K_2SiO_3, $Na_2Si_2O_5$-$K_2Si_2O_5$, Na_2SiO_3-$K_2Si_2O_5$. The liquidus slopes in the $Na_2Si_2O_5$-$K_2Si_2O_5$ system exhibit breaks at 742°C for $Na_2Si_2O_5$ and 920°C for $K_2Si_2O_5$. In the binary Na_2SiO_3-SiO_2 and K_2SiO_3-SiO_2 systems, similar breaks are observed at 706°C on the Na_2O side and 768°C on the SiO_2 side for $Na_2Si_2O_5$ and at 814°C on the K_2O side and 993°C on the SiO_2 side for $K_2Si_2O_5$. This effect was explained by limited solid solutions of $Na_2Si_2O_5$ with SiO_2 and Na_2O and $K_2Si_2O_5$ with SiO_2 and K_2O, correspondingly.

A later study by Schairer et al. [391] admits that there is a solid solution between sodium and potassium disilicates. $KNaSi_2O_5$ compound was found and it is apparently a part of the solid solution series. However, the network topology of an intermediate disilicate $K_{1.33}Na_{0.67}Si_2O_5$ studied by Spek and De Jong [392] is different from the end-member disilicates. Disilicate phase transitions observed in the binary systems were followed in the ternary system.

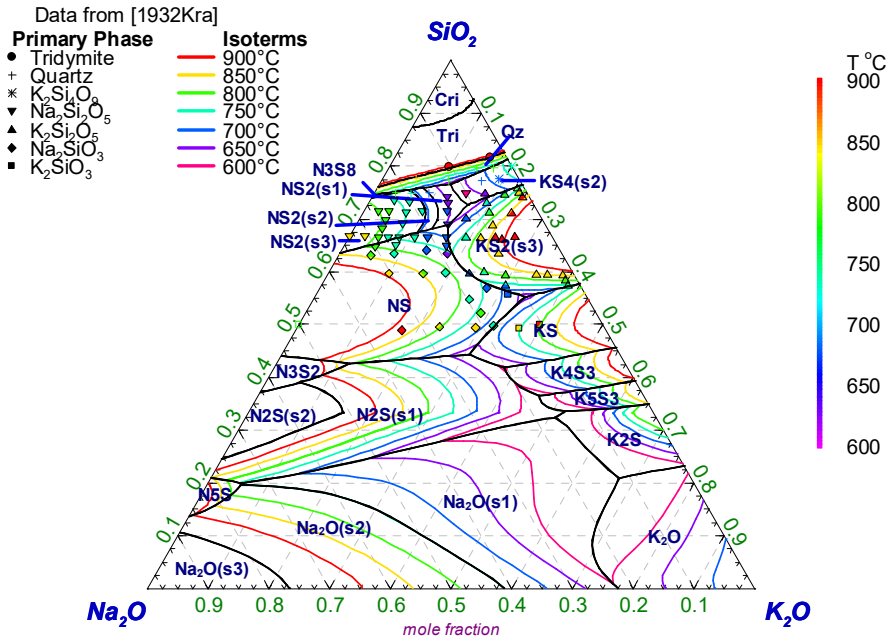

Figure 12.1 Liquidus projection in the Na_2O-K_2O-SiO_2 system. Isotherms from 600° to 900°C. Experimental points [390] and calculated lines.

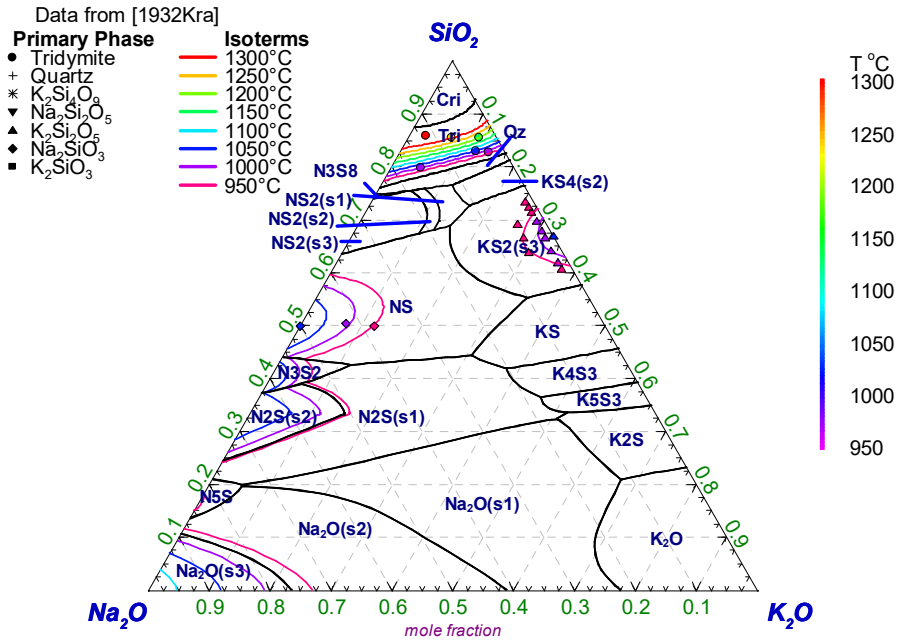

Figure 12.2 Liquidus projection in the Na_2O-K_2O-SiO_2 system. Isotherms from 950° to 1300°C. Experimental points [390] and calculated lines.

Liquidus projections in the system are shown in Figure 12.1-Figure 12.2 in different temperature intervals.

Two sections with constant silica content are presented in Figure 12.3.

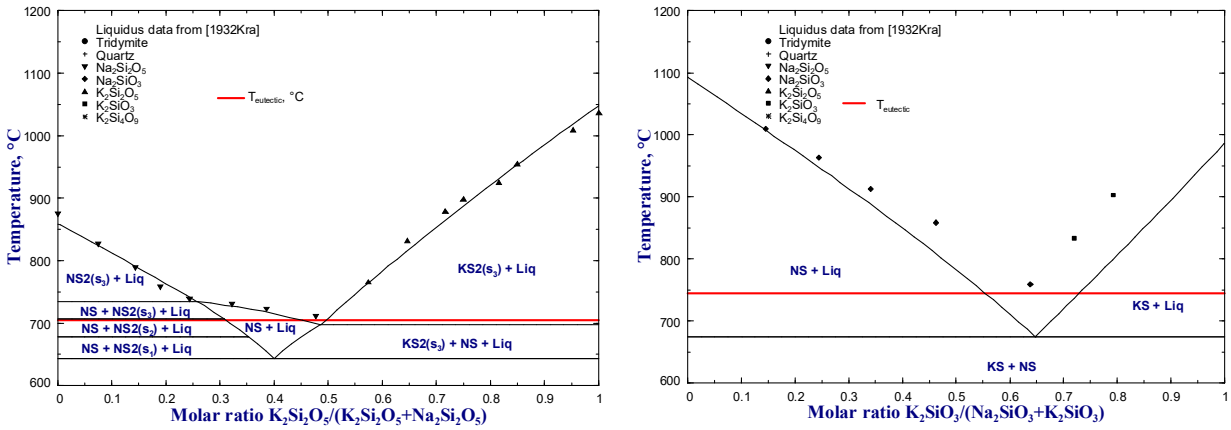

(***a***) (***b***)

Figure 12.3 Phase diagrams in the disilicate (***a***) and metasilicate (***b***) sections of the K_2O-Na_2O-SiO_2 system. Experimental points [390] and calculated lines.

Based on the physical sense, the K_2O-Na_2O-SiO_2 system must be almost ideal because of strong chemical similarity of sodium and potassium. Liquidi in near-ideal systems do not exhibit strong curvature. Keeping this in mind, K_2SiO_3 liquidus in Figure 12.3 (***b***) does not correspond well to the melting point of K_2SiO_3. K_2SiO_3 liquidus points are also off the calculated isotherms in Figure 12.1. An experimental uncertainly in the determination of K_2SiO_3 liquidus in the original paper was assumed; however, it is hard to tell why this discrepancy exists only for K_2SiO_3. It is probable that a complete reaction between K_2CO_3 and SiO_2 with formation of K_2SiO_3 requires more time or higher annealing temperatures.

Invariant points in the K_2O-Na_2O-SiO_2 system are listed in Table 12.1.

Table 12.1 Invariant equilibria in the K_2O-Na_2O-SiO_2 system. The calculated values are shown in bold.

Solid phases	T, °C	Liquid composition, mol%		
		SiO_2	Na_2O	K_2O
KS-NS-KS2	645 [390] **638**	56.63 **55.34**	13.33 **10.05**	30.05 **34.61**
KS2-NS-NS2	665 [390] **647**	63.58 **68.92**	18.47 **15.96**	17.95 **15.12**
KS2-NS2-Qz	540 [390] **500**	75.47 **77.15**	8.48 **5.67**	16.05 **17.18**
NS-KS	745 [390] **675**	50.02 **50.00**	17.32 **17.63**	32.66 **32.37**
NS2-KS2	705 [390] **650**	66.73 **66.67**	16.04 **19.17**	17.24 **14.17**
KS2-NS	680 [390] **770**	60.29 **60.75**	19.16 **17.75**	20.55 **21.50**

The eutectic point KS2-NS2-Qz by Kracek [390] is metastable because the calculated diagram (Figure 12.1-Figure 12.2) exhibits KS4 field where the eutectic point is supposed to be. The same applies to NS2-KS2 eutectic. The reported temperature of 705°C lies close to the NS-KS2 eutectic in the NS2-KS2 section (Figure 12.3, (***a***)).

12.2 Calorimetry data

Rogez and Mathieu [200] performed solution calorimetry of K_2O-Na_2O-SiO_2 glasses in $2PbO{\cdot}B_2O_3$ at 600°C. The compositions were chosen along joins with a constant $K_2O/(Na_2O+K_2O)$ ratio: 0, 1/3, 2/3 and 1. The raw dataset was used in this work for interpolation of the heat of solution in the joins with a constant silica content using a cubic spline interpolation.

Ion exchange experiments with $(Na,K)_2O{\cdot}5SiO_2$ and $(Na,K)_2O{\cdot}6SiO_2$ glasses were performed by Wakabayashi [393]. Molten nitrate mixtures were used as the exchange media, the temperature of experiment was 500°C. The data on the exchange curves was recalculated into the enthalpy of mixing of glasses with an assumption that these glasses have a regular solution behaviour. Similar experiments were carried out by Lezzi and Tomozawa [394]. These studies were performed in order to elucidate the mixed alkali effect in glasses. The available experimental data are summarized in Figure 12.4.

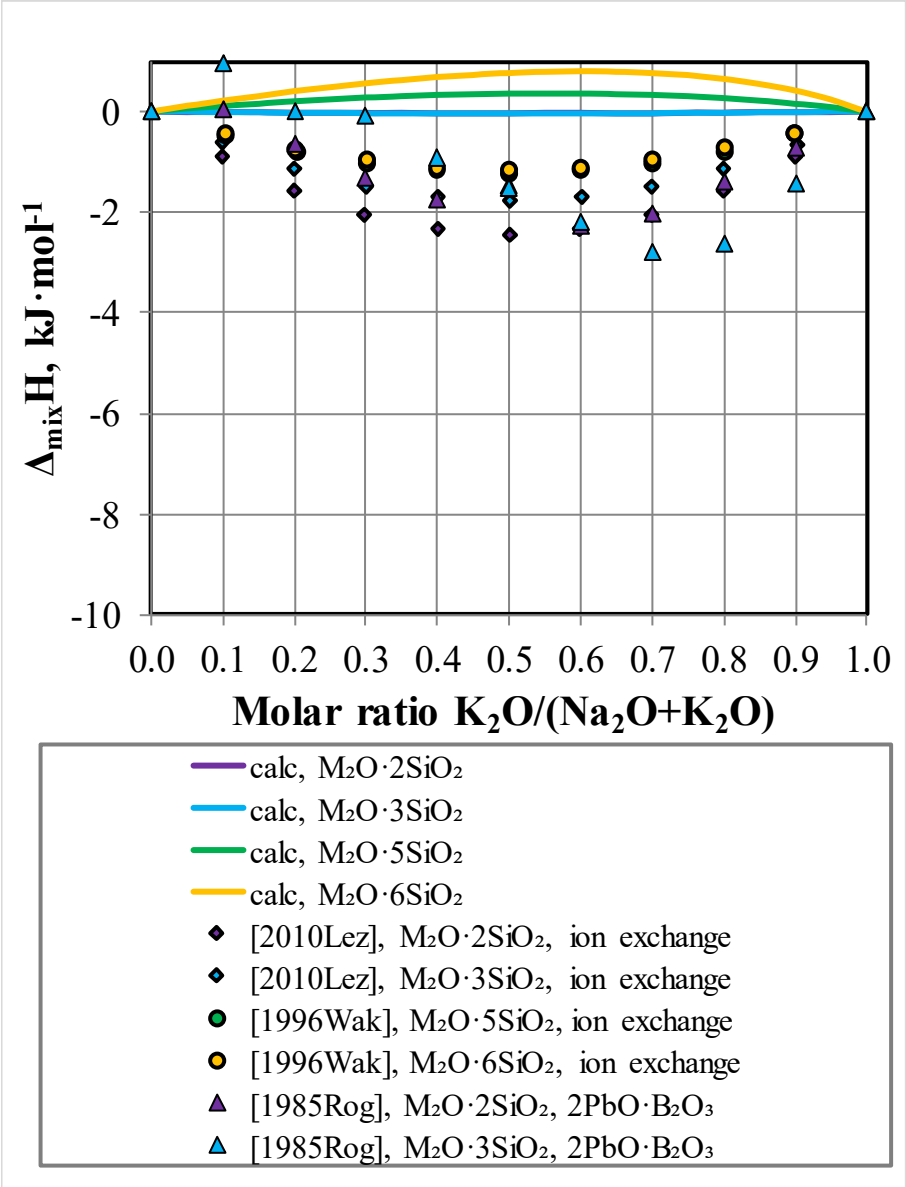

Figure 12.4 The enthalpy of mixing at 500°C for sections with a constant silica content of the K_2O-Na_2O-SiO_2 system. Experimental points [393, 394] and calculated lines.

12.3 Activity data

Chastel et al. [336] measured partial pressures of Na and K over K_2O-Na_2O-SiO_2 melts for compositions with constant silica content by means of the Knudsen cell mass spectroscopy. It is assumed that sodium and potassium oxides decompose into gaseous Na, K and O_2 and the reported values of $\ln(I(K)/I(Na))$ can be recalculated into $\ln(a(K_2O)/a(Na_2O))$ using the following relations:

$$P(\mathrm{Na}) = c \cdot I(\mathrm{Na}) \tag{116}$$

$$P(\mathrm{K}) = c \cdot I(\mathrm{K}) \tag{117}$$

$$P(\mathrm{K})/P(\mathrm{Na}) = I(\mathrm{K})/I(\mathrm{Na}) \tag{118}$$

$$K_{\mathrm{Na,K}} = \frac{P(\mathrm{Na,K})^2 \cdot p(\mathrm{O_2})^{1/2}}{a(\mathrm{Na_2O,K_2O})} \tag{119}$$

$$\frac{K_{\mathrm{K}}}{K_{\mathrm{Na}}} = \frac{a(\mathrm{K_2O})}{a(\mathrm{Na_2O})} \cdot \frac{P(\mathrm{Na})^2}{P(\mathrm{K})^2} = \frac{1}{1} \cdot \frac{P(\mathrm{Na})_0^2}{P(\mathrm{K})_0^2} \tag{120}$$

$$\ln \frac{a(\mathrm{K_2O})}{a(\mathrm{Na_2O})} = 2\left[\ln \frac{I(\mathrm{K})}{I(\mathrm{Na})} - \ln P(\mathrm{K})_0 + \ln P(\mathrm{Na})_0 \right] \tag{121}$$

where $P(\mathrm{Na})_0$ and $P(\mathrm{K})_0$ are the partial pressures of sodium and potassium over pure liquid Na_2O and K_2O which were calculated in *FactSage*. The recalculated data were plotted in form of isotherms and temperature dependencies for fixed compositions in Figure 12.5 and Figure 12.6, correspondingly.

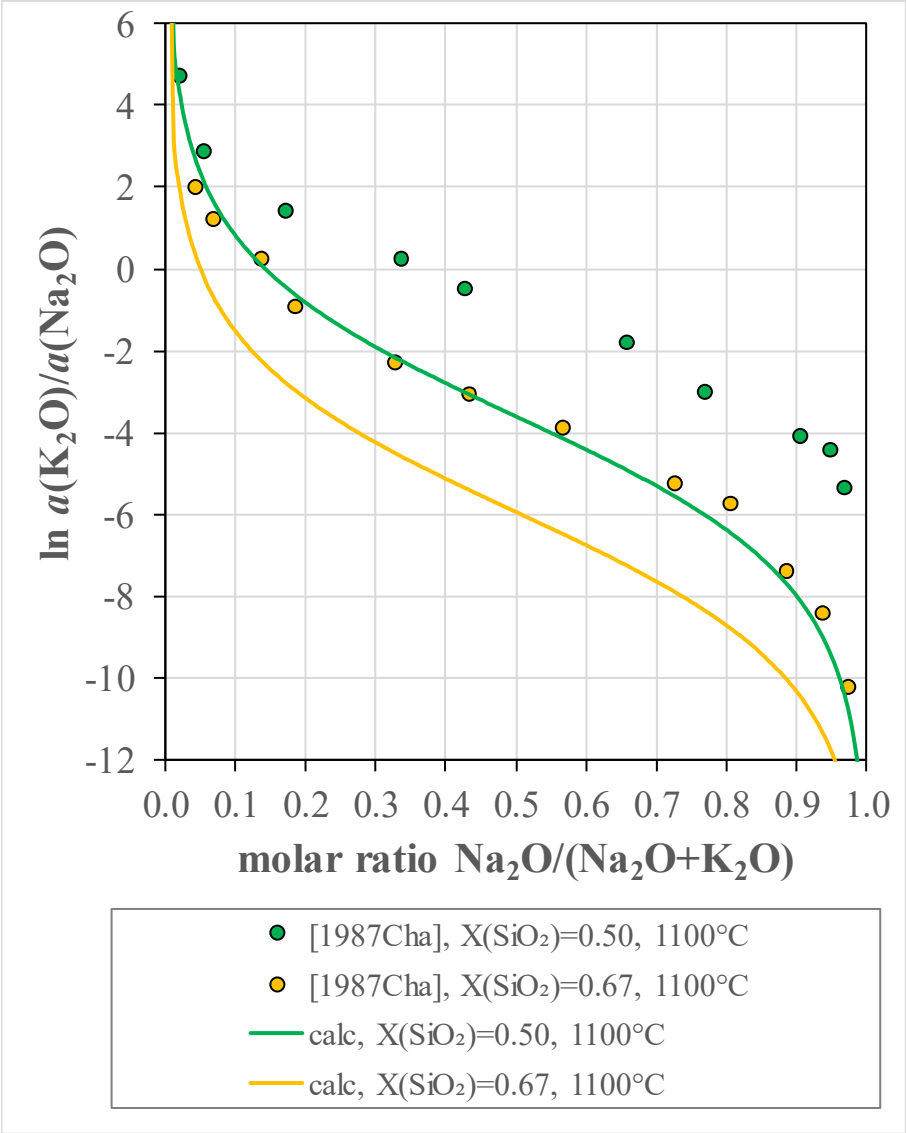

Figure 12.5 Isothermal activity ratio of alkali oxides in the K_2O-Na_2O-SiO_2 system. Experimental points measured by mass spectrometry [336] and calculated lines.

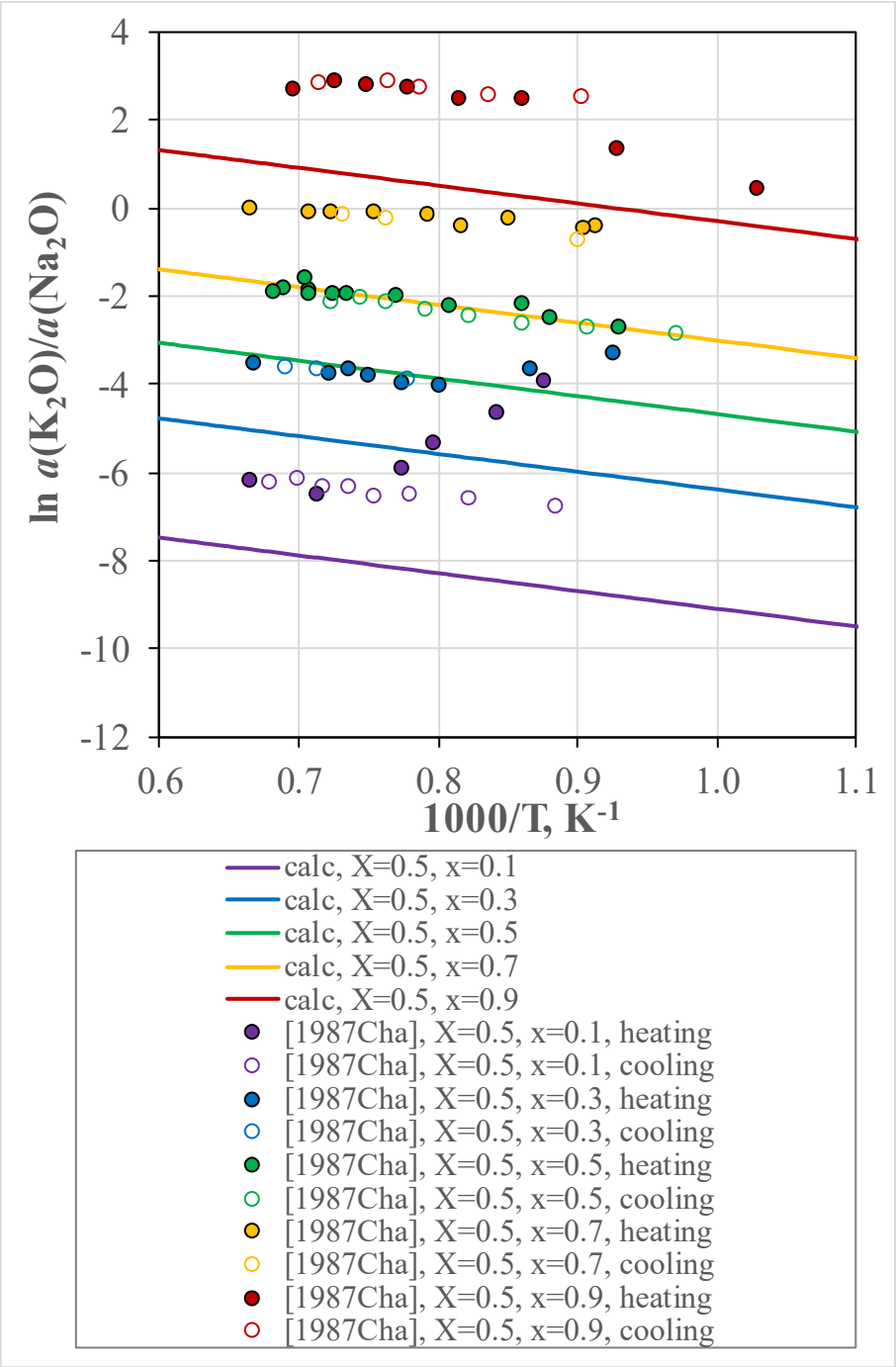
4
2
0
-2
-4
-6
-8
-10
-12
0.6
0.7
0.8
0.9
1.0
1.1
ln a(K2O)/a(Na2O)
1000/T, K-1
calc, X=0.5, x=0.1
calc, X=0.5, x=0.3
calc, X=0.5, x=0.5
calc, X=0.5, x=0.7
calc, X=0.5, x=0.9
[1987Cha], X=0.5, x=0.1, heating
[1987Cha], X=0.5, x=0.1, cooling
[1987Cha], X=0.5, x=0.3, heating
[1987Cha], X=0.5, x=0.3, cooling
[1987Cha], X=0.5, x=0.5, heating
[1987Cha], X=0.5, x=0.5, cooling
[1987Cha], X=0.5, x=0.7, heating
[1987Cha], X=0.5, x=0.7, cooling
[1987Cha], X=0.5, x=0.9, heating
[1987Cha], X=0.5, x=0.9, cooling

(a)

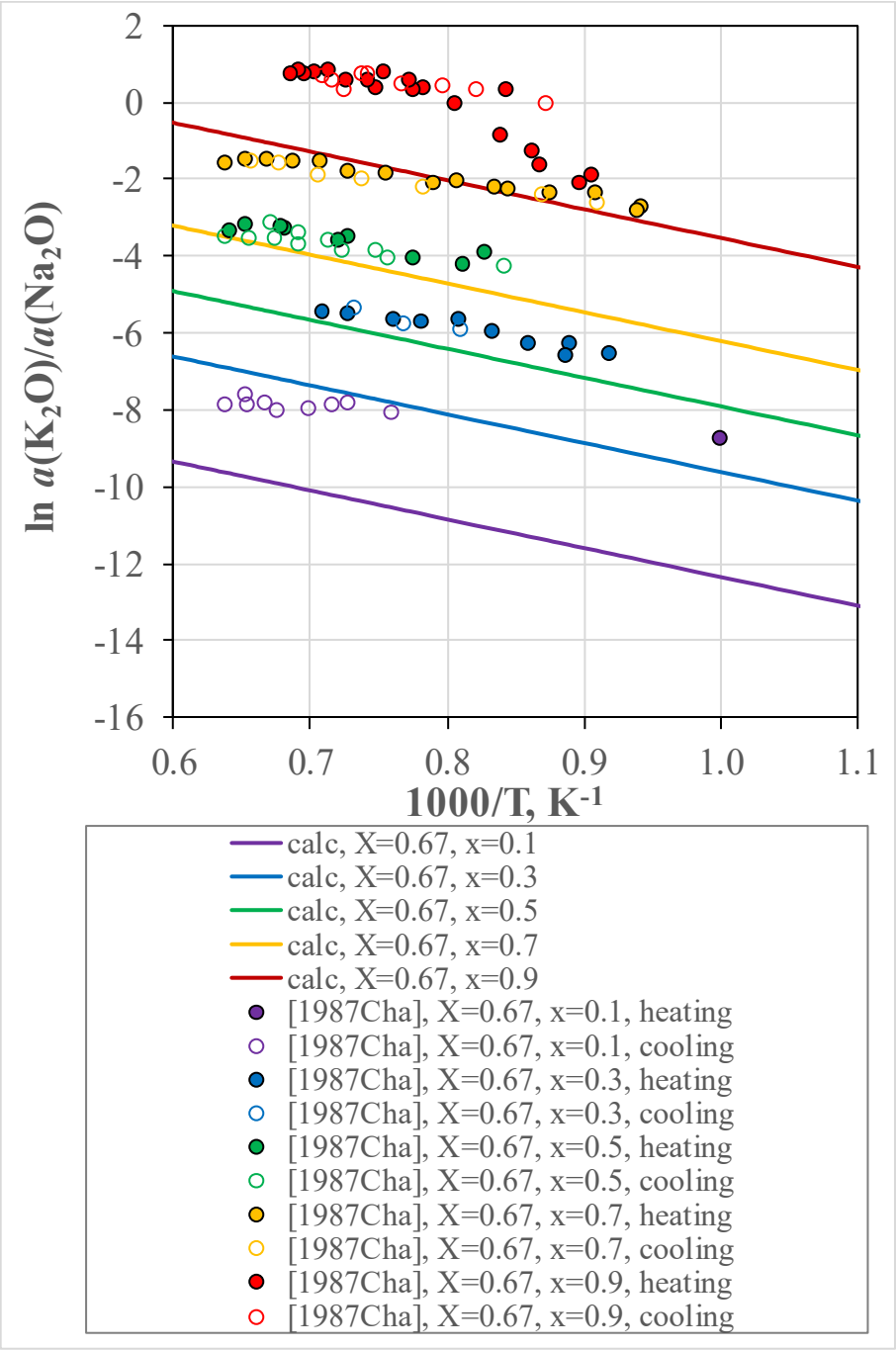
2
0
-2
-4
-6
-8
-10
-12
-14
-16
0.6
0.7
0.8
0.9
1.0
1.1
ln a(K2O)/a(Na2O)
1000/T, K-1
calc, X=0.67, x=0.1
calc, X=0.67, x=0.3
calc, X=0.67, x=0.5
calc, X=0.67, x=0.7
calc, X=0.67, x=0.9
[1987Cha], X=0.67, x=0.1, heating
[1987Cha], X=0.67, x=0.1, cooling
[1987Cha], X=0.67, x=0.3, heating
[1987Cha], X=0.67, x=0.3, cooling
[1987Cha], X=0.67, x=0.5, heating
[1987Cha], X=0.67, x=0.5, cooling
[1987Cha], X=0.67, x=0.7, heating
[1987Cha], X=0.67, x=0.7, cooling
[1987Cha], X=0.67, x=0.9, heating
[1987Cha], X=0.67, x=0.9, cooling

(b)

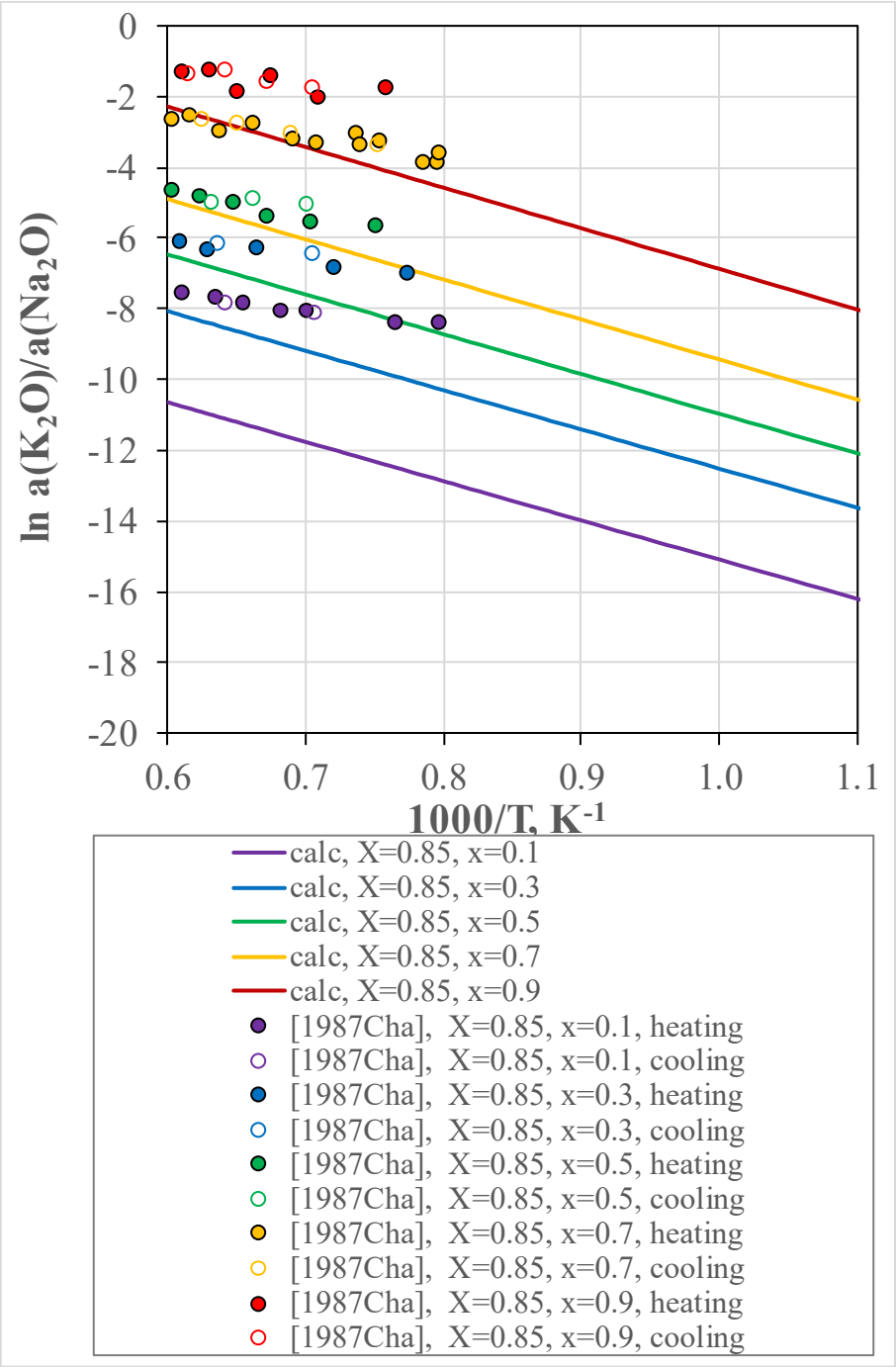

(c)

Figure 12.6 Alkali oxide activity ratios at fixed composition versus the inverse temperature in the series $XSiO_2$ + (1-X)[(1-x)Na_2O + xK_2O]. Experimental points measured by mass spectrometry [336] and calculated lines.

The activity ratios depicted in Figure 12.5-Figure 12.6 show a systematic deviation from the experimental points. There is no simple combination of excess parameters in the K_2O-Na_2O-SiO_2 that would lift the calculated curves; the excess parameters rather change the slope of the curves. As the activities of K_2O and Na_2O are reproduced in the binary systems, we can suppose that there is a systematic error in the data by Chastel et al. [336].

12.4 Optimization results

The Na_2O-SiO_2 and K_2O-SiO_2 subsystems were optimized in this work. There are no experimental data available on the Na_2O-K_2O system. Due to the chemical similarity between Na_2O and K_2O (chemically similar components usually do not have large enthalpies of mixing), the best approximation would be to assume the Na_2O-K_2O system ideal.

The liquid phase in the system was considered ideal which gives an acceptable reproduction of the liquidus. From Figure 12.1, (***a***) and Figure 12.3, (***b***) it can be seen that there are experimental discrepancies in K_2SiO_3 liquidus. Although there are indications that solid solutions of meta and disilicates might exist, their extent of mutual solubility is unclear. The optimization by Kim [18] provides the solid solutions but they are physically inconsistent. It is known that in a series of limited solid solutions where ions of different size exchange, the solution from the side of the end-member with bigger cations (in our case, K_2SiO_3) has a higher solubility of the counterpart end-member. It is related to the asymmetry of a chemical bond; compression of the chemical bonds appearing at a substitution site where a foreign ion is bigger than the host is much less energetically favourable than in the case of a bond extension when a foreign ion is smaller that the host. In the optimization by Kim [18], the solid solution from the Na_2SiO_3 side is larger than the one from the K_2SiO_3 side which contradicts the general rule. It appears that the solid solutions were introduced to improve the quality of fit, but they were not included in the current work to avoid the physical inconsistency.

CHAPTER 13 OPTIMIZATION OF THE K_2O-Na_2O-Al_2O_3-SiO_2 SYSTEM

13.1 Phase diagram

A preliminary $NaAlSiO_4$-$KAlSiO_4$-SiO_2 phase diagram was first published by Bowen and Schairer [395] and later, Schairer [396] gave some additional information about the earlier work. Several solid solutions were reported: carnegieite and nepheline $NaAlSiO_4$ dissolving $KAlSiO_4$ and SiO_2, binary alkali feldspar $NaAlSi_3O_8$-$KAlSi_3O_8$. Bowen and Schairer do not show the field of the orthorhombic $KAlSiO_4$ (kalsilite) as they lacked measurements in this corner. They also remark that there are no discontinuities in the fusion surface between $NaAlSiO_4$ and $KAlSiO_4$ and that there should be a continuous solid solution between nepheline and kalsilite, at least at elevated temperatures. Based on their diagram, Bowen and Schairer draw a conclusion that the majority of natural nepheline samples must crystallize from a liquid with the composition nearby the ternary invariant point Ne-Lc-Fds which explains a small compositional scatter of natural nephelines.

Schairer [396] gives a revised phase diagram of the system (Figure 13.1). The compositions close to the eutectic line Fds-Tri are given but no quenching results are available because dry glasses did not crystallize even during up to 5 years of annealing. Some liquidus temperatures from the work by Bowen and Schairer [395] were lowered at those compositions as they were not annealed for sufficient time in the first study. The system is split into two independent parts by the alkali feldspar join. The compositions richer in silica approach compositions of simplified granitic rock magmas (forming feldspar-silica assemblages) and those poorer approximate simplified alkaline rock magmas which give nepheline as a final crystallization product.

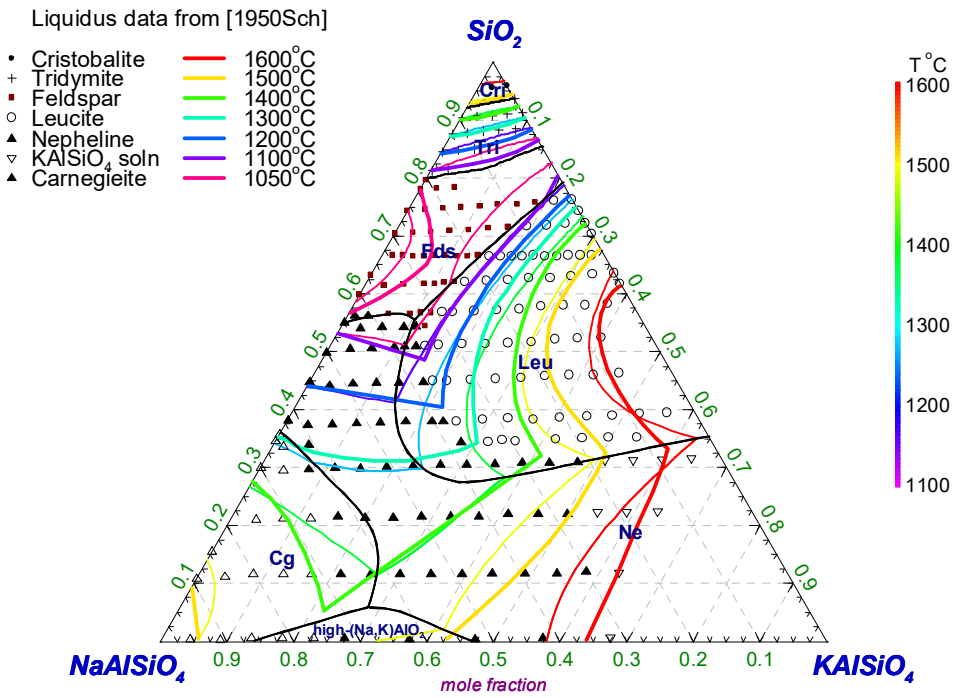

Figure 13.1 Liquidus projection in the SiO_2-$NaAlSiO_4$-$KAlSiO_4$ section of the Na_2O-K_2O-Al_2O_3-SiO_2 system. Experimental [396] (thick curves) and calculated isotherms and univariant lines.

Bowen [50] determined liquidus relations in the section $NaAlSiO_4$-$KAlSiO_4$ using the quenching method. He noted that it was difficult to prepare a pure $KAlSiO_4$ sample due to its elevated melting temperature and volatilization losses of potassium. The presence of the hexagonal and with orthorhombic modification was confirmed; the transition point was 1540°C. An optical identification of the solid phases was complicated as nepheline and kalsilite have similar optical properties. A complete solid solution between $NaAlSiO_4$ and $KAlSiO_4$ end-members was assumed. An eutectic between carnegieite and $KAlSiO_4$ exists at 1404°C.

Subsolidus phase relations in the $NaAlSiO_4$-$KAlSiO_4$ section were investigated in more detail by Tuttle and Smith [43]. They reported two stable $KAlSiO_4$ modifications and one metastable, kaliophilite. A new phase, tetrakalsilite, is produced in mixtures heated at high temperatures in compositions near $Na_{0.25}K_{0.75}AlSiO_4$. Two solid solutions of $NaAlSiO_4$ in kalsilite (hexagonal low-temperature) and in high-temperature $KAlSiO_4$ are found in the K-rich end of the phase diagram. Kalsilite takes up to 20% of nepheline. A nepheline with a mixed $Na_{0.75}K_{0.25}AlSiO_4$ composition was believed to be a separate compound.

Later, it was shown that nepheline and kalsilite form an asymmetric miscibility gap where the sodium-rich side is approximately of $Na_{0.75}K_{0.25}AlSiO_4$ composition [41]. It is related to a peculiarity of the nepheline crystal structure where two types of cationic sites of different size are present. The larger sites (one-fourth of the total number of sites) fit potassium cations very well while the smaller ones are more suitable for sodium cations. Due to this fact, $Na_{0.75}K_{0.25}AlSiO_4$ is a nepheline composition with increased stability. Kalsilite, however, has only one type of cationic sites [44]. The miscibility gap between nepheline and kalsilite was studied by Ferry and Blencoe under different pressures [41].

Energy losses of fitting a small Na^+ in the bigger cavity are so significant, that the pure $NaAlSiO_4$ cannot be found in nature. It contains either some potassium or excess silica. The excess silica creates vacancies in the bigger sites according to the substitution mechanism:

$$Na^{+}+Al^{3+} = Va+Si^{4+} \tag{122}$$

and also increases the stability of nepheline structure.

Kalsilite, however, has only a moderate ability to incorporate excess silica in its structure. Leucite was found in some of the runs [43].

A pure synthetic nepheline of the $NaAlSiO_4$ composition undergoes polymorphic transformations at low temperatures [39]. They are caused by collapsing of the big sites around smaller Na^+ cations and overall decrease of the structure symmetry. Henderson and Roux [39] observed these transitions in sub potassic nephelines. K^+ cations quickly stabilize the high-temperature structure and starting at a certain $KAlSiO_4$ content, these transitions disappear (see Figure 13.2).

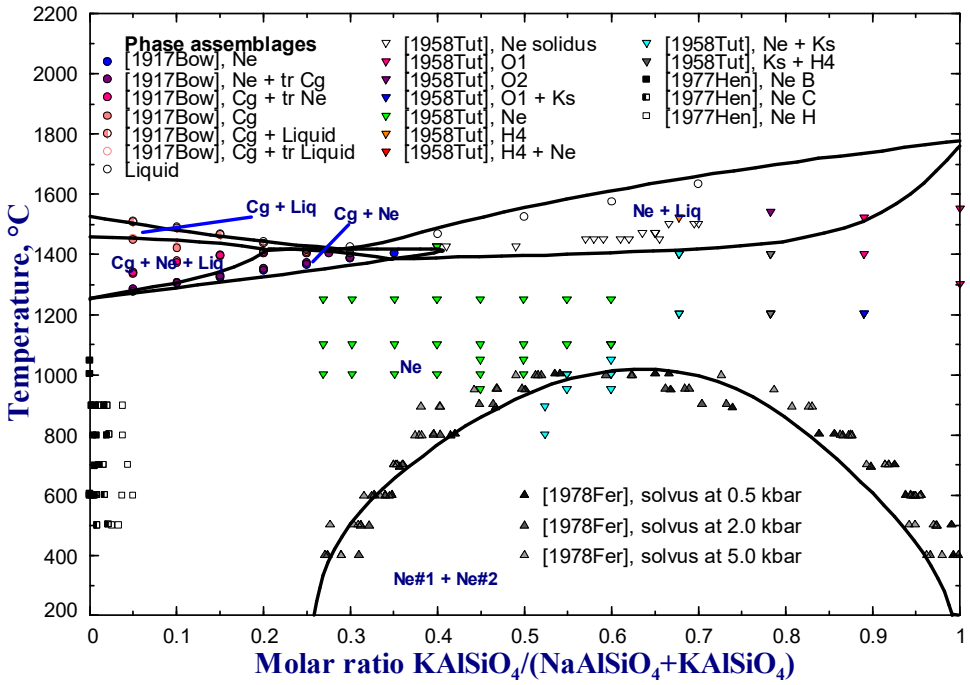

Figure 13.2 Phase diagram of the $NaAlSiO_4$-$KAlSiO_4$ section in the Na_2O-K_2O-Al_2O_3-SiO_2 system. Experimental points [39, 41, 43, 50] and calculated lines.

The effect of excess silica on the nepheline-kalsilite immiscibility was studied by Hovis et al. and Hovis and Crelling [40, 44] (Figure 13.3).

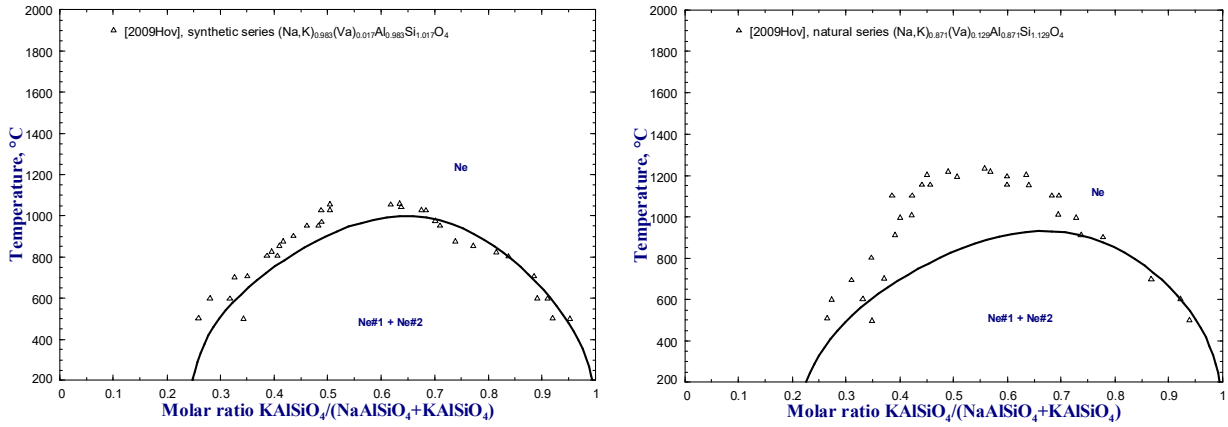

(*a*) (*b*)

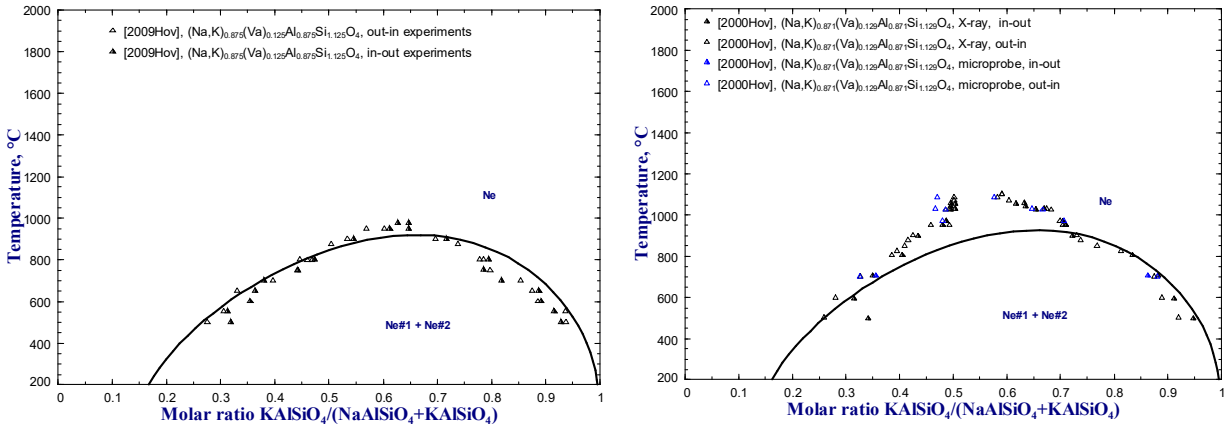

(***c***) (***d***)

Figure 13.3 Nepheline miscibility gap in $NaAlSiO_4$-$KAlSiO_4$ series with different amounts of excess silica: 3.34 mol% (***a***), 9.87 mol% (***b***), 22.22 mol% (***c***), 22.85 mol% (***d***). Experimental points [40, 44] and calculated lines.

Bowen and Schairer [395] published a preliminary report on different parts of the $NaAlSiO_4$-$KAlSiO_4$-SiO_2 system and, in particular, on the alkali feldspar join $NaAlSi_3O_8$-$KAlSi_3O_8$ (Figure 13.4). The end-members exhibit different melting behaviours, albite melts congruently and potassium feldspar decomposes into leucite and liquid. Alkali feldspars with less than 53 mol%Ab form leucite as well.

Schairer [396] also studied the liquidus in the alkali feldspar section $NaAlSi_3O_8$-$KAlSi_3O_8$. This work revises the results obtained by Schairer and Bowen [395]; more compositions had been investigated since the first work. Due to crystallization difficulties, it was impossible to clarify the composition of the feldspar, coexisting with leucite and liquid. It was noted that all feldspar compositions and especially those with more than 50 mol% $KAlSi_3O_8$ give viscous melts which are hard to crystallize. It was also impossible to determine the temperature of the beginning of melting as all mixtures did not crystallize completely upon cooling. Even if crystallized hydrothermally, crystals required annealing at a constant temperature during several weeks to show any signs of melting.

Tuttle and Bowen [397] measured the solvus under hydrothermal conditions using natural samples as a starting material. Solvi for disordered and ordered series of feldspars are available.

Orville [398] determined the solvus using a saline media. Synthetic feldspar materials crystallized hydrothermally from glass were used in the experiments. Experiments were performed with both single- and two-feldspar starting assemblages.

Luth and Tuttle [399, 400] investigated the possibility of deviation of feldspar stoichiometric ratio from the ideal (1:1:6) and its influence on the solvus. To do so, for every fixed Na_2O/K_2O ratio they prepared gels with 3 wt% excess of SiO_2, Al_2O_3, $NaAlSiO_4$+$KAlSiO_4$ and $Na_2Si_2O_5$+$K_2Si_2O_5$ in addition to a stoichiometric $NaAlSi_3O_8$-$KAlSi_3O_8$. An X-ray analysis of crystallized samples was performed. Stoichiometric, persiliceous and peraluminous solvi were plotted at different pressures. A discontinuity in the K-limb was found but it was not confirmed by later independent studies [401].

Goldsmith and Newton [401] studied the feldspar solvus in the temperature range from 300° to 600°C at different pressures of water vapour. It is stated that in the presence of water and under high pressures, the equilibrium is attained fast enough for laboratory measurements. The solvus compositions were bracketed by independent unmixing and homogenisation experiments. There is a clear dependency between the solvus shape and the pressure but the 1 atm solvus can be easily extrapolated from the experimental data. Goldsmith and Newton did not observe any significant difference in the solvus position for completely disordered and partially ordered feldspars; neither did they see a difference for initial compositions with excess silica or alumina. Therefore, they assume that there is no evidence of departure of feldspar compositions from the binary join. Probably, different solvi for peralkaline and peraluminous samples appear due to different rates of equilibration [401, 402]. Peralkaline compositions attain equilibrium easier because of an excess amount of alkali ions in the fluid media.

Lagache and Weisbrod [403] investigated the alkali feldspar solvus by equilibrating feldspars in a NaCl-KCl-H_2O brine under pressures from 0.2 to 2 kbar. No effect of the pressure was detected. They mention that in the majority of runs under hydrothermal conditions gels crystallize into completely disordered feldspars (high albite-sanidine). However, below 500°C and especially in the presence of excess SiO_2, partially disordered feldspars can form during long runs.

Yund and Tullis [404] stress the importance of the elastic strain for the alkali feldspar solvus. So, if a fine mixture of sodium and potassium end-members is equilibrated or a gel is crystallized below

the solvus, the alkali ions would redistribute according to the strain-free solvus. Subsolidus exsolution of alkali feldspars results in an intimate intergrowth of sodic and potassic feldspars, called perthites, with various textures on a wide range of scales. The majority of the works dealing with the alkali feldspar solvus are performed under conditions producing a strain-free solvus. However, Yund and Tullis claim that the equilibration times for a strained solvus must be shorter because the non-homogeneity areas are in the order of a few hundred Ångstrøms and the diffusion of alkali ions is facilitated by the absence of grain boundaries. For example, the coherent solvus was measured by Yund et al. [405] for the maximum microcline-low albite series (partially ordered).

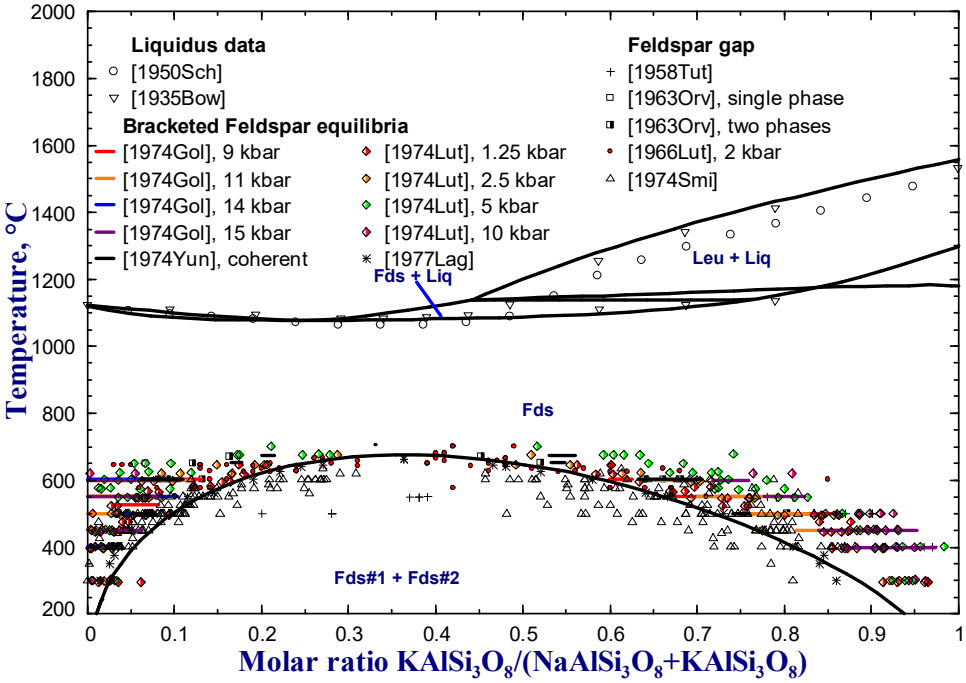

Figure 13.4 Phase diagram of the $NaAlSi_3O_8$-$KAlSi_3O_8$ section in the Na_2O-K_2O-Al_2O_3-SiO_2 system. Experimental data [395-403, 405] and calculated lines.

The phase diagram of the pseudo binary join leucite-albite ($KAlSi_2O_6$-$NaAlSi_3O_8$) was studied by Gupta and Edgar [109]. According to their results, leucite is incompatible with albite and the maximum albite content in alkali feldspars coexisting with leucite is 54 mol%. This conclusion has an important meaning for geological applications. The pseudoeutectic point Lc-Fds at $Lc_{41}Ab_{59}$, 1068±5°C is in a good agreement with the extrapolated value based on the phase diagram by Schairer [396]. Leucite dissolves insignificant amounts of albite (apparently, in the form of

$NaAlSi_2O_6$) but the extent of the solid solution does not exceed 5 mol% Ab. The composition of nepheline coexisting with feldspar at 960°C is $Ne_{68}Ks_{30}Qz_2$ (see Figure 13.5).

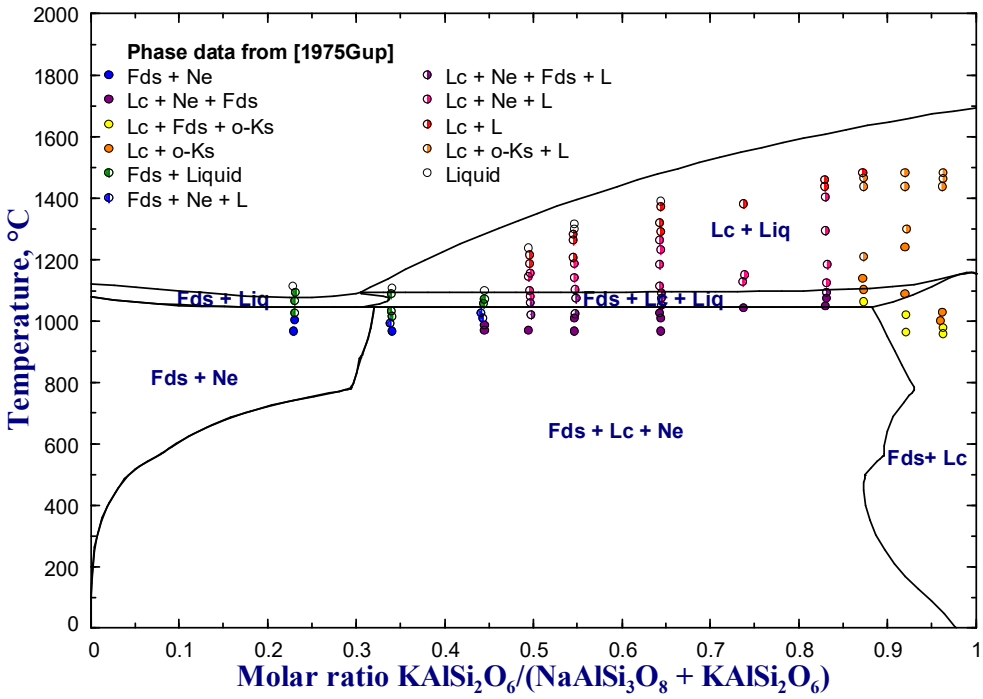

Figure 13.5 Phase diagram of the $NaAlSi_3O_8$-$KAlSi_2O_6$ section in the Na_2O-K_2O-Al_2O_3-SiO_2 system. Experimental data [109] and calculated lines.

The experimental points indicating Lc + o-Ks and Lc + Fds + o-Ks phase assemblages in Figure 13.5 contradict the calculated phase fields. To elucidate this discrepancy, an isothermal section of the $NaAlO_2$-$KAlO_2$-SiO_2 plane at 1200°C was calculated (Figure 13.6). It is seen that the phase fields containing Nepheline solution (which comprises nepheline Ne and kalsilite o-Ks) do not reach the $NaAlSi_3O_8$-$KAlSi_2O_6$ section and cannot possibly be present in Figure 13.5.

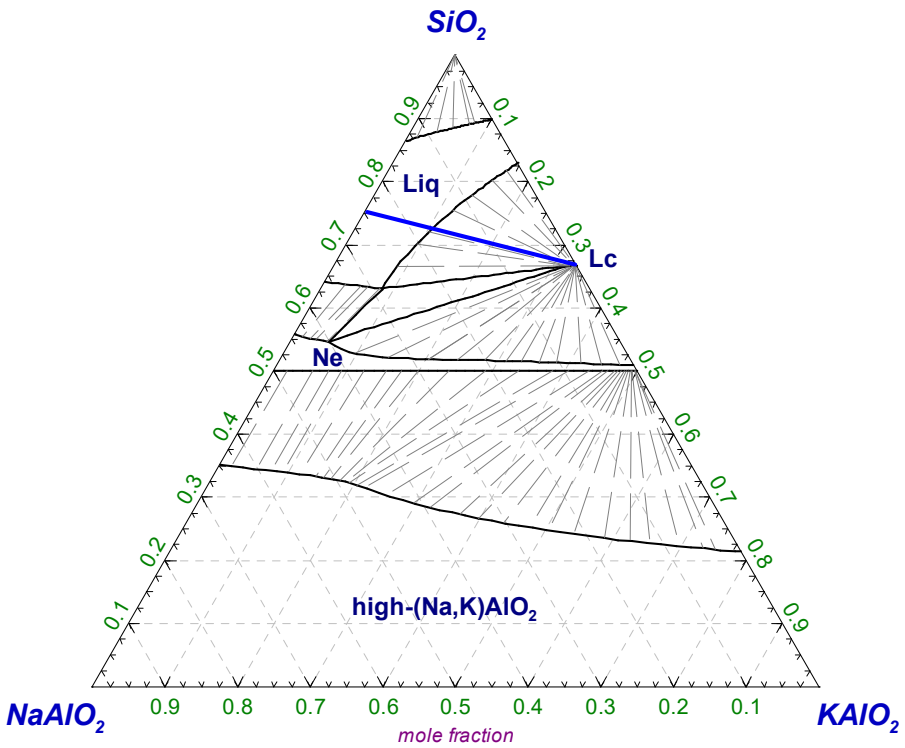

Figure 13.6 Isothermal section of the $NaAlO_2$-$KAlO_2$-SiO_2 plane of the Na_2O-K_2O-Al_2O_3-SiO_2 system at 1200°C showing the coexisting phases. The blue line indicates the $NaAlSi_3O_8$-$KAlSi_2O_6$ section.

The predicted leucite liquidus is higher than the experimental points (Figure 13.5). It is probable that these data are in disagreement with the melting point of leucite in the $KAlO_2$-SiO_2 section (Figure 11.5).

13.2 Calorimetry data

HF solution calorimetry of $NaAlSi_3O_8$-$KAlSi_3O_8$ glasses was performed at 50°C by Hovis [301]. Small negative enthalpies of mixing were obtained. The same section was studied by lead borate solution calorimetry by Brousse et al. [406], Rogez et al. [407] and Chastel et al. [408]. Glasses in the section $Na_{1.6}Al_{1.6}Si_{2.4}O_8$-$K_{1.6}Al_{1.6}Si_{2.4}O_8$ were studied with lead borate solution calorimetry by Hervig and Navrotsky [409]. The enthalpy of mixing of glasses in the $NaAlSi_2O_6$-$KAlSi_2O_6$ section (Figure 13.7) was calculated based on ion exchange data by Lezzi and Tomozawa [410].

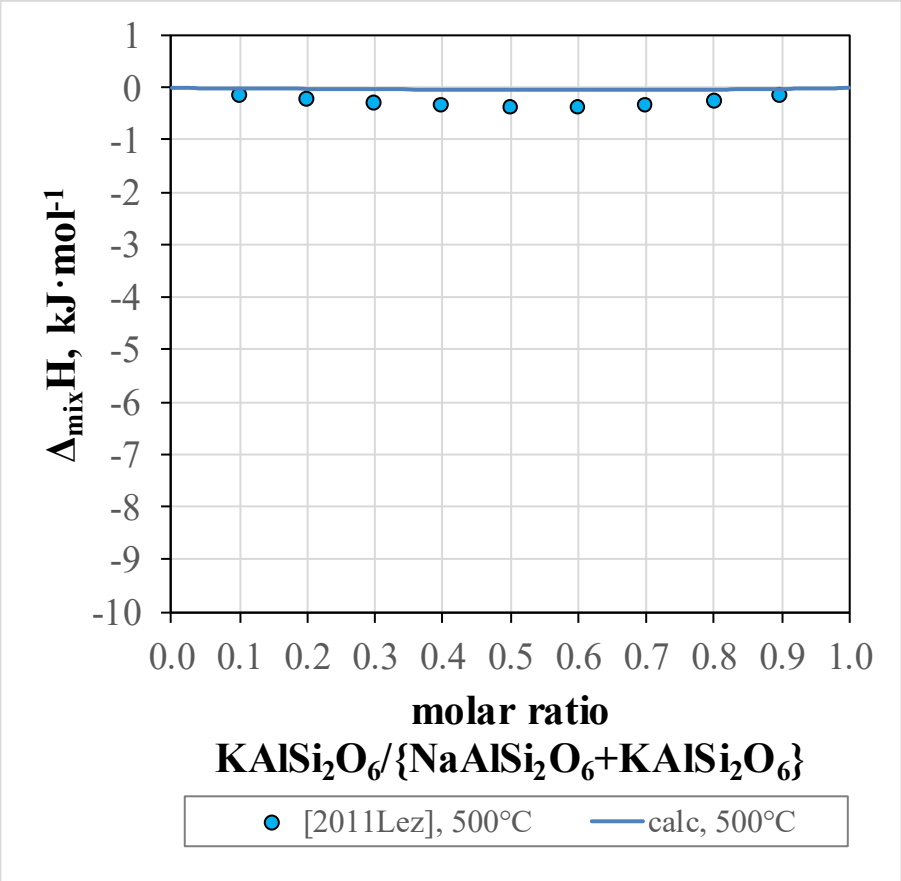

Figure 13.7 The enthalpy of mixing of the liquid in the $NaAlSi_2O_6$-$KAlSi_2O_6$ section. Experimental points [410] and calculated lines.

Enthalpies of solution of the nepheline-kalsilite series with excess silica were measured in HF by Hovis and Roux [42, 313] and compared to the results obtained for series with less content of excess silica (see Figure 13.8). The enthalpies of K-Na mixing increase with Si content.

The heat of the glass-crystal transformation of $Na_{0.7794}K_{0.2206}AlSiO_4$ nepheline was determined with HF calorimetry by Barany [411].

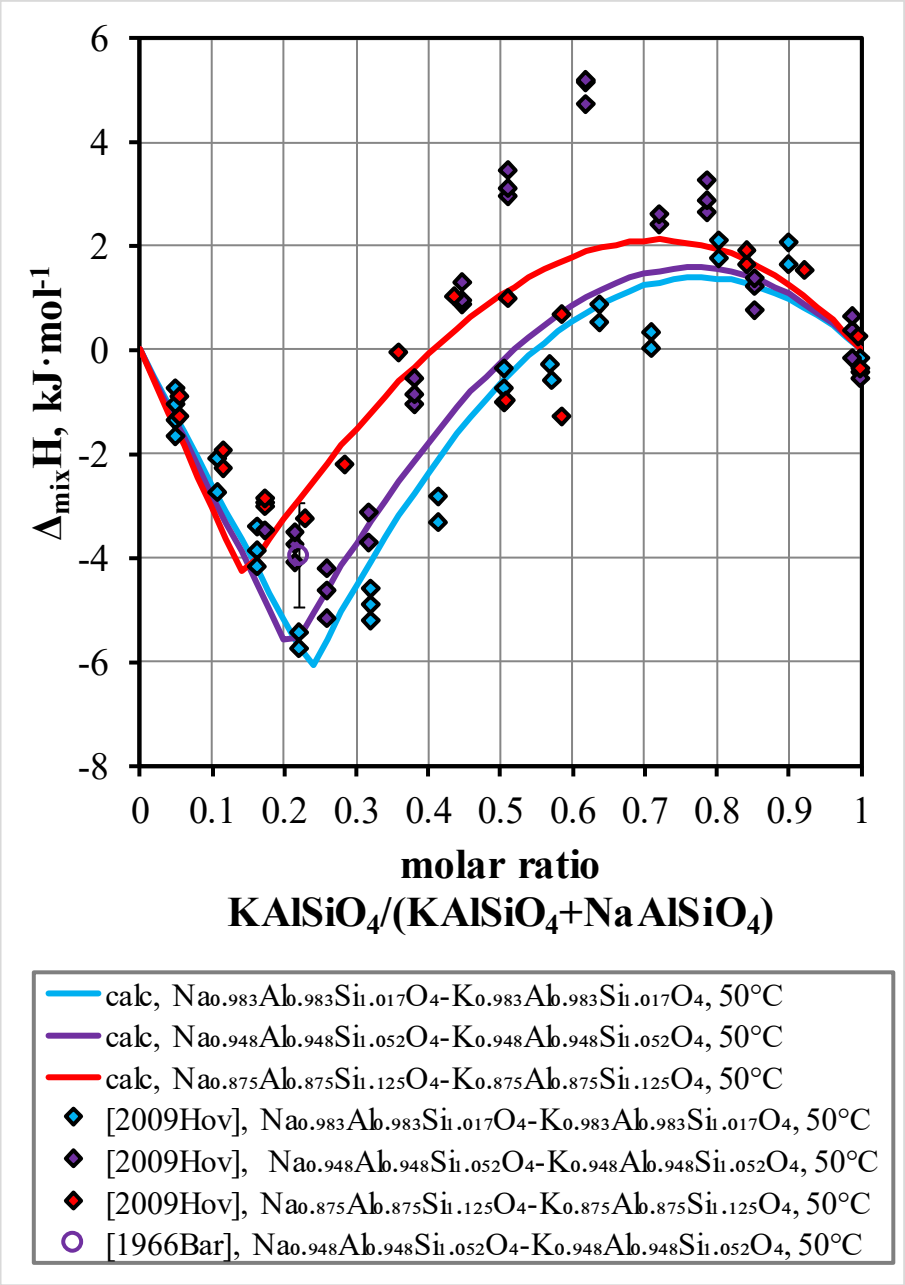

Figure 13.8 The enthalpy of mixing of nepheline solid solution with different amounts of excess silica. Experimental points [44, 411] and calculated lines.

Enthalpies of solution of the feldspar series $NaAlSi_3O_8$-$KAlSi_3O_8$ (disordered, analbite-sanidine) were measured in molten lead borate by Hovis and Navrotsky [412] and Waldbaum and Robie [298]. Their results confirm that the enthalpy of mixing is independent of the temperature, compared to the results obtained by HF calorimetry [413]. Contribution of the elastic strain to the

enthalpy of mixing of alkali feldspars was measured by Hovis et al. [414] with HF solution calorimetry.

HF calorimetry of feldspar series with different degrees of Al/Si order was carried out by Hovis [415]. The enthalpy of mixing of solid solutions increases with the ordering. The experimental data and the calculated curves on the enthalpy of mixing of the solid solution and the liquid in the $NaAlSi_3O_8$-$KAlSi_3O_8$ section are summarized in Figure 13.9.

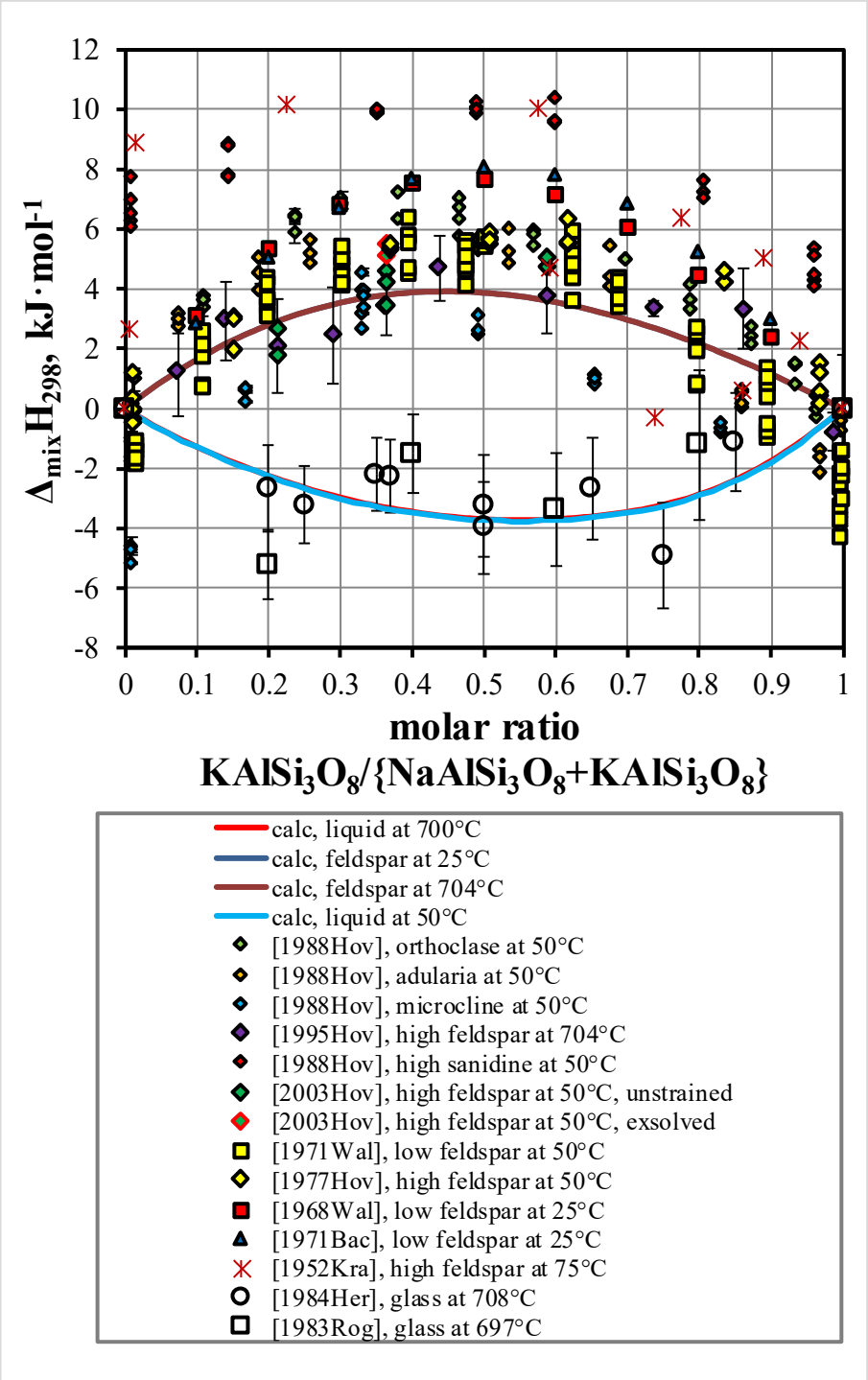

Figure 13.9 The enthalpy of mixing in the $NaAlSi_3O_8$-$KAlSi_3O_8$ section of crystalline feldspars and the liquid. Experimental points [297, 298, 307, 407, 409, 412-416] and calculated lines.

13.3 Activity data

Ion exchange experiments between nephelines and molten alkali nitrates and chlorides were performed by Sobrados and Gregorkiewitz [45] at 350° and 800°C, correspondingly. Synthetic nepheline samples were used with less amount of vacancies and excess silica than the majority of natural nephelines. Zyryanov et al. [417-419] and Perchuk et al. [420] also performed ion exchange between nephelines and (Na,K)Cl melts.

The equilibrium between a nepheline solid solution and a salt melt can be written in the following form:

$$NaAlSiO_4 + KX \leftrightarrow KAlSiO_4 + NaX \tag{123}$$

with the equilibrium constant:

$$K_{eq} = \frac{a(\mathrm{KAlSiO_4}) \cdot a(\mathrm{NaX})}{a(\mathrm{NaAlSiO_4}) \cdot a(\mathrm{KX})} = \exp\left(\frac{-\Delta_r G^\circ}{RT}\right) \tag{124}$$

where

$$\Delta_r G^\circ = g^\circ(KAlSiO_4) + g^\circ(NaX) - g^\circ(NaAlSiO_4) - g^\circ(KX) \tag{125}$$

The activities of components in a corresponding melt were calculated using *FTsalt* database of *FactSage* software. As the result, the ratio of component activities in the nepheline can be calculated (Figure 13.10).

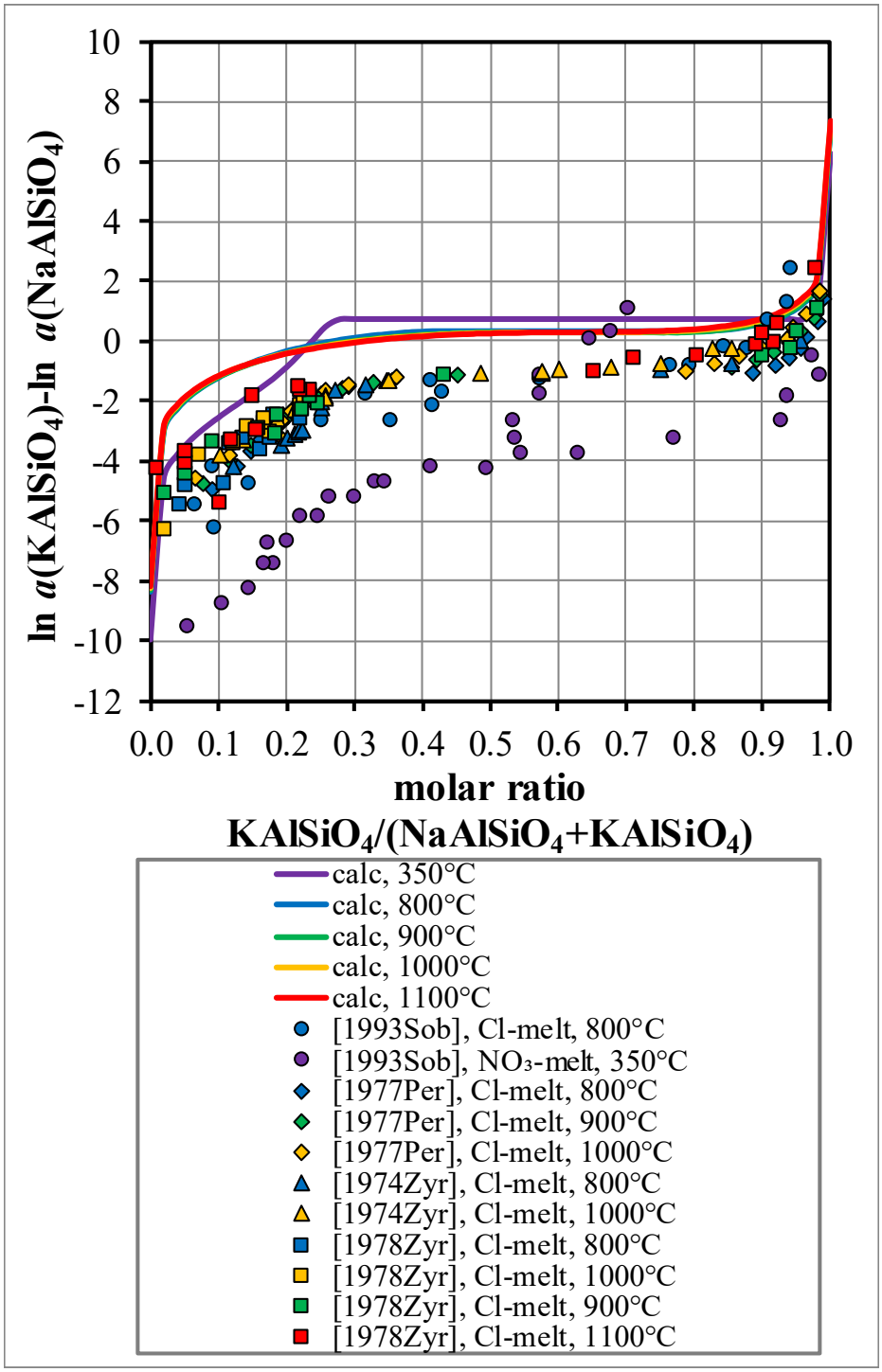

Figure 13.10 Logarithm of the activity ratio of the nepheline end-members as a function of the composition. Experimental points [45, 417, 419, 420] and calculated lines.

Zyryanov et al. [418, 419] performed ion exchange equilibria of nepheline series with a fixed excess silica amount (Figure 13.11).

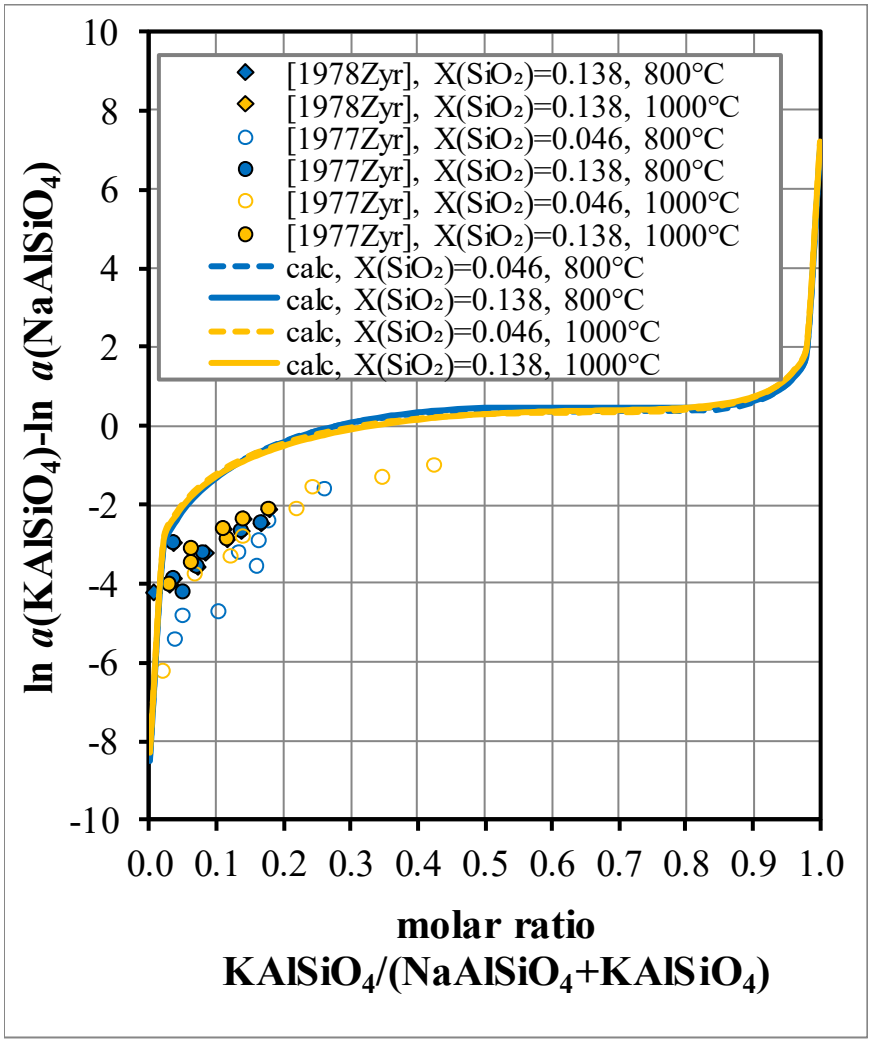

Figure 13.11 Logarithm of the activity ratio of the nepheline end-members as a function of the composition in nepheline solutions with a fixed excess silica content $X(SiO_2)$. Experimental points [418, 419] and calculated lines.

A series of studies deal with the equilibration of alkali feldspars with molten salts [417-421] and brines (concentrated aqueous salt solutions) [398, 419, 420, 422]. It was decided not to take into account the data on equilibria with NaCl-KCl-H_2O fluids as the activities of the components cannot be calculated in *FactSage*. However, the data on molten salts equilibria were used.

Hovis et al. [421] equilibrated two series of topologically monoclinic alkali feldspars with different degree of Al/Si ordering with (Na,K)Br melts at 800°C and 1bar. Equilibrium was achieved from both directions. Zyrianov et al. [417-419] and Perchuk et al. [420] performed equilibrium studies of nepheline/alkali felspar pairs in both aqueous (Na,K)Cl solutions and (Na,K)Cl melts. The molten salts experiments were performed for the range of temperature 800 to 1100°C at about 6 bar pressure with feldspar samples of different degree of ordering.

The equilibrium between a feldspar solid solution and a salt melt can be represented by the following equation:

$$NaAlSi_3O_8+KX \leftrightarrow KAlSi_3O_8+NaX \tag{126}$$

with the equilibrium constant:

$$K_{eq} = \frac{a\left(KAlSi_3O_8\right)\cdot a\left(NaX\right)}{a\left(NaAlSi_3O_8\right)\cdot a\left(KX\right)} = \exp\left(\frac{-\Delta_r G^\circ}{RT}\right) \tag{127}$$

where

$$\Delta_r G^\circ = g^\circ(KAlSi_3O_8)+g^\circ(NaX)-g^\circ(NaAlSi_3O_8)-g^\circ(KX) \tag{128}$$

The activities of components in a corresponding melt were calculated using the *FTsalt* database of *FactSage* software. As the result, the ratio of component activities in the feldspar can be calculated. As equilibrium in (126) is strongly shifted to the right, it was found more convenient to represent the calculated data in a logarithmic form (Figure 13.12).

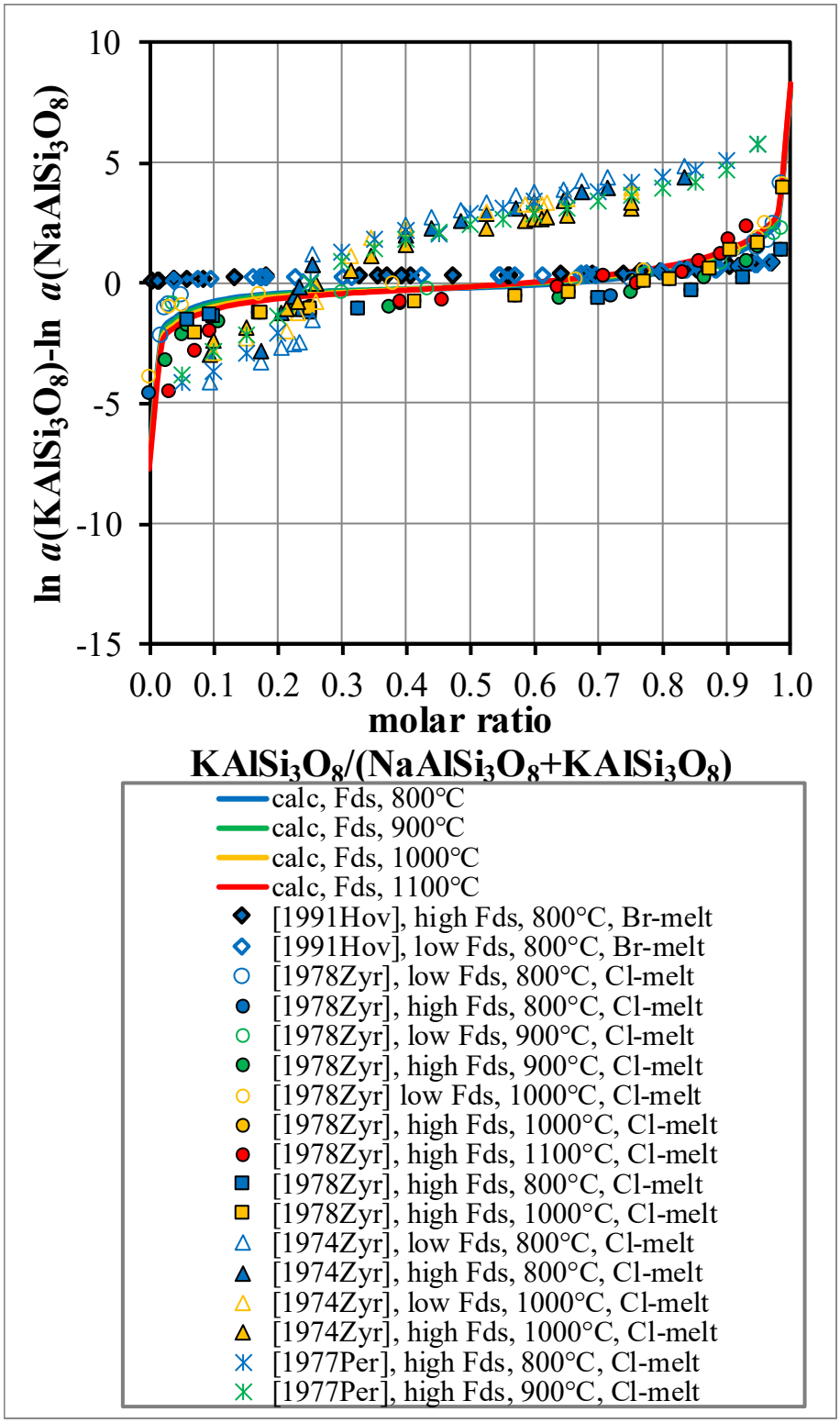

Figure 13.12 Logarithm of the activity ratio of the feldspar end-members as a function of the composition. Experimental data [417-421] and calculated lines.

Rys [164] performed Knudsen cell mass spectrometry measurements with a few samples in the Na_2O-K_2O-Al_2O_3-SiO_2 system (Figure 13.13-Figure 13.14). However, from the optimization of the Na_2O-Al_2O_3-SiO_2 system, it was established that these data are not reliable and cannot be used for optimization.

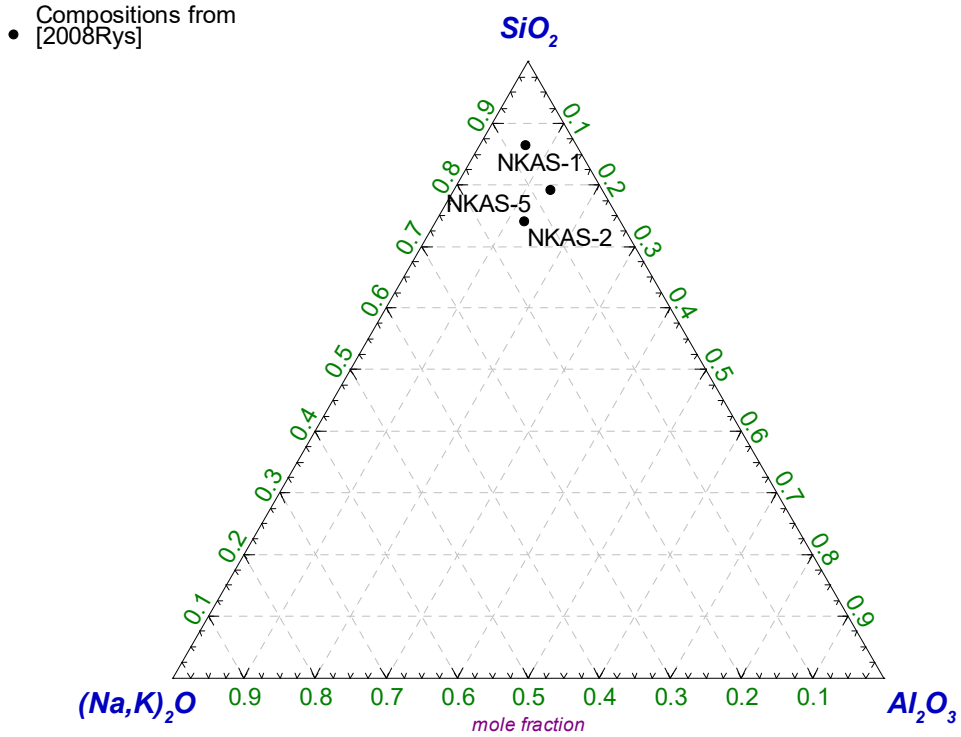

Figure 13.13 Compositions used for activity measurements in the K_2O-Na_2O-Al_2O_3-SiO_2 system [164].

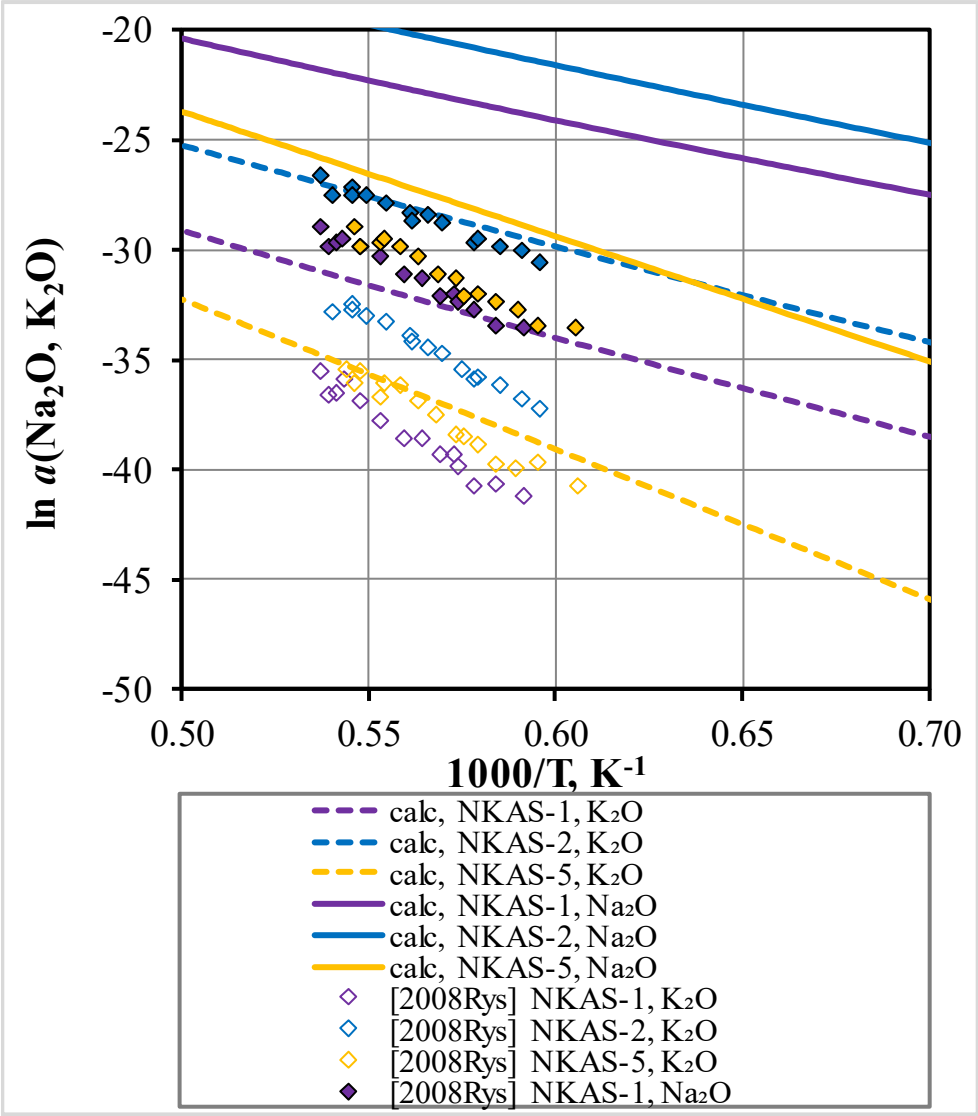

Figure 13.14 Na_2O and K_2O activities as a function of the inverse temperature in a few compositions of the Na_2O-K_2O-Al_2O_3-SiO_2 system. The reference states are the pure liquid Na_2O and K_2O. Experimental data [164] and calculated lines.

13.4 Optimization results

The ternary subsystems Na_2O-Al_2O_3-SiO_2, K_2O-Al_2O_3-SiO_2 and K_2O-Na_2O-SiO_2 were optimized in this work; the Na_2O-K_2O-Al_2O_3 system lacks experimental data and was assumed ideal.

Optimization of the K_2O-Na_2O-Al_2O_3-SiO_2 required only a small correction parameter in the liquid solution (see Table A.15). However, the solid solutions require optimization in order to reproduce the experimental data correctly.

An essential feature of Na-K nephelines is a stable composition at $Na_{0.75}K_{0.25}AlSiO_4$, expressed by $K_2Na_6Al_8Si_8O_{32}$ end-member. Its stability is defined by the enthalpy of mixing. The inverse end-member $Na_2K_6Al_8Si_8O_{32}$ was made unstable because it represents the situation when small cations reside in large cationic sites and vice versa. To reproduce the asymmetric miscibility gap, the interaction parameters between Na and K on the second sublattice are required. Based on physical sense, this interaction must not be significantly influenced by the type of the cation on the first sublattice. Interaction parameters ${}^{0}L_{\mathrm{VaSi_2,KAlSi//NaAlSi}}$ and ${}^{1}L_{\mathrm{VaSi_2,KAlSi//NaAlSi,KAlSi}}$ were added to reproduce the data on the enthalpy of mixing and the miscibility gap at different contents of excess silica.

The parameters in Carnegieite solution were chosen to reproduce the phase fields in the $NaAlSiO_4$-$KAlSiO_4$ phase diagram. As $KAlSiO_4$ pure compound does not exist with the carnegieite structure, $K_4Al_4Si_4O_{16}$ end-member properties were estimated as those of kalsilite $KAlSiO_4$ plus an added Gibbs energy term.

Both end-members of Feldspar solution exist and the miscibility gap in the system implies a positive interaction. The excess terms were chosen to reproduce the slightly asymmetric shape of the gap.

The Gibbs energy of $NaAlSi_2O_6$ end-member of Leucite solution was adjusted to have approximately 5mol% of maximum solubility, according to the information by Gupta and Edgar [109].

No extra terms were added to the aluminate solid solutions. The optimized parameters are summarized in Table A.15.

CHAPTER 14 OPTIMIZATION OF THE CaO-Na_2O-SiO_2 SYSTEM

14.1 Phase diagram

The first studies of phase relations in the Na_2O-CaO-SiO_2 system date back to the beginning of the 20th century. The metasilicate section Na_2SiO_3-$CaSiO_3$ was studied by Kultascheff [423] and by Wallace [424] by differential thermal analysis. Two metasilicate compounds were identified by Kultascheff: $3Na_2SiO_3 \cdot 2CaSiO_3$ and $2Na_2SiO_3 \cdot 3CaSiO_3$. Wallace indicated that the compound $2Na_2SiO_3 \cdot 3CaSiO_3$ is likely a solid solution. However, it appears that dynamic methods are not suited for this system; the melting point of Na_2SiO_3 obtained in these works is 80°C lower than in the studies which used quenching.

Systematic quenching studies of the ternary system were undertaken by Morey and Bowen [86] who were the first to indicate the importance of the undercooling phenomena in this system. According to Morey and Bowen, different parts of the ternary system exhibit drastic changes in the crystallization ability. Samples in the calcium orthosilicate field could not be quenched at all. NC2S3 silicate has the largest primary crystallization field, melts congruently at 1284°C and has an unusually flat liquidus. Another ternary metasilicate, N2CS3, shows an incongruent melting at 1141°C decomposing into NC2S3 and liquid. Devitrite NC3S6 is of great importance to the glass industry and forms in the majority of commercial glasses as a devitrification product. However, it was difficult to locate its primary crystallization field. For some time, the compound was believed to have (1:2:6) stoichiometry. NC3S6 melts incongruently breaking into wollastonite $CaSiO_3$ and liquid. The eutectic $Na_2Si_2O_5$-SiO_2(qz)-NC3S6 has the lowest melting temperature in the system (725°C) and the composition was very difficult to crystallize. A few compositions with less than 50 mol% SiO_2 were investigated too, but the results were not accurate. So, NCS and NC2S2 compounds were found but their melting temperatures were not established. The results by Morey and Bowen [86] were reviewed and rectified later [425] with minor changes in the melting temperatures of compounds and invariant points. Later, Brisi [426] established that the melting point of NCS is 1400°C.

Segnit [117] paid attention to the SiO_2-poor area of the phase diagram. Na_2CO_3, $CaCO_3$ and SiO_2(qz) were used for mixture preparation. It was found that the parts of the phase diagram with

over 15 mol% Na_2O and above 1300°C are significantly affected by Na_2O loss. Apart from the compounds already discovered by Morey and Bowen [86], NC2S2 and N4C3S5 were reported. NC2S2 was mentioned earlier in the work of Thilo [427]. The melting point of NC2S2 was not determined with a great accuracy and is about 1450°C. N4C3S5 melts incongruently and has a small crystallization field. As for the binary phases, the field of $Ca_3Si_2O_7$ was outlined; Ca_2SiO_4 was found to exist as α-modification stabilized by Na_2O solubility (up to 3 mol%, seems to be the greatest in the directions of NCS and NC2S2).

Zhang et al. [428] also studied the silica-poor region of the ternary system. The mixtures were prepared from SiO_2, CaO and Na_2CO_3. The authors did not mention how the degree of carbonate decomposition was controlled. The results seem to be in a good agreement with the data by Segnit [117] on the fields of $Ca_3Si_2O_7$ and NC2S2. The coordinates of the eutectic among NC2S2-NC2S3-NCS were modified. The eutectic point E from the work of Segnit was not confirmed. The authors explain it by a high alkali loss. A new phase NC3S2 was found; it was also mentioned by Montoya et al. [429].

Shahid and Glasser [430] studied the SiO_2-rich part of the system and found a small primary field of NCS5 compound along with $Na_6Si_8O_{19}$ which was usually overlooked by the previous studies. NCS5 undergoes a reversible transformation at 720°C.

Moir and Glasser [87] studied the binary metasilicate section Na_2SiO_3-$CaSiO_3$ in more detail. They have confirmed the existence of NC2S3 and N2CS3. Combeite NC2S3 is not a stoichiometric compound and its composition can vary from 28.5 to 53.5±0.5 mol% Na_2SiO_3. A few polymorphic forms of the combeite solid solution were described. It shows an inversion at 485°C detectable by DTA with the enthalpy of transition of 6.49 $kJ \cdot mol^{-1}$. The high modification could be quenched only for Ca-deficient compositions as the transition becomes slower with excess Na_2SiO_3. Upon prolonged heating below 725°C, Na_2SiO_3-rich solid solutions transform into NC2S3' phase. It is believed to be a polymorph of NC2S3, but the authors did not exclude the possibility that it might have (1:1:2) stoichiometry and an upper stability limit. The detailed nature of the ion substitution in combeite was not elucidated. N2CS3 also forms a solid solution but with a much smaller solubility range. It disproportionates into Na_2SiO_3 and NC2S3 below 700°C. Na_2SiO_3 forms solid solutions with α-$CaSiO_3$ (pseudowollastonite) but not with β-$CaSiO_3$ (wollastonite). The solubility

limit is about 2 mol% Na_2SiO_3. The formation of the solid solution causes the inversion temperature to drop slightly (from 1125° to 1118±5°C).

Ohsato et al. [89] studied the structure of the combeite solid solution. NC2S3 undergoes a reversible phase transformation at 485°C, the transition temperature lowers with an increasing sodium content. Solid solutions form due to Ca↔2Na substitution, the second Na going into a vacant place. Both the low and high solution are trigonal. The high modification has four cationic sites: two with preference for Na and two with preference for Ca. For the low modification, the number of cationic sites increases due to splitting. A mineral combeite found in nature is mentioned with the formula $Na_{2.4}Ca_{1.5}$(Fe, Mn, Mg, Zn)Si_3O_9.

N2CS3 compound is structurally similar to $K_4CaSi_3O_9$ (K2CS3) [93] and $Ca_3Al_2O_6$ (C3A) [91]. NCS compound is isostructural with other alkali-alkali-earth orthosilicates like K_2CaSiO_4, Na_2SrSiO_4, K_2SrSiO_4, etc. [56]. It undergoes a phase transition at 557°C with the enthalpy of transition of 0.67 $kJ \cdot mol^{-1}$ [431].

Blanco et al. [432] studied the influence of Na_2O addition on Ca_2SiO_4 polymorphic transformations. According to the results of several authors, there are two modifications which are able to exist at room temperatures: the stable γ-Ca_2SiO_4 and a metastable β-Ca_2SiO_4. Upon heating, they both transform first into α'-Ca_2SiO_4 and finally into α-Ca_2SiO_4. The specific temperatures of transformations differ with sources.

Akhmetov et al. [433] reported a new compound NCS2 with a cubic or pseudocubic structure. It undergoes certain structural transformations at 700°C and decomposes at around 1200°C into liquid and combeite.

The liquidus projections in different temperature intervals and the metasilicate join are shown in Figure 14.1-Figure 14.2 and Figure 14.3.

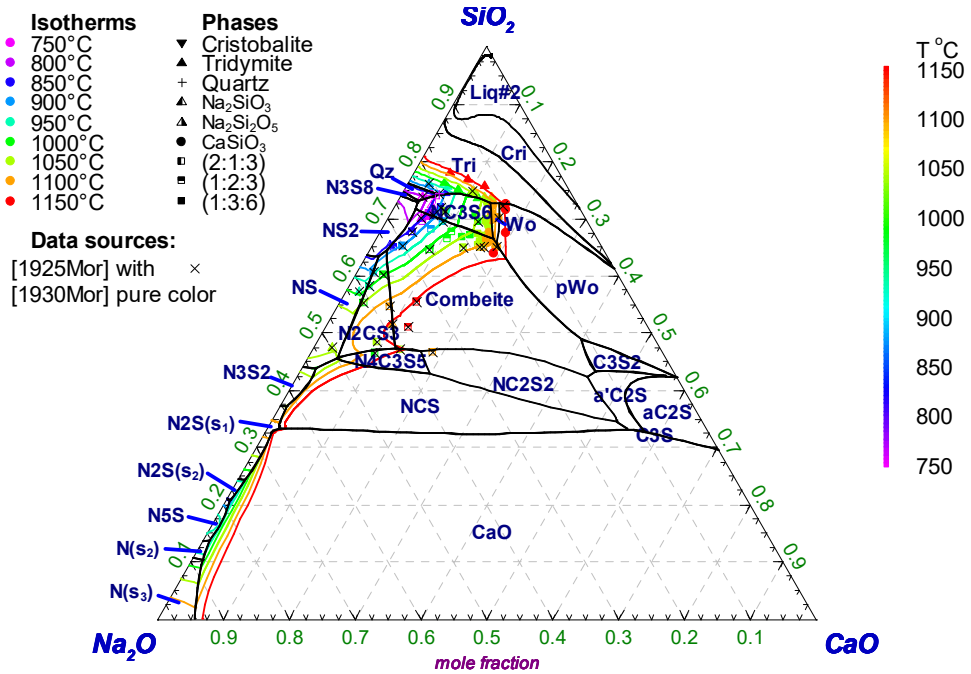

Figure 14.1 Liquidus projection in the CaO-Na_2O-SiO_2 system; isotherms from 750° to 1150°C. Experimental points [86, 425] and calculated lines.

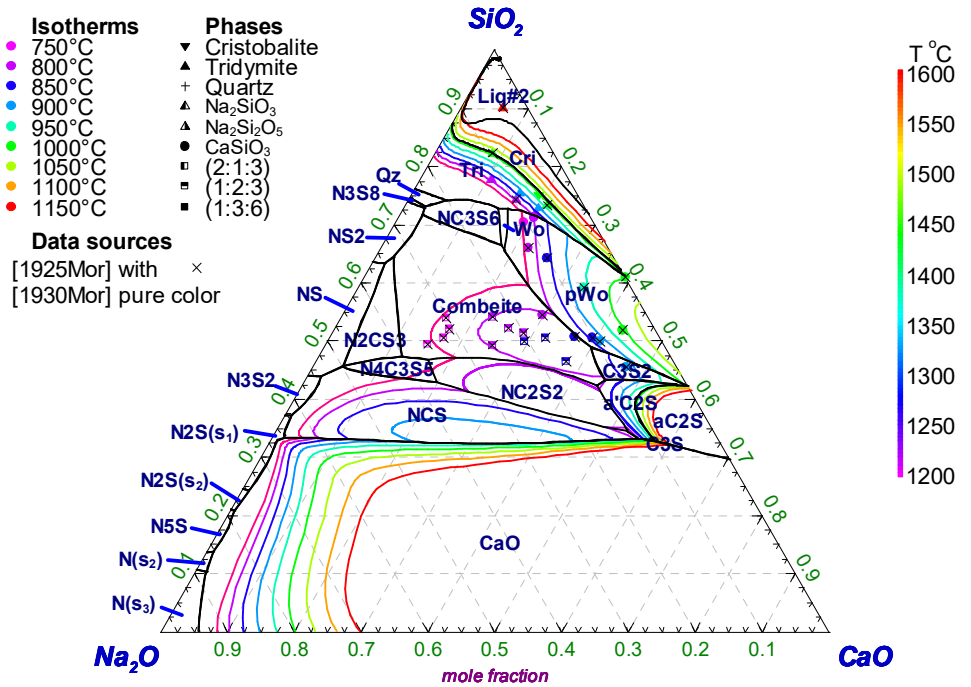

Figure 14.2 Liquidus projection in the CaO-Na_2O-SiO_2 system; isotherms from 1200° to 1600°C. Experimental points [86, 425] and calculated lines.

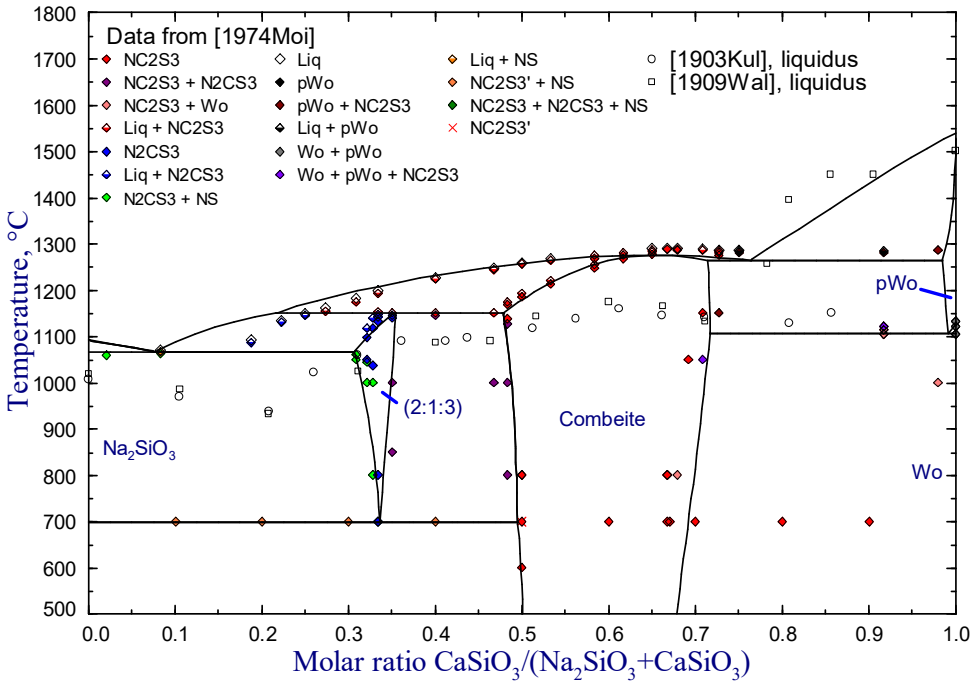

Figure 14.3 Phase diagram in the metasilicate section Na_2SiO_3-$CaSiO_3$ of the Na_2O-CaO-SiO_2 system. Experimental points [87, 423, 424] and calculated lines.

Unfortunately, the liquidus data available in the system mostly lack any order in the compositions chosen for study. However, it was possible to draw a few arbitrary sections through the system which include as many points as possible. These sections are presented in Figure 14.4.

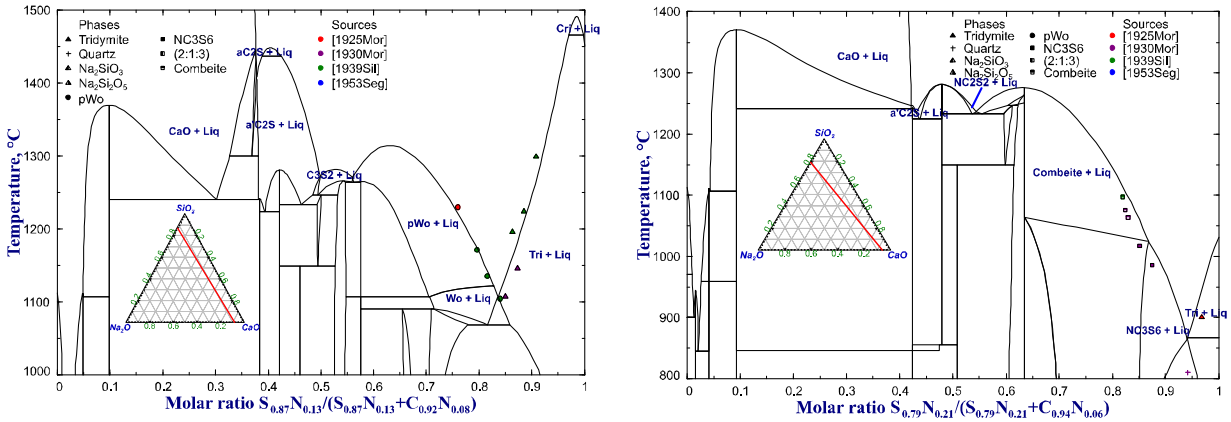

(*a*) (*b*)

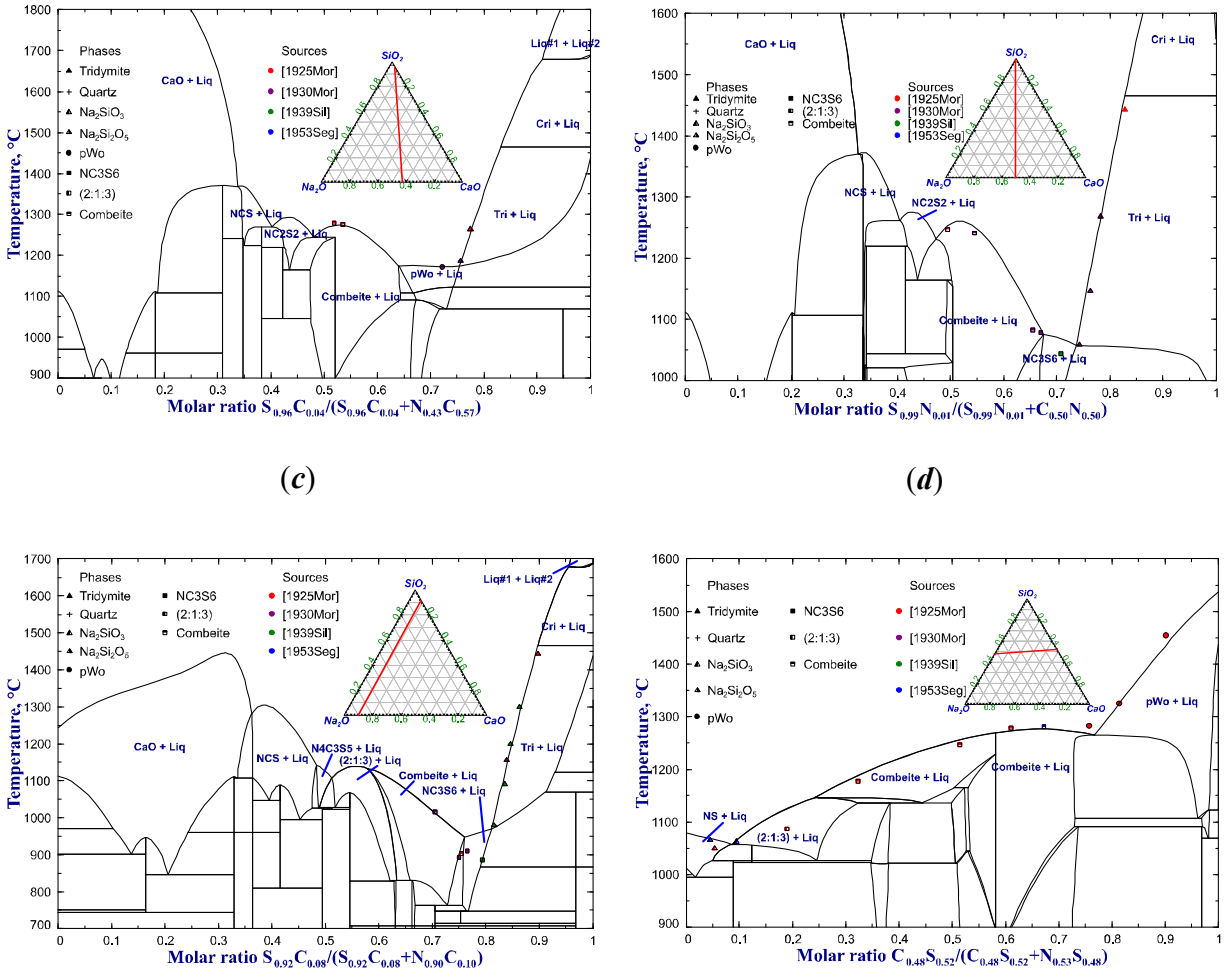

(*c*) (*d*)

(*e*) (*f*)

Figure 14.4 Phase diagrams in the sections drawn through the Na_2O-CaO-SiO_2 system. Experimental points [86, 117, 425, 434] and calculated lines.

The invariant equilibria in the system are summarized in Table 14.1.

Table 14.1 Invariant points in the CaO-Na_2O-SiO_2 system. The calculated values are shown in bold.

Solid phases	**Equilibrium type**	**T, °C**	**Liquid composition, mol%**		
			SiO_2	**Na_2O**	**CaO**
(2:1:3)-Combeite	Peritectic	1141 [86] 1149 [87] **1151**	 **50.00**	 **39.18**	 **10.82**
Combeite	Congruent melting	1284 [86] 1289 [87] **1276**	50.00 **50.00**	16.67 **16.08**	33.33 **33.92**
NC3S6-pWo (Wo?)	Peritectic	1047 [86] 1060 [425] **1091**	67.00 **66.04**	18.00 **16.04**	15.00 **17.92**
Na_2SiO_3-(2:1:3)	Eutectic	1060 [86] 1064 [87] **1067**	 **50.00**	 **46.72**	 **3.28**
Combeite-pWo	Eutectic	1280 [86] 1283 [87] **1269**	 **50.00**	 **11.82**	 **38.18**
$Na_2Si_2O_5$-Combeite	Eutectic	862 [86] **832**	 **65.81**	 **31.56**	 **2.63**
Na_2SiO_3-$Na_2Si_2O_5$-(2:1:3)	Eutectic	821 [86] **828**	61.32 **63.38**	36.73 **34.78**	1.95 **1.85**
$Na_2Si_2O_5$- (2:1:3)-Combeite	Reaction point	827 [86] **830**	61.71 **64.49**	36.13 **32.99**	2.16 **2.52**
$Na_2Si_2O_5$-Combeite-NC3S6	Reaction point	740 [86] **762**	70.96 **71.72**	23.45 **24.91**	5.59 **3.36**
$Na_2Si_2O_5$-NC3S6-Qz	Eutectic	725 [86] 725 [425] **743**	73.71 73.33 **73.10**	20.71 21.30 **23.94**	5.59 5.37 **2.95**
Combeite-NC3S6-Wo	Reaction point	1030 [86] 1060 [425] **1091**	66.20 65.77 **66.53**	18.34 18.13 **15.79**	15.47 16.10 **17.68**
NC3S6-Wo-Tri	Eutectic?	1030 [425] **1100**	73.34 **77.53**	13.12 **11.05**	13.54 **11.41**
Ca_2SiO_4-$Ca_3Si_2O_7$-NC2S2	Reaction point Peritectic	1280 [117] 1278 [428] **1216**	45.38 42.68 **43.26**	8.29 8.46 **13.47**	46.33 48.85 **43.27**
$Ca_3Si_2O_7$-Wo-NC2S2	Eutectic	1270 [117] 1270 [428] **1097**	45.95 44.66 **51.49**	7.72 7.91 **20.00**	46.32 47.43 **28.50**
Combeite-Wo-NC2S2	Eutectic	1255 [117] 1245 [428]	46.86 45.71	11.83 11.15	41.31 43.44

Solid phases	Equilibrium type	T, °C	Liquid composition, mol%		
			SiO_2	Na_2O	CaO
		827	**33.70**	**0.91**	**65.39**
Combeite-NCS-NC2S2	Eutectic	1260 [117] 1258 [428] **1107**	43.33 42.81 **46.15**	22.91 21.22 **41.88**	33.76 35.97 **11.98**
Ca_2SiO_4-NCS-Combeite	Eutectic	1440 [117] **1150**	38.63 **39.30**	21.86 **17.60**	39.5 **43.10**
Combeite-NCS-N4C3S5	Reaction point	1130 [117] **1145**	43.51 **38.63**	38.59 **16.13**	17.9 **45.24**
Combeite-(2:1:3) -N4C3S5	Reaction point	1120 [117] **1135**	44.03 **47.31**	38.81 **40.27**	17.16 **12.42**
Na_2SiO_3- (2:1:3)-N4C3S5	Reaction point	990 [117] **1027**	44.78 **45.72**	43.90 **49.78**	11.32 **4.49**
Na_2SiO_3-NCS-N4C3S5	Reaction point	950 [117] **1025**	41.80 **45.62**	46.87 **49.98**	11.33 **4.40**

14.2 Activity data

Gas equilibration technique was employed by Rego et al. [435]. The samples were equilibrated with a Na_2O-SiO_2 melt with a known Na_2O activity under the CO atmosphere. Sodium vapor obtained during the reaction:

$$Na_2O(liq)+C(cr)\leftrightarrow 2Na(g)+CO(g) \quad (129)$$

allowed to maintain equal sodium oxide activities between the two melts. An investigated melt loses or absorbs sodium oxide according to the difference in the activity with the reference melt. The composition of the investigated melt is analysed.

Mathieu [436] measured Na_2O solubility in Na_2O-free base compositions in the CaO-MgO-SiO_2 system in an atmosphere with a fixed Na(g) partial pressure. Large amounts of $Na_2O{\cdot}2SiO_2$ melt were used as a source of sodium and the partial pressure of oxygen was fixed by Ni/NiO buffer. The operating temperatures were 1250° and 1400°C. The authors present their data in the form of isosolubility lines in the CaO-MgO-SiO_2 base composition triangle and to compare these data with the calculated values, they were replotted in the form of isoactivities. Intersection points of Na_2O isosolubility lines and the CaO-SiO_2 border are plotted in Figure 14.5.

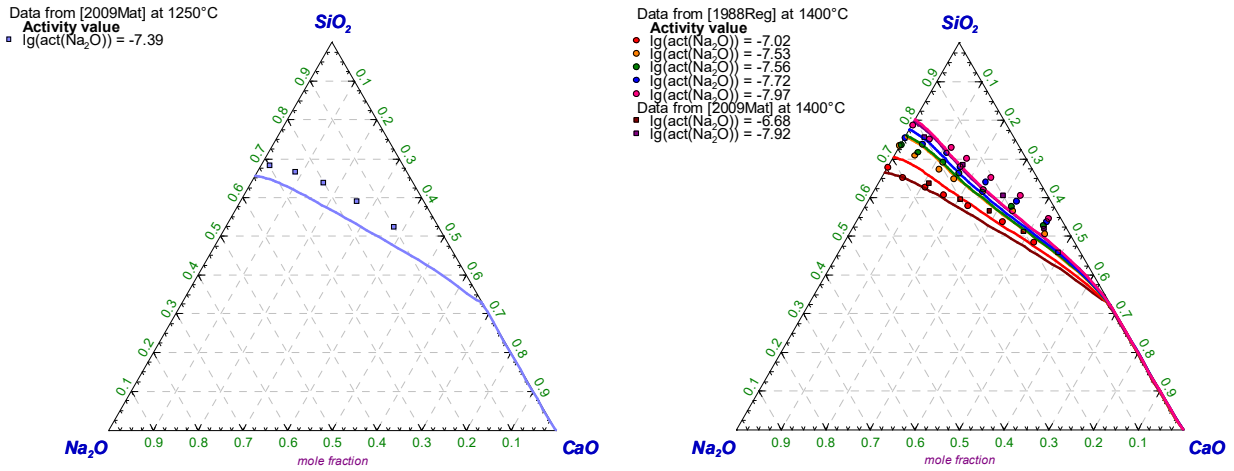

(***a***) (***b***)

Figure 14.5 Isoactivity lines in the Na_2O-CaO-SiO_2 system at 1250°C (***a***) and 1400°C (***b***). The reference state is the pure liquid Na_2O. Experimental points [435, 436] and calculated lines.

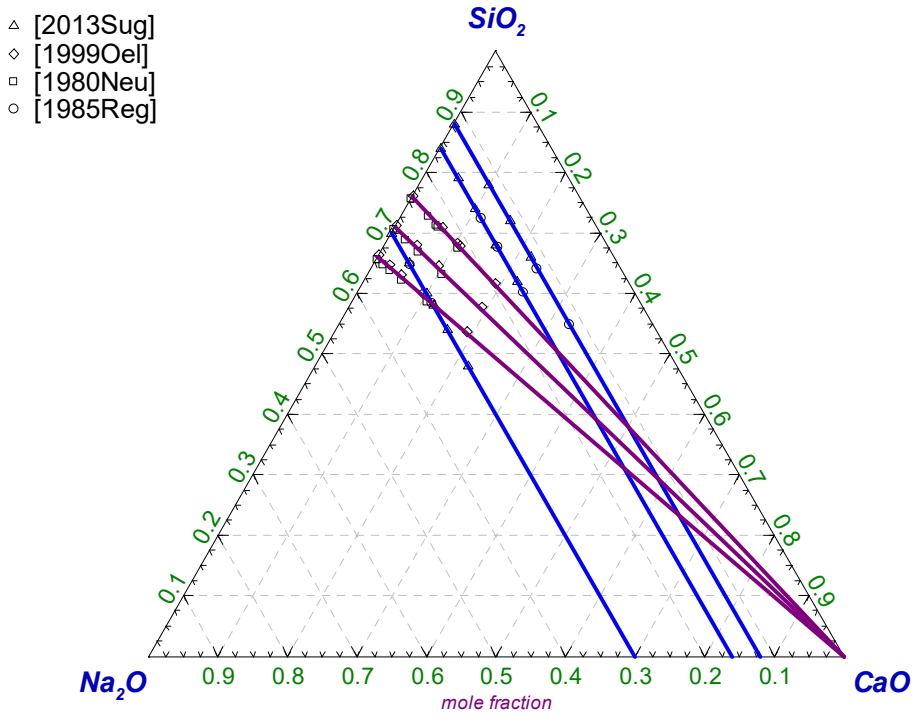

Figure 14.6 Compositions in the Na_2O-CaO-SiO_2 system for which Na_2O activity was measured [214, 229, 319, 437].

Compositions from different studies which measured Na_2O activity were plotted together to analyze the compositional dependence (Figure 14.6). Oeltjen [319] performed mass spectrometry of Na_2O-CaO-SiO_2 slags using a Knudsen cell. Na_2O is a volatile component, decomposing almost exclusively into Na(g) and O_2(g) in the gas phase. By measuring the partial Na(g) pressure, the Na_2O activity in the liquid can be calculated if the partial pressure of Na(g) over the reference state is known. The measurements were performed in isothermal conditions; the composition was varied by adding different amounts of CaO to a binary Na_2O-SiO_2 melt (Figure 14.7). The activity data referred to the liquid Na_2O were used directly in this work without further recalculations.

Neudorf and Elliott [229] studied EMF in Na_2O-CaO-SiO_2 melts using the following electrochemical cell:

$$O_2(Pt)|Na_2O\text{-}WO_3(liq, ref)||Na\text{-}\beta\text{-alumina}||Na_2O\text{-}CaO\text{-}SiO_2|O_2(Pt) \quad (130)$$

In their experiments, the composition of samples was modified by adding different amounts of CaO to binary Na_2O-SiO_2 melts (Figure 14.7). The activity values were taken as recalculated by the authors.

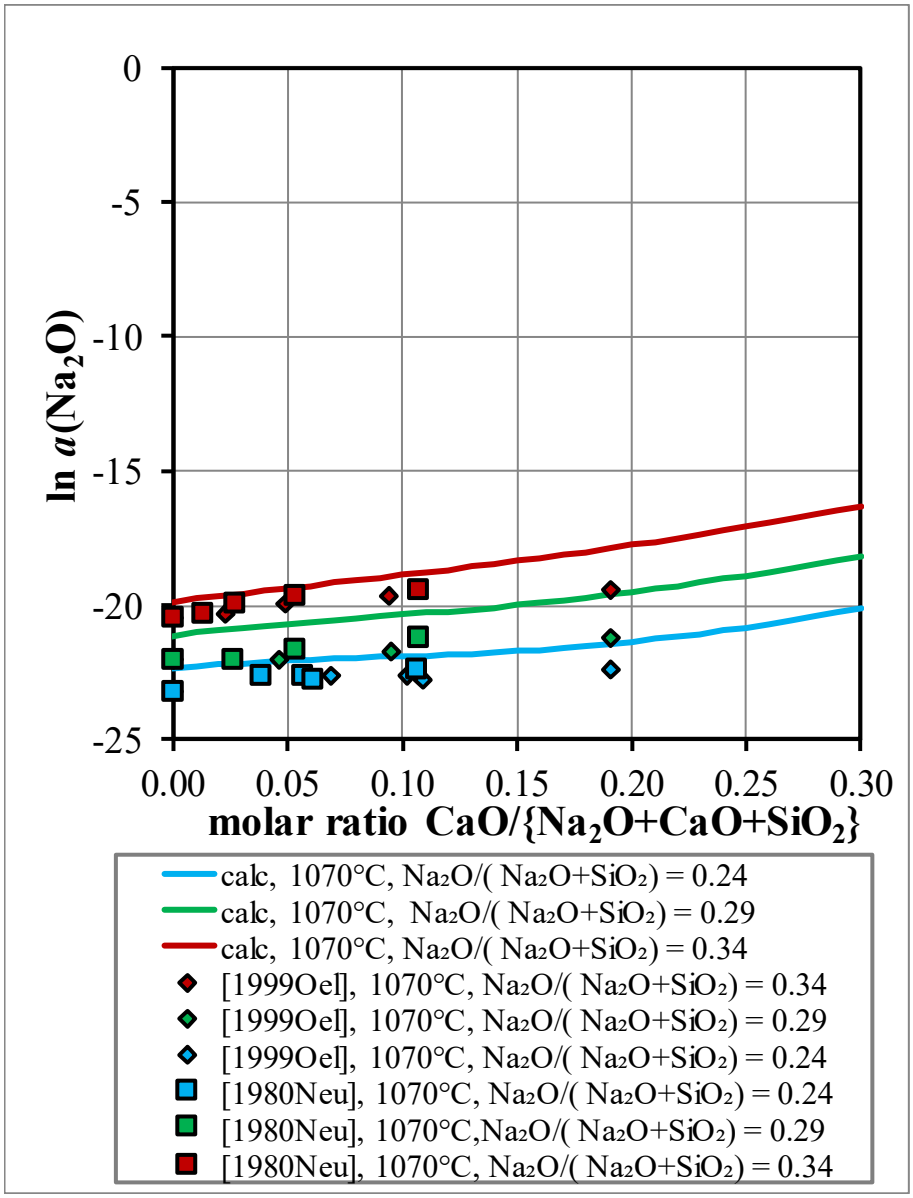

Figure 14.7 Na_2O activity over joins $(Na_2O)_x(SiO_2)_{(1-x)}$-CaO. The reference state is the pure liquid Na_2O. Experimental points [229, 319] and calculated lines.

Sugawara et al. [437] measured EMF in concentration cells of the following type:

$$Pt(O_2)|CaO\text{-}Na_2O\text{-}SiO_2|Na_2O\text{-}Al_2O_3\text{-}SiO_2(ref)|O_2(Pt) \quad (131)$$

A $(Na_2O)_{0.3}(Al_2O_3)_{0.1}(SiO_2)_{0.6}$ melt was used as a reference, the activity data recalculated by the authors were used in this work. The compositional series were designed in a way that CaO and SiO_2 content varied while Na_2O content was fixed (Figure 14.8).

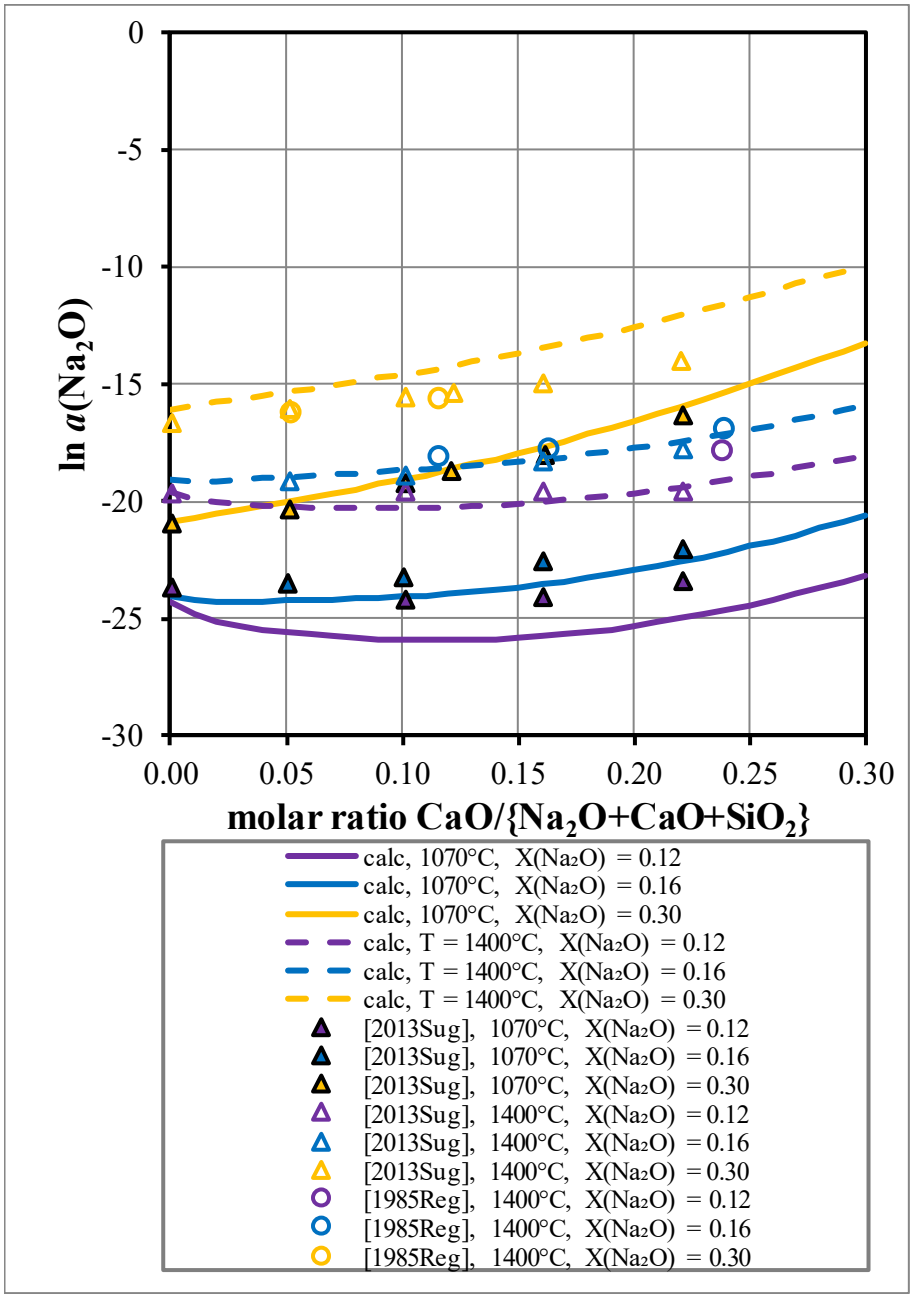

Figure 14.8 Na_2O activity over joins with a constant Na_2O content. The reference state is the pure liquid Na_2O. Experimental points [214, 437] and calculated lines.

14.3 Heat capacity and heat content data

Pankratz [431] measured the heat content of four ternary compounds: Na_2CaSiO_4, $Na_2Ca_2Si_2O_7$, $Na_2CaSi_3O_9$ and $Na_4CaSi_3O_9$ between 298 and 1500K using copper block calorimetry. The

obtained data (see Figure 14.9) indicate that Na_2CaSiO_4 and $Na_2Ca_2Si_3O_9$ undergo reversible transitions at 557° and 477°C with enthalpies of transition of 0.67 and 6.49 kJ·mol^{-1}, correspondingly. As combeite is modeled as a solid solution, we preferred to keep it as one phase and the transition for $Na_2Ca_2Si_3O_9$ is not reproduced. The phase transition of Na_2CaSiO_4 was taken into account in our optimization.

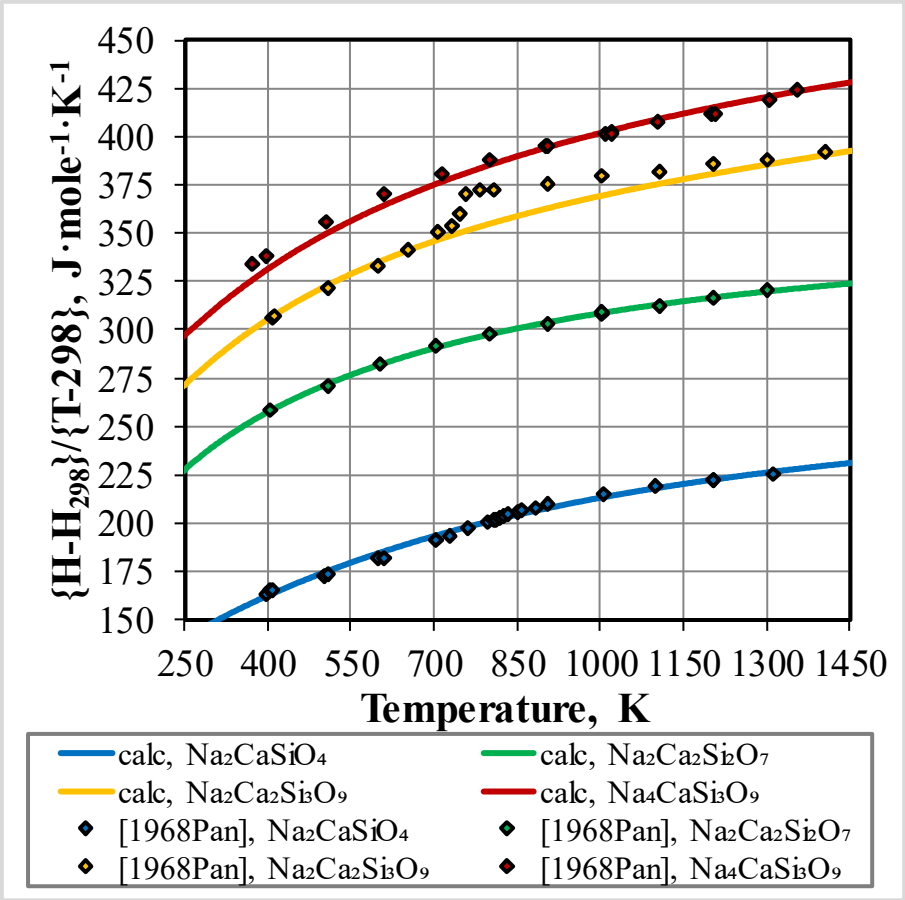

Figure 14.9 The mean heat capacity of Na_2CaSiO_4, $Na_2Ca_2Si_2O_7$ compounds and "$Na_2Ca_2Si_3O_9$" (Combeite) and "$Na_4CaSi_3O_9$" (2:1:3) solid solutions. Experimental points [431] and calculated lines.

14.4 Optimization results

The Na_2O-SiO_2 binary subsystem was optimized in this work; the optimization of the CaO-SiO_2 system by Eriksson et al. [438] was adopted and the Na_2O-CaO subsystem was assumed ideal.

Five ternary stoichiometric compounds were included in the optimization: NCS, NC2S2, N4C3S5, NCS5, NC3S6. Other compounds were not included because of lack of evidence of their existence or stoichiometry. NC2S3 and N2CS3 compounds were modeled as solid solutions, the details on the models are available in Sections 4.8 and 4.9. Simple one-sublattice solution models were used to reproduce the data on alkali solubilities in $CaSiO_3$ and Ca_2SiO_4. The heat capacities of NCS and NC2S2 were evaluated based on the available heat content data. For the rest of the stoichiometric compounds, the heat capacities were taken equal to weighted sums of the heat capacities of Na_2O, CaO and SiO_2 (tridymite). For all the compounds, the initial approximations of the standard entropy were calculated according to the same scheme. However, during the consequent steps of the optimization, these entropy values might have been slightly modified to reproduce the phase equilibria.

As there are no enthalpy data on either the solids or the liquid in the system (except for the Na_2O activity data), the optimization approach was the following: a minimal set of liquid interaction parameters was found to reproduce the liquidus data on the binary compounds whose properties are known from the subsystem optimizations and the enthalpies of the ternary solids were later adjusted in order to reproduce the rest of the phase diagram.

C2N3C1 and N3C2C1 end-members of Combeite solution contain 50 and 66.7 mol% of $CaSiO_3$ which corresponds to the solubility limits of combeite at low temperatures. These end-members were stabilized. The solubility at higher temperatures towards Na_2SiO_3 and $CaSiO_3$ exceeding 50 and 66.7 mol% $CaSiO_3$ is governed by stabilities of N2N3C1 and C3C2C1 end-members, correspondingly. A negative ${}^0L_{Ca//Na2,Ca//Ca}$ parameter is required to avoid a miscibility gap between C2N3C1 and N3C2C1 end-members.

In the case of the Na_2O-CaO-SiO_2 system, only the first two sublattices of (2:1:3) solid solution are non-trivial. The third and the forth sublattices are reserved for alkali and alkali-earth cations, correspondingly. They become non-trivial in case of the presence of potassium and strontium. Two of the four end-members of (2:1:3) solid solution, C1N1N3C1 and N1C1N3C1 have the same composition. Their added Gibbs energy was modified in order to reproduce the upper and the lower decomposition temperatures of the phase. As there are no data on the cation distribution, the end-members were assumed to have the same Gibbs energy. The enthalpy terms of the added Gibbs energy differ slightly (Table A.17); it was required because if they are identical, *FactSage*

calculations take long times due to convergence problems. C1C1N3C1 and N1N1C3C1 end-members define the non-stoichiometry of the phase towards the $CaSiO_3$ and Na_2SiO_3 ends of the Na_2SiO_3-$CaSiO_3$ section, correspondingly.

The added Gibbs energy of Na_2SiO_3 end-member and an excess interaction parameter $q^{11}_{CaSiO_3,Na_2SiO_3}$ of Pseudowollastonite solution were adjusted to reproduce sodium solubility in the Na_2SiO_3-$CaSiO_3$ section. The same applies to α- and α'-C2S solid solutions.

The optimized parameters are summarized in Table A.16-Table A.17.

CHAPTER 15 OPTIMIZATION OF THE Al_2O_3-CaO-Na_2O SYSTEM

15.1 Phase diagram

Investigations of the phase relations in the Al_2O_3-CaO-Na_2O system are complicated by several factors. First, Na_2O has a low melting temperature compared to CaO and Al_2O_3 and therefore, volatilization phenomena can become significant with a rising Na_2O content. Secondly, Na_2O is highly corrosive and does not allow direct heat curve measurements due to its degrading influence on thermocouples [97]. However, the practical interest in the Al_2O_3-CaO-Na_2O system is limited to compositions relatively poor in Na_2O. Calcium aluminates, especially C3A, are important in cement production. Presence of small amounts of CaO and Na_2O plays an important in alumina sintering process. Although there are not a lot of works related to the liquidus determination in the system, quite a lot of studies are devoted to the question of crystal structures and solid solutions, especially the one based on C3A (the main component of Portland cement).

First, some clarity needs to be brought into the stoichiometry of the binary calcium aluminates reported in the literature. The optimization of the CaO-Al_2O_3 system accepted in this work was performed by Eriksson and Pelton [123]. Based on the evidence found in the literature, they confirmed that C5A3 and C12A7 compounds are actually identical and represent a hydrate of $Ca_{12}Al_{14}O_{32}(OH)_2$ composition which does not exist in the anhydrous system [439, 440]. It was also confirmed that C3A5 compound has in fact CA2 stoichiometry [439]. So, the existence of C3A, CA, CA2, CA6 compounds was confirmed and they were included in the *FactSage* database.

The work by Brownmiller and Bogue [97] can be considered as one of the pioneering studies of the ternary system. The authors used quenching in mercury to determine liquidus relations in the Na_2O-low area of the phase diagram. Use of mercury allowed to reach very fast cooling rates due to the fact that mercury is a metal. Two ternary compounds were found: C3N2A5 and C8NA3. The X-ray pattern of C8NA3 is very similar to that of pure C3A and it is reasonable to assume that C8NA3 is a solid solution of Na_2O in tricalcium aluminate. There have been some difficulties to crystallize compositions close to C3N2A5 and there is no solid boundary between $NaAlO_2$ primary crystallization field and the primary field of C3N2A5. Also, the optical properties of crystals change gradually which can be due to a solid solution between $NaAlO_2$ and C3N2A5. However, it

is true only at elevated temperatures and upon cooling the exsolution is observed. C3N2A5 can also be a limiting composition of a solid solution between $NaAlO_2$ and $CaAl_2O_4$ end-members. The following binary subsystems were found: C3A5-C3N2A5, CA-C3N2A5, C5A3-C3N2A5, C3N2A5-NA, CaO-NA (all phases in these sections have compositions which also belong to these sections).

Phase relations in the system NA-CA-Al_2O_3 at 1200°C were determined by Verweij and Saris [96] using quenching and X-ray diffraction. The N2C3A5 compound found by Brownmiller and Bogue was reformulated as NCA2, and a new compound NC3A8 was reported. NCA2 forms a solid solution with $NaAlO_2$ (up to 38 mol% Na_2O at 1200°C). Binary CA6 compound is of special interest in the production of high-pressure sodium discharge lamps. Its structure resembles the structure of Na-β-alumina. It did not form at 1200°C but was found stable at this temperature once formed at higher temperatures. CA6 reacts readily with sodium-containing compounds in the system. Hodge [441] found that CA6 crystals can serve as crystallization centers and catalysts for Na-β-Al_2O_3 formation. However, no stable solid solution between CA6 and Na-β-Al_2O_3 was identified [441].

Zaldat et al. [442] have also built a subsolidus phase diagram of the system at 1400°C. A new ternary phase was discovered, NC4A10 or NC4A9 where a part of Al_2O_3 can be substituted by Cr_2O_3. The phase decomposes into Na_2O and CA2 above 1440°C. In this work, it was considered to be the same phase as NC3A8.

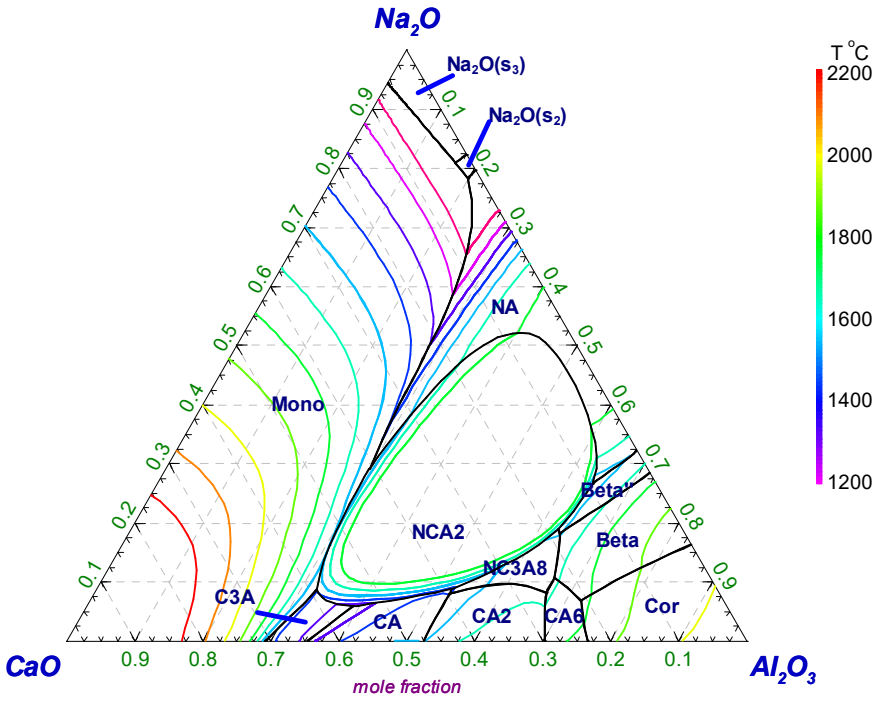

Figure 15.1 Liquidus projection in the Al_2O_3-CaO-Na_2O system.

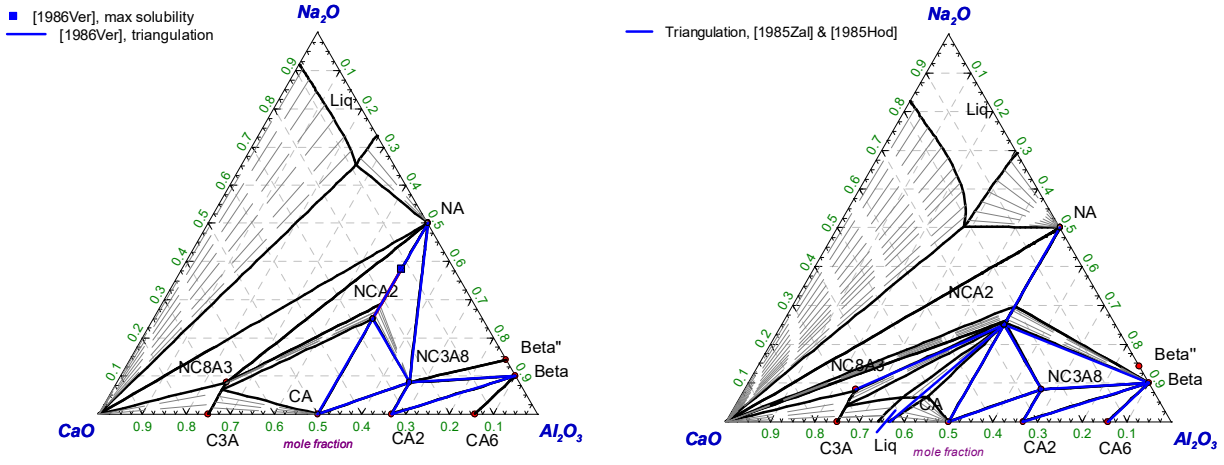

(***a***) (***b***)

Figure 15.2 Subsolidus relations in the Al_2O_3-CaO-Na_2O system at 1200°C (***a***) and 1400°C (***b***). Experimental triangulation [96, 441, 442] and calculated lines.

Liquidus projection in the Al_2O_3-CaO-Na_2O system is shown in Figure 15.1 (no experimental points). Triangulations of the system at 1200° and 1400°C are presented in Figure 15.2. A few sections through the system are collected in Figure 15.3.

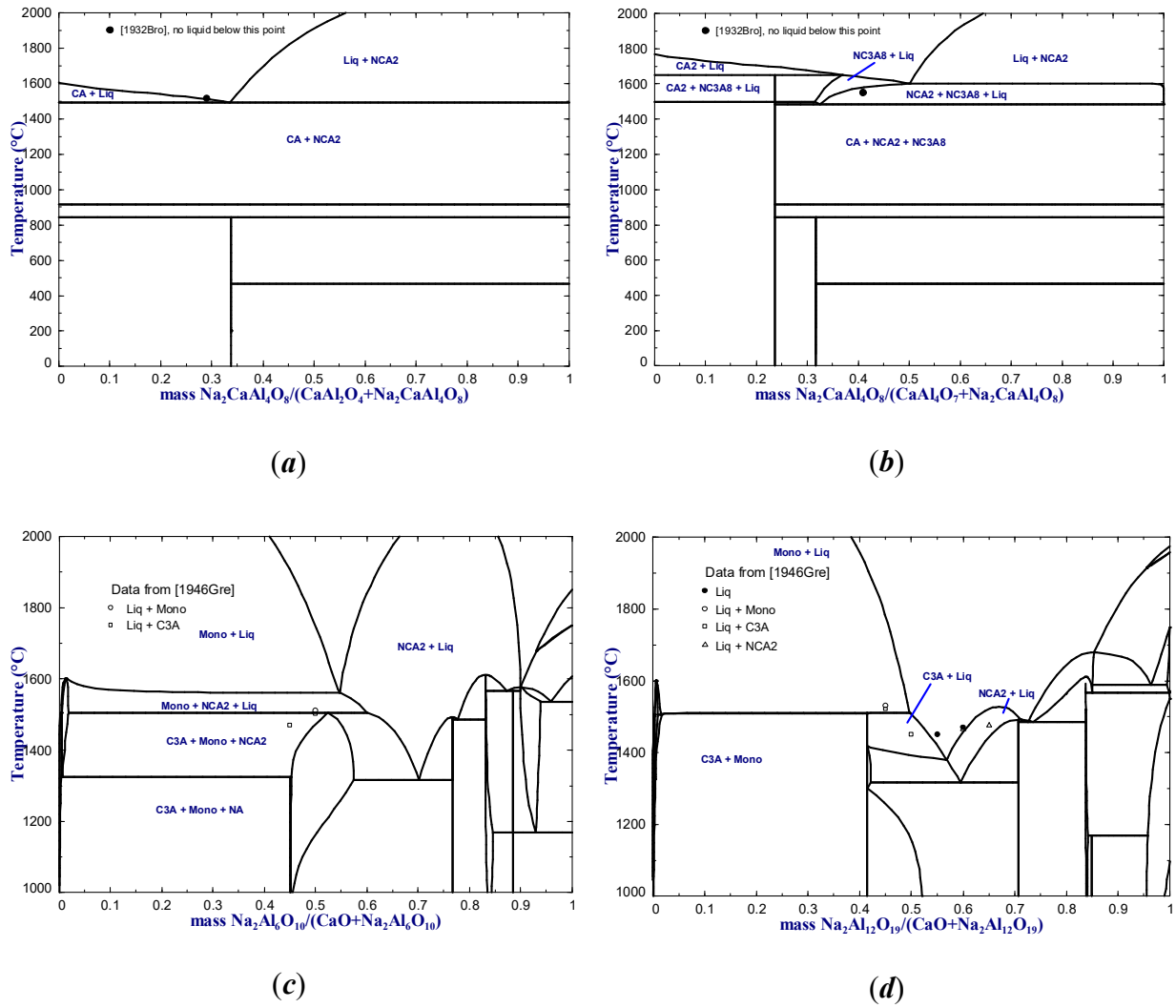

Figure 15.3 Phase diagrams in sections through the CaO-Na_2O-Al_2O_3 system. Experimental points [97, 443] and calculated lines.

The study of clinker materials doped with various elements is important to the cement industry. Alkali oxides are among the most common dopants. In general, significant amounts of Na_2O are detrimental to the clinker quality because upon its addition the hydraulically active compounds (calcium aluminates) are transformed into inert $NaAlO_2$ and CaO. Therefore, the limiting solubilities of Na_2O in calcium aluminates determine the tolerance level to alkali impurities.

A significant amount of works confirm the findings by Brownmiller and Bogue [97] about the solid solution existing between C3A and C8NA3. Conwicke and Day [98] studied the crystal chemistry of the solid solutions in more detail. They found that up to 2.25 wt% Na_2O in C3A the original cubic structure persists while starting from 4.20 wt% Na_2O, the solid solutions have a lower symmetry. Between 2.25 and 4.20 wt%, two structures coexist. The data by Flecher et al. [8] are in a very good agreement with these observations. According to them, the mixed regions are situated between 2.1 and 4.2 wt% Na_2O. The limiting solubility of Na_2O in C3A is 9.0 mol% N3A. The maximum solubility according to Ostrowski and Zelazny [9] is 5.9 wt% Na_2O (which is below the theoretical 7.6 wt% for C8NA3 compound). Also, it was noticed that starting from 5.2 wt% Na_2O, the solid solution is monoclinic. Upon addition of Na_2O, the solid solution undergoes the following symmetry sequence: cubic → orthorhombic → monoclinic. The structural changes were observed both with XRD and IR spectroscopy. These results were confirmed by Lee and Glasser [444] and some other authors. However, the nature of the third phase is less clear. Some researchers describe it as a second orthorhombic phase [445] while others state that it is monoclinic [446]. According to Lee and Glasser [444], the monoclinic solid solution inverts to a tetragonal modification above 550°C. All the modifications can be described with a general formula of $Na_x(Ca_{3-x}Na_x)Al_2O_6$. Apparently, some Ca can be replaced by Na while excess Na required for charge balance occupies vacant positions. The crystal structure of $Ca_{8.5}NaAl_6O_{18}$ was determined by Nishi and Takeuchi [100]. It is orthorhombic and contains Al_6O_{18} rings made of AlO_4 tetrahedra sharing corners. There are 36 available locations altogether for the 34 Ca atoms in the unit cell. The excess locations are preferably distributed in the set of Ca(5) positions to accommodate two of the four Na's per cell. The remaining two Na's are located at the centers of the tetrahedral rings (occupancy of 0.5). Cooperative substitution by Na and K in C3A was studied by Shin and Glasser [99]. It seems that the solubility of K_2O increases in the presence of Na_2O.

According to Ostrowski and Zelazny [9], a solid solution of Na_2O in C12A7 can form (up to 1.8 wt% Na_2O). However, as it was confirmed that the compound is a hydrate, these data were not considered in the current optimization. Apparently, a small solid solution of Na_2O in C5A3 also refers to the same phase. CA properties did not show any noticeable changes with Na_2O presence.

Although CA6 and Na-β-alumina share the same structure, no noticeable mutual solubility has been found [441].

15.2 Optimization results

The Na_2O-Al_2O_3 binary system was optimized in this work. The optimization of the CaO-Al_2O_3 system by Eriksson and Pelton [123] was adopted. The Na_2O-CaO system was assumed ideal.

The compound with NC4A10 or NC4A9 stoichiometry by Zaldat et al. [442] was considered the same as NC3A8 reported elsewhere. The heat capacity of NC3A8 ternary compound was approximated as a weighted sum of the heat capacities of simple oxides. The same applies to the heat capacity of $Na_2CaAl_4O_8$ end-member of NCA2 solid solution; the heat capacity of $Na_4Al_4O_8$ end-member was taken the same as for sodium aluminate.

There are no calorimetric data on either liquid or solid phases in the system; however, the triangulation data at two different temperatures allow to ascertain the enthalpies of formation and the entropies of NCA2 solid solution and NC3A8 compound.

First, for each temperature, an interval of NC3A8 Gibbs energy values which do not violate the experimental triangulation is found. As for the solid solution, a stoichiometric dummy compound NCA2 was created first. For each limiting value of NC3A8 Gibbs energy a possible Gibbs energy interval of NCA2 compound was found as well. It was found that NCA2 intervals get wider when NC3A8 stability increases. So, it was decided to choose the Gibbs energy of NC3A8 close to the most stable value permitted (at each temperature). The temperature dependence of the Gibbs energy allows to derive the enthalpy of formation and the entropy of NC3A8. The Gibbs energy of NCA2 dummy compound was set keeping in mind the Gibbs energy value at the liquidus temperature (Figure 15.3, (***d***)). NCA2 solid solution properties were adjusted to reproduce those of the dummy compound and the maximum solubility in Figure 15.2, (***a***). The properties of C3A solution were adjusted to reproduce its decomposition temperature (Figure 15.3, (***c***)).

Interaction parameters of the liquid were chosen in the following way. First, a negative $\Delta\omega^{\circ}_{\mathrm{NaAl,Ca}}$ interaction was chosen to suppress immiscibility on the combeite liquidus in the CaO-Na_2O-Al_2O_3-SiO_2 system (the $NaAlSiO_4$-Na_2SiO_3-$CaSiO_3$ plane). Bragg type was chosen because it worked more efficient than the others. Ternary $g^{001}_{\mathrm{Al,Ca(NaAl)}}$ and $g^{001}_{\mathrm{NaAl,Al(Ca)}}$ parameters both change NCA2 liquidus in the ternary system but $g^{001}_{\mathrm{Al,Ca(NaAl)}}$ also influences Al_2O_3 liquidus in the $NaAlSiO_4$-$CaAl_2Si_2O_8$ section of the Na_2O-CaO-Al_2O_3-SiO_2 system, so their combination was chosen

accordingly to adjust both NCA2 liquidus in the Al_2O_3-CaO-Na_2O system and corundum primary field in the Na_2O-CaO-Al_2O_3-SiO_2 system. The optimized parameters are summarized in Table A.18 and Table A.19.

CHAPTER 16 OPTIMIZATION OF THE Al_2O_3-CaO-Na_2O-SiO_2 SYSTEM

Besides the obvious importance to geology, the quaternary system Al_2O_3-CaO-Na_2O-SiO_2 presents a certain interest for the glass-making industry. Alumina is used to lower liquidus and immiscibility temperatures as well as to improve the ageing and mechanical properties of sodium calcium silicate glasses.

16.1 The Anorthite-Gehlenite-Nepheline subsystem ($CaAl_2Si_2O_8$-$Ca_2Al_2SiO_7$-$NaAlSiO_4$)

The boundary system $Ca_2Al_2SiO_7$-$NaAlSiO_4$ was studied by Smalley [447]. This system is quaternary. Carnegieite forms solid solutions and the inversion temperature nepheline/carnegieite is lowered. Gehlenite (tetragonal, melts congruently at 1590°C) forms a solid solution although its nature was not determined [447]. The phase diagram of the section is presented in Figure 16.1. The traces of carnegieite under melilite liquidus, noticed by Smalley are apparently traces of sodium aluminate phase whose properties are very similar to carnegieite [55].

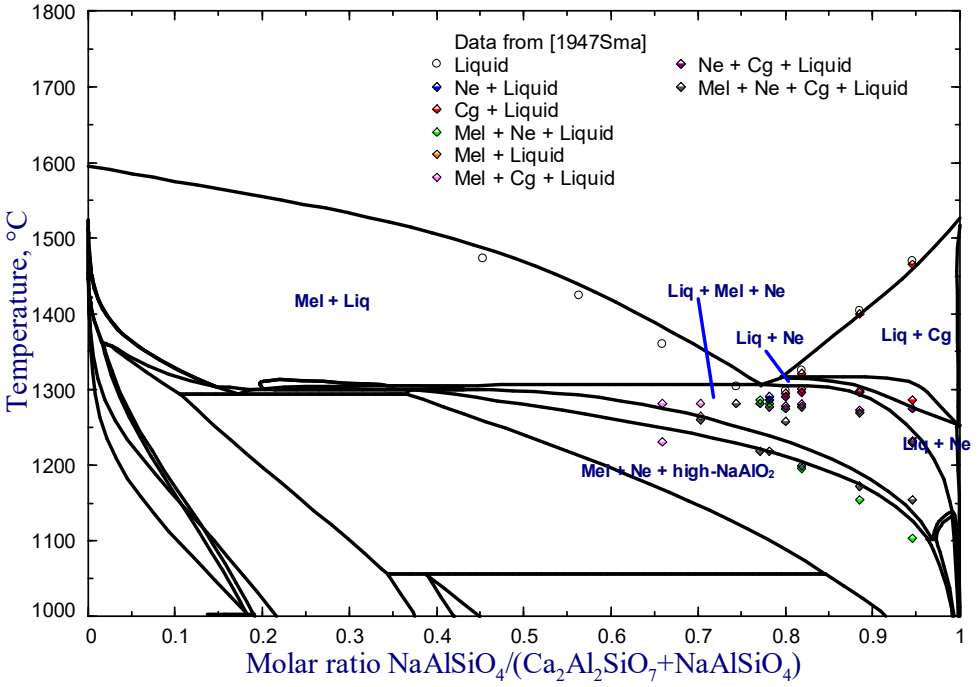

Figure 16.1 Phase diagram of the $Ca_2Al_2SiO_7$-$NaAlSiO_4$ section of the Na_2O-CaO-Al_2O_3-SiO_2 system. Experimental points [447] and calculated lines.

The $NaAlSiO_4$-$CaAl_2Si_2O_8$ boundary was studied by Bowen [52] (Figure 16.2). Synthetic samples of nepheline and anorthite were used in the experiments. All the compositions crystallized readily; the crystallization products were identified optically. Samples were quenched in mercury and heating curves have been registered for the same compositions as well. Only nepheline, carnegieite and anorthite (calcium-rich plagioclase) were reported as solid phases. Nepheline forms a solid solution with anorthite thus raising the carnegieite-nepheline transition temperature. The solubility of anorthite in carnegieite is much less significant. The solidus was measured by finding the temperature at which nepheline solid solution showed first signs of melting. There is an eutectic at 1302°C in the system. The phase diagram of the $CaAl_2Si_2O_8$-$NaAlSiO_4$-$CaSiO_3$ system from Gummer [448] does not entirely agree with the data by Bowen [52]. Gummer assumes that α- or β-alumina may be present in the $NaAlSiO_4$-$CaAl_2Si_2O_8$ boundary although the exact position of its liquidus remains unknown. This observation could also justify the fact that sometimes corundum crystals occur in nepheline-plagioclase bearing rocks.

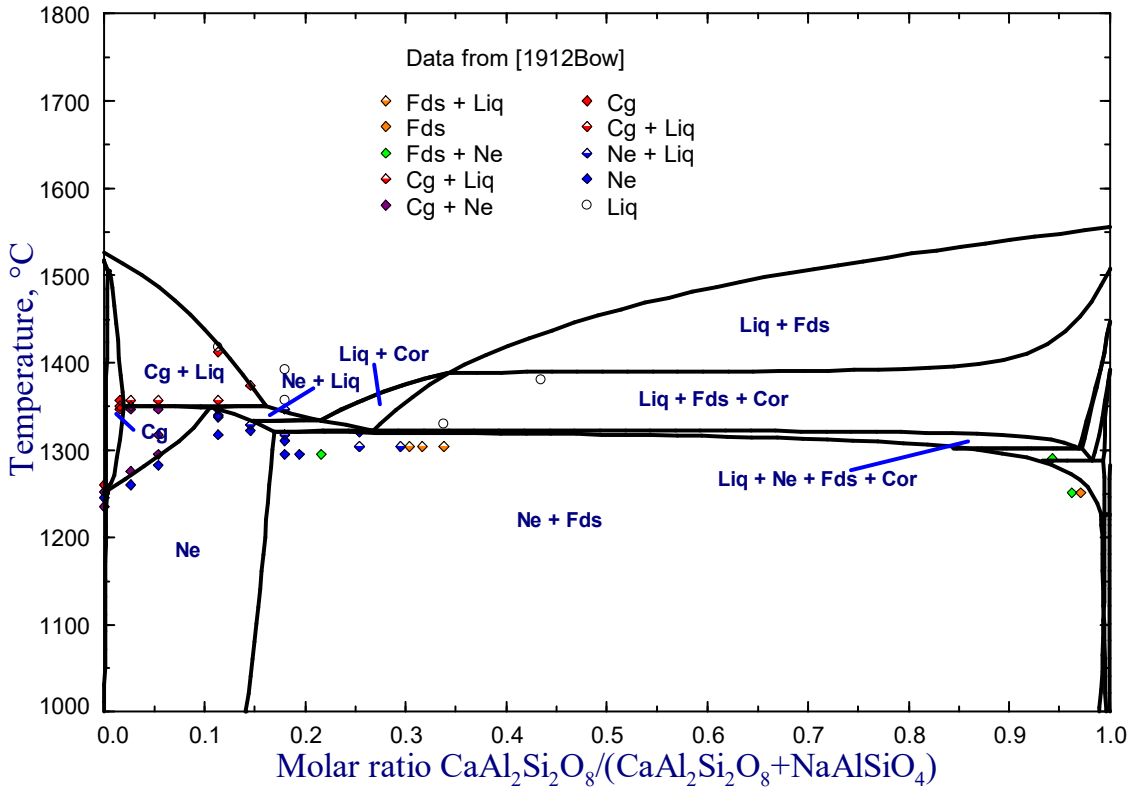

Figure 16.2 Phase diagram of the $CaAl_2Si_2O_8$-$NaAlSiO_4$ section of the Na_2O-CaO-Al_2O_3-SiO_2 system. Experimental points [52] and calculated lines.

The $CaAl_2Si_2O_8$-$Ca_2Al_2SiO_7$-$NaAlSiO_4$ system was investigated by Goldsmith [449] using a quenching method. The system is not ternary because of solid solutions formed by the components. The invariant point in the phase diagram therefore is not a true eutectic but a piercing point. The boundary curve was roughly located inside the compositional tetrahedron and approximated by a straight line running through a composition with 10 wt% of $CaSiO_3$. The formation of solid solutions was confirmed by changes in optical properties compared to the pure end-members. Plagioclase compositions do not differ significantly from the pure anorthite (95-96%) [449]. The pure $CaAl_2Si_2O_8$ melts congruently at 1552°C. Refractive indices of melilites are significantly lower than those for the pure gehlenite $Ca_2Al_2SiO_7$. As Ca is optically "denser" than Na, it is logical to assume that a sodium containing "molecule" enters the melilite structure.

Changes in the inversion temperature between nepheline and carnegieite (1250°C for the pure composition) can be a useful indicator of formation of solid solutions along with changes in optical properties. Usually, nepheline forms more extensive solutions that carnegieite. Goldsmith [449] believes that the $NaAlSiO_4 \leftrightarrow CaAl_2O_4$ substitution mechanism in nephelines is plausible. In that case, the natural samples, containing Ca but not having SiO_2 deficiency could be originated from double substitution $NaAlSiO_4 \leftrightarrow CaAl_2O_4$ and $NaAlSiO_4 \leftrightarrow VaSi_2O_4$. Liquidus projection of the $CaAl_2Si_2O_8$-$Ca_2Al_2SiO_7$-$NaAlSiO_4$ system is given in Figure 16.3.

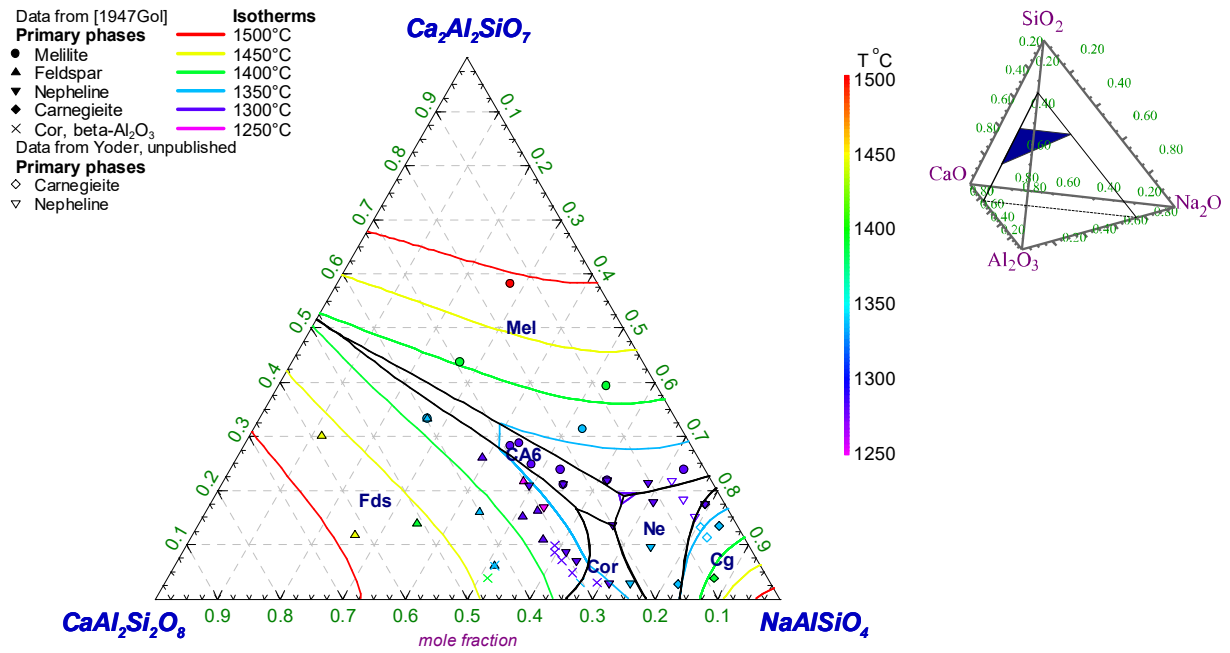

Figure 16.3 Liquidus projection in the $Ca_2Al_2SiO_7$-$CaAl_2Si_2O_8$-$NaAlSiO_4$ plane of the Na_2O-CaO-Al_2O_3-SiO_2 system. Experimental points [449] and calculated lines.

Figure 16.3 features CA6 primary field not present in the available experimental data. During the optimization, it was required to adjust parameters in the CaO-Al_2O_3-Na_2O-SiO_2 and CaO-Al_2O_3-Na_2O systems in order to reproduce the corundum primary field that is present in the $NaAlSiO_4$-$CaAl_2Si_2O_8$ section. However, when the parameters are changed to get the required size of the primary field, CA6 also appears in the liquidus of the $Ca_2Al_2SiO_7$-$CaAl_2Si_2O_8$-$NaAlSiO_4$ system. It can be explained by the fact that CA6 is close to corundum in composition. We can suppose that small quantities of a phase might go undetected in a quenching experiment. According to the literature review in the Al_2O_3-CaO-Na_2O system (Section 15.1), CA6 phase is stable at 1200°C (which is close to the liquidus temperature in Figure 16.3) but does not form due to kinetic reasons [96].

16.2 The Nepheline-CA subsystem ($NaAlSiO_4$-$CaAl_2O_4$)

The $NaAlSiO_4$-$CaAl_2O_4$ system was investigated by Goldsmith [51, 449]. It appears that nepheline is able to include up to 60 wt% of $CaAl_2O_4$ in its structure. The carnegieite solid solution is much more limited (about 5 wt% CA). More of the carnegieite solid solution can form but it is not binary

(excess $NaAlO_2$ is possible). The presence of CA hinders the transition between carnegieite and nepheline and usually it was possible to quench the low-temperature triclinic modification of the carnegieite solution. The study of the system was somewhat complicated by a high Na_2O vapor pressure. CA2 is mostly present instead of CA as a primary phase (it was improperly identified as C3A5 in earlier works). It melts incongruently around 1765°C. Also, α- and β-Al_2O_3 were encountered during the experiments. Determination of α-alumina was complicated by the presence of large amounts of CA2. The authors claim that α- or β-Al_2O_3 has a noticeable primary field in the section although they were not able to define it with good accuracy. Phase diagram of the system is presented in Figure 16.4. The size of α- or β-alumina fields is sensitive to the Na_2O/Al_2O_3 ratio. It is possible that high Na pressure in the system caused the deviation of the real Na_2O/Al_2O_3 ratio in the section from the theoretical values.

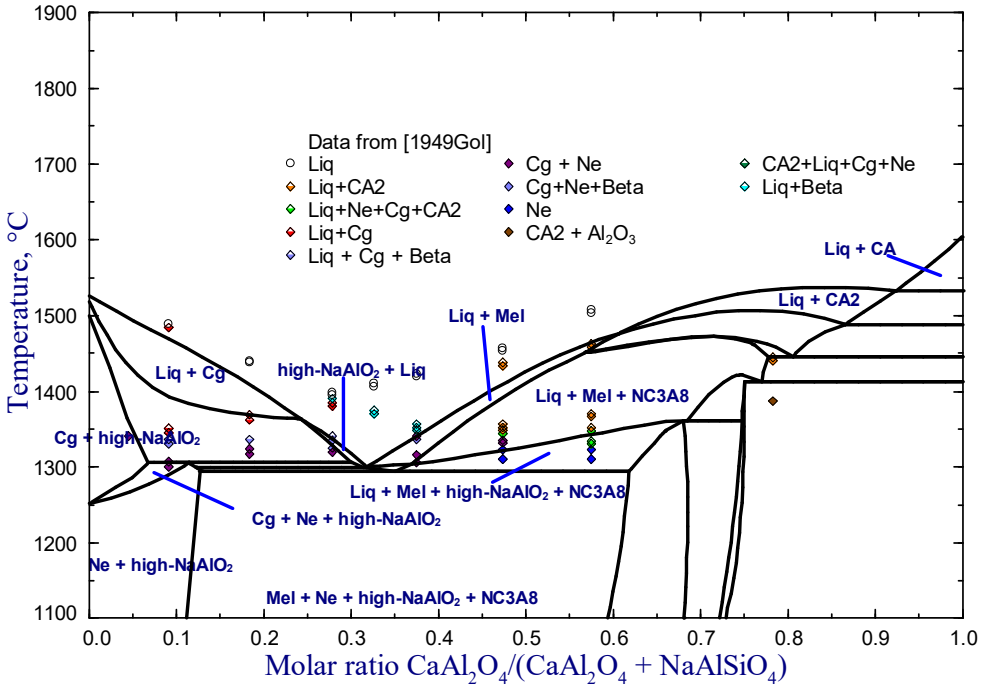

Figure 16.4 Phase diagram of the $CaAl_2O_4$-$NaAlSiO_4$ section of the Na_2O-CaO-Al_2O_3-SiO_2 system. Experimental points [51] and calculated lines.

16.3 The Albite-Nepheline-Wollastonite subsystem ($NaAlSi_3O_8$-$NaAlSiO_4$-$CaSiO_3$)

The system and its boundaries were studied by Foster [73] because of their important applications to geology. Plagioclase (feldspar) contained only small amounts of $CaAl_2Si_2O_8$. Because of the anorthite end-member of the feldspar solution, the system is not truly ternary. $CaSiO_3$ exists in two modifications: high-temperature pseudowollastonite and low-temperature wollastonite. In the $NaAlSiO_4$-$CaSiO_3$ subsystem, no attempts were made to establish the inversion temperature between the two modifications because of a slow inversion rate. However, in the $NaAlSi_3O_8$-$CaSiO_3$ subsystem, the inversion temperature was assigned to 1124°C. Although it is somewhat lower than in the other works, the temperature lowering was not attributed to solid solution formation. The author refers to an unpublished work of Osborn with which they agree about the inversion temperature. The inversion temperature between nepheline and carnegieite is raised by 13°C in the $NaAlSiO_4$-$CaSiO_3$ subsystem. It means that nepheline has a greater solubility of a Ca-containing end-member. From 5 to 10 wt% of $CaSiO_3$ can enter the nepheline structure, probably in the form of $CaAl_2Si_2O_8$. Special attention was given to investigate (1:1) composition in the $NaAlSiO_4$-$CaSiO_3$ system. It corresponds to Na-melilite $CaNaAlSi_2O_7$ which is supposedly an end-member of the melilite solid solution. However, no traces of a new phase were found.

Phase diagrams of the $NaAlSi_3O_8$-$CaSiO_3$ and $NaAlSiO_4$-$CaSiO_3$ boundaries are presented in Figure 16.5 and Figure 16.6, correspondingly. Liquidus projection of the title system is given in Figure 16.7.

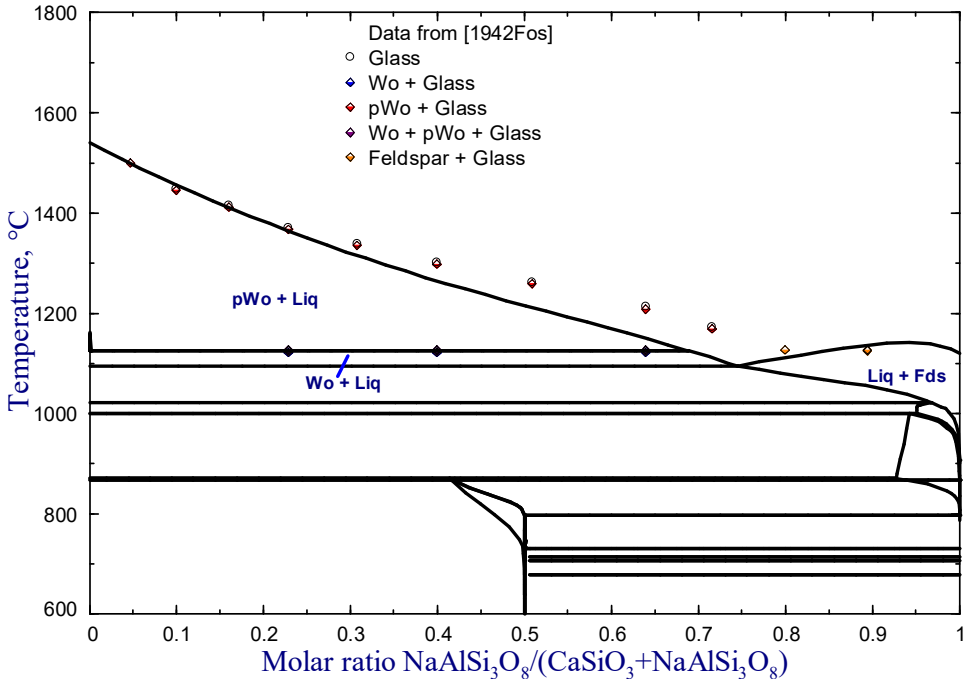

Figure 16.5 Phase diagram of the $CaSiO_3$-$NaAlSi_3O_8$ section of the Na_2O-CaO-Al_2O_3-SiO_2 system. Experimental points [73] and calculated lines.

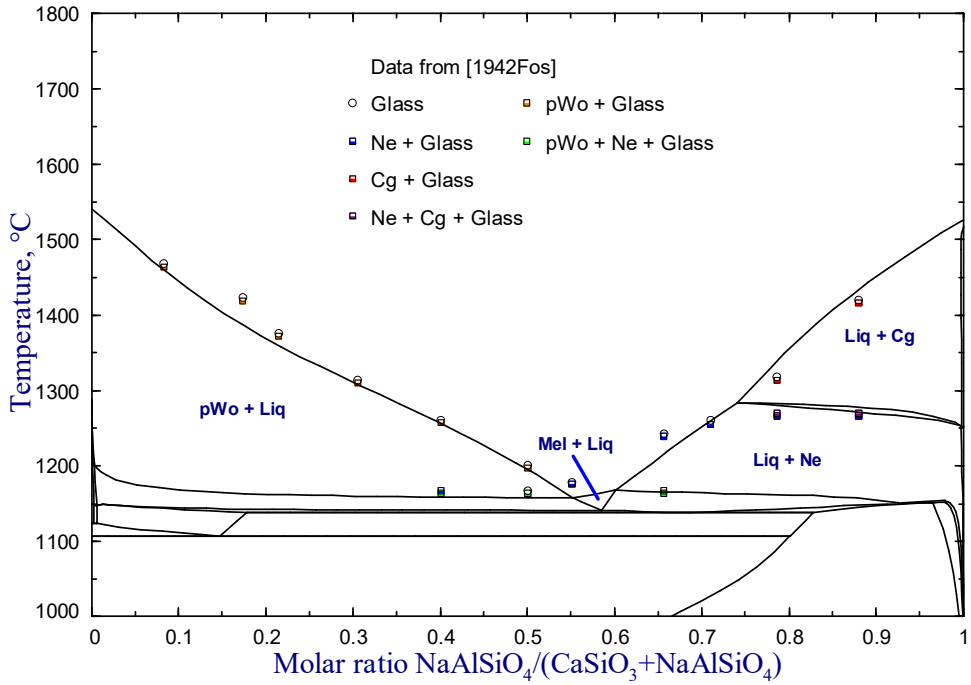

Figure 16.6 Phase diagram of the $CaSiO_3$-$NaAlSiO_4$ section of the Na_2O-CaO-Al_2O_3-SiO_2 system. Experimental points [73] and calculated lines.

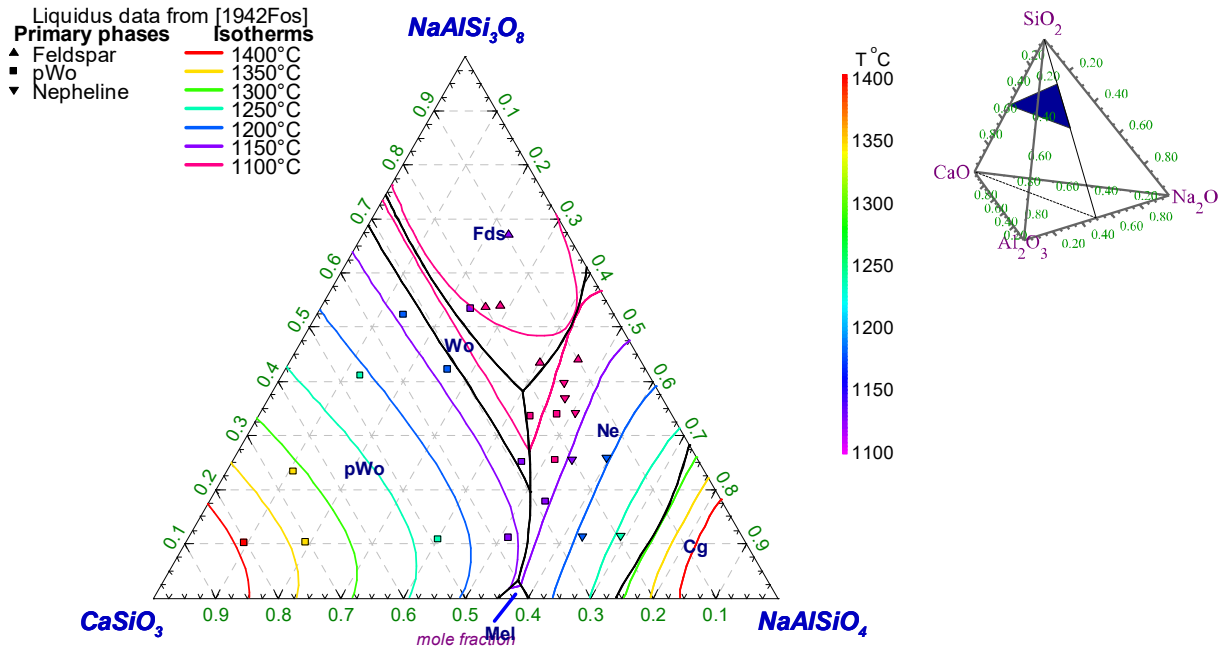

Figure 16.7 Liquidus projection of the $NaAlSi_3O_8$-$CaSiO_3$-$NaAlSiO_4$ plane of the Na_2O-CaO-Al_2O_3-SiO_2 system. Experimental points [73] and calculated lines.

16.4 The Albite-Anorthite subsystem ($NaAlSi_3O_8$-$CaAl_2SiO_8$)

16.4.1 Phase diagram

The study by Bowen [286] was one of the first publications on the $NaAlSi_3O_8$-$CaAl_2Si_2O_8$ system. It is crucial to geological applications as it includes one of the most important solid solution series, plagioclase. The article describes the quenching method in detail, and the consequent works on different parts of the Al_2O_3-CaO-Na_2O-SiO_2 system use essentially the same technique. Both liquidus and solidus were determined; the error margin for liquidus determinations being 2°C and for solidus 4°C. For the compositions rich in albite, the investigators experienced certain crystallization difficulties. The melting point of the pure albite was obtained by extrapolation and the value was considered reliable due to a flat liquidus near the albite composition. The data by Day and Allen [377] who measured heating curves were found to lie close to the liquidus. From the work of these authors alone it was unclear to what the thermal arrests were attributed to.

The subsolidus relations of plagioclase feldspars in Figure 16.8 were taken from a compilation by Smith [68] on phase relations in feldspars. In this work, no distinction was made between different modifications of Na-rich and Ca-rich plagioclases; the miscibility gap, however, is reproduced.

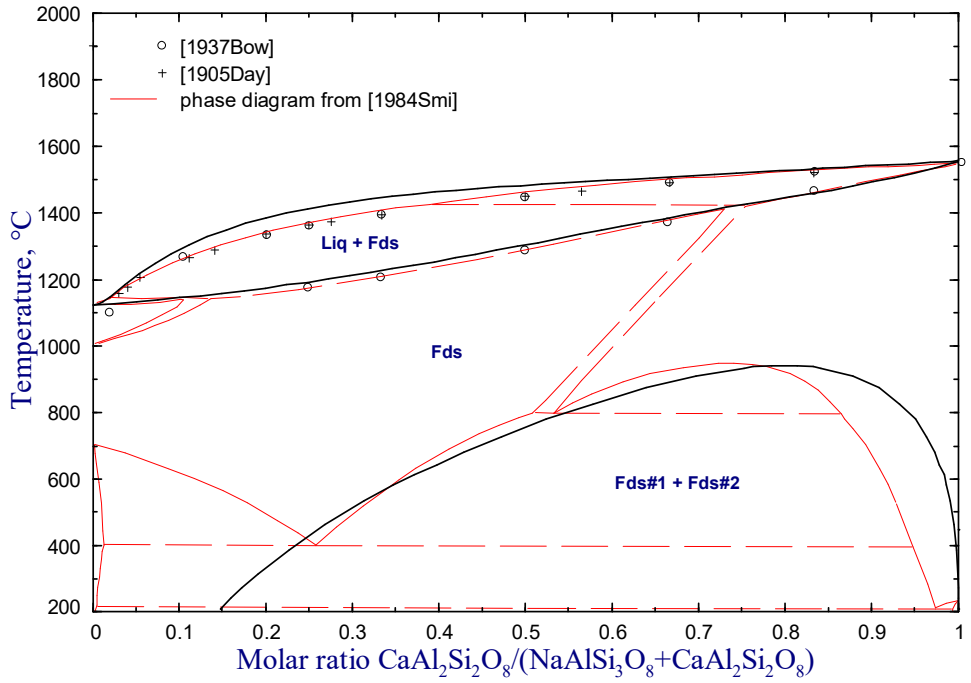

Figure 16.8 Phase diagram of the $NaAlSi_3O_8$-$CaAl_2Si_2O_8$ section of the Na_2O-CaO-Al_2O_3-SiO_2 system. Experimental points [286, 377], the compiled phase diagram by Smith [68] and the calculated lines.

16.4.2 Calorimetry data

To determine the enthalpies of formation of alumosilicates, the solution calorimetry is used. The most popular are the solution calorimetry in 2PbO-B_2O_3 at around 710°C and the calorimetry at 25°C using HF solutions (as a rule, 20 wt% HF solutions are employed). However, HF dissolution experiments with Ca-containing materials can be complicated by the formation of insoluble particles of CaF_2.

The data available in the literature can be divided into calorimetry of glasses and calorimetry of crystals (Figure 16.9). Plagioclases $NaAlS_3O_8$-$CaAl_2Si_2O_8$ are by far the most investigated crystalline compositions in the system.

Navrotsky et al. [315] studied vitreous samples of $NaAlSi_3O_8$-$CaAl_2Si_2O_8$ and $NaAlSi_3O_8$-$CaAl_2Si_2O_8$-SiO_2 compositions by means of lead borate solution calorimetry. From a structural point of view, it was concluded that the mixing between AlO_4 and SiO_4 tetrahedra occurs almost ideally over a wide composition range. Sections in which the degree of SiO_2 network polymerization changes are usually characterized by deviations from the ideal mixing behaviour. It is speculated that $CaAl_2Si_2O_8$ and $NaAlSi_3O_8$ melts have different structure and therefore a non-ideal mixing behaviour arises.

Newton et al. [299] also applied lead borate solution calorimetry but in this case, for crystalline feldspars. It was found that plagioclases are unique among solid solutions because they exhibit an exothermic mixing. It can be explained by the size similarity of Na^+ and Ca^{2+} and a small role of the size mismatch (which always gives a positive contribution to the enthalpy of mixing) between the two end-members.

The influence of the cation size factors was addressed in the work of Benisek et al. [450] who compared the enthalpies of mixing of feldspars in Na-Ca and K-Ca series by means of lead borate solution calorimetry.

It is considered that the non-ideal mixing behaviour of plagioclases is due to different structural states of the solid solution end-members [297, 451]. Between albite with $C\bar{1}$ structure and anorthite with $I\bar{1}$ structure, there must be a line of structural transition. It was shown that after performing necessary stability recalculations for anorthite between the anorthite and albite-like structures, the experimentally measured non-ideality of mixing disappears [450].

The enthalpies of ordering for pure albite and intermediate plagioclase compositions were measured in a series of works [297, 299, 452].

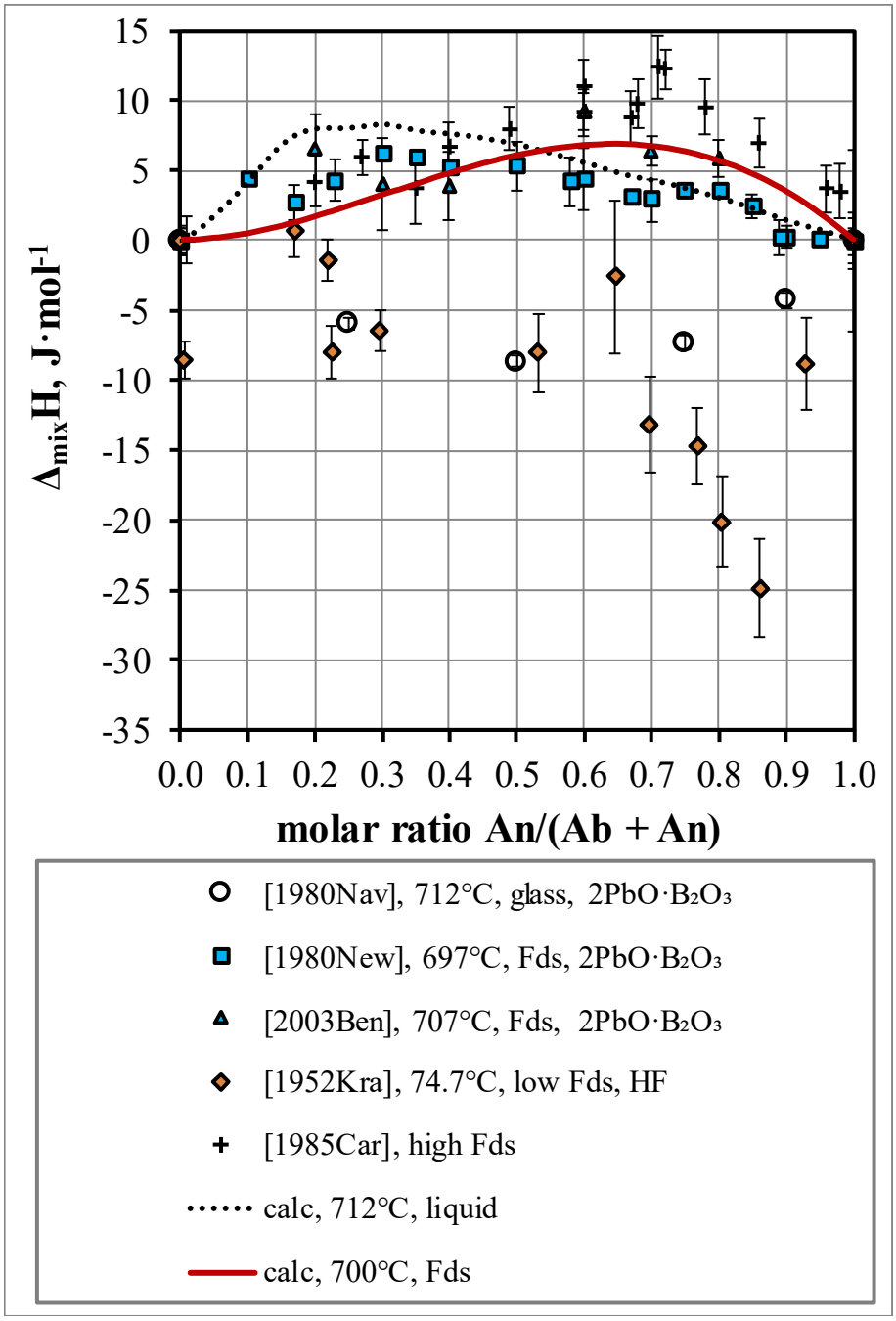

Figure 16.9 The enthalpy of mixing in the $NaAlSi_3O_8$-$CaAl_2Si_2O_8$ section for the liquid and feldspar. Experimental points [297, 299, 315, 450, 452] and calculated lines.

Transposed-temperature-drop calorimetry was performed by Navrotsky et al. [453] according to the scheme:

$$x\text{Ab}(\textit{crystals}, 298\text{K})+(1-x)\text{An}(\textit{crystals}, 298\text{K}) = \text{Ab}_x\text{An}_{1-x}(\textit{melt}, 1500°\text{C}) \qquad (132)$$

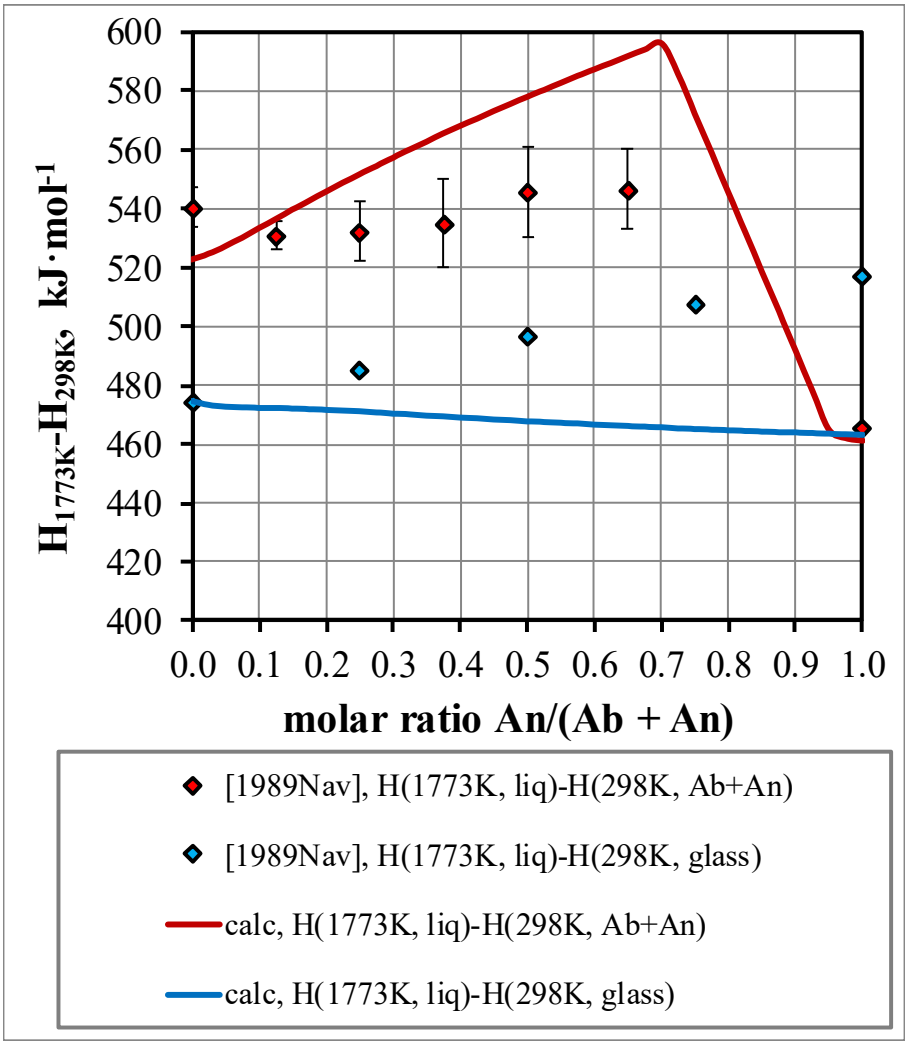

Figure 16.10 The heat content in the albite-anorthite ($NaAlSi_3O_8$-$CaAl_2Si_2O_8$) section. Experimental points [453] and calculated lines.

The results of these experiments and the predicted line are presented in Figure 16.10 in red. The points follow a rising trend until x(An) = 0.7 is reached which corresponds to the liquidus composition at this temperature (Figure 16.8). It means that at the experimental temperature, all compositions richer in An than this point are partially solid; at the point corresponding to the pure anorthite, the crystals did not melt. The coincidence of the predicted line at this point is good which is described by a correct C_P of crystalline anorthite in the database. The fit for intermediate mixtures is not so good. In fact, this is caused by a difference between the true heat capacity of silicate melts and the predicted values (this discrepancy is discussed in detail in section 2.5.1). The series in blue corresponds to drop calorimetry experiments performed with hot silicate melts poured into a

calorimeter where they form glasses. The total heat content is a sum of the heat content of the liquid and the glass. The same discrepancies with the heat content of silicate liquids cause the observed deviation between the measured and the calculated values.

16.4.3 Activity data

The work of Orville [454] on cation exchange between plagioclases and $NaCl$-$CaCl_2$-H_2O brines in the presence of excess quartz is fundamental; it is used as a point of reference for consequent experimental works and its data are used for theoretical investigations in geology. Plagioclase glasses were used as the starting materials. Orville cites sources indicating that synthetic plagioclases can undergo a partial Al/Si ordering under hydrothermal conditions depending on the temperature and the experiment time. The experiments were carried out at 700°C and 2 kbar.

Schliestedt and Wilhelm [455] performed cation exchange equilibria between a synthetic plagioclase and aqueous chloride solution in the temperature range 600-700°C and pressures of 2 and 5 kbar. Gels were used as the starting material. Cation distributions do not change significantly with temperature and pressure. Apparently, plagioclases were disordered. The Ab and An activities recalculated in the original work were used in this study.

The data by Newton et al. [299] were calculated based on the Margules equation from the data on the enthalpy of solution of plagioclases.

Kotelnikov [456] used ion exchange data by Seck [457] to obtain activities of the end-members in $NaAlSi_3O_8$-$CaAl_2Si_2O_8$ feldspars. Kotelnikov et al. [458] studied the cation distribution between plagioclases and an aqueous $NaCl$-$CaCl_2$ solution at 700°C. Plagioclase glasses were used as a starting material. It is noted that hydrothermal conditions can lead to a partial ordering of synthetic plagioclases. The available activity data in plagioclases are summarized in Figure 16.11. There is a good agreement between the data by Kotelnikov [456] (recalculated data by Seck [457]). Worse agreement with the data by Orville [454] could be explained by a partial ordering of samples. A bad description of the data by Newton et al. [299] can be explained by the fact that these activity were calculated and not measured directly.

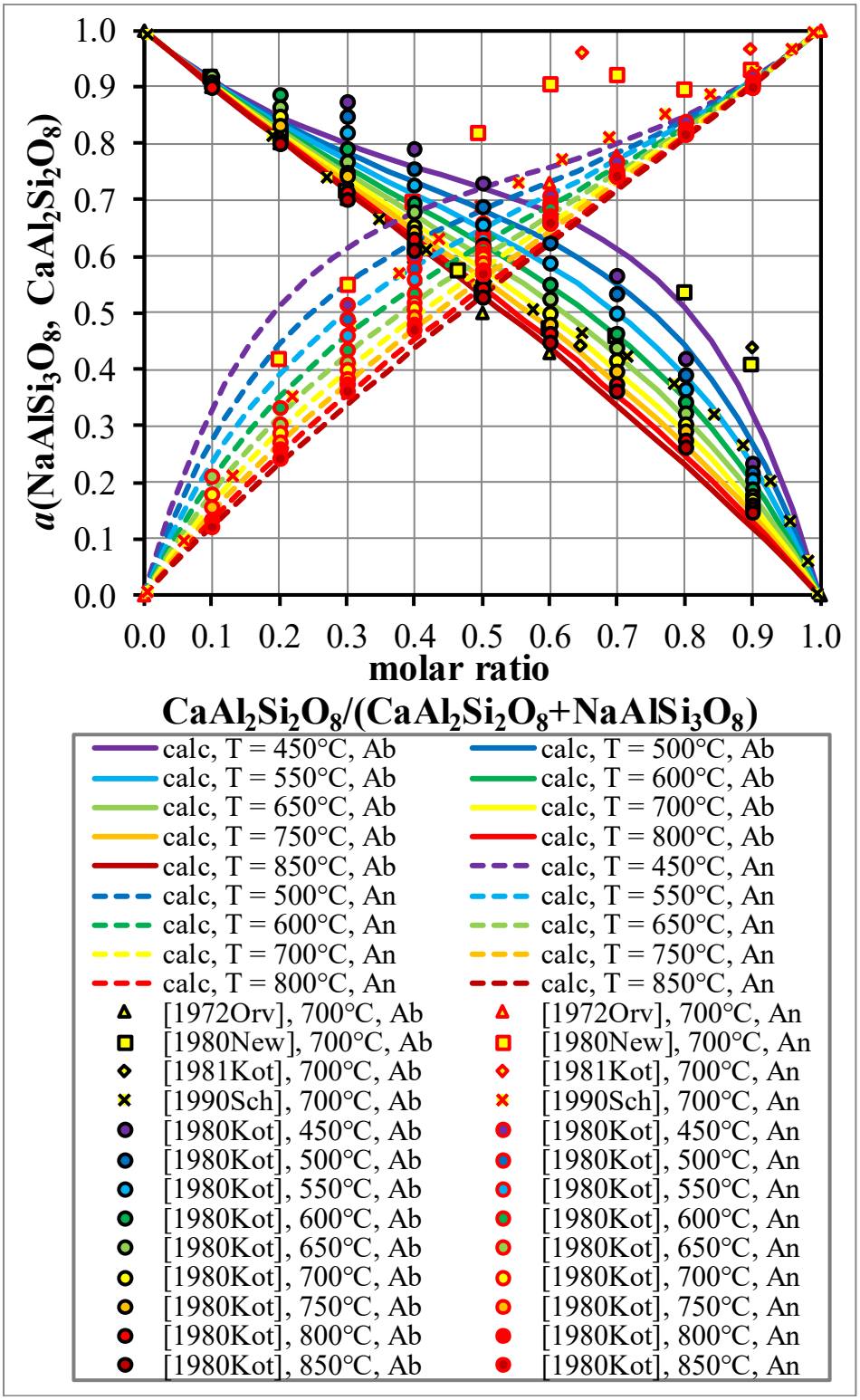

Figure 16.11 Activities of $NaAlSi_3O_8$ and $CaAl_2Si_2O_8$ in plagioclase feldspars at different temperatures. Experimental points [299, 454-456] and calculated lines.

16.5 The Anorthite-Nepheline-Wollastonite subsystem ($CaAl_2Si_2O_8$-$NaAlSiO_4$-$CaSiO_3$)

The system was studied by Juan [72] and by Gummer [448]. According to Gummer [448], the inversion temperature of $CaSiO_3$ does not change substantially; it allows us to conclude that no other substances enter its structure to a significant degree.

The subsystem $NaAlSiO_4$-$CaAl_2Si_2O_8$ is discussed in detail in section 16.1. Liquidus projection of the title system is shown in Figure 16.12.

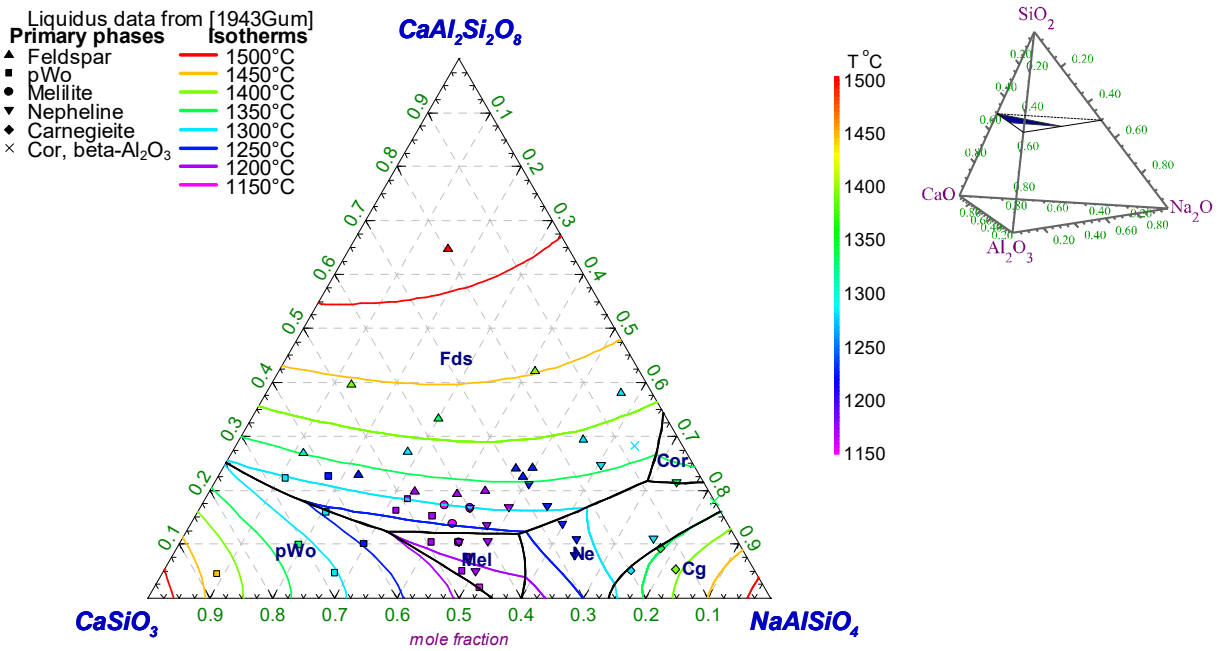

Figure 16.12 Liquidus projection in the $CaAl_2Si_2O_8$-$CaSiO_3$-$NaAlSiO_4$ plane of the Na_2O-CaO-Al_2O_3-SiO_2 system. Experimental points [448] and calculated lines.

16.6 The Gehlenite-Nepheline-Wollastonite subsystem ($Ca_2Al_2SiO_7$-$NaAlSiO_4$-$CaSiO_3$)

Juan [72] studied the $Ca_2Al_2SiO_7$-$NaAlSiO_4$-$CaSiO_3$ system (Figure 16.13). There are four primary fields in the system: melilite, pseudowollastonite, carnegieite and nepheline. The is a maximum on the boundary curve between pseudowollastonite and nepheline at about 6 wt% Geh and 1182±2°C.

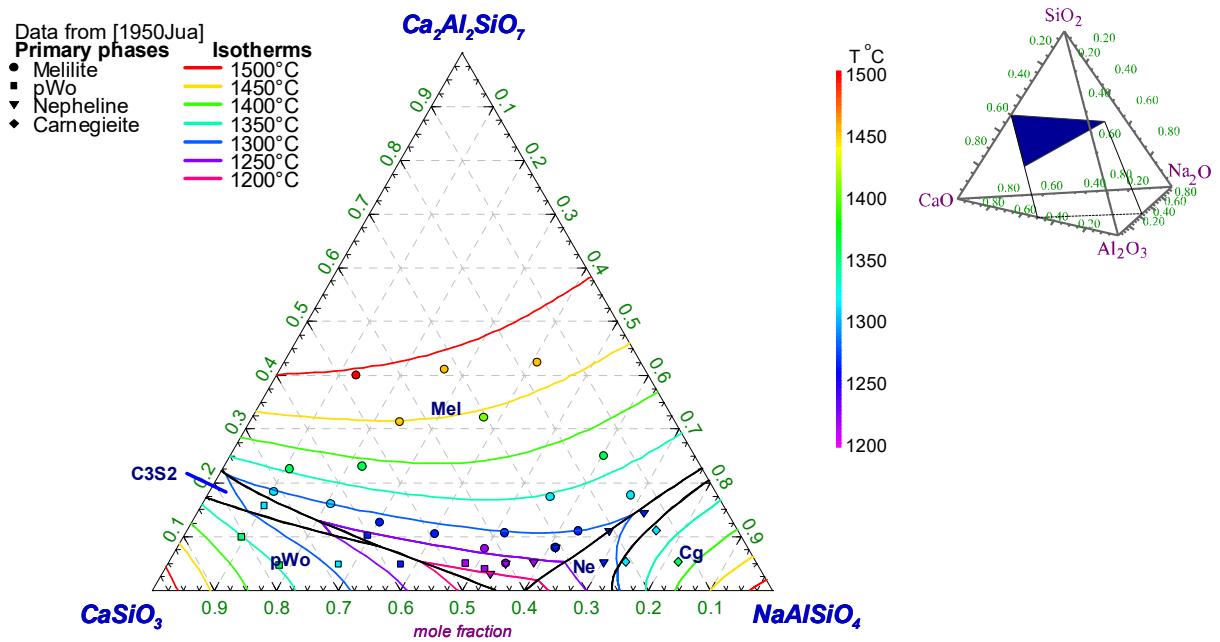

Figure 16.13 Liquidus projection in the $Ca_2Al_2SiO_7$-$CaSiO_3$-$NaAlSiO_4$ plane of the Na_2O-CaO-Al_2O_3-SiO_2 system. Experimental points [72] and calculated lines.

The system also includes the melilite section $Ca_2Al_2SiO_7$-$NaCaAlSi_2O_7$ going from the $CaAl_2SiO_7$ corner to the middle of the $CaSiO_3$-$NaAlSiO_4$ boundary. Its phase diagram was investigated by Schairer et al. [459] and is shown in Figure 16.14. It is generally assumed that sodium can enter the melilite structure in the form of $NaCaAlSi_2O_7$ end-member. However, Schairer et al. [71] has shown that the pure $NaCaAlSi_2O_7$ end-member cannot be obtained under normal pressure and becomes stabilized only under moderate pressures [460]. At 1 atm, the synthesized crystals break down into nepheline $NaAlSiO_4$ and wollastonite $CaSiO_3$. Studies of the $NaAlSiO_4$-$CaSiO_3$ system (which contains the $NaCaAlSi_2O_7$ composition) also confirm the absence of any stable compounds in the $NaAlSiO_4$-$CaSiO_3$ boundary [72, 73]. According to the studies of the $Ca_2Al_2SiO_7$-$CaNaAlSi_2O_7$ system, the content of Na-Mel in the solid solution does not exceed 52 wt% [71].

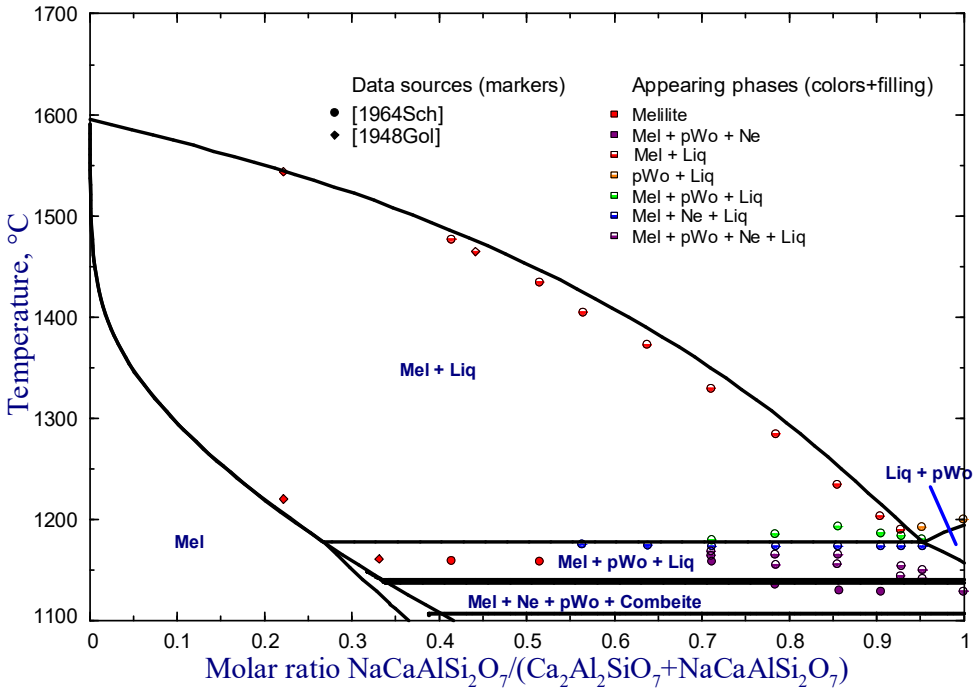

Figure 16.14 Phase diagram of the $Ca_2Al_2SiO_7$-$NaCaAlSi_2O_7$ section of the Na_2O-CaO-Al_2O_3-SiO_2 system. Experimental points [459, 461] and calculated lines.

Yoder [462] studied the $Ca_2Al_2SiO_7$-$CaSiO_3$-$NaAlSiO_4$ system with 10 wt% $CaAl_2Si_2O_8$ by means of quenching and microscopic examination of the products (Figure 16.15). Phase fields of pseudowollastonite, melilite, nepheline and carnegieite are reported. The temperature of the piercing point pWo-Mel-Ne lies between 1169 and 1178°C, the best approximation is 1173°C. The maximum in the Ne-pWo boundary curve found in the $Ca_2Al_2SiO_7$-$CaSiO_3$-$NaAlSiO_4$ system [72] was not reproduced in this plane.

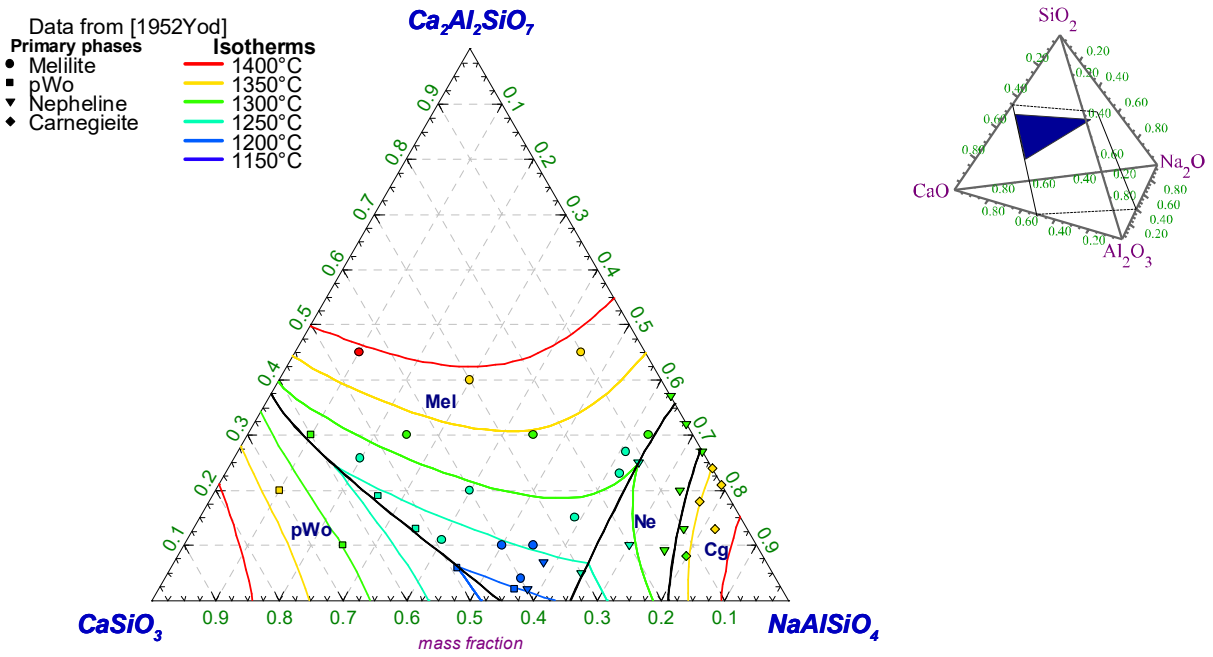

Figure 16.15 Liquidus projection in the $Ca_2Al_2SiO_7$-$CaSiO_3$-$NaAlSiO_4$ + 10 wt% $CaAl_2Si_2O_8$ plane of the Na_2O-CaO-Al_2O_3-SiO_2 system. Experimental points [462] and calculated lines.

16.7 The Nepheline-Wollastonite-Sodium Metasilicate subsystem ($NaAlSiO_4$-$CaSiO_3$-Na_2SiO_3)

Although Na_2SiO_3 is not naturally present as an individual mineral, it is considered as a possible component of residual magmas where soda/alumina ratio exceeds one. It extends the plane of the $NaAlSiO_4$-$CaSiO_3$-$CaAl_2Si_2O_8$ subsystem in the quaternary system and together they are parts of the metasilicate section of the quaternary system Al_2SiO_5-$CaSiO_3$-Na_2SiO_3 (sillimanite-wollastonite-sodium metasilicate). The $NaAlSiO_4$-$CaSiO_3$-Na_2SiO_3 system was studied by Spivak [463] by quenching. The forming phases were examined under a petrographic microscope. The system is not strictly ternary because anorthite enters the nepheline phase. A few isothermal phase diagrams are presented in the source paper but these are rather schematic and do not show the experimental points. Liquidus projection of the title system is presented in Figure 16.16.

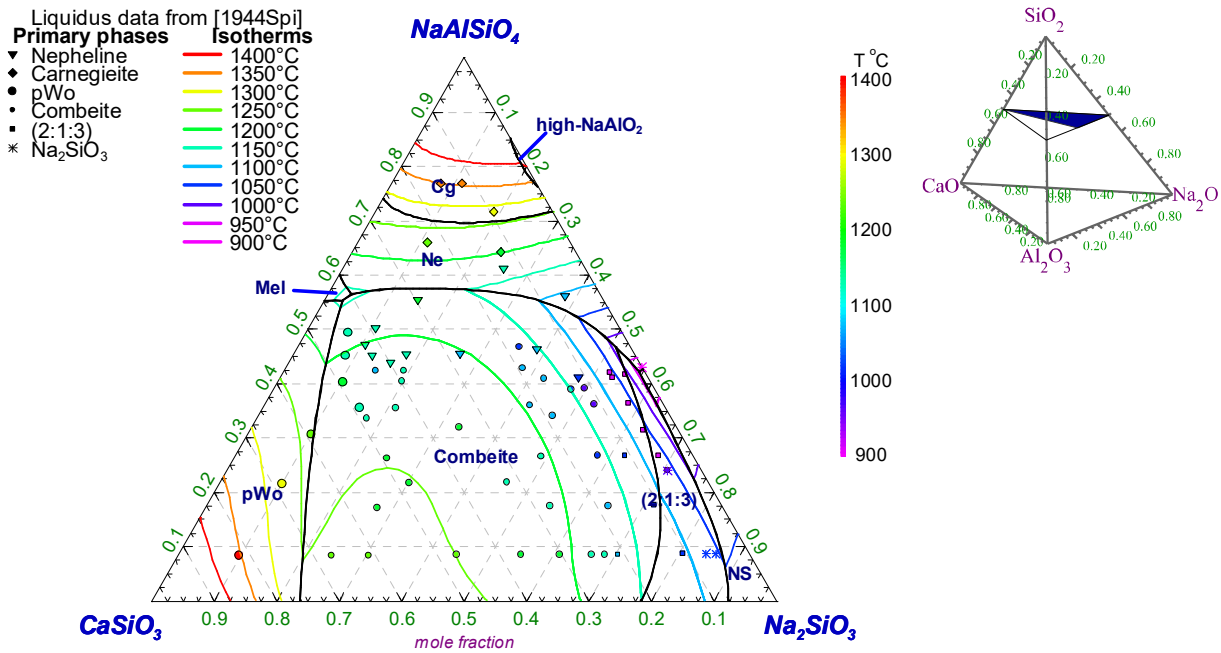

Figure 16.16 Liquidus projection in the $NaAlSiO_4$-$CaSiO_3$-Na_2SiO_3 plane of the Na_2O-CaO-Al_2O_3-SiO_2 system. Experimental points [463] and calculated lines.

16.8 The Ca-Tschermak-Jadeite $CaAl_2SiO_6$-$NaAlSi_2O_6$ system

The $CaAl_2SiO_6$-$NaAlSi_2O_6$ section is mentioned in this work because it is the section where clinopyroxene compositions reside. Neither $CaAl_2SiO_6$ nor $NaAlSi_2O_6$ composition is stable there is no phase diagram available in the literature. Cohen [464] published an estimated enthalpy of mixing of pyroxenes in the quaternary system based on the high pressure equilibration data with grossularite and corundum by Gasparik [80]. These data are presented in Figure 16.17.

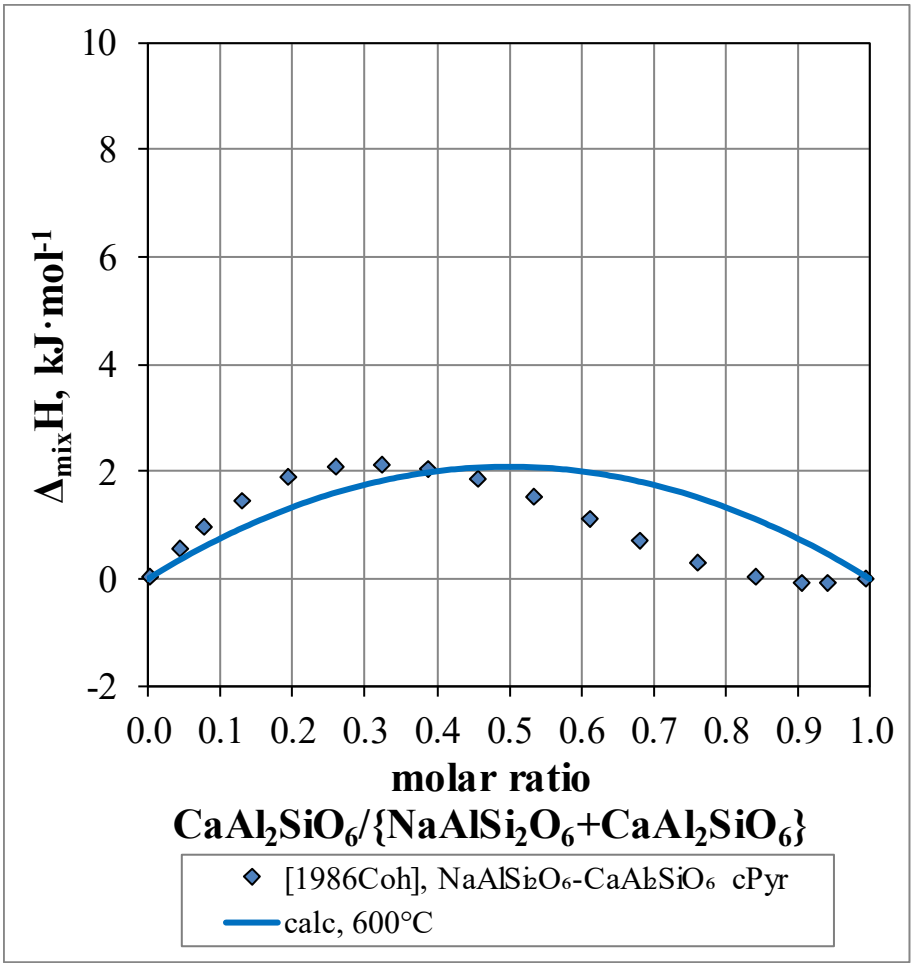

Figure 16.17 The enthalpy of mixing of $CaAl_2SiO_6$-$NaAlSi_2O_6$ clinopyroxenes. Data calculated from equilibria [464] (the points are from a digitized curve) and the calculated line.

16.9 SiO_2-deficient part: Ca_2SiO_4-CaO-$NaAlO_2$-Al_2O_3

Studies of the SiO_2-deficient part of the system were undertaken by Greene and Bogue [443]. More specifically, three planes were studied: Ca_2SiO_4-CaO-$Na_2O{\cdot}6Al_2O_3$, Ca_2SiO_4-CaO-$Na_2O{\cdot}3Al_2O_3$ and Ca_2SiO_4-CaO-$NaAlO_2$. These planes and a boundary to one of them, Ca_2SiO_4-Na2O·$6Al_2O_3$ are shown in Figure 16.18, Figure 16.20-Figure 16.22. During the experiments, the Na_2O volatility and thermoelement corrosion had to be dealt with. To minimize the Na_2O volatility, the annealing times were made as short as possible for the attainment of equilibrium. The thermocouples were frequently recalibrated to reduce the imprecision introduced by the corrosion. The reported phase assemblages usually contained at least one solid phase and the determination of liquidus

temperatures is not possible based on the published data. The absence of NCA2 solid solution among the analysed phases in the data by Greene and Bogue is probably explained by the fact that NCA2 and $NaAlO_2$ have very similar properties as it was established by Brownmiller and Bogue [97] in their work on the CaO-Na_2O-Al_2O_3 system. The liquidus of NCA2 phase is constrained by the optimization of the CaO-Na_2O-Al_2O_3 system and therefore, it extrapolates to the quaternary system.

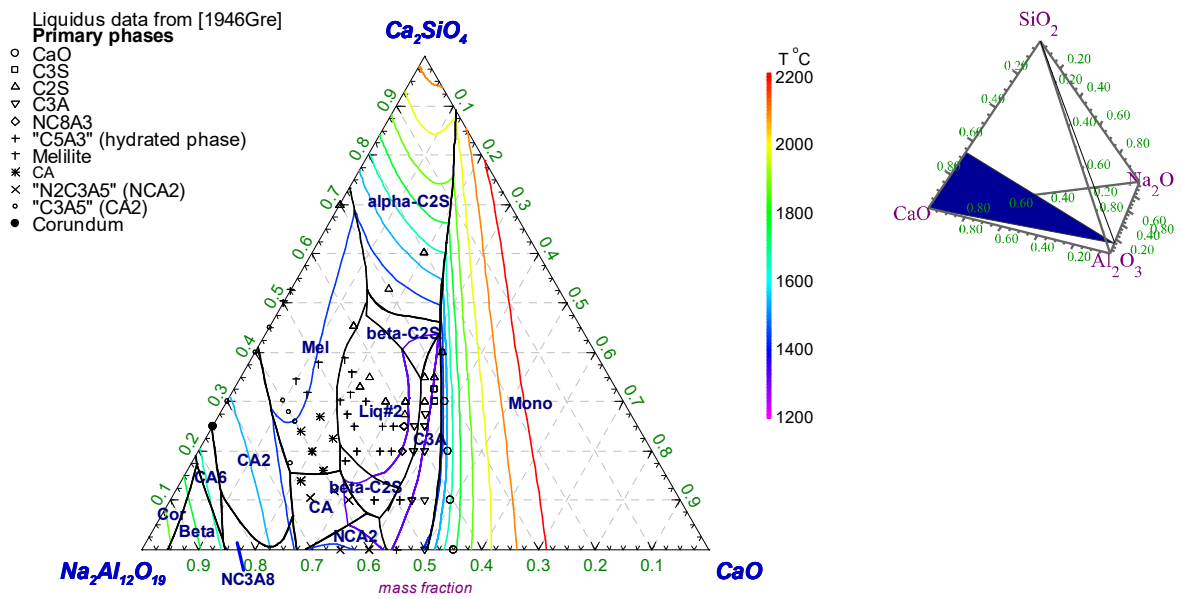

Figure 16.18 Liquidus projection in the Ca_2SiO_4-$Na_2Al_{12}O_{19}$-CaO plane of the Na_2O-CaO-Al_2O_3-SiO_2 system. Experimental points [443] and calculated lines.

To elucidate the nature of the immiscibility gap appearing in the liquidus projection in Figure 16.18, we analysed the direction of tie-lines in it (Figure 16.19).

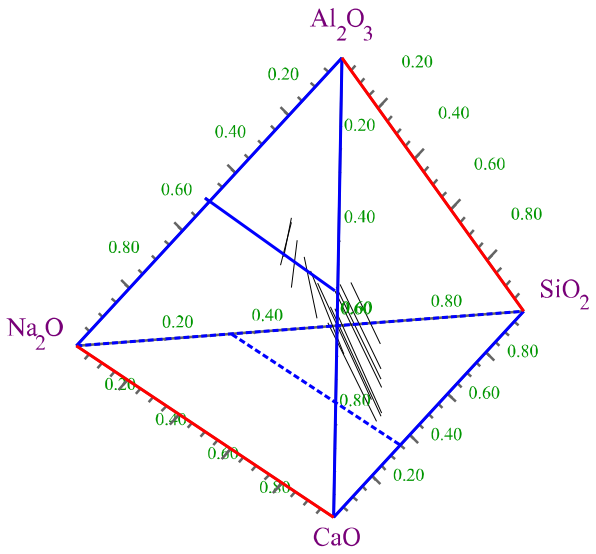

Figure 16.19 Tie-lines of the miscibility gap appearing in the liquidus projection of the Ca_2SiO_4-$Na_2Al_{12}O_{19}$-CaO plane at 1200°C without any solid phases selected. The binary systems with strong negative interactions are shown in blue, the binary systems with ideal or near-ideal interactions are shown in red.

It appears that the tie-lines in Figure 16.19 are approximately directed from the Na_2O-Al_2O_3-CaO ternary system to the Na_2O-CaO-SiO_2 ternary system. In Figure 16.19, the binary systems with substantial negative interaction parameters are highlighted in blue while the systems with nearly ideal interactions are highlighted in red. The blue lines on the Na_2O-Al_2O_3-CaO and Na_2O-CaO-SiO_2 faces connect the maximum SRO compositions in the corresponding binaries. It has also to be noted that these lines repeat the direction of the asymmetric Toop-extrapolations in these systems. In other words, they denote the compositions of stable liquids in the ternary systems Na_2O-Al_2O_3-CaO and Na_2O-CaO-SiO_2. An unstable combination of Na_2O-CaO and Al_2O_3-SiO_2 liquids decomposes into a combination of stable Na_2O-Al_2O_3-CaO and Na_2O-CaO-SiO_2 liquids giving rise to a metastable miscibility gap; the phenomenon is similar to miscibility gaps appearing in reciprocal systems [465]. We suppose that at least a tendency to immiscibility must exist in the described region of the quaternary phase diagram. However, it remains unclear if the gap is supposed to appear at liquidus temperatures. The SiO_2-low region of the quaternary system has never been investigated for the presence of miscibility gaps and they would be difficult to observe at high temperatures for a liquid with low viscosity.

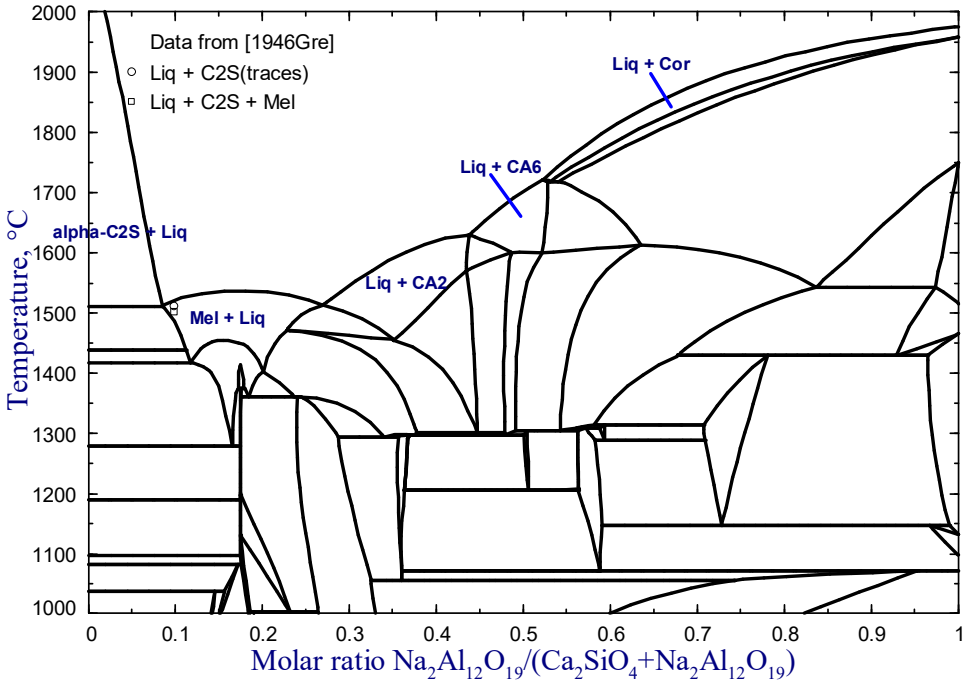

Figure 16.20 Phase diagram of the Ca_2SiO_4-$Na_2Al_{12}O_{19}$ section of the Na_2O-CaO-Al_2O_3-SiO_2 system. Experimental points [443] and calculated lines.

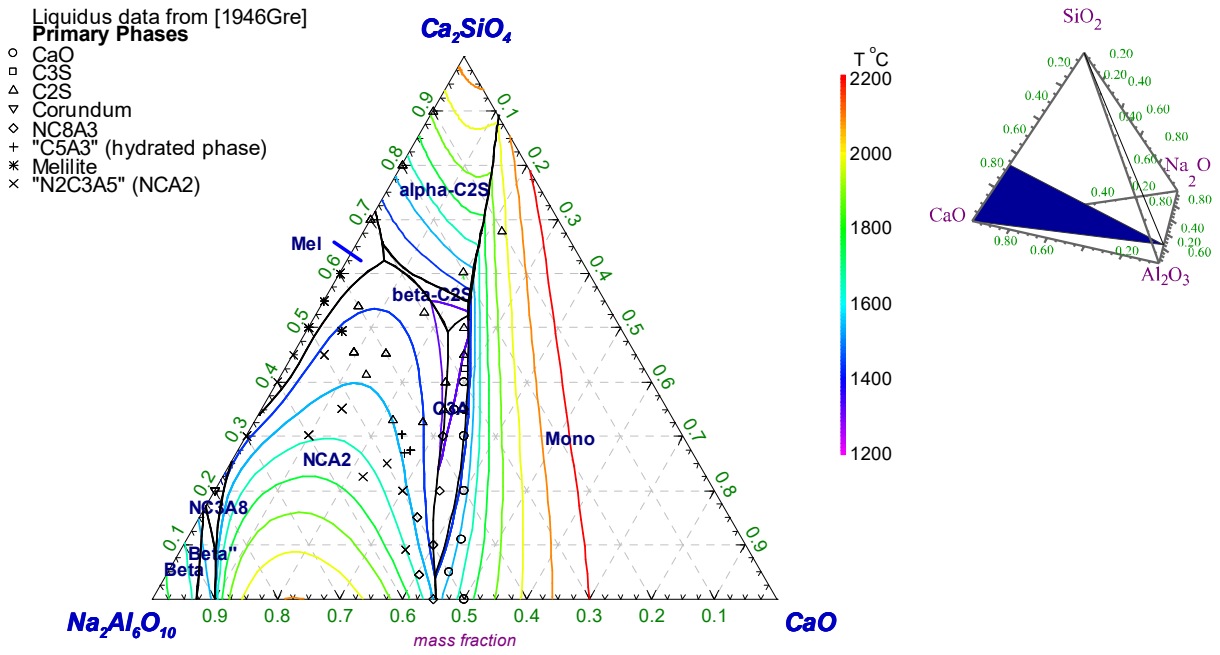

Figure 16.21 Liquidus projection in the Ca_2SiO_4-$Na_2Al_6O_{10}$-CaO plane of the Na_2O-CaO-Al_2O_3-SiO_2 system. Experimental points [443] and calculated lines.

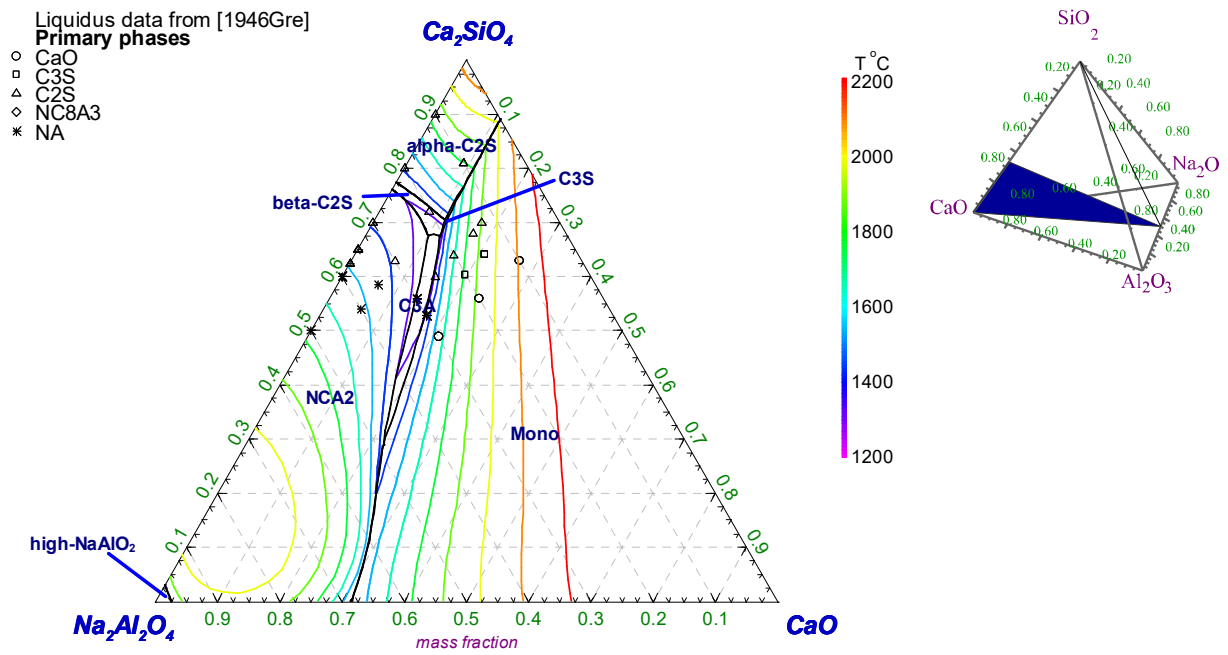

Figure 16.22 Liquidus projection in the Ca_2SiO_4-$Na_2Al_2O_4$-CaO plane of the Na_2O-CaO-Al_2O_3-SiO_2 system. Experimental points [443] and calculated lines.

The subsystem Ca_2SiO_4-$NaAlO_2$ (Figure 16.23) is important in the cement production [466] and Al_2O_3 extraction from slags [467]. According to Greene and Bogue [443], the system is binary with an eutectic at 1405°C. The eutectic temperature found by Korneev and Maltz [467] is lower than 1405°C but it is explained by a partial alkali loss.

Indications of limited solid solutions of $NaAlO_2$ in Ca_2SiO_4 can be found [467, 468]. Refractive indices of C2S crystals measured by Korneev and Mal'ts [467] were shown to lower upon addition of $NaAlO_2$; beyond 5 wt% $NaAlO_2$ the optical properties remained the same. It was concluded that the limiting solubility was 6 wt%. Lin and Maltz [466] also proposed that a solid solution can form based on the data of an optical analysis; the solubility is about 3-5 wt%. Only β-Ca_2SiO_4 forms a solid solution which is beneficial in cement production as β-modification is hydraulically active [469]. It is unclear whether only Na enters the crystal structure or Al is also capable to do so.

Khazanov et al. [470] described that an intermediate phase could form in the system which is stable down to 600°C but its composition was not precisely determined. However, Druzhinina [471]

considered that some calcium aluminates could form in the system. The transition temperatures obtained by DTA (Figure 16.23) were not assigned to actual phase transformations.

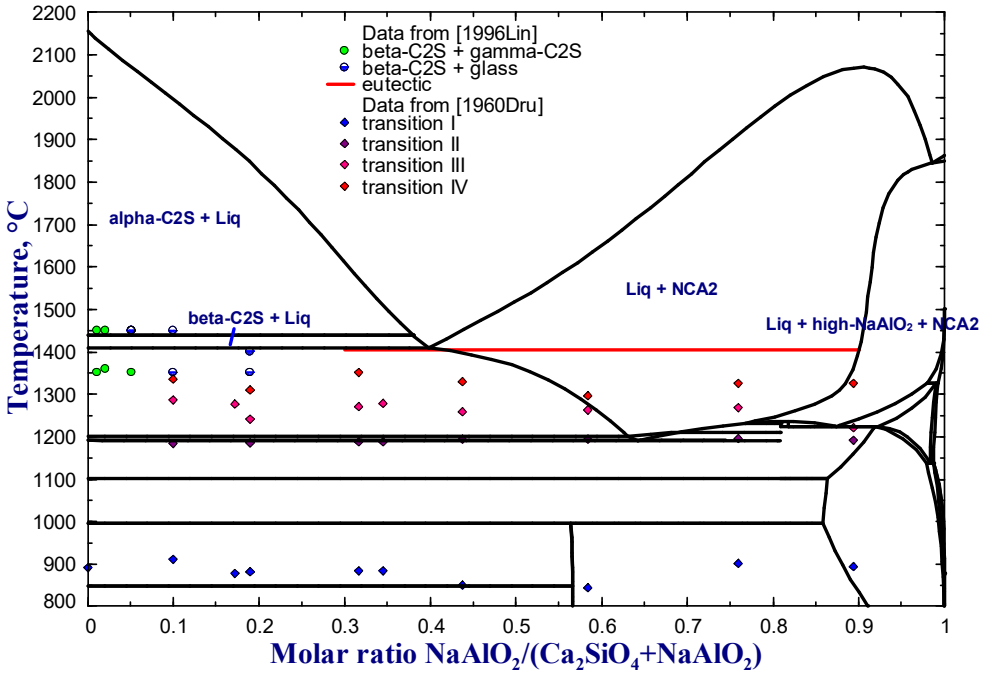

Figure 16.23 Phase diagram of the $NaAlO_2$-Ca_2SiO_4 section of the Na_2O-CaO-Al_2O_3-SiO_2 system. Experimental points [466, 471] and calculated lines.

16.10 Other parts of the quaternary system

16.10.1 Activity data

Mathieu [436] measured Na_2O solubility in Na_2O-free base compositions in the Al_2O_3-CaO-SiO_2 system in an atmosphere with a fixed Na(g) partial pressure. Large amounts of $Na_2O{\cdot}2SiO_2$ melt were used as a source of sodium and the partial pressure of oxygen was fixed by Ni/NiO buffer. The operating temperature was 1400°C. The author presents the data in the form of isosolubility lines in the Al_2O_3-CaO-SiO_2 base composition triangle and to compare these data with calculated values, they were replotted in the form of isoactivities. Intersection points of Na_2O isosolubility lines and sections with a fixed Al_2O_3/CaO ratio are plotted in Figure 16.24.

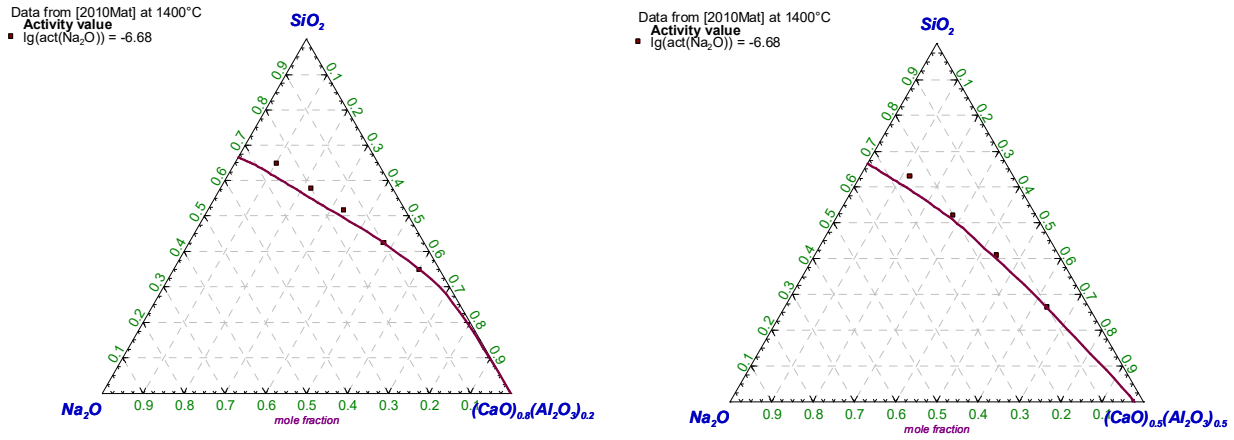

(***a***) (***b***)

Figure 16.24 Isoactivity plots in the SiO_2-Na_2O-$(CaO)_{0.8}(Al_2O_3)_{0.2}$ (***a***) and SiO_2-Na_2O-$(CaO)_{0.5}(Al_2O_3)_{0.5}$ (***b***) sections of the Al_2O_3-CaO-Na_2O-SiO_2 system at 1400°C. The reference state is the pure liquid Na_2O. Points recalculated from the published data [436] and calculated lines.

16.11 Optimization results

The Na_2O-Al_2O_3-SiO_2, Na_2O-CaO-SiO_2 and Al_2O_3-CaO-Na_2O ternary subsystems were optimized in this work (Chapter 8, Chapter 15 and Chapter 14, correspondingly). The optimization of the CaO-Al_2O_3-SiO_2 system was taken from Eriksson and Pelton [123].

Optimization of the quaternary system was joined with the optimization of its subsystems, in particular, the Na_2O-Al_2O_3-SiO_2 and CaO-Na_2O-Al_2O_3 ternaries. So, the extrapolation Na-Al-Si//O with Si apart allows to use an adequate stability of nepheline and albite and to reproduce $CaSiO_3$ liquidus in the quaternary system. If other extrapolations are used, the excess parameters in the quaternary system give rise to miscibility gaps instead of lifting the liquidus unless nepheline is stabilized by about 20 $kJ \cdot mol^{-1}$ below the most stable experimental value.

The standard extrapolation Si-NaAl-Ca//O with Si apart gives a good prediction of the experimental data but it was modified to improve prediction of feldspar liquidus and some other reasons (Table A.20). The excess parameters in the system were chosen to adjust $CaSiO_3$ liquidus.

Excess parameters of Feldspar solid solution were adjusted to reproduce the liquidus, solidus and immiscibility data in the $NaAlSi_3O_8$-$CaAl_2Si_2O_8$ section.

The exchange interaction $\Delta_{CN//A//AS}$ and the Gibbs energy of sodium melilite $NaAlCaSi_2O_7$ were the adjustable parameters for Melilite solid solution. They were changed using the liquidus and solidus data in the $Ca_2Al_2SiO_7$-$NaCaAlSi_2O_7$ section.

The solubility of calcium in Nepheline and Carnegieite is defined by the data in the $NaAlSiO_4$-$CaAl_2Si_2O_8$ and $NaAlSiO_4$-$CaAl_2O_4$ sections, and the Gibbs energy of calcium-containing end-members were adjusted to reproduce the experimental values. An excess parameter ${}^1L_{VaSi_2//NaAlSi,CaAl_2}$ was required to stabilize Nepheline in the $NaAlSiO_4$-$CaAl_2Si_2O_8$ section.

A slightly negative $\Delta_{NC//A//AS}$ exchange parameter was used in Clinopyroxene solution to reproduce the data on the enthalpy of mixing of $CaAl_2SiO_6$-$NaAlSi_2O_6$ pyroxenes.

The optimized parameters are presented in Table A.20.

CHAPTER 17 OPTIMIZATION OF THE CaO-K_2O-SiO_2 SYSTEM

17.1 Phase diagram

Morey et al. [92] studied the system in detail; because of the method of sample preparation (potassium carbonate used as a starting material), the investigated compositions were limited to the area delimited by SiO_2-K_2SiO_3-K_2CaSiO_4-$CaSiO_3$. However, a few compositions were studied beyond this area as well although the authors recommend to rely on them with a precaution. There are a few experimental difficulties encountered in the system. Mixtures with a low content of silica have a high K_2O volatility and are very hydroscopic; compositions rich in silica, especially close to ternary eutectics, are very hard to crystallize. Overall, the equilibration time required to grow crystals varied across the system from a few minutes to weeks. In some cases, it was required to obtain the first crystallization in a hydrothermal bomb. Some compounds have very slow rates of crystallization/dissolution like quartz and a few ternary compounds. Samples in the vicinity of K_2CaSiO_4 composition required quenching in liquid mercury to avoid crystallization.

Compared to the Na_2O-CaO-SiO_2 system, there is no combeite solid solution or any compound with a similar structure. Because of that, primary fields of binary phases, such as $CaSiO_3$ (wollastonite/pseudowollastonite) and K_2SiO_3 extend to the center of the phase diagram to a greater extent.

There is only one compound with SiO_2 content higher than a disilicate composition: KC2S9. The compound melts incongruently at 1050°C; it is hard to crystallize and special attention had to be paid in order to determine its primary crystallization field [92].

There are three ternary compounds in the disilicate join $K_2Si_2O_5$-$CaSi_2O_5$. KC2S6 crystallizes relatively easy, melts incongruently at 1115°C forming $CaSiO_3$ and liquid [92]. K2CS3 melts congruently at 959°C and crystallizes reluctantly from melts [92]. K4CS10 has a flat liquidus surface (congruent melting at 946°C). Also, a metastable liquidus of this phase can be observed in the primary fields of KC2S9 and K2CS6.

KC3S6 compound is structurally analogous to $Na_2Ca_3Si_6O_{16}$ (devitrite) which plays an important role as one of the crystallization products of industrial glasses. Although it is not indicated, the structural similarity can be an indication of a possible solid solution between the sodium and

potassium end-members. The compound melts incongruently at 960°C forming (1:2:6) and liquid/glass [92].

In the metasilicate join K_2SiO_3-$CaSiO_3$ there is no "$K_2Ca_2Si_3O_9$" compound/solid solution analogous to combeite in the Na_2O-CaO-SiO_2 system. However, K2CS3 compound is structurally similar to N2CS3. In the sodium system, the compound has a small non-stoichiometry range; there is no information about the non-stoichiometry of K2CS3 along the K_2SiO_3-$CaSiO_3$ join; it might be very small or might not have been investigated in detail. For the optimization purposes it was considered that K2CS3 does not have a non-stoichiometry range in the K_2O-CaO-SiO_2 system but forms a solid solution with N2CS3.

KCS compound was reported by Morey et al. [92]; it has an analogue in the CaO-Na_2O-SiO_2 system but occupies a much greater field due to the absence of the combeite solid solution. It melts at about 1630°C, probably congruently [92]. However, in a few later works its existence was questioned. The crystallographic findings by Berezhnoi et al. [56] and Hughes [472] contradict the data by Morey et al. [92] who found that the compound has a hexagonal symmetry. Arroyabe et al. [473] and later Chen et al. [474] accepted that KCS points in fact belong to KC2S2 which has a hexagonal symmetry. This hypothesis is supported by the fact that the points supposedly belonging to KCS are very well fitted by KC2S2 liquidus in the current optimization. However, the existence of the true KCS compound is supported by the investigation of Berezhnoi et al. [56] on mixed alkali-alkali earth orthosilicate solutions. The melting point of the compound was estimated at 1333°C based on the melting behaviour of other mixed orthosilicates.

Taylor [118] studied the K_2CaSiO_4-Ca_2SiO_4 section. It was discovered that crystallized samples consist of KCS compound and a new phase. At the molar ratio 11:1 the traces of KCS completely disappear; this way, a new compound, KC23S12 was identified. The author concludes that there is a possibility that this compound forms a solid solution with Ca_2SiO_4, although the X-ray pattern is somewhat different from that of β-Ca_2SiO_4. Due to technical limitations of the employed furnace, the liquidus curve could be obtained only around the eutectic composition between KCS and KC23S12. Quenching method was used to analyze phase compositions at different temperatures, although no details about the quenching media are given. For example, Morey et al. [92] indicate that samples with less than 50 mol% SiO_2 crystallize very fast and require quenching in liquid mercury. These data were not considered in the optimization as Ca_2SiO_4 liquidus cannot appear at

the compositions given by Taylor. Also, the melting point of KCS compound of 1618°C would make KCS liquidus appear at silica content higher than 50 mol% where it was not found by other investigators.

There are other works confirming that to some extent, dicalcium silicate can dissolve certain amount of alkalies (about 1-2 mol%). This amount depends on the modification of Ca_2SiO_4 in question. So, Newman and Wells [475] studied the influence of Na_2O and K_2O additives on the transition temperature in the Ca_2SiO_4 structure.

Chen et al. [474] performed high-temperature equilibration, rapid quenching and electron probe X-ray microanalysis (EPMA). Along with the known binary phases (SiO_2, $CaSiO_3$, Ca_2SiO_4), primary fields of KC2S2 and KC6S4 were reported.

KC2S2 compound was discovered by Arroyabe et al. [473, 476]. They support the hypothesis that KCS reported by Morey et al. [92] and Taylor [118] does not exist and the published data in reality belong to KC2S2 phase. This is confirmed by the current optimization; data points in Figure 17.4, (***a***) are much better reproduced with KC2S2 than with KCS. However, this does not exclude the possibility that some of the points (in other joins) indeed belong to KCS.

KC6S4 is a recently discovered compound. It was studied structurally and spectroscopically by Arroyabe et al. [476] and Ohsato et al. [477]. A small part of its liquidus is reported by Chen et al. [474].

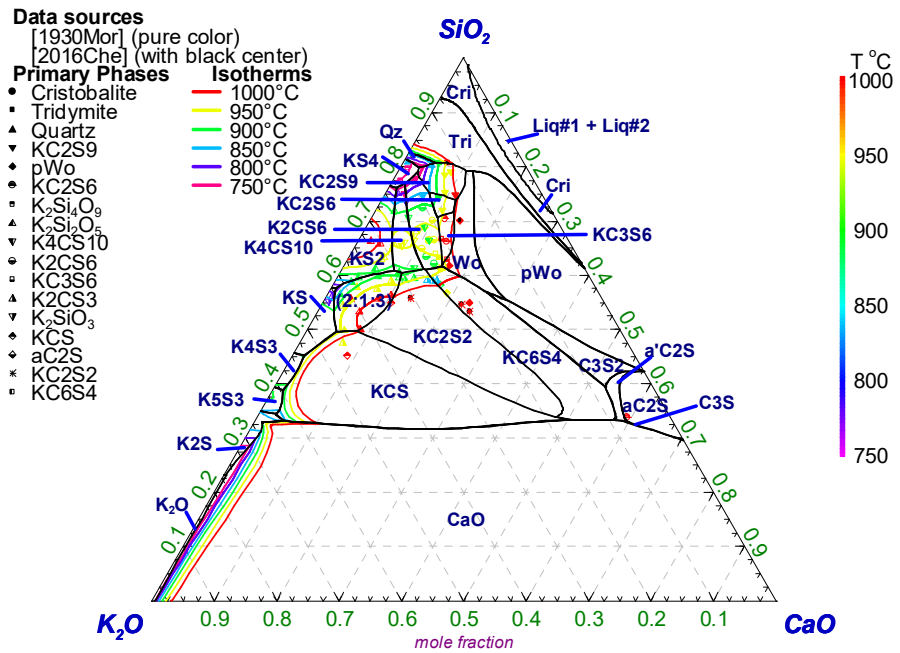

Figure 17.1 Liquidus projection in the CaO-K_2O-SiO_2 system; isotherms from 750° to 1000°C. Experimental points [92, 474] and calculated lines.

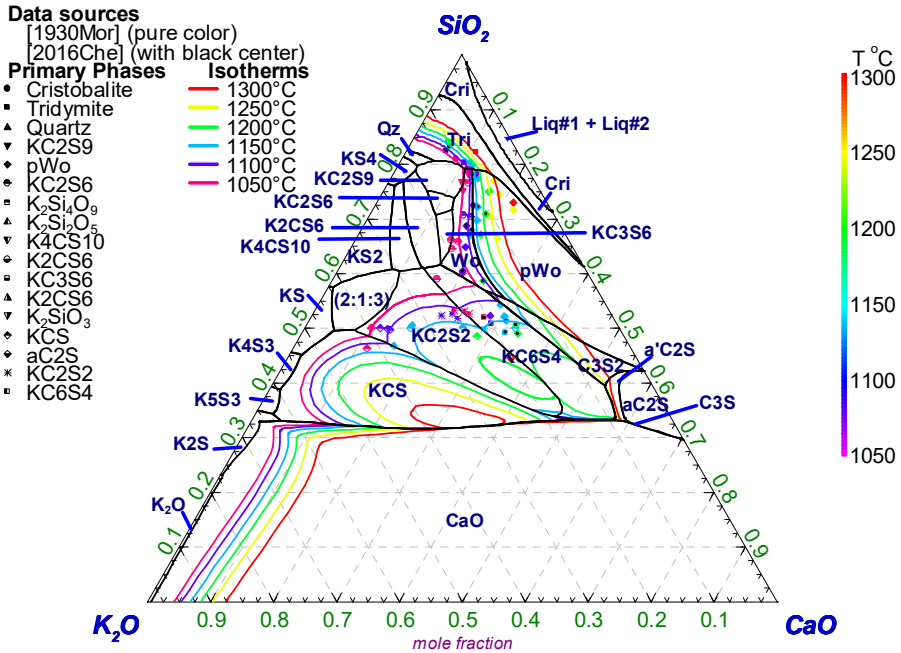

Figure 17.2 Liquidus projection in the CaO-K_2O-SiO_2 system; isotherms from 1050° to 1300°C. Experimental points [92, 474] and calculated lines.

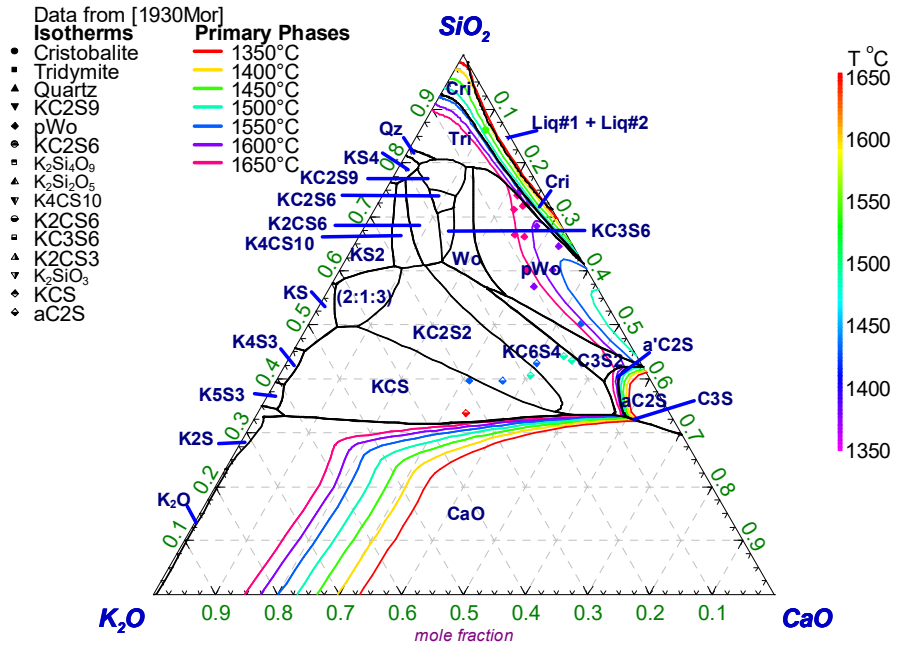

Figure 17.3 Liquidus projection in the CaO-K_2O-SiO_2 system; isotherms from 1350° to 1650°C. Experimental points [92, 474] and calculated lines.

The distortion in isotherms in the liquidus projections (Figure 17.1-Figure 17.3) along the CaO-K_4SiO_4 line means an immiscibility tendency in the system because the CaO-K_4SiO_4 pair is more stable than the K_2O-Ca_2SiO_4 pair. The same phenomenon is observed in the CaO-Na_2O-SiO_2 (Chapter 14), Na_2O-MgO-SiO_2 (Chapter 21) and MgO-K_2O-SiO_2 systems (Chapter 26).

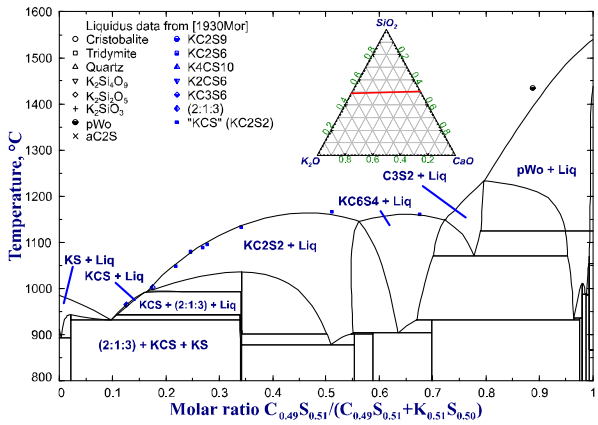

(*a*)

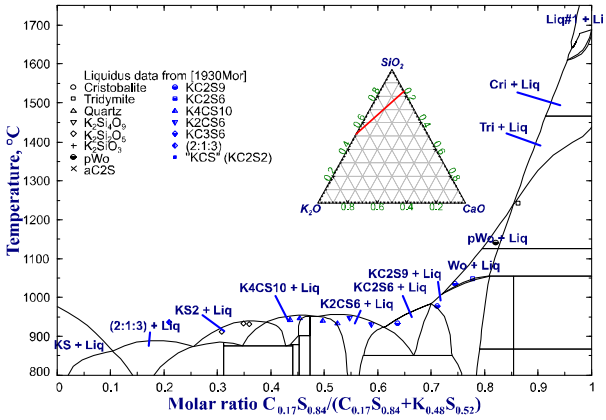

(*b*)

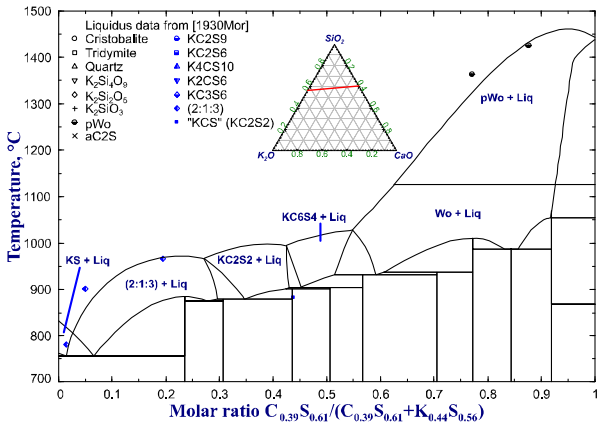
Liquidus data from [1930Mor]
Cristobalite
Tridymite
Quartz
$K_2Si_4O_9$
$K_2Si_2O_5$
K_2SiO_3
pWo
aC2S
KC2S9
KC2S6
K4CS10
K2CS6
KC3S6
(2:1:3)
"KCS" (KC2S2)
pWo + Liq
Wo + Liq
KC6S4 + Liq
KS + Liq
KC2S2 + Liq
(2:1:3) + Liq
Temperature, °C
Molar ratio $C_{0.39}S_{0.61}/(C_{0.39}S_{0.61}+K_{0.44}S_{0.56})$

(*c*)

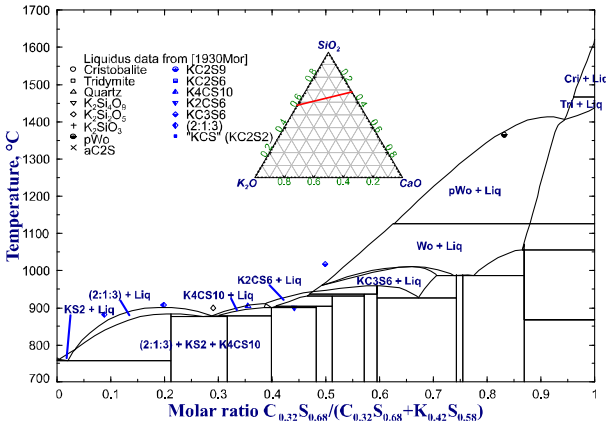
Liquidus data from [1930Mor]
Cristobalite
Tridymite
Quartz
$K_2Si_4O_9$
$K_2Si_2O_5$
K_2SiO_3
pWo
aC2S
KC2S9
KC2S6
K4CS10
K2CS6
KC3S6
(2:1:3)
"KCS" (KC2S2)
Cri + Liq
Tri + Liq
pWo + Liq
Wo + Liq
KC3S6 + Liq
K2CS6 + Liq
K4CS10 + Liq
(2:1:3) + Liq
KS2 + Liq
(2:1:3) + KS2 + K4CS10
Temperature, °C
Molar ratio $C_{0.32}S_{0.68}/(C_{0.32}S_{0.68}+K_{0.42}S_{0.58})$

(*d*)

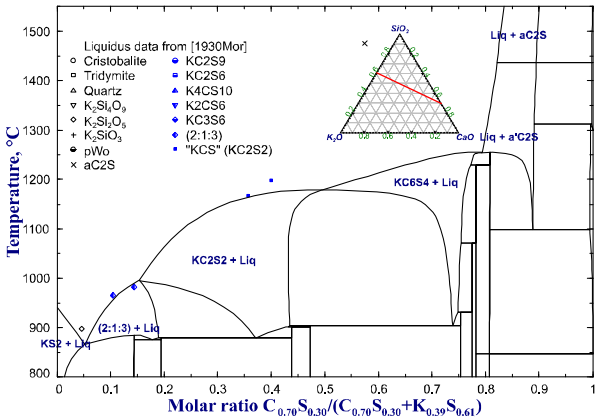
Liquidus data from [1930Mor]
Cristobalite
Tridymite
Quartz
$K_2Si_4O_9$
$K_2Si_2O_5$
K_2SiO_3
pWo
aC2S
KC2S9
KC2S6
K4CS10
K2CS6
KC3S6
(2:1:3)
"KCS" (KC2S2)
Liq + aC2S
Liq + a'C2S
KC6S4 + Liq
KC2S2 + Liq
(2:1:3) + Liq
KS2 + Liq
Temperature, °C
Molar ratio $C_{0.70}S_{0.30}/(C_{0.70}S_{0.30}+K_{0.39}S_{0.61})$

(*e*)

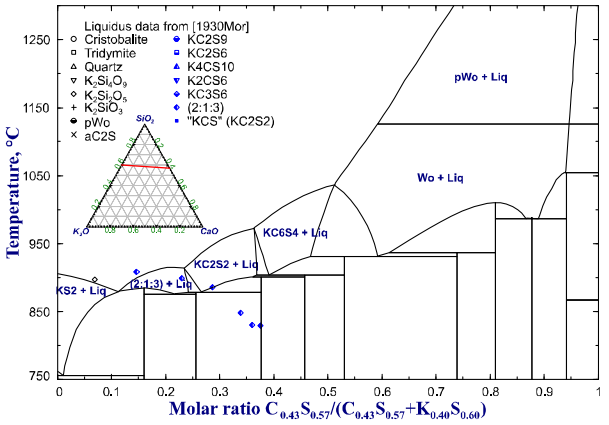
Liquidus data from [1930Mor]
Cristobalite
Tridymite
Quartz
$K_2Si_4O_9$
$K_2Si_2O_5$
K_2SiO_3
pWo
aC2S
KC2S9
KC2S6
K4CS10
K2CS6
KC3S6
(2:1:3)
"KCS" (KC2S2)
pWo + Liq
Wo + Liq
KC6S4 + Liq
KC2S2 + Liq
(2:1:3) + Liq
KS2 + Liq
Temperature, °C
Molar ratio $C_{0.43}S_{0.57}/(C_{0.43}S_{0.57}+K_{0.40}S_{0.60})$

(*f*)

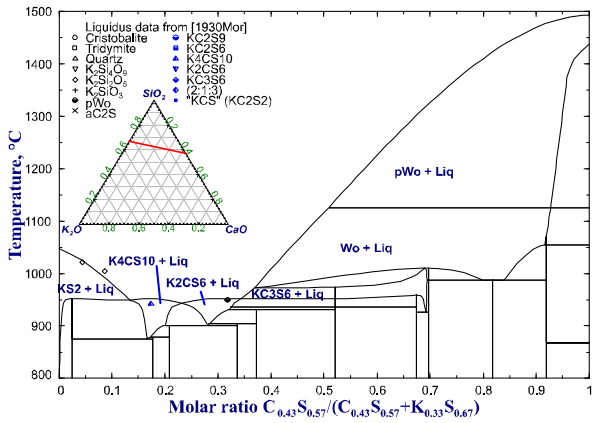
Liquidus data from [1930Mor]
Cristobalite
Tridymite
Quartz
$K_2Si_4O_9$
$K_2Si_2O_5$
K_2SiO_3
pWo
aC2S
KC2S9
KC2S6
K4CS10
K2CS6
KC3S6
(2:1:3)
"KCS" (KC2S2)
pWo + Liq
Wo + Liq
K4CS10 + Liq
KS2 + Liq
K2CS6 + Liq
KC3S6 + Liq
Temperature, °C
Molar ratio $C_{0.43}S_{0.57}/(C_{0.43}S_{0.57}+K_{0.33}S_{0.67})$

(*g*)

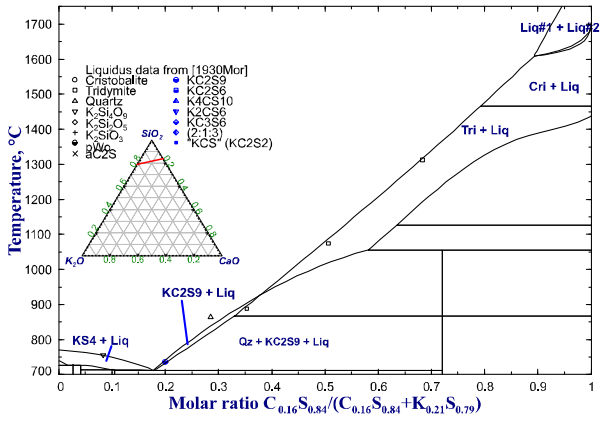
Liquidus data from [1930Mor]
Cristobalite
Tridymite
Quartz
$K_2Si_4O_9$
$K_2Si_2O_5$
K_2SiO_3
pWo
aC2S
KC2S9
KC2S6
K4CS10
K2CS6
KC3S6
(2:1:3)
"KCS" (KC2S2)
Liq#1 + Liq#2
Cri + Liq
Tri + Liq
KC2S9 + Liq
KS4 + Liq
Qz + KC2S9 + Liq
Temperature, °C
Molar ratio $C_{0.16}S_{0.84}/(C_{0.16}S_{0.84}+K_{0.21}S_{0.79})$

(*h*)

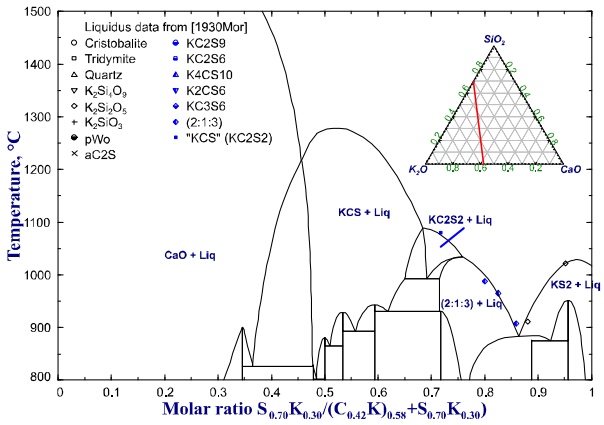
Liquidus data from [1930Mor]
Cristobalite
Tridymite
Quartz
$K_2Si_4O_9$
$K_2Si_2O_5$
K_2SiO_3
pWo
aC2S
KC2S9
KC2S6
K4CS10
K2CS6
KC3S6
(2:1:3)
"KCS" (KC2S2)
CaO + Liq
KCS + Liq
KC2S2 + Liq
(2:1:3) + Liq
KS2 + Liq
Temperature, °C
Molar ratio $S_{0.70}K_{0.30}/(C_{0.42}K)_{0.58}+S_{0.70}K_{0.30})$

(*i*)

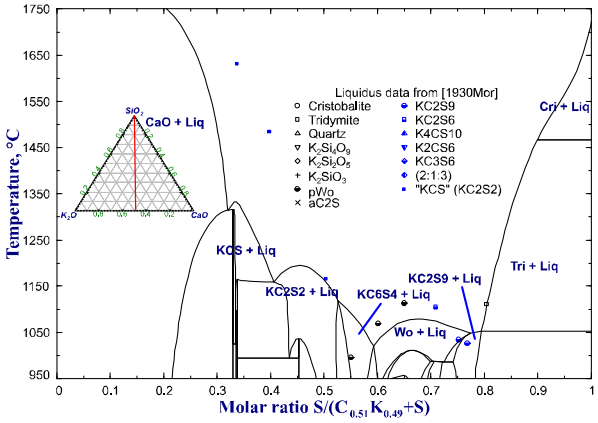
Liquidus data from [1930Mor]
Cristobalite
Tridymite
Quartz
$K_2Si_4O_9$
$K_2Si_2O_5$
K_2SiO_3
pWo
aC2S
KC2S9
KC2S6
K4CS10
K2CS6
KC3S6
(2:1:3)
"KCS" (KC2S2)
CaO + Liq
Cri + Liq
KCS + Liq
KC2S2 + Liq
KC6S4 + Liq
KC2S9 + Liq
Tri + Liq
Wo + Liq
Temperature, °C
Molar ratio $S/(C_{0.51}K_{0.49}+S)$

(*j*)

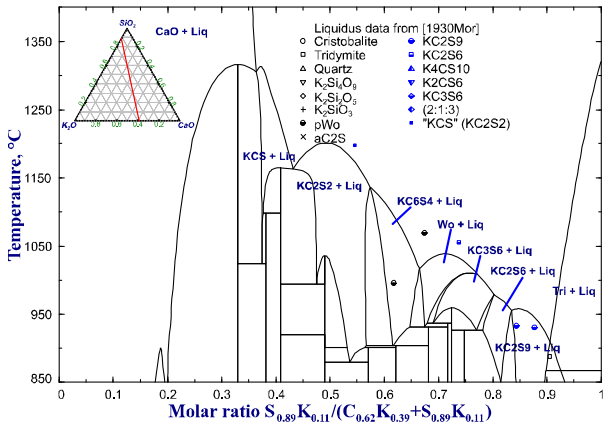
Liquidus data from [1930Mor]
Cristobalite
Tridymite
Quartz
$K_2Si_4O_9$
$K_2Si_2O_5$
K_2SiO_3
pWo
aC2S
KC2S9
KC2S6
K4CS10
K2CS6
KC3S6
(2:1:3)
"KCS" (KC2S2)
CaO + Liq
KCS + Liq
KC2S2 + Liq
KC6S4 + Liq
Wo + Liq
KC3S6 + Liq
KC2S6 + Liq
Tri + Liq
KC2S9 + Liq
Temperature, °C
Molar ratio $S_{0.89}K_{0.11}/(C_{0.62}K_{0.39}+S_{0.89}K_{0.11})$

(*k*)

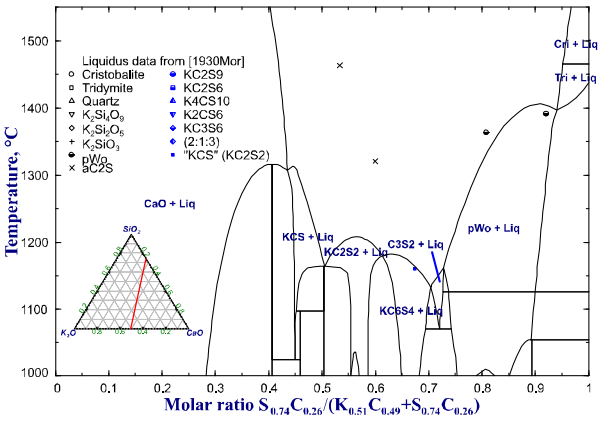
Liquidus data from [1930Mor]
Cristobalite
Tridymite
Quartz
$K_2Si_4O_9$
$K_2Si_2O_5$
K_2SiO_3
pWo
aC2S
KC2S9
KC2S6
K4CS10
K2CS6
KC3S6
(2:1:3)
"KCS" (KC2S2)
Cri + Liq
Tri + Liq
CaO + Liq
KCS + Liq
KC2S2 + Liq
C3S2 + Liq
pWo + Liq
KC6S4 + Liq
Temperature, °C
Molar ratio $S_{0.74}C_{0.26}/(K_{0.51}C_{0.49}+S_{0.74}C_{0.26})$

(*l*)

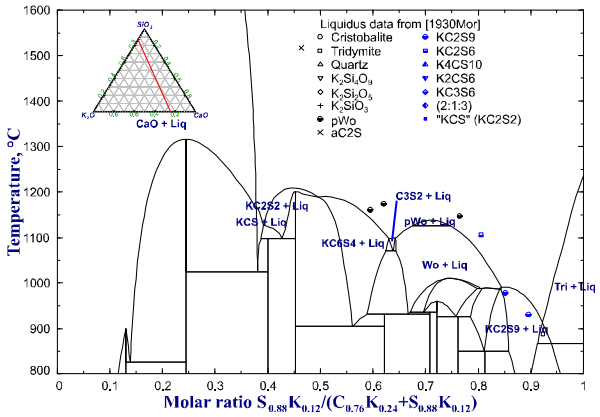
Liquidus data from [1930Mor]
Cristobalite
Tridymite
Quartz
$K_2Si_4O_9$
$K_2Si_2O_5$
K_2SiO_3
pWo
aC2S
KC2S9
KC2S6
K4CS10
K2CS6
KC3S6
(2:1:3)
"KCS" (KC2S2)
CaO + Liq
KC2S2 + Liq
KCS + Liq
C3S2 + Liq
pWo + Liq
KC6S4 + Liq
Wo + Liq
Tri + Liq
KC2S9 + Liq
Temperature, °C
Molar ratio $S_{0.88}K_{0.12}/(C_{0.76}K_{0.24}+S_{0.88}K_{0.12})$

(*m*)

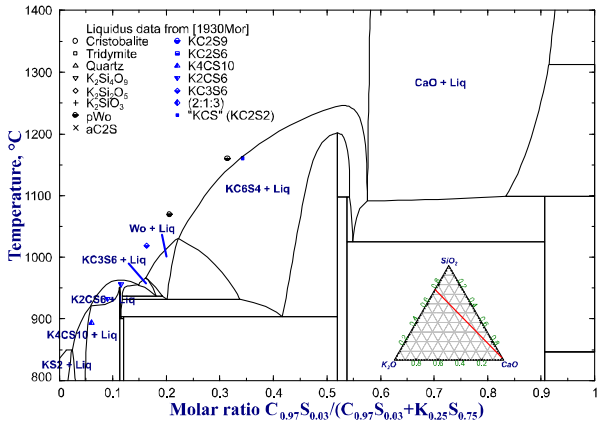
Liquidus data from [1930Mor]
Cristobalite
Tridymite
Quartz
$K_2Si_4O_9$
$K_2Si_2O_5$
K_2SiO_3
pWo
aC2S
KC2S9
KC2S6
K4CS10
K2CS6
KC3S6
(2:1:3)
"KCS" (KC2S2)
CaO + Liq
KC6S4 + Liq
Wo + Liq
KC3S6 + Liq
K2CS6 + Liq
K4CS10 + Liq
KS2 + Liq
Temperature, °C
Molar ratio $C_{0.97}S_{0.03}/(C_{0.97}S_{0.03}+K_{0.25}S_{0.75})$

(*n*)

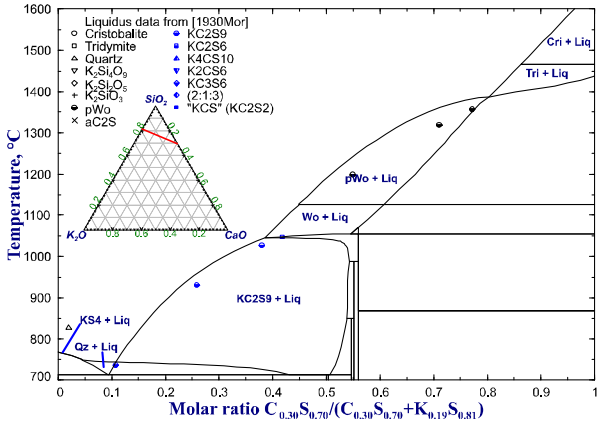

(*o*)

Figure 17.4 Phase diagrams in sections through the K_2O-CaO-SiO_2 system. Experimental points [92] and calculated lines.

Phase diagram data are summarized in Figure 17.1-Figure 17.4. Liquidus data were plotted in liquidus projections; for convenience, there are three isotherm sets for different ranges of temperature (Figure 17.1-Figure 17.3). Although the compositions studied by Morey et al. [92] were not planned to be aligned along joins, it was possible to place most of the points at customary joins (Figure 17.4).

The invariant phase equilibria in the system are listed in Table 17.1.

Table 17.1 Invariant phase equilibria in the K_2O-CaO-SiO_2 system. The calculated values are shown in bold.

Solid phases	Equilibrium type	T, °C	Liquid composition, mol%		
			SiO_2	K_2O	CaO
KC2S6-SiO_2-Wo	Reaction	1080 [92] **946**	70.00 **79.18**	10.00 **11.77**	20.00 **9.05**
KC2S9-KC2S6-SiO_2	Reaction	1050 [92] **1080**	75.00 **75.00**	8.33 **8.33**	16.67 **16.67**
KC2S9-KS4-SiO_2	Eutectic	720 [92] **712**	80.18 **79.86**	17.58 **17.26**	2.24 **2.28**
KS2-KC2S9-KS4	Eutectic	720 [92] **677**	76.82 **75.03**	22.10 **21.44**	1.08 **3.53**
KS2-KC2S9-K4CS10	Reaction	740 [92] –	73.33 –	13.33 –	13.33 –
K4CS10-KC2S9-K2CS6	Reaction	825 [92] **901**	70.37 **69.82**	18.52 **16.97**	11.11 **13.21**
K2CS6-KC2S9-KC3S6	Reaction	910 [92] **880**	71.43 **73.51**	14.29 **17.77**	14.29 **8.72**
KC3S6-KC2S9-KC2S6	Reaction	940 [92] **1011**	66.67 **72.94**	11.11 **13.43**	22.22 **13.64**
KC3S6-KC2S9-Wo	Reaction	1020 [92] **987**	63.16 **71.80**	10.53 **15.72**	26.32 **12.48**
K2CS6-Wo-KC3S6	Reaction	930 [92] **936**	63.64 **62.00**	18.18 **22.46**	18.18 **15.54**
KCS3-K4CS10-K2CS6	Eutectic	890 [92] **866**	60.28 **59.05**	27.19 **25.83**	12.52 **15.12**
K2CS3-K2CS6-Wo	Eutectic	800 [92] **865**	59.63 **58.72**	24.64 **25.39**	15.73 **15.88**
K2CS3-Wo-KC2S2	Reaction	830 [92] **684**	50.00 **65.35**	25.00 **27.31**	25.00 **7.34**
KC2S2-Wo-C2S	Reaction	1180 [92] –	40.00 –	20.00 –	40.00 –
K2CS3-KS2-K4CS10	Eutectic	895 [92] **875**	60.31 **60.81**	30.08 **30.78**	9.61 **8.41**
KS-K2CS3-KS2	Eutectic	770 [92] **756**	56.23 **57.59**	43.50 **41.75**	0.27 **0.66**

17.2 Calorimetry data

Mostly, there is a lack of calorimetric data in the ternary system, only one work is available on the partial enthalpy of mixing of SiO_2 [343] (Figure 17.5). However, the data were not considered as

the data on K_2O-SiO_2 from the same source are in noticeable disagreement with those used in the optimization for the binary system [205]. It was decided not to take the data by Wilding and Navrotsky [343] into account.

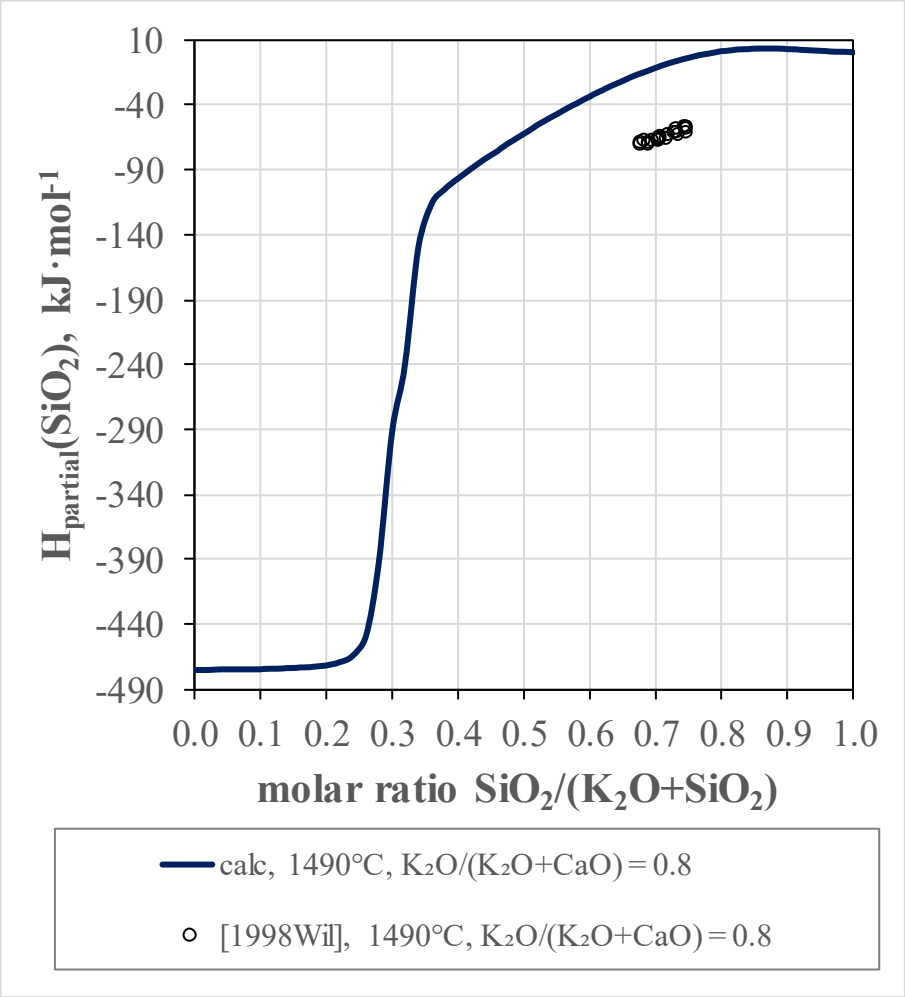

Figure 17.5 The partial enthalpy of SiO_2 in CaO-K_2O-SiO_2 melts ($K_2O/(K_2O+CaO) = 0.8$). Experimental points [343] and the calculated line.

17.3 Heat capacity data

Zhang et al. [478] published an optimization of the ternary systems CaO-Na_2O-SiO_2 and CaO-K_2O-SiO_2 along with the fitted heat capacity data on K4CS10 and KC2S2. The raw data points are not available (apparently, it was a private communication) but judging by the form of the resulting heat capacity curves, one can assume that drop calorimetry was used. However, it was preferred to

use the heat capacities derived from summation as the provided fit [478] has only few C_P-related terms.

17.4 Optimization results

As there are no data on the stability of ternary compounds and/or liquid phase, it had to be guessed. The optimization was performed in the following way: first, liquid parameters were set according to the liquidus points of binary compounds ($CaSiO_3$ and SiO_2). The liquidus points of $K_2Si_2O_5$ and $K_2Si_4O_9$ do not change the results as their fields are narrow. As the thermodynamic properties of the binary compounds are known, this allows to make a good guess of the properties of the liquid phase. It was decided to keep the number of excess Gibbs parameters as few as possible. After the liquid parameters were fixed, the enthalpies of formation of ternary compounds were adjusted to reproduce the corresponding liquidus data. The optimized thermodynamic properties of compounds are summarized in Table A.21 and the excess parameters of solution phases are given in Table A.22.

K2CS3 compound has the same structure as N2CS3 and therefore must be modeled as part of (2:1:3) solid solution. There are no detailed data on the non-stoichiometry of the compound in the K_2O-CaO-SiO_2; it was assumed negligible. K1C1K3C1 and C1K1K3C1 end-members have the same stoichiometry. As there are no data on the cation distribution, they were modeled with the same Gibbs energy with a slight difference to make *FactSage* algorithms converge faster.

The parameters in α-C2S and α'-C2S solid solutions were taken from the work of Kim [18].

The optimized parameters are summarized in Table A.21-Table A.22.

CHAPTER 18 OPTIMIZATION OF THE K_2O-CaO-Al_2O_3 SYSTEM

18.1 Phase diagram

Studies of phase relations in the K_2O-CaO-Al_2O_3 system are complicated by a high volatility of K_2O and high melting temperatures of CaO and Al_2O_3 [479]. Available liquidus data do not cover the whole compositional range of the phase diagram [479].

Van Hoek et al. [480] studied the phase compatibility in the system. They have discovered a ternary compound whose composition is most probably $2K_2O{\cdot}3CaO{\cdot}5Al_2O_3$ (K2C3A5). The compound is present in the subsolidus section at 1100°C [480]; however, liquidus studies by Brownmiller [479] do not mention this compound at all. It can be assumed that the compound decomposes before reaching liquidus temperatures. The Na_2O-CaO-Al_2O_3 system has a compound with the same stoichiometry, N2C3A5 which is part of NCA2 solid solution. There is an indication that K2C3A5 does not have the same structure as NCA2 solid solution [480] and it was treated as an individual compound in this work. It was assumed that it decomposes above 1100°C.

According to Van Hoek et al. [480], the C12A7 compound has a small solubility for K_2O. The solid solution of K_2O in C5A3 from Brownmiller [479] is considered to be the same C12A7 solid solution. As already discussed in Section 15.1, neither C5A3 nor C12A7 actually exist.

Ca-containing β-alumina was obtained by means of an ion exchange in molten salts [480]. However, this solid solution is metastable and decomposes into Al_2O_3 and CA6. Ca-β-alumina and K-β-alumina form a complete metastable solid solution.

CaO-$KAlO_2$ and C5A3-$KAlO_2$ are truly binary subsystems in the ternary system [479].

Shin and Glasser [99] studied Na and K substitution in the $Ca_3Al_2O_6$ compound. K_2O-solubility in the cubic phase is up to 0.75 wt%.

Liquidus projection and an isotherm at 1100°C of the system are given in Figure 18.1 and Figure 18.2, correspondingly.

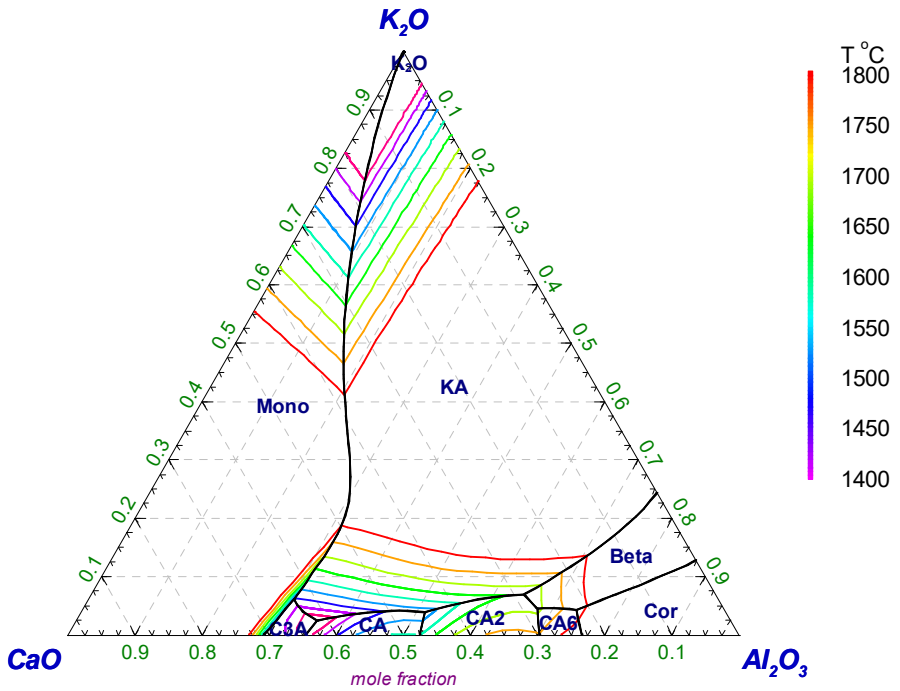

Figure 18.1 Liquidus projection in the K_2O-CaO-Al_2O_3 system.

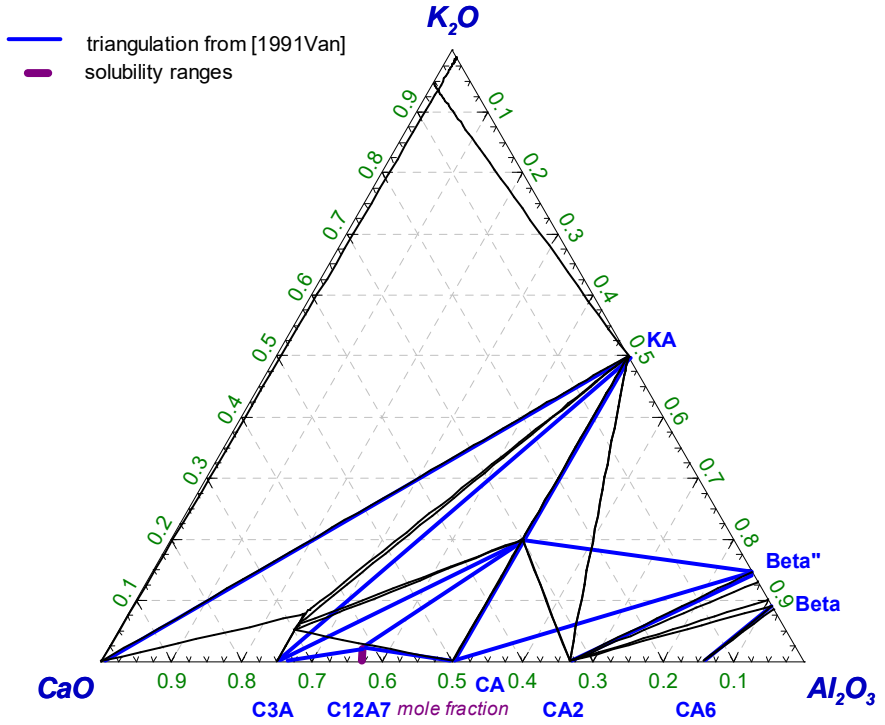

Figure 18.2 Isothermal section in the K_2O-CaO-Al_2O_3 system at 1100°C. Experimental triangulation [480] and calculated lines.

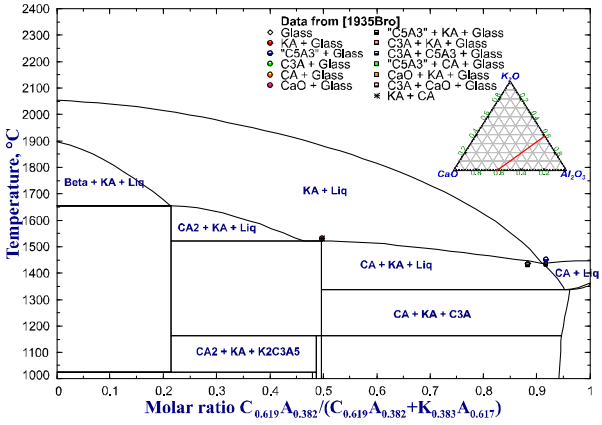
Data from [1935Bro]
Glass
KA + Glass
"C5A3" + Glass
C3A + Glass
CA + Glass
CaO + Glass
"C5A3" + KA + Glass
C3A + KA + Glass
C3A + C5A3 + Glass
"C5A3" + CA + Glass
CaO + KA + Glass
C3A + CaO + Glass
KA + CA
Beta + KA + Liq
KA + Liq
CA2 + KA + Liq
CA + KA + Liq
CA + Liq
CA + KA + C3A
CA2 + KA + K2C3A5
Temperature, °C
Molar ratio $C_{0.619}A_{0.382}/(C_{0.619}A_{0.382}+K_{0.383}A_{0.617})$

(*a*)

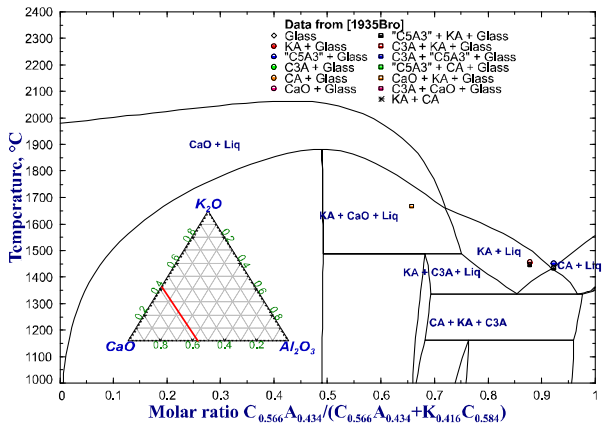
Data from [1935Bro]
Glass
KA + Glass
"C5A3" + Glass
C3A + Glass
CA + Glass
CaO + Glass
"C5A3" + KA + Glass
C3A + KA + Glass
C3A + "C5A3" + Glass
"C5A3" + CA + Glass
CaO + KA + Glass
C3A + CaO + Glass
KA + CA
CaO + Liq
KA + CaO + Liq
KA + Liq
KA + C3A + Liq
CA + Liq
CA + KA + C3A
Temperature, °C
Molar ratio $C_{0.566}A_{0.434}/(C_{0.566}A_{0.434}+K_{0.416}C_{0.584})$

(*b*)

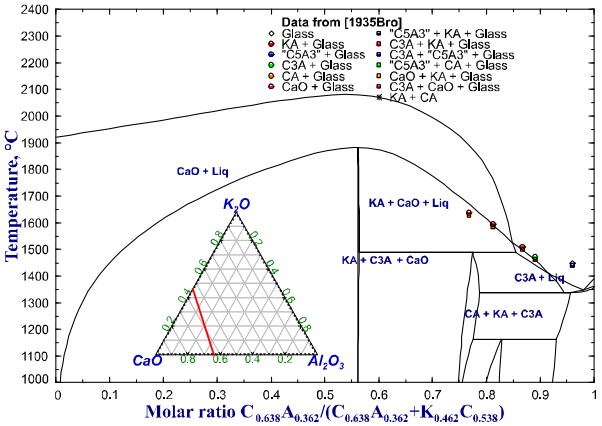
Data from [1935Bro]
Glass
KA + Glass
"C5A3" + Glass
C3A + Glass
CA + Glass
CaO + Glass
"C5A3" + KA + Glass
C3A + KA + Glass
C3A + "C5A3" + Glass
"C5A3" + CA + Glass
CaO + KA + Glass
C3A + CaO + Glass
KA + CA
CaO + Liq
KA + CaO + Liq
KA + C3A + CaO
C3A + Liq
CA + KA + C3A
Temperature, °C
Molar ratio $C_{0.638}A_{0.362}/(C_{0.638}A_{0.362}+K_{0.462}C_{0.538})$

(*c*)

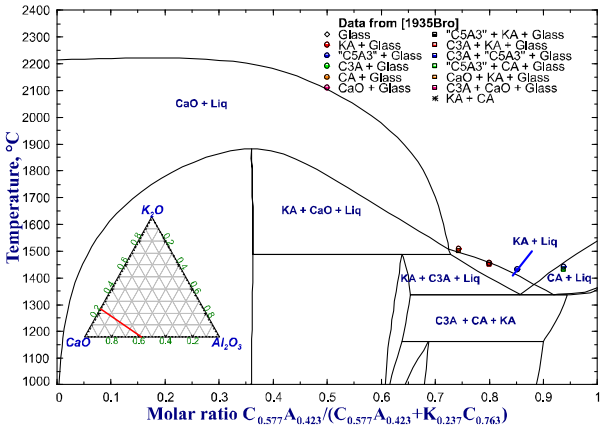
Data from [1935Bro]
Glass
KA + Glass
"C5A3" + Glass
C3A + Glass
CA + Glass
CaO + Glass
"C5A3" + KA + Glass
C3A + KA + Glass
C3A + "C5A3" + Glass
"C5A3" + CA + Glass
CaO + KA + Glass
C3A + CaO + Glass
KA + CA
CaO + Liq
KA + CaO + Liq
KA + Liq
KA + C3A + Liq
CA + Liq
C3A + CA + KA
Temperature, °C
Molar ratio $C_{0.577}A_{0.423}/(C_{0.577}A_{0.423}+K_{0.237}C_{0.763})$

(*d*)

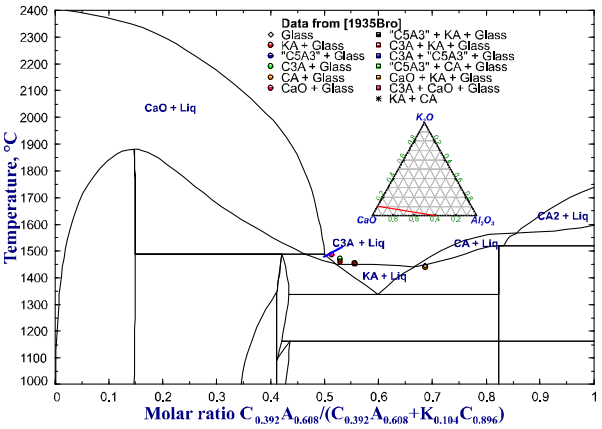
Data from [1935Bro]
Glass
KA + Glass
"C5A3" + Glass
C3A + Glass
CA + Glass
CaO + Glass
"C5A3" + KA + Glass
C3A + KA + Glass
C3A + "C5A3" + Glass
"C5A3" + CA + Glass
CaO + KA + Glass
C3A + CaO + Glass
KA + CA
CaO + Liq
CA2 + Liq
C3A + Liq
CA + Liq
KA + Liq
Temperature, °C
Molar ratio $C_{0.392}A_{0.608}/(C_{0.392}A_{0.608}+K_{0.104}C_{0.896})$

(*e*)

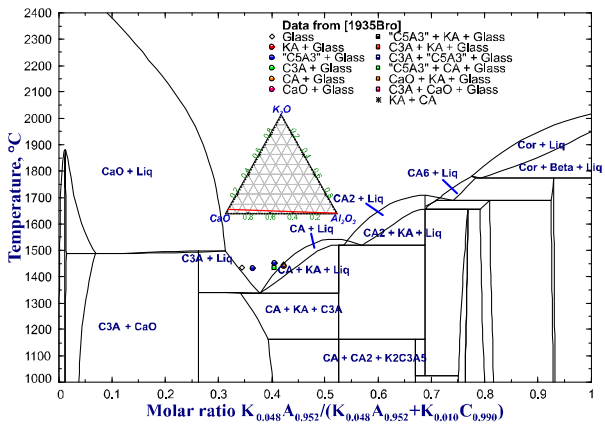
Data from [1935Bro]
Glass
KA + Glass
"C5A3" + Glass
C3A + Glass
CA + Glass
CaO + Glass
"C5A3" + KA + Glass
C3A + KA + Glass
C3A + "C5A3" + Glass
"C5A3" + CA + Glass
CaO + KA + Glass
C3A + CaO + Glass
KA + CA
CaO + Liq
Cor + Liq
Cor + Beta + Liq
CA6 + Liq
CA2 + Liq
CA + Liq
CA2 + KA + Liq
C3A + Liq
CA + KA + Liq
CA + KA + C3A
C3A + CaO
CA + CA2 + K2C3A5
Temperature, °C
Molar ratio $K_{0.048}A_{0.952}/(K_{0.048}A_{0.952}+K_{0.010}C_{0.990})$

(*f*)

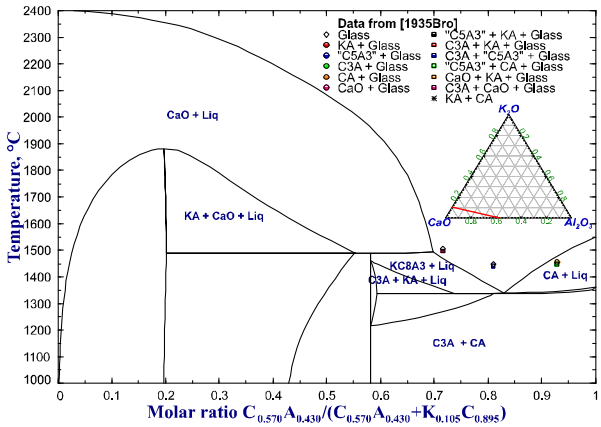

(*g*)

Figure 18.3 Phase diagrams in sections through the K_2O-CaO-Al_2O_3 system. Experimental points [479] and calculated lines. "C5A3" phase is a hydrate which does not exist in the anhydrous system.

Phase diagrams through a few sections in the system are summarized in Figure 18.3.

The triangulation in Figure 18.2 shows that KA-CA2 pair is more stable than CA-Beta" while according to the experimental data, it must be otherwise. Apparently, the Gibbs energies of Beta" solution which was adopted after Kim [18] needs to be modified in order to reproduce the triangulation by Van Hoek et al. [480].

18.2 Optimization results

The K_2O-Al_2O_3 binary system was taken from the work of Kim [18] with modifications (Chapter 10). The optimization of the CaO-Al_2O_3 system by Eriksson and Pelton [123] was adopted and the CaO-K_2O system was assumed ideal.

A small negative $g^{001}_{K,Al(Ca)}$ parameter was used to adjust the liquidus of the binary phases. The heat capacity and the entropy of K2C3A5 compound were estimated as a weighted sum of the corresponding functions of CA and KA. The enthalpy of the compound was set in a way that it decomposes above 1100°C which agrees with the fact that the compound does not appear on the liquidus. The solubility limit of K_2O in C3A solid solution was set according to the available data. The data on K_2O solubility in "C12A7" phase were ignored as Eriksson and Pelton have found

proof in their optimization of the $CaO-Al_2O_3$ system [123] that C12A7 is in fact a hydrate phase that does not exist in the truly anhydrous system. The optimized parameters are summarized in Table A.23-Table A.24.

CHAPTER 19 OPTIMIZATION OF THE K_2O-CaO-Al_2O_3-SiO_2 SYSTEM

19.1 The KC23S12-CaO-C5A3 subsystem

Taylor [118] studied the phase diagram KC23S12-CaO-C5A3 (see Figure 19.1). KC23S12 composition is C2S solid solution including some potassium. While Brownmiller [479] reports a solid solution of K_2O in C5A3, it was not noticed by Taylor. In the optimization of the CaO-Al_2O_3 system by Eriksson and Pelton [123], it was shown that C5A3 compound is actually a hydrate $Ca_{12}Al_{14}O_{32}(OH)_2$ and the compound does not exist in the truly anhydrous system. Liquidus temperatures in some regions of the phase diagram could not be measured because they are beyond the experimental limits. There is a piercing point C2S-C3A-C5A3 at 1310°C.

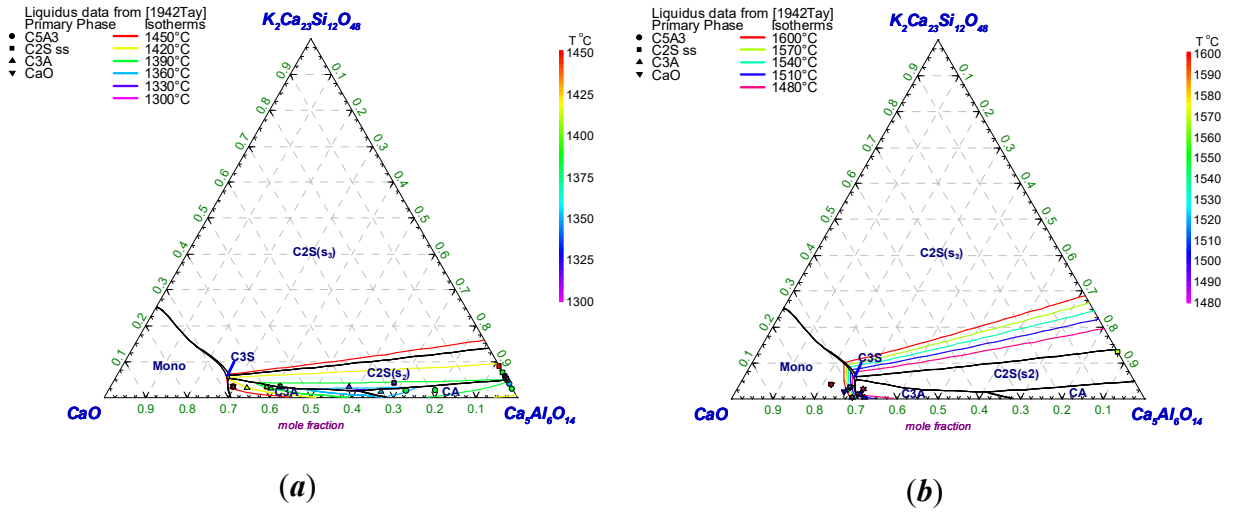

(*a*) (*b*)

Figure 19.1 Liquidus projection in the KC23S12-CaO-C5A3 plane of the CaO-K_2O-Al_2O_3-SiO_2 system. Experimental points [118] and calculated lines.

19.2 The Gehlenite-K-melilite subsystem ($Ca_2Al_2SiO_7$-$KCaAlSi_2O_7$)

Nurse and Midgley [481] studied phase equilibria involving melilite solid solutions. In particular, they studied gehlenite-potassium melilite ($Ca_2Al_2SiO_7$-$KCaAlSi_2O_7$) solid solutions and their melting behaviour (see Figure 19.2). The pure $KCaAlSi_2O_7$ end-member could not be obtained; apparently, it is unstable under atmospheric pressure similar to the sodium end-member [482]. Only

solid solutions with other stable end-members can exist under normal pressure. So, gehlenite $Ca_2Al_2SiO_7$ is able to dissolve up to 20 mol% of $KCaAlSi_2O_7$.

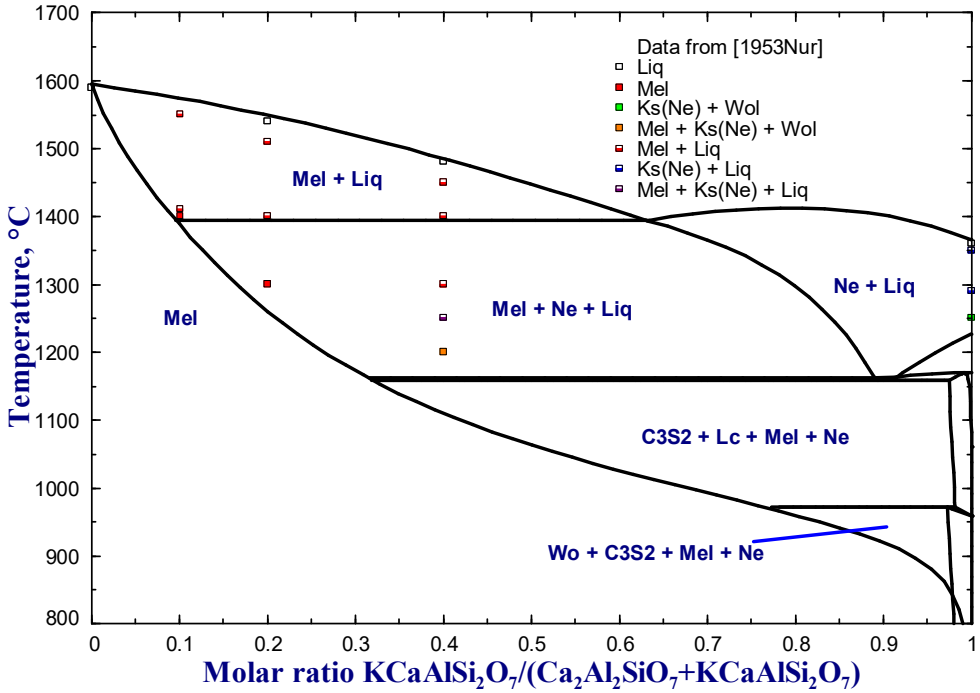

Figure 19.2 Phase diagram in the $Ca_2Al_2SiO_7$-$KCaAlSi_2O_7$ section of the CaO-K_2O-Al_2O_3-SiO_2 system. Experimental points [481] and calculated lines.

19.3 The Anorthite-Leucite-Silica subsystem ($CaAl_2Si_2O_8$-$KAlSi_2O_6$-SiO_2)

Schairer and Bowen [483] studied the $CaAl_2Si_2O_8$-$KAlSi_2O_6$-SiO_2 section of the quaternary system (see Figure 19.3). This is a ternary system where all the phases have compositions laying inside the composition triangle. The $CaAl_2Si_2O_8$-$KAlSi_2O_6$ boundary system has a simple eutectic and shows no evidence of solid solutions (see Figure 19.4).

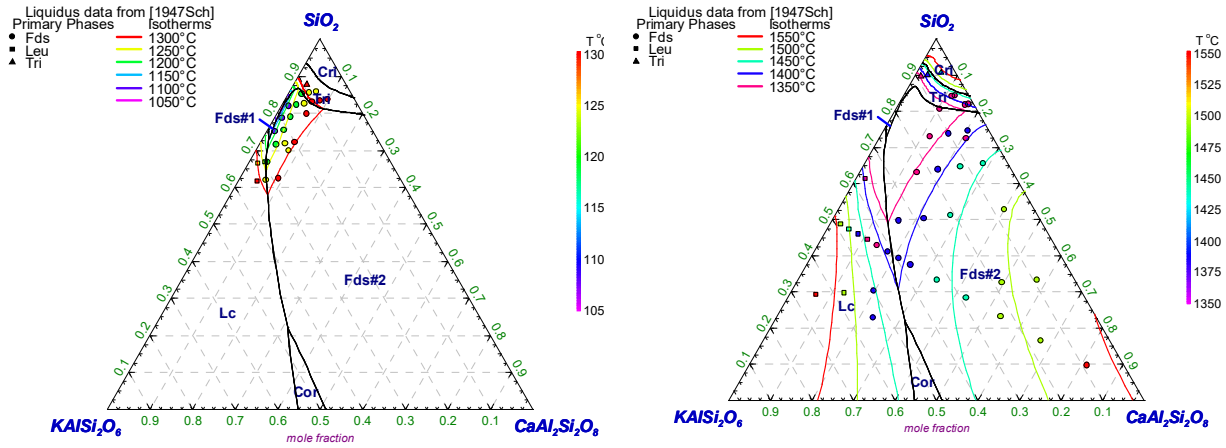

(***a***) (***b***)

Figure 19.3 Liquidus projection in the SiO_2-$KAlSi_2O_6$-$CaAl_2Si_2O_8$ plane of the CaO-K_2O-Al_2O_3-SiO_2 system in different temperature intervals (***a***-***b***). Experimental points [483] and calculated lines.

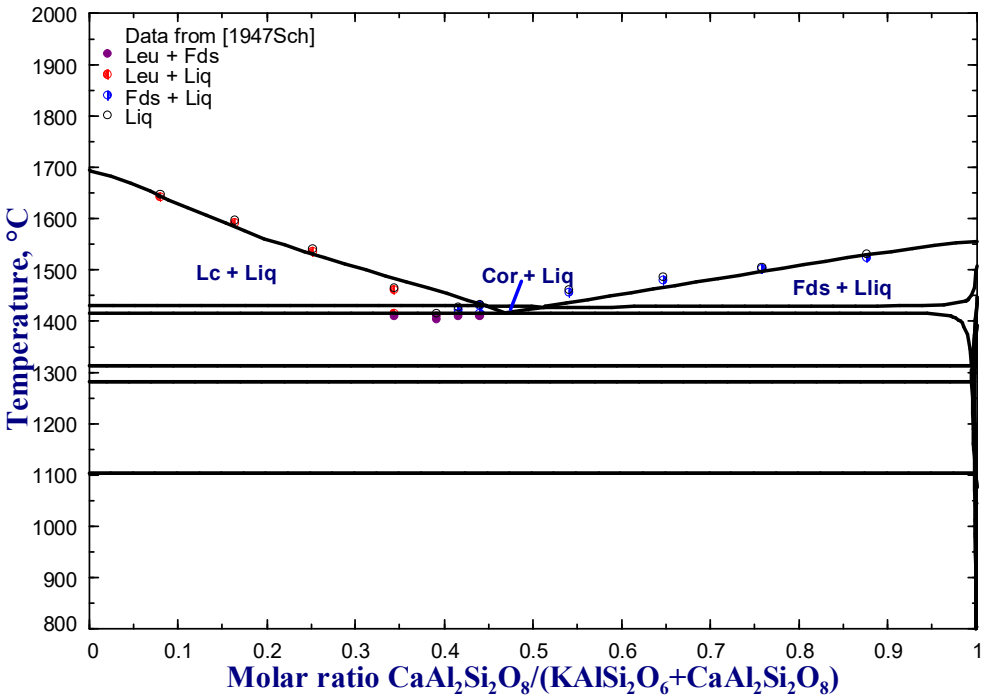

Figure 19.4 Phase diagram in the $CaAl_2Si_2O_8$-$KAlSi_2O_6$ section of the CaO-K_2O-Al_2O_3-SiO_2 system. Experimental data [483] and calculated lines.

In our optimization, there is a portion of the liquidus occupied by corundum. There is experimental evidence that in the CaO-Na_2O-K_2O-Al_2O_3-SiO_2 system corundum appears as a primary phase [484]. To reproduce this behaviour, a certain amount of corundum must appear in the CaO-K_2O-Al_2O_3-SiO_2 system as well. Small amounts of corundum crystals could go unnoticed in the $KAlSi_2O_6$-$CaAl_2Si_2O_8$ section (Figure 19.4).

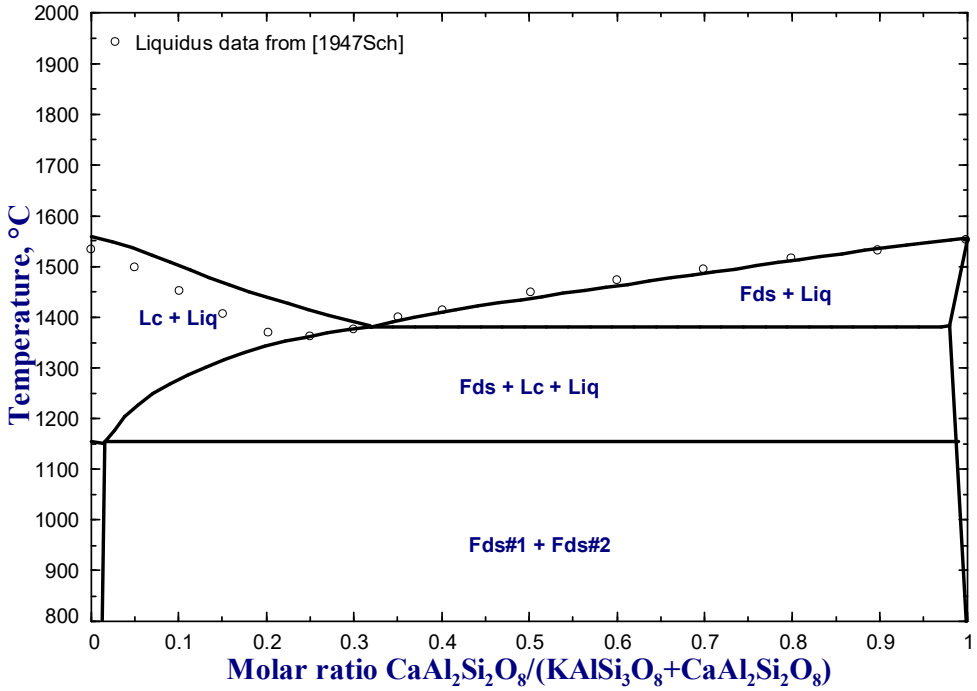

Figure 19.5 Phase diagram in the $CaAl_2Si_2O_8$-$KAlSi_3O_8$ section in the CaO-K_2O-Al_2O_3-SiO_2 system. Experimental data [69, 483] and calculated lines.

Phase diagram of the $KAlSi_3O_8$-$CaAl_2Si_2O_8$ system is shown in Figure 19.5. In the $KAlSi_3O_8$-$CaAl_2Si_2O_8$ feldspar system (sanidine-anorthite) mutual solubility of the end-members is very small under normal pressures although it increases with the pressure [69, 485]. In Figure 19.5, the solubilities were set approximately with regard to the data on ternary feldspars (presented in Section 20.1).

19.4 Calorimetry data

The enthalpies of mixing of (K,Ca)-feldspars were studied by means of lead borate solution calorimetry [450] (see Figure 19.6). Samples were obtained by an ion exchange of plagioclases in molten KCl. As in the $NaAlSi_3O_8$-$CaAl_2Si_2O_8$ system, enthalpy data confirm that there are three

main regions: analbite-like, intermediate and anorthite-like regions. While the excess enthalpies of mixing in the $NaAlSi_3O_8$-$CaAl_2Si_2O_8$ system appear mostly because the end-member symmetry is different, for the $KAlSi_3O_8$-$CaAl_2Si_2O_8$ system the volume mismatch starts to play role as well.

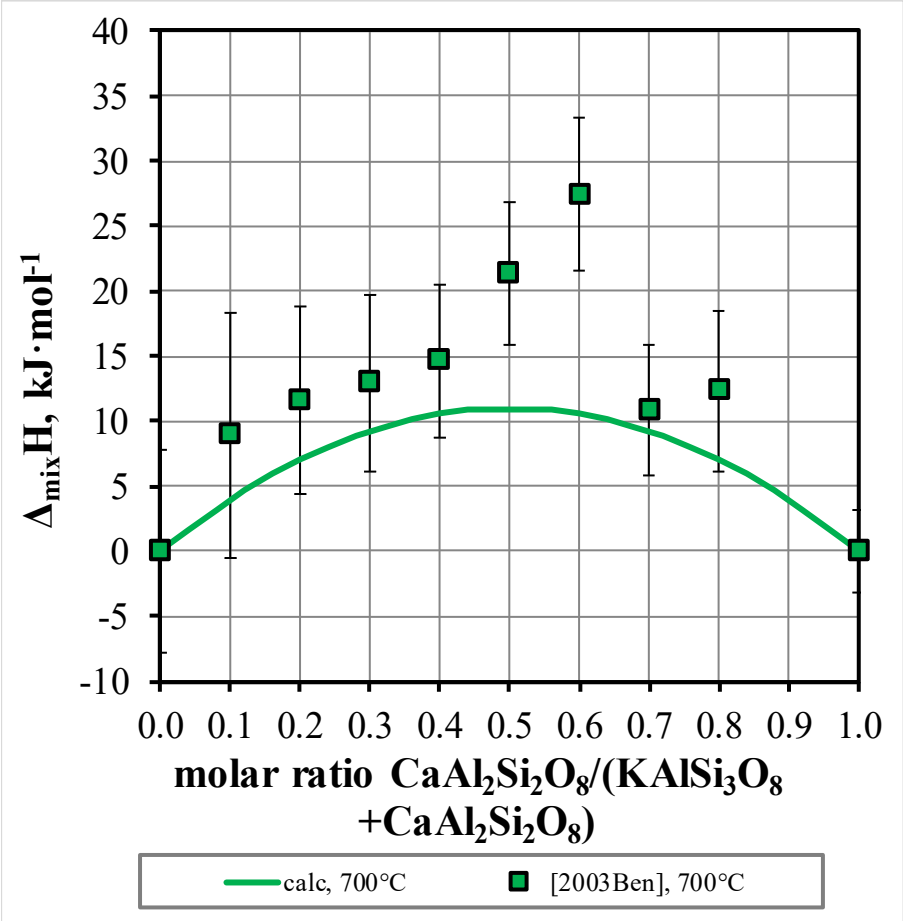

Figure 19.6 The enthalpy of mixing of metastable $KAlSi_3O_8$-$CaAl_2Si_2O_8$ feldspars. Experimental points [450] and the calculated line.

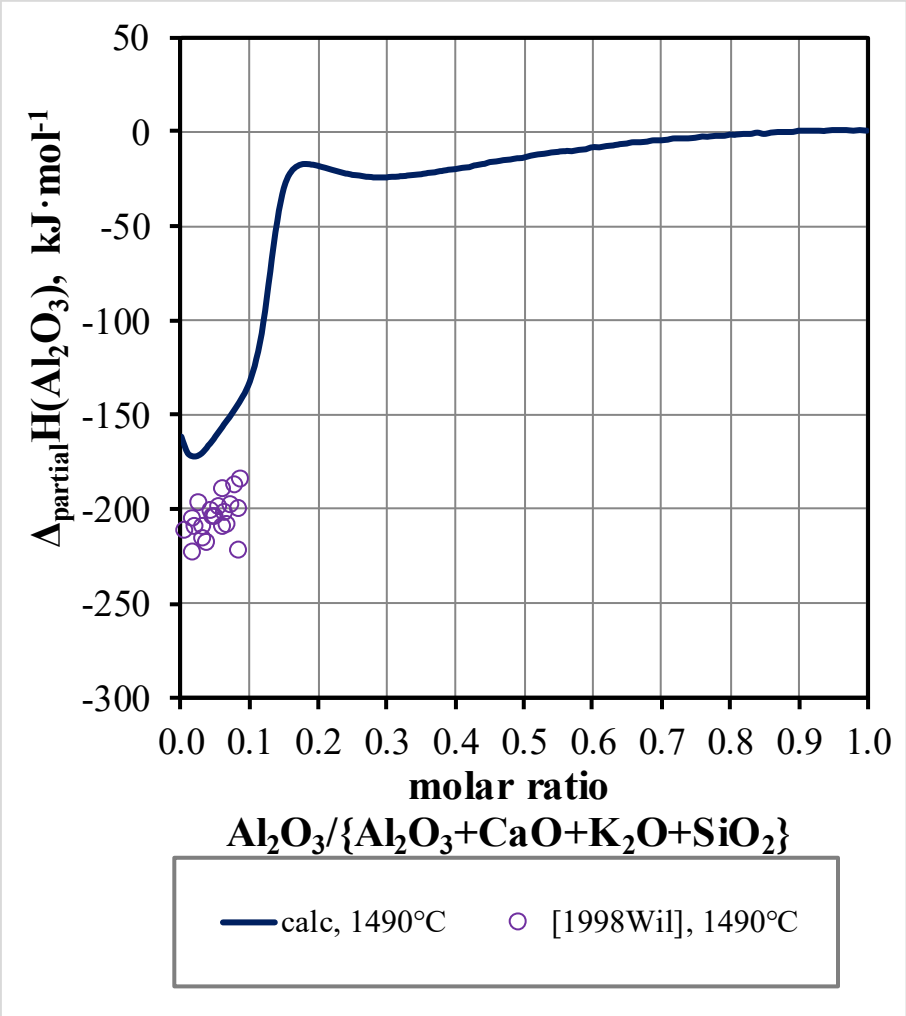

Figure 19.7 The partial enthalpy of Al_2O_3 in $K_2O{\cdot}CaO{\cdot}6SiO_2$ melts. Experimental points [343] and the calculated line.

The enthalpy of solution of corundum in $K_2O{\cdot}CaO{\cdot}6SiO_2$ melts was measured by Wilding and Navrotsky [343] at 1490°C. The enthalpy difference between corundum at 25°C and liquid Al_2O_3 at 1490°C was estimated by them to be 256.7 kJ·mol^{-1}. However, the partial enthalpies published in the same article in the K_2O-SiO_2 and K_2O-CaO-SiO_2 systems are not in agreement with other available experimental data (Section 9.2). A systematic experimental error could explain the discrepancy between the experimental and the calculated values in Figure 19.7.

19.5 Activity data

A series of works performed measurements of K pressures over K_2O-CaO-Al_2O_3-SiO_2 slags using a Knudsen cell [486, 487]. These data were recalculated into activities of the liquid K_2O (Figure 19.8). To do that, an assumption was used that potassium oxide decomposes into K(g) and O_2 in the gas phase and the percentage of other species is negligible. This assumption was confirmed for other potassium oxide systems [346]. To calculate the partial pressure of K(g) over the pure liquid K_2O, properties of K_2O(liq) were taken from *FactSage* databases. Even though there is a large uncertainly regarding the properties of liquid K_2O, consistent usage of a once chosen set of properties for both recalculating the experimental data and calculation of predicted values allows to cancel out this uncertainty.

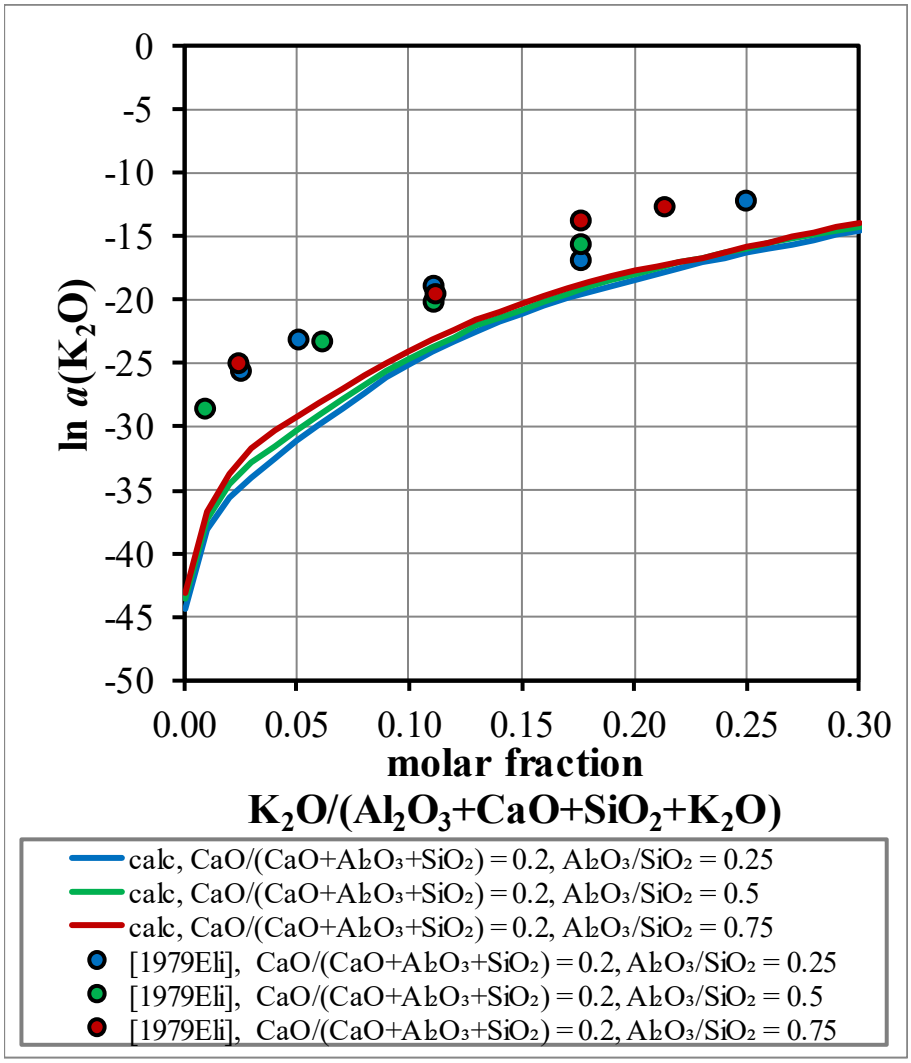

Figure 19.8 K_2O activity at 1430°C as a function of K_2O content at several base CaO-Al_2O_3-SiO_2 compositions. Experimental points [486] and calculated lines.

K_2O activity values at the measured compositions (Figure 19.8) is mostly attributed to the strong interaction between K_2O and SiO_2 while the presence of Al_2O_3 and CaO only slightly modifies the activity. It can be proven by calculating K_2O activity in binary systems with the same SiO_2 content. We suppose that the systematic deviation in K_2O activity in Figure 19.8 is attributed to the quality of the experimental data.

19.6 Optimization results

The K_2O-Al_2O_3-SiO_2, K_2O-CaO-SiO_2 and Al_2O_3-CaO-K_2O ternary subsystems were optimized in this work (Chapter 11, Chapter 17 and Chapter 18, correspondingly). The optimization of the CaO-Al_2O_3-SiO_2 system was adopted after Eriksson and Pelton [123]. It was found that the liquid phase can be treated as ideal. Corundum liquidus starts to appear in the $KAlSi_2O_6$-$NaAlSi_3O_8$ section. The data on the $NaAlSiO_4$-$CaAl_2Si_2O_8$-$KAlSi_2O_6$ plane in the CaO-K_2O-Na_2O-Al_2O_3-SiO_2 system by Gupta and Edgar [484] indicate that corundum is one of the primary phases there. This is an indirect indication that corundum can appear as a primary phase in the CaO-K_2O-Al_2O_3-SiO_2 system as well. The excess parameter of the liquid phase $\omega^{001}_{\mathrm{KAl,Si(Ca)//O,O}}$ serves to control the size of Corundum field and $\omega^{031}_{\mathrm{KAl,Si(Ca)//O,O}}$ parameter is required to avoid a spurious miscibility gap close to the SiO_2 corner arising from positive values of $\omega^{001}_{\mathrm{KAl,Si(Ca)//O,O}}$.

The model parameters $G^{add}_{\mathrm{KCaAlSi_2O_7}}$ and $\Delta_{\mathrm{CK//A//AS}}$ of Melilite solution were adjusted to reproduce the $Ca_2Al_2SiO_7$-$KCaAlSi_2O_7$ diagram in Figure 19.2. The optimized parameters are summarized in Table A.25.

CHAPTER 20 OPTIMIZATION OF THE K_2O-Na_2O-CaO-Al_2O_3-SiO_2 SYSTEM

20.1 Phase diagram

The investigated parts of the quinary system are limited by sections through the end-members with geological importance. So, Gupta and Edgar [109] studied phase relations in the $NaAlSi_3O_8$-$KAlSi_2O_6$-$CaAl_2Si_2O_8$ system (Figure 20.1). Samples with a small fraction of anorthite were highly viscous and hard to crystallize. It was proven that leucite is incompatible with sodium feldspar. The most sodium-rich feldspar coexisting with leucite corresponds to $Ab_{59}Or_{46}$ composition. A narrow solid solution of albite in leucite was found which cannot extend beyond $Lc_{95}Ab_5$ composition.

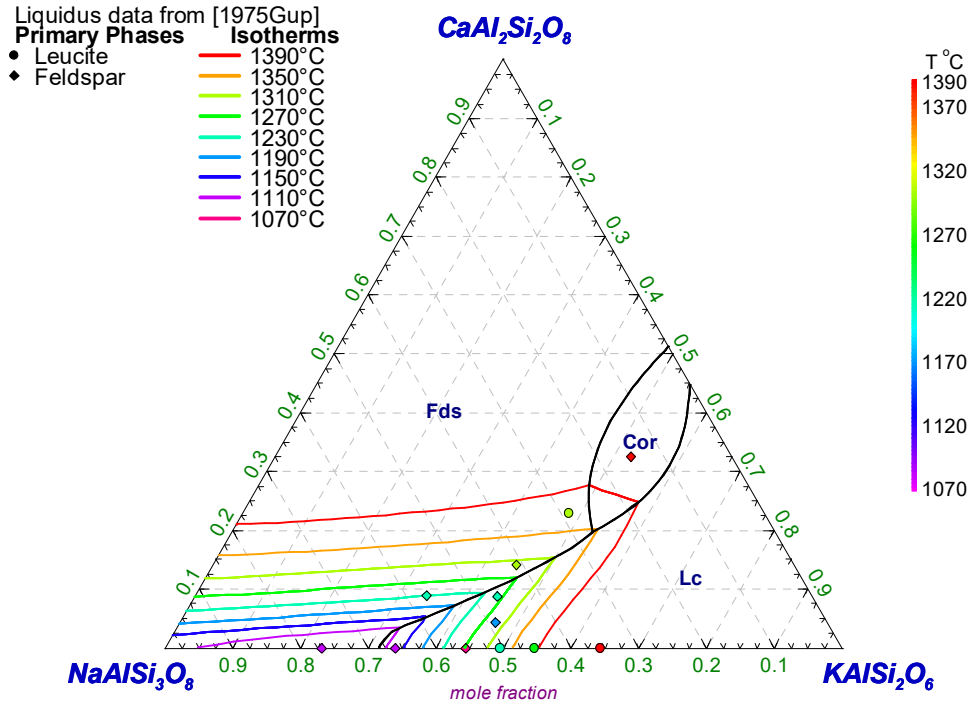

Figure 20.1 Liquidus projection in the $CaAl_2Si_2O_8$-$NaAlSi_3O_8$-$KAlSi_2O_6$ plane of the Na_2O-K_2O-CaO-Al_2O_3-SiO_2 system. Experimental data [109] and calculated lines.

Gupta and Edgar [484] also studied the $NaAlSiO_4$-$KAlSi_2O_6$-$CaAl_2Si_2O_8$ system. Leucite can incorporate some amounts of nepheline (5-10 wt%). Primary phases of corundum and β-alumina

have been observed as well. To prove that corundum is a true primary phase and does not form solely due to alkali loss, control experiments in sealed cylinders were performed.

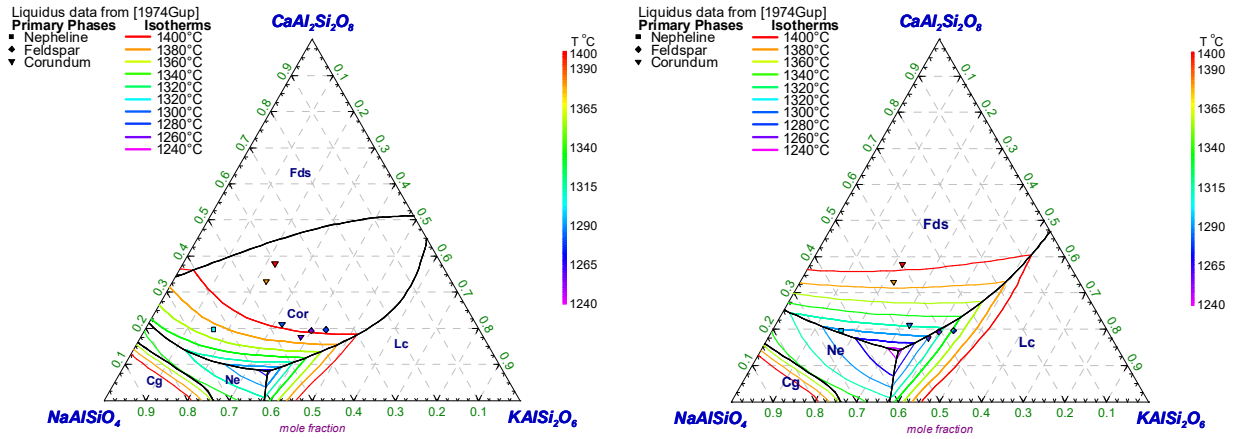

(***a***) (***b***)

Figure 20.2 Liquidus projection in the $CaAl_2Si_2O_8$-$NaAlSiO_4$-$KAlSi_2O_6$ plane of the Na_2O-K_2O-CaO-Al_2O_3-SiO_2 system with (***a***) and without (***b***) Corundum phase included into calculation. Experimental data [484] and calculated lines.

Liquidus projections in the $CaAl_2Si_2O_8$-$NaAlSiO_4$-$KAlSi_2O_6$ system were calculated with and without Corundum phase. It is seen (Figure 20.2, (***b***)) that the calculated isotherms correspond to the experimental points. It is not mentioned by Gupta and Edgar [484] but it is hard to determine the size and position of Corundum field in similar systems (the $CaAl_2Si_2O_8$-$NaAlSiO_4$ section [52], the $Ca_2Al_2SiO_7$-$CaAl_2Si_2O_8$-$NaAlSiO_4$ plane [449]) because corundum forms in very small quantities and the position of its field is strongly influenced by alkali losses.

Liquidus temperatures in the feldspar system $NaAlSi_3O_8$-$KAlSi_3O_8$-$CaAl_2Si_2O_8$ were measured by Franco and Schairer [488] (Figure 20.3).

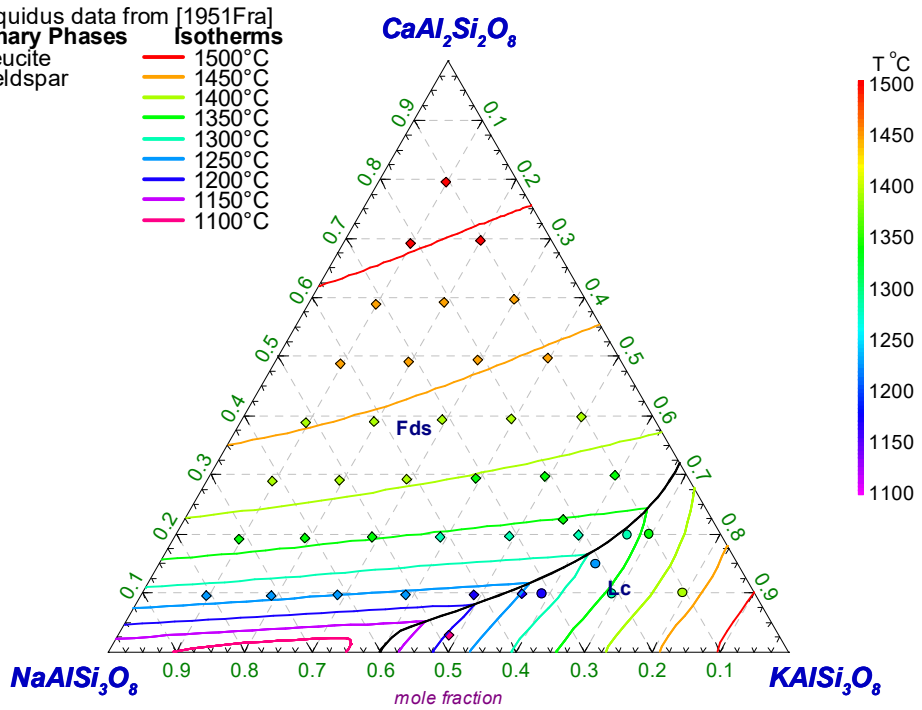

Figure 20.3 Liquidus projection in the $CaAl_2Si_2O_8$-$NaAlSi_3O_8$-$KAlSi_3O_8$ plane of the Na_2O-K_2O-CaO-Al_2O_3-SiO_2 system. Experimental data [488] and calculated lines.

Based on the binary phase diagrams in the feldspar system $NaAlSi_3O_8$-$KAlSi_3O_8$-$CaAl_2Si_2O_8$, one can assume existence of a ternary miscilibity gap. A few works deal with compositions of coexisting alkali feldspars and plagioclases [457, 489, 490]. These data are summarized in Figure 20.4.

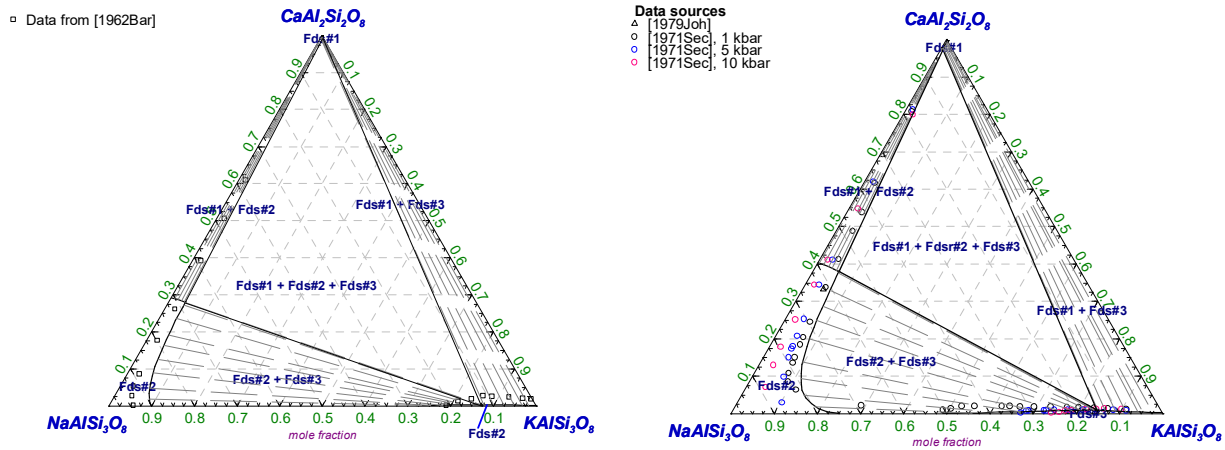

(*a*) (*b*)

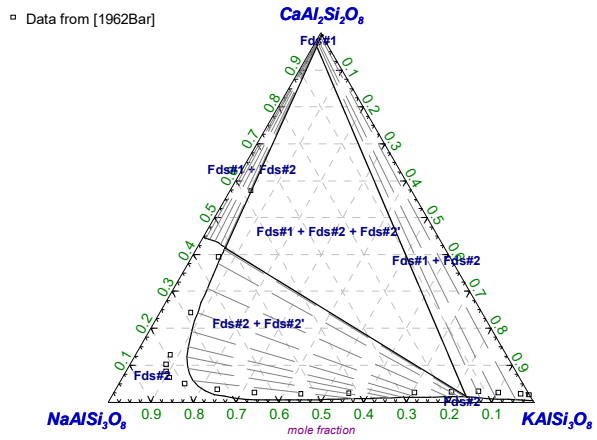

(*c*)

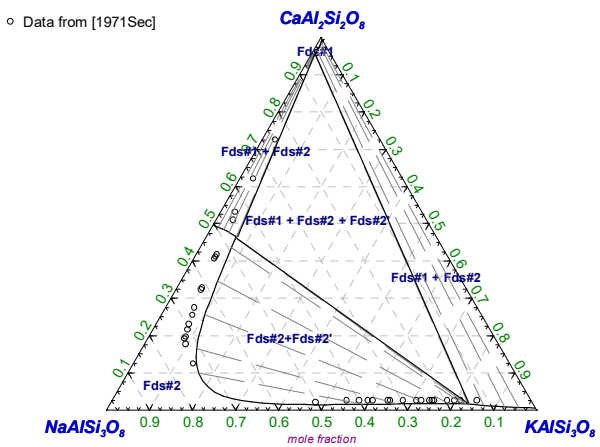

(*d*)

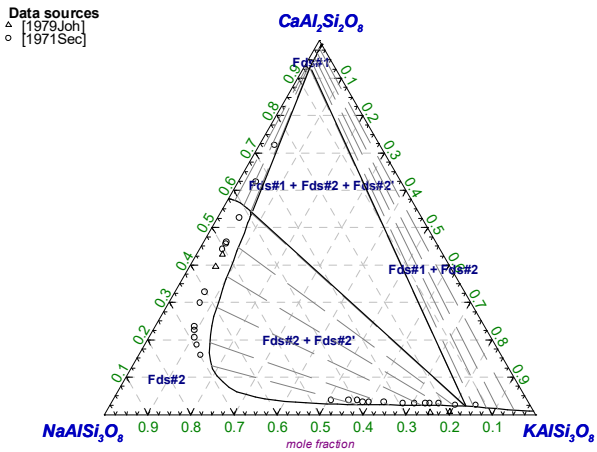

(*e*)

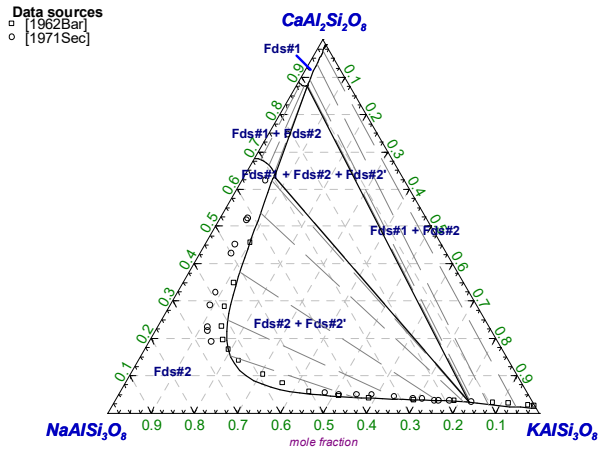

(*f*)

Figure 20.4 Feldspar miscilibity gap at 500°C (***a***), 650°C (***b***), 700°C (***c***), 750°C (***d***), 825°C (***e***), 900°C (***f***). Experimental points [457, 489-491] and calculated lines.

Temperatures of the displacive transformation in ternary feldspars are reported by Kroll and Bambauer [492, 493].

20.2 Calorimetry data

Enthalpies of solution in 20.1 wt% HF for disordered ternary feldspars with a constant anorthite content were measured by Hovis [494]. The data were recalculated into the enthalpy of mixing

(Figure 20.5). Compared to the An-free series, ternary feldspars have a less positive enthalpy of mixing.

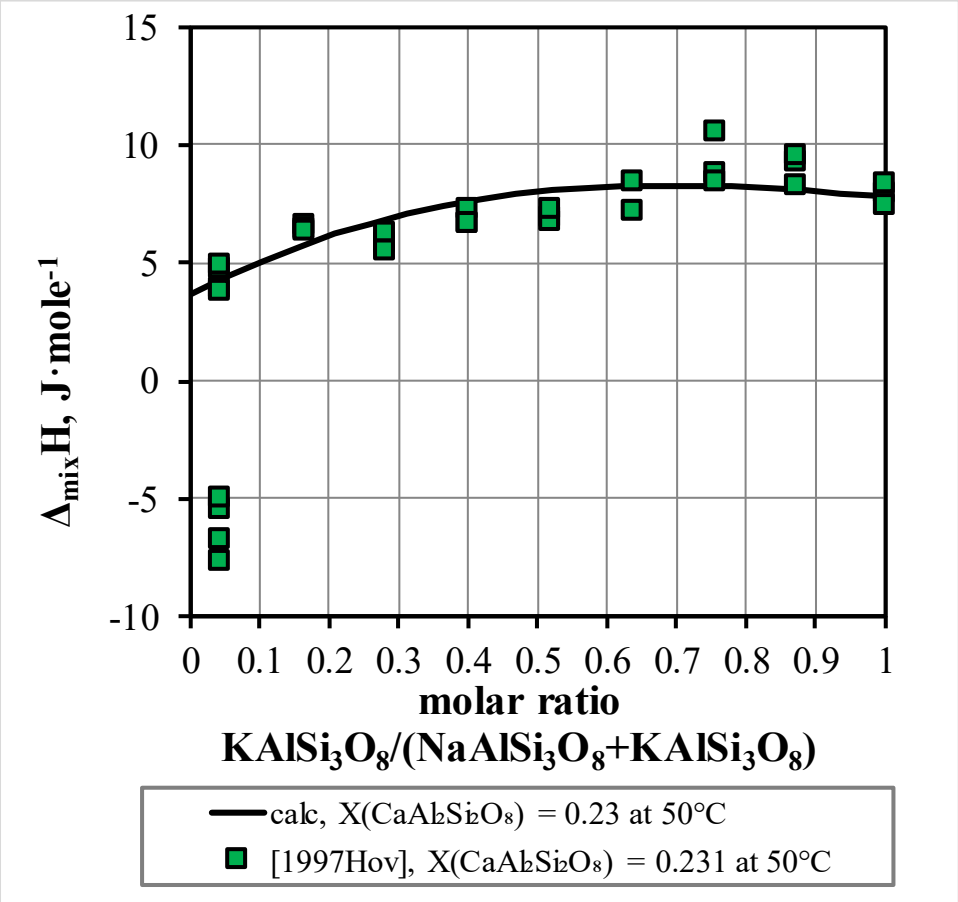

Figure 20.5 The enthalpy of mixing of ternary $NaAlSi_3O_8$-$KAlSi_3O_8$-$CaAl_2Si_2O_8$ feldspars. Experimental points [494] and the calculated line.

20.3 Optimization results

No optimization specific for the quinary system was performed; all presented predictions are based on the available optimizations of the subsystems.

CHAPTER 21 OPTIMIZATION OF THE Na_2O-MgO-SiO_2 SYSTEM

21.1 Phase diagram

There are three disilicate compounds in the Na_2O-MgO-SiO_2 system. NM5S12 was first reported by Schairer et al. [391]; it melts incongruently. Later it was found to decompose into $MgSiO_3$ and liquid at 1200±5°C [495]. This compound is structurally similar to KM5S12 and forms solid solutions with it [496]. There are minerals containing this end-member: roedderite, merrihueite, osumilite. NM2S6 melts incongruently (no details) [391, 495]. The compound was also found by Botvinkin et al [497]. According to Cradwick and Taylor [498], the compound is isostructural with the mineral tuhualite $[Na,K]_2Fe_2Fe_2Si_{12}O_{30}\cdot H_2O$. NMS4 compound was reported by Schairer et al. [391] and by Schairer and Yoder [495]. It melts incongruently [391, 495].

There are two ternary metasilicate compounds in the system. N2M3S5 melts incongruently [391, 495]. There is N2MS3 compound but, apparently, it is not structurally related to N2CS3 compound. It melts incongruently [391, 495].

There are two compounds with a silica content intermediate between disilicates and metasilicates. NMS3 compound melts incongruently [391, 495]. The compound is structurally dissimilar with its K-analogue [495]. Probably, it forms a limited solid solution with $NaAlSiO_4$. NM2S4 melts incongruently [391, 495].

There are three compounds with a silica content less then that of metasilicates. N2M2S3 compound melts incongruently [391, 495]. It has at least three polymorphs (no details given) [495]. The compound was investigated in more detail by Foris et al. [499]; the transition from orthorhombic to cubic is at 645°C. A Na-deficient tetragonal phase was also found. The phase is said to be of carnegieite-type (but direct indications of whether the solid solution actually exists, are not given). The structure, composition and phase relations of other compounds were mainly investigated in the works of Botvinkin et al. [497] and Manuilova [500]. Apparently, these works are not independent as the authors share the same affiliation. NMS compound was found by Hughes [472] but, according to Schairer and Yoder [495], it consists of N2M2S3 and another unidentified phase. If it is true, the unidentified phase must lie in the $NaMg_{0.5}O$-SiO_2 section and has a lower silica content. However, no experimental data on phase equilibria in this region are available. The phase

is also reported by Botvinkin et al. [497] (congruent melting) and by Manuilova [500]. According to Shannon [501], NMS can be produced hydrothermally and it is not the same phase as found by Hughes [472]. NM2S2 compound melts without decomposition [497, 500]. Ternary compounds in the system are summarized in Figure 21.1.

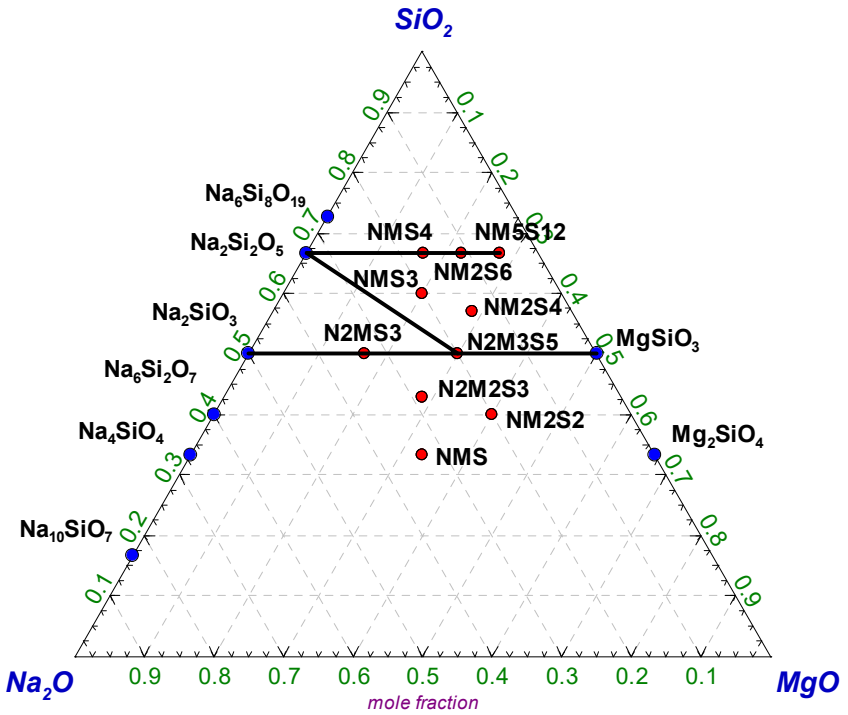

Figure 21.1 Stoichiometric compounds and the investigated sections in the Na_2O-MgO-SiO_2 system.

The metasilicate section Na_2SiO_3-$MgSiO_3$ was investigated by Wallace [424] together with other metasilicate sections: Na_2SiO_3-$CaSiO_3$, Na_2SiO_3-$SrSiO_3$, Na_2SiO_3-$BaSiO_3$, etc. The melts between 20 and 80% $MgSiO_3$ did not crystallize well and only points close to the limiting compositions are available (Figure 21.2). The melting temperature of the pure Na_2SiO_3 composition obtained by Wallace does not coincide with the data available in the Na_2O-SiO_2 system. The same discrepancy was noticed in the optimization of the Na_2O-CaO-SiO_2 system (this work, section Chapter 14). Apparently, DTA method was used giving rise to the undercooling effect. The melting point of $MgSiO_3$, however, is reproduced well. It is probably explained by faster crystallization rates of the compound. The point at around 95 mol% $MgSiO_3$ corresponds to formation of $MgSiO_3$ phase and the crystallization of Mg_2SiO_4 (as seen from the phase diagram) was probably not noticed due to a

weak thermal effect in DTA. In general, the data by Wallace were not considered reliable for the optimization and are only given for reference purposes.

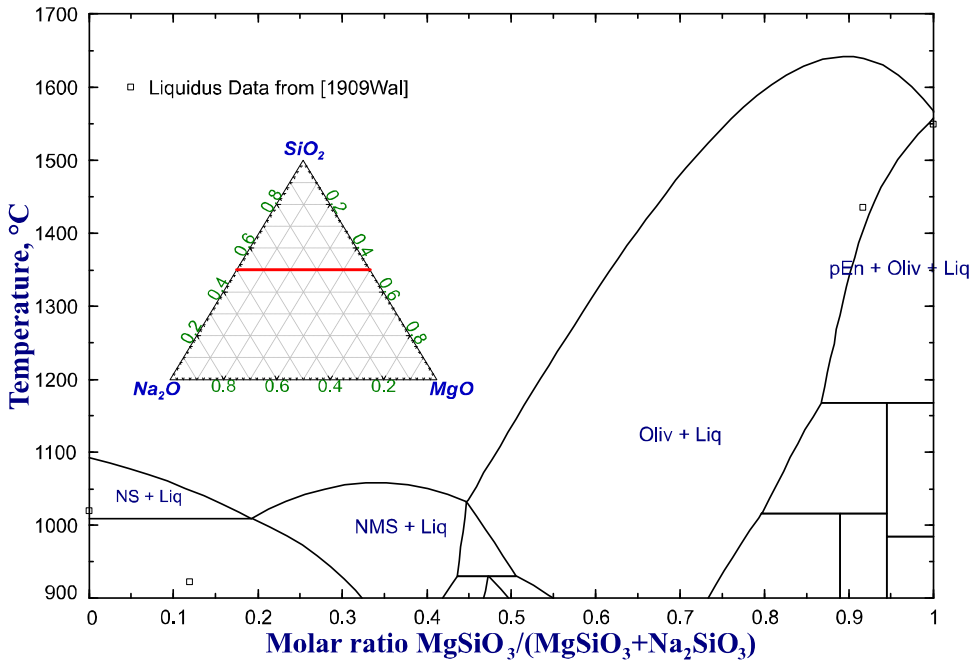

Figure 21.2 Phase diagram in the Na_2SiO_3-$MgSiO_3$ section of the Na_2O-MgO-SiO_2 system. Experimental points [424] and calculated lines.

Phase relations in the system were studied by Schairer et al. [391]. Apparently, their work continues the work of Morey started in the same laboratory [158]. Unfortunately, the authors did not publish all the details about their work and only a schematic phase diagram is available with invariant points. Quenching technique was used with a consequent X-ray identification of the solid phases. The authors mention that an optical identification of crystalline phases which is usually employed in their group is complicated in case of the Na_2O-MgO-SiO_2 system as there are many ternary compounds with similar optical properties and their identification is complicated by the formation of very small intergrown crystals. So, an X-ray identification of the crystalline phases was preferred. Although there are some coincidence reflections of different phases, there are still enough unique reflections for reliable identification of all the compounds. Compositions with more than 50 mol% SiO_2 could be prepared using Na_2SiO_3, SiO_2 and MgO as precursors. However, noticeable Na_2O losses occurred at $X(SiO_2) < 50\%$. In that case, the final composition of each melt had to be determined by a chemical analysis. Furthermore, some of the liquid samples in the SiO_2-

poor region were so fluid that even mercury quenching was not enough to prevent the crystallization. Also, the authors experienced difficulties with the equilibration of high-SiO_2 samples with high viscosity and low liquidus temperatures.

The Na_2SiO_3-Mg_2SiO_4-SiO_2 part of the Na_2O-MgO-SiO_2 system was investigated by Botvinkin et al. [497]. Quenching method was used to determine phase compositions at different temperatures. The authors indicate that in SiO_2 field, only cristobalite was found as a crystallization product and not tridymite. Apparently, in tridymite stability field, cristobalite forms as a faster crystallizing metastable phase. Besides the optical phase identification, an X-ray analysis was used as well. Crystallization difficulties were noticed for compositions in the primary field of NM2S6 compound. Some univariant lines, for example, NMS/NM2S6 univariant line was placed approximately based on the information on the direction of the isotherms nearby. The compositions of NM2S6, NMS and NM2S2 compounds were determined graphically. The authors paid special attention to verify the composition of NM2S6 compound because they had a suspicion that it could have (1:3:6) stoichiometry similar to devitrite in the Na_2O-CaO-SiO_2 system.

Crystallization fields and isotherms by Schairer et al. and Botvinkin et al. are given in Figure 21.3-Figure 21.4. For clarity, the experimental isotherms were separated from the experimental primary fields.

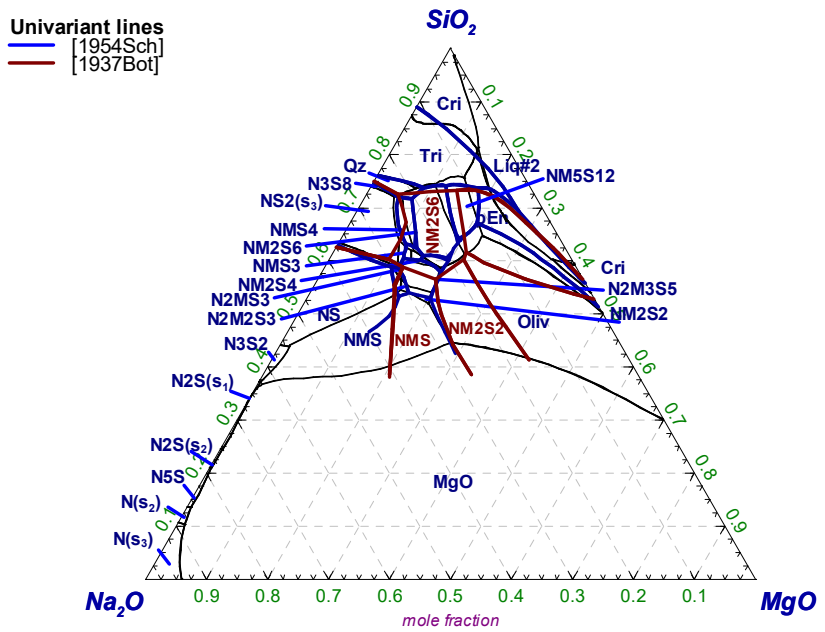

Figure 21.3 Primary fields in the Na_2O-MgO-SiO_2 system. Experimental univariant lines [391, 497] and the calculated phase diagram. The phase labels correspond to the calculated phase diagram and mostly coincide with the fields by Schairer et al. [391]; the field labels by Botvinkin et al. [497] are marked in brown.

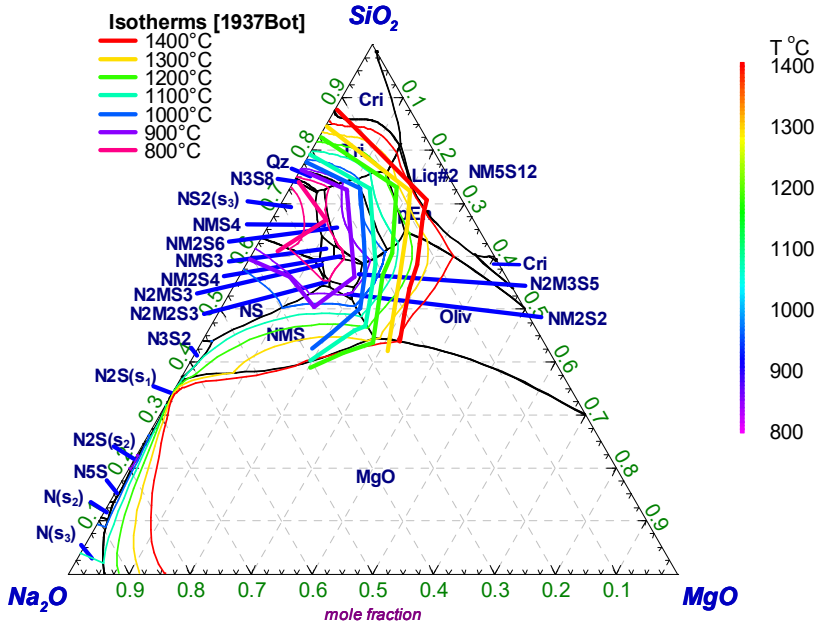

Figure 21.4 Isotherms in the Na_2O-MgO-SiO_2 system. Experimental isotherms (thick lines) [497] and the calculated phase diagram.

Schairer and Yoder [495] finalized the work on the ternary system started by Schairer et al. [391] and presented two sections in the ternary system: NM5S12-$Na_2Si_2O_5$ and N2M3S5-$Na_2Si_2O_5$. No solid solutions in the ternary system were noticed. Also, there is no correlation between the composition and the structure of compounds in the calcium and magnesium systems. The latter can be explained by a significant size difference of Ca^{2+} and Mg^{2+} cations. The NM5S12-$Na_2Si_2O_5$ section includes three ternary compounds: NMS4, NM2S6 and NM5S12 (all disilicates). It is a section which shows the incongruent melting of these ternary compounds (Figure 21.5). It is not binary, as NM5S12 compound decomposes into $MgSiO_3$ and liquid. The calculated phase diagram shows a part of the liquid miscibility gap propagating from the MgO-SiO_2 side of the system. However, the experimental data by Schairer and Yoder [495] do not reflect this as no special attention was paid to the existence of the second liquid phase.

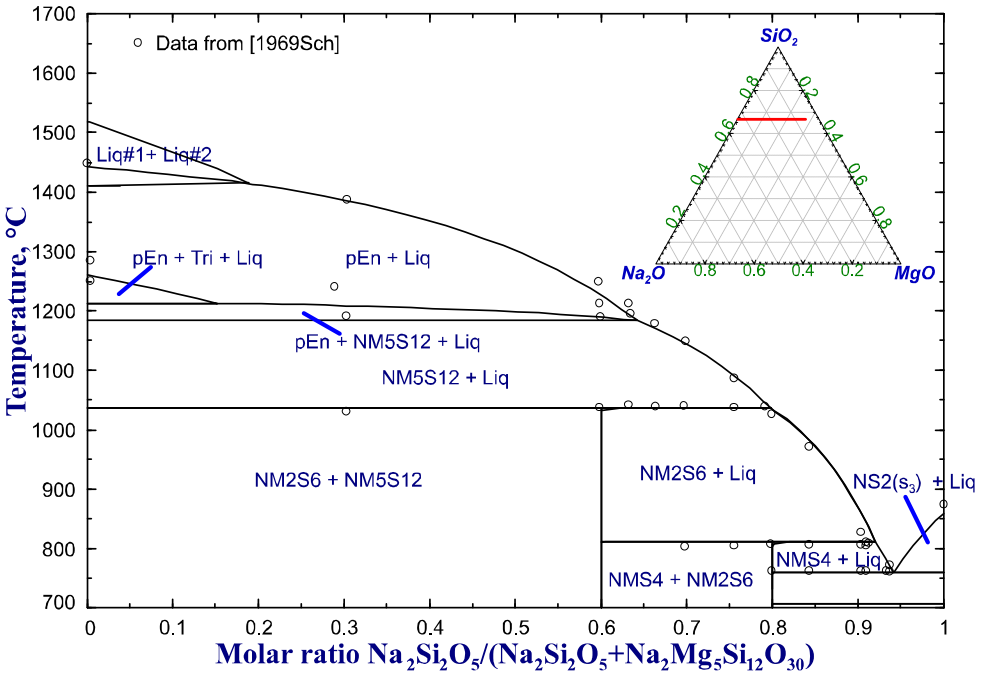

Figure 21.5 Phase diagram in the $Na_2Si_2O_5$-$Na_2Mg_5Si_{12}O_{30}$ section of the Na_2O-MgO-SiO_2 system (the disilicate section). Experimental points [495] and calculated lines.

The N2M3S5-$Na_2Si_2O_5$ section shows the incongruent melting of N2M3S5 compound (Figure 21.6).

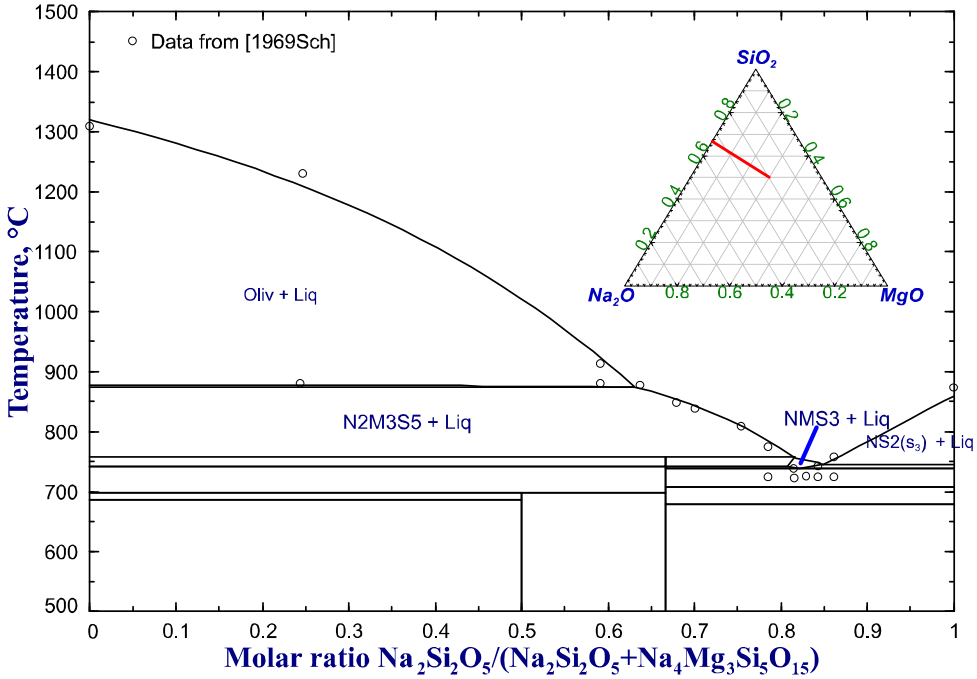

Figure 21.6 Phase diagram in the $Na_2Si_2O_5$-$Na_4Mg_3Si_5O_{15}$ section of the Na_2O-MgO-SiO_2 system. Experimental points [495] and calculated lines.

The phase fields by Schairer et al. [391] and by Botvinkin et al. [497] in Figure 21.3 do not coincide; in this work it was decided to trust the data by Schairer et al. The liquidus was set according to the data by Schairer and Yoder [495]; as their work is a continuation of the work by Schairer et al. [391], the experimental isotherms in Figure 21.4 are not supposed to agree with the calculated ones.

Invariant equilibria in the system are summarized in Table 21.1. The compositions of invariant points are taken from a hand-plotted diagram without experimental points by both Schairer et al. [391] and Morey [158] which could be not precise.

Table 21.1 Invariant phase equilibria in the Na_2O-MgO-SiO_2 system. The calculated values are shown in bold.

Solid phases	**T, °C**	**Liquid composition, mol%**		
		SiO_2	**Na_2O**	**MgO**
NM5S12-Tri-pEn	1250 [158, 391] **1212**	**75.70**	**9.82**	**14.48**
NM5S12-pEn-Oliv	1190 [391]	67.03	12.11	20.86

Solid phases	T, °C	Liquid composition, mol%		
		SiO_2	Na_2O	MgO
	1193 [158] **1168**	**64.64**	**12.45**	**22.91**
NM2S6-NM5S12-Oliv	1040 [158, 391] **816**	64.05 **59.51**	16.37 **22.32**	16.37 **18.16**
NM2S6-NMS4-Oliv	915 [391] 910 [158] **847**	60.50 **58.75**	20.10 **22.26**	20.10 **18.98**
NM2S4-N2M3S5-Oliv	868 [391] 875 [158] **843**	57.82 **58.52**	22.64 **22.53**	22.64 **18.95**
N2M3S5-N2M2S3-M2S	865 [391] 860 [158] **864**	52.99 **52.90**	26.84 **27.89**	26.84 **19.20**
N2M2S3-N2M3S5-N2MS3	798 [391] 795 [158] **776**	53.93 **56.46**	29.87 **29.71**	29.87 **13.83**
NS-N2M2S3-N2MS3	825 [391] 820 [158] **779**	53.31 **56.32**	31.82 **30.01**	31.82 **13.67**
NS-NS2-N2MS3	735 [158, 391] **744**	58.82 **59.34**	30.23 **29.89**	30.23 **10.77**
NS2-N2MS3-N2M3S5	713 [158, 391] **735**	58.78 **59.69**	29.13 **28.48**	29.13 **11.84**
NS2-N2M3S5-NMS3	713 [391] 715 [158] **732**	60.44 **58.92**	27.47 **29.39**	27.47 **11.69**
NS2-NMS3-NMS4	733 [391] 748 [158] **752**	63.23 **63.82**	25.74 **26.54**	25.74 **9.64**
NS2-Qz-NMS4	725 [391] 720 [158] 733 [495] **731**	72.03 **72.29**	22.52 **23.09**	22.52 **4.62**
NM2S6-NM2S4-NMS3	785 [391] 780 [158] **776**	61.07 **62.26**	24.03 **25.32**	24.03 **12.42**
NM2S6-NMS4-NMS3	773 [391] 775 [158] **781**	62.37 **61.48**	24.30 **25.10**	24.30 **13.42**
N2M3S5-NM2S4-NMS3	780 [391] 785 [158] **770**	60.20 **59.87**	24.84 **26.45**	24.84 **13.68**

Solid phases	T, °C	Liquid composition, mol%		
		SiO_2	Na_2O	MgO
NM2S6-NMS4-Qz	775 [391] 785 [158] 780 [495] **771**	71.65 **72.59**	20.39 **21.71**	20.39 **5.70**
Tri-Qz-NM2S6	867 [158, 391] 870 [495] **867**	73.83 **65.61**	17.42 **11.46**	17.42 **22.92**
Tri-NM5S12-NM2S6	1018 [391, 495] 1013 [158] **993**	74.21 **74.57**	13.57 **15.23**	13.57 **10.20**
Cri-Tri-pEn	1470 [158, 391] **1465**	69.77 **53.71**	4.14 **0.00**	4.14 **46.29**

The invariant points by Botvinkin et al. [497] are not shown in Table 21.1 because of their inconsistency with the data by Schairer et al. [391], Morey [158], Schairer and Yoder [495] and the current optimization.

21.2 Activity data

Gas equilibration technique was used by Rego et al. [435] to obtain isoactivity lines in the Na_2O-MgO-SiO_2 system. The log $a(Na_2O(liq))$ was from about -8.0 to -7.0. An investigated melt was heated in a graphite crucible which shared the gas atmosphere with a large amount of a binary Na_2O-SiO_2 melt, also equilibrated with graphite, used for reference purposes.

The sodium vapor, obtained during the reaction:

$$Na_2O(liq)+C(cr)\leftrightarrow 2Na(g)+CO(g) \quad (133)$$

allowed to maintain equal sodium oxides activities between two melts. The investigated melt loses or absorbs sodium oxide according to the difference in the activity between two melts. The composition of the investigated melt is analysed.

Mathieu [436] measured Na_2O solubility in Na_2O-free base compositions in the CaO-MgO-SiO_2 system in an atmosphere with a fixed Na(g) partial pressure. Large amounts of $Na_2O{\cdot}2SiO_2$ melt were used as a source of sodium and the partial pressure of oxygen was fixed by a Ni/NiO buffer. The operating temperatures were 1250° and 1400°C. The authors present their data in the form of isosolubility lines in the CaO-MgO-SiO_2 base composition triangle and to compare these data with

calculated values, these were replotted in the form of isoactivities. Intersection points of Na_2O isosolubility lines and the MgO-SiO_2 border are plotted in Figure 21.7.

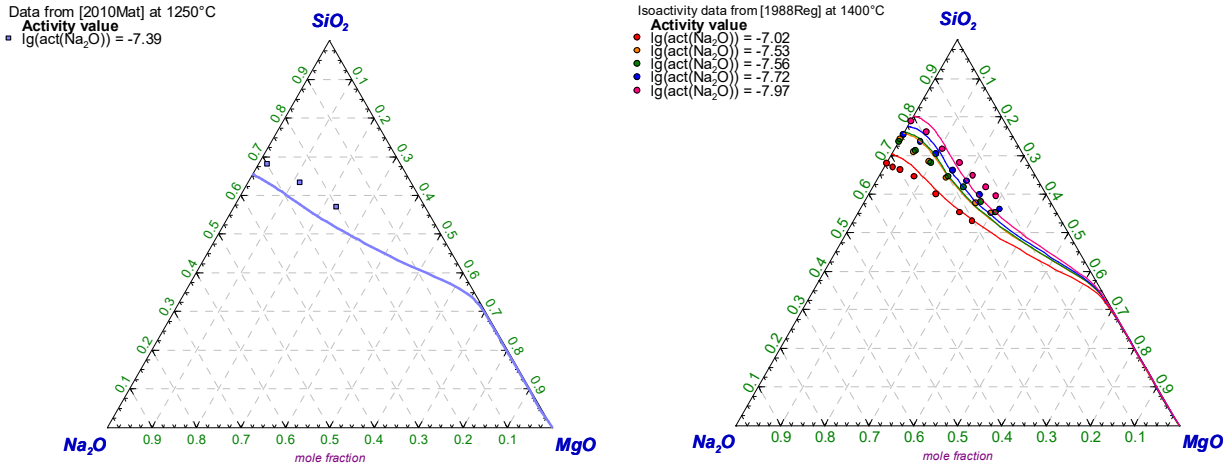

(***a***) (***b***)

Figure 21.7 Isoactivity lines in the Na_2O-MgO-SiO_2 system at 1250°C (***a***) and 1400°C (***b***). The reference state is the pure liquid Na_2O. Experimental points [435, 436] and calculated lines.

EMF measurements in a cell:

$$Ag|Na_2O{\cdot}3SiO_2||(1\text{-}x)Na_2O{\cdot}xMgO{\cdot}3SiO_2|Ag \tag{134}$$

were performed at different temperatures for trisilicate compositions by Smith and Rindone [226] (Figure 21.8). There are also isothermal data available at 500°C (Figure 21.9). To calculate the activity of Na_2O in the reference melt, the same oxide database was used as for the optimization to maintain consistency.

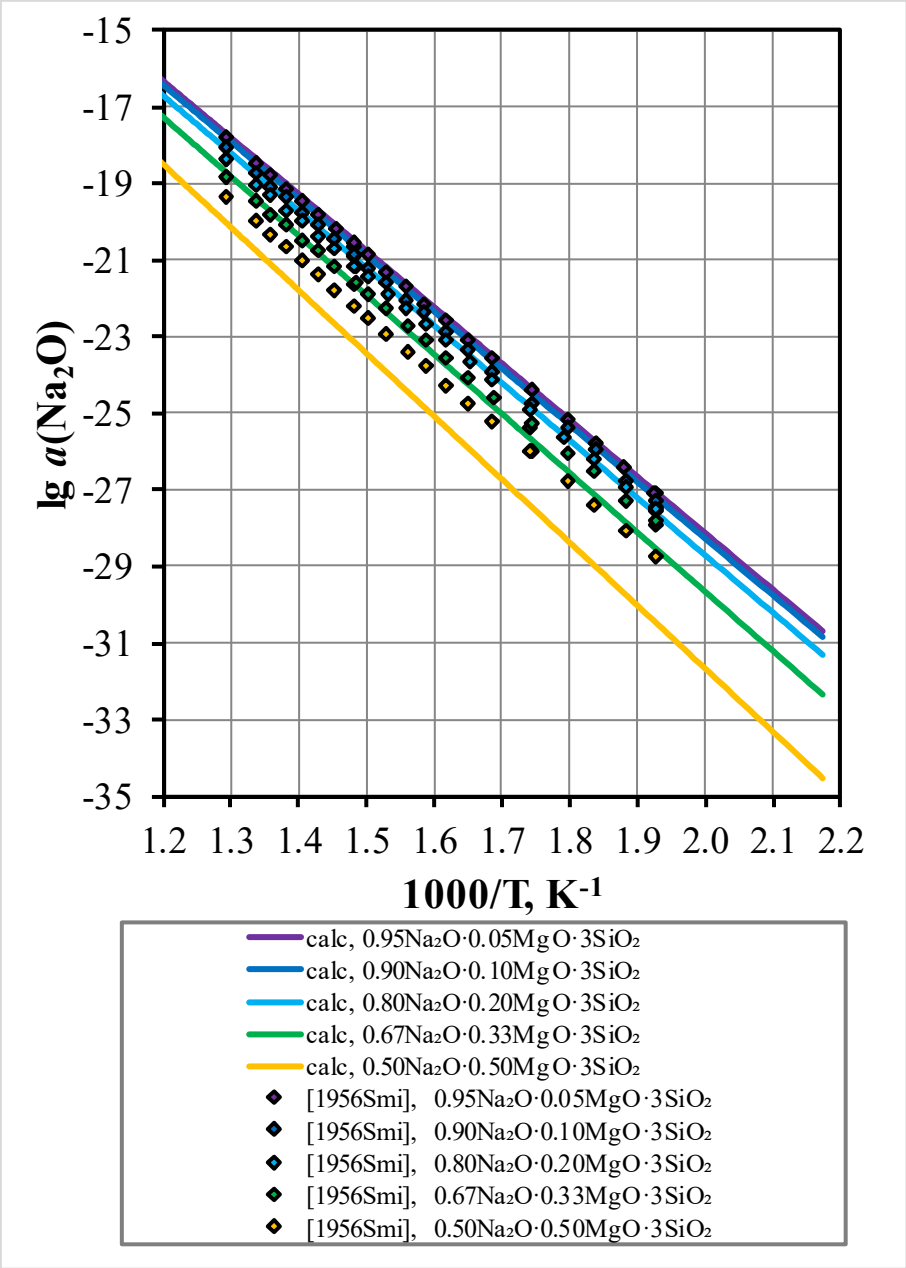

Figure 21.8 Temperature dependence of Na_2O activity of the liquid phase at compositions in the trisilicate section. The reference state is the pure liquid Na_2O. Experimental points [226] and calculated lines.

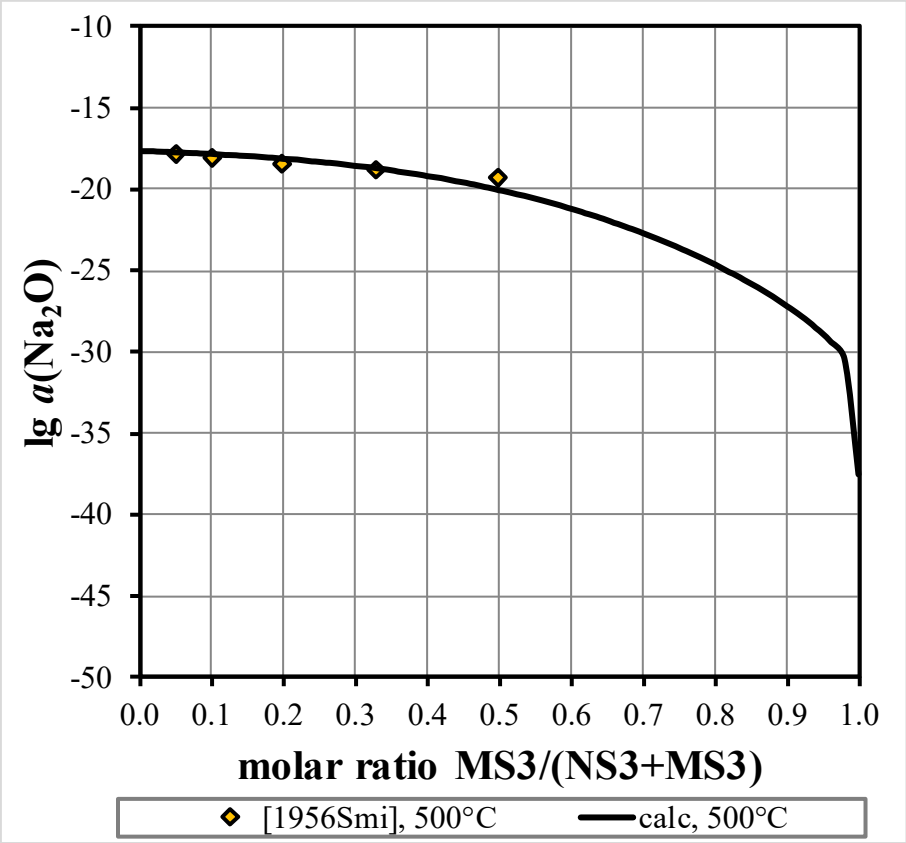

Figure 21.9 Na_2O activity of the liquid phase along the trisilicate section at 500°C. The reference state is the pure liquid Na_2O. Experimental points [226] and the calculated line.

21.3 Optimization results

The Na_2O-SiO_2 binary system was optimized in this work, an optimization of the MgO-SiO_2 by Wu et al. [502] was adopted, and the Na_2O-MgO binary was considered ideal.

As there are no data concerning the thermodynamic properties of the ternary compounds in the literature, their C_P and entropies were estimated as weighted combinations of the functions of binary compounds. Later, if needed, the entropies could be adjusted. Excess parameters in the liquid phase were set using the liquidus data on the binary compounds (mostly $MgSiO_3$ and Mg_2SiO_4) whose properties are already known. The enthalpies and, if needed, the entropies of the ternary compounds were adjusted to reproduce the corresponding phase diagram data. The optimized parameters are summarized in Table A.26-Table A.27.

CHAPTER 22 OPTIMIZATION OF THE CaO-MgO-Na_2O-SiO_2 SYSTEM

22.1 Phase diagram

A few authors studied various planes and sections in the quaternary CaO-MgO-Na_2O-SiO_2 system because of its value for glass-making applications. A new quaternary compound $Na_2Ca_4Mg_2Si_4O_{15}$ was mentioned by Hausner and Suppaner [503]. Only an X-ray pattern was reported and no thermodynamic or phase equilibria data could be found in the literature. Planes in the quaternary system with 5 and 10 wt% MgO were studied by Shahid and Glasser [504] (see Figure 22.1, Figure 22.2). Silverman [505] studied the SiO_2-rich part of the SiO_2-Na_2O-($CaO_{0.5}MgO_{0.5}$) system (see Figure 22.3).

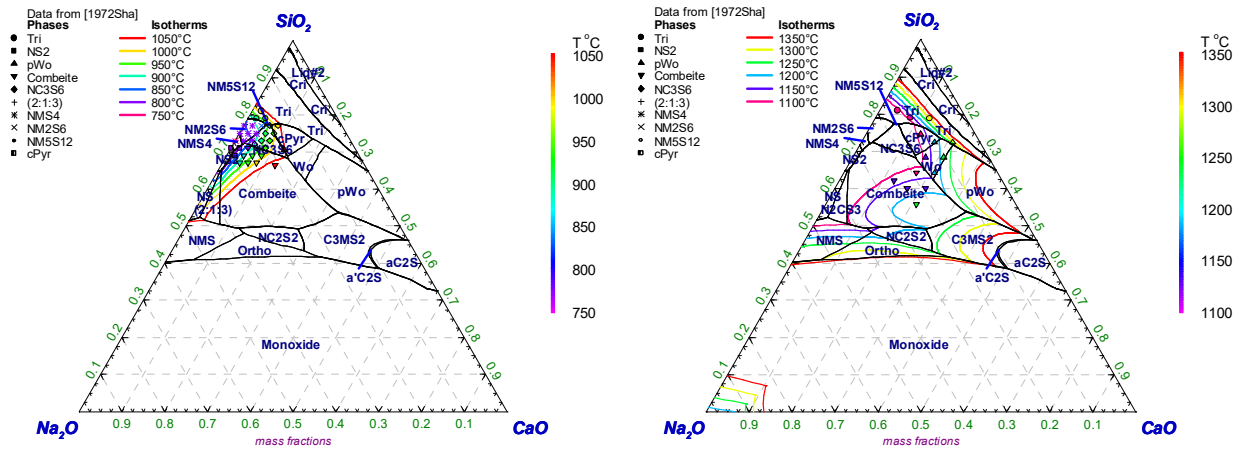

(***a***) (***b***)

Figure 22.1 Liquidus projection in the 5 wt% MgO plane of the CaO-MgO-Na_2O-SiO_2 system. Isotherms from 750° to 1050°C (***a***) and 1100° to 1350°C (***b***). Experimental points [504] and calculated lines.

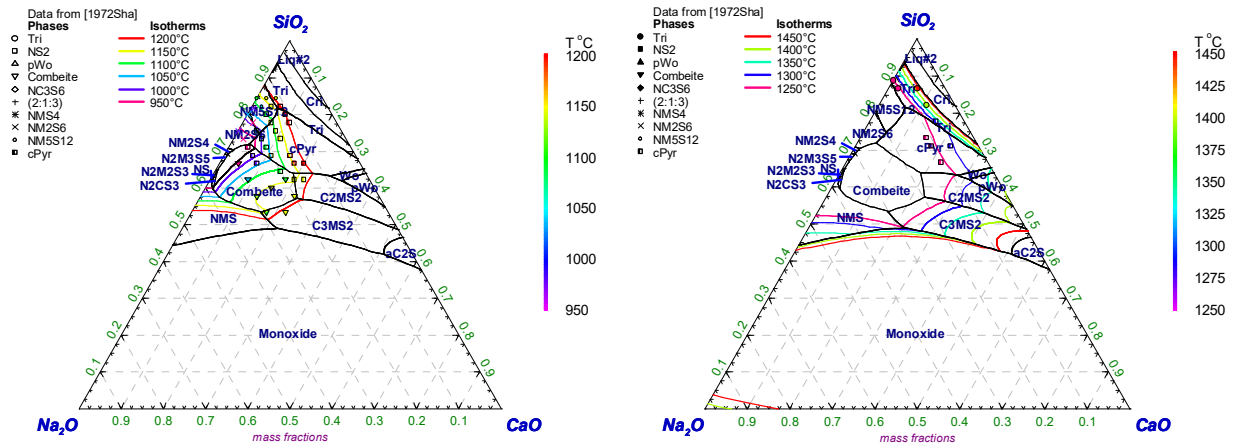

(***a***) (***b***)

Figure 22.2 Liquidus projection in the 10 wt% MgO plane of the CaO-MgO-Na_2O-SiO_2 system. Isotherms from 950° to 1200°C (***a***) and 1250° to 1450°C (***b***). Experimental points [504] and calculated lines.

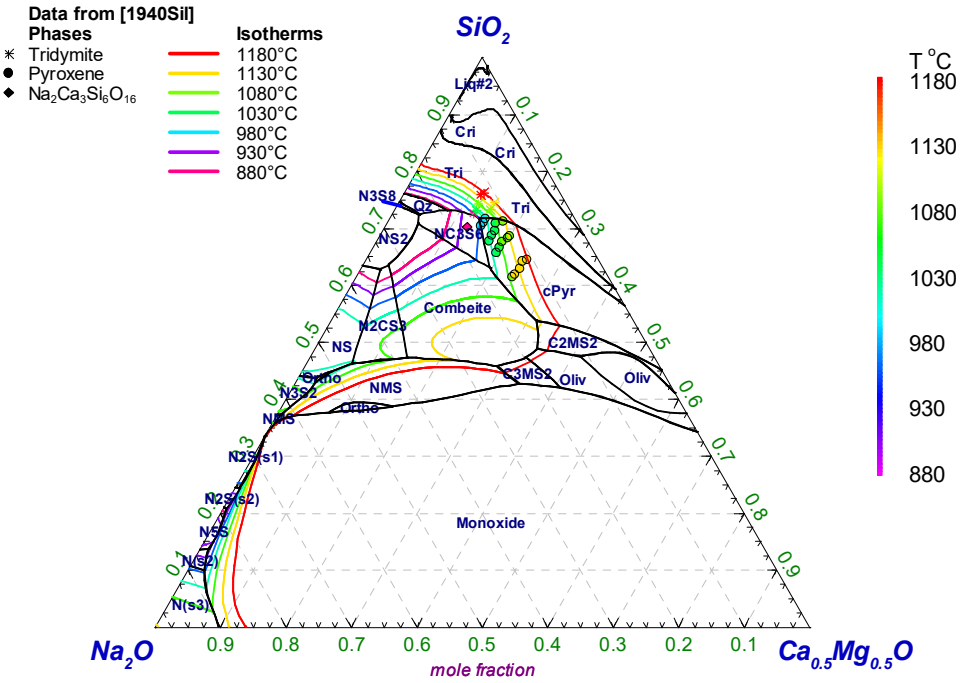

Figure 22.3 Liquidus projection in the SiO_2-Na_2O-$Ca_{0.5}Mg_{0.5}O$ plane of the CaO-MgO-Na_2O-SiO_2 system. Experimental points [505] and calculated lines.

The effect of substitution of CaO by MgO in various starting compositions in the $CaO-Na_2O-SiO_2$ system as well as of addition of MgO to base compositions is reported by several authors [506-511]. The base compositions (not substituted) in the $CaO-Na_2O-SiO_2$ system are plotted in Figure 22.4. The sections obtained through addition of MgO to base $CaO-Na_2O-SiO_2$ compositions are plotted in Figure 22.5, the CaO/MgO substitution sections are presented in Figure 22.6.

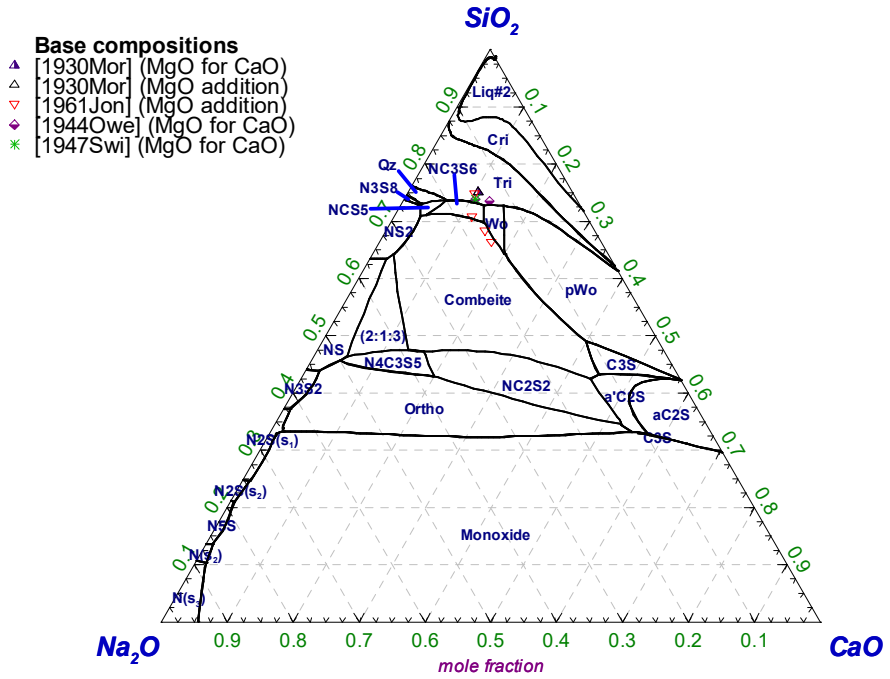

Figure 22.4 Base compositions of the sections studied in the $CaO-MgO-Na_2O-SiO_2$ system [506-511]. Sections have either CaO replaced by MgO or MgO was added to a base composition.

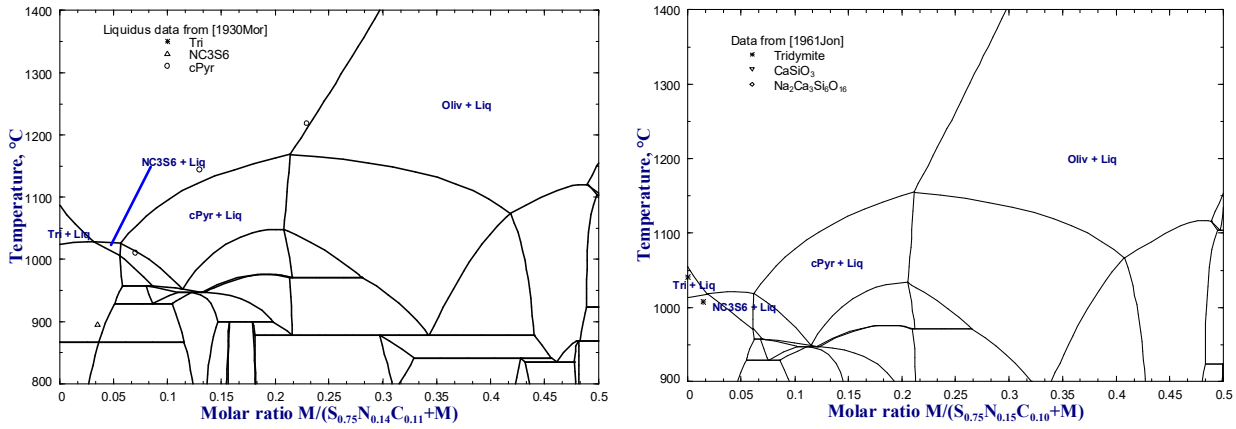

(*a*) (*b*)

Figure 22.5 Phase diagrams in sections obtained by a gradual addition of MgO to fixed Na_2O-CaO-SiO_2 compositions. Experimental points [508, 509] and calculated lines.

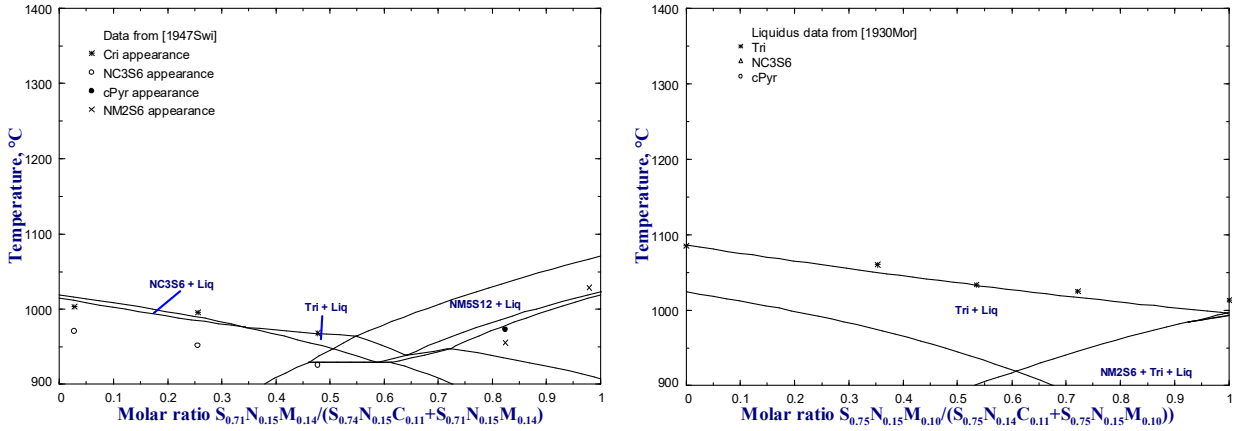

(*a*) (*b*)

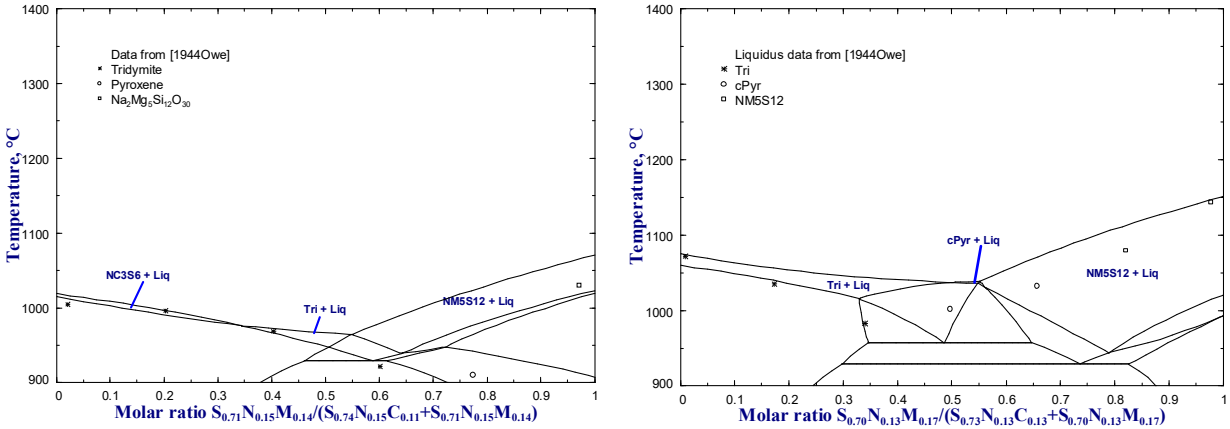

(*c*) (*d*)

Figure 22.6 Phase diagrams of sections obtained by a gradual replacement of CaO for MgO to fixed Na_2O-CaO-SiO_2 compositions. Experimental points [508, 510, 511] and calculated lines.

22.2 Activity data

Mathieu et al. [512] measured Na_2O solubility in Na_2O-free base compositions in the CaO-MgO-SiO_2 system in an atmosphere with a fixed Na(g) partial pressure. Large amounts of $Na_2O{\cdot}2SiO_2$ melt were used as a source of sodium and the partial pressure of oxygen was fixed by a Ni/NiO buffer. The operating temperatures were 1250° and 1400°C. The authors present their data in the form of isosolubility lines in the CaO-MgO-SiO_2 base composition triangle and to compare these data with calculated values, these were replotted in the form of isoactivities. Intersection points of Na_2O isosolubility lines and sections with a fixed CaO/MgO ratio are plotted in Figure 22.7-Figure 22.9.

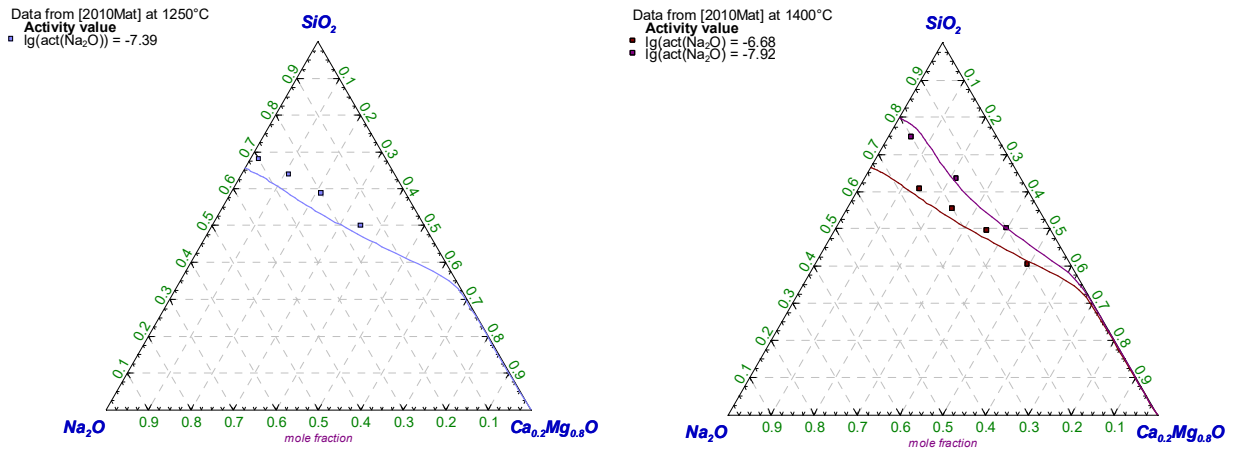

(***a***) (***b***)

Figure 22.7 Na_2O isoactivity plots in the SiO_2-Na_2O-$Ca_{0.2}Mg_{0.8}O$ section of the CaO-MgO-Na_2O-SiO_2 system at 1250°C (***a***) and 1400°C (***b***). Points recalculated from the published data [512] and calculated lines.

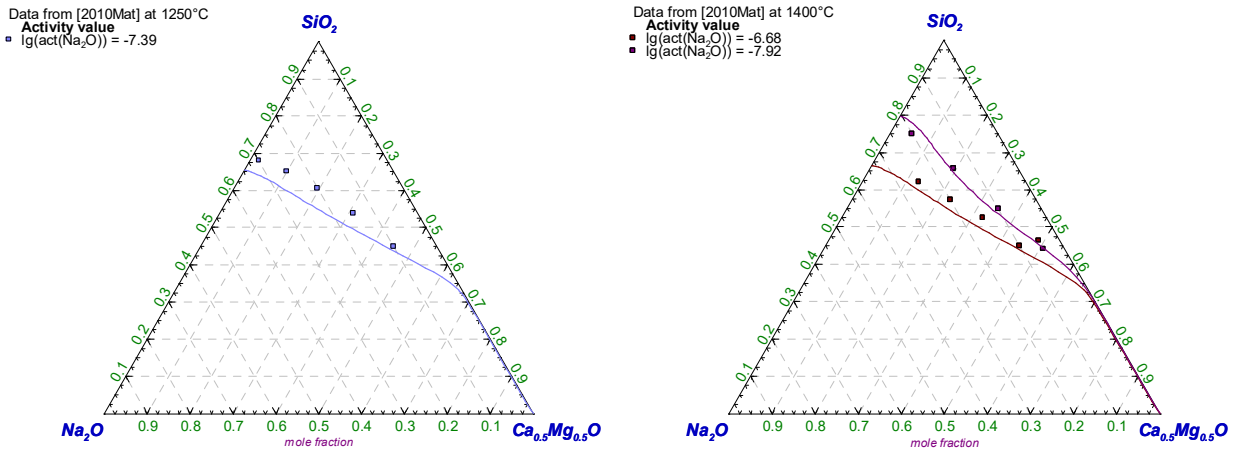

(***a***) (***b***)

Figure 22.8 Na_2O isoactivity plots in the SiO_2-Na_2O-$Ca_{0.5}Mg_{0.5}O$ section of the CaO-MgO-Na_2O-SiO_2 system at 1250°C (***a***) and 1400°C (***b***). Points recalculated from the published data [512] and calculated lines.

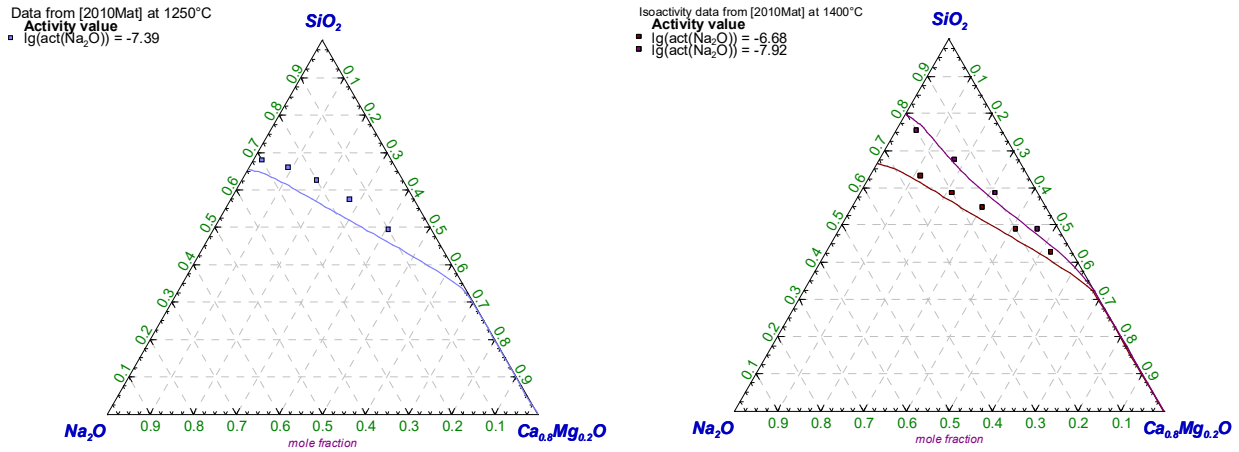

(***a***) (***b***)

Figure 22.9 Na_2O isoactivity plots in the SiO_2-Na_2O-$Ca_{0.8}Mg_{0.2}O$ section of the CaO-MgO-Na_2O-SiO_2 system at 1250°C (***a***) and 1400°C (***b***). The reference state is the pure liquid Na_2O. Points recalculated from the published data [512] and calculated lines.

Kim et al. [513] performed EMF measurements of a float glass composition $70.2SiO_2 \cdot 13.2Na_2O \cdot 10.0CaO \cdot 5.9MgO$ at different temperatures in a cell of the following type:

$$O_2(Pt)|Na_2O\text{-}WO_3(liq)||Na^+\text{-}\beta\text{-}Al_2O_3||melt|O_2(Pt) \quad (135)$$

Their data are plotted in Figure 22.10.

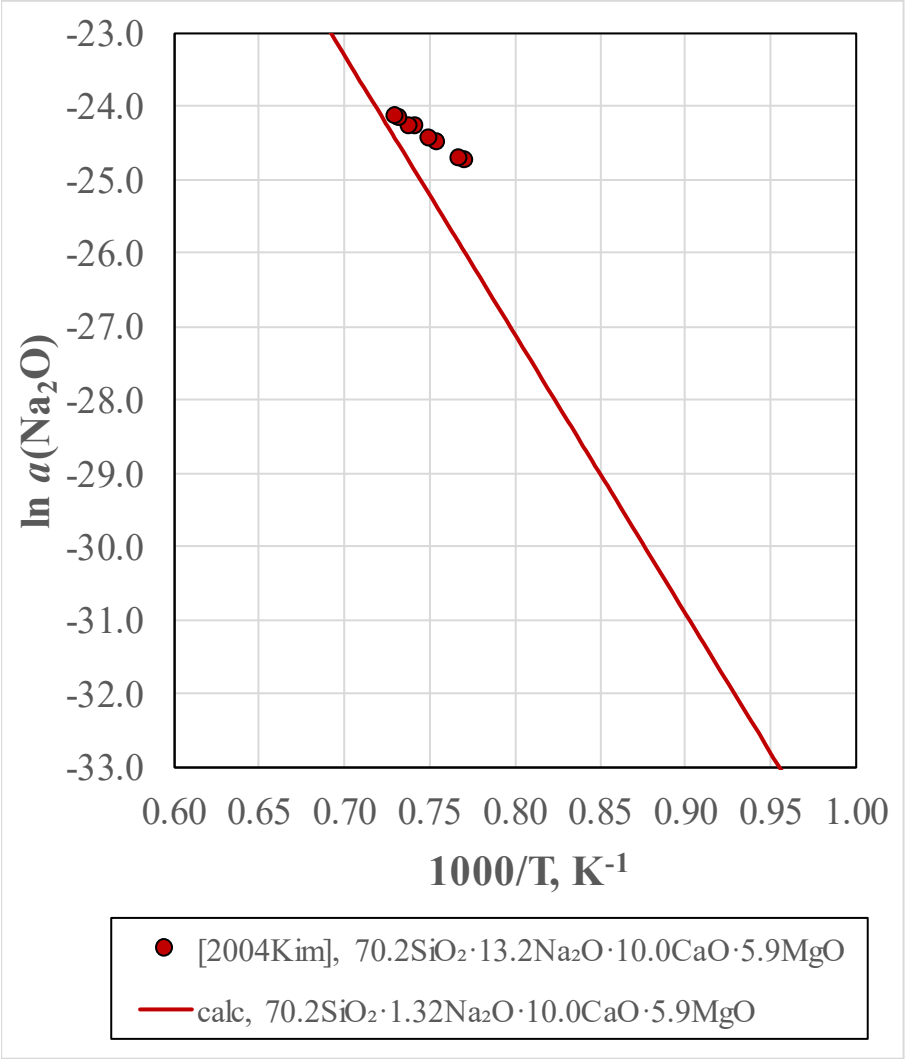

Figure 22.10 Activity of Na_2O as a function of the inverse temperature for a fixed composition in the CaO-MgO-Na_2O-SiO_2 system. The reference state is the pure liquid Na_2O. Experimental points [513] and the calculated line.

22.3 Optimization results

The phase diagrams in the CaO-MgO-Na_2O-SiO_2 were calculated based only on the optimizations of the binary and ternary subsystems; no additional parameters were used. However, some data in the quaternary system, for example, the slope of tridymite liquidus (see Figure 22.6, (***b***)) were used to adjust the parameters in the Na_2O-MgO-SiO_2 system as there are no data available on tridymite liquidus in the ternary system.

CHAPTER 23 OPTIMIZATION OF THE $MgO-Al_2O_3-Na_2O$ SYSTEM

23.1 Phase diagram

The studies of phase relations in the $Na_2O-MgO-Al_2O_3$ system are limited to the studies of MgO-stabilized β-aluminas. From the practical point of view, MgO-substituted β-aluminas are important as solid electrolytes. Addition of MgO and Li_2O makes them more resistant and durable [105]. There are no available data on the liquidus in the system because of experimental difficulties related to its measurement. The calculated liquidus projection is shown in Figure 23.2.

Alsen [258] presents isotherms at 1870 and 1950K of the Al_2O_3-rich corner of the phase diagram. MgO is dissolved in β”-alumina solid solution up to around 10 mol%. No other compounds or solid solutions were registered.

The phase diagram from a work by Weber and Venero [104] (Figure 23.1) features a few MgO-containing compounds with β-alumina structure. According to this phase diagram, β-alumina dissolves MgO, forming a solid solution, and there are three more separate phases: β’’-alumina (apparently not the same as in the $Na_2O-Al_2O_3$ system), β’’’- and β’’’’-aluminas. A later study by Van Hoek et al. [514] indicates that β’’’ and β’’’’ form a solid solution.

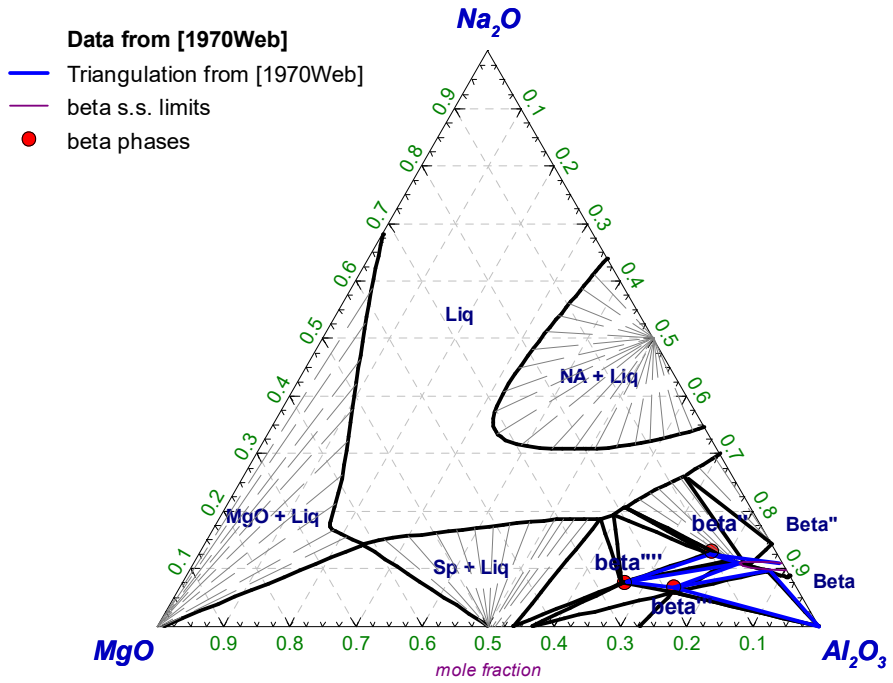

Figure 23.1 An isothermal section of the Na_2O-MgO-Al_2O_3 phase diagram at 1700°C. Experimental data [104] and calculated lines.

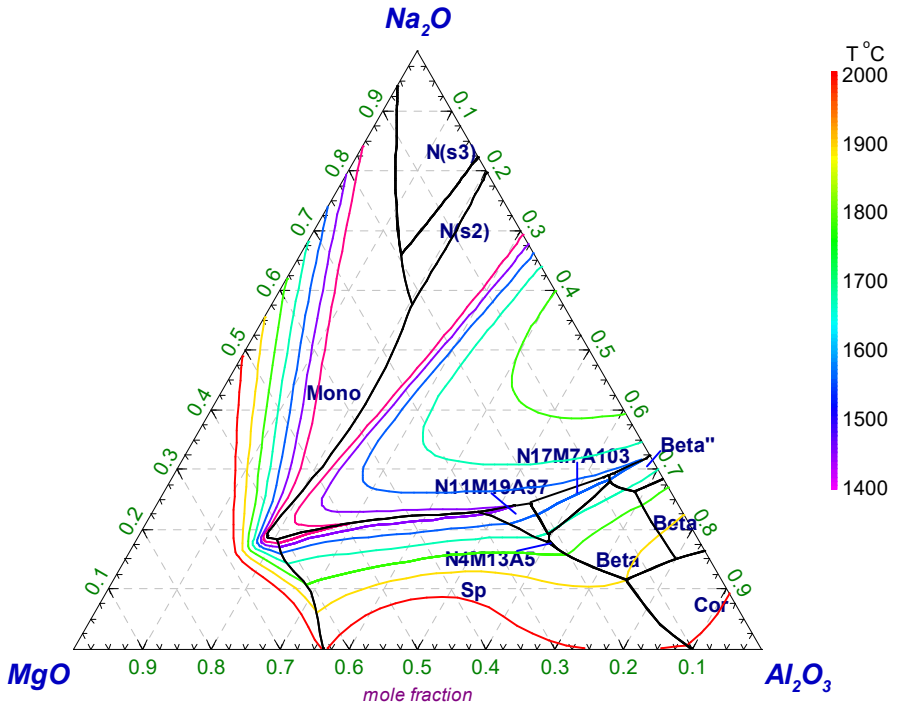

Figure 23.2 Liquidus projection in the MgO-Al_2O_3-Na_2O system.

23.2 Optimization results

The Na_2O-Al_2O_3 binary system was optimized in this work; the Na_2O-MgO system was assumed ideal. The optimization of the MgO-Al_2O_3 by Jung et al. [515] was adopted.

The liquid was assumed ideal. The end-members of Beta and Beta" solid solutions were evaluated according to the same schemes as for the K_2O-MgO-Al_2O_3 system and the corresponding model parameters have the same values (taken from the work of Kim [18]). The formulas of the ternary compounds β''-, β'''- and β''''-aluminas were evaluated based on their compositions in Figure 23.1: $Na_{17}Mg_7Al_{103}O_{170}$, $Na_8Mg_{13}Al_{102}O_{170}$, $Na_{11}Mg_{19}Al_{97}O_{170}$. Their heat capacities and the entropies were evaluated according to additive schemes from the corresponding functions of $NaAlO_2$, MgO and Al_2O_3. The enthalpies of the compounds were adjusted to be compatible with the experimental triangulation. The properties of the compounds are listed in Table A.26.

CHAPTER 24 OPTIMIZATION OF THE MgO-Na_2O-Al_2O_3-SiO_2 SYSTEM

Phase equilibrium data in the quaternary systems are mostly represented by geologically important regions.

24.1 The Forsterite-Nepheline-Silica subsystem (Mg_2SiO_4-$NaAlSiO_4$-SiO_2)

Parts of the central plane $NaAlO_2$-SiO_2-MgO are the most investigated in the quaternary system. However, as the system was studied because of its importance in geological applications, only subsystems with mineral end-members are covered in the literature. Nepheline-forsterite-silica system was studied as a part of the "simple basalt tetrahedron" nepheline-forsterite-silica-diopside [516]. Schairer and Yoder [516] present the liquidus of the $NaAlSiO_4$-Mg_2SiO_4-SiO_2 system (Figure 24.1); they give the experimental compositions with the primary phases and manually drawn isotherms without detailed information in each point. The liquidus is dominated by olivine and enstatite fields coming close to the Mg-free boundary. The system is not ternary at liquidus temperatures because of the spinel field extending from the $NaAlSiO_4$-Mg_2SiO_4 boundary. However, at lower temperatures spinel disappears and the system becomes ternary. The join albite-enstatite $NaAlSi_3O_8$-$MgSiO_3$ splits the phase diagram in a way that nepheline and enstatite are incompatible and should not coexist in mineral assemblages. There are several piercing and invariant points in the system: Sp-Cg-Ne at 1290±5°C, Sp-Ne-Oliv at 1155±5°C, Ne-Fds-Oliv at 1058±5°C, a binary eutectic Fds-Oliv at 1103±2°C, Fds-Oliv-pEn at 1095±5°C, Fds-Tri-pEn at 1045°C (Table 24.1). The subsystem albite-forsterite-silica ($NaAlSi_3O_8$-Mg_2SiO_4-SiO_2) was later studied in more detail by Schairer and Yoder [517] who published a preliminary phase diagram.

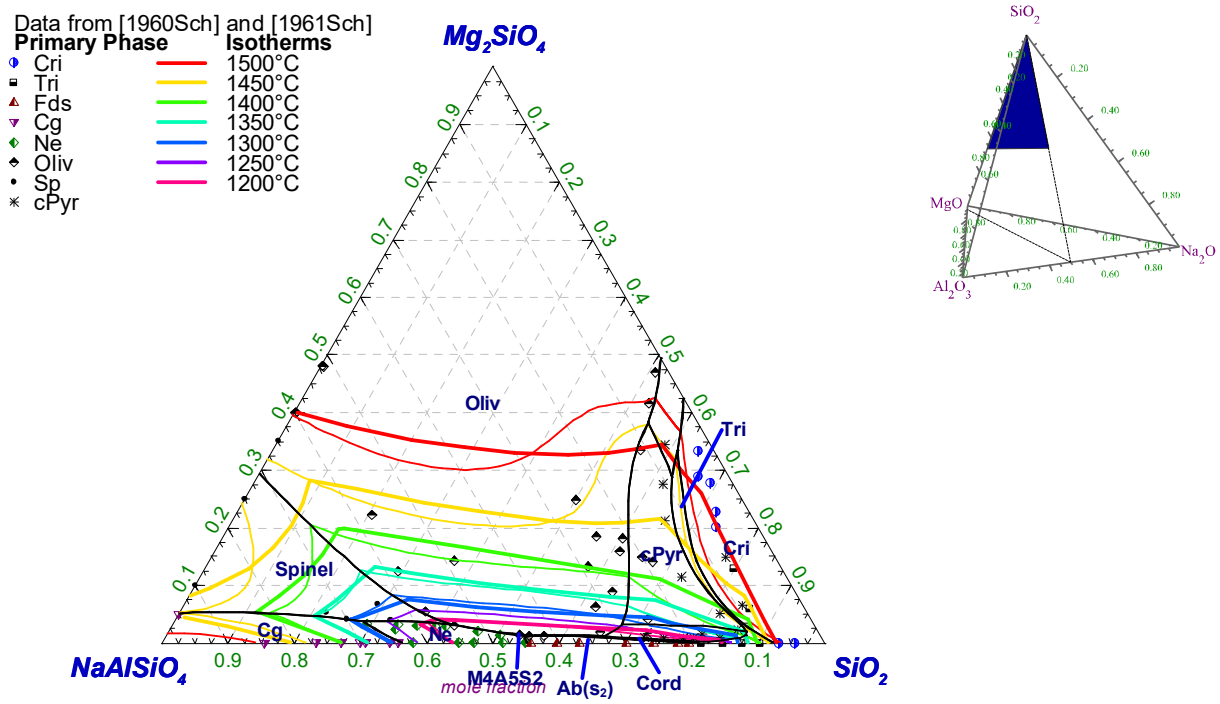

Figure 24.1 Liquidus projection in the Mg_2SiO_4-$NaAlSiO_4$-SiO_2 plane of the MgO-Na_2O-Al_2O_3-SiO_2 system. Experimental points and isotherms (thick lines) [516, 518] and calculated lines.

Schairer and Yoder [516] also give a phase diagram of the $NaAlSi_3O_8$-Mg_2SiO_4 (albite-forsterite) binary system (Figure 24.2). It is a simple eutectic system with the eutectic point lying close to albite. Later, Yoder [519] republishes the same diagram with a correction of the melting point of forsterite. According to Yoder [519], $MgSiO_3$ and $NaAlSi_2O_6$ form pyroxene solid solutions under high pressures.

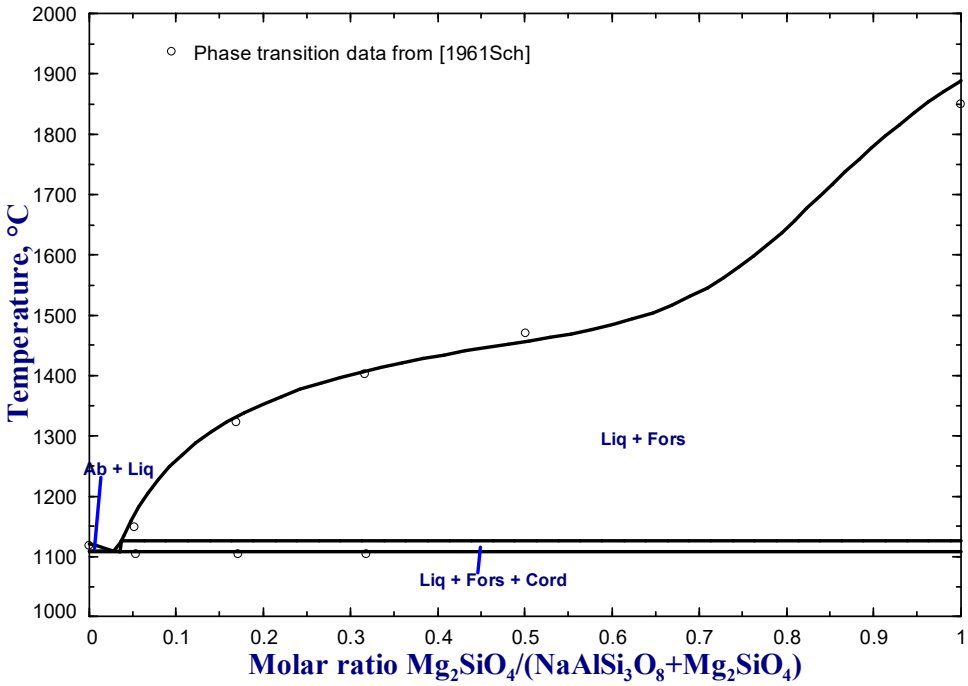

Figure 24.2 Phase diagram in the $NaAlSi_3O_8$-Mg_2SiO_4 section of the MgO-Na_2O-Al_2O_3-SiO_2 system. Experimental points [516] and calculated lines.

Mao and Schairer [520] performed quenching experiments in the $NaAlSi_2O_6$-Mg_2SiO_4 section (jadeite-forsterite, Figure 24.3). As jadeite is unstable under normal pressures, nepheline crystallizes as the primary phase at its composition. Also, nepheline appears as a second solid phase at 1098±5°C at mixed compositions.

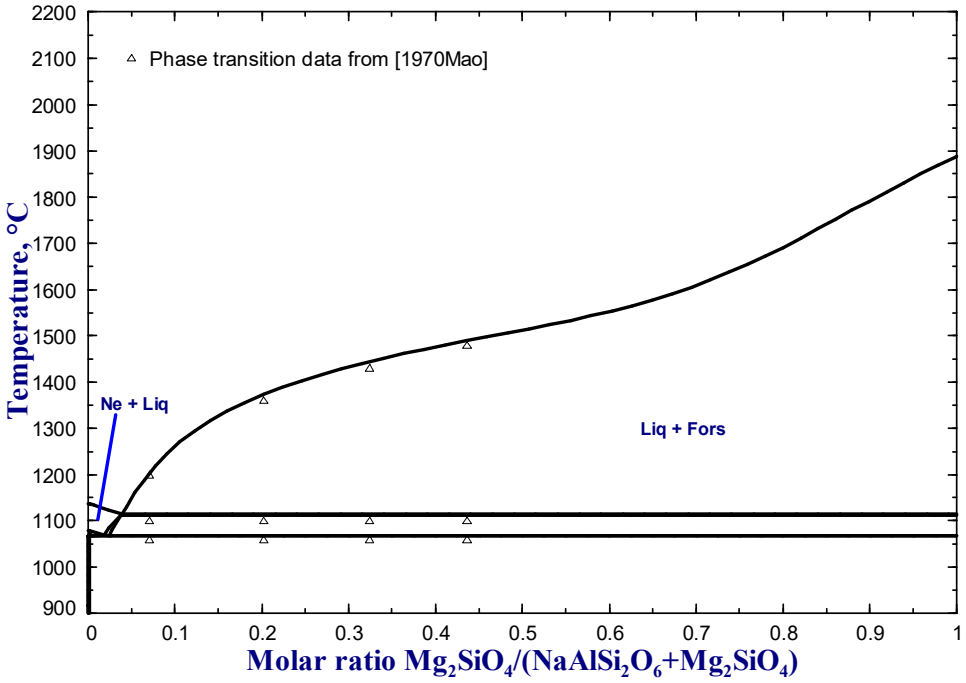

Figure 24.3 Phase diagram in the $NaAlSi_2O_6$-Mg_2SiO_4 section of the MgO-Na_2O-Al_2O_3-SiO_2 system. Experimental points [520] and calculated lines.

Table 24.1 Piercing/invariant points in the nepheline-forsterite-silica plane ($NaAlSiO_4$-Mg_2SiO_4-SiO_2) of the Na_2O-Al_2O_3-MgO-SiO_2 system. The calculated values are shown in bold.

Piercing/invariant point	**Temperature, °C**
Sp-Cg-Ne	1290±5 [516] **1280** (calc)
Sp-Ne-Oliv	1155±5 [516] **1176** (calc)
Ne-Fds-Oliv	1058±5 [516] **1074** (calc)
a binary eutectic Fds-Oliv	1103±2 [516] **1107** (calc)
Fds-Oliv-pEn	1095±5 [516] **1149** (calc)
Fds-Tri-pEn	1045 [516] **1145** (calc)

24.2 The Spinel-Nepheline-Silica subsystem ($MgAl_2O_4$-$NaAlSiO_4$-SiO_2)

The phase diagram of the $MgAl_2O_4$-$NaAlSiO_4$-SiO_2 system (spinel-nepheline-silica) was studied by Schairer and Yoder [521]. In their short publication, only the studied compositions and the primary fields are indicated without information on the liquidus temperature. This is a ternary system except for the compositions which form mullite as the primary phase. However, at lower temperatures, mullite is consumed by a reaction with liquid and the system becomes truly ternary.

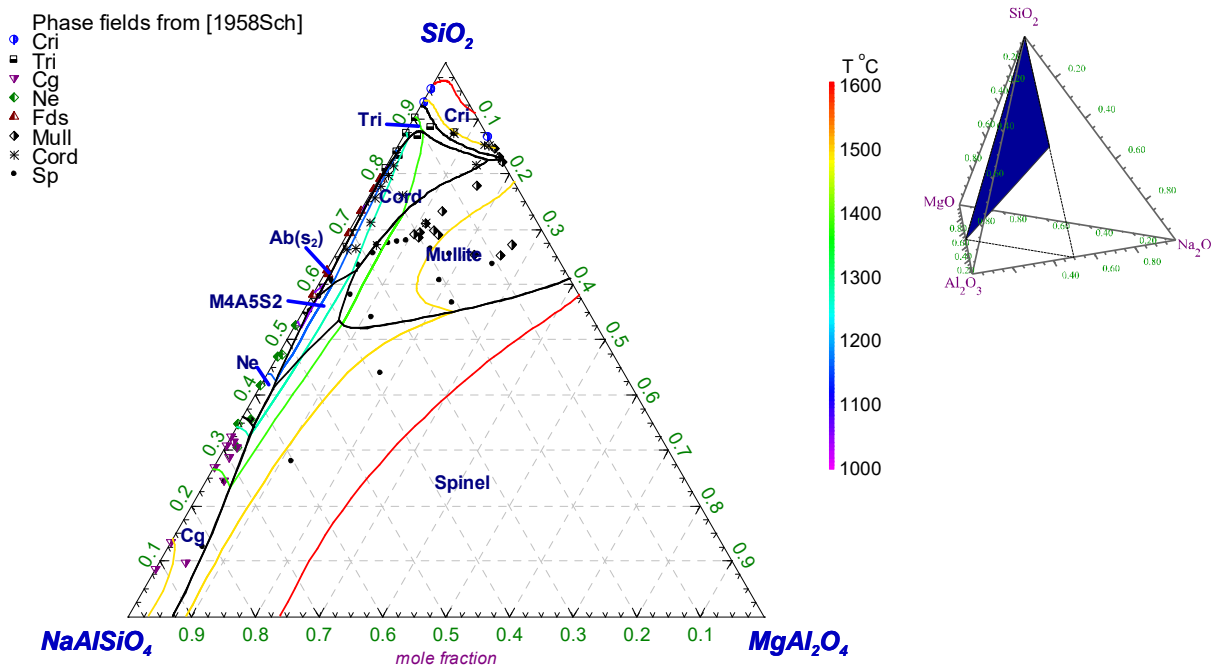

Figure 24.4 Liquidus projection in the SiO_2-$NaAlSiO_4$-$MgAl_2O_4$ plane of the MgO-Na_2O-Al_2O_3-SiO_2 system. Experimental points [521] and calculated lines.

The SiO_2-$MgAl_2O_4$ boundary belongs to the MgO-Al_2O_3-SiO_2 system optimized by Jung et al. [515]. The calculated boundary between Mullite and Spinel is shifted towards Spinel field if compared to the experimental data (Figure 5.1, (***d***)). We assume that the large Mullite field in Figure 24.4 would become smaller and reproduce the experimental points much better if Mullite/Spinel boundary were more accurate in the MgO-Al_2O_3-SiO_2 system.

There is a number of invariant and piercing points in the system (Table 24.2).

Table 24.2 Piercing/invariant points in the spinel-nepheline-silica plane ($MgAl_2O_4$-$NaAlSiO_4$-SiO_2) of the Na_2O-Al_2O_3-MgO-SiO_2 system. The calculated values are shown in bold.

Piercing/invariant point	Temperature, °C
Mull-Cord-Tri	1438±5 [521] **1443** (calc)
Sp-Mull-Cord	1345±5 [521] **1284** (calc, metastable)
Cord-Fds-Tri	1045±10 [521] **1134** (calc)
Sp-Fds-Cord	1095±5 [521] **1048** (calc, metastable)
Ne-Fds-Sp	1055±5 [521] **1073** (calc)
Cg-Ne-Sp	1280 [521] **1285** (calc)
Ne-Sp	~1490 [521] **1404** (calc)

24.3 The Forsterite-Albite-Cordierite subsystem (Mg_2SiO_4-$NaAlSi_3O_8$-$Mg_2Al_4Si_5O_{18}$)

Phase relations in the forsterite-albite-cordierite system (Mg_2SiO_4-$NaAlSi_3O_8$-$Mg_2Al_4Si_5O_{18}$) were studied by Schairer [522] because of the importance of the system in elucidating the process of magma crystallization. The source article presents the studied composition, the primary fields and manually drawn isotherms (Figure 24.8).

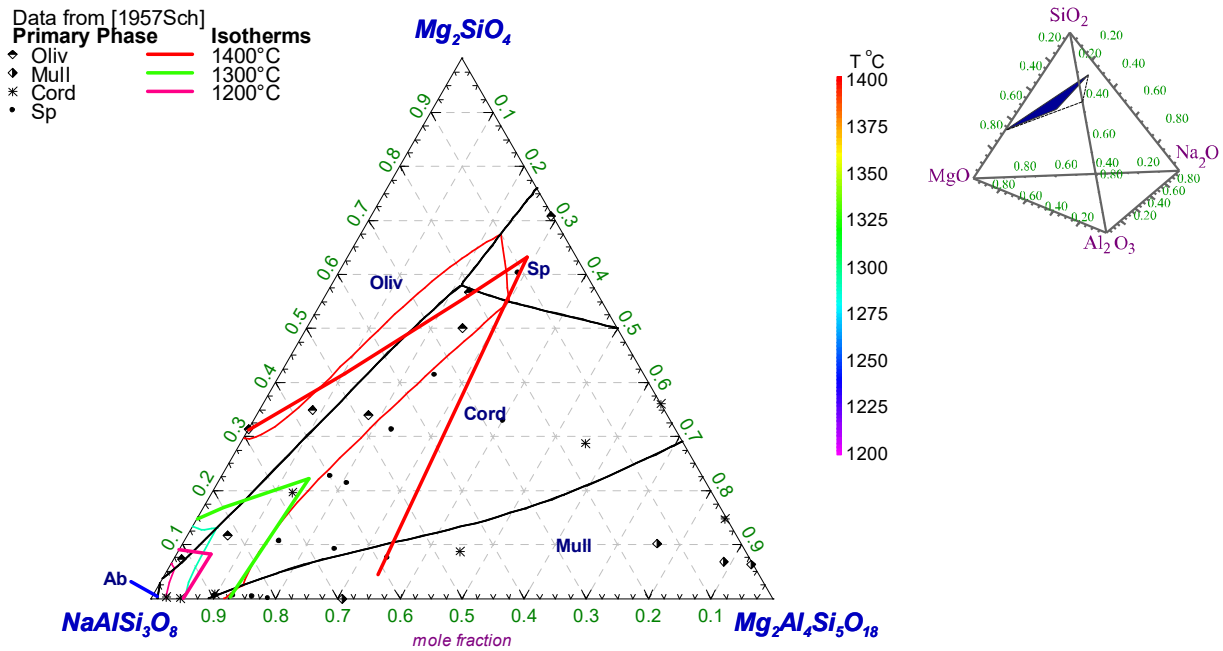

Figure 24.5 Liquidus projection in the Mg_2SiO_4-$NaAlSi_3O_8$-$Mg_2Al_4Si_5O_{18}$ plane of the MgO-Na_2O-Al_2O_3-SiO_2 system. Experimental points and isotherms (thick lines) [522] and calculated lines.

In the original phase diagram by Schairer and Yoder [522], there is a large spinel field and two small disconnected cordierite fields. However, the calculated liquidus projection (Figure 24.5) features a large cordierite field and a small Spinel field starting from the Mg_2SiO_4-$Mg_2Al_4Si_5O_{18}$ boundary system. We suppose that due to crystallization difficulties of the ternary magnesium alumosilicate $Mg_2Al_4Si_5O_{18}$, a fast-crystallizing metastable spinel was observed in the majority of the points in the cordierite primary field. In fact, if the diagram in Figure 24.5 is calculated with the ternary magnesium alumosilicates omitted from the calculation, the Spinel field goes down close to the $NaAlSi_3O_8$-$Mg_2Al_4Si_5O_{18}$ boundary.

There are two piercing points Sp-Cord-Mull at 1408±3°C, Oliv-Sp-Cord at 1297±3°C, a ternary eutectic Oliv-Cord-Fds at 1095±3°C and a binary eutectic Fds-Oliv at 1095±3°C (Table 24.3).

Table 24.3 Piercing/invariant points in the forsterite-albite-cordierite plane (Mg_2SiO_4-$NaAlSi_3O_8$-$Mg_2Al_4Si_5O_{18}$) of the Na_2O-Al_2O_3-MgO-SiO_2 system. The calculated values are shown in bold.

Piercing/invariant point	Temperature, °C
Sp-Cord-Mull	1408±3 [522] Not available (calc)
Oliv-Sp-Cord	1297±3 [522] **1371** (calc)
Oliv-Cord-Fds	1095±3 [522] **1128** (calc, metastable)
Fds-Oliv	1095±3 [522] **1107** (calc)

24.4 The Enstatite-Albite-Cordierite subsystem ($MgSiO_3$-$NaAlSi_3O_8$-$Mg_2Al_4Si_5O_{18}$)

Schairer [522] studied liquidus relations in the enstatite-albite-cordierite system ($MgSiO_3$-$NaAlSi_3O_8$-$Mg_2Al_4Si_5O_{18}$) because of the importance of the system in elucidating the process of magma crystallization. The source article presents the studied composition, the primary fields and manually drawn isotherms.

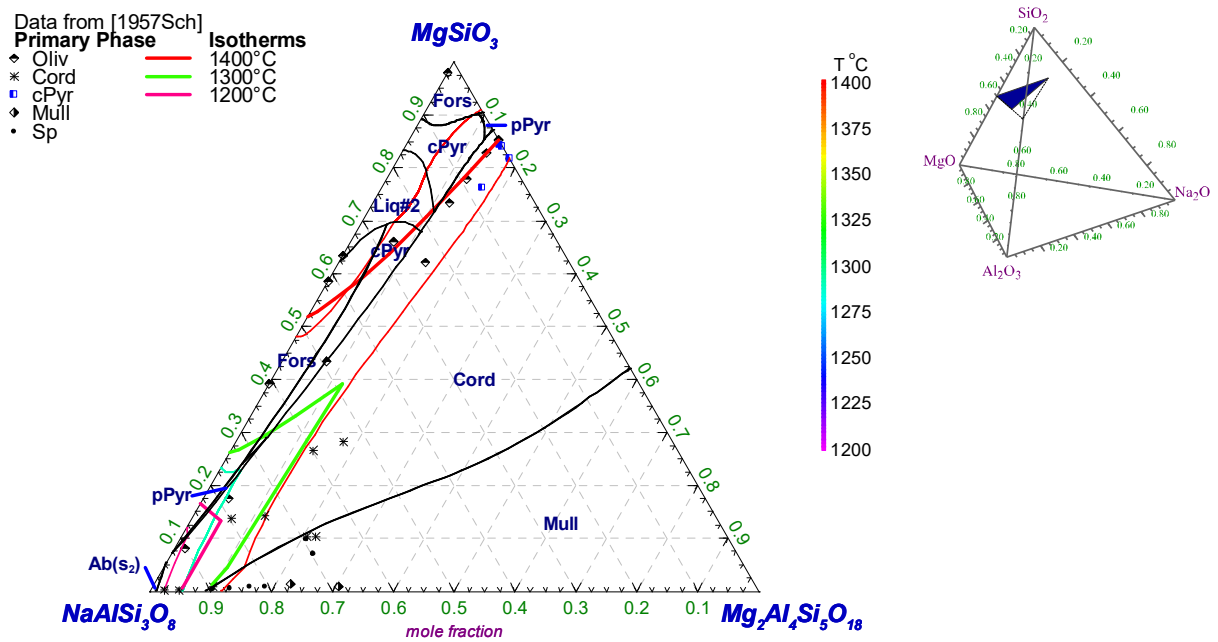

Figure 24.6 Liquidus projection in the $MgSiO_3$-$NaAlSi_3O_8$-$Mg_2Al_4Si_5O_{18}$ plane of the MgO-Na_2O-Al_2O_3-SiO_2 system. Experimental points and isotherms (thick lines) [522] and calculated lines.

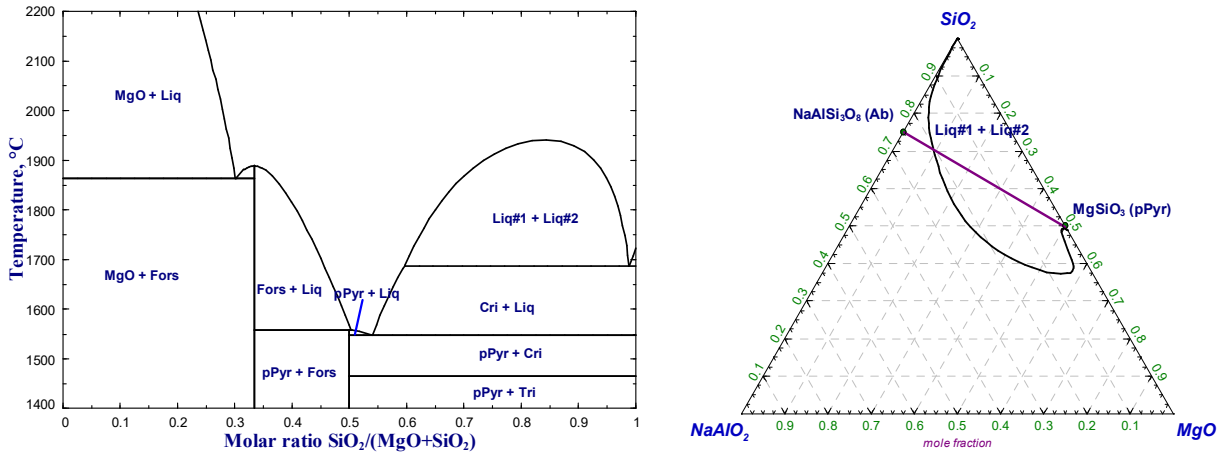

(***a***) (***b***)

Figure 24.7 Phase diagram of the MgO-SiO_2 system featuring the binary miscibility gap (***a***) and an isothermal section $NaAlO_2$-MgO-SiO_2 (only liquid phase) at 1200°C showing the propagation of the binary miscibility gap into the quaternary system (***b***).

The immiscibility gap in the liquidus projection in Figure 24.6 originates from the binary miscibility gap of the MgO-SiO_2 system as shown in Figure 27.7. The extension of the binary gap into the $NaAlO_2$-MgO-SiO_2 plane intersects the $NaAlSi_3O_8$-$MgSiO_3$ section. Probably, Schairer [522] did not report the gap because it is not detectable by quenching.

There are three piercing points in the system: pPyr-Oliv-Cord at 1343±5°C, Cord-Mull-Sp at 1378±5°C and Oliv-Cord-Fds at 1095±5°C (Table 24.4).

Table 24.4 Piercing/invariant points in the enstatite-albite-cordierite plane ($MgSiO_3$-$NaAlSi_3O_8$-$Mg_2Al_4Si_5O_{18}$) of the Na_2O-Al_2O_3-MgO-SiO_2 system. The calculated values are shown in bold.

Piercing/invariant point	**Temperature, °C**
pPyr-Oliv-Cord	1343±5 [522] **1324** (calc)
Cord-Mull-Sp	1378±5 [522] Not available (calc)
Oliv-Cord-Fds	1095±5 [522] **1116** (calc, metastable)

24.5 The Silica-Albite-Cordierite subsystem (SiO_2-$NaAlSi_3O_8$-$Mg_2Al_4Si_5O_{18}$)

Phase relations in the silica-albite-cordierite system (SiO_2-$NaAlSi_3O_8$-$Mg_2Al_4Si_5O_{18}$) were studied by Schairer [522] because of the importance of the system in elucidating the process of magma crystallization. The source article presents the studied composition, the primary fields and manually drawn isotherms (Figure 24.8).

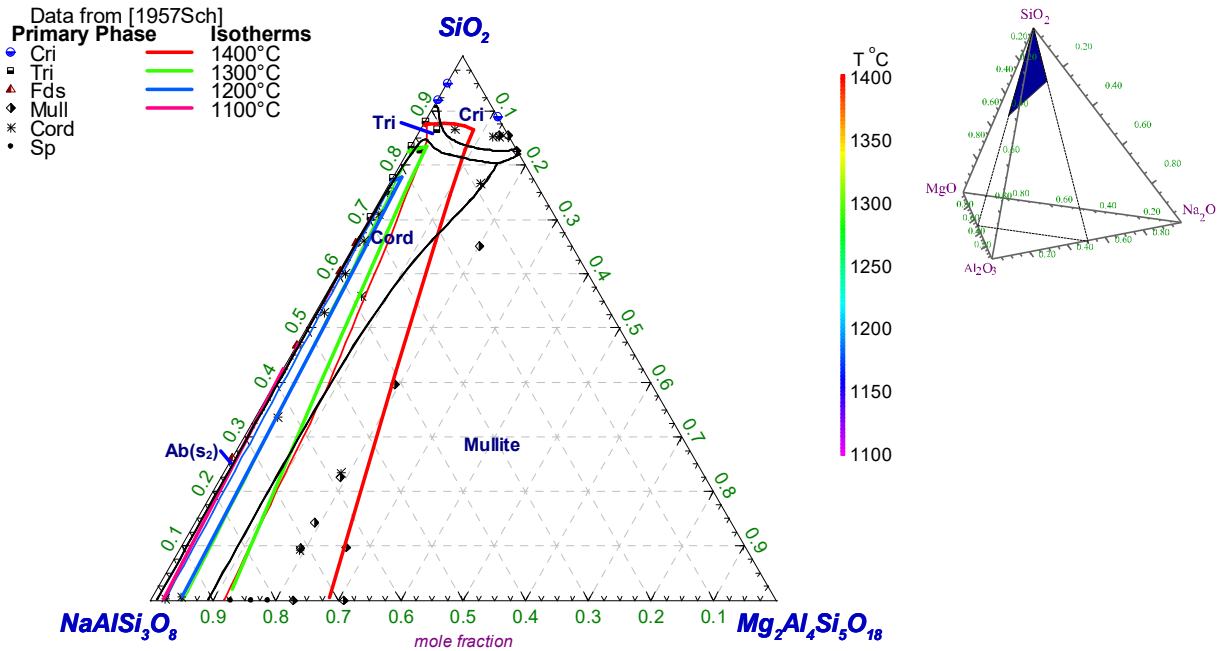

Figure 24.8 Liquidus projection in the SiO_2-$NaAlSi_3O_8$-$Mg_2Al_4Si_5O_{18}$ plane of the MgO-Na_2O-Al_2O_3-SiO_2 system. Experimental points and isotherms (thick lines) [522] and calculated lines.

There are two piercing points Mull-Cord-Tri at 1460±5°C, Mull-Cord-Sp at 1345±5°C and a ternary eutectic Fds-Cord-Tri at 1045±5°C. There is also a binary eutectic Fds-Cord at 1098±5°C (Table 24.5).

Table 24.5 Piercing/invariant points in the silica-albite-cordierite plane (SiO_2-$NaAlSi_3O_8$-$Mg_2Al_4Si_5O_{18}$) of the Na_2O-Al_2O_3-MgO-SiO_2 system. The calculated values are shown in bold.

Piercing/invariant point	Temperature, °C
Mull-Cord-Tri	1460±5 [522] **1444** (calc)
Mull-Cord-Sp	1345±5 [522] Not available (calc)
Fds-Cord-Tri	1045±5 [522] **1096** (calc)
Fds-Cord	1098±5 [522] **1113** (calc)

24.6 Other sections

Mathieu [436] measured Na_2O solubility in Na_2O-free base compositions in the Al_2O_3-MgO-SiO_2 system in an atmosphere with a fixed Na(g) partial pressure. Large amounts of $Na_2O{\cdot}2SiO_2$ melt were used as a source of sodium and the partial pressure of oxygen was fixed by a Ni/NiO buffer. The operating temperatures were 1250° and 1400°C. The author presents the data in the form of isosolubility lines in the Al_2O_3-MgO-SiO_2 base composition triangle and to compare these data with calculated values, there were replotted in the form of isoactivities. Intersection points of Na_2O isosolubility lines and sections with a fixed Al_2O_3/MgO ratio are plotted in Figure 24.9.

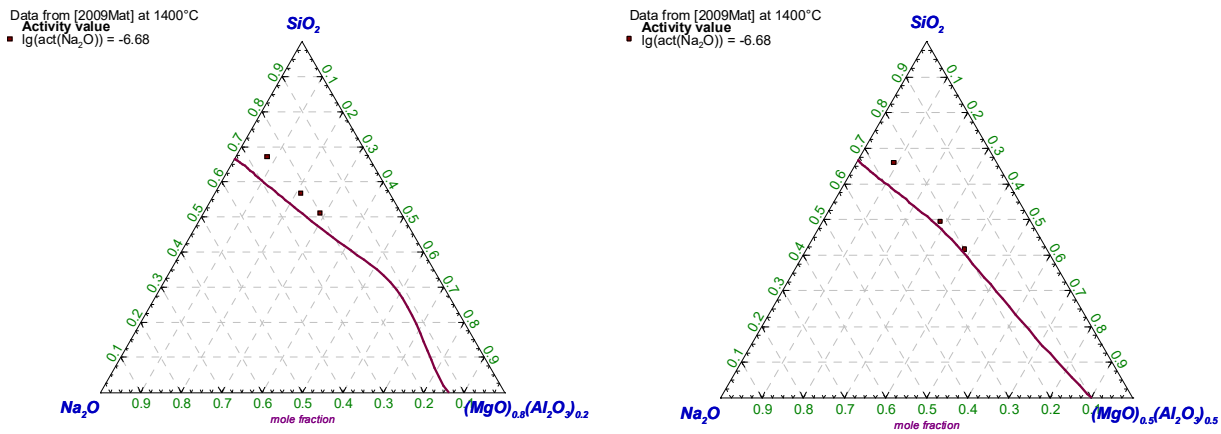

(***a***) (***b***)

Figure 24.9 Isoactivity plots in the SiO_2-Na_2O-$(MgO)_{0.8}(Al_2O_3)_{0.2}$ (***a***) and SiO_2-Na_2O-$(MgO)_{0.5}(Al_2O_3)_{0.5}$ (***b***) sections of the Al_2O_3-MgO-Na_2O-SiO_2 system at 1400°C. The reference state is the pure liquid Na_2O. Points recalculated from the published data [436] and calculated lines.

24.7 Optimization results

The existence of $NaAlO_2$ associate species in the model of the liquid means that in the quaternary Na_2O-Al_2O_3-MgO-SiO_2 there might be ternary parameters of interaction among SiO_2, MgO and $NaAlO_2$ which do not affect the equilibria in the subsystems. In fact, there are no other binary and ternary combinations of species which would influence the quaternary system without affecting the subsystems. The interactions between SiO_2, MgO and $NaAlO_2$ would be most noticeable in the

central plane of the system, $NaAlO_2$-SiO_2-MgO. A few parameters were introduced to raise the liquidus in the $NaAlSi_2O_6$-Mg_2SiO_4 and $NaAlSi_3O_8$-Mg_2SiO_4 sections which belong to the $NaAlO_2$-SiO_2-MgO plane. The optimized parameters are summarized in Table A.30.

CHAPTER 25 OPTIMIZATION OF THE $MgO-CaO-Na_2O-Al_2O_3-SiO_2$ SYSTEM

Phase equilibria in the $MgO-CaO-Na_2O-Al_2O_3-SiO_2$ system are very complex and have a high significance for geological applications. However, in many cases, these equilibria can be viewed as a sum of equilibria in simpler subsystems.

25.1 The Albite-Anorthite-Diopside subsystem ($NaAlSi_3O_8$-$CaAl_2Si_2O_8$-$CaMgSi_2O_6$)

The albite-diopside boundary was studied along with the albite-anorthite-diopside system ($NaAlSi_3O_8$-$CaAl_2Si_2O_8$-$CaMgSi_2O_6$) by Bowen [523] (Figure 25.1). The experimental data show the appearance temperatures of feldspar and clinopyroxene. It was unclear why the experimental feldspar liquidus has a maximum; Mg solubility in feldspar is negligible. It is hard to detect traces of glass in samples, therefore, there is a large uncertainty in the data on the beginning of melting.

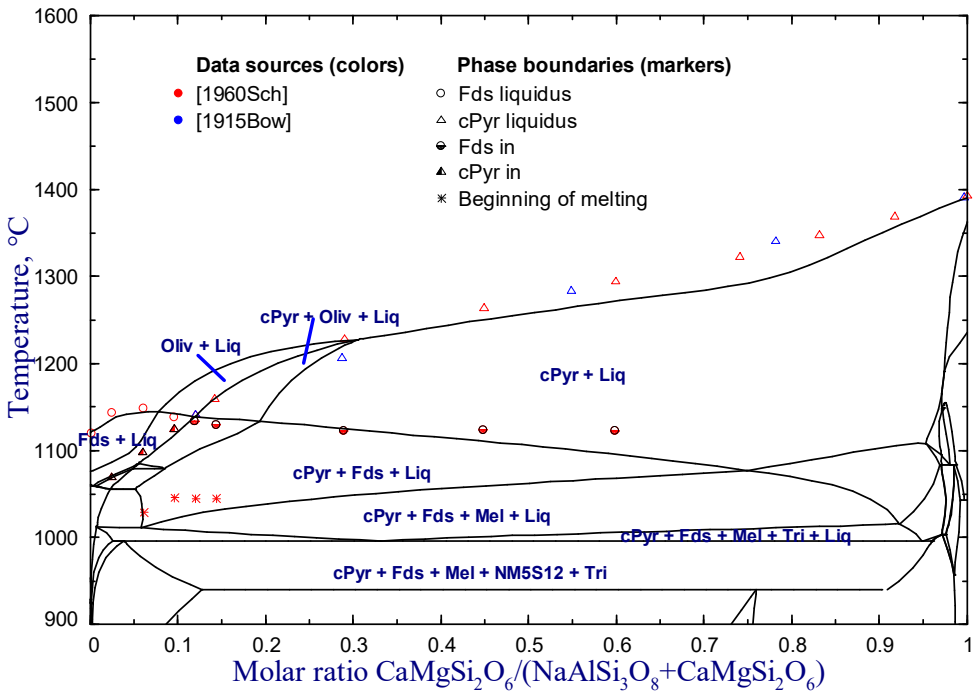

Figure 25.1 Phase diagram in the $CaMgSi_2O_6$-$NaAlSi_3O_8$ section of the $CaO-MgO-Al_2O_3-Na_2O-SiO_2$ system. Experimental points [523, 524] and calculated lines.

Murphy [525] studied the albite-anorthite-diopside system ($NaAlSi_3O_8$-$CaAl_2Si_2O_8$-$CaMgSi_2O_6$, Figure 25.2). It is a simple system with two primary crystallization fields of clinopyroxene and feldspar. Some Na_2O losses were observed during glass crystallization (up to 3.5% of sodium content in the course of four days). Feldspar solid solution contains up to 1 mol% of Mg in the form of $CaMgSi_3O_8$ end-member. Pyroxenes in this system mainly consist of diopside $CaMgSi_2O_6$ (87-93%), enstatite $Mg_2Si_2O_6$ (3-6%), Ca-tschermakite $CaAl_2SiO_6$ (0.5-9%) and contain only 0-2% of jadeite $NaAlSi_2O_6$. Their results about pyroxene compositions are confirmed by Kushiro and Schairer [526]. An insignificant jadeite solubility in pyroxene under normal pressures was confirmed by Schumoff-Deleano [527] during attempts to prepare mixed crystals of diopside and jadeite; the optical properties of the obtained crystals remained the same as for the pure diopside. The compositions of the coexisting phases (feldspar-pyroxene-liquid) were studied by Kushiro [528].

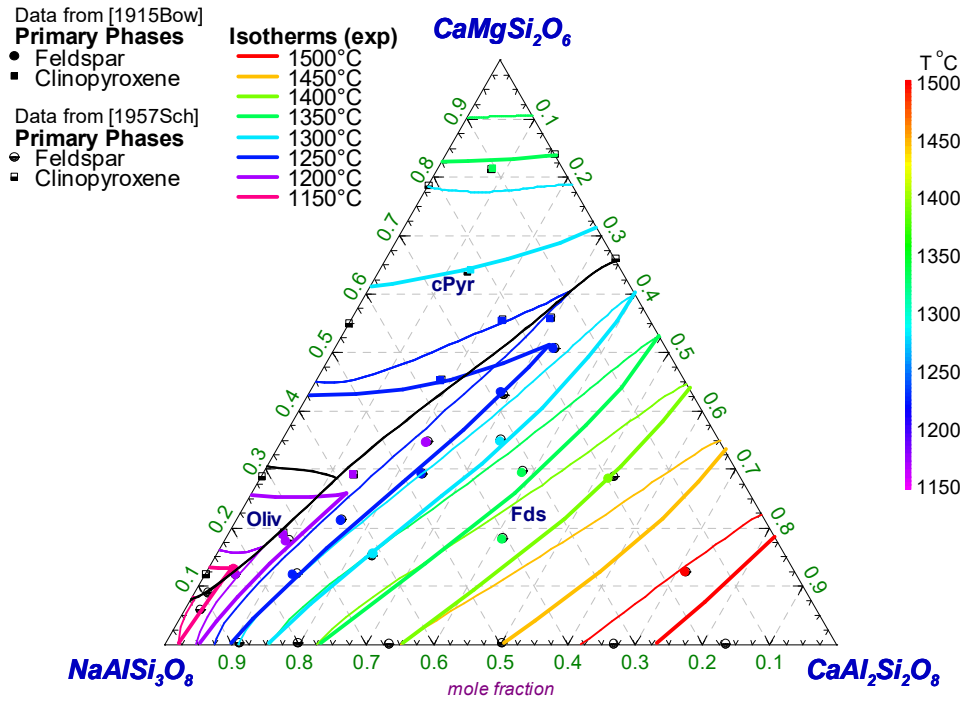

Figure 25.2 Liquidus projection in the $CaMgSi_2O_6$-$NaAlSi_3O_8$-$CaAl_2Si_2O_8$ plane of the CaO-MgO-Na_2O-Al_2O_3-SiO_2 system. Experimental points and isotherms (thick lines) [523, 529] and calculated lines.

The enthalpy of solution of $NaAlSi_3O_8$- $CaMgSi_2O_6$ glasses were measured by Navrotsky et al. [315]. The data by Weill et al. [530] appear to be the same as from Navrotsky et al. [315]. The data were recalculated into the enthalpy of mixing; as the operating temperature is above the glass transition temperature, no correction for glass transition was required (Section 2.5.2). The data are presented in Figure 25.3.

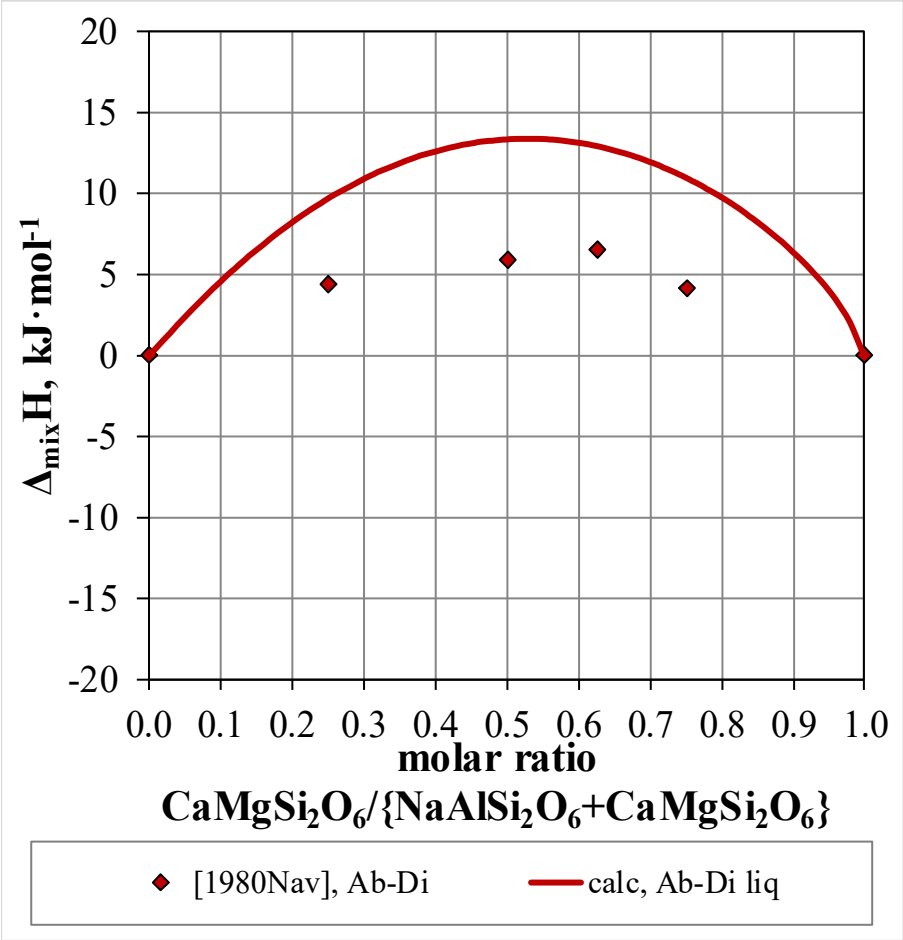

Figure 25.3 The enthalpy of mixing of liquid in the $NaAlSi_3O_8$-$CaMgSi_2O_6$ section of the CaO-MgO-Al_2O_3-Na_2O-SiO_2 system recalculated from glass calorimetry data. Experimental points [315] and calculated lines.

25.2 The Albite-Anorthite-Forsterite subsystem ($NaAlSi_3O_8$-$CaAl_2Si_2O_8$-Mg_2SiO_4)

The albite-anorthite-forsterite system ($NaAlSi_3O_8$-$CaAl_2Si_2O_8$-Mg_2SiO_4) was studied by Schairer and Yoder [531] (Figure 25.4). It is not a ternary system as spinel appears at liquidus starting from the Mg_2SiO_4-$CaAlSi_2O_8$ boundary. However, in this boundary, the spinel phase disappears below 1318±3°C. There is a piercing point between olivine, feldspar and spinel at 1290°C (Table 25.1). Isotherms at 1280° and 1300°C showing the compositions of coexisting liquids and feldspars are given as well (Figure 25.5).

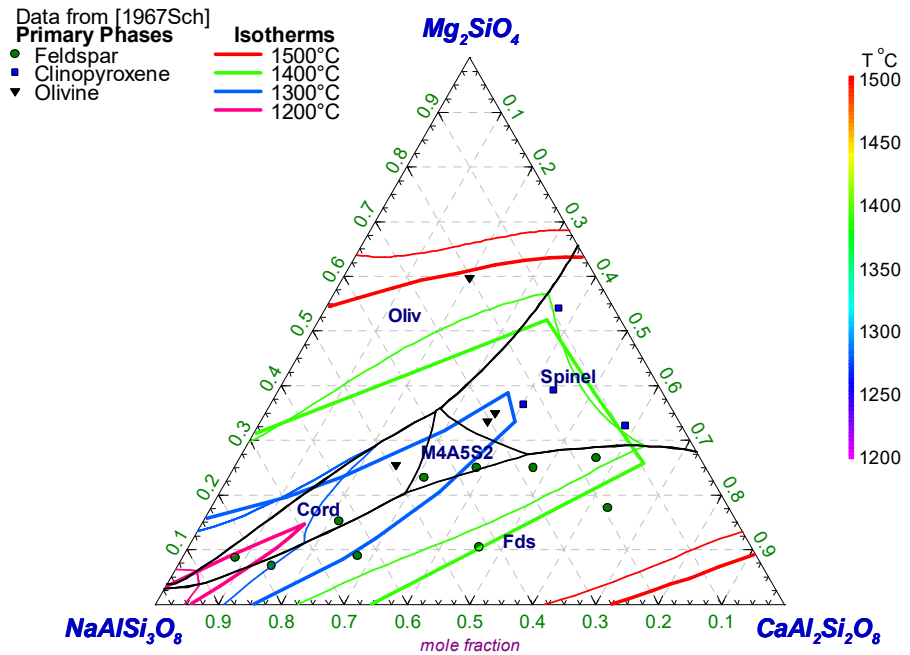

Figure 25.4 Liquidus projection in the Mg_2SiO_4-$NaAlSi_3O_8$-$CaAl_2Si_2O_8$ plane of the CaO-MgO-Na_2O-Al_2O_3-SiO_2 system. Experimental points and isotherms (thick lines) [531] and calculated lines.

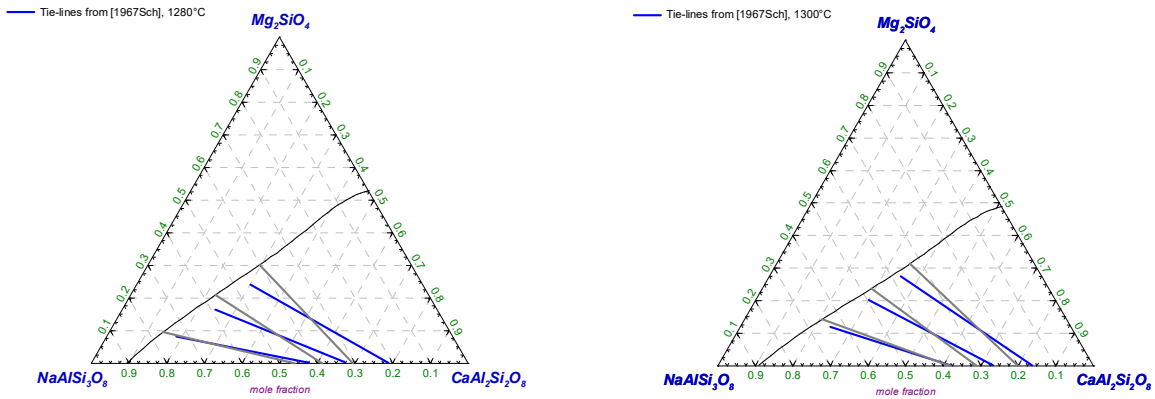

(***a***) (***b***)

Figure 25.5 Isotherms of the Mg_2SiO_4-$NaAlSi_3O_8$-$CaAl_2Si_2O_8$ plane of the CaO-MgO-Na_2O-Al_2O_3-SiO_2 system at 1280°C (***a***) and 1300°C (***b***). Experimental [531] and calculated tie-lines.

Table 25.1 Piercing points in the Mg_2SiO_4-$NaAlSi_3O_8$-$CaAl_2Si_2O_8$ plane (forsterite-albite-anorthite) of the CaO-MgO-Na_2O-Al_2O_3-SiO_2 system. The calculated values are shown in bold.

Piercing point	Temperature, °C
Oliv-Fds-Sp	1290 [531] **1259** (calc)

25.3 The Albite-Anorthite-Akermanite subsystem ($NaAlSi_3O_8$-$CaAl_2Si_2O_8$-$Ca_2MgSi_2O_7$)

The albite-anorthite-akermanite system ($NaAlSi_3O_8$-$CaAl_2Si_2O_8$-$Ca_2MgSi_2O_7$) was studied by Schairer and Yoder [532, 533] (Figure 25.6). The pyroxene primary field appears propagating from the $NaAlSi_3O_8$-$Ca_2Mg_2Si_2O_7$ boundary. The piercing point cPyr-Fds-Mel is at 1228±3°C (Table 25.2). Pyroxene compositions in the system are somewhat aluminous, indicating the presence of a solid solution. Crystals of nepheline and wollastonite solid solutions were noticed under the liquidus surface. Compositions of the solid solutions could not be determined because of their complex nature.

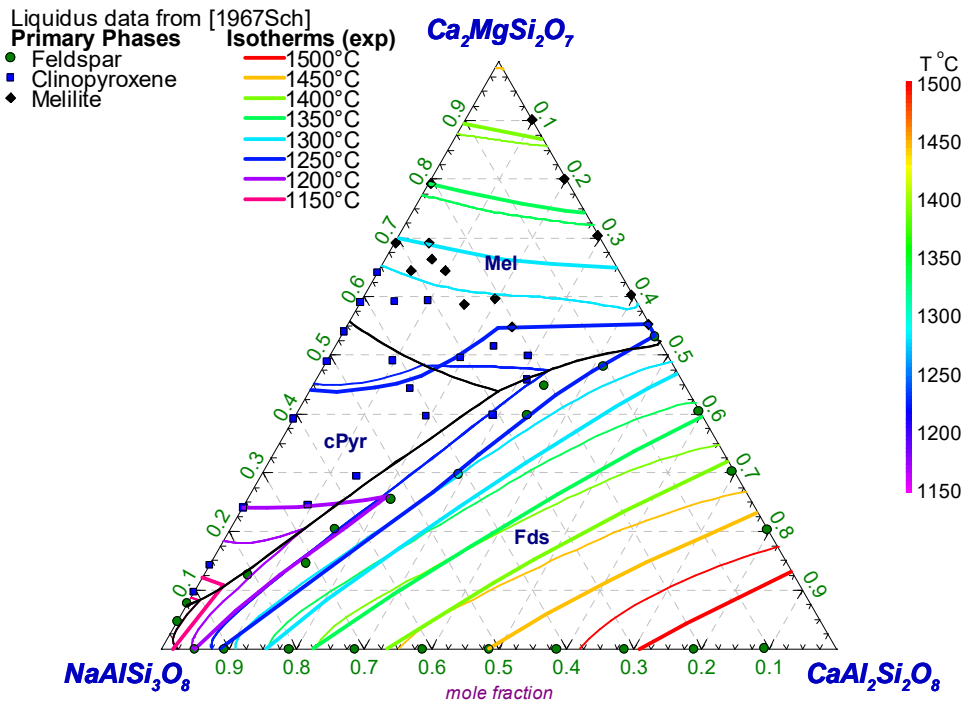

Figure 25.6 Liquidus projection in the $Ca_2MgSi_2O_7$-$NaAlSi_3O_8$-$CaAl_2Si_2O_8$ plane of the CaO-MgO-Na_2O-Al_2O_3-SiO_2 system. Experimental points and isotherms (thick lines) [532] and calculated lines.

Table 25.2 Piercing points in the $Ca_2MgSi_2O_7$-$NaAlSi_3O_8$-$CaAl_2Si_2O_8$ plane (akermanite-albite-anorthite) of the CaO-MgO-Na_2O-Al_2O_3-SiO_2 system. The calculated values are shown in bold.

Piercing point	Temperature, °C
cPyr-Fds-Mel	1228 [532, 533] **1234** (calc)

25.4 The Akermanite-Nepheline-Wollastonite subsystem ($Ca_2MgSi_2O_7$-$NaAlSiO_4$-$CaSiO_3$)

Schairer and Yoder [534] studied the akermanite-Na-Mel phase diagram ($Ca_2MgSi_2O_7$-$NaCaAlSi_2O_7$) under atmospheric pressure and at 20 kb (Figure 25.7). Pure $NaCaAlSi_2O_7$ end-member is not stable under normal pressures and decomposes into a mixture of $CaSiO_3$ and $NaAlSiO_4$. Only the solid solution between akermanite and Na-melilite exists under atmospheric pressure (up to 62 mol% $NaCaAlSi_2O_7$). However, if the pressure is increased, it becomes stable. Starting from about 4 kb, a complete solid solution exists between the end-members. Also, a scatter

plot of naturally occurring melilites in the composition plane $Ca_2MgSi_2O_7$-$NaCaAlSi_2O_7$-$Ca_2Al_2SiO_7$ is given [482].

Liquidus temperatures of the mixed crystal series $Ca_2MgSi_2O_7$-$NaCaAlSi_2O_7$ were studied with a heating stage microscope by Christie [535]. There is a common agreement in the literature that the pure akermanite becomes unstable at lower temperatures although there are disagreements about which phases it decomposes to, probably because the experiments were run under hydrothermal conditions [536-539]. According to the work by Schairer et al. [71], akermanite partially decomposes at temperatures below 1385°C forming pseudowollastonite/wollastonite and later diopside at 1240±10°C. No other phases were found in noticeable amounts. It was confirmed by Schairer et al. [71] that Na-melilite crystals decompose into a mixture of $NaAlSiO_4$ and $CaSiO_3$ under 1 atm pressure. The maximum soda melilite content in the $Ca_2MgSi_2O_7$-$NaCaAlSi_2O_7$ join is about 50%.

The akermanite-nepheline-wollastonite system ($Ca_2MgSi_2O_7$-$NaAlSiO_4$-$CaSiO_3$) was studied by Schairer and Yoder [540] (Figure 25.9) as well as the $Ca_2MgSi_2O_7$-$NaCaAlSi_2O_7$ section within it. Detailed information on phase appearances is given. The primary phases are nepheline/carnegieite, melilite and pseudowollastonite; there is one piercing point Ne-Mel-pWo at 1171±3°C (Table 25.3). The boundary system $Ca_2MgSi_2O_7$-$NaAlSiO_4$ was investigated by Onuma and Yagi [541] (Figure 25.8).

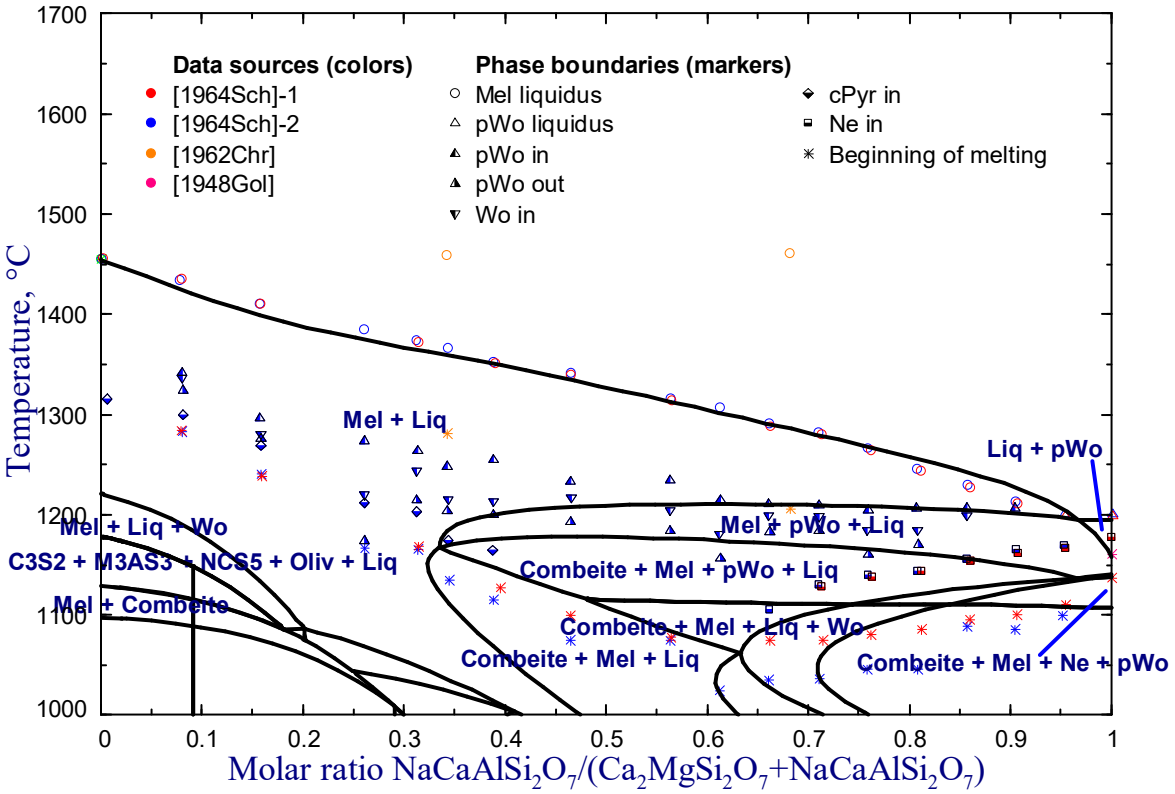

Figure 25.7 Phase diagram in the $Ca_2MgSi_2O_7$-$NaCaAlSi_2O_7$ section of the CaO-MgO-Al_2O_3-Na_2O-SiO_2 system. Experimental points [459, 461, 534, 535, 542] and calculated lines.

According to Schairer et al. [71], the partial decomposition of pure $Ca_2MgSi_2O_7$ (the CaO-MgO-SiO_2 system) with formation of pseudowollastonite/wollastonite happens at a temperature much higher than the calculated one. Moreover, the inversion temperature pWo/Wo changes with the composition in Figure 25.7. The authors explain it by the formation of a solid solution of magnesium in wollastonite. The discrepancy between the experimental data and the calculated transitions arises because of the properties of compounds and solid solutions in the CaO-MgO-SiO_2 system. Any modifications leading to the correction go beyond the scope of the current work which is limited to the optimization of the alkali-containing systems.

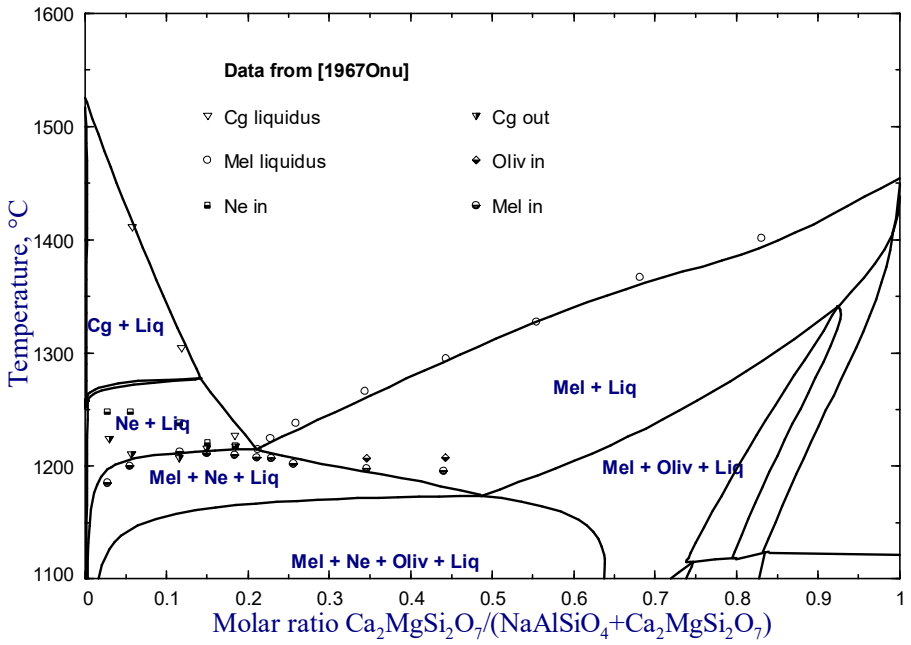

Figure 25.8 Phase diagram in the $Ca_2MgSi_2O_7$-$NaAlSiO_4$ section of the CaO-MgO-Al_2O_3-Na_2O-SiO_2 system. Experimental points [541] and calculated lines.

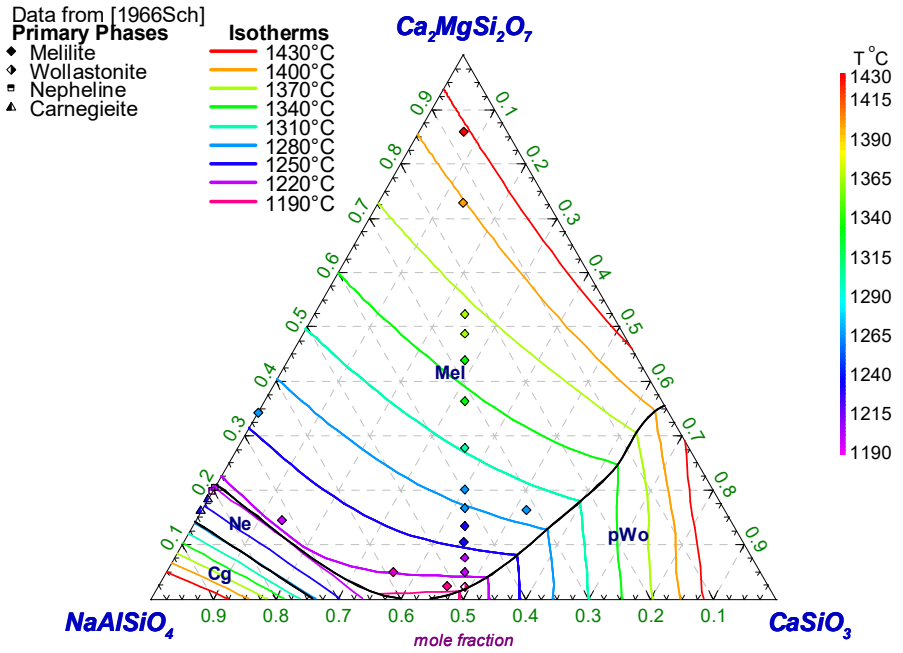

Figure 25.9 Liquidus projection in the $Ca_2MgSi_2O_7$-$NaAlSiO_4$-$CaSiO_3$ plane of the CaO-MgO-Na_2O-Al_2O_3-SiO_2 system. Experimental points [540] and calculated lines.

Table 25.3 Piercing points in the $Ca_2MgSi_2O_7$-$NaAlSiO_4$-$CaSiO_3$ plane (akermanite-nepheline-wollastonite) of the CaO-MgO-Na_2O-Al_2O_3-SiO_2 system. The calculated values are shown in bold.

Piercing point	Temperature, °C
Ne-Mel-pWo	1171 [540] **1165** (calc)

25.5 The Na-Melilite-Gehlenite-Akermanite subsystem ($NaCaAlSi_2O_7$-$Ca_2Al_2SiO_7$-$Ca_2MgSi_2O_7$)

The sodium melilite-gehlenite-akermanite ternary system ($NaCaAlSi_2O_7$-$Ca_2Al_2SiO_7$-$Ca_2MgSi_2O_7$) was studied by Schairer et al. [71, 459].

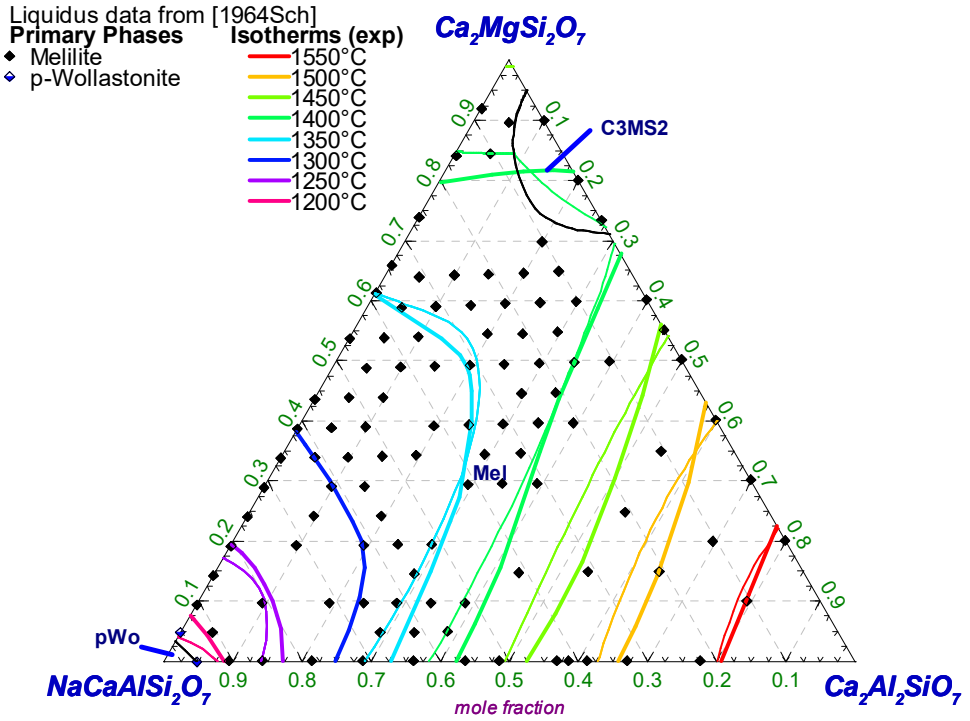

Figure 25.10 Liquidus projection in the $Ca_2MgSi_2O_7$-$NaCaAlSi_2O_7$-$Ca_2Al_2SiO_7$ plane of the CaO-MgO-Na_2O-Al_2O_3-SiO_2 system. Experimental points and isotherms (thick lines) [459] and calculated lines.

Merwinite C3MS2 liquidus in Figure 25.10 starts from the alkali-free boundary section $Ca_2MgSi_2O_7$-$Ca_2Al_2SiO_7$ that belongs to the CaO-MgO-Al_2O_3-SiO_2 system. In the $Ca_2MgSi_2O_7$-

$Ca_2Al_2SiO_7$ section, merwinite disappears close to solidus temperatures. The origin of this phase is not quite clear; the current optimization was based on the existing optimization of the CaO-MgO-Al_2O_3-SiO_2 system [515, 543].

Isothermal sections of the $Ca_2MgSi_2O_7$-$NaCaAlSi_2O_7$-$Ca_2Al_2SiO_7$ system are available from Schairer et al. [71].

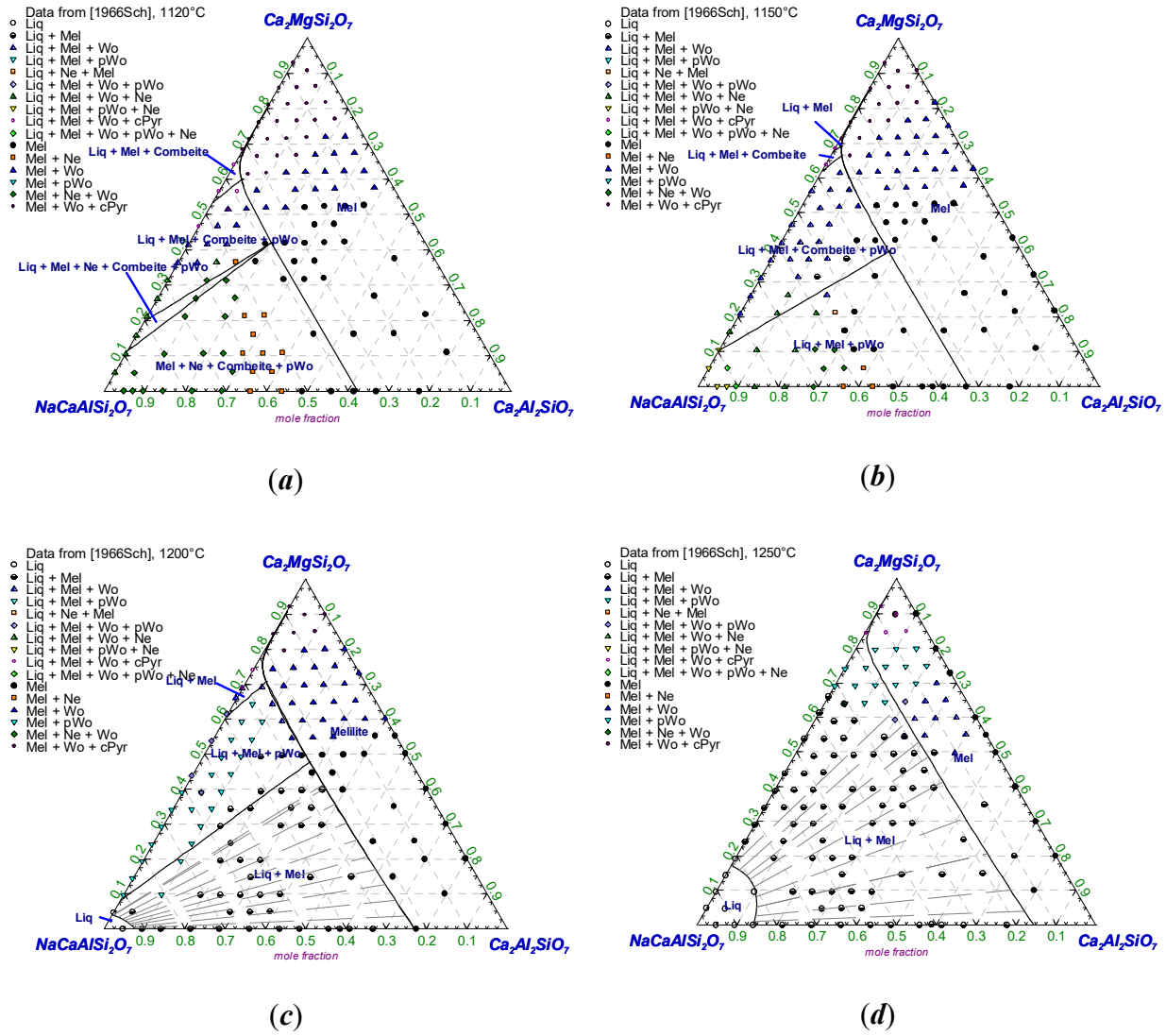

Figure 25.11 Isothermal sections in the $Ca_2MgSi_2O_7$-$NaCaAlSi_2O_7$-$Ca_2Al_2SiO_7$ plane (akermanite-soda melilite-gehlenite) of the CaO-MgO-Na_2O-Al_2O_3-SiO_2 system: 1120°C (***a***), 1150°C (***b***), 1200°C (***c***), 1250°C (***d***). Experimental points [71] and calculated lines.

Wollastonite and pseudowollastonite reported by Schairer et al. [71] were found in negligible amounts that could not be analysed by X-ray but were identified by optical microscopy. The presence of wollastonite/pseudowollastonite in Figure 25.11 starts from the $Ca_2MgSi_2O_7$ corner. Pure akermanite partially decomposes under the liquidus temperature producing small amounts of wollastonite/pseudowollastonite as it can be seen from Figure 25.7. Akermanite end-member in the oxide database also produces them but at a much lower temperature. However, as $Ca_2MgSi_2O_7$ end-member belongs to an alkali-free system CaO-MgO-SiO_2, changing its properties goes beyond the scope of the current work.

25.6 The Akermanite-Nepheline-Diopside subsystem ($Ca_2MgSi_2O_7$-$NaAlSiO_4$-$CaMgSi_2O_6$)

The nepheline-diopside join ($NaAlSiO_4$-$CaMgSi_2O_6$) was first investigated by Bowen [544] and later by Schairer et al. [545] (Figure 25.12). The system is very complex, all crystalline phases are solid solutions. The primary phases are carnegieite, nepheline, olivine and pyroxene. Melilite also forms at subliquidus temperatures.

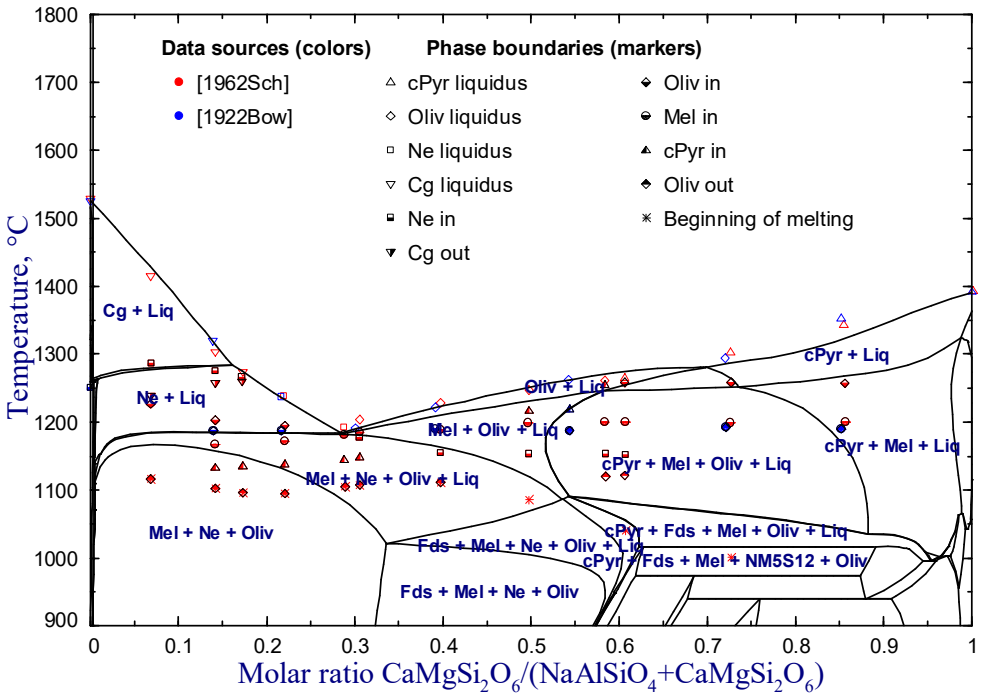

Figure 25.12 Phase diagram in the $CaMgSi_2O_6$-$NaAlSiO_4$ section of the CaO-MgO-Al_2O_3-Na_2O-SiO_2 system. Experimental points [544, 545] and calculated lines.

The akermanite-nepheline-diopside system ($Ca_2MgSi_2O_7$-$NaAlSiO_4$-$CaMgSi_2O_6$) as well as the boundary $Ca_2MgSi_2O_7$-$NaAlSiO_4$ system were investigated by Onuma and Yagi [541]. The nepheline-carnegieite inversion in the $Ca_2MgSi_2O_7$-$NaAlSiO_4$ system occurs over a wide temperature range which indicates that both phases are solid solutions. Melilite phase does not have the pure $Ca_2MgSi_2O_7$ composition; birefringence measurements indicate that melilite contains noticeable amounts of a sodium end-member. The refractive index of the pyroxene indicates that diopside also forms a solid solution, probably incorporating $CaAl_2SiO_6$ end-member. The pseudoternary system features an olivine crystallization field originating from the $NaAlSiO_4$-$CaMgSi_2O_6$ boundary. There are two piercing points in the system: Oliv-Mel-cPyr at 1212°C and Ne-Oliv-Mel at 1169°C.

The akermanite-nepheline-diopside system ($Ca_2MgSi_2O_7$-$NaAlSiO_4$-$CaMgSi_2O_6$) was investigated by Schairer and Yoder [540]. Experimental compositions are given along with detailed information on phase appearances. This system is not ternary, it features olivine primary crystallization field originating from the $NaAlSiO_4$-$CaMgSi_2O_6$ boundary along with

nepheline/carnegieite, melilite and diopside crystallization fields. There are two piercing points in the system: Ne-Mel-Oliv at 1178±5°C and Mel-Oliv-cPyr at 1213±3°C (Table 25.4).

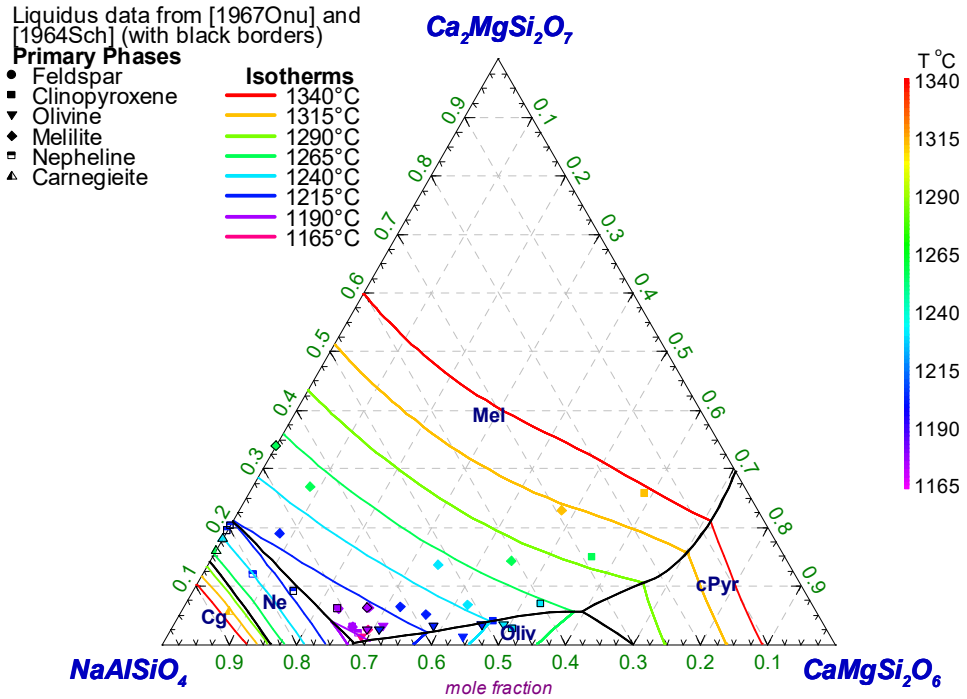

Figure 25.13 Liquidus projection in the $Ca_2MgSi_2O_7$-$NaAlSiO_4$-$CaMgSi_2O_6$ plane of the CaO-MgO-Na_2O-Al_2O_3-SiO_2 system. Experimental points [540] and calculated lines.

The presence of Clinopyroxene points in the Melilite field in Figure 25.13 can be explained by the phase diagram of the $Ca_2MgSi_2O_7$-$CaMgSi_2O_6$ boundary from the optimization of the CaO-MgO-SiO_2 by Jung et al. [546] presented in Figure 25.14. Akermanite (Melilite) liquidus is not perfectly reproduced and the eutectic point is at x($CaMgSi_2O_6$) = 0.70 rather than at 0.62-0.65.

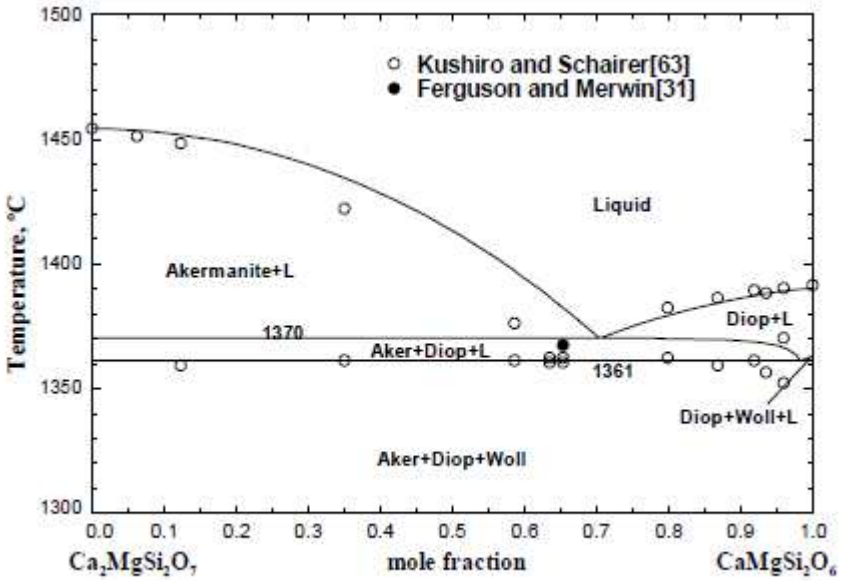

Fig. 19. Calculated phase diagram of the $Ca_2MgSi_2O_7$–$CaMgSi_2O_6$ section.

Figure 25.14 Phase diagram in the $Ca_2MgSi_2O_7$-$CaMgSi_2O_6$ section of the CaO-MgO-SiO_2 system taken from the original optimization by Jung et al. [546].

Table 25.4 Piercing points in the $Ca_2MgSi_2O_7$-$NaAlSiO_4$-$CaMgSi_2O_6$ plane (akermanite-nepheline-diopside) of the CaO-MgO-Na_2O-Al_2O_3-SiO_2 system. The calculated values are shown in bold.

Piercing point	**Temperature, °C**
Oliv-Mel-cPyr	1213 [540] 1212 [541] **1267** (calc)
Ne-Oliv-Mel	1178 [540] 1169 [541] **1183** (calc)

25.7 The Diopside-Nepheline-Wollastonite subsystem ($CaMgSi_2O_6$-$NaAlSiO_4$-$CaSiO_3$)

The diopside-nepheline-wollastonite system ($CaMgSi_2O_6$-$NaAlSiO_4$-$CaSiO_3$) was studied by Schairer and Yoder [540] (preliminary data, Figure 25.15). Detailed information on phase appearances is given. There are four piercing points in the system: Ne-Wo-Mel, Mel-cPyr-Oliv, Ne-Mel-Oliv and Mel-cPyr-Oliv, although the temperatures are not given.

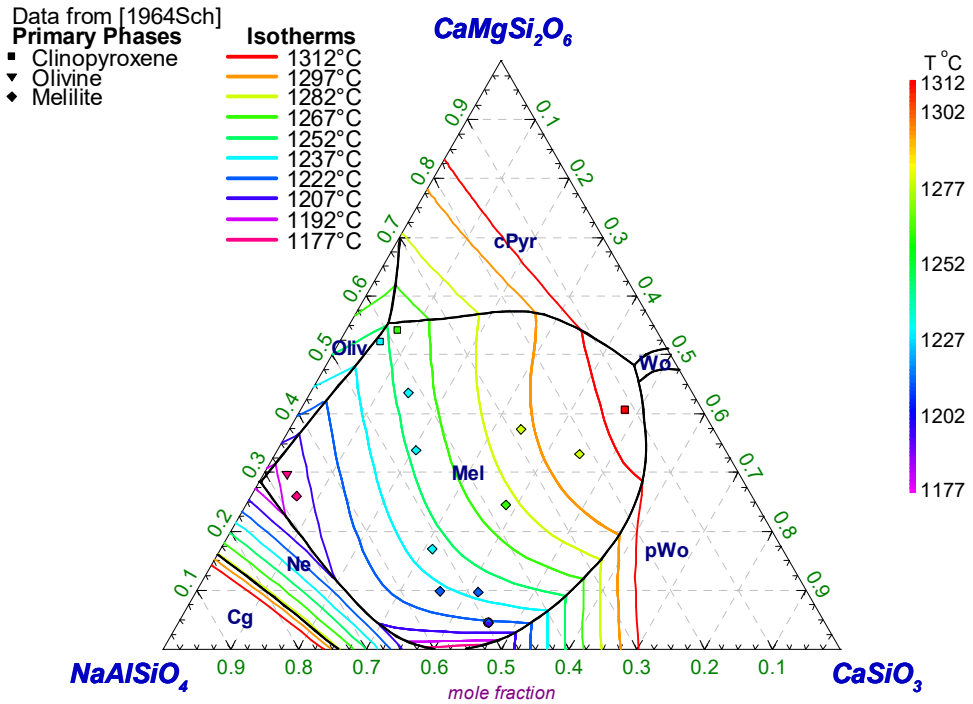

Figure 25.15 Liquidus projection in the $CaMgSi_2O_6$-$NaAlSiO_4$-$CaSiO_3$ of the CaO-MgO-Na_2O-Al_2O_3-SiO_2 system. Experimental points [540] and calculated lines.

25.8 The Forsterite-Nepheline-Diopside subsystem (Mg_2SiO_4-$NaAlSiO_4$-$CaMgSi_2O_6$)

The nepheline-forsterite-diopside system ($NaAlSiO_4$-Mg_2SiO_4-$CaMgSi_2O_6$) was investigated by Schairer and Yoder [517] (Figure 25.16). It is not a ternary system as spinel primary crystallization field appears in the liquidus. Melilite solid solution appears as one of the phases during the crystallization but does not have its own primary field. There is a piercing point Sp-Ne-Oliv at 1245±5°C (Table 25.5).

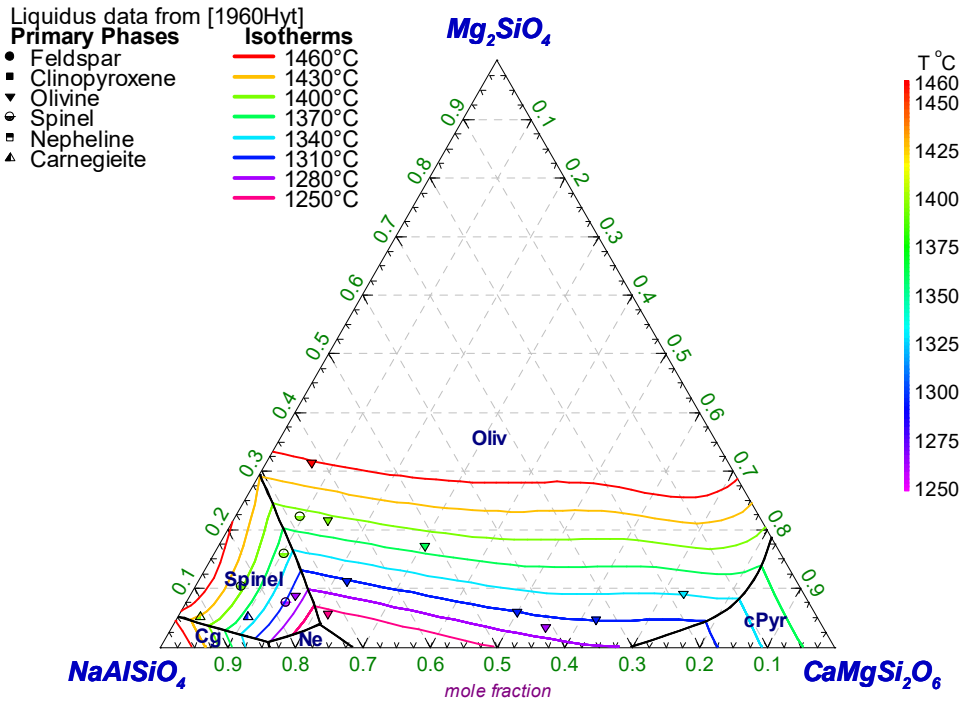

Figure 25.16 Liquidus projection in the Mg_2SiO_4-$NaAlSiO_4$-$CaMgSi_2O_6$ plane of the CaO-MgO-Na_2O-Al_2O_3-SiO_2 system. Experimental points [547] and calculated lines.

Table 25.5 Piercing points in the Mg_2SiO_4-$NaAlSiO_4$-$CaMgSi_2O_6$ plane (forsterite-nepheline-diopside) of the CaO-MgO-Na_2O-Al_2O_3-SiO_2 system. The calculated values are shown in bold.

Piercing point	Temperature, °C
Sp-Ne-Oliv	1245±5 [517] **1216** (calc)

25.9 The Anorthite-Nepheline-Diopside subsystem ($CaAl_2Si_2O_8$-$NaAlSiO_4$-$CaMgSi_2O_6$)

The nepheline-anorthite-diopside system ($NaAlSiO_4$-$CaAl_2Si_2O_8$-$CaMgSi_2O_6$) was studied by Schairer et al. [548]. Apart from carnegieite/nepheline, pyroxene and feldspar primary fields, olivine, spinel and β-alumina primary fields appear in the phase diagram. Only the boundaries of primary fields are given and the temperatures of the piercing points: Oliv-cPyr-Fds at 1165±5°C, Oliv-Ne-Fds at 1160±2°C, Ne-Fds-Sp at 1168±2°C, Ne-Sp-Fds at 1263±3°C, Ne-Fds-β-alumina at 1298±3°C (Table 25.6).

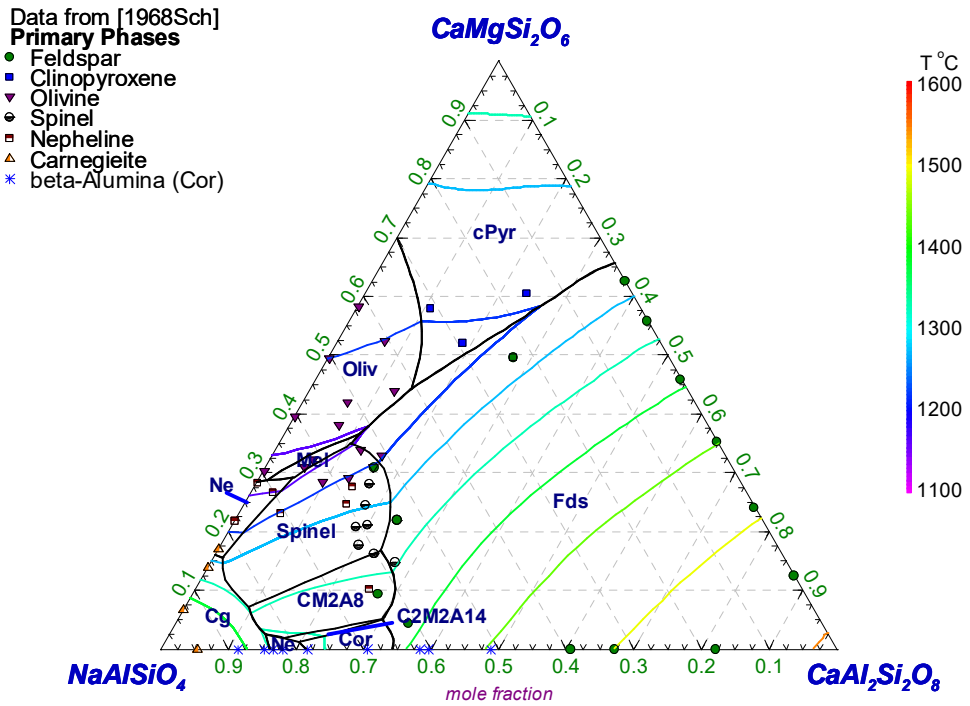

Figure 25.17 Liquidus projection in the $CaMgSi_2O_6$-$NaAlSiO_4$-$CaAl_2Si_2O_8$ plane of the CaO-MgO-Na_2O-Al_2O_3-SiO_2 system. Experimental points [548] and calculated lines.

We suppose that the appearance of the ternary phase CM2A8 (Figure 25.17) is not seen in the experiments by Schairer et al. [548] because ternary phases usually have much higher crystallization times compared to binary phases: it is easier for two types of cations to organize in a certain way to build the crystal structure than for three.

Table 25.6 Piercing points in the $CaMgSi_2O_6$-$NaAlSiO_4$-$CaAl_2Si_2O_8$ plane (diopside-nepheline-anorthite) of the CaO-MgO-Na_2O-Al_2O_3-SiO_2 system. The calculated values are shown in bold.

Piercing point	**Temperature, °C**
Oliv-cPyr-Fds	1165±5 [548] **1214** (calc)
Oliv-Ne-Fds	1160±2 [548] **1183** (calc, metastable)
Ne-Fds-Sp	1168±2 [548] **1150** (calc, metastable)
Ne-Sp-Fds	1263±3 [548] **1310** (calc, metastable)
Ne-Fds-β-alumina (Cor)	1298±3 [548] **1292** (calc, metastable)

25.10 The Nepheline-Diopside-Silica subsystem ($NaAlSiO_4$-$CaMgSi_2O_6$-SiO_2)

The nepheline-diopside-silica system ($NaAlSiO_4$-$CaMgSi_2O_6$-SiO_2) was studied by Schairer and Yoder [524] (Figure 25.19). Experimental compositions, primary phases and isotherms are available for the system. The primary phases are clinopyroxene (probably containing some amount of Al-end-members), complex nepheline and carnegieite solid solutions, feldspar, tridymite/cristobalite and olivine. There are three piercing points in the system: Ne-Oliv-cPyr at 1138±3°C, Ne-cPyr-Fds at 1118±3°C, cPyr-Fds-Tri at 1073±3°C (Table 25.7). This system is split into two subsystems by the join $NaAlSi_3O_8$-$CaMgSi_2O_6$. Compositions richer in silica than this join, contain silica polymorphs among the crystallization products. Compositions poorer in silica, however, contain nepheline. So, the phase diagram explains the fact that nephelines and quartz are incompatible in nature. A peculiar feature of the $NaAlSi_3O_8$-$CaMgSi_2O_6$ join is that feldspar liquidus has a maximum at $Ab_{0.91}Di_{0.09}$ composition. However, its reason is unclear. The jadeite-diopside join ($NaAlSi_2O_6$-$CaMgSi_2O_6$) was also investigated as a part of the pseudoternary system.

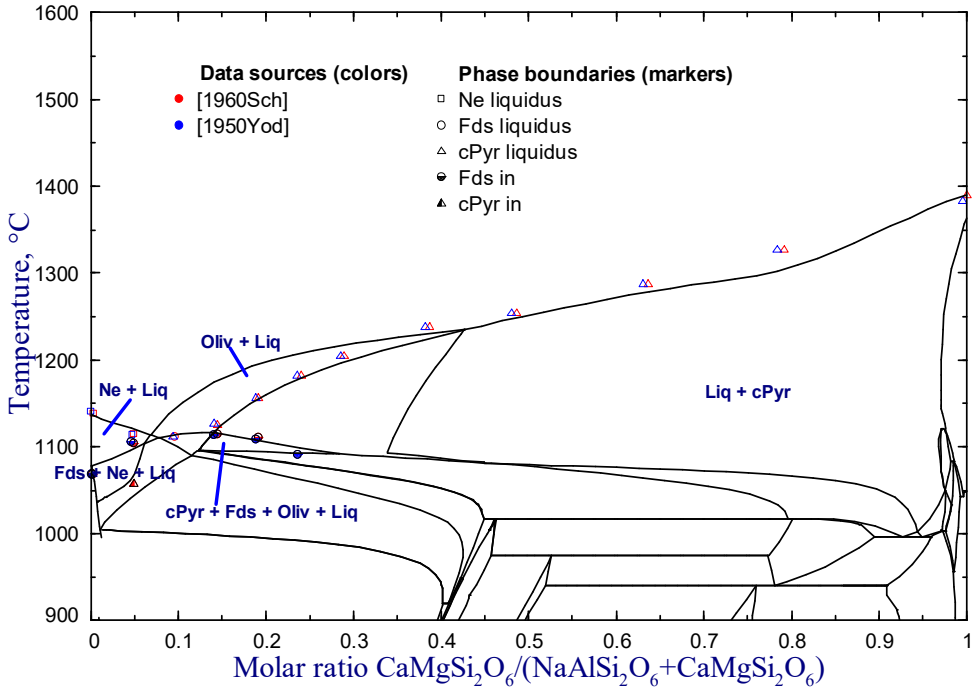

Figure 25.18 Phase diagram of the $CaMgSi_2O_6$-$NaAlSi_2O_6$ section of the CaO-MgO-Al_2O_3-Na_2O-SiO_2 system. Experimental points [81, 524] and calculated lines.

There is an olivine primary field in Figure 25.18 which is not reported in the literature. In our model, the position of olivine (forsterite) liquidus is fixed in the MgO-Na_2O-Al_2O_3-SiO_2 system by available experimental data (Figure 24.2, Figure 24.3) and it extrapolates to the quinary system. We can suppose that small quantities of olivine crystals might go undetected in quenching experiments.

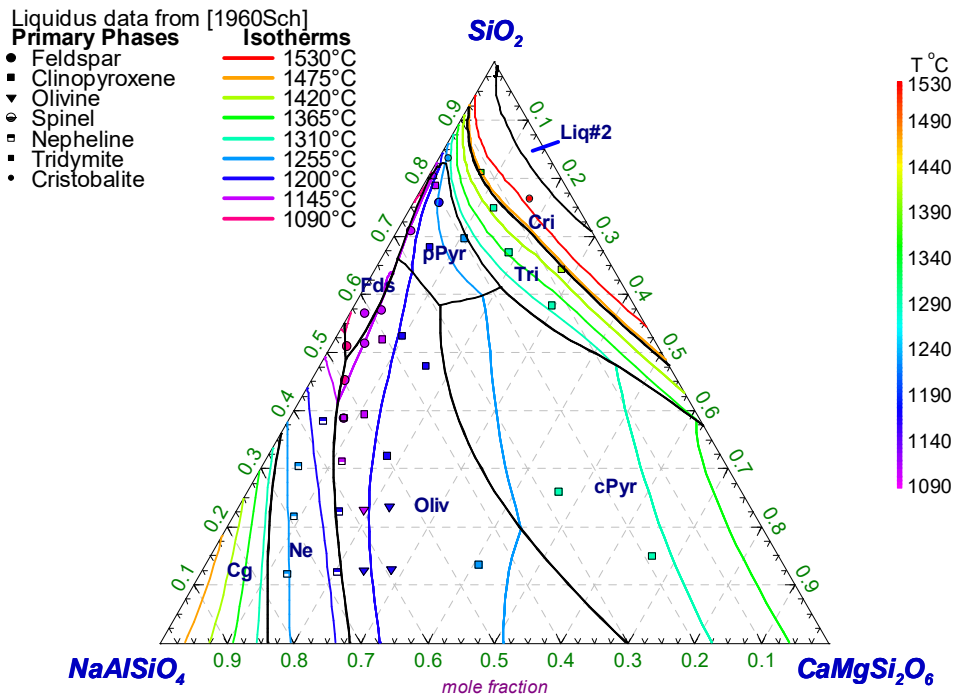

Figure 25.19 Liquidus projection in the SiO_2-$NaAlSiO_4$-$CaMgSi_2O_6$ plane of the CaO-MgO-Na_2O-Al_2O_3-SiO_2 system. Experimental points [524] and calculated lines.

Table 25.7 Piercing points in the SiO_2-$NaAlSiO_4$-$CaMgSi_2O_6$ plane (silica-nepheline-diopside) of the CaO-MgO-Na_2O-Al_2O_3-SiO_2 system. The calculated values are shown in bold.

Piercing point	Temperature, °C
Ne-Oliv-cPyr	1138±3 [524] Not available
Ne-cPyr-Fds	1118±3 [524] **1115** (calc, metastable)
cPyr-Fds-Tri	1073±3 [524] **1138** (calc, metastable)

Some natural clinopyroxenes contain significant amounts of sodium in the form of jadeite. Diopside $CaMgSi_2O_6$ and jadeite $NaAlSi_2O_6$ can form a solid solution under elevated pressures.

Apparently, naturally occurring sodium-containing clinopyroxenes were formed under pressure in the Earth crust. X-ray studies by Rossi et al. [549] indicate that there is a miscibility gap between diopside and jadeite and a zone of ordered structure called omphacite. The enthalpy of solution in lead borate at 970K was measured for Di-Jd solutions by Wood et al. [79], Cohen [78], Newton et al. [550] (Figure 25.20). The obtained data indicate a positive enthalpy of mixing; considering that jadeite is unstable under the atmospheric pressure, the solubility of jadeite in diopside must be quite small.

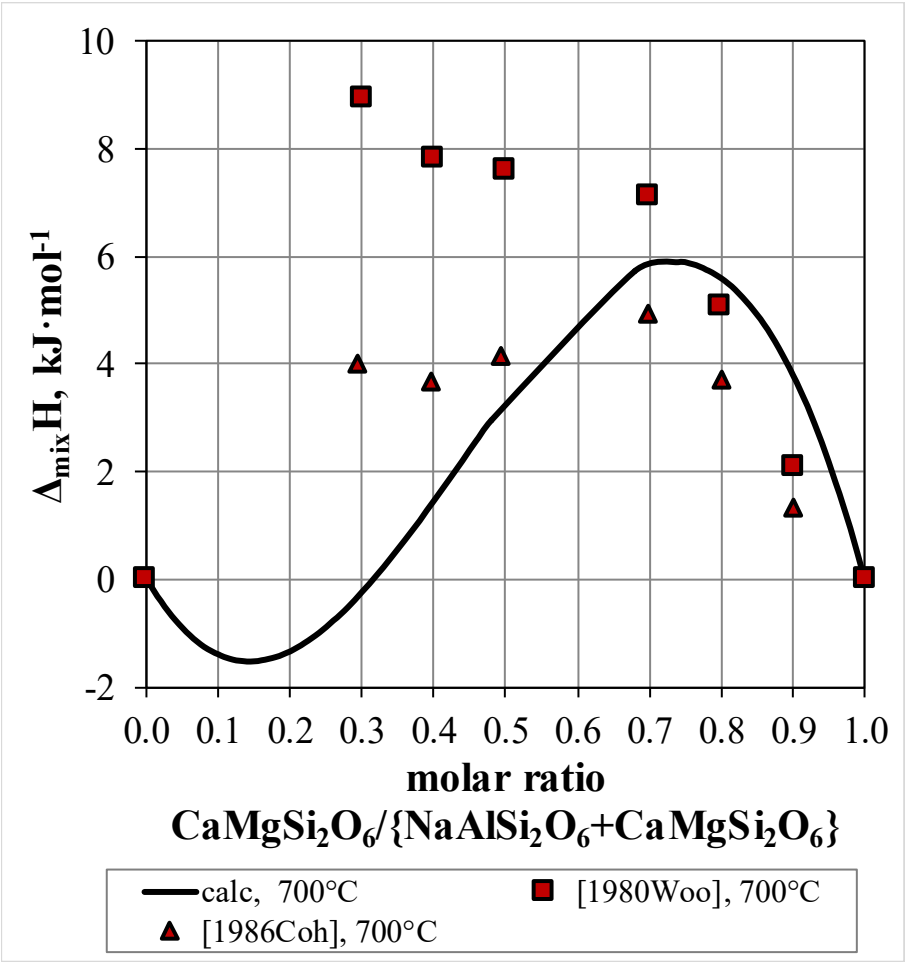

Figure 25.20 The enthalpy of mixing of Clinopyroxene solid solution along the diopside-jadeite join ($CaMgSi_2O_6$-$NaAlSi_2O_6$). Experimental points [78, 79] and the calculated line.

Holland [551] and Gasparik [80, 552] measured jadeite activity in clinopyroxenes of $NaAlSi_2O_6$-$CaMgSi_2O_6$ composition by equilibrating them with quartz and high albite in hydrothermal conditions at different pressures. Holland used disordered samples because at 600°C

clinopyroxenes form an intermediate ordered form called omphacite. The activities of end-members of Clinopyroxene solid solution are summarized in Figure 25.21.

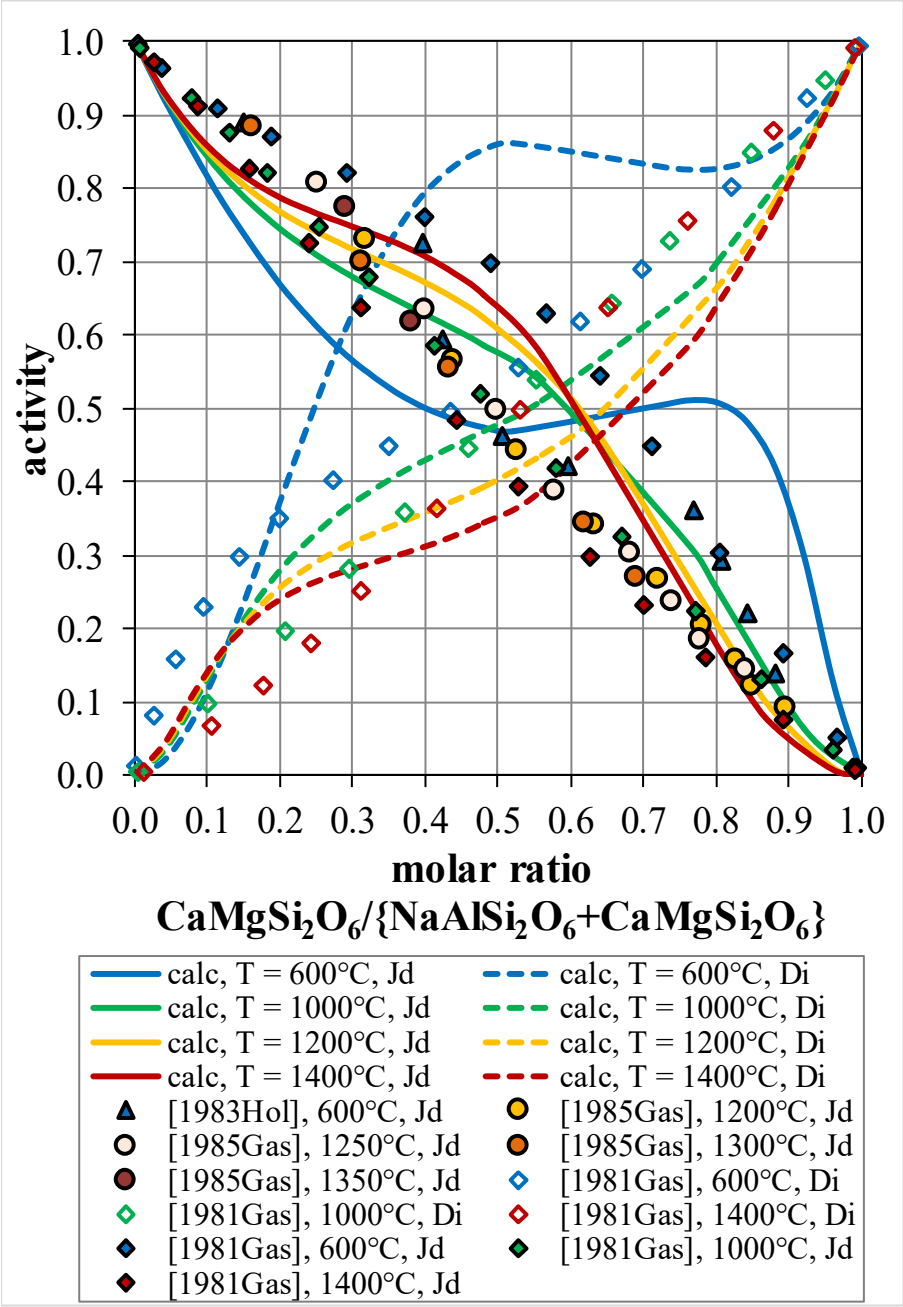

Figure 25.21 End-member activities in Clinopyroxene $NaAlSi_2O_6$-$CaMgSi_2O_6$ solid solution at different temperatures. Experimental points [80, 551, 553] and calculated lines.

25.11 The Akermanite-Albite-Diopside subsystem ($Ca_2MgSi_2O_7$-$NaAlSi_3O_8$-$CaMgSi_2O_6$)

The akermanite-albite-diopside system ($Ca_2MgSi_2O_7$-$NaAlSi_3O_8$-$CaMgSi_2O_6$) was studied by Schairer and Yoder [540] (Figure 25.22). Detailed information on phase appearances is given. The liquidus structure is quite simple; feldspar, pyroxene and melilite primary fields are present without any piercing points.

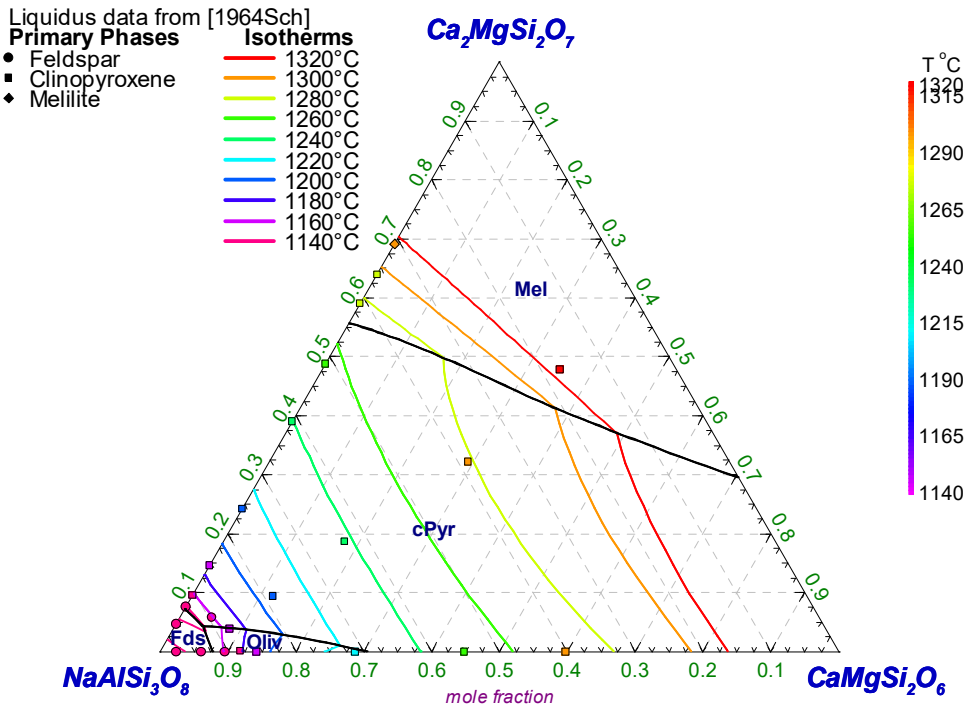

Figure 25.22 Liquidus projection in the $Ca_2MgSi_2O_7$-$NaAlSi_3O_8$-$CaMgSi_2O_6$ plane of the CaO-MgO-Na_2O-Al_2O_3-SiO_2 system. Experimental points [540] and calculated lines.

25.12 The Forsterite-Albite-Diopside subsystem (Mg_2SiO_4-$NaAlSi_3O_8$-$CaMgSi_2O_6$)

The forsterite-albite-diopside system (Mg_2SiO_4-$NaAlSi_3O_8$-$CaMgSi_2O_6$) was studied by Schairer and Yoder [521] (Figure 25.23). It is a ternary system with a simple piercing point (the temperature is not indicated) and no solid solutions, the majority of the liquidus projection is occupied with the

forsterite primary crystallization field. The experimental points are mostly located along the forsterite-diopside univariant line.

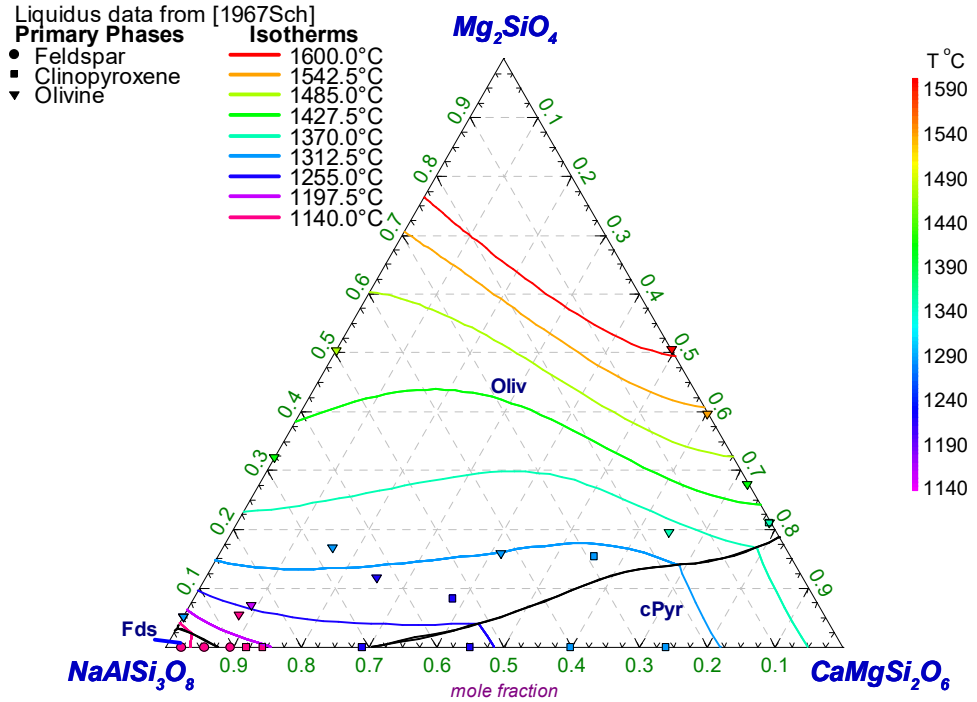

Figure 25.23 Liquidus projection in the Mg_2SiO_4-$NaAlSi_3O_8$-$CaMgSi_2O_6$ plane (olivine-albite-diopside) in the CaO-MgO-Na_2O-Al_2O_3-SiO_2 system. Experimental points [521] and calculated lines.

25.13 The Enstatite-Albite-Diopside subsystem ($MgSiO_3$-$NaAlSi_3O_8$-$CaMgSi_2O_6$)

The enstatite-albite-diopside system ($MgSiO_3$-$NaAlSi_3O_8$-$CaMgSi_2O_6$) was investigated by Schairer and Morimoto [554] (Figure 25.24). There is one piercing point in the phase diagram: pPyr-Fds-cPyr at 1130±2°C (Table 25.8). The detailed quenching information for the experimental points is not given, only the experimental compositions, the primary phases and the isotherms are presented. A few isothermal sections are also available.

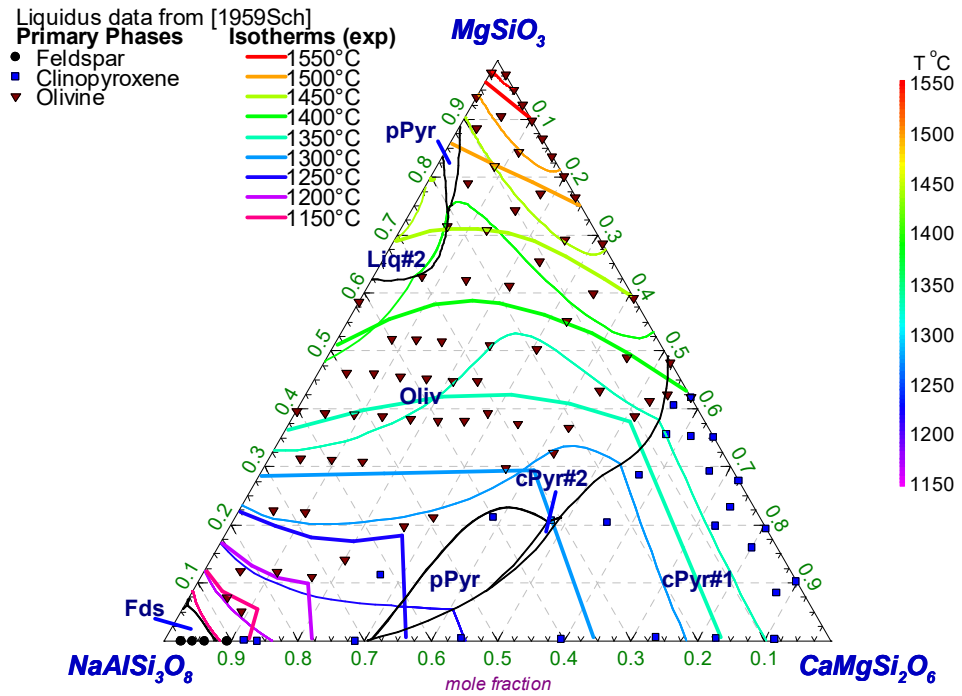

Figure 25.24 Liquidus projection in the $MgSiO_3$-$NaAlSi_3O_8$-$CaMgSi_2O_6$ plane of the CaO-MgO-Na_2O-Al_2O_3-SiO_2 system. Experimental points and isotherms (thick lines) [554] and calculated lines.

The origin of the miscibility gap appearing on the liquidus projection (Figure 25.24) is explained in Section 24.4.

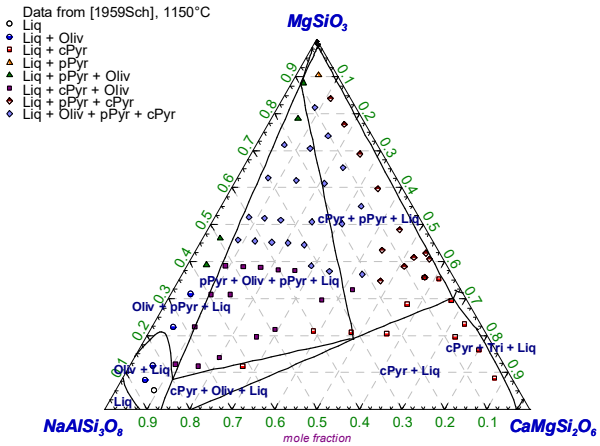

(*a*)

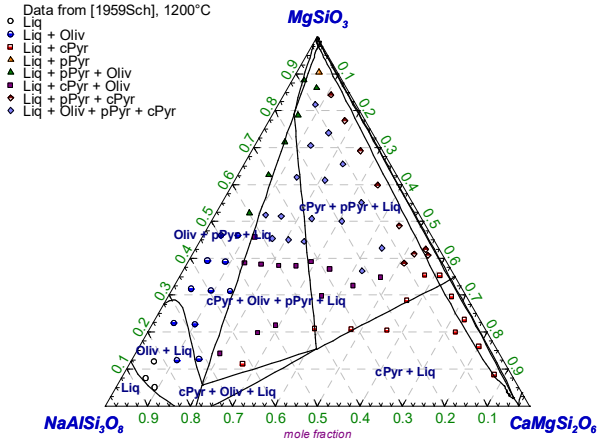

(*b*)

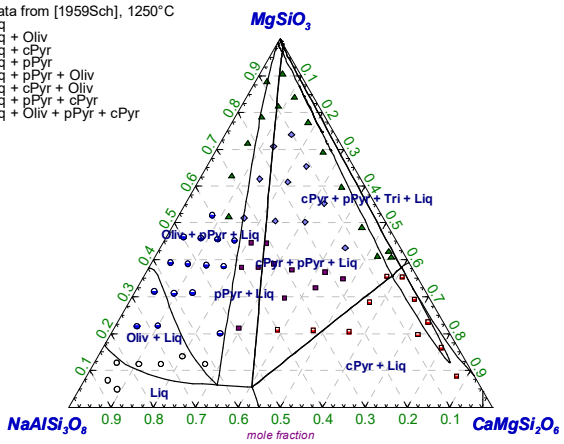

(*c*)

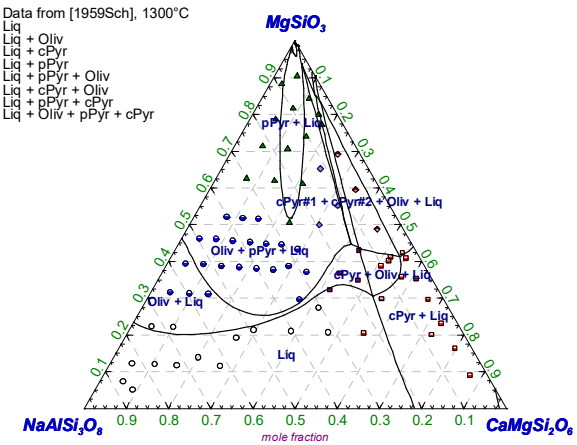

(*d*)

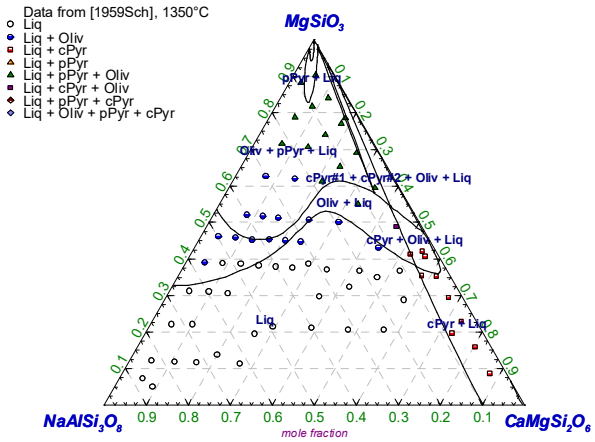

(*e*)

Figure 25.25 Isothermal sections of the $MgSiO_3$-$NaAlSi_3O_8$-$CaMgSi_2O_6$ plane in the CaO-MgO-Na_2O-Al_2O_3-SiO_2 system at 1150°C (***a***), 1200°C (***b***), 1250°C (***c***), 1300°C (***d***), and 1350°C (***e***). Experimental points [554] and calculated lines.

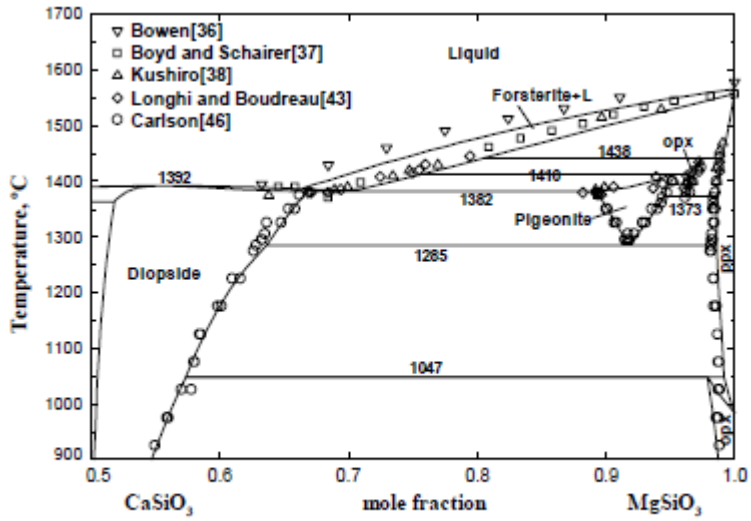

Fig. 11. Calculated phase diagram of the $CaMgSi_2O_6$–$MgSiO_3$ section.

Figure 25.26 Phase diagram of the $MgSiO_3$-$CaMgSi_2O_6$ boundary from the optimization by Jung et al. [546].

The phase diagram in the Na-free boundary section $MgSiO_3$-$CaMgSi_2O_6$ is presented in Figure 25.26. The isothermal sections of this boundary at 1150, 1200, 1250, 1300 and 1350°C do not contain liquid; the solid phases in Figure 25.25 either do not include sodium (Olivine, Protopyroxene) or include it in small amounts that do not affect the equilibria (Clinopyroxene). This means that the same solid phases must be stable if $NaAlSi_3O_8$ is added to $MgSiO_3$-$CaMgSi_2O_6$. For example, at 1300 and 1350°C there is no Protopyroxene present in the $MgSiO_3$-$CaMgSi_2O_6$ phase diagram while the data by Schairer and Morimoto [554] indicate its presence. We can suppose that the Ca-rich Clinopyroxene from Figure 25.26 has crystallization difficulties and was not observed. The same concerns Orthopyroxene phase which is stable in the calculated phase diagram (Figure 25.26) but is not present among the observed phases by Schairer and Morimoto [554].

Table 25.8 Piercing points in the $MgSiO_3$-$NaAlSi_3O_8$-$CaMgSi_2O_6$ plane (enstatite-albite-diopside) of the CaO-MgO-Na_2O-Al_2O_3-SiO_2 system. The calculated values are shown in bold.

Piercing point	Temperature, °C
pPyr-Fds-cPyr	1130±2 [554] **1154** (calc, metastable)

25.14 The Wollastonite-Albite-Akermanite subsystem ($CaSiO_3$-$NaAlSi_3O_8$-$Ca_2MgSi_2O_7$)

The wollastonite-albite-akermanite system ($CaSiO_3$-$NaAlSi_3O_8$-$Ca_2MgSi_2O_7$) was studied by Schairer and Yoder [540] (Figure 25.27). Detailed information on phase appearances is given. There are three piercing points in the system: Ab-Wo-cPyr at 1095±10°C, Wo-pWo-Mel at 1320±5°C and Wo-cPyr-Mel at 1268±3°C (Table 25.9).

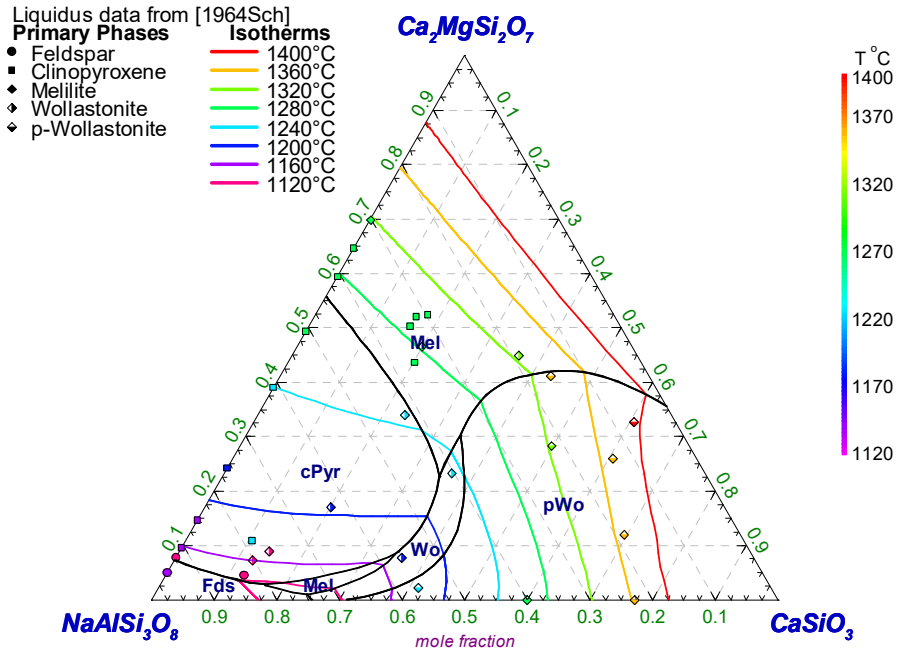

Figure 25.27 Liquidus projection in the $Ca_2MgSi_2O_7$-$NaAlSi_3O_8$-$CaSiO_3$ plane of the CaO-MgO-Na_2O-Al_2O_3-SiO_2 system. Experimental points [540] and calculated lines.

Table 25.9 Piercing points in the $Ca_2MgSi_2O_7$-$NaAlSi_3O_8$-$CaSiO_3$ plane (akermanite-albite-wollastonite) of the CaO-MgO-Na_2O-Al_2O_3-SiO_2 system. The calculated values are shown in bold.

Piercing point	Temperature, °C
Fds-Wo-cPyr	1095±10 [540] **1100** (calc, metastable)
Wo-pWo-Mel	1320±5 [540] **1253** (calc)
Wo-cPyr-Mel	1268±3 [540] **1224** (calc)

25.15 The Nepheline-Albite-Akermanite subsystem ($NaAlSiO_4$-$NaAlSi_3O_8$-$Ca_2MgSi_2O_7$)

The akermanite-nepheline-albite system ($Ca_2MgSi_2O_7$-$NaAlSiO_4$-$NaAlSi_3O_8$) was studied by Schairer and Yoder [540] (Figure 25.28). Detailed information on phase appearances is given. There are two piercing points, Ne-Mel-cPyr at 1100±5°C and Ne-cPyr-Fds at 1083±5°C (Table 25.10).

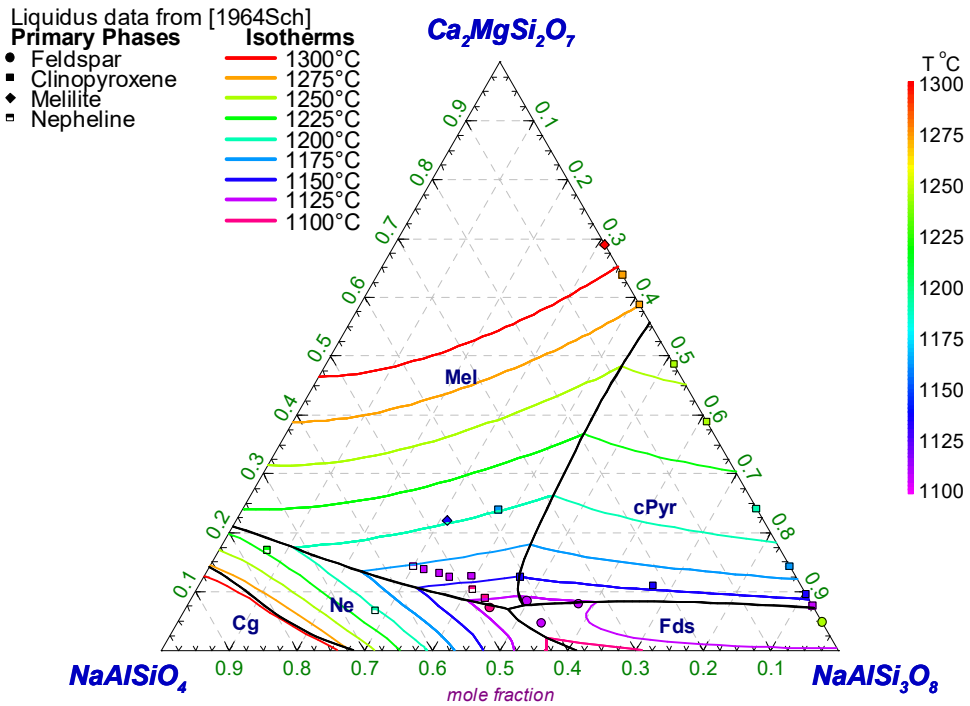

Figure 25.28 Liquidus projection in the $Ca_2MgSi_2O_7$-$NaAlSiO_4$-$NaAlSi_3O_8$ plane of the CaO-MgO-Na_2O-Al_2O_3-SiO_2 system. Experimental points [540] and calculated lines.

Table 25.10 Piercing points in the $Ca_2MgSi_2O_7$-$NaAlSiO_4$-$NaAlSi_3O_8$ plane (akermanite-nepheline-albite) of the CaO-MgO-Na_2O-Al_2O_3-SiO_2 system. The calculated values are shown in bold.

Piercing point	Temperature, °C
Ne-Mel-cPyr	1100±5 [540] **1108** (calc)
Ne-cPyr-Fds	1083±5 [540] **1105** (calc)

25.16 Other sections

Mathieu [436] measured Na_2O solubility in Na_2O-free base compositions in the CaO-MgO-SiO_2-5 mol%Al_2O_3 system in an atmosphere with a fixed Na(g) partial pressure. Large amounts of $Na_2O{\cdot}2SiO_2$ melt were used as a source of sodium and the partial pressure of oxygen was fixed by Ni/NiO buffer. The operating temperature was 1400°C. The author presents the data in the form of isosolubility lines in the CaO-MgO-SiO_2-5 mol%Al_2O_3 base composition triangle and to compare these data with calculated values, they were replotted in the form of isoactivities. Intersection points of Na_2O isosolubility lines and sections with a fixed CaO/MgO ratio are plotted in Figure 25.29.

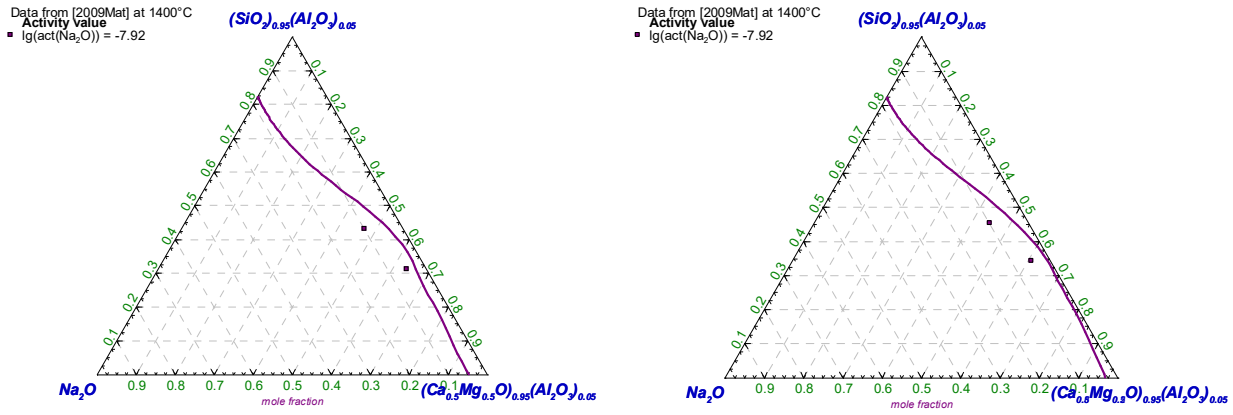

(***a***) (***b***)

Figure 25.29 Isoactivity plots in the $(SiO_2)_{0.95}(Al_2O_3)_{0.05}$-$Na_2O$-$(Ca_{0.5}Mg_{0.5}O)_{0.95}(Al_2O_3)_{0.05}$ (***a***) and $(SiO_2)_{0.95}(Al_2O_3)_{0.05}$-$Na_2O$-$(Ca_{0.8}Mg_{0.2}O)_{0.95}(Al_2O_3)_{0.05}$ (***b***) sections of the Al_2O_3-CaO-MgO-Na_2O-SiO_2 system at 1400°C. The reference state is the pure liquid Na_2O. Points recalculated from the published data [436] and calculated lines.

25.17 Optimization results

The sodium-containing quaternary subsystems were optimized in this work; the CaO-MgO-Na_2O-Al_2O_3 system lacks experimental data and was optimized as the part of the quinary system. The optimization of the CaO-MgO-Al_2O_3-SiO_2 system was taken from Jung et al. [515, 543].

According to the experimental data, melilite forms a solid solution with a significant solubility in the system. Clinopyroxene has only an insignificant solubility of the sodium end-member. An

excess parameter in the liquid $q^{001}_{\mathrm{Mg,NaAl(Ca)}}$ was added to adjust the liquidi of clinopyroxene and olivine in the system. The melilite liquidus was adjusted by using an exchange parameter $\Delta_{\mathrm{CN//AM//S}}$. The optimized parameters are summarized in Table A.31.

CHAPTER 26 OPTIMIZATION OF THE K_2O-MgO-SiO_2 SYSTEM

26.1 Phase diagram

Phase equilibria in the K_2O-MgO-SiO_2 system were studied in detail by Roedder [114, 115]. Four ternary compounds were found in the system. KMS melts congruently at about 1650°C with high K_2O losses. KMS3 and KMS5 also melt congruently at 1134±1° and 1089±1°C. According to X-ray analysis, KMS5 has two polymorphic modifications. X-ray analysis of KMS3 revealed that it undergoes a solid-solid transition which, however, was not confirmed by DTA and optical studies. Roedderite KM5S12 melts incongruently at 1174±2°C decomposing into $MgSiO_3$ and liquid.

Later, Roth [46] discovered two more compounds, K5M5S11 and K2M2S5. According to Roth, KMS3 melts incongruently.

A remarkable feature of the K_2O-MgO-SiO_2 system is that the K_2MgSiO_4-SiO_2 join is isostructural with the $KAlO_2$-SiO_2 join in the K_2O-Al_2O_3-SiO_2 system (Figure 26.5). The compounds in this join have Al-containing analogues. So, KMS has a cubic structure derived from a stuffed cristobalite structure [555] and is isostructural with $KAlO_2$. This compound also exists in low- and high-T forms with the transition at 508°C and $\Delta_{tr}H$ = 1.68 kJ·mol^{-1}. KMS can dissolve excess silica to some extent which only increases its similarity to $KAlO_2$. The powder pattern of KMS3 is like the one for kalsilite $KAlSiO_4$. Schairer [556] has found a thermal evidence of a solid solution between $KAlSiO_4$ and KMS3. KMS5 is structurally isomorphous with leucite [114-116] and, according to Roth [46], KMS5 and $KAlSi_2O_6$ form a complete solid solution. Like leucite, the compound can exist in an ordered and a disordered form [116]. However, it remains mysterious why no Mg-containing kalsilites or leucites were found in nature; all Mg inclusions in natural samples can be explained by the presence of either olivine or diopside.

Roedderite KM5S12 is isostructural with NM5S12 and is an end-member of a rare merrihueite-roedderite mineral group [557].

The liquidus projections in the system are shown in Figure 26.1-Figure 26.3 for different temperature intervals.

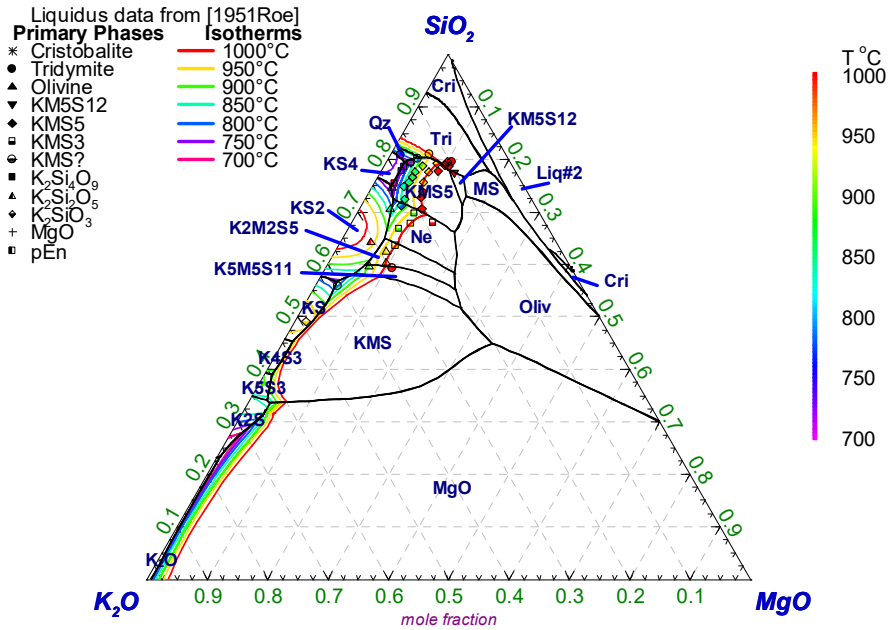

Figure 26.1 Liquidus projection in the K_2O-MgO-SiO_2 system; isotherms from 700 to 1000°C. Experimental points [114, 115] and calculated lines.

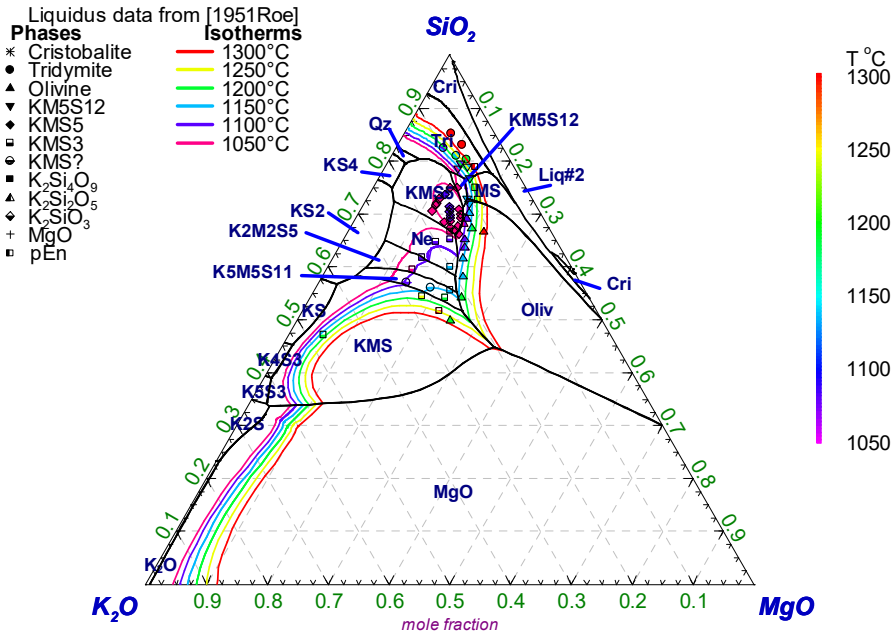

Figure 26.2 Liquidus projection in the K_2O-MgO-SiO_2 system; isotherms from 1050° to 1300°C. Experimental points [114, 115] and calculated lines.

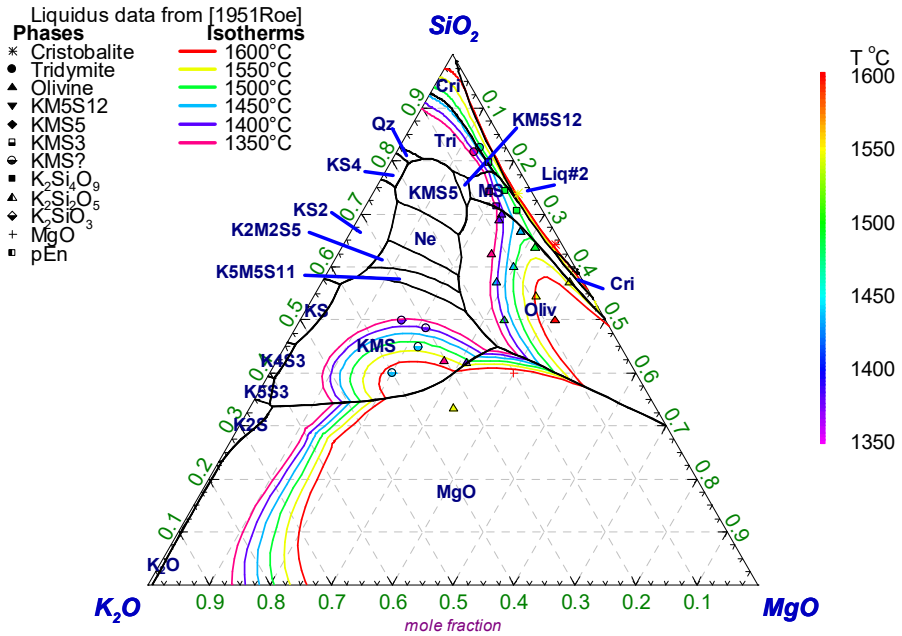

Figure 26.3 Liquidus projection in the K_2O-MgO-SiO_2 system; isotherms from 1350° to 1600°C. Experimental points [114, 115] and calculated lines.

There is a small bump in the liquidus projection (Figure 26.1-Figure 26.3) along the MgO-K_4SiO_4 line. It appears because the K_4SiO_4-MgO pair is more stable that the diagonal pair K_2O-Mg_2SiO_4 which causes the immiscibility tendency. However, no miscibility gap forms. The same phenomenon can be observed in the CaO-Na_2O-SiO_2 (Chapter 14), CaO-K_2O-SiO_2 (Chapter 17) and Na_2O-MgO-SiO_2 systems (Chapter 21).

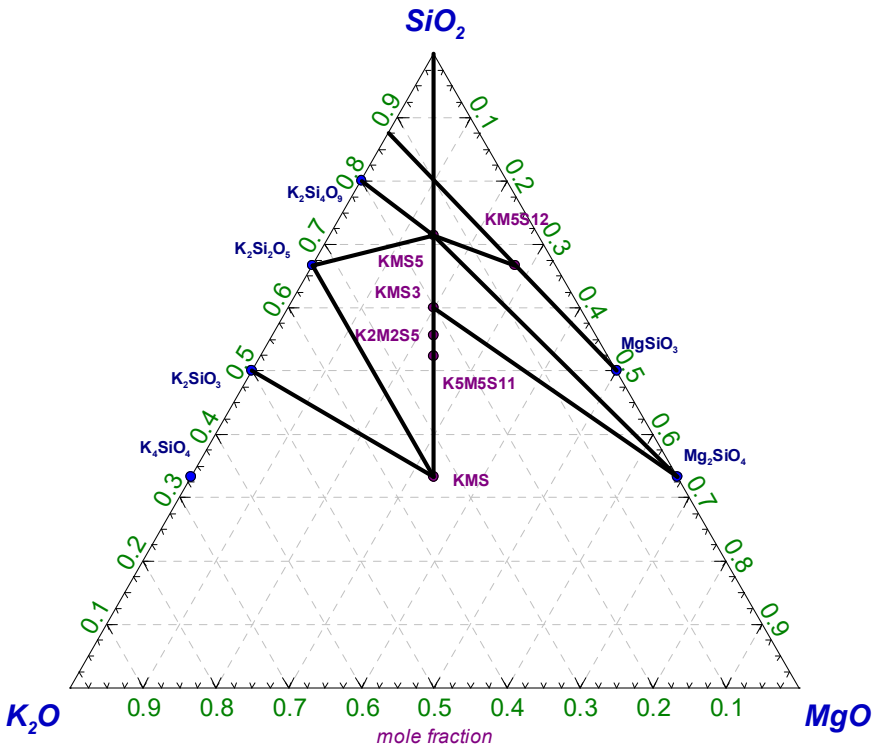

Figure 26.4 Sections through the K_2O-MgO-SiO_2 system [46, 114].

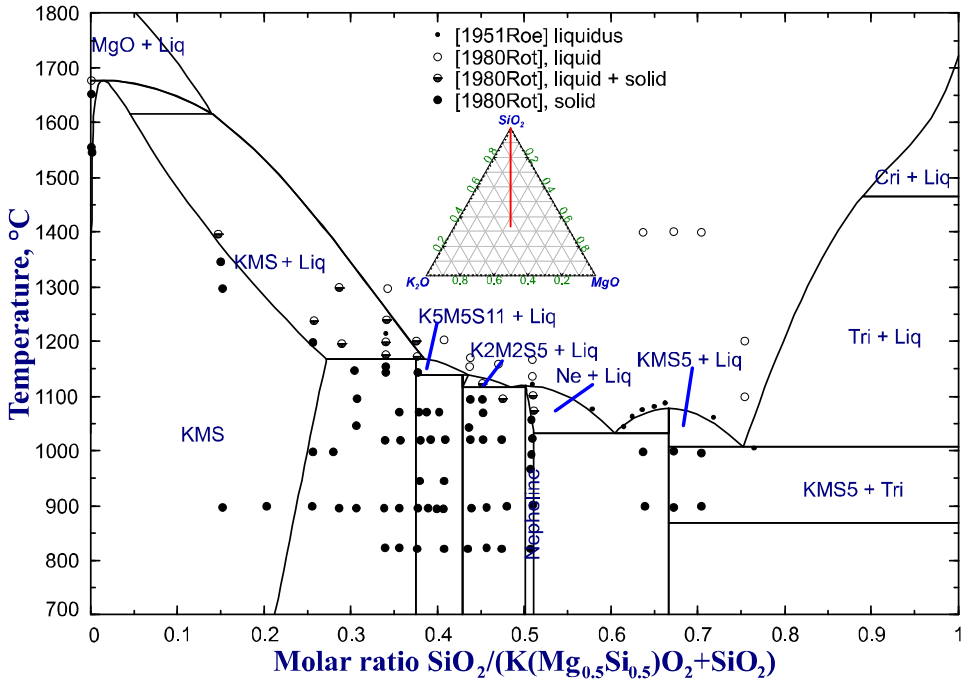

Figure 26.5 Phase diagram of the $K(Mg_{0.5}Si_{0.5})O_2$-SiO_2 section of the K_2O-MgO-SiO_2 system. Experimental points [46, 114] and calculated lines.

The main $(K_2O)_{0.5}(MgO)_{0.5}$-SiO_2 section through the system in Figure 26.5 contains all but one of the ternary compounds and shows their mutual solubility and melting relations.

A few sections through the ternary system in the work by Roedder [114] were presented without experimental points, only as manually traced curves (Figure 26.4). They were digitized and are shown in Figure 26.6.

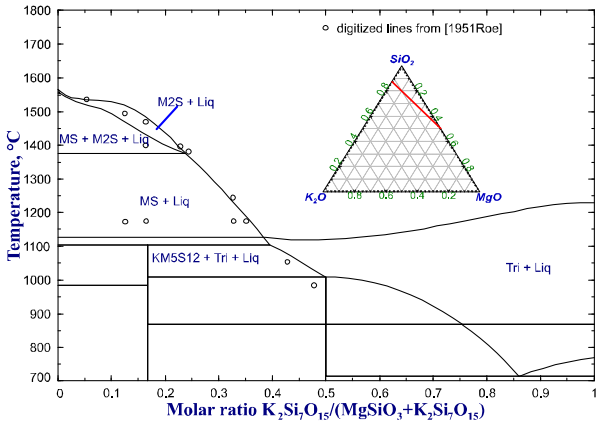
digitized lines from [1951Roe]
M2S + Liq
MS + M2S + Liq
MS + Liq
KM5S12 + Tri + Liq
Tri + Liq
Temperature, °C
Molar ratio $K_2Si_7O_{15}/(MgSiO_3+K_2Si_7O_{15})$

(*a*)

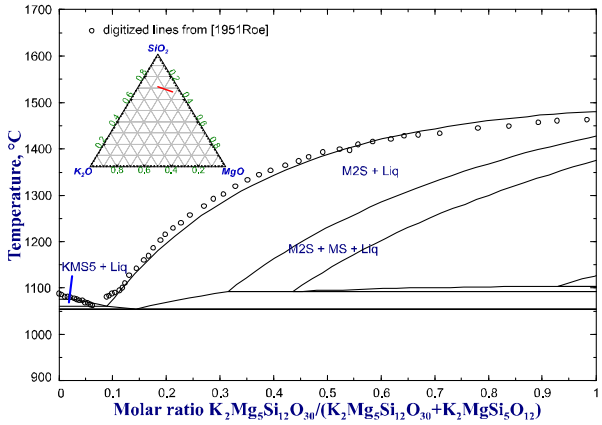
digitized lines from [1951Roe]
M2S + Liq
M2S + MS + Liq
KMS5 + Liq
Temperature, °C
Molar ratio $K_2Mg_5Si_{12}O_{30}/(K_2Mg_5Si_{12}O_{30}+K_2MgSi_5O_{12})$

(*b*)

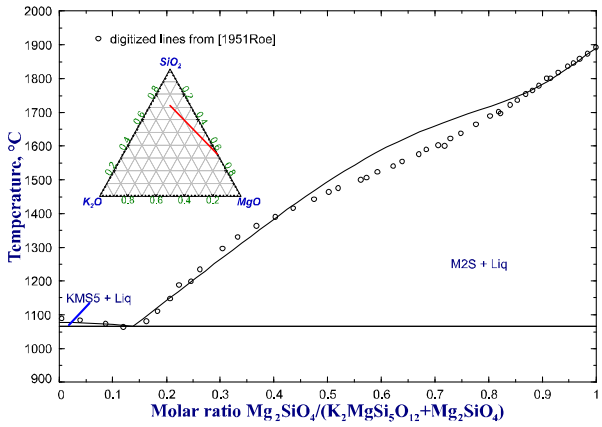
digitized lines from [1951Roe]
M2S + Liq
KMS5 + Liq
Temperature, °C
Molar ratio $Mg_2SiO_4/(K_2MgSi_5O_{12}+Mg_2SiO_4)$

(*c*)

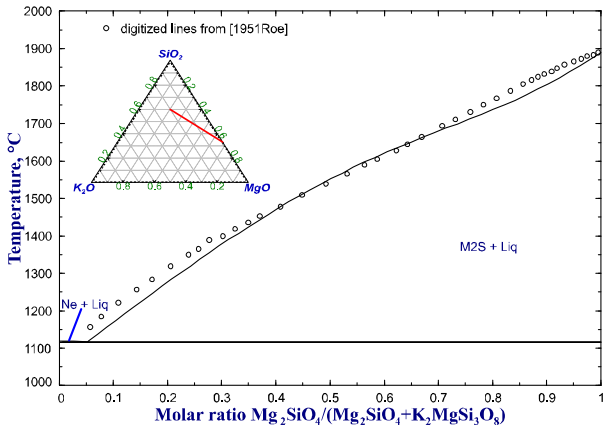
digitized lines from [1951Roe]
M2S + Liq
Ne + Liq
Temperature, °C
Molar ratio $Mg_2SiO_4/(Mg_2SiO_4+K_2MgSi_3O_8)$

(*d*)

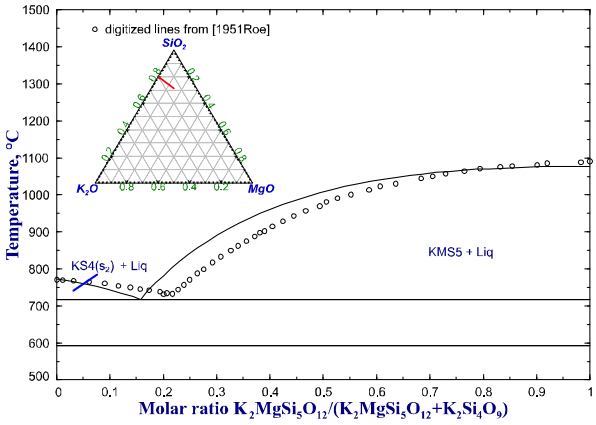
digitized lines from [1951Roe]
KMS5 + Liq
KS4(s2) + Liq
Temperature, °C
Molar ratio $K_2MgSi_5O_{12}/(K_2MgSi_5O_{12}+K_2Si_4O_9)$

(*e*)

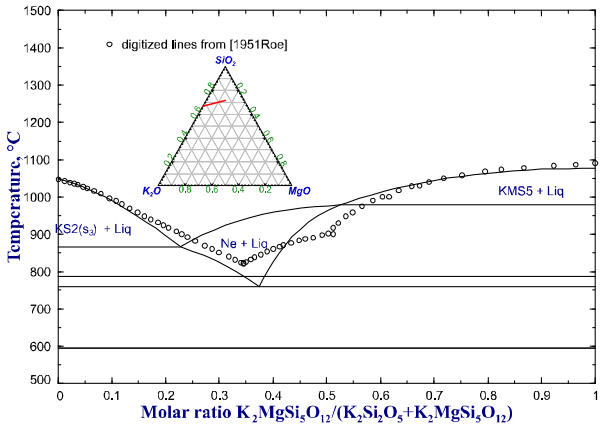
digitized lines from [1951Roe]
KMS5 + Liq
KS2(s3) + Liq
Ne + Liq
Temperature, °C
Molar ratio $K_2MgSi_5O_{12}/(K_2Si_2O_5+K_2MgSi_5O_{12})$

(*f*)

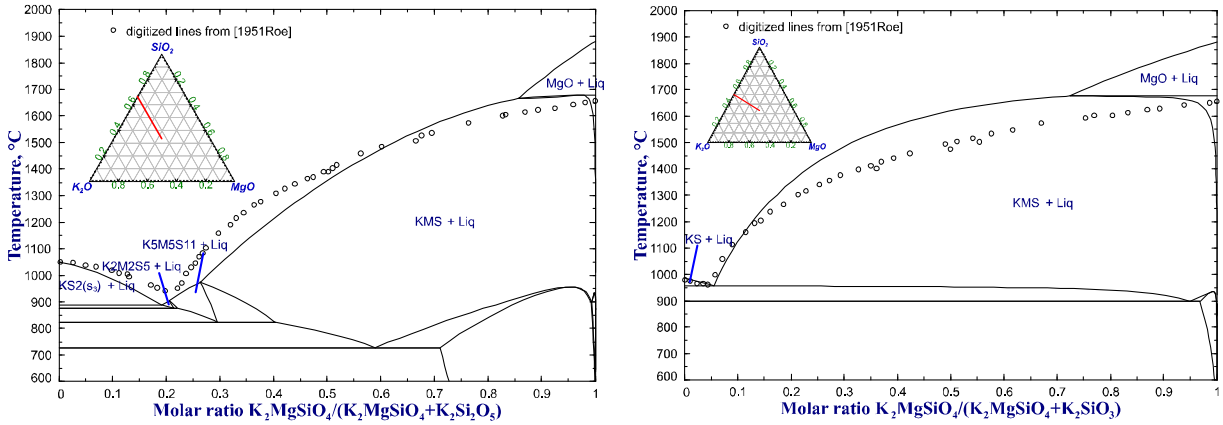

(***g***) (***h***)

Figure 26.6 Phase diagrams in different sections through the K_2O-MgO-SiO_2 system: $MgSiO_3$-$K_2Si_7O_{15}$ (***a***), $K_2MgSi_5O_{12}$-$K_2Mg_5Si_{12}O_{30}$ (***b***), $K_2MgSi_5O_{12}$-Mg_2SiO_4 (***c***), $K_2MgSi_3O_8$-Mg_2SiO_4 (***d***), $K_2Si_4O_9$-$K_2MgSi_5O_{12}$ (***e***), $K_2Si_2O_5$-$K_2MgSi_5O_{12}$ (***f***), $K_2Si_2O_5$-K_2MgSiO_4 (***g***), K_2SiO_3-K_2MgSiO_4 (***h***). Digitized lines from the source (shown as points) [114] and calculated lines.

The invariant points in the ternary system are summarized in Table 26.1.

Table 26.1 Invariant equilibria in the K_2O-MgO-SiO_2 system. The calculated values are shown in bold.

Solid phases	**T, °C**	**Equilibrium type**	**Liquid composition, mol%**		
			SiO_2	**K_2O**	**MgO**
KMS5	1089 [114] **1077**	Melting	71.42 **71.43**	14.29 **14.29**	14.29 **14.29**
KMS3	1134 [114] **1118**	Melting	60.00 **60.00**	20.00 **20.00**	20.00 **20.00**
KMS	1650 [114] **1664**	Melting	33.32 **36.89**	33.33 **36.89**	33.34 **26.23**
Tri-KMS5	987 [114] **1007**	Eutectic	79.65 **77.96**	10.12 **11.02**	10.23 **11.02**
pEn-KM5S12	1174 [114] **1055**	Reaction	75.80 **68.79**	8.59 **12.53**	15.61 **18.68**
KMS5-KM5S12	1063 [114] **1055**	Eutectic	70.71 **70.30**	13.02 **12.22**	16.28 **17.47**
KMS5-Oliv	1053 [114] **1066**	Eutectic	68.82 **69.00**	13.29 **13.37**	17.88 **17.63**
KMS5-KMS3	1030 [114]	Eutectic	67.00	16.43	16.57

Solid phases	T, °C	Equilibrium type	Liquid composition, mol%		
			SiO_2	K_2O	MgO
	1029		**66.91**	**16.55**	**16.55**
KMS5-KS4	730 [114] **718**	Eutectic	77.64 **78.23**	18.46 **18.82**	3.91 **2.96**
KMS3-KS2	933 [114] **913**	Eutectic	63.71 **64.29**	27.55 **28.57**	8.74 **7.14**
KMS3-Oliv	1131 [114] **1116**	Eutectic	59.41 **59.14**	19.61 **19.36**	20.98 **21.50**
KMS-KS2	910 [114] **864**	Eutectic	59.41 **59.63**	33.29 **33.33**	7.29 **7.04**
KMS-KS	950 [114] **954**	Eutectic	48.31 **48.69**	48.48 **48.69**	3.21 **2.63**
KMS?-MgO	>1650 [114] **1664**	–	– **36.89**	– **36.89**	– **26.23**
KMS-KMS3	1110 [114] **1081**	Eutectic	55.84 **55.55**	22.18 **22.23**	21.99 **22.23**
pEn-Cri-Tri	1470 [114] **1471**	Inversion	92.07 **77.89**	4.08 **4.30**	3.85 **17.81**
pEn-Tri-KM5S12	1165 [114] **1103**	Reaction	79.51 **76.67**	7.39 **9.22**	13.10 **14.12**
Tri-KM5S12-KMS5	963 [114] **1007**	Eutectic	79.23 **77.93**	9.82 **11.01**	10.95 **11.05**
Tri-KMS5-KS4	715 [114] **712**	Eutectic	79.80 **79.83**	16.97 **17.31**	3.24 **2.85**
Oliv-pEn-KM5S12	1155 [114] **1091**	Reaction	72.31 **72.95**	10.49 **10.66**	17.19 **16.38**
Oliv-KM5S12-KMS5	1042 [114] **1054**	Eutectic	69.05 **71.35**	13.08 **12.09**	17.86 **16.55**
Oliv-KMS3-KMS5	1013 [114] **1028**	Eutectic	65.92 **66.12**	15.68 **15.98**	18.40 **17.90**
KMS3-KMS5-KS2	795 [114] **760**	Reaction	69.96 **72.33**	22.17 **23.07**	7.87 **4.59**
KMS5-KS2-KS4	685 [114] **689**	Eutectic	74.70 **75.04**	21.18 **21.98**	4.12 **2.98**
KMS3-KMS-KS2	905 [114] **773**	Eutectic	60.60 **60.58**	29.26 **31.36**	10.13 **8.06**
KMS3-KMS-Oliv	1105 [114] **930**	Eutectic	54.50 **55.61**	22.06 **22.29**	23.44 **22.10**
KMS-Oliv-MgO	1350 [114] **1268**	Reaction	42.96 **44.85**	23.49 **20.28**	33.55 **34.87**
KMS-KS2-KS	720 [114] **709**	Eutectic	56.19 **56.76**	42.88 **40.22**	0.92 **3.02**

According to the phase diagram (Figure 26.1-Figure 26.3), there are K2M2S5 and K5M5S11 compounds which were not detected by Roedder [114] and because of their primary fields, there are no stable invariant equilibria KMS3-KS2, KMS3-Oliv, KMS-KS2, KMS-KS, KMS3-KMS-KS2, KMS3-KMS-Oliv. Table 26.1 gives metastable invariant points for these phase assemblages.

26.2 Activity data

The influence of MgO on EMF in potassium trisilicate glasses was investigated by Smith and Rindone [226]. They studied substituted glasses in the $(1\text{-}x)K_2O{\cdot}xMgO{\cdot}3SiO_2$ series where the base $K_2O{\cdot}3SiO_2$ composition served as the reference. To calculate EMF values into K_2O activity, K_2O activity of the reference melt was calculated using the same oxide database as used for the optimization to achieve self-consistency. The data were published in both temperature- and composition-dependent forms (Figure 26.7 and Figure 26.8, correspondingly).

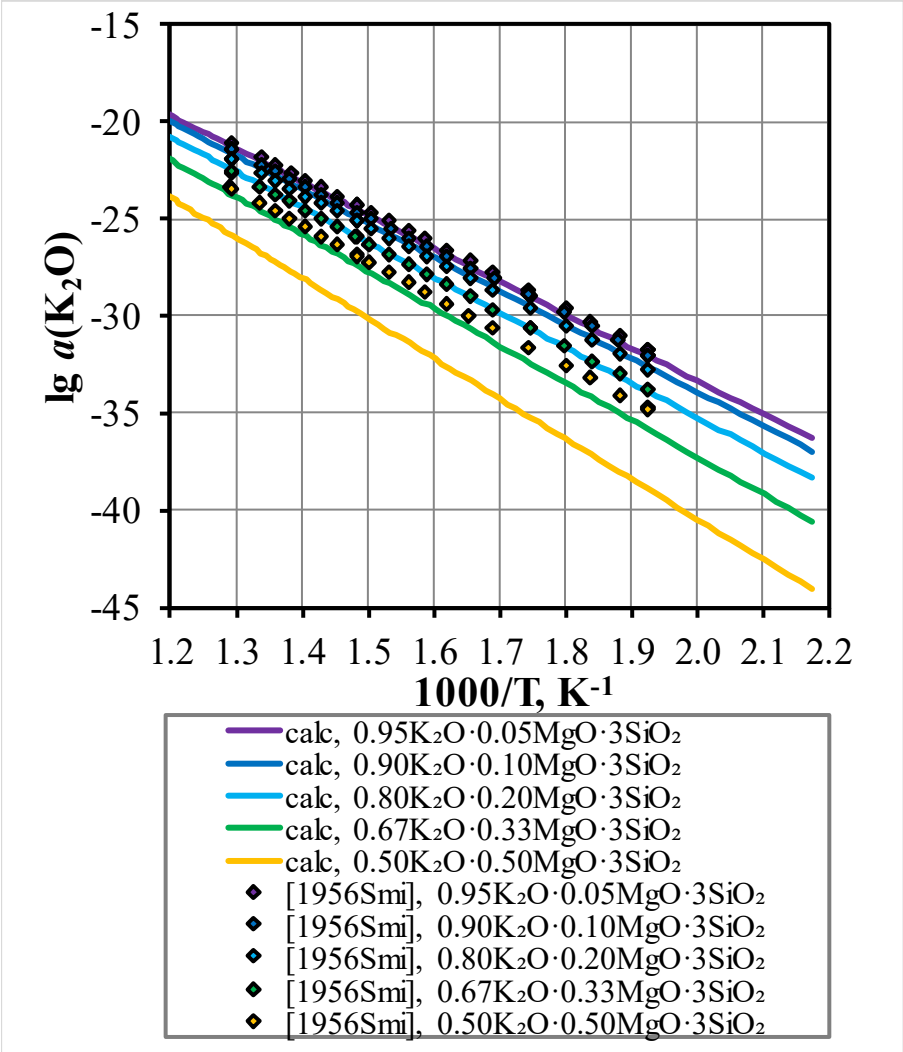

Figure 26.7 Temperature dependence of K_2O activity of the liquid phase at compositions in the trisilicate section. The reference state is the pure liquid K_2O. Experimental points [226] and calculated lines.

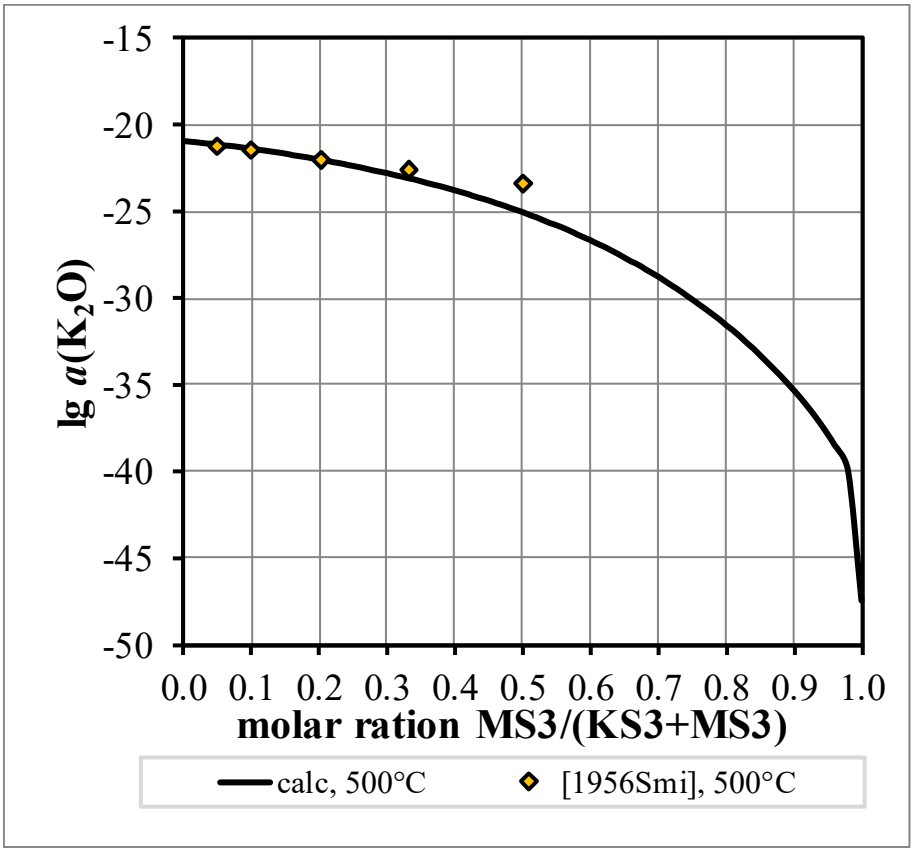

Figure 26.8 K_2O activity of the liquid phase along the trisilicate section at 500°C. The reference state is the pure liquid K_2O. Experimental points [226] and the calculated line.

26.3 Optimization results

The K_2O-SiO_2 binary system was optimized in this work. The optimization of the MgO-SiO_2 system was adopted after Wu et al. [502]. The K_2O-MgO system was assumed ideal.

As there are no thermodynamic data concerning the ternary compounds, the optimization of the system was performed in the following way. First, a simple set of excess parameters in the liquid solution was used to reproduce the liquidus relations of the binary phases whose properties are already known. Then, the properties of the ternary compounds were adjusted to reproduce the rest of the data. The heat capacities of ternary compounds were estimated as weighted sums of the heat capacities of oxides. The enthalpies of formation and, if required, the entropies were corrected in order to reproduce the phase diagram data.

KMS3 compound has a non-stoichiometry range, dissolving excess silica. The compound has the kalsilite structure and must, therefore, be modeled as part of Nepheline solid solution. There are two end-members in the system, $K_8Mg_4Si_{12}O_{32}$ and $K_6Mg_3Si_{13}O_{32}$. Their Gibbs energies are defined by the melting point of the compound and the solubility limit, correspondingly.

KMS compound has a considerable non-stoichiometry range dissolving excess silica. It exists in two modifications and is structurally identical to $KAlO_2$. It is modeled by high-$(Na,K)AlO_2$ and low-$(Na,K)AlO_2$ solid solutions. As SiO_2 end-members of the solutions are already fixed by the optimizations of the other systems, the solubility is modeled by excess interaction terms. There are no data on the composition dependence of the transition temperature; the interaction terms are identical in both solutions.

The optimized parameters are shown in Table A.32 and Table A.33.

CHAPTER 27 MODELING APPROACH TO BORON-CONTAINING SYSTEMS

27.1 Structure of boron-containing melts

Similar to SiO_2, B_2O_3 can be viewed as an acidic network-forming oxide. However, the structural complexity of B_2O_3-containing melts exceeds the complexity of melts containing silica. The coordination number of silicon is fixed and is equal to four. The addition of a network-modifying agent results only in a subsequent breaking of Si-O-Si bonds and formation of sheets, chains, rings or isolated SiO_4^{2-} tetrahedral units depending on the concentration of the network-modifying agent. There are two main factors that make B_2O_3-containing systems different. First, boron is able to change its coordination and is usually present as a mixture of three- and four-coordinated atoms. Second, boron with the coordination number three and a planar configuration has more degrees of freedom of arrangement in 3D structures. The structure of melts and glasses cannot be studied by the conventional X-ray diffraction method as it is sensitive only to the long-range order present in crystalline bodies. ^{11}B NMR spectroscopy is able to distinguish between coordination numbers of boron [558] but it is still unable to give information about finer details of the structure. Structural investigations of melts and glasses were greatly enhanced with the development of IR, Raman spectroscopy and X-ray scattering.

It is generally assumed that the pure amorphous boron oxide changes its structure depending on the temperature. So, at temperatures lower that about 600°C, Raman spectra indicate the presence of a highly symmetrical vibrational mode, inactive in IR spectra. The only reasonable explanation of this fact is the presence of six-membered rings, called boroxol units (see Figure 27.1).

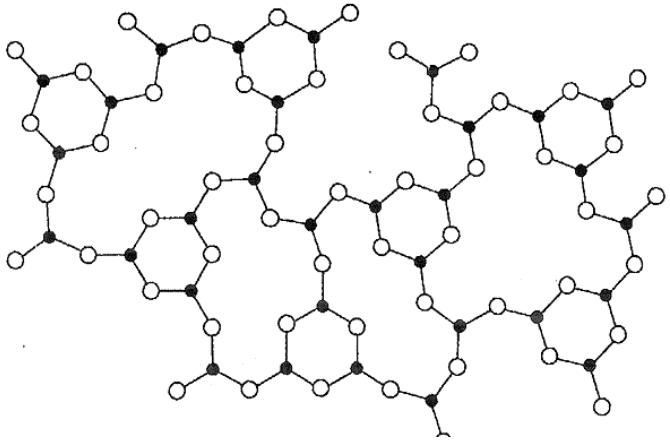

Figure 27.1 The schematic representation of the B_2O_3 glass structure. The image is taken from Krogh-Moe [559].

The presence of boroxol units was also confirmed by the radial distribution function, obtained by X-ray scattering by Strong [560].

Upon heating, the vibrational band of boroxol disappears, indicating that boron oxide transforms to a disordered state. This transition is accompanied by noticeable changes in physical properties, in particular, the density. The viscosity exhibits a non-Arrhenian behavior (Figure 27.2, (***b***)).

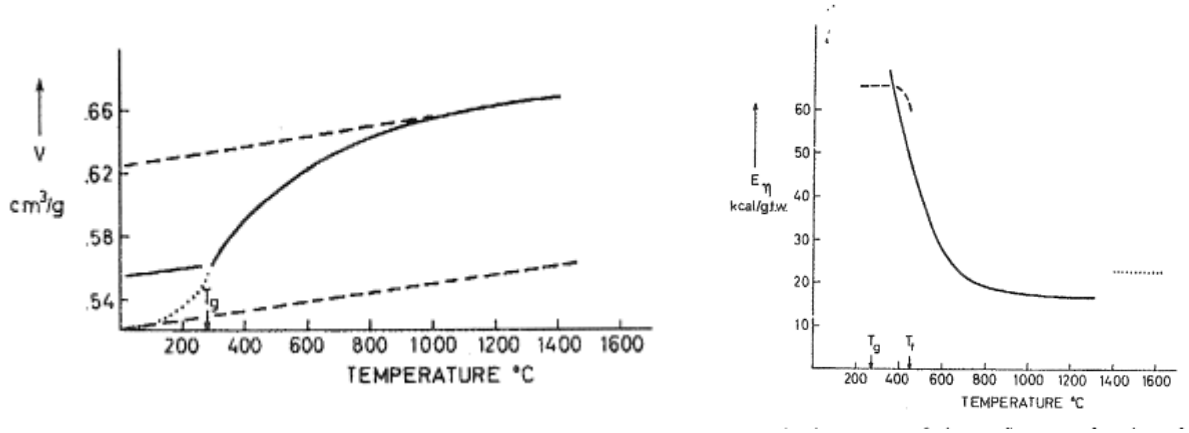

(***a***) (***b***)

Figure 27.2 Specific volume of vitreous and liquid B_2O_3 (***a***) and the apparent activation energy of viscous flow for B_2O_3 (***b***). The images are taken from Krogh-Moe [559].

According to Jellison and Bray [561], boroxol groups have a low degree of interconnectivity with other groups, containing four-coordinated boron. This can be a plausible explanation of the metastable miscibility gap appearing in alkali oxide-boron oxide systems. As it can be seen in Figure 27.3 (***b***), the presence of boroxol is not favored if network-modifiers are added.

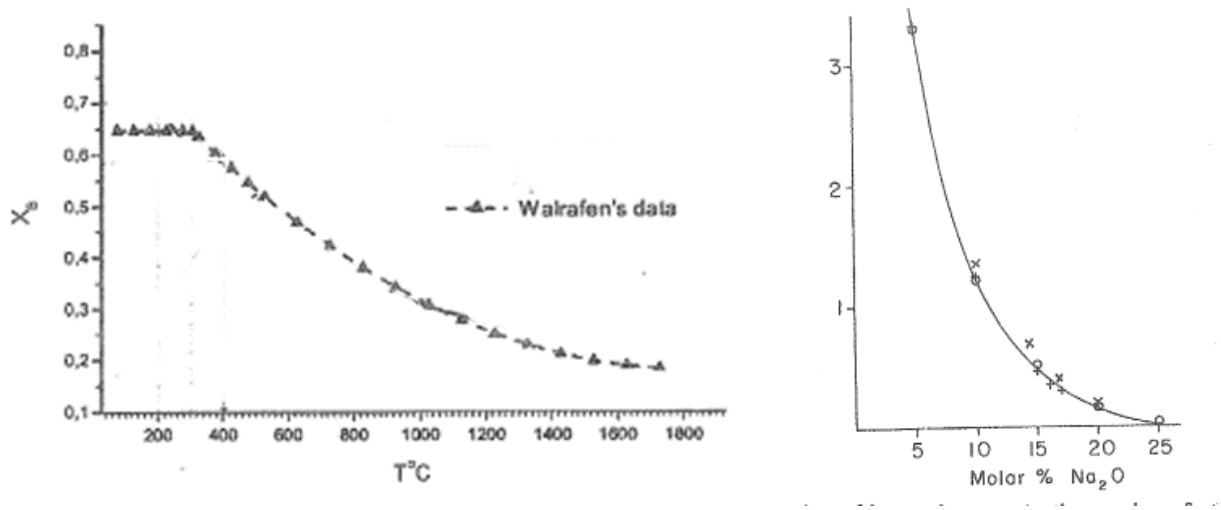

(***a***) (***b***)

Figure 27.3 The concentration of boroxol rings in pure B_2O_3 as a function of temperature (***a***) and the ratio of the number of boron atoms in boroxol groups to the number of other boron atoms in Na_2O-B_2O_3 mixtures at 298K (***b***). The images are taken from Vedishcheva and Shakhmatkin (modified) [562] and Jellison and Bray [561], correspondingly.

NMR studies of Na_2O-B_2O_3 glasses [561] indicated that B^{IV} concentration first grows with Na_2O content to the maximum ratio $B^{IV}/B^{III} = 1$ and then drops back to zero. To explain that, they suggested that B^{IV} can be connected only to four B^{III} or one B^{IV} and three B^{III}. B^{IV} is not stable if surrounded by more than one B^{IV} and the B^{IV} concentration drop is explained by the backward conversion of four-coordinated boron to isolated BO_3^{3-} anions.

The major structural units present in alkali borate glasses and melts are presented in Figure 27.4. Li_2O-B_2O_3 glasses are given as an example but the choice of the alkali cation does not matter a lot.

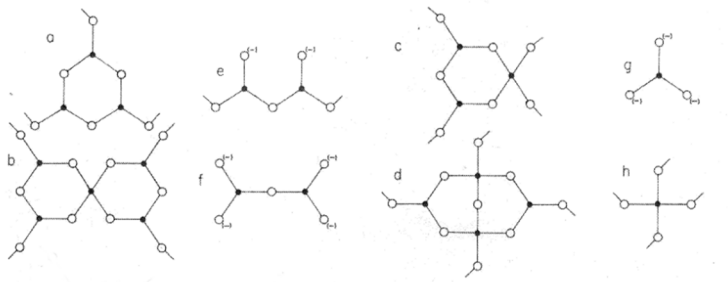

Figure 27.4 The main structural units present in Li_2O-B_2O_3 glasses: boroxol unit (***a***), pentaborate unit (***b***), triborate unit (***c***), diborate unit (***d***), metaborate unit (***e***), pyroborate unit (***f***), orthoborate unit (***g***), loose BO_4 unit (***h***). The image is taken from Bray and Lui [563].

Corresponding sodium-containing melts are characterized by the presence of a tetraborate group instead of triborate and pentaborate groups. As it can be seen from Figure 27.5, tetraborate is equivalent to a triborate and a pentaborate group joined together [563].

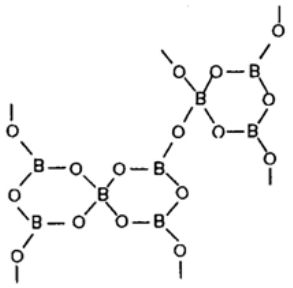

Figure 27.5 Tetraborate group present in Na_2O-B_2O_3 melts. The image is taken from Bray and Lui [563].

27.2 Short-range ordering of boron-containing melts

Short-range ordering in a system indicates that there is a significant preference of species of type A to be surrounded by species B and vice versa. This usually appears as a strong interaction A-B indicating that the reaction:

$$A\text{-}A + B\text{-}B \leftrightarrow 2A\text{-}B \tag{136}$$

is strongly shifted to the right. The composition at which the short-range ordering reaches its maximum is called the maximum short-range ordering (SRO) composition; its position depends on the ratio of the coordination numbers of A and B.

Short-range ordering decreases the configurational entropy of the system compared to an ideal randomly mixed solution; the enthalpy of mixing and the Gibbs energy of mixing change sharply at the maximum SRO composition. Partial properties of the phase (activity, partial enthalpy) change significantly over a narrow compositional interval at the maximum SRO composition. Some other, non-thermodynamic properties can also exhibit similar behaviour (viscosity, ion conductivity).

Analysis of the experimental data available in the Na_2O-B_2O_3 system indicates that there are two maximum SRO compositions. The main one is located at about $x(B_2O_3) = 0.25$ as is seen from the enthalpy of mixing in the system. The second composition of maximum SRO is located at $x(B_2O_3) = 0.80$ which corresponds to the tetraborate composition. Its presence is confirmed by the data on the partial enthalpy [564] and Na_2O activity [565-570]. Another fact that makes the alkali borate systems special is that the metastable miscibility gap is located right below the short-range composition; as a rule, these phenomena are mutually exclusive.

27.3 Metastable miscibility gap anomaly in alkali oxide-boron oxide systems

Metastable miscibility gaps are quite common in binary systems consisting of a network former and a network modifier. Alkali silicate and alkali-earth silicate systems are a good example of that. The critical temperature changes in the series MO-SiO_2, where M = Mg, Ca, Sr, Ba (see Figure 27.6). There is a pretty good correlation between the critical temperature and the charge/radius ratio of the cation. The shape of the miscibility gap can be predicted using the Debye-Hückel theory, i.e. the miscibility gap arises due to electrostatic interactions of cations with the silica network.

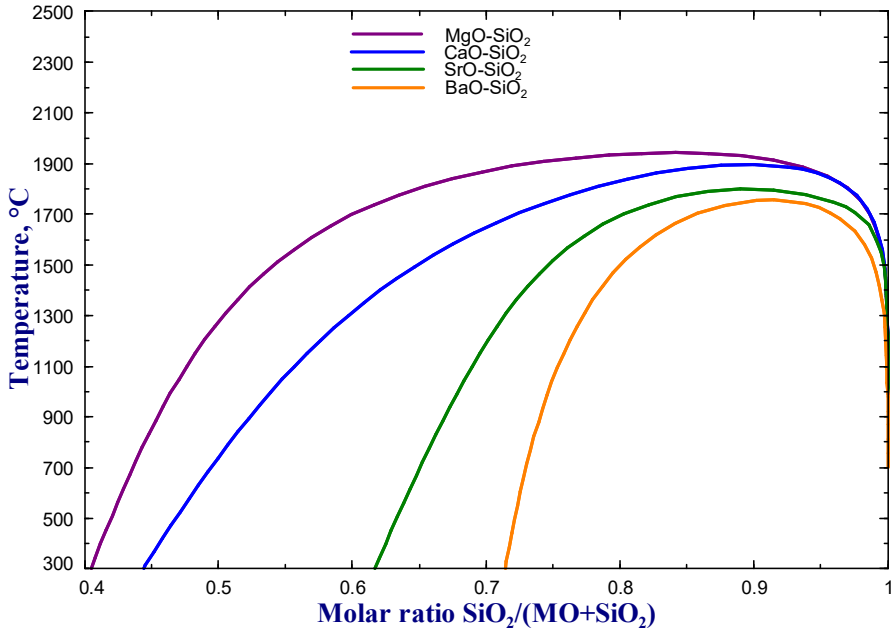

Figure 27.6 Miscibility gaps in the MO-SiO_2 systems, where M = Mg, Ca, Sr, Ba, calculated based on the existing optimizations in the *FToxid* database.

However, the alkali borate systems fall off the general trend and exhibit only insignificant variations of the critical temperature for different alkali cations (Figure 27.7).

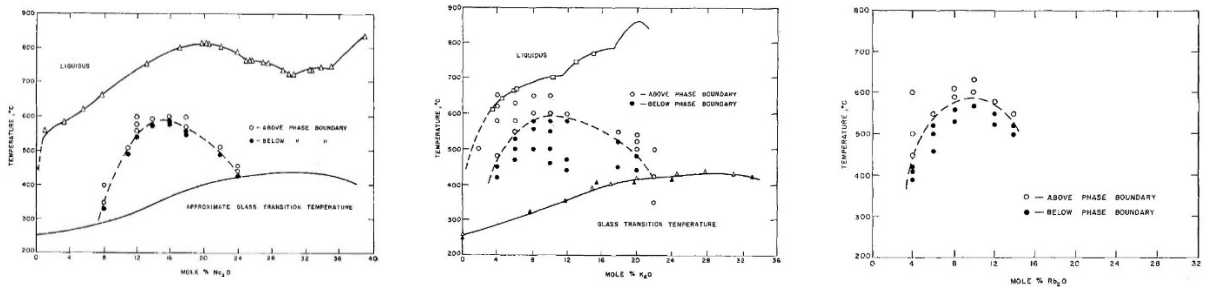

(***a***) (***b***) (***c***)

Figure 27.7 Metastable miscibility gaps in Na_2O-B_2O_3 (***a***), K_2O-B_2O_3 (***b***), Rb_2O-B_2O_3 (***c***) systems. The images are taken from Shaw and Uhlmann [571].

The critical temperature for alkali borate systems approximately coincides with the temperature at which boroxol disappears from borate melts. Given the insensitivity of the T_C to alkali cation and the low connectivity of boroxol groups with B^{IV} [561], we assume that the miscibility gaps arise due to the presence of boroxol groups segregated from the rest of the alkali-

containing phase. The immiscibility disappears completely at temperatures higher than the boroxol decomposition temperature and the same compositions start to exhibit a moderate short-range ordering tendency.

27.4 Ternary miscibility gaps in M_2O-B_2O_3-SiO_2 systems

The properties of ternary M_2O-B_2O_3-SiO_2 melts change significantly with composition. So, in the low alkali region there is a metastable miscibility gap as shown in Figure 27.8. The tie-lines (not shown in Figure 27.8) run from the Na_2O-B_2O_3 side to SiO_2 corner [572, 573]. This miscibility gap is important for industrial applications because glasses prepared in the immiscibility region form a porous interconnected structure with very good thermal and mechanical properties after a chemical treatment [574, 575].

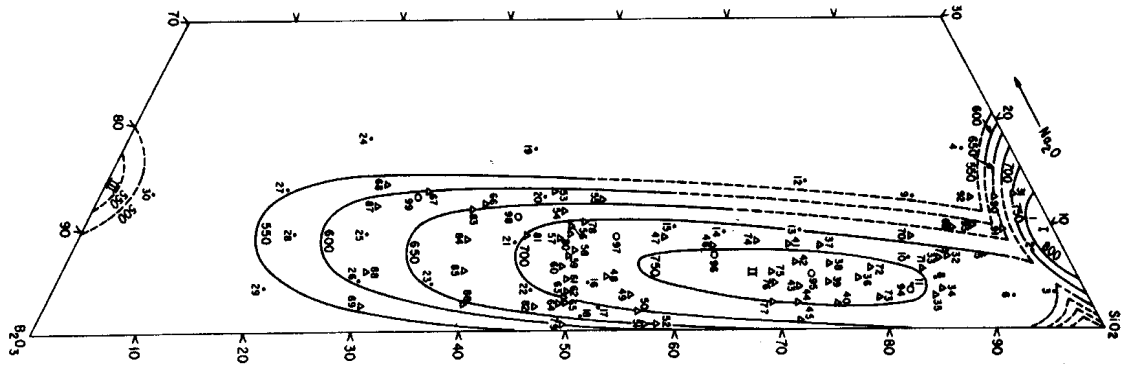

Figure 27.8 Metastable miscibility gap in the Na_2O-B_2O_3-SiO_2 system. The image is taken from Haller et al. [575].

In this work, it is proposed that ternary miscibility gaps appear due to the following exchange reaction:

$$xB_2O_3+(Na_2O)_{1-x}(SiO_2)_x \leftrightarrow (Na_2O)_{1-x}(B_2O_3)_x+xSiO_2 \quad (137)$$

The reaction (137) is shifted to the right thus forming a stable pair of reactants which leads to immiscibility phenomena. In fact, the reason why the miscibility gap appears is somewhat similar to the reason for miscibility gaps in reciprocal salt systems [465].

27.5 Liquid phase model

A good solution model must represent all the essential features of a system in a natural way. For example, for a system with a short-range ordering the Modified Quasichemical Model could be used as it was specifically designed for this kind of systems. It is obvious that the Na_2O-B_2O_3 system requires the short-range ordering to be accounted for. However, there are two maximum SRO compositions and the standard MQM allows to have only one. The second composition could be reproduced if an extra species were to be introduced in the model. Usually, an additional species is added based on the structural data of melts.

As it was shown before, there are many structural units in the Na_2O-B_2O_3 glasses and melts. It would not be wise to include them all in the model; each extra species greatly increases the number of degrees of freedom of a model: one would need to constrain the stabilities and the parameters of cross-interactions. It is usually hard to find a physically consistent way to set these degrees of freedom; an incorrect or an inconsistent optimization could lead to difficult-to-find artefacts in the multicomponent systems, such as spurious miscibility gaps. Usually, it is recommended to use as few species and degrees of freedom as possible to represent all the essential experimental features.

Obviously, the model must expand the two-sublattice Modified Quasichemical Model used for other subsystems in the project (the B_2O_3-SiO_2 system by Decterov et al. [15]). The optimizations of the alkali-non-boron systems and boron systems without alkalies provide us with Na^+, $(Na_2)^{2+}$ and B^{3+} species on the cationic sublattice. Alkali dimer $(Na_2)^{2+}$ is only relevant for silica-containing systems with a caging effect. Planar configuration of boron in pure boron oxide allows for newly introduced Na^+ cations to migrate over the network independently. No noticeable amounts of the dimer should be found in the Na_2O-B_2O_3 system. The main composition of maximum SRO (short-range ordering) must be represented by the Na^+-B^{3+} interaction. The structural data indicate that at $0.75Na_2O$-$0.25B_2O_3$ composition there are BO_3^{3-} and Na^+ ions in the liquid. To reproduce the second maximum SRO composition at $x(B_2O_3) = 0.80$, an extra species was added. There are at least three different ways to do that.

The extra species could be NaB^{4+}, somewhat similar to $NaAl^{4+}$. The second maximum SRO composition would appear due to the NaB^{4+}-B^{3+} interaction. This variant was called the monoborate model. NaB^{4+} species would account for B^{IV} in the liquid.

The second model was proposed based on the observation that B^{IV} fraction does not exceed 0.5. The structural unit with the same B^{IV} fraction is diborate $Na_2B_4^{14+}$; half of boron atoms in a unit are four-coordinated. We could assume that the second maximum SRO composition appears due to $Na_2B_4^{14+}$-B^{3+} interaction. The advantage of the diborate model is that ^{IV}B fraction never exceeds 0.5.

The third model assumes that the tetraborate itself is included as the extra species (tetraborate model). However, B^{IV} content would not exceed 0.25 and there is no possible way to reproduce the binary miscilibity gap data as the gap is situated right below the associate composition.

After multiple trials with all the three models, it was decided to use the monoborate model. A correct choice of the interaction parameters makes B^{IV} fraction not to exceed 0.5 and it is even possible to reproduce the metastable miscibility gap consistently with the rest of the experimental data within the binary system. This model also works much better if other components are added, such as SiO_2.

CHAPTER 28 OPTIMIZATION OF THE Na_2O-B_2O_3 SYSTEM

28.1 Phase diagram

The phase diagram of the Na_2O-B_2O_3 system was investigated by many methods (Figure 28.1). For example, Morey and Merwin [576] performed quenching of samples. The heating curve method with precrystallized samples was employed by Jenckel [577] and Milman and Bouaziz [578]. A group of authors used oscillation technique [334, 579]. The oscillation method consists in measuring the amplitude and the frequency of an oscillating thin plate immersed in a liquid as a function of its viscosity. The parameters of oscillation are highly sensitive to changes of the phase composition. The method is described in detail in the work of Kaplun and Meshalkin [580]. Golubkov and Shakhmatkin [581] used SAXS technique to measure the liquidus. Visual polythermal method was employed by Vartbaronov and Bergman [582]. The visual polythermal method consists in visual observation of the crystallization process of a transparent liquid with temperature.

Similar to the Na_2O-SiO_2 system, mixture properties change significantly with the composition. The cheapest and most convenient way to prepare a sample is to use H_3BO_3 and Na_2CO_3 as precursors. However, mixtures with more than 50 mol% of Na_2O cannot be prepared this way and pure Na_2O had to be used as a reagent [583], as in the work by Milman and Bouaziz [578]. Compositions rich in B_2O_3 (80-100 mol%) are difficult to crystallize [577, 578], and it is very hard to get rid of traces of water [576]. Na_2O-B_2O_3 melts are characterized by high volatility of both sodium and boron oxides. $NaBO_2$(g) is a stable gaseous species, and boron oxide volatility increases significantly with addition of Na_2O [576].

The Na_2O-B_2O_3 system has many stoichiometric compounds but none of them seem to form solid solutions with noticeable solubility ranges.

Many stoichiometric compounds in the system have polymorphic modifications, stable over a certain temperature range or metastable. The Na_2O-B_2O_3 phase diagram is remarkable in the sense that many of these modifications have slow transformation rates and it is often possible to register metastable phase equilibria.

Sodium orthoborate Na_3BO_3 was reported by Milman and Bouaziz [578]. It has a congruent melting point at 675°C. The crystal structure was reported by Koenig and Hoppe [584].

Sodium pyroborate $Na_4B_2O_5$ melts congruently [576, 578, 585].

$Na_6B_4O_9$ compound decomposes at 575°C but could not be identified by X-ray.

Sodium metaborate $NaBO_2$ melts congruently [576-579] and has two polymorphic modifications with the transformation temperature of 730°C [578]. The crystal structure was reported by Fang [586] and by Marezio et al. [587].

$Na_4B_6O_{11}$ is a "hanging" phase; it has a lower and upper stability limit [578]. However, the compound was not confirmed by X-ray [588] and its existence was questioned by Liang [589].

Sodium diborate $Na_2B_4O_7$ is a congruently melting phase [578]. It has three polymorphic modifications (high-*T* α, medium-T β and low-*T* γ) [576, 579]. According to DTA curves, the transformations occur at 560° and 640°C [590]. However, calculations based on calorimetry data showed that only γ- and α-phases are truly stable (with transition temperature of 571°C) while β-phase is always metastable [590].

$Na_4B_{10}O_{17}$ is another "hanging" phase with a lower and upper stability limit and its existence was not confirmed by X-ray. According to Kaplun and Meshalkin [579], the heat of the upper decomposition reaction is significant while for the lower decomposition it is hard to detect. Liang [589] proved that the phase is metastable.

Sodium triborate NaB_3O_5 forms either a stable peritectic [576, 578] or shows a metastable congruent melting [578]. According to Kaplun and Meshalkin [579], the compound melts congruently (stable). A metastable liquidus of the compound was reported [334, 577]. Krogh-Moe studied the crystal structure of α-NaB_3O_5 [591] and β-NaB_3O_5 [592].

Sodium tetraborate $Na_2B_8O_{13}$ has a stable α- and a metastable β-modification [578]. The congruent melting points of both modifications have been measured [576-578, 593]. A metastable liquidus of β-$Na_2B_8O_{13}$ was reported by Jenckel [577]. The crystal structure of β-modification was studied by Penin et al. [594], α-modification by Hyman et al. [595] and Bubnova et al. [596].

Sodium pentaborate NaB_5O_8 has three polymorphic modifications (α, β, γ) [578]. It forms a peritectic [578, 579, 597].

Sodium enneaborate NaB_9O_{14} melts with formation of a peritectic and has three stable modifications with transformation temperatures of 325°C for γ/β and 643°C for β/α [578]. This compound is very hard to obtain, annealing times of one month were required [578]. It is possible that some authors who do not report the compound may have overlooked its formation.

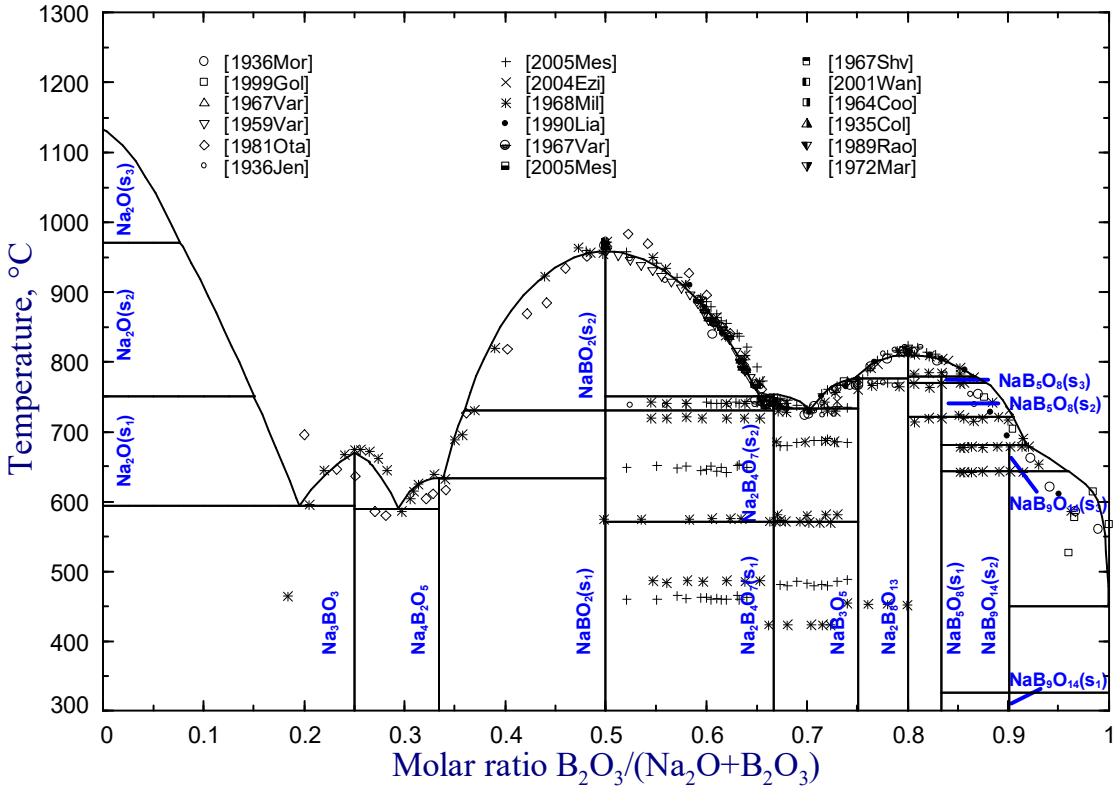

Figure 28.1 Phase diagram of the Na_2O-B_2O_3 system. Experimental points [334, 576-578, 581, 582, 589, 598-608] and calculated lines.

The metastable miscibility gap in the Na_2O-B_2O_3 system (Figure 28.2) was investigated by Shaw and Uhlmann [571]. Glass samples were held in a furnace with a thermal gradient; the annealed samples were investigated by the direct-transmission electron microscopy. It is noted that light scattering techniques do not work in this case because of a very small range of homogeneity. Du et al. [609] studied the immiscibility of a single composition at 500°C by XRD, NMR and SEM techniques. There are a few other works dealing with the immiscibility phenomena in the sodium borate system but apparently, they all cite the same experimental data by Shaw and Uhlmann [571].

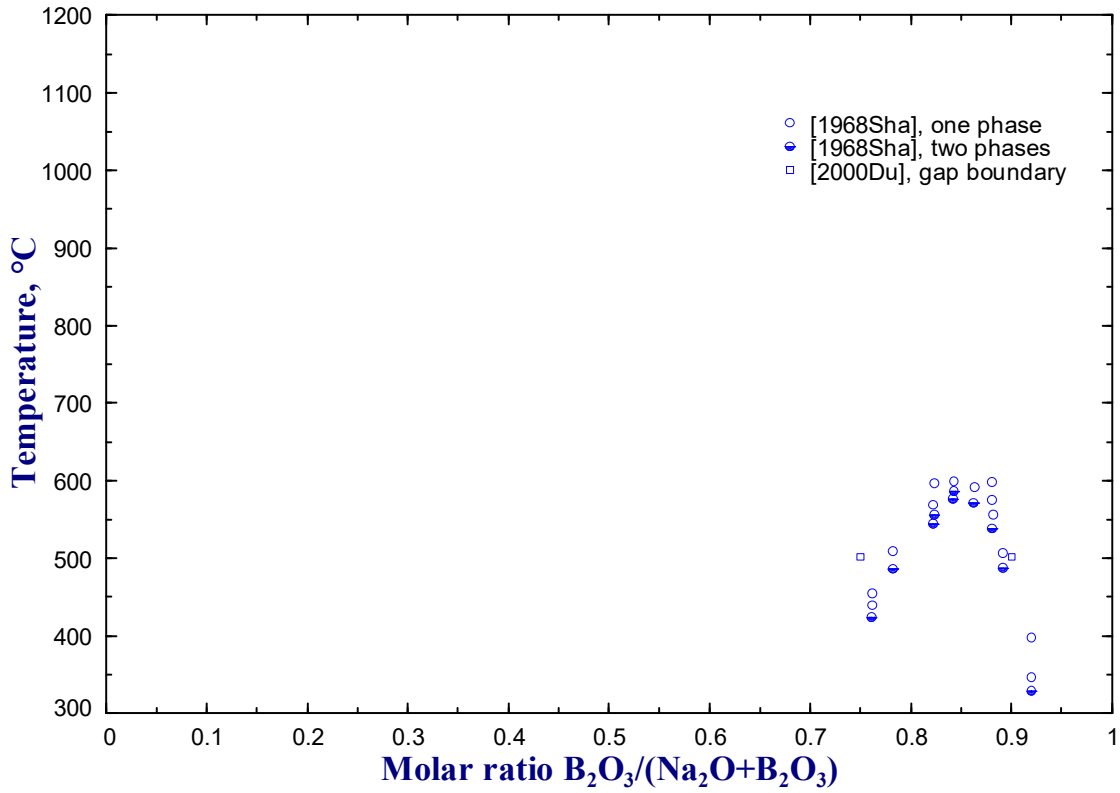

Figure 28.2 Metastable miscibility gap in the Na_2O-B_2O_3 system. Experimental points [571, 609].

In the present study it was decided not to reproduce the metastable miscibility gap. The reason why it was not reproduced is discussed in detail in section 28.6.

28.2 Calorimetry data

Several types of solution calorimetry in the Na_2O-B_2O_3 system can be found in the literature. Julsrud and Kleppa [610] performed a direct calorimetry using $NaBO_2$ and B_2O_3 as starting compositions. The experiments were performed under a nitrogen atmosphere at 975±2°C. Both components were maintained and brought to reaction at the operating temperature. The reproducibility of calibrations was ±1%. B_2O_3 and $NaBO_2$ were prepared from H_3BO_3 and $Na_2B_2O_4{\cdot}2H_2O$ by calcining them at high temperatures. The partial enthalpies are also given but were determined by the tangent method (good agreement with the results by Ostvold and Kleppa [564]). Fan [197] performed direct reaction calorimetry of pure Na_2O and B_2O_3. A mixture of crystalline Na_2O and glassy B_2O_3 were dropped into a calorimeter at a constant temperature above the glass transition temperature. Na_2O was obtained from NaN_3 and $NaNO_3$. The compositions

with more than 80 mol% Na_2O were not investigated because of their high corrosive effect on the calorimeter walls. To recalculate the raw data, the author took enthalpy increments and the heat of melting of Na_2O from Barin et al. [611] which is in a good agreement with *FactSage* databases. The data of Julsrud and Kleppa [610] are in a good agreement with those by Fan [197], although they are not independent: to recalculate the enthalpy of mixing of $NaBO_2$-B_2O_3 to the enthalpy of mixing of Na_2O-B_2O_3, a value of $\Delta_f H(NaBO_2)$ was taken from Fan [197]. In this work, the data on the enthalpy of mixing of both sources [197, 610] were taken directly from the work of Fan [197] without additional recalculations. We assume that direct reaction calorimetry is not well suited for alkali borate systems similar to alkali silicate systems. Although the reaction starts quite intensely, its last stage is sluggish and the obtained enthalpy of mixing is less negative that the real value.

The solution calorimetry of Na_2O-B_2O_3 liquids, glasses and crystalline solids allows to overcome this drawback. The acid calorimetry is one of the common examples. One of the most popular solution media is diluted HNO_3 (usually, 2N concentration). Calorimetric measurements were performed at 298K [612-620] and at 273K [621]. Shul'ts et al. [613] took special precautions to avoid sample hydration and indicated that the disagreement with other works [617, 619] arise from the water presence in their samples. To recalculate the solution calorimetry data in 2N HNO_3, the value of −33.47 kJ·mol^{-1} for solution of vitreous B_2O_3 from Yoshio and Takahashi [619] and −351.04 kJ mol^{-1} for solution of crystalline Na_2O from Shartsis and Capps [617] were used. The latter was calculated based on the values of the heat of neutralization of dilute solutions of a strong base by a strong acid and the heat of solution of Na_2O in water. The heat of transformation of crystalline Na_2O to liquid Na_2O was calculated using the *FToxid* database.

Adami and Joe [622] performed the solution calorimetry of crystalline sodium borates in HCl solution. The value of $\Delta_f H(Na_2O(cr))$ used by Adami and Joe to recalculate the results into the enthalpies of formation from oxides was -415.9±4.2 kJ·mol^{-1} which is in a good agreement with the value of −418.02 kJ·mol^{-1} from *FactSage*.

The glass calorimetry data were recalculated into the enthalpy of mixing of liquid according to the procedure described in Section 2.5.2. The recalculated calorimetry data on glasses and liquids are summarized in Figure 28.3.

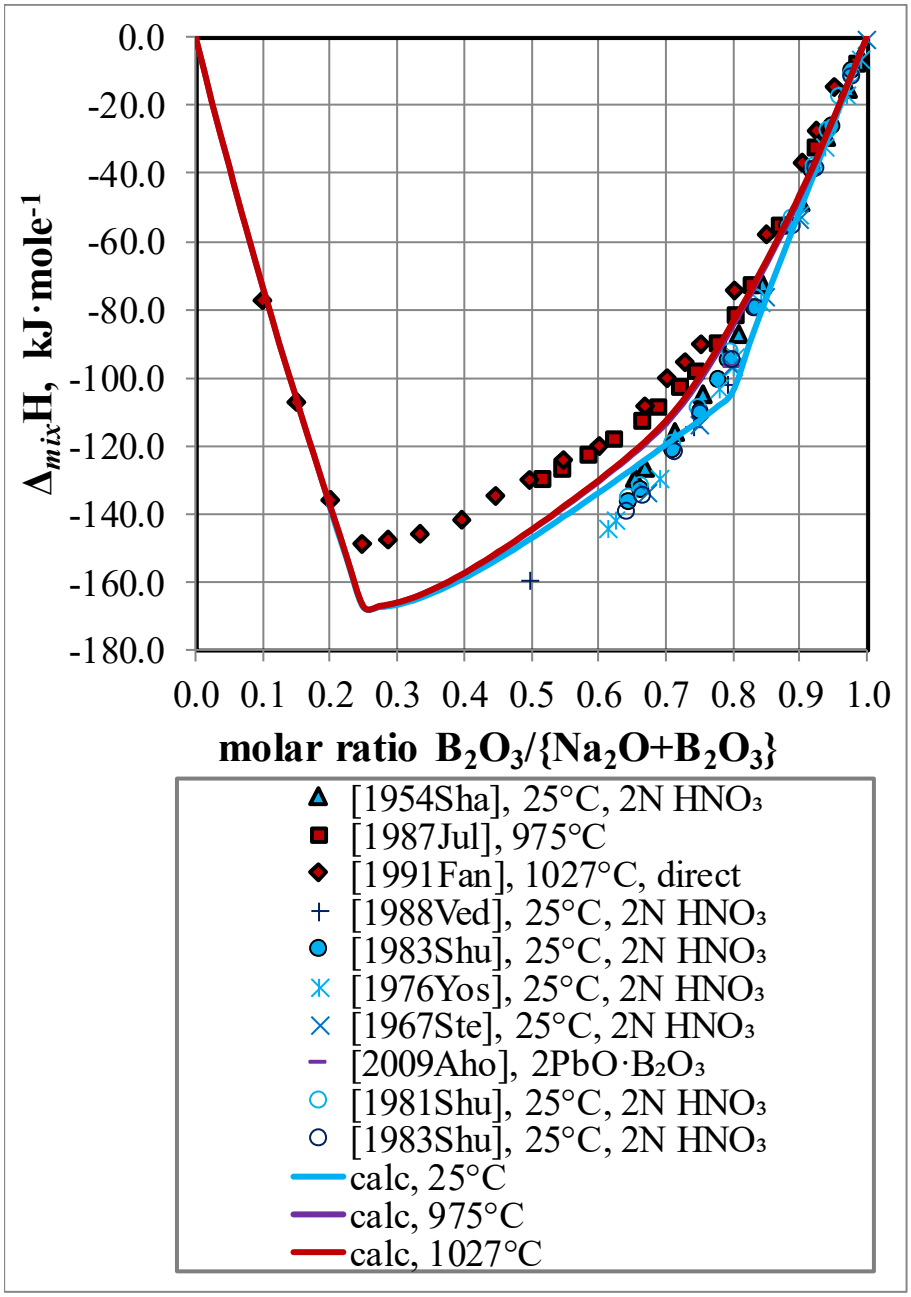

Figure 28.3 The enthalpy of mixing of the liquid phase in the Na_2O-B_2O_3 system. Experimental points [197, 201, 610, 614, 616-619, 623] and calculated lines.

The recalculated data on crystalline solids are gathered together in Figure 28.4. Cooper and Scarpiello [605] and Slough and Jones [624] assessed the available data in the literature and published the recommended values of the enthalpy of formation of sodium borate compounds.

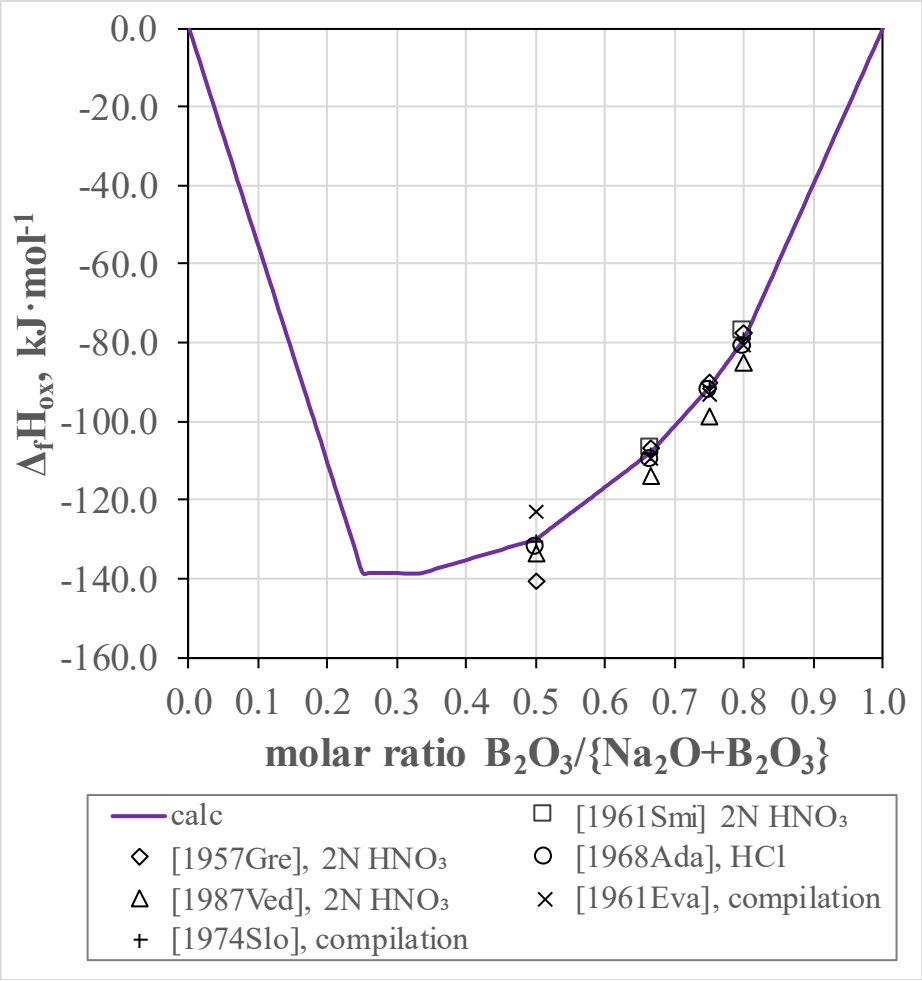

Figure 28.4 The enthalpy of formation from oxides of crystalline compounds in the Na_2O-B_2O_3 system. Experimental points [615, 620-622, 624, 625] and the calculated line.

Ostvold and Kleppa measured the partial enthalpy of B_2O_3 in liquid sodium borates at 985°C. The data were taken directly from the source without any recalculations. Their data are presented in Figure 28.5.

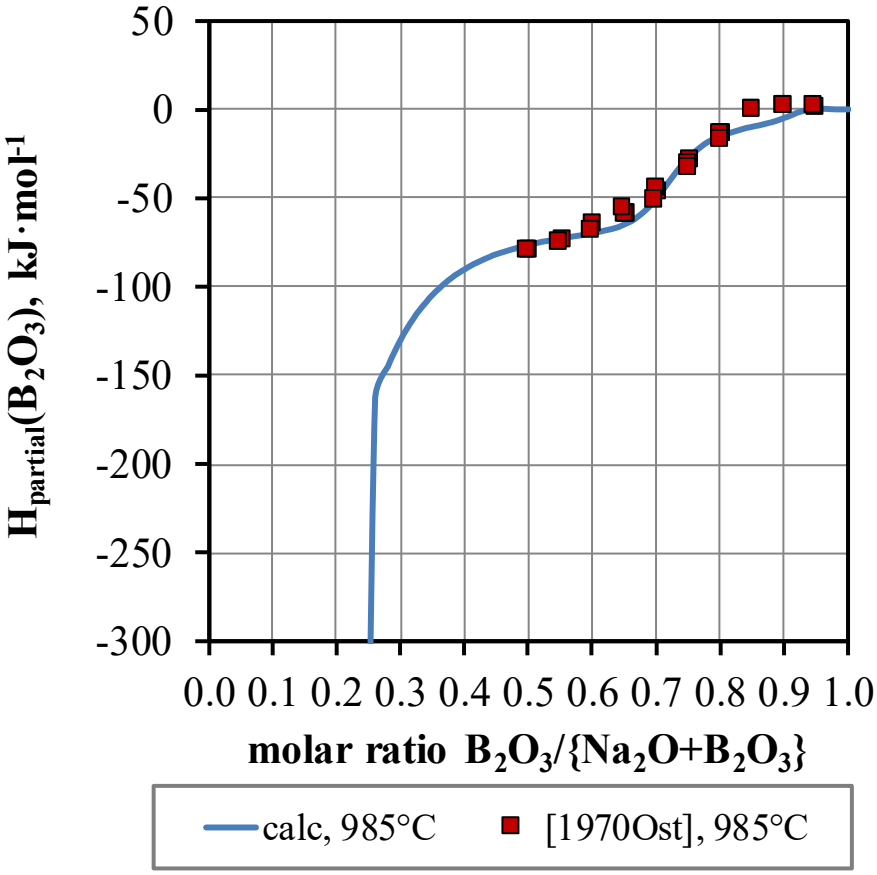

Figure 28.5 The partial enthalpy of B_2O_3 in the Na_2O-B_2O_3 system. Experimental points [564] and the calculated line.

28.3 Activity data

There is a series of works dealing with measurement of Na_2O activities in Na_2O-B_2O_3 melts and glasses. Park and Min measured Na_2O activity using equilibration with an Ag-Na alloy (which was considered as a Henrian solution of Na in Ag) in a CO/CO_2 atmosphere [626, 627].

Voronkova and Ivanova [568] and Asai [628] measured EMF of sodium borate melts with $Na_2B_4O_7$ melt as a reference. Itoh et al. performed analogous measurements with $Na_2B_4O_7$ melt as a reference [566] and a $(Na_2O)_{0.05}(B_2O_3)_{0.95}$ melt as a reference [565]. Sato et al. [569] also performed measurements with a $(Na_2O)_{0.05}(B_2O_3)_{0.95}$ reference. A reference melt with a very low sodium oxide content (0.7-1.0 mol% Na_2O) was employed by Stegmaier and Dietzel [570]. Kuehne [567] used a

reference with the composition $0.28Na_2O{\cdot}0.72B_2O_3$ which is close to diborate. One of the problems of reference melts with low Na_2O content is high hygroscopicity.

Unless indicated otherwise, all EMF data were recalculated in this work to Na_2O activity with the standard state of Na_2O(liq). The properties of the pure liquid Na_2O were taken from *FactSage* databases. Na_2O activity in reference melts was also calculated with the same *FactSage* database as used for the optimization.

Kozhina and Shul'ts employed a pre-crystallized $(Na_2O)_{0.32}(Al_2O_3)_{0.17}(SiO_2)_{0.51}$ glass as a reference for EMF measurements [222]. The data were presented in form of Na_2O chemical potential recalculated to Na_2O(liq) standard state. There are no indications about the Na_2O reference activity used for recalculations and the data were accepted without additional recalculations.

Shakhmatkin and Shul'ts measured EMF of Na_2O-B_2O_3 melts at 700-1000°C [629, 630]. A $(Na_2O)_{0.2}(SiO_2)_{0.8}$ melt was used as a reference. Measured EMF values changed with time reaching a maximum and slowly going down. This maximum was considered as the equilibrium value and the subsequent decrease was explained by a partial mixing. The data were presented in form of Na_2O chemical potential and no recalculation was made as the initial EMF data are unavailable.

Mass spectroscopic measurements of vapor pressures are reported by Shul'ts et al. [631]. $NaBO_2$ is a predominant species over melts with a sufficient Na_2O content but B_2O_3 vaporization is also possible. These data were not taken into consideration because there are multiple species present in the vapor phase and the ways to recalculate the vapor pressure data into the activities are ambiguous [631].

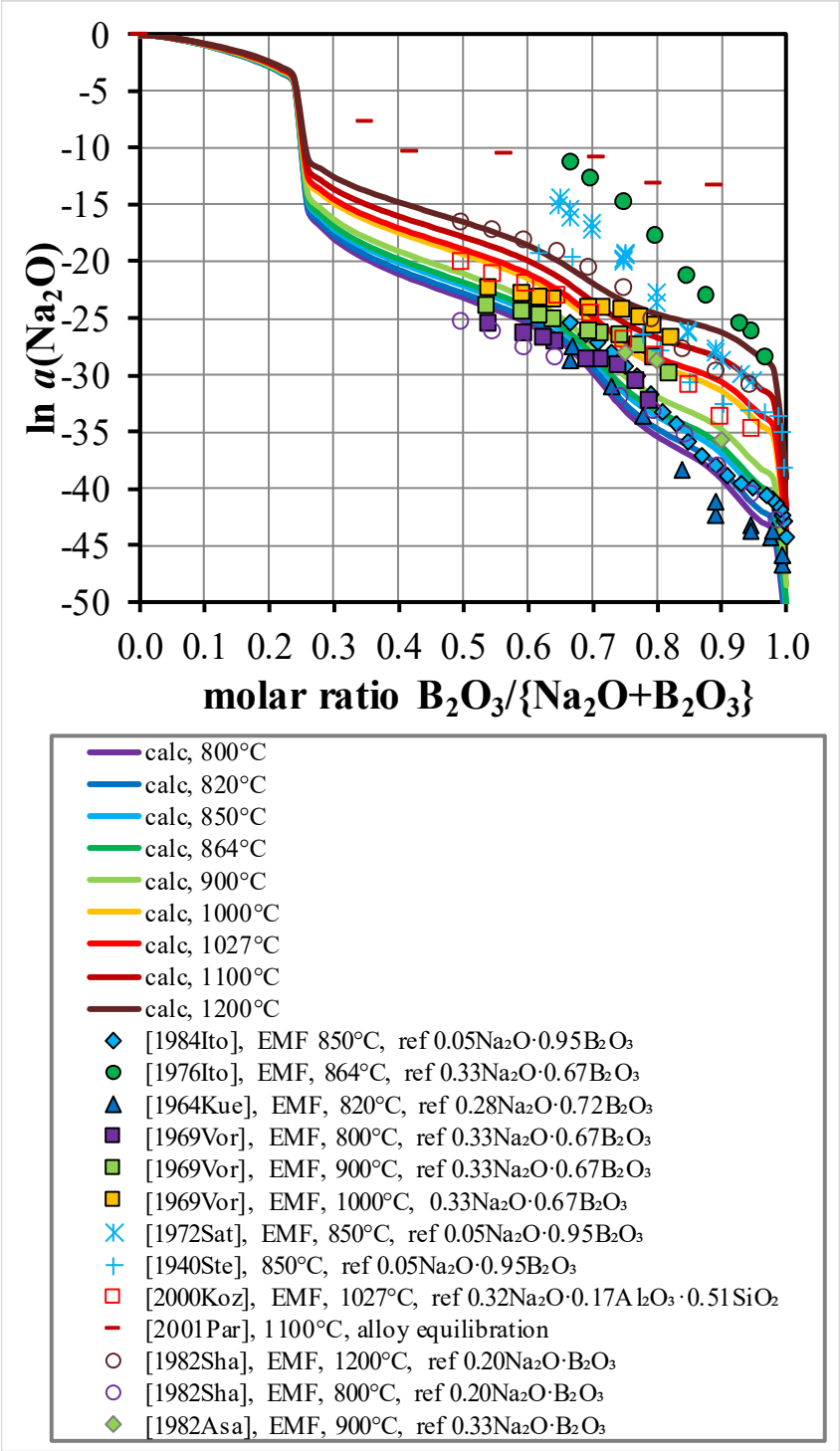

Figure 28.6 Na_2O activity in the liquid phase in the Na_2O-B_2O_3 system. The reference state is the pure liquid Na_2O. Experimental points [565-570] and calculated lines.

The activity data are summarized in Figure 28.6. We explain the disagreement of the data by Sato et al. [569] and Stegmaier and Dietzel [570] by the fact that $0.05Na_2O{\cdot}B_2O_3$ melt was used as a reference, a composition which is very hydroscopic. The uncontrolled water absorption can lead to significant deviations from the true EMF values. Apparently, Itoh et al. [565] managed to avoid water absorption although it is not mentioned in their work. The data by Park and Min [626, 627] do not agree with the rest of the data; we can assume that the problem lies in the experimental method they used.

28.4 Species distribution data

There is a significant amount of work related to Nuclear Magnetic Resonance Spectroscopy (NMR) of alkali borate glasses and species. Characteristic spectra emitted by boron nuclei are influenced by their nearest neighbours and, in particular, the coordination number. Integration of the signals allows to calculate the relative content of three- and four-coordinated boron in a sample. Both ^{10}B and ^{11}B NMR can be performed [561, 609, 632-635].

Another method of investigating the boron coordination is Raman spectroscopy. There are characteristic bands in a spectrum which correspond to the three- and four-coordinated boron. This technique also allows to perform measurements at elevated temperatures and see the structural differences of glasses and melts [636].

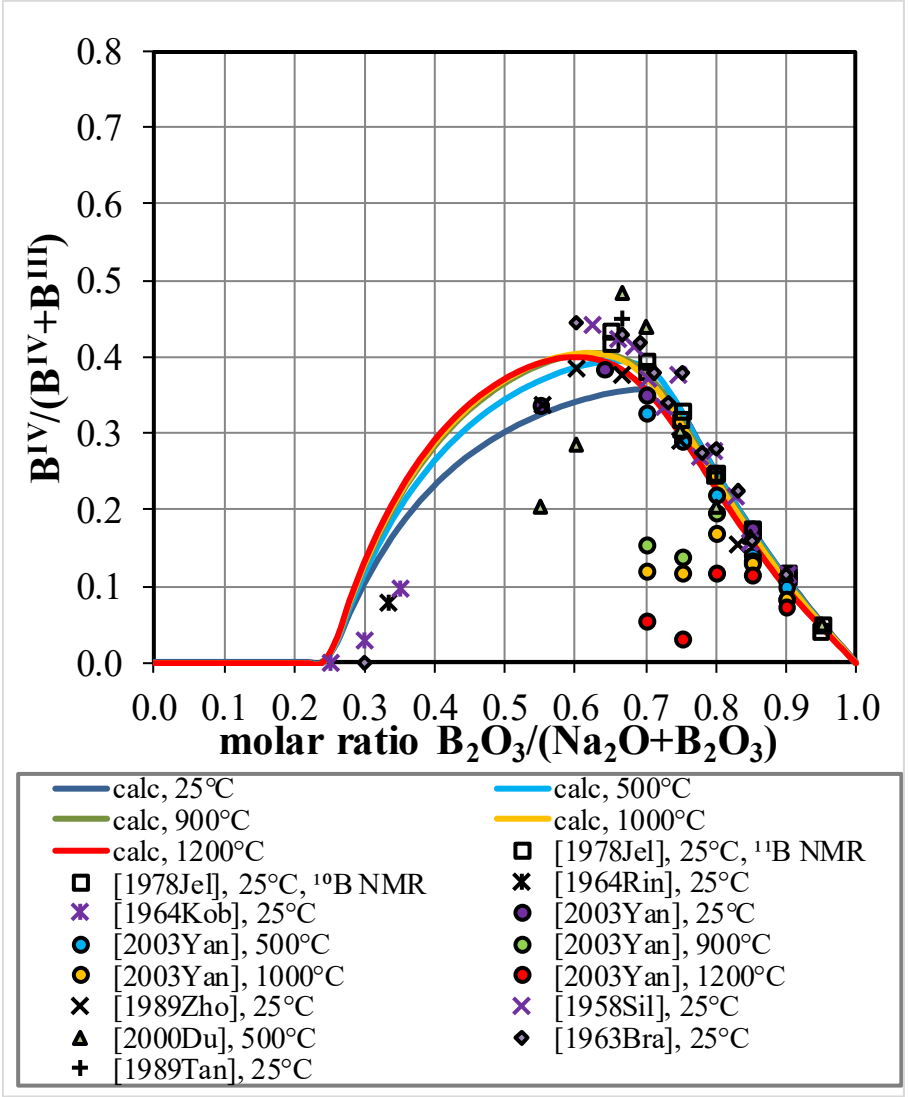

Figure 28.7 Distribution of the four-coordinated boron in Na_2O-B_2O_3 glasses and melts. Experimental points [561, 609, 632-639] and calculated lines.

The data on boron coordination in binary glasses and melts are summarized in Figure 28.7. It confirms the general ideas about boron conversion upon addition of alkali oxides (Section 27.1). The amount of the four-coordinated boron increases linearly until it reaches 1:1 ratio with B^{III} which corresponds to diborate species. It is formulated (Section 27.1) that four-coordinated boron can have up to one four-coordinated boron as a neighbor and because of that the conversion of B^{III} to B^{IV} proceeds until the B^{IV}/B^{III} ratio reaches 1. If more Na_2O is added, four-coordinated boron converts back to three-coordinated breaking up bridging oxygen bonds.

28.5 Heat capacity and heat content data

Adiabatic heat capacity measurements are available for $NaBO_2$ [640, 641] (Figure 28.8) and $Na_2B_4O_7$ [640] (Figure 28.9).

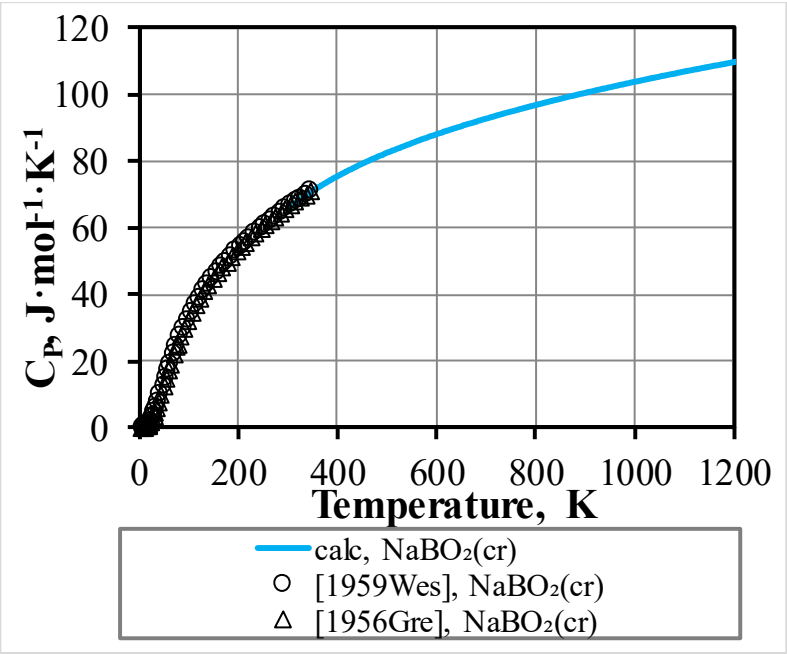

Figure 28.8 The heat capacity of sodium metaborate $NaBO_2$. Experimental points [640, 641] and the calculated line.

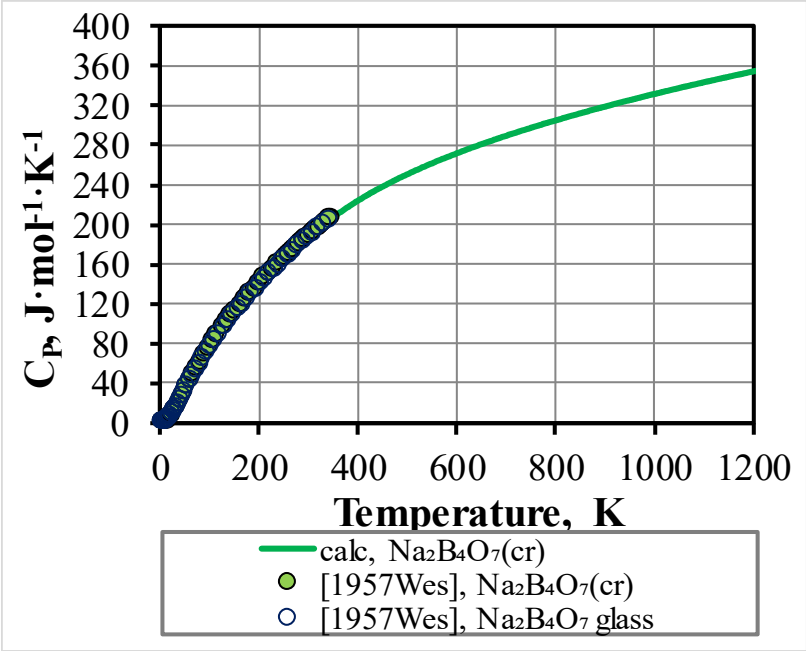

Figure 28.9 The heat capacity of sodium diborate $Na_2B_4O_7$. Experimental points [642] and the calculated line.

Heat content data were measured for $NaBO_2$ [643], $Na_2B_4O_7$ [620, 643], NaB_3O_5 [643], $Na_2B_8O_{13}$ [620, 643] (see Figure 28.10).

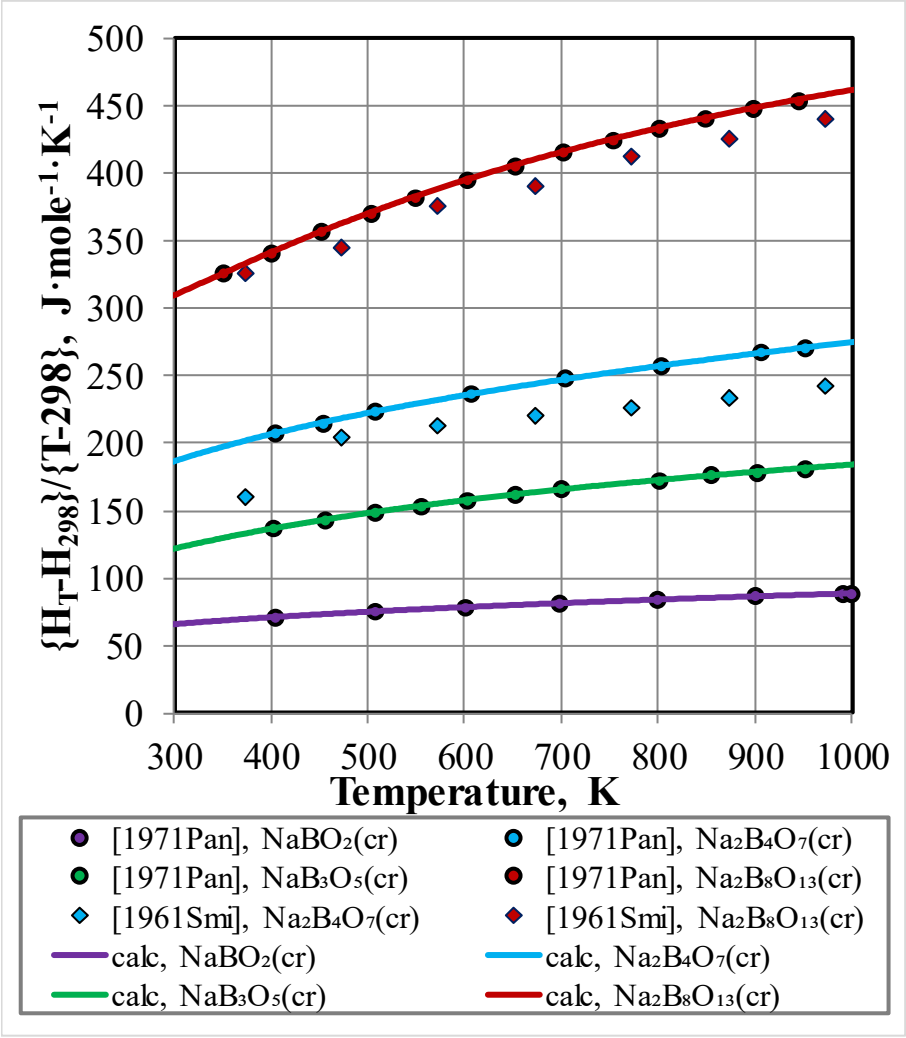

Figure 28.10 The heat content of four compounds in the Na_2O-B_2O_3 system. Experimental points [620, 643] and calculated lines.

28.6 Optimization results

The heat capacities of $NaBO_2$, $Na_2B_4O_7$, NaB_3O_5 and $Na_2B_8O_{13}$ were fitted after the available data according to the procedure described in Section 2.2; the standard entropies of $NaBO_2$ and $Na_2B_4O_7$ were set according to the values obtained by integration of the low-temperature C_P data. The remaining heat capacities and entropies were approximated as weighted sums of the corresponding functions of Na_2O and B_2O_3. The enthalpies of formation were assessed based on the experimental values or were later adjusted to reproduce the phase diagram.

The main $\Delta g^{\circ}_{\mathrm{Na,B}}$ interaction parameter was chosen to reproduce the enthalpy of mixing; its temperature dependence is defined by the curvature of the Na_3BO_3 liquidus. The stability of $NaBO_2$ associate is a variable parameter in the system; a few trials with different stabilities have shown that nothing in particular changes in the optimizations of the Na_2O-B_2O_3 and Na_2O-B_2O_3-SiO_2 systems. A more stable associate would require less negative interaction parameters and vice versa. However, it does not bring significant changes in the quality of optimization. For a given $NaBO_2$ stability, the $NaBO_2$ liquidus can be adjusted by $g^{01}_{\mathrm{Na,B}}$ parameter. The temperature term of $NaBO_2$ stability is responsible for the curvature of $NaBO_2$ liquidus. The B_2O_3-rich part of the phase diagram is adjusted by three NaB-B interaction parameters. The Na_2O-rich part of the phase diagram is set in the following way: first, a substantial negative NaB-Na interaction is set to avoid spurious miscibility gaps around Na_3BO_3. However, the interaction should not be strong enough to disturb the B^{IV} distribution curve. Two other interactions parameters, $g^{10}_{\mathrm{Na,B}}$ and $g^{10}_{\mathrm{Na,NaB}}$ are used to make Na_2O liquidus steeper.

Default coordination numbers were used for Na-B and Na-NaB pairs. However, large coordination numbers of NaB-B pair are required in order to reproduce the ternary miscibility gap in the Na_2O-B_2O_3-SiO_2 system (Chapter 29). The optimizations of the Na_2O-B_2O_3 and the Na_2O-B_2O_3-SiO_2 systems were performed simultaneously; these coordination numbers were adjusted to get the good critical temperature of the ternary miscibility gap.

In principle, it is possible to reproduce the binary miscibility gap as well. To do that, significant temperature terms must be used in the $g^{10}_{\mathrm{NaB,B}}$ and $\Delta g^{\circ}_{\mathrm{NaB,B}}$ parameters. As it was discussed previously (section 27.3), the true nature of alkali borate miscibility gaps derives from the presence of boroxol units and their bad connectivity with four-coordinated boron; boroxol-rich and B^{IV}-rich liquids unmix. An adequate representation of the phenomenon would require including a boroxol species in the model and to reoptimize all the boron-containing systems, even those without alkalies which is far beyond the scope and the capabilities of the current research project. If the miscibility gap is caused by a strong temperature dependence of NaB-B interaction, this would affect the extrapolation properties in the higher order systems. It was considered that the binary gap was of far less interest for practical database applications than good predicting properties in the

multicomponent systems. So, an optimization without strong *T*-terms of NaB-B interaction was preferred.

The optimized parameters are summarized in Table A.34 and Table A.35.

CHAPTER 29 OPTIMIZATION OF THE Na_2O-B_2O_3-SiO_2 SYSTEM

29.1 Phase diagram

Determination of liquidus in the Na_2O-B_2O_3-SiO_2 system is complicated by the volatility of sodium metaborate [644] and long crystallization times over almost the whole compositional range [645]. Even in the $NaBO_2$-Na_2SiO_3 section, compositions near the Na_2SiO_3 end showed a hysteresis of heating curve [644]. The quenching method is considered to be the most reliable, although DTA of precrystallized samples seems to work fine as well [646].

The study by Morey [645] was performed using the quenching technique and is considered to be the most reliable. $NaBO_2$ crystallizes so readily that it cannot be quenched to glass. In the lower-temperature part of its field, however, **weeks or months** were required to start crystallization. Mixtures near the ternary invariant points could be crystallized only in water fluid media, the eutectics were located by extrapolation. The compositions close to the B_2O_3-SiO_2 side were difficult to prepare due to their high viscosity. $NaBSiO_4$ compound can be crystallized in presence of water under high pressure. In anhydrous mixtures, it forms only if the glass is seeded. The seeded runs were performed separately from the rest of the trials.

The need of seeding is a probable reason why Ghanbari-Ahari and Cameron [646] did not observe the formation of $NaBSiO_4$ using DTA of precrystallized samples. $NaBSiO_4$ crystallization is sluggish and requires preliminary seeding and long annealing times to occur. Their phase diagram shows Na_4SiO_4 field, but it was probably contaminated with Na_2CO_3. The heating rate of 10°C/min was used, only heating curves were registered.

The liquidus surface in the Na_2O-B_2O_3-SiO_2 system for compositions with more than 60 wt% SiO_2 was investigated by Rockett and Foster [647]. The liquidus was studied by the traditional quenching method at temperatures higher than 1000°C and more than 5 mol% Na_2O or by the solution method employed for the B_2O_3-SiO_2 system [648]. The solution method consists in achieving complete dissolution of a solid phase in a viscous liquid at different temperatures. The crystalline phases were identified using a petrographic microscope and the X-ray. Tridymite was the major primary phase; the melts in the area of its supposed crystallization were very viscous. The ternary miscibility gap is metastable and does not appear above the liquidus. Only manually

drawn liquidus isotherms are available from the work by Rockett and Foster without detailed information on quenching experiments. These isotherms were digitized for the $NaBO_2$-SiO_2 and Na_3BO_3-SiO_2 sections (Figure 29.2, Figure 29.3, (***c***)). However, in the original phase diagram by Rockett and Foster, the isotherms have large curvature around the $NaBO_2$-SiO_2 section and thus there might be a relatively large uncertainty about the silica liquidus in this section.

The $NaBO_2$-Na_2SiO_3 section was studied by DTA by Van Klooster [644]. As molten alkali metaborates are very volatile, crucibles had to be covered.

Rockett and Foster [649] investigated the tetraborate-silica $Na_2B_8O_{13}$-SiO_2 section of the ternary system. Sealed platinum crucibles were used to avoid Na_2O and B_2O_3 losses, the equilibration time varied between 10 min and 200 hr. The crystalline phases were identified by the X-ray and optical microscopy. Only one modification of sodium tetraborate was observed; the transformation temperature Cri/Tri is lowered by 50°C compared to the pure silica. The authors suggest that a coupled substitution is possible in cristobalite, however, no peak shifts were noticed in the X-ray diffraction pattern. The eutectic temperature reported here is 50°C higher than the one given by Morey [645].

Reedmergnerite, $NaBSi_3O_8$, is a mineral isostructural to low albite [650]. According to Appleman and Clark [650], it melts incongruently at 821±4°C. However, Morey [645] failed to synthesize it even in hydrothermal conditions and the phase was not reported by Rockett and Foster [647]

Figure 29.1 shows the liquidus projection in the ternary system based on the data by Morey [645].

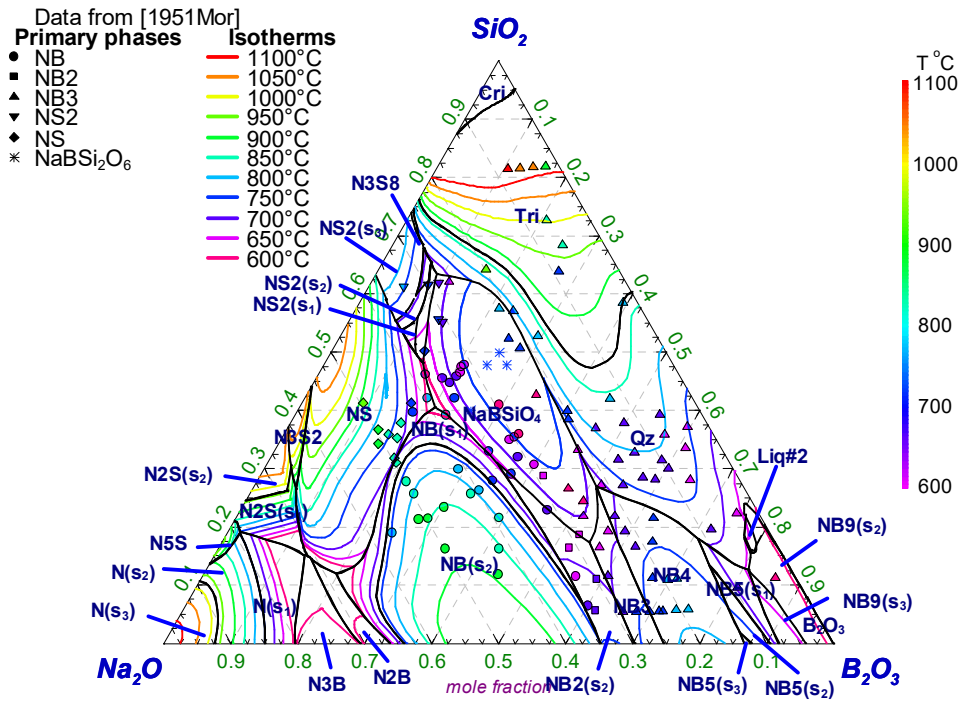

Figure 29.1 Liquidus projection in the Na_2O-B_2O_3-SiO_2 system. Experimental points [645] and calculated lines.

Figure 29.2-Figure 29.3 summarize the data on various sections through the ternary system.

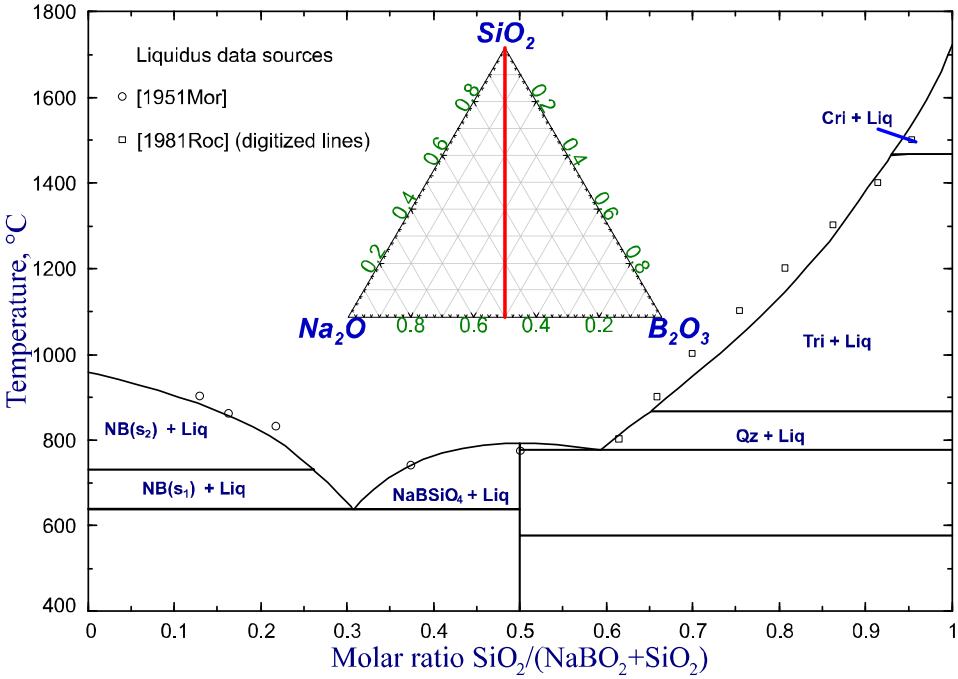

Figure 29.2 Phase diagram of the $NaBO_2$-SiO_2 section of the Na_2O-B_2O_3-SiO_2 system. Experimental points [645, 647] and calculated lines.

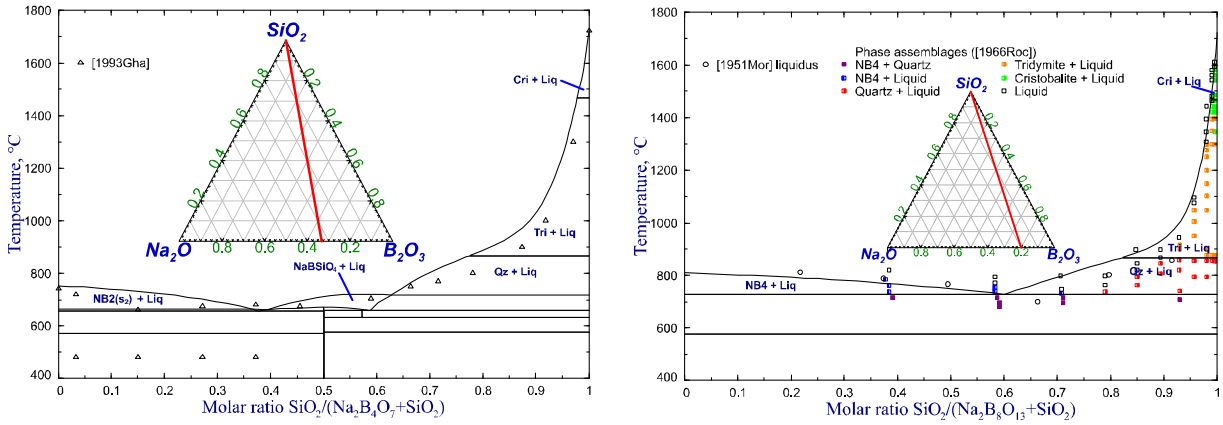

(*a*) (*b*)

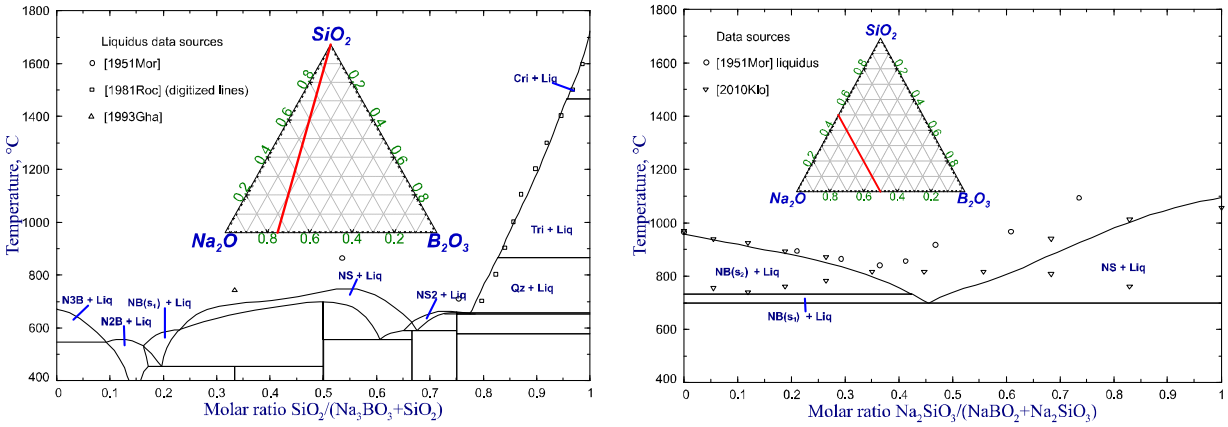

(*c*) (*d*)

Figure 29.3 Phase diagrams of sections through the Na_2O-B_2O_3-SiO_2 system: $Na_2B_4O_7$-SiO_2 (***a***), $Na_2B_8O_{13}$-SiO_2 (***b***), Na_3BO_3-SiO_2 (***c***), Na_2SiO_3-$NaBO_2$ (***d***). Experimental points [644-647, 649] and calculated lines.

29.2 Miscibility gap

Immiscibility phenomena in sodium borosilicate glasses are important from the point of view of the technology of porous glasses with good thermal properties. Usually, industrial glasses are annealed at around 600°C until phase separation occurs and the boron-rich phase is leached out afterwards [574, 575].

Thach Lan [572] studied the immiscibility by the electron microscopy and also gives the compositions of the coexisting phases. Galakhov and Alekseeva [573] observed the opalescence in sodium borosilicate glasses. The direction of tie-lines in the two-phase region and the compositions of the coexisting phases were determined as well. Scholes and Wilkinson [651] proposed tie-lines at 550°C based on electron microscopy data. Haller et al. [575] annealed sodium borosilicate glasses in a gradient temperature furnace. The immiscibility was observed from the opalescence. As there are the binary Na_2O-SiO_2 gap and the ternary gap, a three-liquid equilibrium must exist at low temperatures. Polyakova [652-654] reports that the ternary miscibility gap has, in fact, both upper and lower critical temperatures. Glasses were synthetized, annealed at a constant temperature until the phase separation occurs and then studied by DTA. In DTA curves, two glass transition temperatures can be identified related to the low- and high-viscosity phases. Also, in some samples,

a third glass transition temperature was registered (three-liquid equilibrium). As the temperature at which glasses were annealed is lowered, the two glass transition temperatures become closer to each other and only one endothermic effect is observed at 433°C. The upper immiscibility temperatures were refined using opalescence observations. Wakabayashi et al. [655] observed phase separation in sodium borosilicate glasses by measuring the electrical conductivity and using TEM. Alekseeva et al. [656] continued the work on the miscibility gap [573] with special attention to the high-viscous area rich in silica. For example, one of the drawbacks of the work of Galakhov and Alekseeva [573] is small sizes of glass samples used in experiments which often led to undesired crystallization. T_{misc} was determined by observing the clearance of opalescent glasses. Opalescence in glasses along the tetraborate-silica join was observed by Rockett et al. [574]. We assume that the lower miscibility temperature, reported in the works of Polyakova [652-654] and Rockett et al. [574] arise due to a spinodal decomposition of glasses at low temperatures. Ultrafine homogeneity area do not show opalescence and would not have distinct peaks on DTA.

Immiscibility isotherms in the Na_2O-B_2O_3-SiO_2 system are given in Figure 29.4.

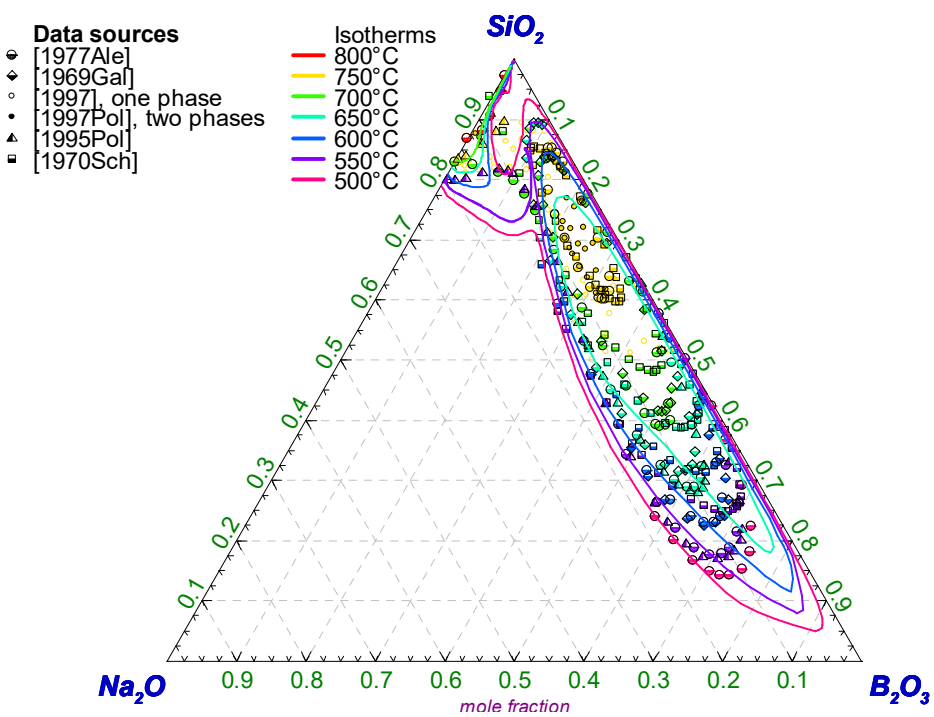

Figure 29.4 Isothermal projections of the metastable miscibility gap in the Na_2O-B_2O_3-SiO_2 system. Experimental points [573, 651, 653, 654, 656] and calculated lines.

Figure 29.5 shows two polythermal sections through the gap, one with a constant SiO_2 content and another with a constant Na_2O/B_2O_3 ratio. The immiscibility temperatures at $x(SiO_2) > 0.50$ are not described in a perfect way; it also leads to the fact that 750°C does not appear among the calculated isotherms in Figure 29.4. Raising the immiscibility temperature in that region (Figure 29.5, (***b***)) by excess parameters of the liquid would inevitably cause a significant rise of the tridymite liquidus temperature in the $Na_2B_8O_{13}$-SiO_2 section (Figure 29.3, (***b***)). We explain this discrepancy by the fact that the predicted entropy of mixing along the $Na_2B_8O_{13}$-SiO_2 join is too high. It is also confirmed by the enthalpy of mixing in the $Na_2B_8O_{13}$-SiO_2 system (Figure 29.9) which is more positive than the experimental data. A possible explanation to this discrepancy would be the existence of a ternary associate which would allow for a very low entropy of mixing in the section. There is evidence in the literature that a ternary $NaBSi_4^{16+}$ associate exists [657]. However, the current model does not include ternary associates because it would greatly increase the complexity of the system and leave too many parameter models unconstrained. A possible consequence of unproperly constrained model parameters are, for example, spurious miscibility gaps in multicomponent systems. The current optimization with only one binary associate was considered satisfactory.

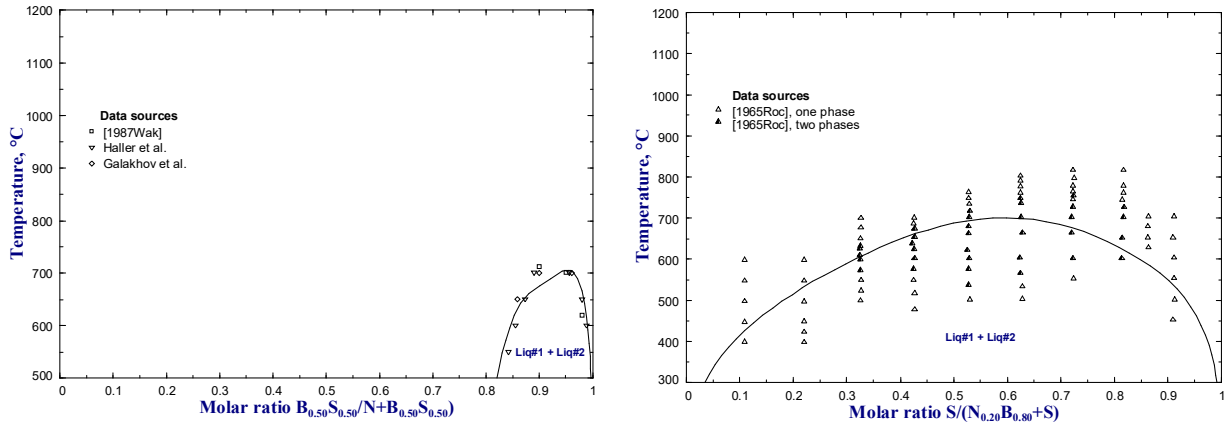

(***a***) (***b***)

Figure 29.5 Polythermal sections through the metastable miscibility gap in the Na_2O-B_2O_3-SiO_2 system. Experimental points [574, 575, 655, 658] and calculated lines.

29.3 Calorimetry data

A few authors investigated heats of solution of sodium borosilicate glasses in HCl [659, 660] but because a porous non-soluble residue was reported, these data were not used.

Enthalpies of mixing in the $NaBO_2$-SiO_2 section (Figure 29.6) were measured by Julsrud and Kleppa [661] at 1120°C by a solid-liquid calorimetry. Small amounts of crystalline quartz were added to a $NaBO_2$-SiO_2 melt and the integral enthalpy of mixing was calculated by summation of the gradual heat effects taking into account the varying mass of the mixture. Lead borate solution calorimetry at about 700°C was performed by Navrotsky [662] (the reported data are the same as from Hervig and Navrotsky [663]) and by De Yoreo et al. [303]. Apparently, the work by Navrotsky [662] is the continuation of the work by De Yoreo et al. [303].

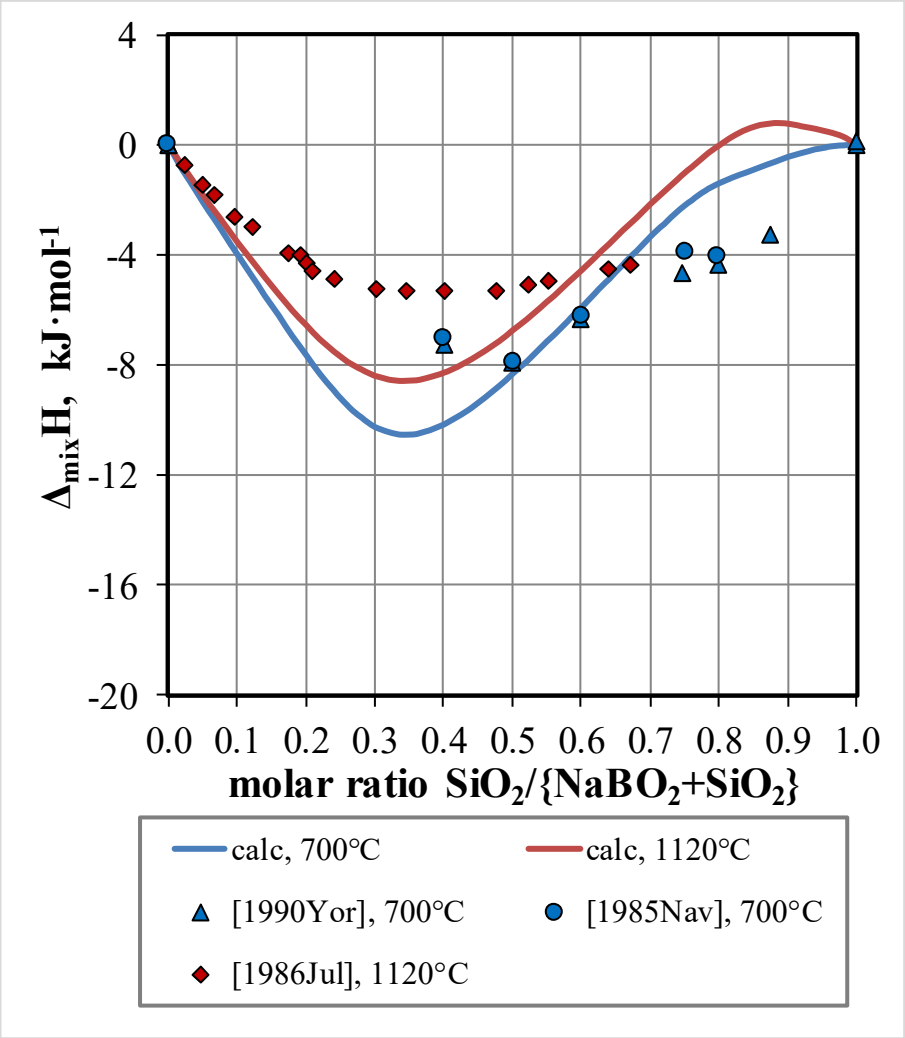

Figure 29.6 The enthalpy of mixing in the $NaBO_2$-SiO_2 section of the Na_2O-B_2O_3-SiO_2 system at different temperatures. Experimental points [303, 661, 664] and calculated lines.

The calorimetry data by Julsrud and Kleppa [661] can also be used to derive the partial enthalpy of SiO_2 in the $NaBO_2$-SiO_2 section (Figure 29.7).

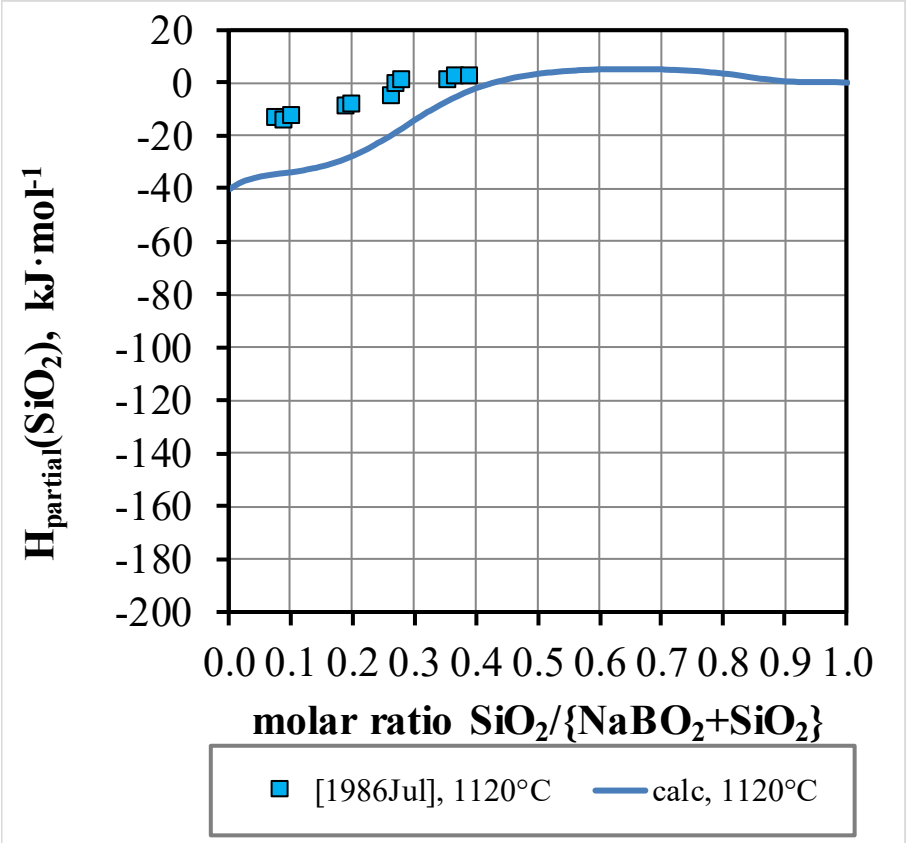

Figure 29.7 The partial enthalpy of SiO_2 in the $NaBO_2$-SiO_2 section of the Na_2O-B_2O_3-SiO_2 system at 1121°C. Experimental points [661] and calculated lines.

Navrotsky et al. [664] performed lead borate solution calorimetry of glasses in the Na_2O-B_2O_3-SiO_2 system with different Na_2O/B_2O_3 ratio. The data in the $NaBO_2$-SiO_2 section are the same as from Navrotsky [662], the sections Na_3BO_3-SiO_2 and $Na_2B_8O_{13}$-SiO_2 were also studied. The solution data for Na_3BO_3 is absent, therefore, it is not possible to recalculate the data on the Na_3BO_3-SiO_2 section into enthalpy of mixing data directly. However, it was possible to calculate the heat of solution of liquid sodium orthoborate in lead borate at 700°C using auxiliary data on the heat of solution of crystalline Na_2O, $\Delta_{soln}H(Na_2O(cr)) = -172.21$ kJ·mol^{-1} [300] and of liquid B_2O_3, $\Delta_{soln}H(B_2O_3(liq)) = -56.62$ kJ·mol^{-1} [664]. To do that, the enthalpy of formation of liquid Na_3BO_3 from the crystalline Na_2O and liquid B_2O_3 evaluated in the optimization of the Na_2O-B_2O_3 system (−121.42 kJ·mol^{-1}, this work) was used. The resulting value of −21.89 kJ·mol^{-1} was used to recalculate the data in Figure 29.8.

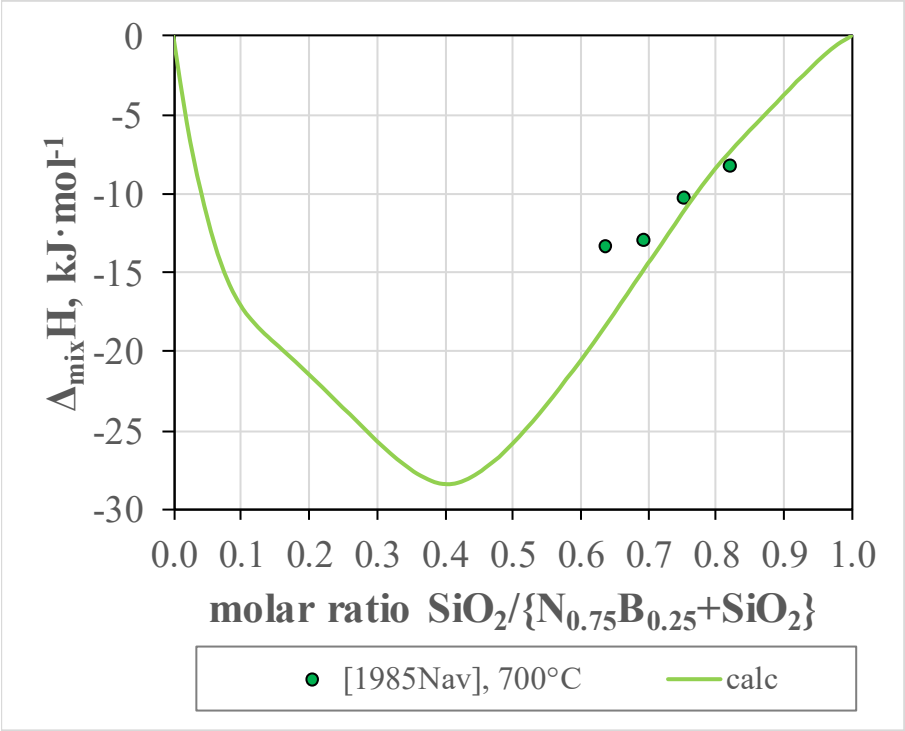

Figure 29.8 The enthalpy of mixing in the Na_3BO_3-SiO_2 section of the Na_2O-B_2O_3-SiO_2 system. Experimental points [664] and calculated lines.

The enthalpy of mixing in the $Na_2B_8O_{13}$-SiO_2 section is given in Figure 29.9.

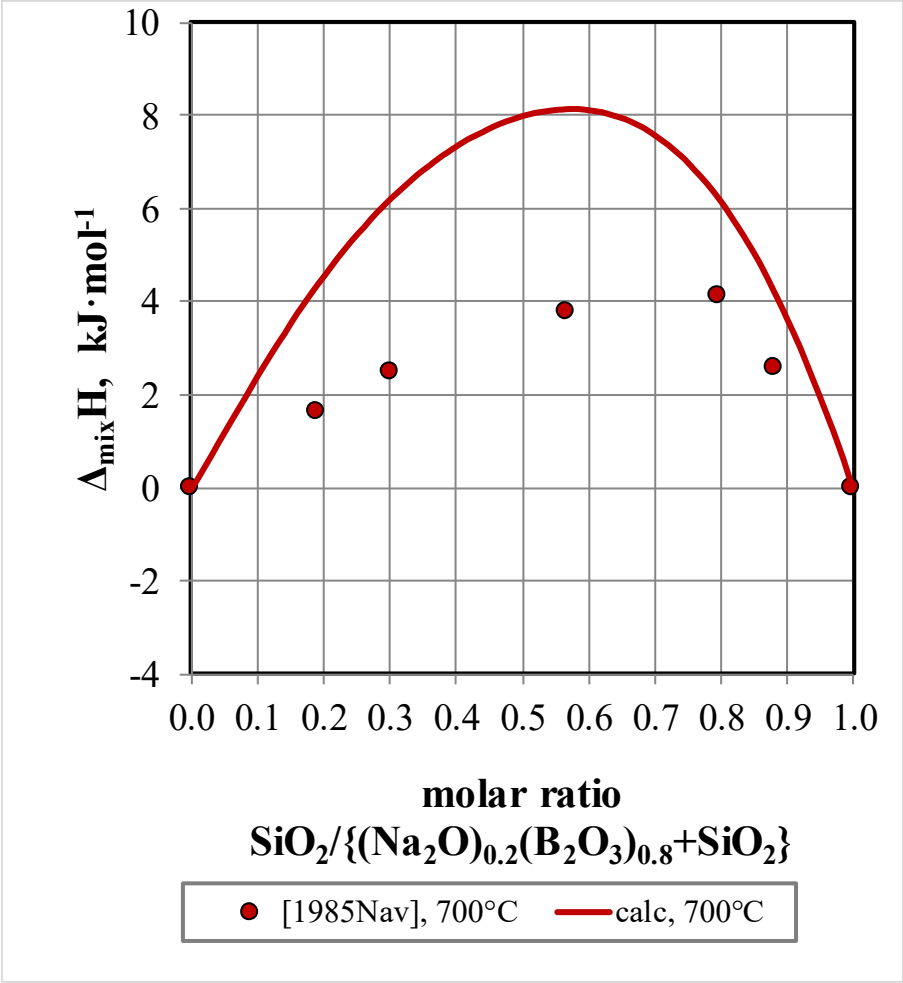

Figure 29.9 The enthalpy of mixing in the $Na_2B_8O_{13}$-SiO_2 section of the Na_2O-B_2O_3-SiO_2 system. Experimental points [664] and calculated lines.

A possible reason of the positive deviation of the calculated enthalpy of mixing from the experimental values is discussed in Section 29.2.

Ahoussou et al. [201] carried out HF and lead borate calorimetry of glasses with 20 mol% Na_2O (Figure 29.10). The data on HF were recalculated according to the procedure described in Section 2.5.2.

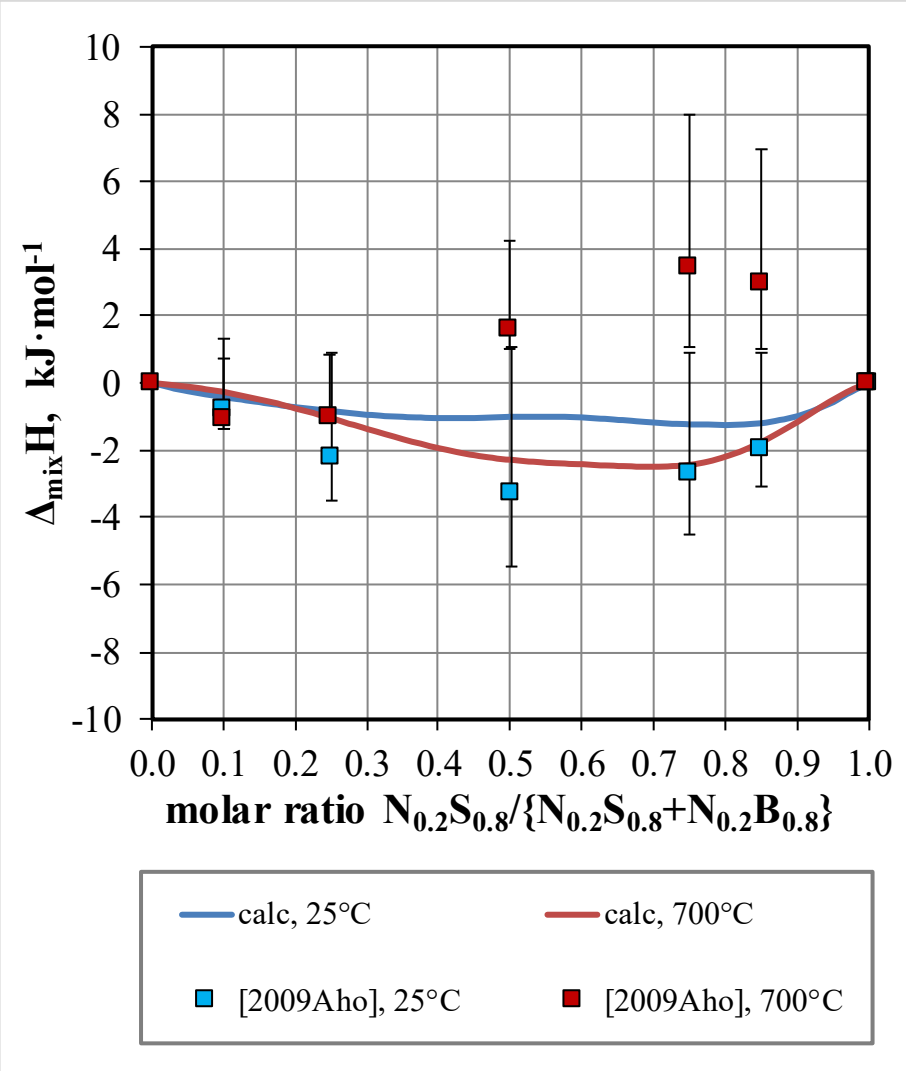

Figure 29.10 The enthalpy of mixing at 20 mol% Na_2O of the Na_2O-B_2O_3-SiO_2 system at different temperatures. Experimental points [201] and calculated lines.

29.4 Activity data

Abdelouhab et al. [233] performed EMF measurements of a few SiO_2-rich sodium borosilicate melts in a cell with Na-alumina solid electrolyte and a C-type melt as the reference (multicomponent mixture, apparently, of industrial significance). The activity values were taken as recalculated by the authors. Asai and Yokokawa [665] used an EMF cell of the following type:

$$O_2(Pt)|Na_2O{\cdot}2B_2O_3,ref||Na_2O\text{-}B_2O_3\text{-}SiO_2|O_2(Pt) \quad (138)$$

where molten sodium diborate was used as the reference. The EMF data were recalculated in this work using Na_2O activity of the reference melt calculated in *FactSage*.

A similar cell was employed by Kozhina and Shultz [222] but the reference melt was $31.95Na_2O \cdot 16.82Al_2O_3 \cdot 51.23SiO_2$. The activities calculated by the authors were used directly in this work because the raw EMF data were not published.

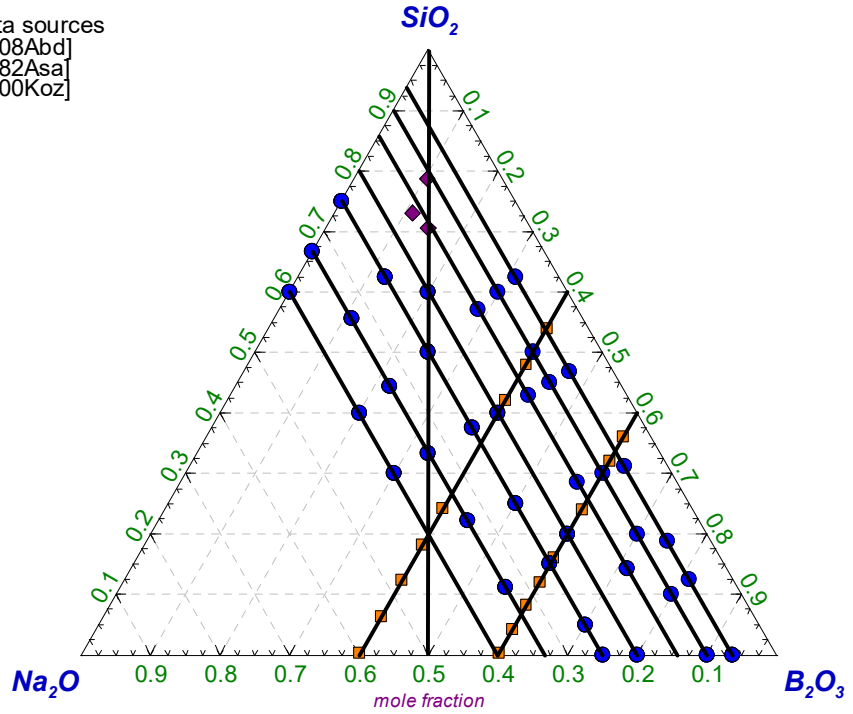

Figure 29.11 Compositions in the Na_2O-B_2O_3-SiO_2 system at which Na_2O activities were studied [222, 233, 665] and the isothermal sections plotted through them in this work.

The investigated compositions are summarized in Figure 29.11. Temperature-activity dependencies that are directly obtained from the EMF data are somewhat cumbersome to present because of a large amount of data; instead, it was decided to use these data to derive compositional dependencies of Na_2O activity. Thus, the values at the limiting compositions, belonging to the already optimized binary subsystems can be an indication of the overall reliability of the datasets. Based on the compositional trends, a few sections were drawn through the points: a series with a fixed Na_2O content, allowing to observe fine variations of Na_2O activity on B_2O_3/SiO_2 substitution (Figure 29.13), two series with a fixed B_2O_3 content (Figure 29.14) and the central $NaBO_2$-SiO_2 join (Figure 29.12).

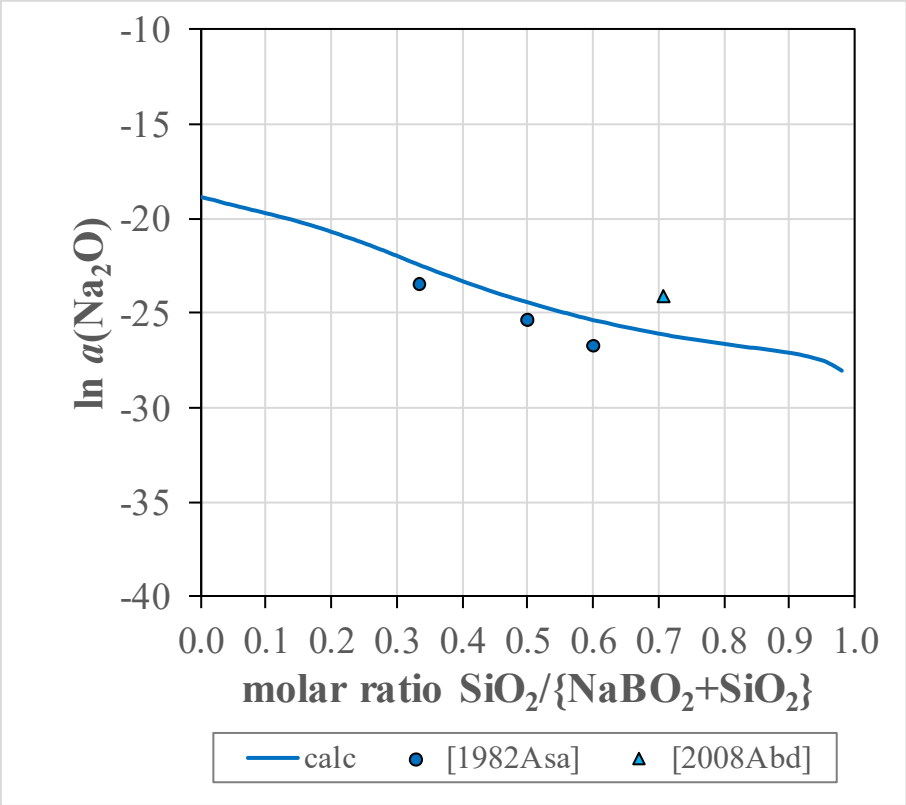

Figure 29.12 Na_2O activity at 900°C along the $NaBO_2$-SiO_2 section. Experimental points [233], points interpolated from experimental data [665] and the calculated line.

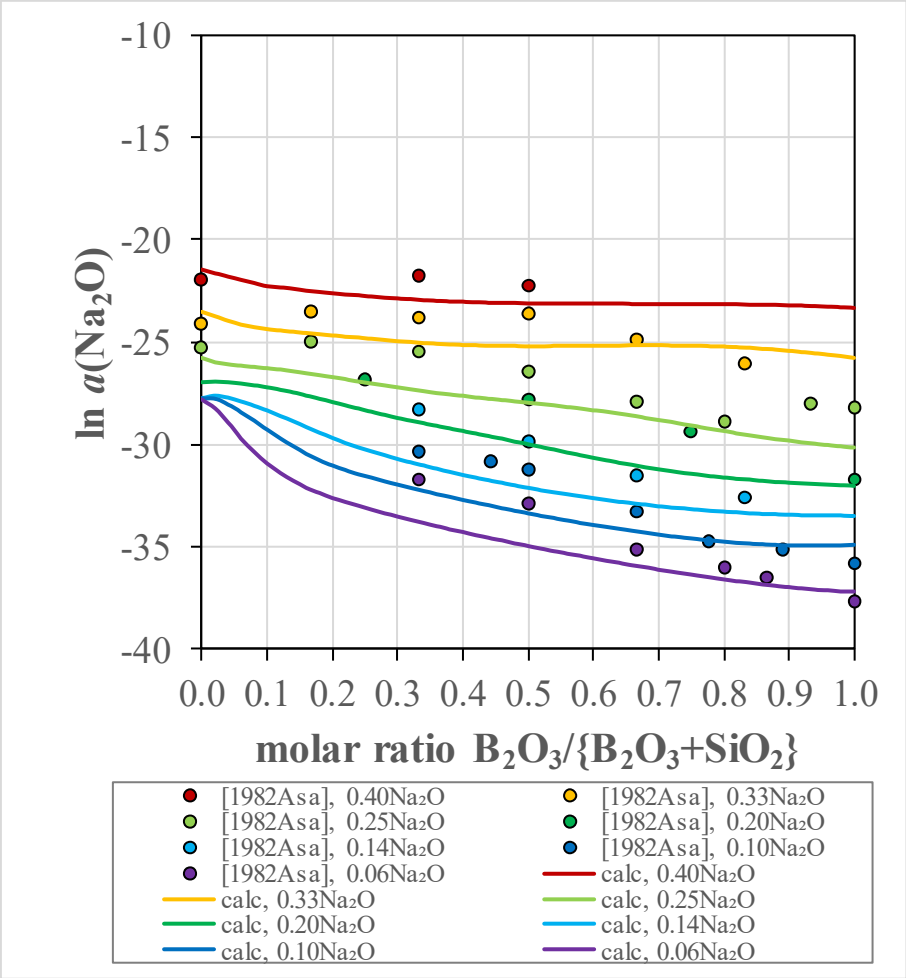

Figure 29.13 Na_2O activity at 900°C in sections with a constant Na_2O content. The reference state is the pure liquid Na_2O. Points interpolated from experimental data [665] and calculated lines.

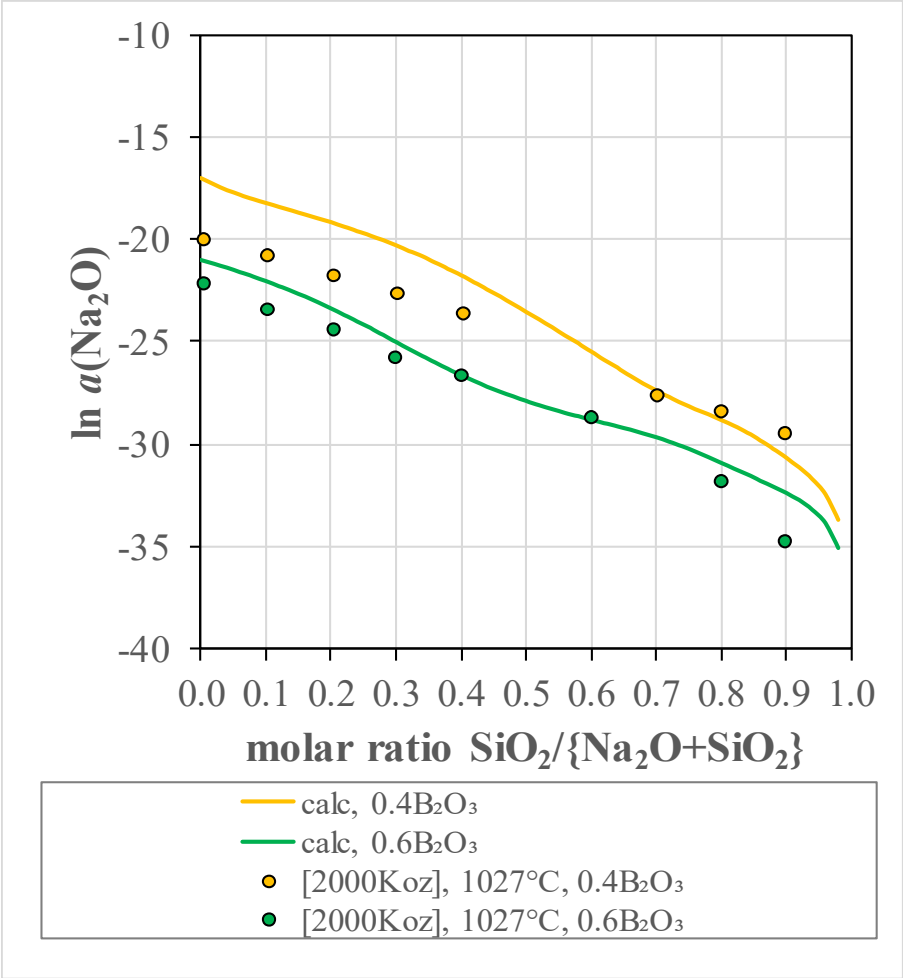

Figure 29.14 Na_2O activity at 1027°C in sections with a constant B_2O_3 content. The reference state is the pure liquid Na_2O. Experimental points [222] and calculated lines.

29.5 Optimization results

The Na_2O-SiO_2 and the Na_2O-B_2O_3 subsystems of the ternary system were optimized in this work (Chapter 6 and Chapter 28). For the B_2O_3-SiO_2 system, the optimization by Decterov et al. was adopted [15].

There are no heat capacity or heat content data on the ternary compound, $NaBSiO_4$. Its heat capacity and the standard entropy were evaluated as weighted sums of the corresponding functions of $NaBO_2$ and SiO_2 (tridymite); the enthalpy of formation was adjusted to reproduce the phase diagram data. It was decided not to include $NaBSi_3O_8$ compound in the optimization as a few authors failed to obtain it.

Special attention needs to be made to the grouping of species in the system. There are five combinations by three of species in the system. It was decided to keep the groupings including the alkali dimer $(Na_2)^{2+}$ the same as the corresponding groupings with simple Na^+. In the Na-Si-NaB//O grouping, Na_2O is set apart as Si and NaB are network formers while Na_2O is a network modifier. In the B-Si-NaB//O grouping, Si is set apart because only this configuration allows to obtain a properly elongated ternary miscibility gap. Analogous to the Na-Si-NaB//O grouping, it would be logical that in the Na-Si-B//O Na must be apart as Si and B have similar properties. However, this grouping makes the metastable Na_2O-SiO_2 gap descend along the SiO_2-$NaBO_2$ section down to the Na_2O-B_2O_3 boundary. This incorrect gap extrapolation was resistant to any kind of ternary excess parameters within the range of values allowed for by the rest of the experimental data. The only way to supress it was to choose a somewhat unusual Si-apart grouping which restricts the Na_2O-SiO_2 derived gap to a small area. This grouping leads to a moderate spurious miscibility gap approximately along the $NaBO_2$-Na_2SiO_3 section which, however, could be suppressed by $q^{101}_{\mathrm{Na,Si(B)}}$ parameter.

The rest of the parameters work in the following way. $\Delta g^{\circ}_{\mathrm{NaB,Si}}$ parameter sets the liquidus along the $NaBO_2$-SiO_2 join, $g^{101}_{\mathrm{B,Si(NaB)}}$ parameter tunes the ternary gap, $q^{001}_{\mathrm{Na,Si(NaB)}}$ and $q^{002}_{\mathrm{NaB,Si(Na)}}$ parameters work along the $NaBO_2$-Na_2SiO_3 join. An interaction parameter with the sodium dimer $q^{001}_{\mathrm{Na_2,Si(B)}}$ is required to make some liquidus kinks to disappear.

The optimized parameters are summarized in Table A.36-Table A.37.

CHAPTER 30 OPTIMIZATION OF THE K_2O-B_2O_3 SYSTEM

30.1 Phase diagram

The K_2O-B_2O_3 system features multiple compounds and no solid solutions. Some compounds have two or three polymorphic modifications. Due to the slow kinetics of phase transformations, some of the polymorphs can show metastable melting behavior [666]. Compounds with high B_2O_3 content are difficult to crystallize from melts: for example, KB_9O_{14} could be obtained only with seeding with CsB_9O_{14} by Toledano [666] and Polyakova and Tokareva [667] failed to find it. Compositions high in B_2O_3 have also a tendency for glass-forming [668].

As a rule, samples for measurements are prepared from H_3BO_3 and K_2CO_3. Samples with more than 35 mol% K_2O are highly hydroscopic [667]. Similar to the Na_2O-B_2O_3 system, it can be assumed that K_2CO_3 does not decompose with less than 50 mol% B_2O_3 in a mixture and any results obtained in the composition region of 0-50 mol% B_2O_3 belong to the KBO_2-K_2CO_3 system. In fact, Rza-Zade and Mamedova [669] present liquidus temperature in the whole composition region from 0 to 100 mol% B_2O_3 but the melting temperature of the mixture with 0 mol% B_2O_3 corresponds to K_2CO_3 rather than to K_2O (Figure 30.1). This fact can be easily seen from the liquidus point corresponding to the pure K_2O (902°C instead of 740°C). The melting point of K_2CO_3 measured by DTA is in the range 900-905°C [670]. The liquidus data by Rza-Zade and Mamedova [669] at compositions with more than 50 mol% K_2O are omitted because the samples contained unreacted potassium carbonate. The $K_4B_2O_5$ compound was reported [669], but it is not indicated whether a chemical analysis of carbonates was performed.

Generally, the liquidus was measured either by DTA by heating crystallized samples [666, 667, 669] or by the oscillation method [671, 672]. In short, the oscillation method consists in measuring the amplitude and the frequency of an oscillating thin plate immersed in a liquid as a function of its viscosity. The parameters of oscillation are highly sensitive to changes of the phase composition. The method is described in detail in the work of Kaplun and Meshalkin [580].

There are a lot of similarities between the compounds in the Na_2O-B_2O_3 and K_2O-B_2O_3 systems. We assume that there exists a potassium orthoborate compound K_3BO_3 although none of the studies mention it. It can be explained by the fact that in the sodium borate system the compound could be

obtained only if crystalline Na_2O was used as a source of sodium oxide and it could not be obtained with Na_2CO_3. It is even harder to carry out experiments with pure K_2O and apparently, nobody was much concerned with the K_2O-rich part of the phase diagram. We estimated the melting point of K_3BO_3 to be approximately equal to the melting point of Na_3BO_3 because, for example, the melting points of $NaBO_2$ and KBO_2 do not differ significantly.

Potassium metaborate KBO_2 melts congruently [666] and apparently undergoes two polymorphic modifications at 440° and 780°C [669, 673]. The structure of the compound was investigated by Zachariasen [674].

Potassium diborate $K_2B_4O_7$ has triclinic structure [675] and melts congruently [666]. One polymorphic transformation at 390°C was reported by Mamedova et al. [673].

Potassium triborate KB_3O_5 is triclinic [675]. It can show either a stable incongruent or a congruent metastable behaviour. No polymorphs were reported for this compound.

"Potassium tetraborate" was first thought to have the same stoichiometry as its sodium analogue, but a later investigation of the crystal structure has shown that its true stoichiometry is $K_{10}B_{38}O_{62}$ [676]. The compound melts congruently and does not have polymorphic modifications.

Potassium pentaborate KB_5O_8 has several polymorphic modifications. There is a monoclinic γ-KB_5O_8 metastable at all temperatures, an orthorhombic low-T β-KB_5O_8 and an orthorhombic α-KB_5O_8 stable at liquidus temperatures [666]. The compound can form a stable peritectic [668, 669, 672] and a metastable peritectic [667, 672]. Metastable congruent melting is also possible [672].

Potassium enneaborate KB_9O_{14} melts incongruently [666] and is difficult to crystallize from melts.

Kaplun and Meshalkin [672] reported two "hanging" phases, $K_4B_6O_{11}$ and $K_4B_{10}O_{17}$ with upper and lower decomposition temperatures. However, the presence of $K_4B_6O_{11}$ was not confirmed by X-ray and $K_4B_{10}O_{17}$ was found only in one sample and the results with its presence could not be reproduced.

The phase diagram of the K_2O-B_2O_3 system is given in Figure 30.1.

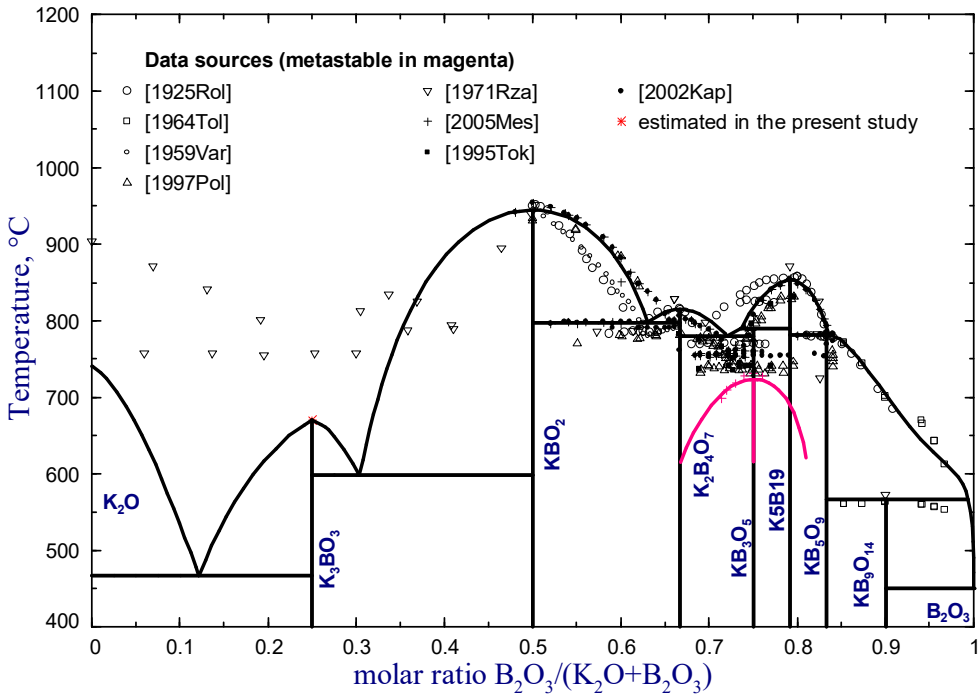

Figure 30.1 Phase diagram of the K_2O-B_2O_3 system. Experimental data [334, 598, 666-669, 672, 677] and calculated lines. Stable equilibria are shown in black, the metastable in magenta.

The metastable miscibility gap in the potassium borate system was investigated by Shaw and Uhlmann [571]. Glass samples were held in a furnace with a thermal gradient; the annealed samples were investigated by the direct-transmission electron microscopy. It is noted that light scattering techniques do not work in this case because of a very small range of homogeneity.

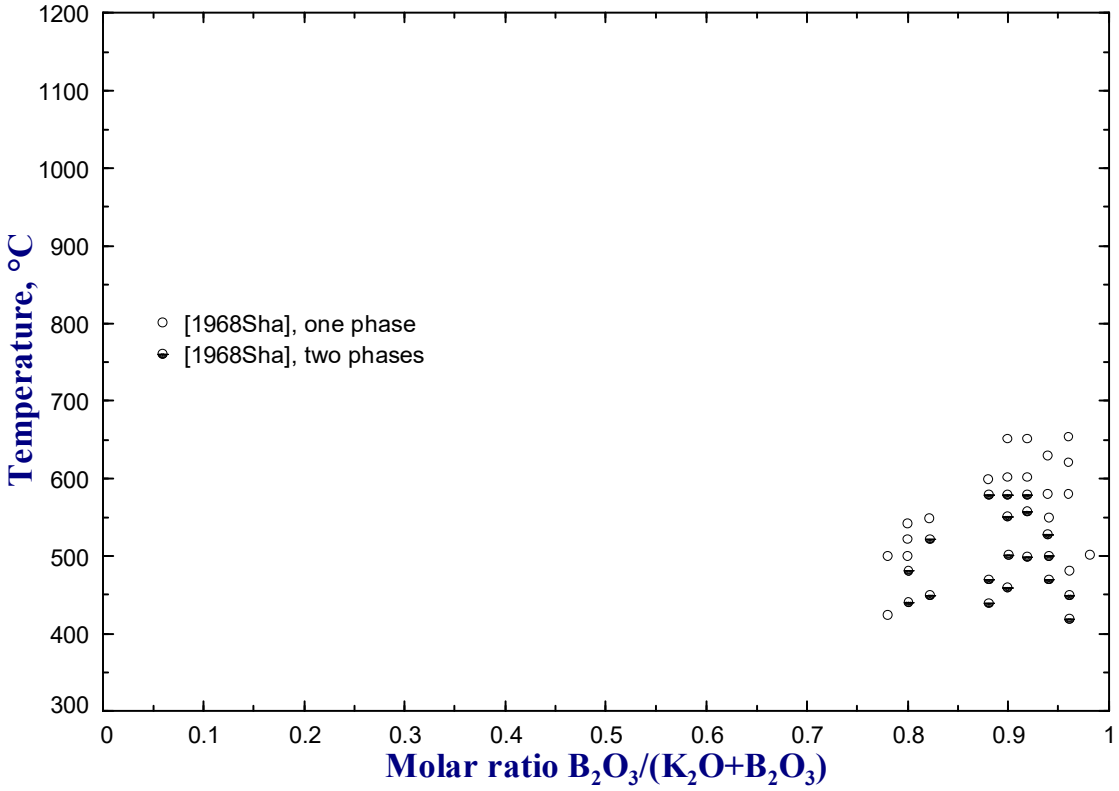

Figure 30.2 Metastable miscibility gap in the K_2O-B_2O_3 system. Experimental points [571].

In the present study it was decided not to reproduce the metastable miscibility gap as discussed in section 28.6 and similar to the Na_2O-B_2O_3 system.

30.2 Calorimetry data

There is a series of works in the literature devoted to the solution calorimetry of glasses and crystalline solids in the K_2O-B_2O_3 system.

A popular solvent used for solution calorimetry was 2N HNO_3 [617-620, 678]. Shartsis and Capps [617] noted that small samples had to be used to avoid the formation of insoluble H_3BO_3. Shartsis and Capps [617] reported the calculated value of the heat of solution of K_2O(cr) which is −428.44 kJ·mol^{-1}. Later, Shul'ts et al. [618] used their value to recalculate their own data. Also, the enthalpy of solution of pure B_2O_3(gl) of −33.47 kJ·mol^{-1} was adopted after Shartsis and Capps [617]. These values were used to recalculate the data from the rest of the sources.

The lead borate calorimetry of samples was performed by Ahoussou et al. [342]. To recalculate their data, enthalpy of solution of B_2O_3(gl) of −56.62 kJ·mol^{-1} from Navrotsky et al. [664] and K_2O(cr) of −266.23 kJ·mol^{-1} from Zygan et al. [195] were used.

Ahoussou et al. [679-681] performed a solution calorimetry of glasses in 6N HF + 4N HNO_3 acid mixture. Unfortunately, their data is the only of the kind; neither the authors or any other sources report enthalpies of solution of pure K_2O(cr) and B_2O_3 in the same solution media. Therefore, their data were not used for the optimization. The same problem was encountered with the data by Hattori and Taniguchi [682] who performed solution calorimetry measurements in 0.2N HNO_3.

The glass calorimetry data were recalculated into the enthalpy of mixing of liquid according to the procedure described in Section 2.5.2.

The recalculated data are summarized in Figure 30.3.

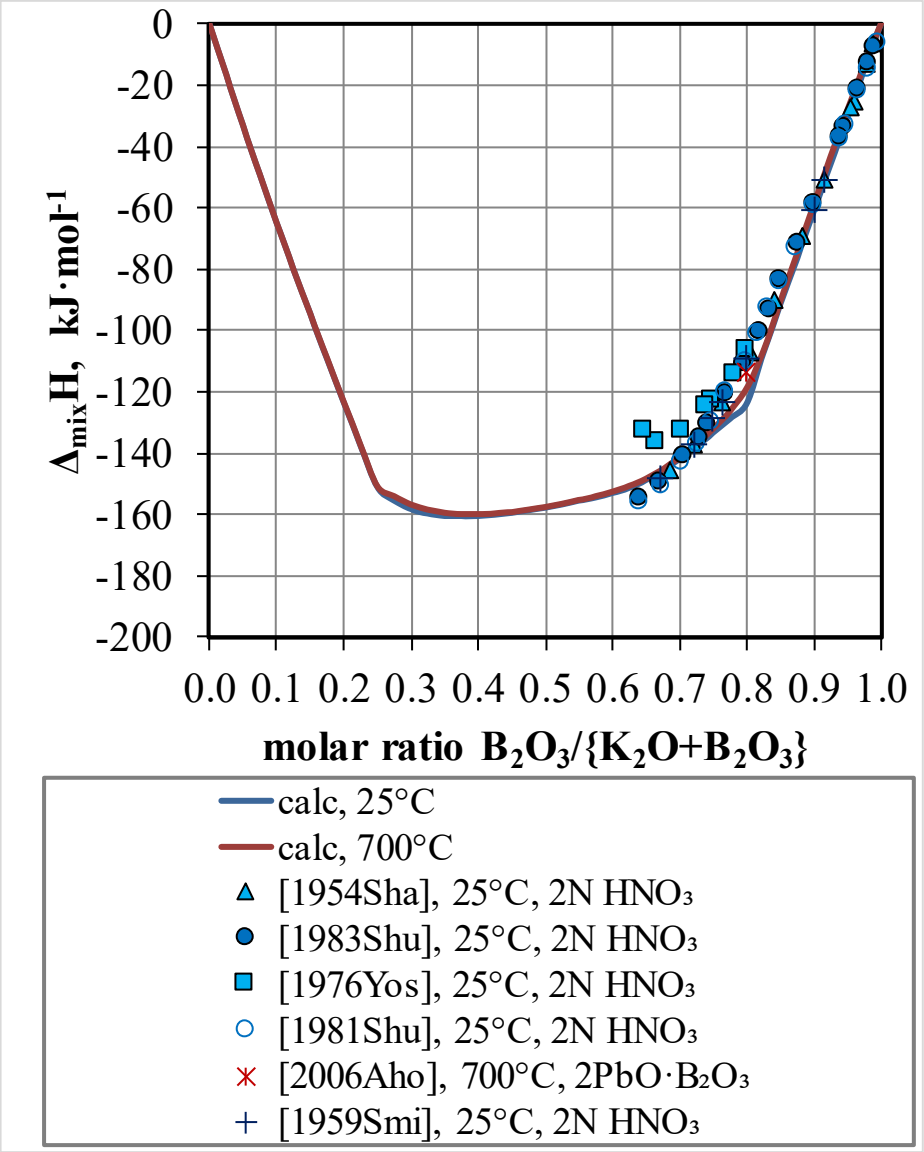

Figure 30.3 The enthalpy of mixing of the liquid phase in the K_2O-B_2O_3 system. Experimental points [342, 614, 617-619, 683] and calculated lines.

The data on crystalline solids, recalculated into the enthalpy of formation from oxides are given in Figure 30.4.

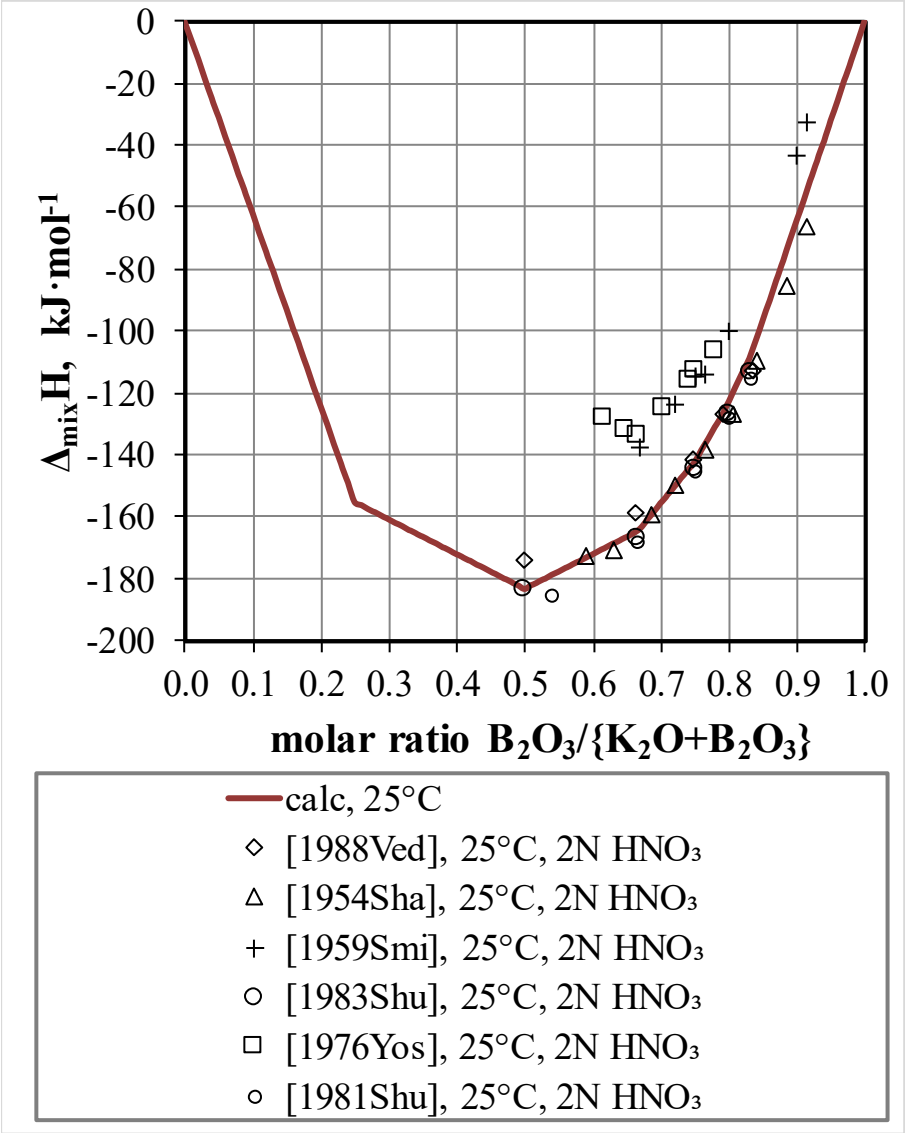

Figure 30.4 The enthalpy of formation of crystalline solids from oxides in the K_2O-B_2O_3 system. Experimental points [614, 616-619, 683] and the calculated line.

It is hard to tell why the points by Yoshio and Takahashi [619] and Smith [683] are less negative than the rest of the data. The data by Smith are reproduced well in Figure 30.3; thus, we can exclude possible errors related to the calorimetry procedure. Probably, the crystal samples were not completely crystallized. The points by Yoshio and Takahashi [619] are somewhat less negative than the rest of the data in Figure 30.3; we can assume a systematic experimental error.

Ostvold and Kleppa [564] report the partial enthalpy of B_2O_3 in K_2O-B_2O_3 melts. However, they noted that these data might be a subject to a systematic error because KBO_2 used for sample preparation was contaminated with K_2CO_3. Their data are shown in Figure 30.5.

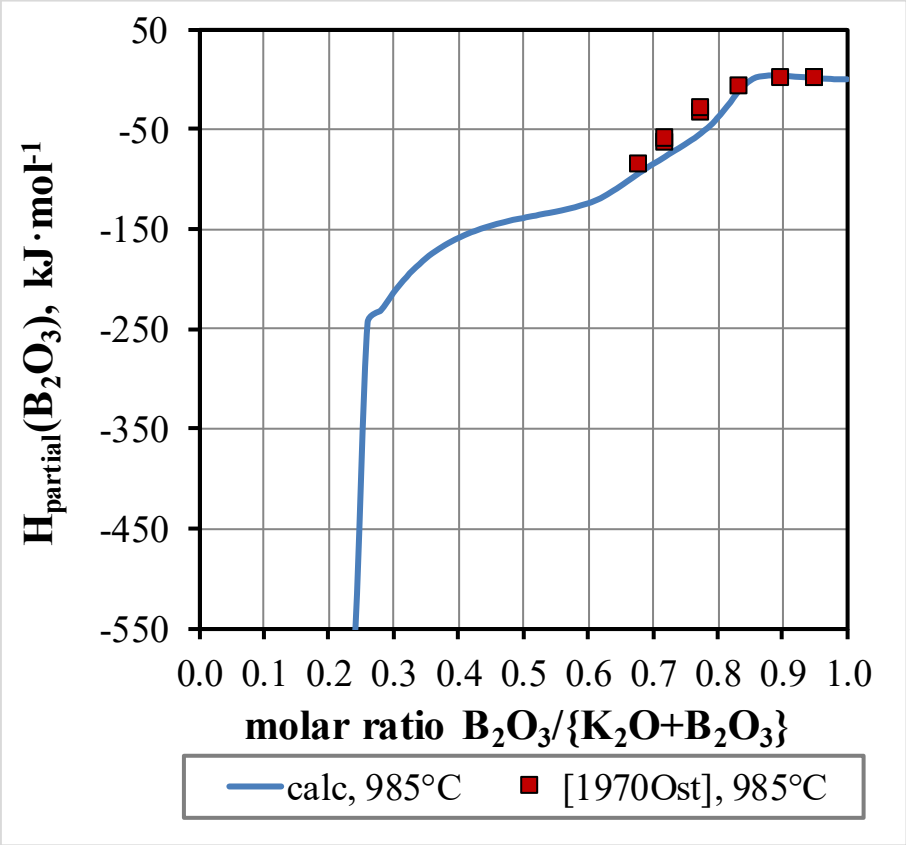

Figure 30.5 The partial enthalpy of B_2O_3 in the K_2O-B_2O_3 melts. Experimental points [564] and the calculated line.

30.3 Activity data

Activities of K_2O in the liquid phase in the K_2O-B_2O_3 system can be obtained from EMF data. Usually, a concentration cell with a reference glass or melt is used. Itoh et al. [566] employed $(K_2O)_{0.05}(B_2O_3)_{0.95}$ as the reference. Stegmaier and Dietzel used $(K_2O)_{0.0056}(B_2O_3)_{0.9944}$ as the reference [570]. Shakhmatkin and Shul'ts [630] do not report the composition of the reference melt but they give the absolute values of K_2O activity recalculated with pure liquid K_2O as the standard state. The data by Borisov and Ukhvatova [217] were not used as they did not publish the composition of the reference melt and the absolute values of EMF. As in the Na_2O-B_2O_3 system,

one of the possible sources of errors in EMF measurements can be contamination with traces of water.

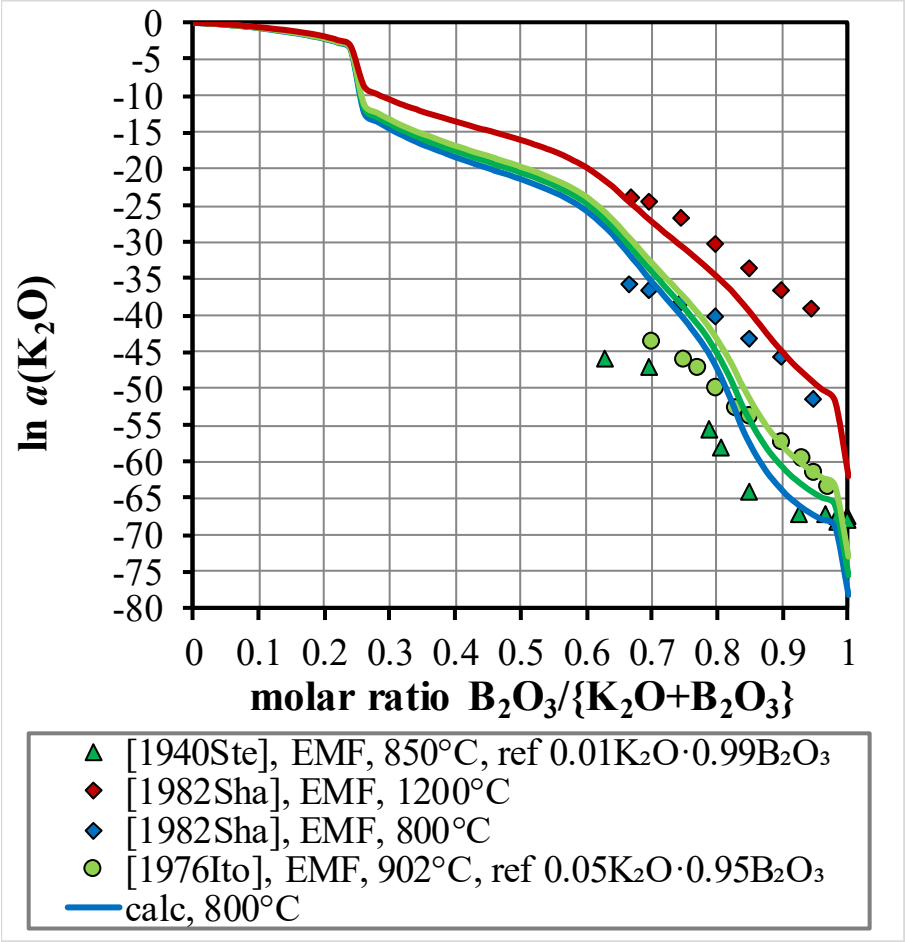

Figure 30.6 K_2O activity of the liquid phase in the K_2O-B_2O_3 system. The reference state is the pure liquid K_2O. Experimental points [566, 570, 630] and calculated lines.

The recalculated K_2O activities are presented in Figure 30.6. Unless the original EMF data are unavailable (Shakhmatkin and Shul'ts [630]), K_2O activity of reference melts was calculated using the same database as used in the optimization. As the reference melts mentioned by the original sources lie close to pure B_2O_3, we assume that the experimental data might not be exact due to water absorption. Hygroscopicity of B_2O_3-rich melts is a serious problem that has to be dealt with in the Na_2O-B_2O_3 system (Section 28.3) and in the K_2O-B_2O_3 it is supposed to be even higher.

30.4 Heat capacity and heat content data

Paukov et al. reported the low-temperature heat capacity of crystalline KBO_2 measured in an adiabatic calorimeter [684] (Figure 30.7).

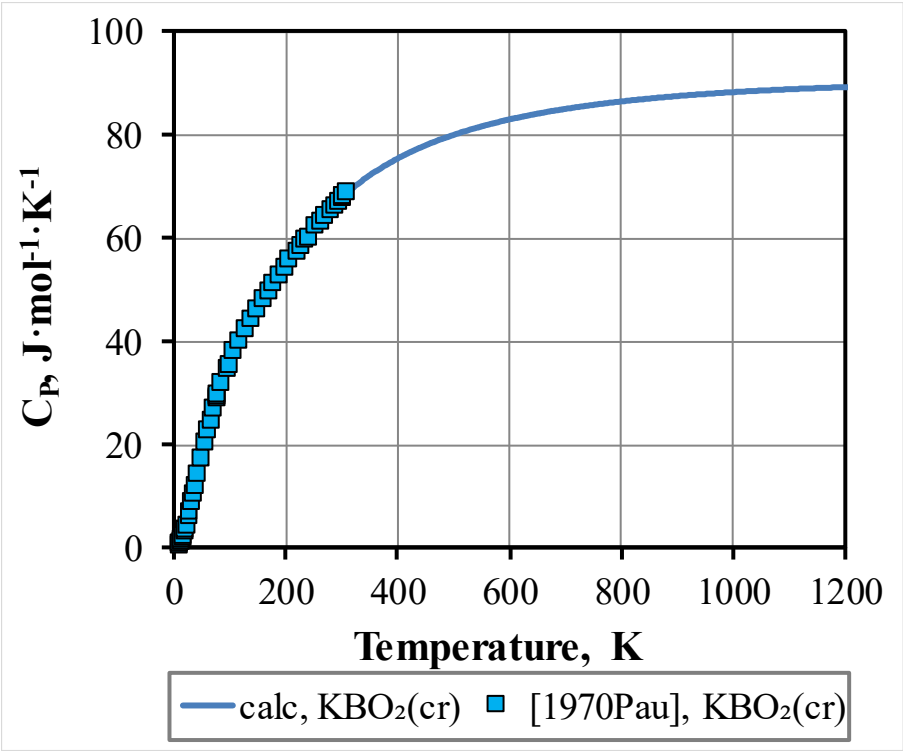

Figure 30.7 The heat capacity of potassium metaborate KBO_2. Experimental points [684] and the calculated line.

Smith and Rindone reported heat content measurements of vitreous and crystallized compositions in the K_2O-B_2O_3 system [620] (Figure 30.8). The heat capacity of glasses was approximated as the sum of the heat capacities of the simple oxides in the crystalline state below the glass transition temperature and the heat capacity of the liquid above it.

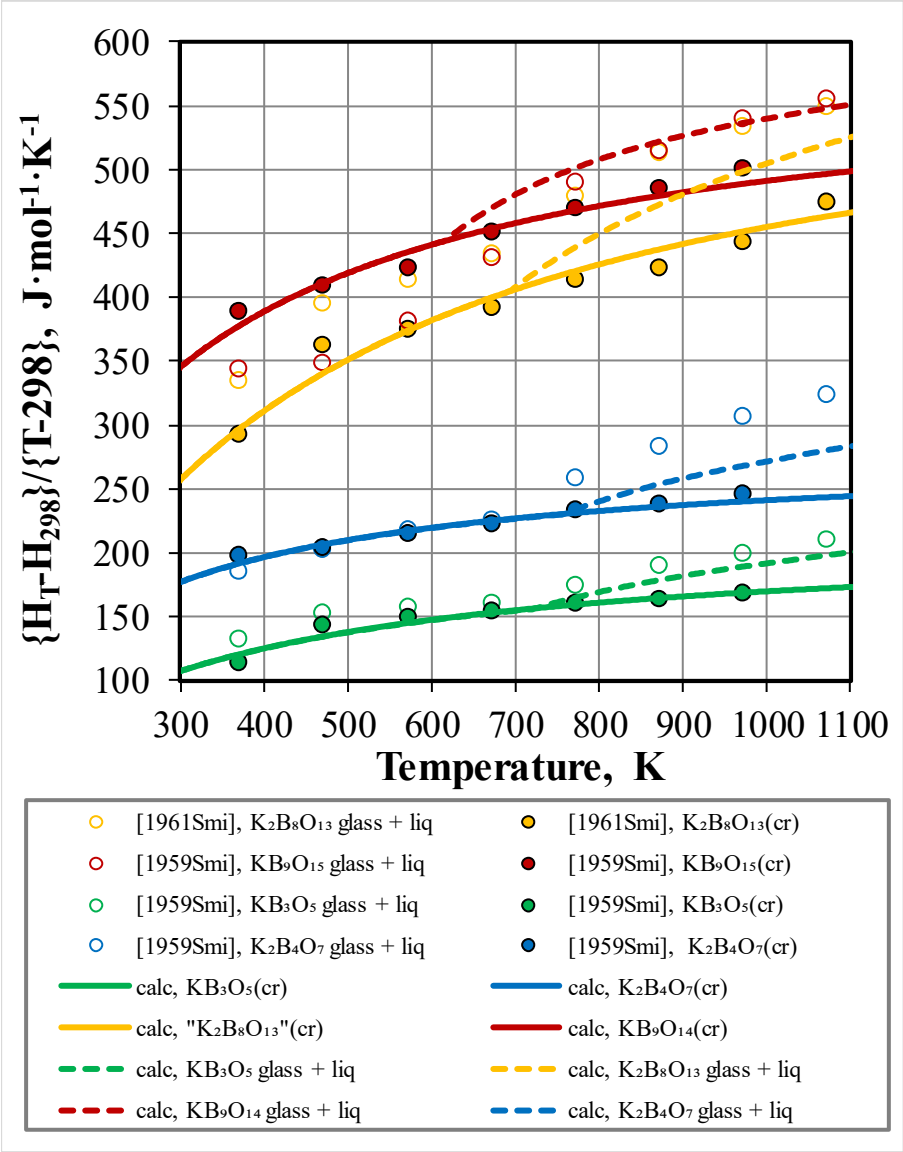

Figure 30.8 The mean heat capacity of potassium borates. Experimental points [683] and calculated lines.

30.5 Optimization results

The optimization approach in the K_2O-B_2O_3 system closely follows that of the Na_2O-B_2O_3 system. If the heat capacity and the entropy data are unavailable for some compounds, they were estimated as weighted sums of other compounds and/or simple oxides. The experimental enthalpies of formation were either adopted or they were later adjusted to fit the phase diagram.

Again as in the Na_2O-B_2O_3 system, the absolute value of the Gibbs energy of KBO_2 associate does not have great importance for the extrapolation properties in the multicomponent systems. Its value is constrained by the fact that KBO_2 is stable at 50 mol% composition based on NMR data and the fact that a still negative $g^{01}_{K,B}$ parameter is needed to avoid immiscibility at 50 mol%.

A large negative $\Delta g^{\circ}_{K,B}$ parameter sets the extent of the enthalpy of mixing; $g^{10}_{K,B}$, $\Delta g^{\circ}_{K,KB}$, $g^{10}_{K,KB}$ and $g^{001}_{K,B(KB)}$ parameters all adjust the liquidi of K_2O, K_3BO_3, and help prevent spurious miscibility gaps. $g^{01}_{K,B}$ parameter lowers KBO_2 liquidus. $\Delta g^{\circ}_{KB,B}$, $g^{10}_{KB,B}$ and $g^{01}_{KB,B}$ parameters shape the liquidus at the compositions richer in B_2O_3 than KBO_2. It is possible to reproduce the metastable miscibility gap in the system (Figure 30.2) but it was not done because of the same reasons as described in the optimization section on the Na_2O-B_2O_3 system (Section 28.6). Similar to the Na_2O-B_2O_3 system, the coordination numbers of KB-B pair were increased to make the ternary miscibility gap in the K_2O-B_2O_3-SiO_2 system appear. The exact values of the coordination numbers were found in a coupled optimization of the binary and the ternary systems.

The optimized parameters are summarized in Table A.38 and Table A.39.

CHAPTER 31 OPTIMIZATION OF THE K_2O-B_2O_3-SiO_2 SYSTEM

31.1 Phase diagram

The ternary phase diagram was extensively investigated in the works of Polyakova and Tokareva [677, 685] using DTA. A few ternary compounds were found and characterized by X-ray. Among them, $KBSi_2O_6$ seems to be more characterized than the others. Its primary crystallization field appears in the liquidus with a congruent melting point. There is some uncertainty about the true composition of $K_5B_7Si_3O_{19}$ (or $K_6B_8Si_3O_{21}$ [685]) and $K_{12}B_{10}Si_{14}O_{25}$. These two compounds already decompose at temperatures below 700°C.

$KBSi_2O_6$ analogues are absent from the Li_2O-B_2O_3-SiO_2 and the Na_2O-B_2O_3-SiO_2 phase diagrams. It seems that the compound stability increases with the radius of the alkali cation. $RbBSi_2O_6$ is the most stable in the alkali metal series. $KBSi_2O_6$ is structurally similar to leucite $KAlSi_2O_6$ [111, 112]. According to Mazza et al. [113], $KBSi_2O_6$ has two modifications (low-*T* tetragonal and high-*T* cubic) with the transition somewhere between 410° and 515°C.

Crystals of $KBSi_3O_8$ were obtained hydrothermally and investigated by Krzhizhanovskaya et al. [686] and Kimata [687]. The compound exists in two modifications: monoclinic, isostructural with aluminosilicate feldspars and the orthorhombic modification, structurally similar to danburite $CaB_2Si_2O_8$. The phase is stable up to 600°C and decomposes into $KBSi_2O_6$ and SiO_2.

Liquidus projection in the system is shown in Figure 31.1 and phase diagram in a few sections of the system are presented in Figure 31.2-Figure 31.3.

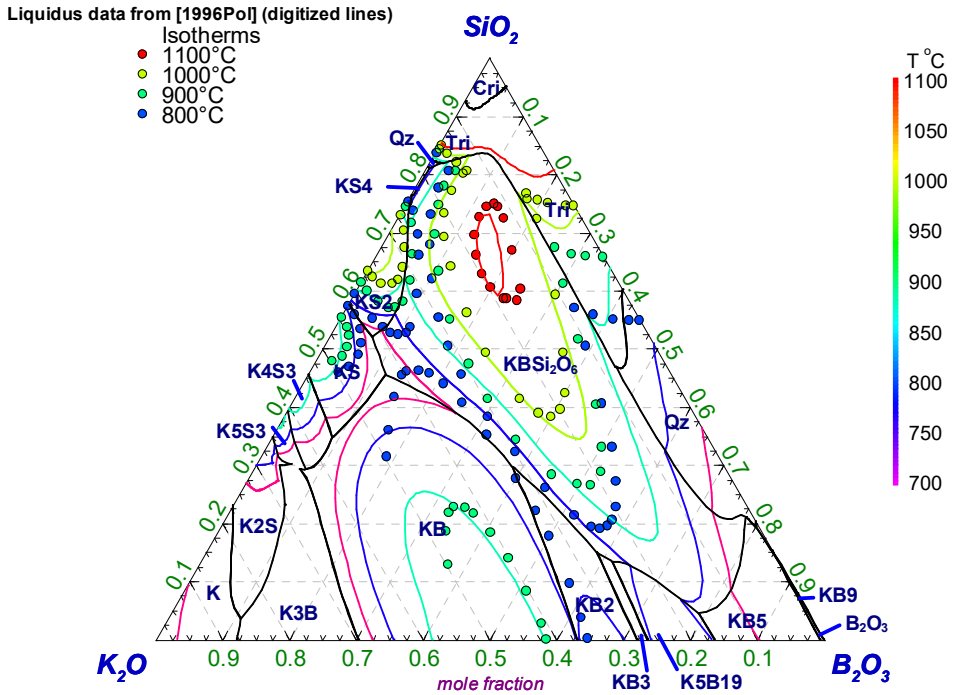

Figure 31.1 Liquidus projection in the K_2O-B_2O_3-SiO_2 system. Experimental points [685] and calculated lines.

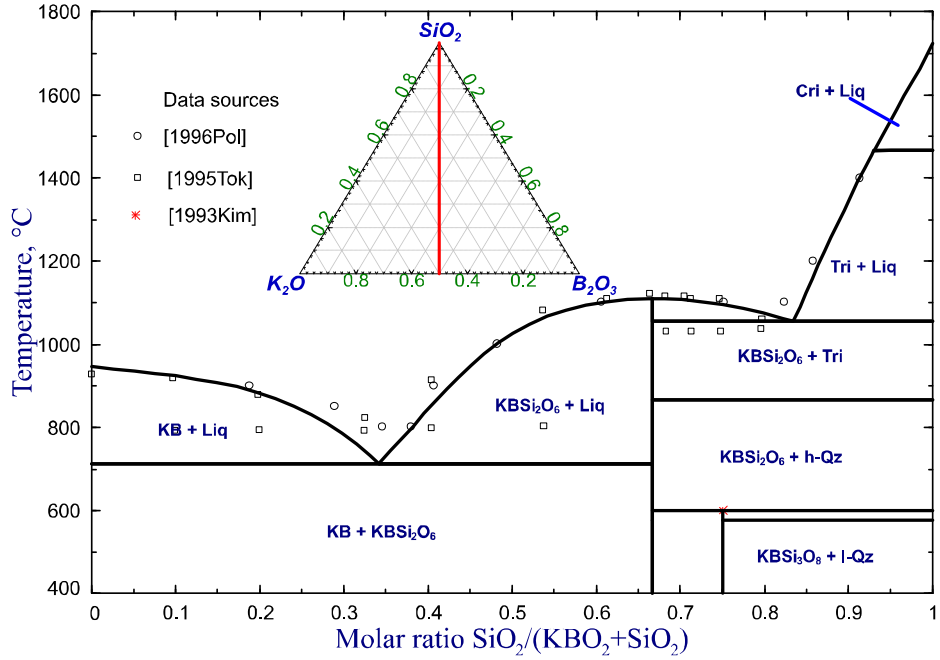

Figure 31.2 Phase diagram in the KBO_2-SiO_2 section of the K_2O-B_2O_3-SiO_2 system. Experimental points [677, 685] and calculated lines.

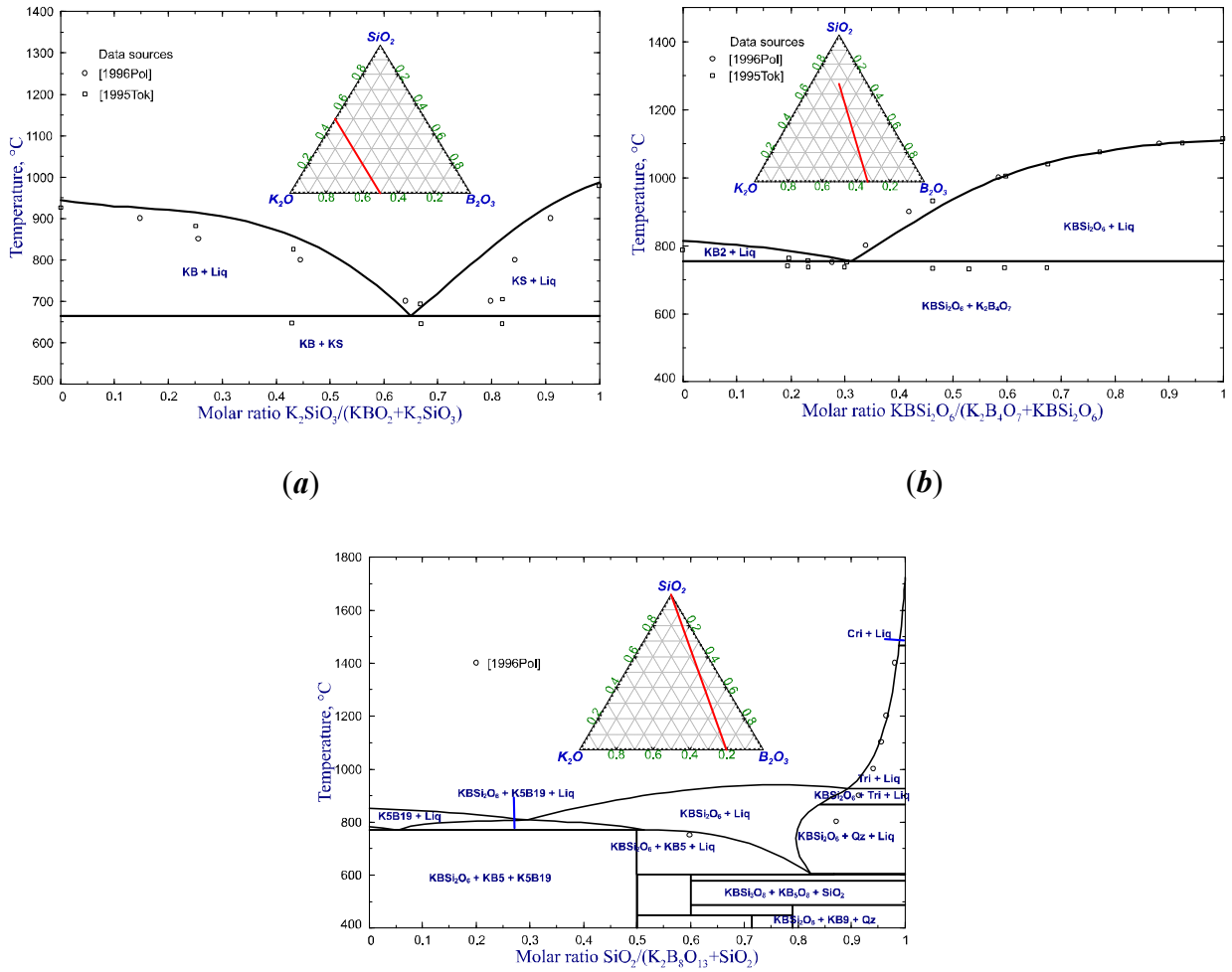

(***a***) (***b***)

(***c***)

Figure 31.3 Phase diagrams in sections through the K_2O-B_2O_3-SiO_2 system: K_2SiO_3-KBO_2 (***a***), $K_2B_4O_7$-$KBSi_2O_6$ (***b***), $K_2B_8O_{13}$-SiO_2 (***c***). Experimental points [677, 685] and calculated lines.

31.2 Miscibility gap

The immiscibility region in the K_2O-B_2O_3-SiO_2 has the same nature as in the Li_2O-B_2O_3-SiO_2 and Na_2O-B_2O_3-SiO_2 systems. According to Taylor and Owen [688], the consolute temperature is 629±5°C (4±1 mol% K_2O, 30±8 mol%B_2O_3 and 66±8 mol% SiO_2).

Taylor and Owen [688] determined the immiscibility temperature by observations of the opalescence clearance. Polyakova [653] and Polyakova and Tokareva [685] studied the

immiscibility in the ternary system using DTA of homogeneous glasses observing glass transition temperatures of two glass phases.

Isotherms of the miscibility gap are given in Figure 31.4 and polythermal sections through the gap along the long and the short axes are shown in Figure 31.5.

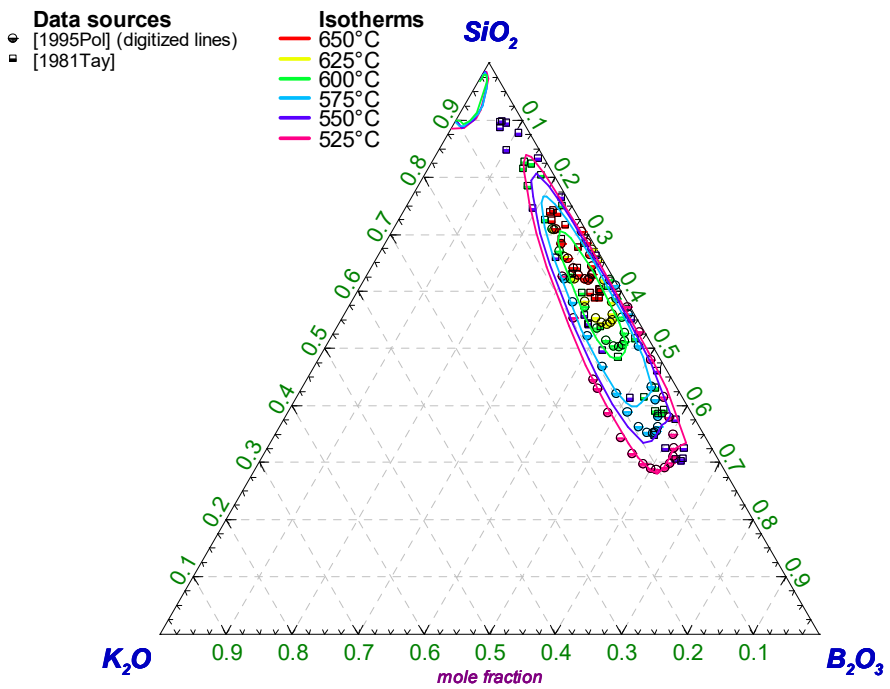

Figure 31.4 Isothermal projections of the metastable miscibility gap in the K_2O-B_2O_3-SiO_2 system. Experimental points [653, 688] and calculated lines.

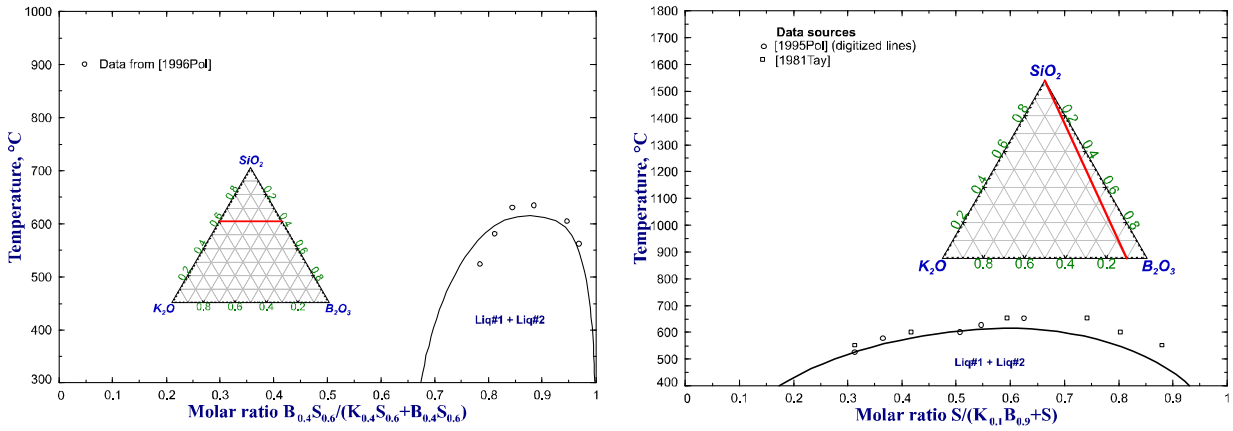

(***a***) (***b***)

Figure 31.5 Polythermal sections through the metastable miscibility gap in the K_2O-B_2O_3-SiO_2 system. Experimental points [653, 685, 688] and calculated lines.

The position of the miscibility gap is somewhat underestimated close to the SiO_2-rich corner (Figure 31.5, (***b***)) which also explains why the isotherms at 625° and 650°C are not available in Figure 31.4. Apparently, this has the same explanation as in the Na_2O-B_2O_3-SiO_2 system (Section 29.2).

31.3 Calorimetry data

The $0.8[xB_2O_3$-$(1-x)SiO_2]$-$0.2K_2O$ section was investigated by lead borate solution calorimetry at 973K [342] and acid calorimetry at 298K [680] (Figure 31.6).

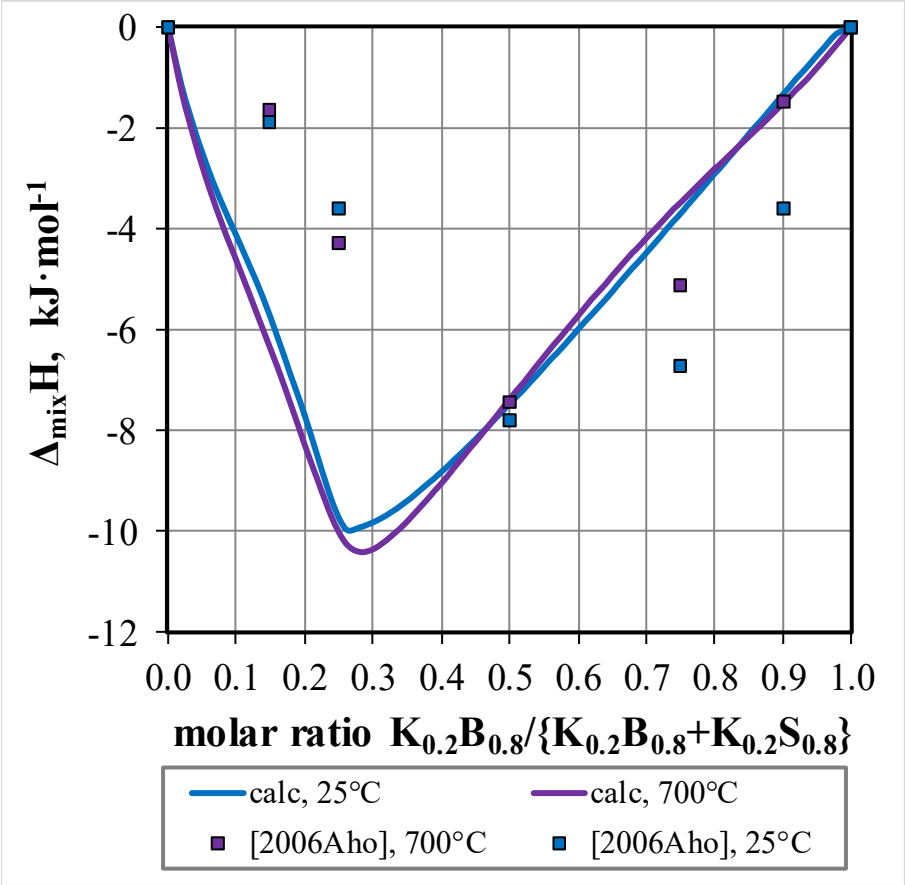

Figure 31.6 The enthalpy of mixing in the K_2O-B_2O_3-SiO_2 system at 20 mol% K_2O. Experimental points [342] and calculated lines.

31.4 Optimization results

The binary systems K_2O-B_2O_3 and K_2O-SiO_2 were optimized in this work (Chapter 9 and Chapter 30). For the B_2O_3-SiO_2 system, the optimization by Decterov et al. was adopted [15].

There are two ternary compounds in the system, $KBSi_2O_6$ and $KBSi_3O_8$, which were considered during the optimization. Unfortunately, there are no calorimetry data available on these compounds. The heat capacity and the entropy of $KBSi_2O_6$ and $KBSi_3O_8$ compounds were approximated as a sum of heat capacities and entropies of KBO_2 and SiO_2. Later, the enthalpies of formation of the compounds were adjusted in order to fit the phase equilibrium data.

The K_2O-B_2O_3-SiO_2 is the only system where the extrapolation rules are different from the sodium counterpart. The K-KB-Si//O extrapolation is K-Toop. Unlike the Na_2O-B_2O_3-SiO_2 system, it was found that in the K-B-Si//O system, K-Toop extrapolation on K-KB-Si//O gives better results.

The phase diagram of the KBO_2-SiO_2 section was modeled by KB-Si interaction ($\Delta g^{\circ}_{\mathrm{KB,Si}}$ and $g^{01}_{\mathrm{KB,Si}}$ parameters). The liquidus in the $K_2B_8O_{13}$-SiO_2 section and the ternary gap were adjusted by $g^{001}_{\mathrm{Si,KB(B)}}$, $g^{001}_{\mathrm{KB,B(Si)}}$ and $g^{002}_{\mathrm{KB,B(Si)}}$ parameters. The liquidus in the K_2SiO_3-KBO_2 section was adjusted by $g^{001}_{\mathrm{K,Si(KB)}}$ and $g^{101}_{\mathrm{K,Si(KB)}}$ parameters: the first one changes KBO_2 liquidus and eliminates a spurious miscibility gap, and the second one raises the liquidus and the eutectic point. A similar parameter, $g^{021}_{\mathrm{K,Si(KB)}}$, was used to model the liquidus in the left upper part of the phase diagram (Figure 31.1).

The optimized parameters are summarized in Table A.40 and Table A.41.

CHAPTER 32 OPTIMIZATION OF THE K_2O-Na_2O-B_2O_3 SYSTEM

32.1 Phase diagram

All available data on phase equilibria in the system are contained in the area with $X(B_2O_3) \geq 0.5$.

The monoborate section $NaBO_2$-KBO_2 (Figure 32.1) was investigated by Bergman and Vartbaronov [689] by the visual polythermal method. The visual polythermal method consists in visual observation of the crystallization process of a transparent liquid with temperature. It was noted that monoborate compositions do not present any crystallization difficulties. The same section was also studied by Van Klooster [690] by DTA. Van Klooster also took precautions to minimize losses due to evaporation.

A series of articles [582, 689, 690] proposed that $NaBO_2$ and KBO_2 solid end-members form a solid solutions series since the melting occurred over a certain temperature range. Unfortunately, Van Klooster [690] could not investigate the mixed crystals optically because of their low quality. In the works of Qiao et al. [691] and Rao et al. [607] the existence of the monoborate solid solution was confirmed by an X-ray analysis and the liquidus curve was measured using DTA. Van Klooster [690] performed DTA and reported that there is a limited mutual solubility at lower temperatures but as the temperature grows, the solid solution becomes continuous.

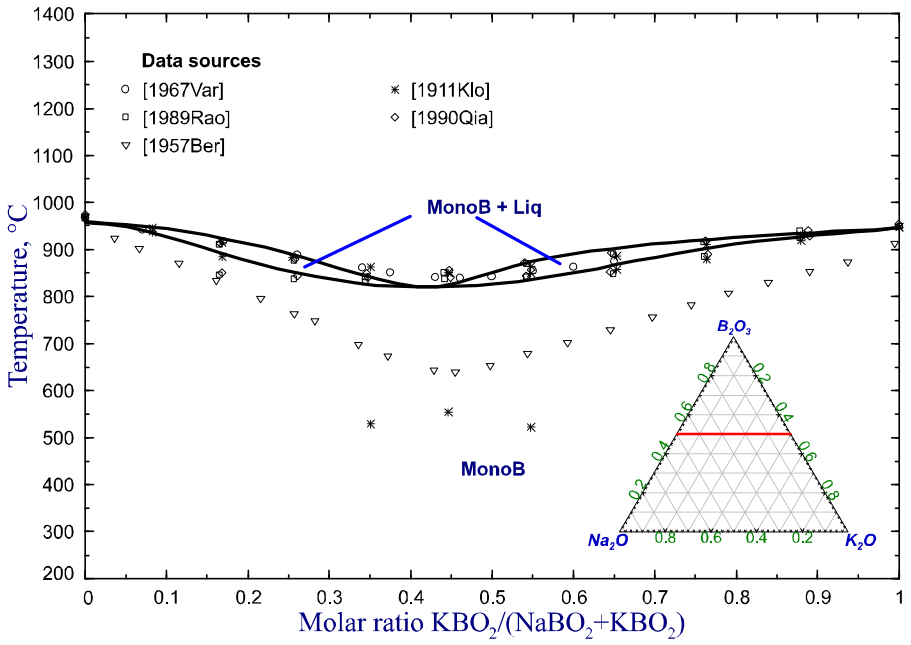

Figure 32.1 Phase diagram of the monoborate $NaBO_2$-KBO_2 section of the Na_2O-K_2O-B_2O_3 system. Experimental points [582, 607, 689-691] and calculated lines.

It was impossible to achieve both a miscibility gap in Monoborate and a narrow liquidus-solidus split as indicated in Figure 32.1. We assume the indications of a subsolidus miscibility gap [690] unreliable since no additional confirmation of its existence, besides DTA, was given.

The diborate section $Na_2B_4O_7$-$K_2B_4O_7$ was investigated by Bergman and Vartbaronov [692] by the visual polythermal method (Figure 32.2). The authors experienced certain difficulties with crystallization. A solid solution exists between the end-members which becomes discontinuous at temperatures below 510°C. Apparently, its existence was supposed from the mixture behavior upon heating. The diborate solid solutions were investigated by X-ray method [693].

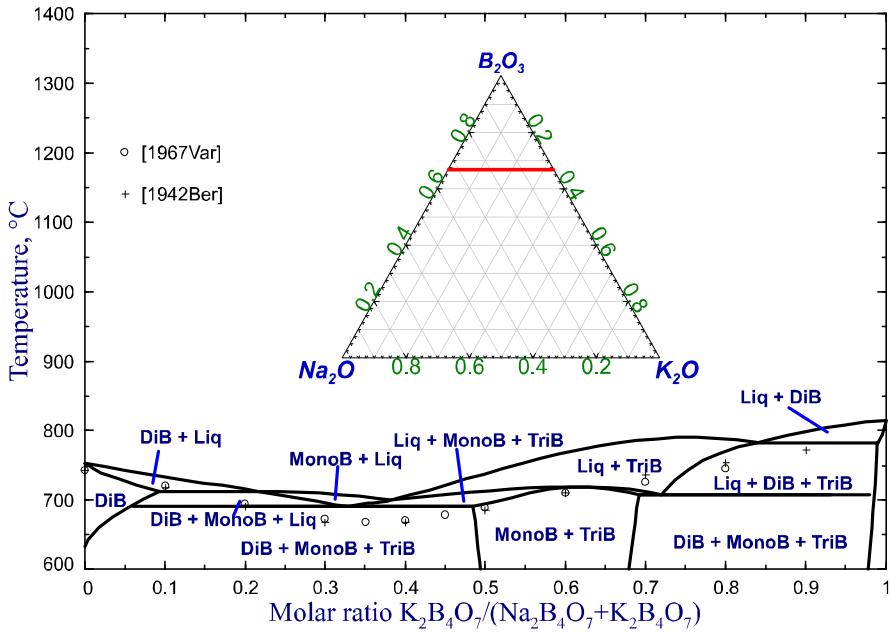

Figure 32.2 Phase diagram of the diborate $Na_2B_4O_7$-$K_2B_4O_7$ section of the Na_2O-K_2O-B_2O_3 system. Experimental points [582, 694] and calculated lines.

The triborate section NaB_3O_5-KB_3O_5 was studied by means of X-ray diffraction, DSC and the annealing and quenching techniques by Bubnova et al. [695] (Figure 32.3). Solid solutions $Na_{1-x}K_xB_3O_5$ ($0.5 < x \leq 1.0$) based on KB_3O_5 phase were found.

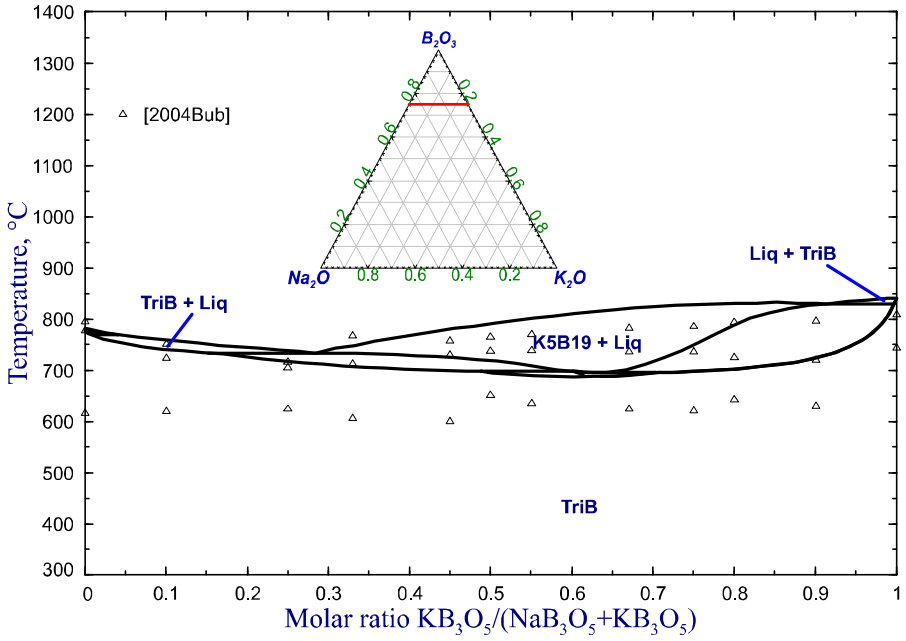

Figure 32.3 Phase diagram of the triborate NaB_3O_5-KB_3O_5 section of the Na_2O-K_2O-B_2O_3 system. Experimental points [695] and calculated lines.

Also, the reciprocal system (Na,K)||(BO_2, B_4O_7) was investigated by Vartbaronov and Bergman [582, 601] by the visual polythermal method. The diborate-monoborate cross-sections are given in Figure 32.4.

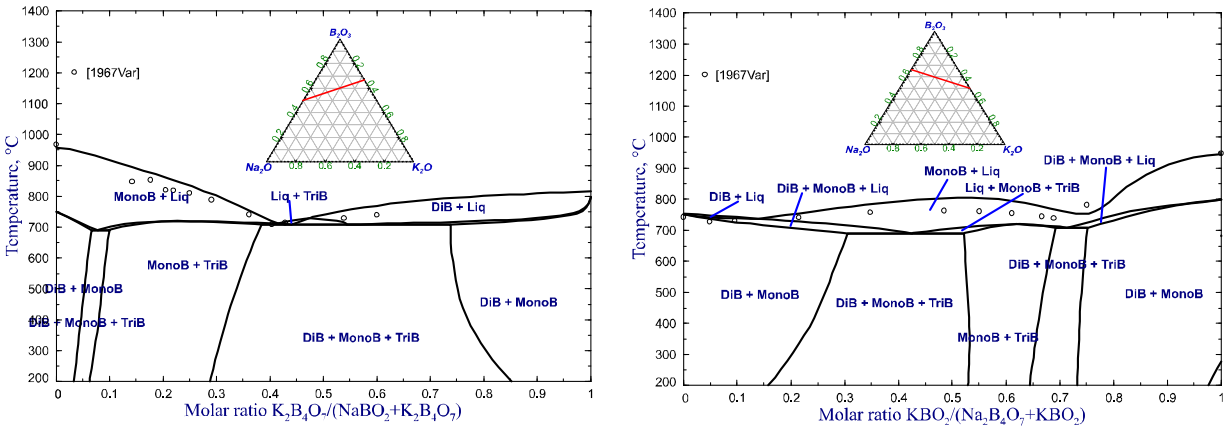

(***a***) (***b***)

Figure 32.4 Phase diagrams of the diborate-monoborate cross-sections: $K_2B_4O_7$-$NaBO_2$ (***a***) and $Na_2B_4O_7$-KBO_2 (***b***). Experimental points [582] and calculated lines.

32.2 Calorimetry data

Glass solution calorimetry was performed for $(Na_2O\text{-}K_2O)_{1-x}(B_2O_3)_x$ series with different B_2O_3 content (Figure 32.5, Figure 32.6). Usually, $HF+HNO_3$ [696] or diluted HNO_3 [682] were used as solvents at 25°C. The recalculation of the glass calorimetry data into the enthalpy of mixing is straight-forward. Since the glass transition temperatures are almost the same along sections with constant B_2O_3 content, it can be shown that the enthalpy of mixing for the glass is essentially the same as the enthalpy of mixing for the liquid, assuming that the heat capacities of both glass and liquid can be adequately estimated by the Neumann–Kopp rule from the heat capacities of pure glass and liquid oxides.

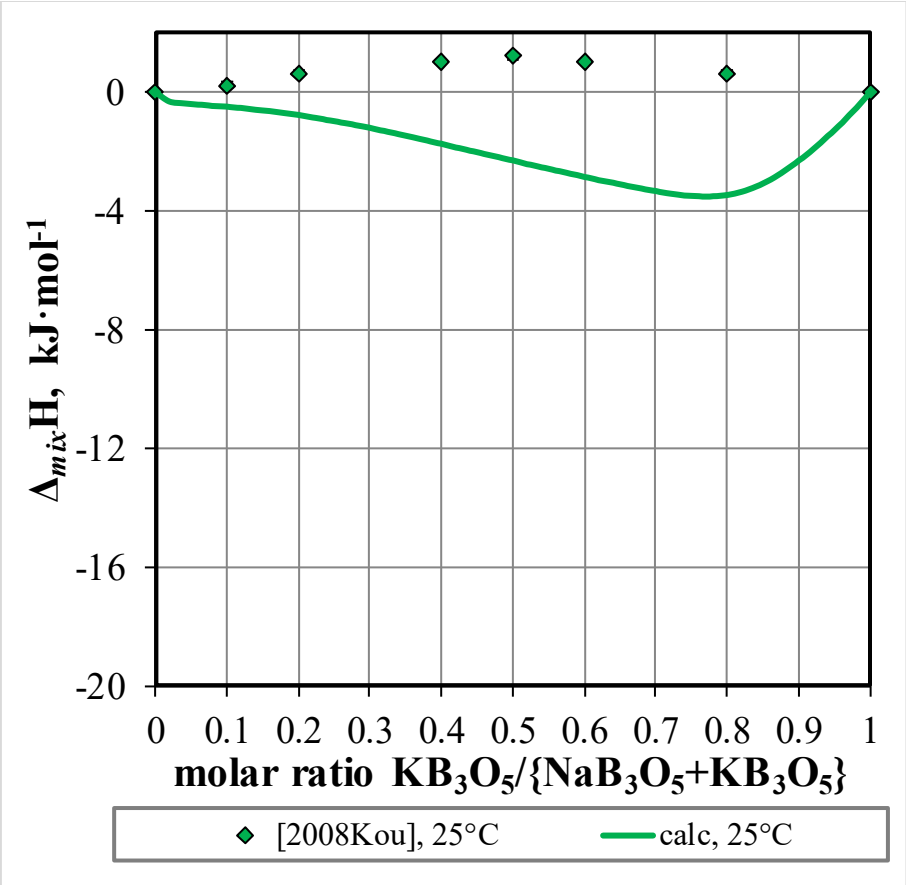

Figure 32.5 The enthalpy of mixing of the liquid phase in the triborate section $NaB_3O_5\text{-}KB_3O_5$ at 25°C. Experimental points [696] and the calculated line.

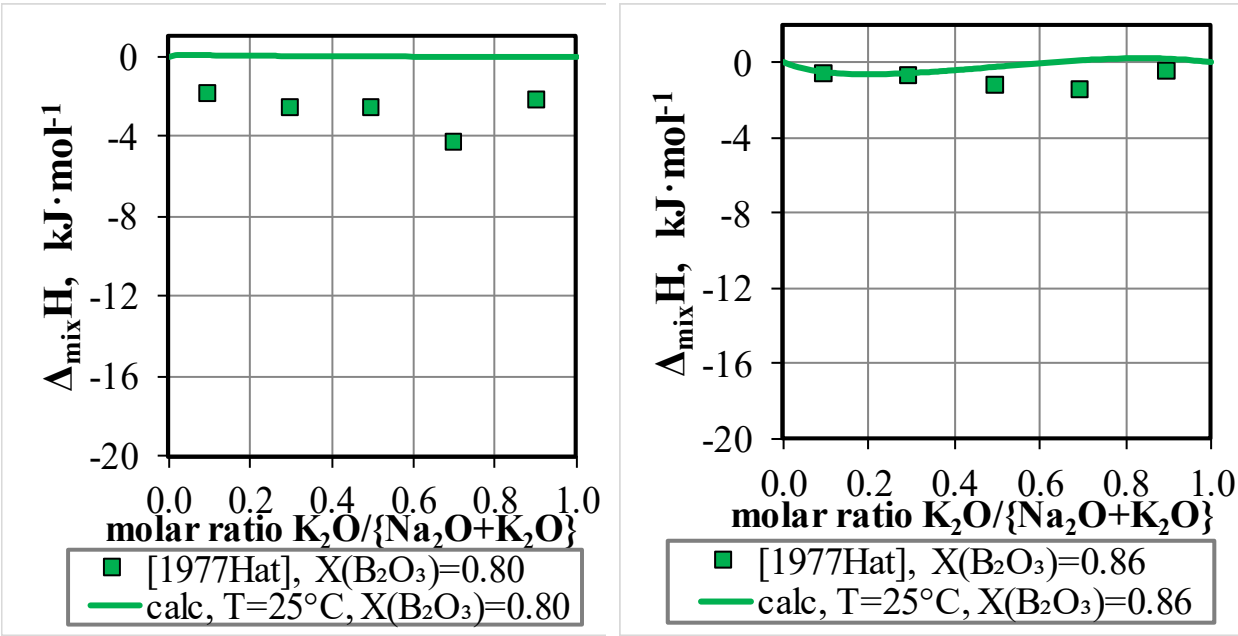

(***a***) (***b***)

Figure 32.6 The enthalpy of mixing of the liquid phase in the section with 80 mol% (***a***) and 86 mol% (***b***) B_2O_3 at 25°C. Experimental points [682] and calculated lines.

32.3 Optimization results

The binary Na_2O-B_2O_3 and K_2O-B_2O_3 systems were optimized in this work (Chapter 28 and Chapter 30) while the Na_2O-K_2O system was assumed ideal.

There are no new compounds in the system; however, mono-, di- and triborates form solid solutions. In case where more than one stable polymorph exists, a generic end-member is created (see section 2.3). For sodium and potassium triborates, several polymorphs exist but one of them is stable.

The default Kohler extrapolation among NaB-KB-B//O,O was chosen. Because of chemical and structural similarity of B, NaB and KB species, the interaction parameters among them must be of the same order of magnitude. If there are moderately negative parameters of interaction NaB-B and KB-B there should be also a moderate negative interaction NaB-KB ($\Delta g^{\circ}_{NaB,KB}$). The second liquid

parameter, $g^{101}_{B,KB(NaB)}$ is required to compensate for a liquidus asymmetry, probably caused by uneven interactions in the Na_2O-B_2O_3 and K_2O-B_2O_3 systems.

The interactions parameters in the solid solutions were chosen in order to reproduce the liquidus. Unfortunately, it was not possible to reproduce the subsolidus immiscibility of monoborates (Figure 32.1).

The optimized parameters are summarized in Table A.42.

CHAPTER 33 CONCLUSION AND RECOMMENDATIONS

During this research project, the alkali-containing part of the Na_2O-K_2O-CaO-MgO-Al_2O_3-B_2O_3-SiO_2 system was optimized. Due to the substantial amount of data, only the most important parts of the optimized systems appear in this thesis including the Na_2O-K_2O-CaO-Al_2O_3-SiO_2, Na_2O-CaO-MgO-Al_2O_3-SiO_2, K_2O-MgO-SiO_2 and the Na_2O-K_2O-B_2O_3-SiO_2 subsystems.

The existing approach to the experimental data processing has been improved in some ways. A physically consistent model of the heat capacity of solids without phase transitions was used for assessment and extrapolation of heat capacity and heat content data. A unifying approach to modeling of solution end-members with multiple modifications was proposed and applied. A method to recalculate the properties of glasses into the properties of liquids with the same composition was proposed and used throughout the work. A semi-automated optimization procedure was developed and adopted. A nonlinear least squares algorithm was applied to search for an optimal parameter set in each system. The general principles and the dataflow chart of the semi-automated optimization procedure were given and explained.

Based on the available structural data, models of the solid solutions present in the Na_2O-K_2O-CaO-MgO-Al_2O_3-B_2O_3-SiO_2 system were developed, revised and/or extended. When applicable, selection of specific models was accompanied by detailed explanations and illustrations to overcome a common lack in readers' knowledge of crystallography and crystal chemistry.

The current database was developed as part of a large oxide database within the *FactSage* package. Special attention was paid to the limitations and inconsistencies of this database including underestimated values of the heat content of silicate liquids, the systematic deviation of the Mullite/Corundum boundary from experiments by independent authors in various ternary systems with the Al_2O_3-SiO_2 boundary and others. Unfortunately, to introduce the necessary changes to the full database was not feasible in the timeframe of the current research project. These inconsistencies were pointed out first, for the future researchers and, secondly, for the users to be aware of the weak points of this database.

Our novel "caging" hypothesis was introduced as a way to explain the systematic discrepancies of cristobalite liquidus data in the series of binary systems between an alkali oxide and silica. The modeling approach, based on the "caging" hypothesis, which includes extra dimer species Na_2^{2+}

and K_2^{2+} was developed and successfully applied. The caging phenomenon was especially remarkable in the Na_2O-SiO_2 and the Li_2O-SiO_2 systems. Although, the optimization of the Li_2O-SiO_2 system goes beyond the scope of the current work, we are confident that the quality of the optimization of the lithia-containing systems would significantly benefit from the introduction of a dimer species on the cationic sublattice.

The charge compensation effect in the Na_2O-Al_2O_3-SiO_2 and K_2O-Al_2O_3-SiO_2 systems was accounted for by the introduction of the associate species $NaAl^{4+}$ and KAl^{4+}.

The structure and properties of alkali-containing borate melts and glasses were discussed in detail; the choice of the modeling approach based on the structural information was explained and validated. The origin and nature of the binary metastable miscibility gap in the systems Na_2O-B_2O_3 and K_2O-B_2O_3, as well as the ternary metastable miscibility gap in the Na_2O-B_2O_3-SiO_2 and K_2O-B_2O_3-SiO_2 systems, were analyzed and discussed. The essential features of these systems were modeled and reproduced with an explanation of the limitations of the existing database that do not allow the reproduction of the binary miscibility gap.

In general, optimization studies are limited to binary and ternary systems while the properties and equilibria in higher-order systems are assumed to extrapolate reasonably well. Here, a special effort was made to characterize and illustrate the abundant experimental data in the multicomponent systems.

The system in question has been relatively well studied and characterized in the literature. However, there are still areas which have not been studied experimentally. Sample preparation plays an important role regarding the compositions available for studies. The most conventional source of alkali oxide is carbonates Na_2CO_3 and K_2CO_3. The degree to which carbonates decompose in mixtures determines the maximum content of alkali oxides in prepared samples. For example, the maximum content of Na_2O and K_2O in silicate samples cannot exceed 50 mol%; the same applies to alkali aluminate samples. All samples containing more alkali oxide require the use of much less available pure Na_2O and K_2O as reagents. It is one of the main reasons why the alkali oxide-rich parts of the Na_2O-SiO_2, K_2O-SiO_2, Na_2O-B_2O_3 and K_2O-B_2O_3 systems have been investigated relatively poorly or even not at all.

Besides the difficulties in preparation, mixtures of alkali oxides with CaO, MgO and Al_2O_3 (refractory oxides) have both very high liquidus temperatures and high partial pressures of alkalies which make them extremely challenging for liquidus determination. Also, alkali oxides are extremely corrosive at high temperatures; expensive crucibles made of gold or other inert materials need to be used, thermocouples need to be frequently recalibrated and replaced. For example, the liquidus in the $CaO-Na_2O-Al_2O_3$ and the $CaO-K_2O-Al_2O_3$ systems has been investigated only close to the $CaO-Al_2O_3$ binary system; the liquidi in the $MgO-Na_2O-Al_2O_3$ and the $MgO-K_2O-Al_2O_3$ systems have not been investigated at all. Samples with a low content of silica or boron oxide are difficult to quench which made yet another obstacle to the investigation of certain compositions in the $CaO-Na_2O-SiO_2$, $CaO-K_2O-SiO_2$, $MgO-Na_2O-SiO_2$, $MgO-K_2O-SiO_2$ systems.

The current model of the $Na_2O-K_2O-CaO-MgO-Al_2O_3-B_2O_3-SiO_2$ system has been optimized with the data available in the literature. It is possible that the lack of experimental data in certain composition regions (as described above) affected the accuracy of the model. The lack of experimental data in these regions is mainly caused by experimental difficulties that have not been yet overcome and not by a general lack of interest in these region by the scientific community.

However, we assume that the lack of data in alkali-rich, silica poor regions does not affect the overall quality of the model. For example, in the $CaO-K_2O-SiO_2$ system, there are data lacking (or unreliable) beyond the K_2SiO_3 composition in the K_2O-SiO_2 binary subsystem and at the compositions with less than 50 mol% of silica in the ternary system. However, the extrapolation rules for the Gibbs energy in the liquid phase (asymmetric Toop model with SiO_2 as the special component) makes sure that the Gibbs energy in the K_2O-SiO_2 subsystem is projected into ternary compositions with the same content of silica. The contribution of the Gibbs energy from the K_2O-CaO binary system (which has a high uncertainty but is not supposed to be large) is very small compared to the contributions from the K_2O-SiO_2 and the $CaO-SiO_2$ systems; it does not affect the area with $X(SiO_2) > 50$ mol% in any significant way. The same applies to systems with more components. The uncertainly of the model is localised within the region with a small SiO_2 (and B_2O_3) content and with a high alkali content.

REFERENCES

1. Gy, R., *Ion exchange for glass strengthening.* Mater. Sci. Eng., B, 2008. **149**(2): p. 159-165.
2. *Boron in glass and glass fibre.* http://www.etiproducts.com/.
3. Seyfarth, A., *Boron in glass determination using WDXRF.* Adv. X-Ray Anal., 2008. **51**: p. 269-274.
4. *Use of borates in glass and glass fibre.* http://ec.europa.eu/geninfo.
5. Besmann, T.M., K.E. Spear, and E.C. Beahm. *Assessment of Nepheline Precipitation in Nuclear Waste Glass via Thermochemical Modeling*. in *Materials Research Society Symposium Proceedings (2000), 608(Scientific Basis for Nuclear Waste Management XXIII)*. 2000. Materials Research Society.
6. Spear, K.E. and M.D. Allendorf, *Thermodynamic Analysis of Alumina Refractory Corrosion by Sodiumor Potassium Hydroxide in Glass Melting Furnaces.* J. Electrochem. Soc., 2002. **149**(12): p. B551-B559.
7. Allendorf, M.D. and K.E. Spear, *Thermodynamic Analysis of Silica Refractory Corrosionin Glass-Melting Furnaces.* J. Electrochem. Soc., 2001. **148**(2): p. B59-B67.
8. Flecher, K.E., H.G. Midgley, and A.E. Moore, *The binary system $3CaO{\cdot}Al_2O_3$-$Na_2O{\cdot}8CaO{\cdot}3Al_2O_3$ within the system CaO-Al_2O_3-Na_2O.* Magaz. Concrete Res., 1965. **17**(53): p. 171-176.
9. Ostrowski, C. and J. Zelazny, *Solid solutions of calcium aluminates C3A, C12A7 and CA with sodium oxide.* J. Therm. Anal. Calorim., 2004. **75**(3): p. 867-885.
10. Yao, Y.-F.Y. and J.T. Kummer, *Ion-exchange properties of and rates of ionic diffusion in β-alumina.* J. Inorg. Nucl. Chem., 1967. **29**(9): p. 2453-2475.
11. Chartrand, P. and A.D. Pelton, *Modeling the Charge Compensation Effect in Silica-rich Na_2O-K_2O-Al_2O_3-SiO_2 Melts.* CALPHAD, 1999. **23**(2): p. 219-230.
12. Denisov, Y.V. and A.A. Zubovich, *Boson peak and medium-range order structure of alkali borate glasses.* Glass Phys. Chem., 2003. **29**(4): p. 345-352.
13. Jung, I.-H., S.A. Decterov, and A.D. Pelton, *Thermodynamic Modeling of the CaO-MgO-Al_2O_3-SiO_2 System.* in preparation.
14. Decterov, S.A. and A.D. Pelton, *A thermodynamic database for B_2O_3-containing systems*. 2006. p. 25 pp.
15. Decterov, S.A., V. Swamy, and I.-H. Jung, *Thermodynamic modeling of the B_2O_3-SiO_2 and B_2O_3-Al_2O_3 systems.* Int. J. Mater. Res., 2007. **98**(10): p. 987-994.
16. Swamy, V., I.-H. Jung, and S.A. Decterov, *Thermodynamic modeling of the Al_2O_3-B_2O_3-SiO_2 system.* J. Non-Cryst. Solids, 2009. **355**(34-36): p. 1679-1686.

17. Wu, P., G. Eriksson, and A.D. Pelton, *Optimization of the Thermodynamic Properties and Phase Diagrams of the Na_2O-SiO_2 and K_2O-SiO_2.* J. Am. Ceram. Soc., 1993. **76**(8): p. 2059-64.

18. Kim, D., *Coupled Experimental Study and Thermodynamic Optimization of the K_2O-Na_2O-CaO-MgO-Al_2O_3-SiO_2*, in *Department of Mining and Materials Engineering*. 2017, McGill University: Montreal, Quebec, Canada.

19. Kim, D.-G., B. Konar, and I.-H. Jung, *Coupled Experimental Study and Thermodynamic Optimization of the K_2O-MgO and K_2O-MgO-SiO_2 Systems.* Metall. Mater. Trans. B, 2017. **48**(5): p. 2788-2803.

20. Kim, D.-G., B. Konar, and I.-H. Jung, *Thermodynamic optimization of the K_2O-Al_2O_3-SiO_2 system.* Ceram. Int., 2018. **44**(14): p. 16712-16724.

21. Kang, Y.-B. and P. Chartrand, *Calculation of property diagram as a Zero-Phase Fraction line of auxiliary phase.* CALPHAD, 2016. **55**: p. 69-75.

22. Voronin, G.F. and A.L. Voskov, *Calculation of phase equilibria and construction of phase diagrams by convex hull method.* Moscow University Chemistry Bulletin, 2013. **68**(1): p. 1-8.

23. Voronin, G.F. and I.B. Kutsenok, *Universal Method for Approximating the Standard Thermodynamic Functions of Solids.* J. Chem. Eng. Data, 2013. **58**(7): p. 2083-2094.

24. Richet, P. and Y. Bottinga, *Thermochemical Properties of Silicate Glasses and Liquids: A Review.* Rev. Geophys., 1986. **24**(1): p. 1-25.

25. http://www.crct.polymtl.ca/fact/factsage/Intrsage.pdf. (Montreal).

26. Richet, P., R.A. Robie, and B.S. Hemingway, *Entropy and Structure of Silicate Glasses and Melts.* Geochim. Cosmochim. Acta, 1993. **57**(12): p. 2751-2766.

27. Pelton, A.D., et al., *The Modified Quasichemical Model. I - Binary Solutions.* Metall. Mater. Trans. B, 2000. **31**(4): p. 651-659.

28. Pelton, A.D. and P. Chartrand, *The Modified Quasichemical Model. II - Multicomponent Solutions.* Metall. Mater. Trans. A, 2001. **32**(6): p. 1355-1360.

29. Chartrand, P. and A.D. Pelton, *On the Choice of "Geometric" Thermodynamic Models.* J. Phase Equilib., 2000. **21**(2): p. 141-147.

30. Hillert, M., *The Compound Energy Formalism.* J. Alloys Compd., 2001. **320**(2): p. 161-176.

31. Angel, R.J. and C.T. Prewitt, *Crystal structure of mullite: A re-examination of the average structure.* Am. Mineral., 1986. **71**(11-12): p. 1476-1482.

32. Fischer, R.X., et al., *Crystal structure of synthetic $Al_4B_2O_9$: a member of the mullite family closely related to boralsilite.* Am. Mineral., 2008. **93**(5-6): p. 918-927.

33. Edgar, A.D., *Chemistry, occurrence and paragenesis of feldspathoids: a review*, in *Feldspars and Feldspathoids*, W.L. Brown, Editor. 1984, D. Reidel Publishing Company. p. 501-532.

34. Buerger, M.J., G.E. Klein, and G. Donnay, *Determination of the crystal structure of nepheline.* Am. Mineral., 1956. **39**: p. 805-818.

35. Cellai, D., et al., *X-ray study of the trigonal → hexagonal phase transition in metamorphic kalsilite.* Am. Mineral., 1999. **84**(11-12): p. 1950-1955.

36. Graetsch, H. and I. Topalovic-Dierdorf, *^{29}Si MAS NMR spectrum and superstructure of modulated tridymite L3-To(MX-1).* Eur. J. Mineral., 1996. **8**(1): p. 103-113.

37. Hovis, G.L., et al., *X-ray powder diffraction and sodium-23, aluminum-27, and silicon-29 MAS-NMR investigation of nepheline-kalsilite crystalline solutions.* Am. Mineral., 1992. **77**(1-2): p. 19-29.

38. Dollase, W.A. and W.M. Thomas, *The crystal chemistry of silica-rich, alkali-deficient nepheline.* Contrib. Mineral. Petrol., 1978. **66**(3): p. 311-18.

39. Henderson, C.M.B. and J. Roux, *Inversions in sub-potassic nephelines.* Contrib. Mineral. Petrol., 1977. **61**(3): p. 279-298.

40. Hovis, G.L. and J.A. Crelling, *The Effects of Excess Silicon on Immiscibility in the Nepheline-Kalsilite System.* Am. J. Sci., 2000. **300**: p. 238-249.

41. Ferry, J.M. and J.G. Blencoe, *Subsolidus phase relations in the nepheline-kalsilite system at 0.5, 2.0, and 5.0 kbar.* Am. Mineral., 1978. **63**(11-12): p. 1225-1240.

42. Hovis, G.L. and J. Roux, *Thermodynamic mixing properties of nepheline-kalsilite crystalline solutions.* Am. J. Sci., 1993. **293**(10): p. 1108-27.

43. Tuttle, O.F. and J.V. Smith, *The Nepheline-Kalsilite System. II. Phase Relations.* Am. J. Sci., 1958. **256**: p. 571-589.

44. Hovis, G.L., A. Mott, and J. Roux, *Thermodynamic, phase equilibrium, and crystal chemical behavior in the nepheline-kalsilite system.* Am. J. Sci., 2009. **309**(5): p. 397-419.

45. Sobrados, I. and M. Gregorkiewitz, *Ion exchange between tectosilicates with the nepheline-kalsilite framework and molten MNO_3 or MCl (M = Li, Na, K, Ag).* Phys. Chem. Miner., 1993. **20**(6): p. 433-441.

46. Roth, R.S., *Phase Equilibriums Research in Portions of The Potassium Oxide-Magnesium Oxide-Iron(III) Oxide-Aluminum Oxide-Silicon Dioxide System.* Adv. Chem. Ser.186/ Solid state Chem: Contemp Overview, 1980. **254 (5499)**: p. 391-408.

47. Richet, P., et al., *Thermodynamics of Open Networks:Ordering and Entropy in $NaAlSiO_4$ Glass, Liquid, and Polymorphs.* Phys. Chem. Miner., 1990. **17**(5): p. 385-394.

48. Kelley, K.K., et al., *Thermodynamic Properties of Sodium-Aluminum and Potassium-Aluminum Silicates.* Rept.-US Bur Mines , Report of Investigation #4955, 1953. **4955**: p. 1-21.

49. Greig, J.W. and T.F.W. Barth, *The system $Na_2O{\cdot}Al_2O_3{\cdot}2SiO_2$ (nephelite, carnegieite) $Na_2O{\cdot}Al_2O_3{\cdot}6SiO_2$ (albite).* Am. J. Sci., 1938. **35A**(5): p. 93-112.

50. Bowen, N.L., *Sodium potassium nephelites.* Am. J. Sci., 1917. **43**: p. 115-132.

51. Goldsmith, J.R., *Some aspects of the system $NaAlSiO_4$-$CaO{\cdot}Al_2O_3$.* Am. Mineral., 1949. **34**(12): p. 471-493.

52. Bowen, N.L., *The Binary System: $Na_2Al_2Si_2O_8$ (Nephelite, Carnegieite), $CaAl_2Si_2O_8$ (Anorthite).* Am. J. Sci., 1912. **33 (4th ser)**: p. 551-573.

53. Thery, J. and D. Briancon, *Structure and properties of sodium aluminate.* Rev. Int. Hautes Temp. Refract., 1964. **1**(3): p. 221-227.

54. Beletskii, M.S., et al., *Reaction of Sodium Aluminate with Potassium Aluminate.* Tr., Vses. Nauchn.-Issled. Alyumin.-Magnievyi Inst., 1960. **46**: p. 34-39.

55. Schairer, J.F. and N.L. Bowen, *The system Na_2O-Al_2O_3-SiO_2.* Am. J. Sci., 1956. **254**(731): p. 129-195.

56. Berezhnoi, A.S., et al., *Characteristics of polycomponent high-basicity silicates of the sodium oxide-potassium oxide-calcium oxide-magnesium oxide-silicon dioxide system.* Izv. Akad. Nauk SSSR, Neorg. Mater., 1976. **12**(9): p. 1653-1658.

57. Kroll, H., *Feldspate im System $KAlSi_3O_6$-$CaAl_2Si_2O_8$-$NaAlSi_3O_6$: Al,Si-Verteilung und Gitterparameter, Phasen-Transformationen und Chemismus*. 1971: Wilhelms-Universitiit. Mtnster.

58. Harlow, G.E., *The anorthoclase structures: the effects of temperature and composition.* Am. Mineral., 1982. **67**(9-10): p. 975-996.

59. Winter, J.K., F.P. Okamura, and S. Ghose, *A high-temperature structural study of high albite, monalbite, and the analbite → monalbite phase transition.* Am. Mineral., 1979. **64**(3-4): p. 409-423.

60. Kroll, H., *Determination of aluminum, silicon distribution in alkali feldspars from x-ray powder data.* Neues Jahrb. Mineral., Monatsh., 1971(2): p. 91-94.

61. Kroll, H., *Estimation of the aluminum, silicon distribution of feldspars from the lattice translations Tr[110] and Tr[1(vin)110]. I. Alkali feldspars.* Contrib. Mineral. Petrology, 1973. **39**(2): p. 141-156.

62. Brown, W.L. and I. Parsons, *Alkali feldspars: ordering rates, phase transformations, and behavior diagrams for igneous rocks.* Mineral. Mag., 1989. **53**(3): p. 25-42.

63. Goldsmith, J.R. and D.M. Jenkins, *The high-low albite relations reveled by reversal of degree of order at high pressures.* Am. Mineral., 1985. **70**: p. 911-923.

64. Donnay, G. and J.D.H. Donnay, *Symmetry change in the high-temperature alkali feldspar series.* Am. J. Sci., Bowen Vol. Pt., 1952. **1**: p. 115-132.

65. Laves, F., *Phase relations of the alkali feldspars. II. The stable and pseudo-stable phase relations in the alkali feldspar system.* J. Geol., 1952. **60**: p. 549-574.

66. Merkel, G.A. and J.G. Blencoe, *Thermodynamic procedures for treating the monoclinic/triclinic inversion as a high-order phase transition in equations of state for binary analbite-sanidine feldspars.* Adv. Phys. Geochem., 1982: p. 243-284.

67. Smith, J.V., *Phase diagrams for alkali feldspars.* Intern. Geol. Congr., Rept. 21st Session, Copenhagen, 1960. **Pt. 21**: p. 185-193.

68. Smith, J.V., *Phase relations of plagioclase feldspars*, in *Feldspars and Feldspathoids*, W.L. Brown, Editor. 1984, D. Reidel Publishing Company. p. 55-94.

69. Ai, Y. and D.H. Green, *Phase Relations in the System Anorthite-Potassium-Feldspar At 10 Kbar with Emphasis on Their Solid Solutions.* Mineral. Mag., 1989. **53(371)**: p. 337-45.

70. Smith, J.V., *Re-examination of the crystal structure of melilite.* Am. Mineral., 1953. **38**(1): p. 643-661.

71. Schairer, J.F., J.H.S. Yoder, and C.E. Tilley, *The High-Temperature Behavior of Synthetic Melilites in the Join Gehlenite-Soda Melilite-Akermanite.* Carnegie Inst. Washington Yearb. (1966), 1966. **65**: p. 217-226.

72. Juan, V.C., *The system $CaSiO_3$-$Ca_2Al_2SiO_7$-$NaAlSiO_4$.* J. Geol., 1950. **58**(1): p. 1-15.

73. Foster, W.R., *The system $NaAlSi_3O_8$-$CaSiO_3$-$NaAlSiO_4$.* J. Geol., 1942. **50**(1): p. 152-173.

74. Prostakova, V., et al., *Experimental investigation and thermodynamic modeling of the ($NiO + CaO + SiO_2$), ($NiO + CaO + MgO$) and ($NiO + CaO + MgO + SiO_2$) systems.* J. Chem. Thermodyn., 2015. **86**: p. 130-142.

75. Deer, W.A., R.A. Howie, and J. Zussman, *An Introduction to the Rock Forming Minerals*. 1966: Longman House, Hong Kong. 528 pp.

76. Okamura, F.P., S. Ghose, and H. Ohashi, *Structure and Crystal Chemistry of Calcium Tschermak's Pyroxene, $CaAlAlSiO_6$.* Am. Mineral., 1974. **59**(5-6): p. 549-557.

77. C., P.D., *Volume anomaly and the impure ferroelastic phase transition in leucite*, in *Phase Transitions in Ferroelastic and Co-Elastic Crystals*, E.K.H. Salje, Editor. 1990, Cambridge University. p. 350-366.

78. Cohen, R.E., *Thermodynamic solution properties of aluminous clinopyroxenes: nonlinear least squares refinements.* Geochim. Cosmochim. Acta, 1986. **50**(4): p. 563-75.

79. Wood, B.J., et al., *Thermochemistry of jadeite-diopside pyroxenes.* Geochim. Cosmochim. Acta, 1980. **44**(9): p. 1363-1371.

80. Gasparik, T., *Thermodynamic properties of pyroxenes in the NCMAS system saturated with silica*. 1981, State Univ. New York: Stony Brook, NY, USA p. 146 pp.

81. Yoder, H.S., Jr., *The jadeite problem. II.* Am. J. Sci., 1950. **248**: p. 312-334.

82. Mao, H.K., *The System Jadeite ($NaAlSi_2O_6$)-Anorthite ($CaAl_2Si_2O_8$) at High Pressures.* Carnegie Inst. Washington Yearb. (1969-1970), 1969: p. 163-170.

83. Khanukhova, L.T., et al., *Solid solutions of pyroxenes in the sodium aluminosilicate ($NaAlSi_2O_6$)-calcium aluminosilicate ($CaAl_2SiO_6$)-silica system at 35 kbar and 1200°C.* Dokl. Akad. Nauk SSSR, 1976. **231**(1): p. 185-187 [Petrogr].

84. Prewitt, C.T. and C.W. Burnham, *Crystal structure of jadeite, $NaAlSi_2O_6$.* Am. Mineral., 1966. **51**(7): p. 956-975.

85. Jung, I.-H., *Critical Evaluation and Thermodynamic Modeling of Phase Equilibria in Multicomponent Oxide Systems*, in *Département de génie chimique*. 2003, École Polytechnique de Montréal: Montreal (Canada). p. 338 pp.

86. Morey, G.W. and N.L. Bowen, *The Ternary System Sodium Metasilicate-Calcium Metasilicate-Silica.* J. Soc. Glass Technol., 1925. **9**(1): p. 226-264.

87. Moir, G.K. and F.P. Glasser, *Phase equilibriums in the system sodium silicate-calcium silicate.* Phys. Chem. Glasses, 1974. **15**(1): p. 6-11.

88. Moir, G.K. and F.P. Glasser, *Solid solutions and phase equilibriums in the systems sodium silicate-strontium silicate and sodium silicate-calcium silicate-strontium silicate.* Trans. Brit. Ceram. Soc., 1974. **73**(6): p. 199-206.

89. Ohsato, H., Y. Takeuchi, and I. Maki, *Structural study of the phase transition of sodium calcium silicate ($Na_4Ca_4[Si_6O_{18}]$).* Acta Crystallogr., Sect. B Struct. Sci., 1990. **B46**(2): p. 125-131.

90. Ohsato, H., I. Maki, and Y. Takeuchi, *Structure of Sodium Calcium Silicate ($Na_2CaSi_2O_6$).* Acta Cryst., 1985. **C41**(11): p. 1575-1577.

91. Fischer, R.X. and E. Tillmanns, *Crystal structure of sodium calcium silicate ($Na_4CaSi_3O_9$) and its structural relations to potassium strontium germanate ($K_4SrGe_3O_9$) and calcium aluminate ($Ca_3Al_2O_6$).* Z. Kristallogr., 1984. **166**(3-4): p. 245-256.

92. Morey, G.W., F.C. Kracek, and N.L. Bowen, *The Ternary System K_2O-CaO-SiO_2.* J. Soc. Glass Technol., 1930. **14**(54): p. 149-187.

93. Gunawardane, R.P. and F.P. Glasser, *Crystal chemistry and synthesis of ternary silicates and germanates containing alkali (sodium ion, potassium ion) and alkaline earth (calcium ion, strontium ion, barium ion) cations.* Z. Anorg. Allg. Chem., 1975. **411**(2): p. 163-172.

94. Gunawardane, R.P. and F.P. Glasser, *The system potassium oxide-barium oxide-silicon dioxide.* J. Am. Ceram. Soc., 1976. **59**(5-6): p. 233-236.

95. Gunawardane, R.P. and F.P. Glasser, *Phase Equilibriums and Crystallization of Melts in the System Sodium Oxide-Barium Oxide-Silicon Dioxide.* J. Am. Ceram. Soc., 1974. **57**(5): p. 201-204.

96. Verweij, H. and C.M.P.M. Saris, *Phase Formation in the System $Na_2O{\cdot}Al_2O_3$-$CaO{\cdot}A_2O_3$-Al_2O_3 at 1200°C in Air.* J. Am. Ceram. Soc., 1986. **69**(2): p. 94-98.

97. Brownmiller, L.T. and R.H. Bogue, *System: CaO-Na_2O-Al_2O_3.* Bur. Standards J. Research, R.P. 414, 1932. **8**(2): p. 289-307.

98. Conwicke, J.A. and D.E. Day, *Crystalline solubility of soda in tricalcium aluminate.* J. Am. Ceram. Soc., 1964. **47**(12): p. 654-655.

99. Shin, G.Y. and F.P. Glasser, *Interdependence of sodium and potassium substitution in tricalcium aluminate.* Cem. Concr. Res., 1983. **13**(1): p. 135-140.

100. Nishi, F. and Y. Takeuchi, *Aluminum oxide (Al_6O_{18}) rings of tetrahedra in the structure of sodium calcium aluminate ($Ca_{8.5}NaAl_6O_{18}$).* Acta Crystallogr., Sect. B, 1975. **B31**(4): p. 1169-1173.

101. Rankin, G.A. and H.E. Merwin, *The Ternary System CaO-Al_2O_3-MgO.* J. Am. Chem. Soc., 1916. **38**(3): p. 568-588.

102. Ridgway, R.R., A.A. Klein, and W.J. O'Leary, *The preparation and properties of so-called "beta-alumina".* Trans. Electrochem. Soc., 1936. **70**: p. 71-88.

103. Choudhury, N.S., *Electromotive force measurements on cells involving beta-alumina solid electrolyte.* J. Electrochem. Soc., 1973. **120**(12): p. 1663-1667.

104. Weber, N. and A.F. Venero, *Revision of the phase diagram $NaAlO_2$-Al_2O_3.* 72nd Annual Meeting of the Am. Ceram. Soc., May, Philadelphia 5-JI-70, 1970. **7**: p. 141.

105. Kummer, J.T., *β-Alumina electrolytes.* Progr. Solid State Chem. (Progress in Solid State Chemistry), 1972: p. 141-175.

106. Tomilov, N.P., *Phase diagram of the sodium aluminate ($NaAlO_2$)-alumina system and nonstoichiometry of the β-alumina phases.* Izv. Sib. Otdel. Akad. Nauk. SSSR, Ser. Khim. Nauk, 1986. **6**: p. 92-98.

107. Kracek, F.C., K.J. Neuvonen, and G. Burley, *A thermodynamic study of the stability of jadeite.* Washington Acad. Sci. Jour., 1951. **41**: p. 373-383.

108. Dove, M.T., et al., *On the role of aluminum-silicon ordering in the cubic-tetragonal phase transition of leucite.* Am. Mineral., 1993. **78**(5-6): p. 486-492.

109. Gupta, A.K. and A.D. Edgar, *Leucite-sodium-feldspar incompatibility.* Mineral. Mag., 1975. **40**(312): p. 377-384.

110. Mazzi, F., E. Galli, and G. Gottardi, *The crystal structure of tetragonal leucite.* Am. Mineral., 1976. **61**(1): p. 108-115.

111. Voldan, J., *Crystallization of a three-component compound in the system potassium oxide-boron oxide-silicon dioxide.* Silikaty (Prague), 1979. **23**(2): p. 133-141.

112. Voldan, J., *Crystallization of alkali metal borosilicates of the leucite type.* Stekloobraznoe Sostoyanie, 1983. **7th**: p. 142-143.

113. Mazza, D., et al., *Boron for aluminum substitution in the $KAlSi_2O_6$ leucite structure.* J. Eur. Ceram. Soc., 1997. **17**(7): p. 951-955.

114. Roedder, E.W., *The system K_2O-MgO-SiO_2. I. II.* Am. J. Sci., 1951. **249**: p. 81-130, 224-248.

115. Roedder, E.W., *The system K_2O-MgO-SiO_2. I. II.* Am. J. Sci., 1951. **249**(2): p. 224-248.

116. Kohn, S.C., et al., *An NMR study of structure and ordering in synthetic $K_2MgSi_5O_{12}$, a leucite analog.* Phys. Chem. Miner., 1991. **18**(2): p. 144-152.

117. Segnit, E.R., *Further Data on the System Na_2O-CaO-SiO_2.* Am. J. Sci., 1953. **251**(8): p. 586-601.

118. Taylor, W.C., *Phase-equilibrium studies involving the potash compounds of portland cement.* J. Res. Nat. Bur. Stand., 1942. **29**(4): p. 437-451.

119. Schairer, J.F. and N.L. Bowen, *The System K_2O-Al_2O_3-SiO_2.* Am. J. Sci., 1955. **253**: p. 681-746.

120. Rankin, G.A. and F.E. Wright, *The Ternary System CaO-Al_2O_3-SiO_2.* Am. J. Sci., (4th series), 1915. **39**: p. 1-79.

121. Rankin, G.A. and H.E. Merwin, *The Ternary System MgO-Al_2O_3-SiO_2.* Am. J. Sci., 1918. **45**: p. 301-325.

122. Chen, S., et al., *Experimental study of phase equilibria in the PbO-Al_2O_3-SiO_2 system.* Metall. Mater. Trans. B, 2001. **32B**(6): p. 997-1005.

123. Eriksson, G. and A.D. Pelton, *Critical Evaluation and Optimization of the Thermodynamic Properties and Phase Diagrams of the CaO-Al_2O_3, Al_2O_3-SiO_2, and CaO-Al_2O_3-SiO_2 Systems.* Metall. Trans., 1993. **24**: p. 807-816.

124. Bowen, N.L. and J.W. Greig, *The System Al_2O_3-SiO_2.* J. Am. Ceram. Soc., 1924. **7**(4): p. 238-254.

125. Toropov, N.A. and F.Y. Galakhov, *The System Alumina-Silica.* Dokl. Akad. Nauk SSSR, 1951. **778**(2): p. 299-302.

126. Gelsdorf, G., H. Mueller-Hesse, and H.E. Schwiete, *Incorporation experiments on synthetic mullite and substitution experiments with gallium oxide and germanium dioxide. II.* Arch. Eisenhuettenwes., 1958. **29**(8): p. 513-519.

127. Toropov, N.A. and F.Y. Galakhov, *Solid Solutions in the Al_2O_3-SiO_2 System.* Izvest. Akad. Nauk SSSR, Otdel Khim.Nauk, 1958. **1**: p. 8-11.

128. Aramaki, S. and R. Roy, *Revised equilibrium phase diagram for the system Al_2O_3-SiO_2.* Nature, 1959. **184**: p. 631-2.

129. Welch, J.W., *A New Interpretation of the Mullite Problem.* Nature, 1960. **186**(4724): p. 545-546.

130. Aramaki, S. and R. Roy, *Revised Phase Diagram for the System Al_2O_3-SiO_2.* J. Am. Ceram. Soc., 1962. **45**(5): p. 229-242.

131. Horibe, T. and S. Kuwabara, *Thermo-Analytical Investigation of Phase Equilibria in the Al_2O_3-SiO_2 System.* Bull. Chem. Soc. Jpn., 1967. **40**(4): p. 972-982.

132. Staronka, A., H. Pham, and M. Rolin, *Cooling Curve Study on the Silica-Alumina System.* Rev. Int. Hautes Temp. Refract, 1968. **5**(2): p. 111-115.

133. Davis, R.F. and J.A. Pask, *Diffusion and Reaction Studies in the System Al_2O_3-SiO_2.* J. Am. Ceram. Soc., 1972. **55**(10): p. 525-531.

134. Aksay, I.A. and J.A. Pask, *The Silica-Alumina System: Stable and Metastable Equilibria at 1.0 Atmosphere.* Science (Washington, D.C.), 1974. **183**(4120): p. 69.

135. Aksay, I.A. and J.A. Pask, *Stable and Metastable Equilibria in the System SiO_2-Al_2O_3.* J. Am. Ceram. Soc., 1975. **58**(11-12): p. 507-512.

136. Okada, K. and N. Otsuka, *Change in Chemical Composition of Mullite Formed from $2SiO_2 \cdot 3Al_2O_3$ Xerogel During the Formation Process.* J. Am. Ceram. Soc., 1987. **70**(10): p. C245-C247.

137. Klug, F.J., S. Prochazka, and R.H. Doremus, *Alumina-Silica Phase Diagram in the Mullite Region.* J. Am. Ceram. Soc., 1987. **70**: p. 750-759.

138. Prochazka, S. and F.J. Klug, *Infrared-transparent mullite ceramic.* J. Am. Ceram. Soc., 1983. **66**(12): p. 874-880.

139. Gielisse, P.J. and W.R. Foster, *Research on Phase Equilibria between Boron Oxides and Refractory Oxides, Including Silicon and Aluminum Oxides*. 1961: The Ohio State University Research Foundation, Columbus 12, Ohio. p. 1-10.

140. Dietzel, v.A. and H. Scholze, *Untersuchungen im System B_2O_3-Al_2O_3-SiO_2.* Glastech. Ber., 1955. **28**(2): p. 47-51.

141. Lambotte, G. and P. Chartrand, *Thermodynamic optimization of the (Na_2O + SiO_2 + NaF + SiF_4) reciprocal system using the Modified Quasichemical Model in the Quadruplet Approximation.* J. Chem. Thermodyn., 2011. **43**(11): p. 1678-1699.

142. Konar, B., M.-A. Van Ende, and I.-H. Jung, *Critical evaluation and thermodynamic optimization of the Li-O, and Li_2O-SiO_2 systems.* J. Eur. Ceram. Soc., 2017. **37**(5): p. 2189-2207.

143. Kracek, F.C., *The Binary System Li_2O-SiO_2.* J. Phys. Chem., 1930. **34**(12): p. 2641-2650.

144. Murthy, M.K. and F.A. Hummel, *Phase Equilibria in the System Lithium Metasilicate-Forsterite-Silica.* J. Am. Ceram. Soc., 1955. **38**(2): p. 55-63.

145. Kracek, F.C., *The System Sodium Oxide-Silica.* J. Am. Chem. Soc., 1930. **34**(4): p. 1583-1598.

146. Morey, G.W. and N.L. Bowen, *The Binary System Sodium Metasilicate-Silica.* J. Phys. Chem., 1924. **28**(11): p. 1167-1179.

147. Kracek, F.C., N.L. Bowen, and G.W. Morey, *The System Potassium Metasilicate-Silica.* J. Phys. Chem., 1929. **33**(12): p. 1857-1879.

148. Bockris, J.O.M., J.D. Mackenzie, and K.J. A., *Viscous Flow in Silica and Binary Liquid Silicates.* Trans. Faraday Soc., 1955. **51**(12): p. 1734-1748.

149. Kracek, F.C., N.L. Bowen, and G.W. Morey, *Equilibrium Relations and Factors Influencing Their Determination in the System K_2SiO_3-SiO_2.* Phys. Chem., 1937. **41**(9): p. 1183-1193.

150. Alekseeva, Z.D., *The diagram of the Rb_2SiO_3-SiO_2 system.* Russ. J. Inorg. Chem., 1963. **8**(6): p. 741-744.

151. Greig, J.W., *Immiscibility in Silicate Melts. Part I.* Am. J. Sci., 5th Ser., 1927. **13**(73): p. 1-44.

152. Kracek, F.C., *The Cristobalite Liquidus in the Alkali Oxide-Silica Systems and the Heat of Fusion of Cristobalite.* J. Am. Chem. Soc., 1930. **52**(4): p. 1436-1442.

153. D'Ans, J.L.J., *Untersuchungen im system Na_2O-SiO_2-ZrO_2.* Z. Anorg. Allg. Chem., 1930. **191**(1): p. 1-35.

154. Kracek, F.C., *Phase Equilibrium Relations in the System Na_2SiO_3-Li_2SiO_3-SiO_2.* J. Am. Chem. Soc., 1939. **61**(10): p. 2863-2877.

155. Willgallis, A. and K.J. Range, *Zur Polymorphie des $Na_2Si_2O_5$.* Glastech. Ber, 1964. **37**: p. 194-200.

156. Williamson, J. and F.P. Glasser, *The crystallization of $Na_2O \cdot 2SiO_2$-SiO_2 glasses.* Phys. Chem. Glasses, 1966. **7**(4): p. 127-138.

157. Boivin, P., et al., *Determination of temperature and enthalpy of melting of alkali disilicates by differential calorimetric analysis.* J. Mater. Sci., 1993. **28**(7): p. 1834-1838.

158. Morey, G.W., *Geophysical Laboratory.* Geophysical Laboratory, Carnegie Institute of Washington, 1953. **Paper No. 1215**: p. 39-96.

159. Matveev, M.A., *Thermographic study of sodium and lithium silicates.* Tr. Inst. - Mosk. Khim.-Tekhnol. Inst. im. D. I. Mendeleeva, 1962. **37**: p. 49-57.

160. Williamson, J. and F.P. Glasser, *Phase Relations In The System $Na_2Si_2O_5$-SiO_2.* Science, 1965. **148**(4): p. 1589 -1591.

161. Schairer, J.F. and J.H.S. Yoder, *The Compound $3Na_2O \cdot 8SiO_2$ in the system $Na_2O \cdot SiO_2$.* Carnegie Inst. Washington Yearb. (1969-1970), 1969: p. 160-163.

162. Loeffler, J., *Alkaline Phase of the Sodium Oxide-Silicon Dioxide System.* Glastech. Ber., 1969. **42**(3): p. 92-96.

163. Meshalkin, A.B. and A.B. Kaplun, *Phase equilibria in the Na_2O-SiO_2 system.* Russ. J. Inorg. Chem., 2003. **48**(10): p. 1567-1569.

164. Rys, M., *Investigation of thermodynamic properties of alkali metals in oxide systems relevant to coal slags*. 2008. p. 132 pp.

165. D'Ans, J. and J. Loeffler, *Study of the system Na_2O-SiO_2-ZrO_2.* Z. Anorg. Allg. Chem., 1969. **191**(12): p. 1-34.

166. Krakau, K.A., E.J. Mukhin, and M.S. Geinrich, *Equilibrium diagram of the system Na_2O-PbO-SiO_2.* Akad. Nauk S.S.S.R., Otdel. Khim. Nauk, Acad. Nauk S.S.S.R. i Gosudarst. Ordena Lenina Opticheskii Inst., Sbornik Statei, 1949: p. 15-38.

167. Bouaziz, R., G. Papin, and A.P. Pollet, *L'oxyde de sodium et le systeme binaire: oxyde-hydroxyde de sodium.* Acad. Sci., 1966. **262C**: p. 1051-1054.

168. Willgallis, A., *Silicon Dioxide-Sodium Oxide-Sodium Fluoride System.* Glastech. Ber., 1969. **42**(12): p. 506-509.

169. Borisov, A.F., V.I. Zadumin, and I.V. Timoshenko, *Evaluation of the ratio of crystalline and vitreous phases by an emf method.* Stekloobraznoe Sostoyanie, Tr. Vses. Simp., 3rd, 1974: p. 172-175.

170. Borisov, A.F. and R.S. Borisova, *Potentiometric studies of crystallization in silicate systems.* Fiz. Khim. Stekla, 1987. **13**(1): p. 29-33.

171. Andreev, N.S., et al., *The chemically heterogeneous structure of binary sodium and lithium silicate glasses.* Stekloobraznoe Sostoyanie, Inst. Khim. Silikatov, Akad. Nauk SSSR, Gos. Optich. Inst., Zavod Khudozhestvennogo Stekla, Leningr. Elektrotekhn. Inst., Tr. Simpoziuma, Leningrad, 1963. **1962**(1): p. 46-53.

172. Hammel, J.J. *Experimental evidence for spinodal decomposition in glasses of the Na_2O-SiO_2 system*. in *7th International Congress on Glass, International Commossion on Glass*. 1965. Brussels.

173. Andreev, N.S. and T.I. Ershova, *Interparticle interference during light scattering by submicro-inhomogeneous glass.* Dokl. Akad. Nauk SSSR, 1967. **172**(6): p. 1299-1302.

174. Moriya, Y., D.H. Warrington, and R.W. Douglas, *Metastable liquid-liquid immiscibility in some binary and ternary alkali silicate glasses.* Phys. Chem. Glasses, 1967. **8**(1): p. 19-25.

175. Porai-Koshits, E.A. and V.I. Aver'yanov, *Primary and secondary phase separation of sodium silicate glasses.* J. Non-Cryst. Solids, 1968. **1**(1): p. 29-38.

176. Tomozawa, M. and R.A. Obara, *Effect of minor third components on metastable immiscibility boundaries of binary glasses.* J. Amer. Ceram. Soc., 1973. **56**(7): p. 378-381.

177. Topping, J.A. and M.K. Murthy, *Effect of small additions of alumina and gallium(III) oxide on the immiscibility temperature of sodia silica glasses.* J. Amer. Ceram. Soc., 1973. **56**(5): p. 270-275.

178. Haller, W., D.H. Blackburn, and J.H. Simmons, *Miscibility Gaps in Alkali-Silicate Binaries - Data and Thermodynamic Interpretation.* J. Am. Ceram. Soc., 1974. **57**(3): p. 120-126.

179. Mazurin, O.V., G.P. Roskova, and V.I. Aver'yanov, *Factors determining the character of phase-separating glasses.* Fiz. Khim. Stekla, 1975. **1**(2): p. 110-117.

180. Stevens, C.G. and E.T. Turkdogan, *Heat of Formation of Sodium Di-Silicate.* Trans. Faraday Soc., 1955. **51**: p. 356-360.

181. King, E.G., *Heats of formation of crystalline calcium orthosilicate, tricalcium silicate, and zinc orthosilicate.* J. Am. Chem. Soc., 1951. **73**: p. 656-588.

182. Torgeson, D.R. and T.G. Sahama, *A Hydrofluoric Acid Solution Calorimeter and the Determination of the Heats of Formation of M_2SiO_4, $MgSiO_3$, and $CaSiO_3$.* J. Am. Chem. Soc., 1948. **70**(6): p. 2156-2160.

183. Hummel, C. and H.E. Schwiete, *Thermochemische Untersuchungen im System Na_2O-SiO_2 Teil I: Lösungskalorimetrische Untersuchung von Bildungs- und Reaktionswarmen.* Glastech. Ber., 1959. **32**: p. 327-335.

184. Hummel, C. and H.E. Schwiete, *Thermochemical investigations in the system SiO_2Na_2O. II. Heats of solution and enthalpy-temperature functions, as functions of the alkali concentration.* Glastech. Ber., 1959. **32**: p. 413-420.

185. Takahashi, K. and T. Yoshio, *Thermochemical investigations of glasses. II. Oxygen-alkali metal bond energy in alkali silicates. (R_2O-SiO_2).* Yogyo Kyokai Shi, 1970. **78**(902): p. 329-337.

186. Hovis, G.L., *Resolution of a systematic interlaboratory discrepancy in recent calorimetric data, and the heats of solution of quartz, low albite, adularia, and gibbsite.* Am. Mineral., 1982. **67**(9-10): p. 950-5.

187. Hemingway, B.S. and R.A. Robie, *Enthalpies of formation of low albite ($NaAlSi_3O_8$), gibbsite ($Al(OH)_3$), and $NaAlO_2$; revised values for $\Delta_f H°_{298}$ and $\Delta_f G°_{298}$ of some aluminosilicate minerals.* J. Res. U. S. Geol. Surv. (Journal of Research of the U. S. Geological Survey), 1977. **5**(4): p. 413-429.

188. Roth, W.A. and H. Troitzsch, *Beitrag zur Thermochemie der Kieselsaure und Einiger Silikate.* Zeitschr. Anorg. Chem., 1949. **260**: p. 337-344.

189. Kroger, C. and G. Kreitlow, *Die Lösungs-und Bildungswarmen der Natronkalksilikate.* Glastech. Ber., 1956. **29**: p. 393-400.

190. Charlu, T.V., R.C. Newton, and O.J. Kleppa, *Enthalpies of Formation of 970 K of Compounds in the System Magnesia-Alumina Silica from High Temperature Solution Calorimetry.* Geochim. Cosmochim. Acta, 1975. **39**(11): p. 1487-1497.

191. Hlabse, T. and O.J. Kleppa, *The thermochemistry of jadeite.* Am. Mineral., 1968. **53**(7-8): p. 1281-1292.

192. Shearer, J.A. and O.J. Kleppa, *Enthalpies of Formation of Spinel ($MgAl_2O_4$), Pyroxene ($MgSiO_3$), Olivine (Mg_2SiO_4), Kyanite (Al_2SiO_5), and Sillimanite (Al_2SiO_5) by Oxide Melt Solution Calorimetry.* J. Inorg. Nucl. Chem., 1973. **35**(4): p. 1073-1078.

193. Petrovic, I., P.J. Heaney, and A. Navrotsky, *Thermochemistry of the new silica polymorph moganite.* Phys. Chem. Miner., 1996. **23**(2): p. 119-126.

194. Kiseleva, I.A., et al., *Thermodynamic properties of alkali feldspars.* Geokhimiya, 1990. **3**: p. 406-413.

195. Zygan, V.N., et al., *Thermochemistry of the dissolution of oxide phases containing alkali metals.* Izv. Akad. Nauk SSSR, Neorg. Mater., 1978. **14**(6): p. 1087-1089.

196. Jeffes, J.H.E., F.D. Richardson, and J. Pearson, *Heats of formation of manganous orthosilicate and manganous sulfide.* Trans. Faraday Soc., 1954. **50**: p. 364-370.

197. Fan, M., *Thermochemische Untersuchung der Schmelzen Na_2O-SiO_2, Na_2O-GeO_2, Na_2O-B_3O_3 und Li_2O-B_2O_3.* 1991, Technischen Hochschule Aachen: Aachen, Germany. p. 99 pp.

198. Tischer, R.E., *Heat of annealing in simple alkali silicate glasses.* J. Amer. Ceram. Soc., 1969. **52**(9): p. 499-503.

199. Hovis, G.L., M.J. Toplis, and P. Richet, *Thermodynamic Mixing Properties of Sodium Silicate Liquids and Implications for Liquid-Liquid Immiscibility.* Chem. Geol., 2004. **213**(1-3): p. 173-186.

200. Rogez, J. and J.C. Mathieu, *Enthalpy of formation in the system sodium oxide-potassium oxide-silica.* Phys. Chem. Liq., 1985. **14**(4): p. 259-272.

201. Ahoussou, A.P., et al., *Contribution to thermochemical studies of 0.8[xB_2O_3-(1 - x)SiO_2]-0.2Na_2O glasses.* Chin. Chem. Lett., 2009. **20**(2): p. 245-249.

202. Roth, W.A. and H. Richter, *The heats of formation of iron slags from the oxides.* Arch. Eisenhuettenwes., 1938. **11**: p. 417-419.

203. Takahashi, K. and T. Yoshio, *Thermodynamic quantities of alkali silicates in the temperature range from 25°C to melting point.* Yogyo Kyokai Shi, 1973. **81**(12): p. 524-533.

204. Takahashi, K. and T. Yoshio, *Thermochemical investigations on glass. I. Energy relations in alkali silicates by solution calorimetry.* Yogyo Kyokai Shi, 1970. **78**(893): p. 29-38.

205. Morishita, M., A. Navrotsky, and M.C. Wilding, *Direct measurement of relative partial molar enthalpy of SiO_2 in SiO_2-M_2O (M = Li, Na, K, Cs) binary and SiO_2-CaO-Al_2O_3 ternary melts.* J. Am. Ceram. Soc., 2004. **87**(8): p. 1550-1555.

206. McCready, N.W., *The Thermodynamic Properties of Sodium Silicate.* J. Phys. Colloid. Chem., 1948. **52**: p. 1277-1283.

207. Kroger, C. and E. Fingas, *The systems alkali oxide-CaO-Al_2O_3-SiO_2-CO_2. V. Stable equilibrium in the system Na_2O-SiO_2-CO_2 and the CO_2 pressure in the reaction of K_2CO_3 and K_2SiO_3.* Z. Anorg. Allg. Chem., 1935. **225**: p. 1-23.

208. Adams, L.H. and L.W. Cohen, *Enthalpy Changes as Determined from Fusion Curves in Binary Systems.* Am. J. Sci., 1966. **264**(7): p. 543-561.

209. Naylor, B.F., *High-temperature Heat Contents of Sodium Metasilicate and Sodium Disilicate.* J. Am. Chem. Soc., 1945. **67**(3): p. 466-467.

210. Goto, K.S., S. Yamaguchi, and K. Nagata. *The Chemical Activity of Component Oxides in Sodium Oxide-Based Slags*. in *Proc. 2nd Int. Symp. Metall. Slags Fluxes*. 1984. Metall. Soc. AIME, Warrendale, PA.

211. Zaitsev, A.I., N.E. Shelkova, and B.M. Mogutnov, *Thermodynamics of Na_2O-SiO_2 melts.* Inorg. Mater., 2000. **36**(6): p. 529-543.

212. Matousek, J., *Methods for measuring and significance of the vapor pressure of the volatile components of silicate melts.* Sb. Vys. Sk. Chem.-Technol. Praze, Chem. Technol. Silik., 1975. **L6**: p. 193-213.

213. Tsukihashi, S. and N. Sano, *Measurement of the Activity of Na_2O in Na_2O-SiO_2 Melts by Chemical Equilibration Method.* Tetsu to Hagane, 1985. **71**(1-2): p. 815-822.

214. Rego, D.N., G.K. Sigworth, and W.O. Philbrook, *Thermodynamic Study of Na_2O-SiO_2 Melts at 1300° and 1400°C.* Metall. Mater. Trans. B, 1985. **16B**(2): p. 313-323.

215. Zaitsev, A.I., et al., *Thermodynamic properties and phase equilibria in the Na_2O-SiO_2 system.* Phys. Chem. Chem. Phys., 1999. **1**(8): p. 1899-1907.

216. Borisov, A.F. and V.I. Solov'ev, *Liquation in a sodium silicate system studied by an emf. method.* Likvatsionnye Yavleniya v Steklakh, Tr. Vses. Simp., 1st, 1969: p. 54-59.

217. Borisov, A.F. and L.S. Ukhvatova, *Electromotive force in low-alkali borate melts.* Stekloobraznoe Sostoyanie, Tr. Vses. Simp., 3rd, 1974: p. 168-172.

218. Shakhmatkin, B.A. and M.M. Shul'ts, *Thermodynamic Properties of Glass-Forming Melts in the System Na_2O-SiO_2 between 800 and 1200°C.* Fiz. Khim. Stekla, 1980. **6**: p. 129-135.

219. Yamaguchi, S., A. Imai, and K.S. Goto, *Measurement of activity of Na_2O-SiO_2 Binary Melt Using beta-Alumina as a Solid electrolyte.* J. Japan Inst. Metals, 1983. **47**(9): p. 736-742.

220. Ravaine, D., E. Azandegbe, and J.L. Souquet, *Potentiometric measurements of electrochemical cells consisting of fused silicates; interpretation of results by a statistical model.* Silic. Ind., 1975. **40**: p. 333-340.

221. Tsaplin, A.A., et al., *Thermodynamic properties and phase equilibria in Na_2O-SiO_2 and K_2O-SiO_2 systems.* Schr. Forschungszent. Juelich, Reihe Energietech./Energy Technol., 2000. **15**(Pt. 1, High Temperature Materials Chemistry, Part 1): p. 59-62.

222. Kozhina, E.L. and M.M. Shultz, *Thermodynamic properties of sodium-containing glassforming oxide melts.* Ceram.-Silik., 2000. **44**(3): p. 91-97.

223. Shul'ts, M.M., Stolyarova, and G.G. Ivanov, *A Mass Spectroscopy Study of the Thermodynamic Properties of Melts and Glasses in the Na_2O-SiO_2 System.* Fiz. Khim. Stekla, 1987. **13**: p. 168-172.

224. Rudnyi, E.B., et al., *Ion equilibria. A new technique for measurement of low oxygen and alkali partial pressures.* High Temp. Sci., 1990. **26**: p. 165-174.

225. Borisov, A.F. and V.I. Solov'ev, *Concentration differential of potentials in silicate melts.* Stekloobraznoe Sostoyanie, 1971. **5**(1): p. 231-235.

226. Smith, G.S. and G.E. Rindone, *Acid-base relationship in glass systems. Application of the oxygen electrode in galvanic cells with glasses of different compositions.* Glass Ind., 1956. **37**: p. 437-43,454,456.

227. Kohsaka, S., S. Sato, and T. Yokokawa, *E.m.f. Measurements of Molten Oxide Mixtures. III. Sodium Oxide + Silicon Dioxide.* J. Chem. Thermodyn., 1979. **11**(6): p. 547-551.

228. Itoh, H. and T. Yokokawa, *Thermodynamic Activity of Na_2O in Na_2O-SiO_2-Al_2O_3 Melt.* Trans. Jap. Inst. Metals, 1984. **25**(12): p. 879-884.

229. Neudorf, D.A. and J.F. Elliot, *Thermodynamic Properties of Na_2O-SiO_2-CaO melts at 1000 to 1100°C.* Metall. Trans., 1980. **11B**: p. 607-614.

230. Rudnyi, E.B., et al., *Use of the ion-molecule equilibrium method to determine the activity of an alkali metal oxide in sodium silicate melts.* Fiz. Khim. Stekla, 1988. **14**(2): p. 218-225.

231. Piacente, V. and J. Matousek, *Alkali vapor pressures over some simple silicate melts.* Collect. Czech. Chem. Commun., 1983. **48**(6): p. 1528-1531.

232. Frohberg, M.G., E. Caune, and M.L. Kapoor, *Measurement of the activity of the oxygen ions in the fluid systems sodium oxide-silicon dioxide and potassium oxide-silicon dioxide.* Arch. Eisenhuttenwes., 1973. **44**(8): p. 585-588.

233. Abdelouhab, S., et al., *Determination of Na_2O activities in silicate melts by EMF measurements.* J. Non-Cryst. Solids, 2008. **354**(26): p. 3001-3011.

234. Kelley, K.K., *The Specific Heats at Low Temperatures of Crystalline Ortho-,Meta-, and Disilicates of Sodium.* J. Am. Chem. Soc., 1939. **61**(2): p. 471-473.

235. Labban, A., et al., *Heat capacities and derived thermodynamic properties of lithium, sodium, and potassium disilicates from T = (5 to 350) K in both vitreous and crystalline states.* J. Chem. Thermodyn., 2007. **39**(7): p. 991-1000.

236. Tashiro, M., *Method for the continuous measurement of the high-temperature heat content of glasses and of fused salts.* Glass Ind., 1956. **37**: p. 549-552.

237. Richet, P., Y. Bottinga, and C. Tequi, *Heat capacity of sodium silicate liquids.* J. Am. Ceram. Soc., 1984. **67**(1): p. C6-C8.

238. Takahashi, K., et al., *High temperature thermodynamic properties of several binary alkali silicate glasses.* Mem. Sch. Eng., Okayama Univ., 1967. **2**(1): p. 55-61.

239. Richet, P. and D.R. Neuville, *Thermodynamics of silicate melts: configurational properties.* Advances in Physical Geochemistry, 1992. **10**(Thermodyn. Data): p. 132-161.

240. Richet, P., *From physical properties to structure: the low-temperature heat capacity of silicate glasses.* Int. Congr. Glass, Proc., 20th, 2004: p. 07 047/1-07 047/8.

241. Ushakov, V.M., et al., *Heat capacities and enthalpies of formation of sodium silicate glasses.* Probl. Kalorim. Khim. Termodin., Dokl. Vses. Konf., 10th, 1984. **2**: p. 411-413.

242. Yageman, V.D. and G.M. Matveev, *Heat capacity of glasses of the silica-sodium silicate (SiO_2-$Na_2O \cdot 2SiO_2$) system.* Fiz. Khim. Stekla, 1982. **8**(2): p. 238-245.

243. Moynihan, C.T., et al., *Heat capacity and structural relaxation of mixed-alkali glasses.* J. Am. Ceram. Soc., 1976. **59**(3-4): p. 137-140.

244. Yageman, V.D. and G.M. Matveev, *Experimental values of enthalpy and heat capacity of silicon dioxide-sodium silicate (SiO_2-$Na_2Si_2O_5$) system melts.* Fiz. Khim. Stekla, 1980. **6**(5): p. 602-608.

245. Schwiete, H.E. and G. Ziegler, *Specific heat of glasses.* Glastech. Ber., 1955. **28**: p. 137-146.

246. Rolin, M. and R.H. Thanh, *Phase Diagram of Na_2O-Al_2O_3, CaO-Al_2O_3, La_2O_3-Al_2O_3.* Rev. Hautes Temp. Refract., 1965. **2**(2): p. 175-185.

247. Bunzel, E.G. and E.J. Kohlmeyer, *Thermal Properties of Sodium Compounds, Especially of Na_2O and Na_2S and Their Reactions with Metals.* Z. Anorg. Chem., 1947. **254**(1-2): p. 1-30.

248. Matignon, C., *Action of high temperatures on some refractory substances.* Compt. Rend., 1923. **177**: p. 1290-1293.

249. Christensen, A.U., K.C. Conway, and K.K. Kelley, *High-Temperature Heat Contents and Entropies of Aluminates and Ferrites of Lithium and Sodium, and of Lithium Titanate.* U. S. Bur. Mines RI, 1960. **RI 5565**: p. 1-7.

250. Rolin, M. and P.H. Thanh, *Phase diagrams of nonreactive mixtures with molybdenum. I. Apparatus for freezing point curves up to 2100°C.* Bull. Soc. Chim. Fr., 1963(5): p. 1030-1035.

251. Bouaziz, R., G. Papin, and A.P. Rollet, *Chimie Minerale.-L'oxyde de sodium et le systeme binaire: oxyde-hydroxyde de sodium.* Compt. Rend. (Ser. C), 1966. **262**: p. 1051-1054.

252. Liebertz, J., *Formation and region of existence of the two sodium-β-aluminum oxide phases.* Ber. Deut. Keram. Ges., 1972. **49**(9): p. 288-290.

253. Ampian, S.G., *X-ray diffraction and optical microscopic data on several important phases in the binary systems $CaO-Al_2O_3$, $CaO-SiO_2$, and $Na_2O-Al_2O_3$.* Bur. Mines Rep. Invest., 1964. **6428**(4): p. 53 pp.

254. Otsubo, Y., K. Yamaguchi, and Y. Kawamura, *Thermal Behavior of Alkali Metal Aluminates.* Nippon Kagaku Zasshi, 1962. **83**: p. 352-353.

255. Thery, J., et al., *Structure and properties of alkaline aluminates.* Bull. Soc. Chim. Fr., 1961: p. 973-975.

256. Yamaguchi, G. and K. Suzuki, *Structures of alkali polyaluminates.* Bull. Chem. Soc. Jap., 1968. **41**(1): p. 93-99.

257. Scholder, R. and M. Mansmann, *Compounds of the so-called "β-alumina type".* A. Anorg. Allg. Chem., 1963. **321**(5-6): p. 246-261.

258. Alsen, M., *On the homogeneity range of β"-alumina in the sodium oxide-magnesium oxide-alumina system.* Solid State Ionics, 1986. **20**(1): p. 17-23.

259. Duncan, G.K. and A.R. West, *The stoichiometry of β"-alumina: phase diagram studies in the system sodium oxide-magnesium oxide-lithium oxide-aluminum oxide.* Solid State Ionics, 1988. **28-30**(Pt. 1): p. 338-343.

260. Coughlin, J.P., *Heats of Formation of Crystalline Aluminates of Sodium and Lithium.* J. Am. Chem. Soc., 1957. **79**(10): p. 2397-2399.

261. Koehler, M.F., R. Barany, and K.K. Kelley, *Heats and Free Energies of Formation of Ferrites and Aluminates of Calcium, Magnesium, Sodium, and Lithium*. 1961. p. 14 pp.

262. Hemingway, B.S. and H.T.J. Haselton, *A Reeavaluation of the Calorimetric Data for the Enthalpy of Formation of Some K- and Na-Bearing Silicate Minerals*. 1994: United States Department of the Interior U. S. Geological Survey. p. 33 pp.

263. Zhang, L., et al., *Reference Electrode of Simple Galvanic Cells for Developing Sodium Sensors for Use in Molten Aluminium.* Metall. Mater. Trans. B, 1996. **27B**: p. 794-800.

264. Dubreuil, A., M. Malenfant, and A.D. Pelton, *Thermodynamic stability of β-alumina.* J. Electrochem. Soc., 1981. **128**(9): p. 2006-2008.

265. Brisley, R.J. and D.J. Fray, *Determination of the sodium activity in aluminum and aluminum silicon alloys using sodium beta alumina.* Metall. Trans., 1983. **14B**: p. 435-440.

266. Elrefaie, F.A. and W.W. Smeltzer, *Thermodynamic properties of the ionic conducting phases of sodium-aluminum-oxygen system between 800 and 1200K.* Solid State Ionics, 1984: p. 517-524.

267. Jacob, K.T., K. Swaminathan, and O.M. Sreedharan, *Potentiometric determination of activities in the two-phase fields of the system sodium oxide-(α)alumina.* Electrochim. Acta, 1991. **36**: p. 791-798.

268. Itoh, M., K. Kimura, and Z. Kozuka, *Measurement of Na_2O Activity in Beta-Alumina by EMF Method.* Trans. Jpn. Inst. Met., 1985. **26**(5): p. 353-61.

269. Choudhury, N.S., *Thermochemical stability of β- and β"-alumina electrolytes in sodium sulfur cells. I. The activities of sodium oxide and aluminum oxide.* J. Electrochem. Soc., 1986. **133**: p. 425-429.

270. Kale, G.M., *Sodium oxide-alumina system: activity of sodium oxide in (alpha + beta)- and (beta + beta")-alumina.* Metall. Trans. B, 1992. **23B**(6): p. 833-839.

271. Ji, C. and Y. Jiang, *Thermodynamic stability of beta-alumina.* Chin. J. Met. Sci. Technol., 1988. **4**(1): p. 40-3.

272. Nafe, H., F. Meyer, and F. Aldinger, *The equilibrium between Na-β- and Na-β"-alumina as a function of the phase composition.* Electrochim. Acta, 2000. **45**(10): p. 1631-1638.

273. Choudhury, N.S., *Electromotive force measurements on cells involving beta-alumina solid electrolyte.* J. Electrochem. Soc., 1973. **120**(12): p. 1663-7.

274. Nafe, H. and G.M. Kale, *On the thermodynamic activity of Na_2O in Na-beta-alumina.* Mater. Res. Bull., 2002. **37**(6): p. 1063-1069.

275. Elrefaie, F.A., *Thermodynamic properties of Na-Al-O, Ni-Al-O, Fe-Al-O systems*. 1979, McMaster University, Hamilton, ON, Canada: Hamilton.

276. Rog, G., A. Kozlowska-Rog, and K. Zakula, *Determination of the Standard Gibbs Free Energies of Formation of the Sodium Aluminates by emf Measurements.* J. Chem. Thermodyn., 1992. **24**(1): p. 41-4.

277. Rog, G., S. Kozinski, and A. Kozlowska-Rog, *The application of NASICON ($Na_3Zr_2Si_2PO_{12}$) to the thermodynamic study of beta-alumina.* Electrochim. Acta, 1983. **28**(1): p. 43-45.

278. Rog, G. and A. Kozlowska-Rog, *Thermodynamic Properties of Sodium Polyaluminates.* Solid State Ionics, 1982. **7**(4): p. 291-294.

279. Kozlowska-Rog, A. and G. Rog, *Thermodynamic stability of beta-aluminas.* Szklo Ceram., 1985. **36**(1): p. 1-3.

280. Kumar, R.V. and D.A.R. Kay, *Thermodynamic stabilities of some β and β"-aluminas.* Metall. Trans. B, 1985. **16B**(2): p. 295-301.

281. Elrefaie, F.A. and W.W. Smeltzer, *The stability of β-Al_2O_3 ($Na_2O \cdot 11Al_2O_3$) in oxygen atmospheres.* J. Electrochem. Soc. (Journal of the Electrochemical Society), 1981. **128**(7): p. 1443-1447.

282. Rog, G., A. Kozlowska-Rog, and K. Zakula, *Determination of the standard free enthalpies of formation of sodium aluminates.* Pol. J. Chem. (Polish Journal of Chemistry), 1991. **65**(4): p. 631-5.

283. King, E.G., *Heat Capacities at Low Temperatures and Entropies at 298.16K. of Aluminates and Ferrites of Lithium and Sodium.* J. Am. Chem. Soc., 1955. **77**(12): p. 3189-3190.

284. McWhan, D.B., et al., *Low-temperature heat capacity of alkali-metal and silver β-aluminas.* Phys. Rev. B, 1977. **15**(2): p. 553-560.

285. Bjorkstam, J.L., P. Ferloni, and M. Villa, *^{23}Na second-order quadrupolar shifts and heat capacity anomalies in sodium β-alumina.* J. Chem. Phys., 1980. **73**(6): p. 2932-2936.

286. Bowen, N.L., *The Melting Phenomena of the Plagioclase Feldspars.* Am. J. Sci., 1913. **35 (5190)**: p. 577-599.

287. Bowen, N.L. and J.W. Greig, *The crystalline modifications of $NaAlSiO_4$.* Am. J. Sci., 1925. **10**: p. 204-212.

288. De Pablo-Galan, L. and W.R. Foster, *Investigation of Role of Beta Alumina in the System Na_2O-Al_2O_3-SiO_2.* J. Am. Ceram. Soc., 1959. **42**(10): p. 491-498.

289. Anovitz, L.M. and J.G. Blencoe, *Dry melting of high albite.* Am. Mineral., 1999. **84**(11-12): p. 1830-1842.

290. Navrotsky, A., C. Capobianco, and J. Stebbins, *Some thermodynamic and experimental constraints on the melting of albite at atmospheric and high pressure.* J. Geol. (Journal of Geology), 1982. **90**(6): p. 679-698.

291. Boettcher, A., et al., *Melting in feldspar-bearing systems to high pressures and the structures of aluminosilicate liquids.* Geology, 1984. **12**(4): p. 202-204.

292. Tilley, C.E., *The ternary system: Na_2SiO_3-$Na_2Si_2O_5$-$NaAlSiO_4$.* Mineral. Petrogr. Mitt., 1933. **43**(1): p. 406-421.

293. Kracek, F.C., *The System Sodium Oxide-Silica.* J. Phys. Chem., 1930. **34**(7): p. 1583-1598.

294. Henderson, C.M.B. and A.B. Thompson, *The low-temperature inversion in sub-potassic nephelines.* Am. Mineral., 1980. **65**(9-10): p. 969-979.

295. Holm, J.L. and O.J. Kleppa, *Thermodynamics of the Disordering Process in Albite.* Am. Mineral., 1968. **53**(1-2): p. 123-133.

296. Blinova, G.K. and I.A. Kiseleva, *Calorimetric Study of Structural Transformations of Plagioclases.* Geokhimiya, 1982. **5**: p. 713-719.

297. Kracek, F.C. and K.J. Neuvonen, *Thermochemistry of plagioclase and alkali feldspars.* Am. J. Sci., 1952. **250A**: p. 293-318.

298. Waldbaum, D.R. and R.A. Robie, *Calorimetric investigation of sodium-potassium mixing and polymorphism in the alkali feldspars.* Z. Kristallogr., Kristallgeom., Kristallphys., Kristallchem., 1971. **134**(5/6): p. 381-420.

299. Newton, R.C., T.V. Charlu, and O.J. Kleppa, *Thermochemistry of the high structural state plagioclases.* Geochim. Cosmochim. Acta, 1980. **44**(7): p. 933-941.

300. Petrovic, I. and A. Navrotsky, *Thermochemistry of Na-faujasites with varying Si/Al ratios.* Microporous Mater., 1997. **9(1,2)**: p. 1-12.

301. Hovis, G.L., *A hydrofluoric acid solution calorimetric investigation of glasses in the systems $NaAlSi_3O_8$-$KAlSi_3O_8$ and $NaAlSi_3O_8$-Si_4O_8.* Geochim. Cosmochim. Acta, 1984. **48**(3): p. 523-525.

302. Roy, B.N. and A. Navrotsky, *Thermochemistry of Charge-Coupled Substitutions in Silicate Glasses: the Systems $MAlO_2$-SiO_2 (M = Li,Na,K,Rb,Cs,Mg,Ca,Sr,Ba,Pb).* J. Am. Ceram. Soc., 1984. **67**(9): p. 606-610.

303. De Yoreo, J.J., A. Navrotsky, and D.B. Dingwell, *Energetics of the charge-coupled substitution Si^{4+} -> Na^{+} + T^{3+} in the glasses $NaTO_2$-SiO_2 (T=Al, Fe, Ga, B).* J. Am. Ceram. Soc., 1990. **73**(7): p. 2068-2072.

304. Navrotsky, A. and Z.-R. Tian, *Systematics in the enthalpies of Formation of Anhydrous Aluminosilicate Zeolites, Glasses, and Dense Phases.* Chem. Eur. J., 2001. **7**(4): p. 769-774.

305. Kelley, K.K., *Heats and free energy of formation of anhydrous silicates*, in *U. S. Bur.Mines, Rept. Invest.* 1962. p. 32.

306. Robie, R. and D.R. Waldbaum, *Thermodynamic properties of minerals and related substances at 298.15°K (25.0°C) and one atmosphere (1.013 bars) pressure and at higher temperature.* Geol. Surv. Bull. (US), 1968. **1259**(7): p. 1-256.

307. Waldbaum, D.R., *High-Temperature Thermodynamic Properties of Alkali Feldspars.* Contrib. Mineral. Petrol. (Berlin), 1968. **17**(1): p. 71-77.

308. Barin, I., *Thermodynamic Data for Pure Substances*. 1989: VCH, Weinheim, Germany. 1829 pp.

309. Holland, T.J.B. and R. Powell, *An Enlarged and Updated Internally Consistent Thermodynamic Dataset with Uncertainties and Correlations: The System K_2O-Na_2O-CaO-MgO-MnO-FeO-Fe_2O_3-Al_2O_3-TiO_2-SiO_2-C-H_2-O_2.* J. Metamorph. Geol., 1990. **8**: p. 89-124.

310. Ghiorso, M.S. and R.O. Sack, *Chemical mass transfer in magmatic processes IV. A revised and internally consistent thermodynamic model for the interpolation and extrapolation of liquid-solid equilibria in magmatic systems at elevated temperatures and pressures.* Contrib. Mineral. Petrol., 1995. **119**(2-3): p. 197-212.

311. Robie, R.A. and B.S. Hemingway, *Thermodynamic Properties of Minerals and Related Substances at 298.15K and 1 Bar Pressure and at High Temperatures*. 1995: U. S. Geological Survey, Denver.

312. Gottschalk, M., *Internally consistent thermodynamic data for rock-forming minerals in the system SiO_2-TiO_2-Al_2O_3-Fe_2O_3-CaO-MgO-FeO-K_2O-Na_2O-H_2O-CO_2.* Eur. J. Mineral., 1997. **9**(1): p. 175-223.

313. Hovis, G.L. and J. Roux, *Thermodynamic of excess silicon in nepheline and kalsilite crystalline solutions.* Eur. J. Mineral., 1999. **11**(5): p. 815-827.

314. Richet, P. and Y. Bottinga, *Glass transitions and thermodynamic properties of amorphous silicon dioxide, $NaAlSi_nO_{2n+2}$, and $KAlSi_3O_8$.* Geochim. Cosmochim. Acta, 1984. **48**(3): p. 453-470.

315. Navrotsky, A., et al., *Thermochemistry of glasses and liquids in the systems $CaMgSi_2O_6$-$CaAl_2Si_2O_8$-$NaAlSi_3O_8$, SiO_2-$CaAl_2Si_2O_8$-$NaAlSi_3O_8$, and SiO_2-Al_2O_3-CaO-Na_2O.* Geochim. Cosmochim. Acta, 1980. **44**(10): p. 1409-23.

316. Yokokawa, T., et al., *Thermodynamic Activity of Na_2O in the Metals; Na_2O-B_2O_3-Al_2O_3, Na_2O-B_2O_3-SiO_2, and Na_2O-SiO_2-Al_2O_3.* 1983: p. 197-200.

317. Yokokawa, T., K. Kawamura, and K. Suzumura, *Electrochemistry of silicate melts.* Dyn. Processes Mater. Transp. Transform. Earth's Inter., 1990: p. 83-96.

318. Graham, P.W.L. and G.E. Rindone, *Properties of sodium aluminosilicate glasses. IV. Relative acidities and some thermodynamic properties.* J. Am. Ceram. Soc., 1964. **47**(1): p. 19-24.

319. Oeltjen, L., *Vorhersage thermodynamischer Eigenschaften von Kohlenschlacken mittels Modellrechnungen*. 1999, Institut fur Werkstoffe und Verfahren der Energietechnik: Aachen.

320. De Ligny, D., et al., *Heat Capacity and Entropy of Rutile (TiO_2) and Nepheline ($NaAlSiO_4$).* Phys. Chem. Miner., 2002. **29**(4): p. 267-272.

321. Stebbins, J.F., I.S.E. Carmichael, and D.E. Weill, *The High Temperature Liquid and Glass Heat Contents and the Heats of Fusion of Diopside, Albite, Sanidine and Nepheline.* Am. Mineral., 1983. **68**(7-8): p. 717-730.

322. Hemingway, B.S., et al., *Heat capacity and thermodynamic properties of coesite and jadeite, reexamination of the quartz-coesite equilibrium boundary.* Am. Mineral., 1998. **83**(5-6): p. 409-418.

323. Openshaw, R.E., et al., *The heat capacities at low temperatures and entropies at 298.15K of low albite, analbite, microcline, and high sanidine.* J. Res. U. S. Geol. Surv., 1976. **4**(2): p. 195-204.

324. Haselton, H.T.J., et al., *Calorimetric investigation of the excess entropy of mixing in analbite-sanidine solid solutions : lack of evidence for sodium, potassium short-range order and implications for two-feldspar thermometry.* Am. Mineral., 1983. **68**(3-4): p. 398-413.

325. Salje, E., et al., *Thermodynamics of Sodium Feldspar. II: Experimental Results and Numerical Calculations.* Phys. Chem. Miner., 1985. **12**(2): p. 99-107.

326. Hemingway, B.S., K.M. Krupka, and R.A. Robie, *Heat capacities of the alkali feldspars between 350 and 1000K from differential scanning calorimetry, the thermodynamic functions of the alkali feldspars from 298.15 to 1400K, and the reaction quartz + jadeite = analbite.* Am. Mineral., 1981. **66**(11-12): p. 1202-1215.

327. Krupka, K.M., R.A. Robie, and B.S. Hemingway, *High-temperature heat capacities of corundum, periclase, anorthite, $CaAl_2Si_2O_8$ glass, muscovite, pyrophyllite, $KAlSi_3O_8$ glass, grossular, and $NaAlSi_3O_8$ glass.* Am. Mineral., 1979. **64**(1-2): p. 86-101.

328. Robie, R.A., B.S. Hemingway, and W.H. Wilson, *Low-temperature heat capacities and entropies of feldspar glasses and of anorthite.* Am. Mineral., 1978. **63**(1-2): p. 109-23.

329. Richet, P. and Y. Bottinga, *Heat capacity of liquid silicates: new measurements on sodium aluminosilicate and potassium silicate.* Geochim. Cosmochim. Acta, 1980. **44**(10): p. 1535-1541.

330. Stebbins, J.F., et al., *High Temperature Heat Contents and Heat Capacities of Liquids and Glasses in the System $NaAlSi_3O_8$-$CaAl_2Si_2O_8$.* Contrib. Mineral. Petrol., 1982. **80**(3): p. 276-84.

331. Goranson, R.W. and F.C. Kracek, *An Experimental Investigation of the Phase Relations of Potassium Tetrasilicate under Pressure.* J. Phys. Chem., 1932. **36 (Springer-Verlag)**(3): p. 913-926.

332. Bon, A. and C. Gleitzer, *Potassium metasilicate-potassium oxide systems.* C. R. Acad. Sci., Ser. C, 1973. **277**(21): p. 1109-1011.

333. Schartau, W. and R. Hoppe, *New alkali metal silicates.* Naturwissenschaften, 1973. **60**(5): p. 256.

334. Meshalkin, A.B. and A.B. Kaplun, *The complex investigation of the phase equilibria and melt characteristics in borate and silicate systems.* J. Cryst. Growth, 2005. **275**(1-2): p. e115-e119.

335. Stypula, A., et al., *Technological Problems in the Manufacture of Potassium Water Glass.* Szklo Ceram., 1998. **49**(4): p. 2-5.

336. Chastel, R., et al., *Excess thermodynamic functions in ternary sodium oxide-potassium oxide-silica melts by Knudsen cell mass spectrometry.* Chem. Geol., 1987. **62**(1-2): p. 19-29.

337. Steiler, J.M., *Etude Thermodynamique des Laitiers Liquides du Systeme K_2O-SiO_2.* Comm. Eur. Communities, [Rep.] EUR, 1982: p. 21-1/21-36.

338. Beyer, R.P., et al., *Thermodynamic properties of potassium metasilicate and disilicate*. 1980, Bur. Mines. p. 24 pp.

339. Borisova, N.V. and V.M. Ushakov, *High-temperature Calorimetry of Glasses and Crystals in the K_2O-SiO_2 System.* Glass Phys. Chem., 1998. **24**(4): p. 318-322.

340. Kawamoto, Y. and M. Tomozawa, *Prediction of Immiscibility Boundaries of the Systems K_2O-SiO_2, K_2O-Li_2O-SiO_2, K_2O-Na_2O-SiO_2, and K_2O-BaO-SiO_2.* J. Am. Ceram. Soc., 1981. **64**(5): p. 289-292.

341. Geisinger, K.L., et al., *Potassium silicate ($K_2Si_4O_9$): Energetics and vibrational spectra of glass, sheet silicate, and wadeite-type phases.* Am. Mineral., 1987. **72**: p. 984-994.

342. Ahoussou, A.P., J. Rogez, and A. Kone, *Enthalpy of mixing in 0.8[xB_2O_3-(1-x)SiO_2]-0.2K_2O melts at 973K.* Thermochim. Acta, 2006. **447**(1): p. 109-111.

343. Wilding, M.C. and A. Navrotsky, *The Dissolution of Silica and Alumina in Silicate Melts: in situ High Temperature Calorimetric Studies.* N. Jb. Miner. Abh., 1998. **172**(2-3): p. 177-201.

344. Spencer, P.J., *Thermodynamic properties of silicates.* Nat. Phys. Lab. U. K., 1973. **Div. Chem. Stand., Rep. (1973),No. 21**: p. 36 pp.

345. Kozhina, E.L., *Thermodynamic properties of potassium silicate-system melts.* Fiz. Khim. Stekla, 1990. **16**(5): p. 679-684.

346. Plante, E.R., *Vapor pressure measurements of potassium over potassium oxide-silicon dioxide solutions by a Knudsen effusion, mass spectrometric method.* NBS Spec. Publ. (U. S.), 1979. **561-1**: p. 265-281.

347. Zaitsev, A.I., et al., *Thermodynamic properties of K_2O-SiO_2 melts.* Zh. Fiz. Khim., 2000. **74**(6): p. 1021-1028.

348. Callow, R.J., *Activities in alkali oxide-silica melts.* Trans. Faraday Soc., 1950. **46**: p. 663-673.

349. Plante, E.R., D.W. Bonnell, and J.W. Hastie, *Experimental and theoretical determination of oxide glass vapor pressures and activities.* Adv. Fusion Glass, Proc. Int. Conf., 1st, 1988: p. 26 .1-26 .18.

350. Plante, E.R., C.D. Olson, and T. Negas. *Interaction of K_2O with slag in open cycle, coal fired MHD*. in *6th international Conference on Magnetohydrodynamic Electrical Power Generation*. 1975.

351. Preston, E. and W.E.S. Turner, *Study of the volatilization from potassium-oxide-silica glasses.* J. Soc. Glass Technol., 1933. **27**: p. 122-144.

352. Eliezer, N., et al., *Vapor pressure measurement studies on slag-seed component equilibriums: the silica-potassium oxide system*. 1977, Dep. Chem., Montana State Univ., Bozeman, MT, USA. p. 230-235.

353. Stull, D.R., et al., *Low Temperature Heat Capacities of 15 Inorganic Compounds.* J. Chem. Eng. Data., 1970. **15**: p. 52-56.

354. Beyer, R.P. and G.E. Daut, *Low-temperature heat capacities of potassium disilicate.* J. Chem. Eng. Data, 1979. **24**(3): p. 170-171.

355. Moya, J.S., E. Criado, and S. De Aza, *The potassium oxide.aluminum oxide-aluminum oxide system.* J. Mater. Sci., 1982. **17**(8): p. 2213-2217.

356. Roth, R.S., J.R. Dennis, and H.F. McMurdie, *Phase Diagrams for Ceramists*. Phase Diagrams for Ceramists. Vol. VI. 1987, Westerville, OH: American Ceramic Society. 515.

357. Schaefer, G.W., A.P. de Kroon, and F. Aldinger, *Influence of precursor chemistry on phase evolution and stability range in the potassium-beta alumina system.* Mater. Res. Soc. Symp. Proc., 1995. **393** (Materials for Electrochemical Energy Storage and Conversion-Batteries, Capacitors and Fuel Cells): p. 61-66.

358. Eliezer, I. and R.A. Howald, *High-Temperature Thermodynamics and Phase Equilibria in the Potassium Oxide-Aluminium Oxide System.* High Temp. Sci., 1978. **10**(1): p. 1-16.

359. Sokolowski, J. and A. Kotarba, *The structure of potassium aluminium oxide $KAlO_2$.* Mater. Sci. Forum, 2000. **321-324**: p. 954-959.

360. P., d.K.A., G.W. Schafer, and F. Aldinger, *Crystallography of potassium aluminate $K_2O{\cdot}Al_2O_3$.* J. Alloys Compd., 2001. **314**(1-2): p. 147-153.

361. Bennington, K.O. and G.E. Daut, *The standard formation data for potassium aluminate ($KAlO_2$).* Thermochim. Acta, 1988. **124**: p. 241-245.

362. Itoh, M. and Z. Kozuka, *Thermodynamic stability of K^+-β-alumina.* J. Am. Ceram. Soc., 1988. **71**(1): p. C36-C39.

363. Kale, G.M. and K.T. Jacob, *Thermodynamic stability of potassium β-alumina.* Metall. Trans. B, 1989. **20**(5): p. 687-691.

364. Marinkovic, M., R. Woodriff, and I. Eliezer, *New method for vapor pressure measurement applicable to potassium over coal slag.* Spectrochim. Acta, Part B, 1978. **33B**(10-12): p. 765-775.

365. Beyer, R.P., M.J. Ferrante, and R.R. Brown, *Thermodynamic Properties of $KAlO_2$.* J. Chem. Thermodyn., 1980. **12**(10): p. 985-991.

366. Arakelyan, O.T., *Polymorphism and Isomorphism of Some Phases of the System Na_2O (or K_2O)-Al_2O_3-Fe_2O_3.* Khim. I Prakt. Primen. Silik., Inst. Khim. Silik., Akad. Nauk SSSR, 1960: p. 63-73.

367. Cook, L.P., *Interfacially controlled phenomena in the potassium carbonate-potassium aluminate ($KAlO_2$) system*, in *Mater. Sci. Res.* 1981. p. 143-154.

368. Anthony, P.J. and A.C. Anderson, *Specific heats of lithium, sodium, potassium, and silver β-alumina below 1 K.* Phys. Rev. B, 1977. **16**(8): p. 3827-2828.

369. Schairer, J.F. and N.L. Bowen, *Melting Relations in the Systems Na_2O-Al_2O_3-SiO_2 and K_2O-Al_2O_3-SiO_2.* Am. J. Sci., 1947. **245**: p. 193-204.

370. Husheer, S.L.G., J.G. Thompson, and A. Melnitchenko, *Cristobalite-Related Phases in the $KAlO_2$-$KAlSiO_4$ System.* J. Solid State Chem., 1999. **147**(2): p. 624-630.

371. Cook, L.P., et al., *The system potassium oxide-aluminum oxide-silicon dioxide. Part 1. Phases on the $KAlSiO_4$-$KAlO_2$ join.* Am. Mineral., 1977. **62**(11-12): p. 1180-1190.

372. Li, C., A.F. Reid, and S. Saunders, *Nonstoichiometric Alkali Ferrites and Aluminates in the Systems $NaFeO_2$-TiO_2, $KFeO_2$-TiO_2, $KAlO_2$-TiO_2, and $KAlO_2$-SiO_2.* J. Solid State Chem., 1971. **3**(4): p. 614-620.

373. Boysen, H., *Neutron scattering and phase transitions in leucite*, in *Phase Transitions in Ferroelastic and Co-Elastic Crystals*, E.K.H. Salje, Editor. 1990, Cambridge University Press: New York. p. 334-349.

374. Palmer, D.C., A. Putnis, and E.K.H. Salje, *Twinning in tetragonal leucite.* Phys. Chem. Miner., 1988. **16**(3): p. 298-303.

375. Palmer, D.C., U. Bismayer, and E.K.H. Salje, *Phase transitions in leucite: Order parameter behavior and the Landau potential deduced from Raman spectroscopy and birefringence studies.* Phys. Chem. Miner., 1990. **17**(3): p. 259-265.

376. Palmer, D.C. and E.K.H. Salje, *Phase transitions in leucite: Dielectric properties and transition mechanism.* Phys. Chem. Miner., 1990. **17**(5): p. 444-452.

377. Day, A.L. and E.T. Allen, *The isomorphism and thermal properties of the feldspars.* Am. J. Sci., 1905. **4**(19): p. 93-143.

378. Morey, G.W. and N.L. Bowen, *The melting of potash feldspar.* Am. J. Sci., 1922. **4**(19): p. 1.

379. Helgeson, H.C., et al., *Summary and critique of the thermodynamic properties of rock-forming minerals.* Am. J. Sci., 1978. **278A**: p. 1-229.

380. Senderov, E.E. and A.M. Bychkov, *Physicochemical conditions for the formation of structural modifications of alkali feldspars in petrogenesis.* Sov. Geol., 1979(9): p. 33-44.

381. Barth, T.F.W., *Diffusive transformation sanidine-microcline.* Estud. Geol. (Madrid), 1959. **15**: p. 31-38.

382. Schumm, R.H., *Thermodynamic Properties of Solid Alkali Aluminosilicates at Elevated Temperatures*. 1981, U. S. Department of Commerce; National Technical Information Service. p. 1-46.

383. Hovis, G.L., *Solution calorimetric and x-ray investigation of aluminum-silicon distribution in monoclinic potassium fledspars.* Feldspars, Proc. NATO Advan. Study Inst., 2nd (Feldspars, Proceedings of a NATO Advanced Study Institute , 2nd), 1974: p. 114-144.

384. Robie, R.A., B.S. Hemingway, and J.R. Fisher, *Thermodynamic Properties of Minerals and Related Substances at 298.15 K and 1 Bar (10^5 Pascals) Pressure and at Higher Temperatures*. U.S. Geological Survey Bulletin. Vol. 1452. 1978: Government Printing Office Washington, D. C. 456.

385. Lange, R.A., I.S.E. Carmichael, and J.F. Stebbins, *Phase transitions in leucite ($KAlSi_2O_6$), orthorhombic $KAlSiO_4$, and their iron analogs ($KFeSi_2O_6$, $KFeSiO_4$).* Am. Mineral., 1986. **71**(7-8): p. 937-945.

386. Paukov, I.E., I.A. Belitsky, and B.A. Fursenko, *Heat capacity and thermodynamic functions of leucite at low temperatures.* Thermochim. Acta, 2002. **387**(1): p. 23-28.

387. Hirao, K. and N. Soga, *The heat capacity and a phase transition in leucite-type compounds.* Yogyo Kyokaishi, 1982. **90**(7): p. 390-396.

388. Pankratz, L.B., *High-Temperature Heat Contents and Entropies of Dehydrated Analcite, Kaliophilite, and Leucite*. 1968: Bureau of Mines Report of Investigations. p. 8 pp.

389. Kelley, K.K., *Contributions to the Data on Theoretical Metallurgy XIII. High-Temperature Heat-Content, Heat-Capacity, and Entropy Data for the Elements and Inorganic Compounds.* Bulletin 584 , Bureau of Mines, 1960. **584**(8): p. 1-232.

390. Kracek, F.C., *The Ternary System: K_2SiO_3-Na_2SiO_3-SiO_2.* J. Phys. Chem., 1932. **36**(10): p. 2529-2542.

391. Schairer, J.F., J.H.S. Yoder, and A.G. Keene, *The systems Na_2O-MgO-SiO_2 and Na_2O-FeO-SiO_2.* Carnegie Inst. Washington Yearb. (1954), 1954. **53**: p. 123.

392. Spek, A.L. and B.H.W.S. de Jong, *Potassium sodium phyllosilicate, $K_{1.33}Na_{0.67}Si_2O_5$.* Acta Crystallogr., Sect. E Struct. Rep. Online, 2005. **61**(8): p. i188-i190.

393. Wakabayashi, H., *The relationship between kinetic and thermodynamic properties in mixed alkali glass.* J. Non-Cryst. Solids, 1996. **203**(Optical and Electrical Properites of Glasses): p. 274-279.

394. Lezzi, P.J. and M. Tomozawa, *Enthalpy of mixing of mixed alkali glasses.* J. Non-Cryst. Solids, 2010. **356**(28-30): p. 1439-1446.

395. Bowen, N.L. and J.F. Schairer, *Preliminary report on equilibrium relations between feldspathoids, alkalifeldspars, and silica.* Transactions, American Geophysical Union, 1935. **16**(1): p. 325-328.

396. Schairer, J.F., *The Alkali-Feldspar Join in the System $NaAlSiO_4$-$KAlSiO_4$-SiO_2.* J. Geol., 1950. **58**(5): p. 512-517.

397. Tuttle, O.F. and N.L. Bowen, *Origin of granite in the light of experimental studies in the system $NaAlSi_3O_8$-$KAlSi_3O_8$-SiO_2-H_2O.* Geol. Soc. AM. Mem., 1958. **74**: p. 1-153.

398. Orville, P.M., *Alkali [metal] ion exchange between vapor and feldspar phases.* Am. J. Sci., 1963. **261**(73): p. 201-237.

399. Luth, W.C. and O.F. Tuttle, *The alkali feldspar solvus in the system sodium oxide-potassium oxide-aluminum oxide-silica-water.* Am. Mineral., 1966. **51**(9-10): p. 1359-1373.

400. Luth, W.C., R.F. Martin, and P.M. Fenn, *Peralkaline alkali feldspar solvi.* Feldspars, Proc. NATO Advan. Study Inst., 2nd, 1974: p. 297-312.

401. Goldsmith, J.R. and R.C. Newton. *Determination of the alkali feldspar solvus*. in *Feldspars, Proc. NATO Advan. Study Inst., 2nd*. 1974. Crane, Russak Co., Inc. New York, N. Y.

402. Smith, P. and I. Parsons, *Alkali-feldspar solvus at 1 kilobar water vapor pressure.* Mineral. Mag., 1974. **39**(307): p. 747-767.

403. Lagache, M. and A. Weisbrod, *The system: two alkali feldspars-potassium chloride-sodium chloride-water at moderate to high temperatures and low pressures.* Contrib. Mineral. Petrol., 1977. **62**(1): p. 77-101.

404. Yund, R.A. and J. Tullis, *Subsolidus Phase Relations in the Alkali Feldspars with Emphasis on Coherent Phases*, in *Feldspar Mineralogy*, P.H. Ribbe, Editor. 1983, BookCrafters, Inc., Chelsea, Michigan 48118. p. 141-176.

405. Yund, R.A.M.A.C. and H.B. E., *Coarsening Kinetics of the Exsolution Microstructure in Alkali Feldspar.* Contrib. Mineral. Petrol., 1974. **48**(1): p. 45-55.

406. Brousse, C., et al., *Enthalpy of Mixing of the Orthose-Albite Glassy System ((Na, K)$AlSi_3O_8$).* Mater. Res. Bull., 1982. **17**(1): p. 125-132.

407. Rogez, J., et al., *Thermodynamic study of the albite-orthoclase system by dissolution calorimetry and Knudsen cell mass spectrometry.* Bull. Mineral., 1983. **106**(1-2): p. 119-128.

408. Chastel, R., et al., *Thermodynamic study of the albite-orthose system by Knudsen effusion coupled with a mass spectrometer, and by dissolution calorimetry.* J. Calorim. Anal. Therm., 1981: p. HT5(1-7).

409. Hervig, R.L. and A. Navrotsky, *Thermochemical study of glasses in the system $NaAlSi_3O_8$-$KAlSi_3O_8$-Si_4O_8 and the join $Na_{1.6}Al_{1.6}Si_{2.4}O_8$-$K_{1.6}Al_{1.6}Si_{2.4}O_8$.* Geochim. Cosmochim. Acta, 1984. **48**(3): p. 513-522.

410. Lezzi, P.J. and M. Tomozawa, *Effect of alumina on enthalpy of mixing of mixed alkali silicate glasses.* J. Non-Cryst. Solids, 2011. **357**(10): p. 2086-2092.

411. Barany, R., *Glass-ctystal transformation of nephiline and wollastonite and heat of formation of nepheline.* U. S. Bur. Mines Rept. Inv., 1966. **6784**: p. 8.

412. Hovis, G.L. and A. Navrotsky, *Enthalpies of mixing for disordered alkali feldspars at high temperature: A test of regular solution thermodynamic models and a comparison of hydrofluoric acid and lead borate solution calorimetric techniques.* Am. Mineral., 1995. **80**(3-4): p. 280-284.

413. Hovis, G.L. and D.R. Waldbaum, *A solution calorimetric investigation of potassium-sodium mixing in a sanidine analbite ion-exchange series.* Am. Mineral., 1977. **62**(7-8): p. 680-686.

414. Hovis, G.L., et al., *Elastic Strain Enthalpies of Exsolution: HF Solution Calorimetric Experiments on Alkali Aluminosilicate and Aluminogermanate Feldspars.* Am. Mineral., 2003. **88**(4): p. 547-555.

415. Hovis, G.L., *Enthalpies and volumes related to potassium-sodium mixing and aluminum-silicon order/disorder in alkali feldspars.* J. Petrol., 1988. **29**(4): p. 731-63.

416. Bachinski, S.W. and G. Mueller, *Experimental determinations of the microcline-low albite solvus.* J. Petrology, 1971. **12**(2): p. 329-356.

417. Zyryanov, V.N. and P.I. Dorogokupets, *Equilibriums of solid solutions of nepheline and alkaline feldspar at 800-1000° in alkali chloride melts.* Ocherki Fiz.-Khim. Petrol., 1974: p. 72-81.

418. Zyryanov, V.N., L.L. Perchuk, and K.K. Podlesskii, *Effect of a silicon dioxide excess in nepheline on its phase correspondence with alkaline feldspar.* Geokhimiya, 1977(1): p. 56-62.

419. Zyrianov, V.N., L.L. Perchuk, and K.K. Podlesskii, *Nepheline-alkali feldspar equilibriums: I. Experimental data and thermodynamic calculations.* J. Petrol., 1978. **19**(1): p. 1-44.

420. Perchuk, L.L., K.K. Podlesskii, and V.N. Zyryanov, *Thermodynamic functions of mixing for nepheline and alkali feldspar solid solutions at 1000 > T > 400°.* Zap. Vses. Mineral. O-va., 1977. **106**(1): p. 45-52.

421. Hovis, G.L., F. Delbove, and M.R. Bose, *Gibbs energies and entropies of potassium-sodium mixing for alkali feldspars from phase equilibrium data: Implications for feldspar solvi and short-range order.* Am. Mineral., 1991. **76**(5-6): p. 913-27.

422. Merkel, G.A., *Thermodynamic Mixing Properties of Binary Analbite-Sanidine Feldspars.* (1984) 163 pp. Avail.: Univ. Microfilms Int., Order No. DA8419638 From: Diss. Abstr. Int. B 1985, 45(10), 3184, 1984: p. 1-150.

423. Kultascheff, N.V., *The melting point of calcium silicate ($CaSiO_3$), sodium silicate (Na_2SiO_3), and of their mixtures.* Z. Anorg. Chem., 1903. **35**: p. 186-193.

424. Wallace, R.C., *Mineralogisch-chemische Mitteilungen aus dem institut fur physikalische chemie in Gottingen. III. Über die binaren Systeme des Natriummetasilicats mit Lithium-, Magnesium-, Calcium-, Strontium-, und Barium- metasilicat; des Lithiummetasilicats mit Kalium-, Magnesium-, Calcium-, Strontium- und Bariummetasilicat; und über das Dreistoffsystem Na_2O-Al_2O_3-SiO_2.* Z. Anorg. Chem., 1909. **63**: p. 1-48.

425. Morey, G.W., *The Devitrification of Soda-Lime-Silica Glasses.* J. Am. Ceram. Soc., 1930. **13**(10): p. 683-713.

426. Brisi, C., *The system Na_2CaSiO_4-calcium fluoride.* Atti accad. sci. Torino, Classe sci. fis. mat. e nat., 1951. **85**: p. 325-330.

427. Thilo, E., *The constitution of silicates.* Angew. Chem., 1951. **63**: p. 201-206.

428. Zhang, Z., et al., *Phase equilibria in the Na_2O-CaO-SiO_2 system.* J. Am. Ceram. Soc., 2011. **94**(9): p. 3088-3093.

429. Montoya, B.G., et al., *Alternative batch compositions in the glass-forming region of the Na_2O-CaO-SiO_2 system.* J. Non-Cryst. Solids, 2003. **329**(1-3): p. 22-26.

430. Shahid, K.A. and F.P. Glasser, *Phase Equilibria in the Glass Forming Region of the System Na_2O-CaO-SiO_2.* Phys. Chem. Glasses, 1971. **12**(2): p. 50-57.

431. Pankratz, L.B., *High-temperature heat contents and entropies of four crystalline sodium calcium silicates*. 1968, Albany Met. Res. Center, Bur. of Mines, Albany, OR, USA. p. 8 pp.

432. Blanco, M.N., H.J. Thomas, and E. Pereira, *Alkali metal oxide effect on dicalcium silicate polymorphism. I. Thermal analysis of the system.* Rev. Latinoam. Ing. Quim. Quim. Apl., 1975. **5**(2): p. 125-134.

433. Akhmetov, S.F., et al., *Ternary compounds in the sodium oxide-calcium oxide-silica system.* Tr. Khim.-Met. Inst., Akad. Nauk Kaz. SSR, 1970. **15**: p. 141-148.

434. Silverman, W.B., *Effect of Alumina on Devitrification of Soda-Lime-Silica Glasses.* J. Am. Ceram. Soc., 1939. **22**(11): p. 378-384.

435. Rego, D.N., G.K. Sigworth, and W.O. Philbrook, *Thermodynamic activity of sodium oxide in sodium oxide-calcia-silica, sodium oxide-magnesia-silica and sodium oxide-calcia-silica-alumina melts at 1400°C.* Metall. Trans. B, 1988. **19**(4): p. 655-661.

436. Mathieu, R., *Solubilité du sodium dans les silicates fondus*. 2009, Institut National Polytechnique de Lorraine.

437. Sugawara, T., et al., *Na_2O activity and thermodynamic mixing properties of SiO_2-Na_2O-CaO melt.* J. Non-Cryst. Solids, 2013. **371-372**: p. 58-65.

438. Eriksson, G., et al., *Critical Evaluation and Optimisation of the Thermodynamic Properties and Phase Diagrams of the MnO-SiO_2 and CaO-SiO_2 Systems.* Can. Metall. Q., 1994. **33**(1): p. 13-21.

439. Lagerqvist, K., S. Wallmark, and A. Westgren, *X-Ray Studies of the CaO-Al_2O_3 and SrO-Al_2O_3 Systems.* Z. Anorg. Allg. Chem., 1937. **234**: p. 1-16.

440. Nurse, R.W., J.H. Welch, and A.J. Majumdar, *The CaO-Al_2O_3 System in a Moisture-Free Atmosphere.* Trans. Brit. Ceram. Soc., 1965. **64**(9): p. 409-418.

441. Hodge, J.D., *Alkaline earth effects on the reaction of sodium with aluminum oxide.* Proc. - Electrochem. Soc., 1985. **85-2**(High Temp. Lamp Chem.): p. 261-270.

442. Zaldat, G.I., M.S. Kupriyanova, and A.L. Tubolev, *High-Alumina Region of the Sodium Oxide-Calcium Oxide-Aluminum Oxide System.* Izv. Akad. Nauk SSSR, Neorg. Mater., 1985. **21**(1): p. 51-3.

443. Greene, K.T. and R.H. Bogue, *Phase equilibrium relations in a portion of the system Na_2O-CaO-Al_2O_3-SiO_2.* J. Res. Nat. Bur. Stand. RP 1699, 1946. **36**(2): p. 185-207.

444. Lee, F.C. and F.P. Glasser, *Powder diffraction data for compounds in the series $Na_x(Ca_{3-x}Na_x)Al_2O_5$.* J. Appl. Crystallogr., 1979. **12**(4): p. 407-410.

445. Regourd, M., et al., *Polymorphism of solid solutions of sodium oxide in tricalcium aluminate.* J. Appl. Crystallogr., 1973. **6**(Pt. 5): p. 355-364.

446. Maki, I., *Nature of the prismatic dark interstitial material in portland cement clinker.* Cem. Concr. Res., 1973. **3**(3): p. 295-313.

447. Smalley, R.G., *The system $NaAlSiO_4$-$Ca_2Al_2SiO_7$.* J. Geol., 1947. **55**(1): p. 31.

448. Gummer, W.K., *The system $CaSiO_3$-$CaAlSi_2O_3$-$NaAlSiO_4$.* J. Geol., 1943. **51**(11-12): p. 503-531.

449. Goldsmith, J.R., *The system $CaAl_2Si_2O_8$-$Ca_2Al_2SiO_7$-$NaAlSiO_4$.* J. Geol., 1947. **55**(5): p. 381-404.

450. Benisek, A., et al., *Enthalpies in (Na, Ca)- and (K, Ca)-Feldspar Binaries: a High Temperature Solution Calorimetric Study.* Contrib. Mineral. Petrol., 2003. **145**(1): p. 119-129.

451. Carpenter, M.A. and J.M. Ferry, *Constraints on the thermodynamic mixing properties of plagioclase feldspars.* Contrib. Mineral. Petrol., 1984. **87**(2): p. 138-148.

452. Carpenter, M.A., J.D.C. McConnell, and A. Navrotsky, *Enthalpies of ordering in the plagioclase feldspar solid solution.* Geochim. Cosmochim. Acta, 1985. **49**(4): p. 947-966.

453. Navrotsky, A., et al., *Calorimetry of Silicate Melts at 1773K: Measurement of Enthalpies of Fusion and of Mixing in the Systems Diopside-Anorthite-Albite and Anorthite-Fosterite.* Contrib. Mineral. Petrol., 1989. **101**(1): p. 122-130.

454. Orville, P.M., *Plagioclase Cation Exchange Equilibriums with Aqueous Chloride Solution. Results at 700°C and 2000°C Bars in the Presence of Quartz.* Am. J. Sci., 1972. **272**: p. 234-272.

455. Schliestedt, M. and W. Johannes, *Cation Exchange Equilibria between Plagioclase and Aqueous Chloride Solution at 600 to 700 °C and 2 to 5 kbar.* Eur. J. Mineral., 1990. **2**(3): p. 283-295.

456. Kotel'nikov, A.R., *Calculation of mixing functions for a plagioclase solid solution.* Geokhimiya, 1980. **2**: p. 226-30.

457. Seck, H.A., *Coexisting alkali feldspars and plagioclases in the system $NaAlSi_3O_8$-$KAlSi_3O_8$ $CaAl_2Si_2O_8$-H_2O [albite-orthoclase-anorthite-water] in the temperature range of 650 °C to 900 °C.* Neues Jahrb. Mineral., Abh., 1971. **115**(3): p. 315-345.

458. Kotel'nikov, A.R., A.M. Bychkov, and N.I. Chernavina, *The Distribution of Calcium between Plagioclase and a Water-Salt Fluid at 700 °C and Pfl = 1000 kg/cm^2.* Geochem. Int., 1981. **18**: p. 61-75.

459. Schairer, J.F., J.H.S. Yoder, and C.E. Tilley, *Behavior of Melilites in the Join Gehlenite-Soda Melilite-Akermanite at One-Atmosphere Pressure.* Carnegie Inst. Washington Yearb. (1964-1965), 1964. **64**(11-12): p. 95-100.

460. Yoder, H.S.J., *Soda melilite.* Carnegie Inst. Washington Yearb. (1963-1964), 1963. **63**(10): p. 86-89.

461. Goldsmith, J., *Some melilite solid solutions.* J. Geol., 1948. **56**: p. 437-447.

462. Yoder, H.S.J., *The 10 per cent $CaAl_2Si_2O_8$ plane in the system $CaSiO_3$-$CaAl_2SiO_7$-$NaAlSiO_4$-$CaAl_2Si_2O_8$.* J. Geol., 1952. **60**: p. 586-593.

463. Spivak, J., *The system $NaAlSiO_4$-$CaSiO_3$-$NaSiO_3$.* J. Geol., 1944. **52**: p. 24-52.

464. Cohen, R., *Thermodynamic solution properties of aluminous clinopyroxenes: Nonlinear least squares refinements.* Geochim. Cosmochim. Acta, 1986. **50**: p. 563-575.

465. Saboungi, M.L., et al., *Phase diagrams of reciprocal molten salt systems. Calculations of liquid-liquid miscibility gaps.* J. Phys. Chem., 1974. **78**(11): p. 1091-1096.

466. Lin, I.J. and N. Maltz, *Interactions and phase changes in the system $2CaO \cdot SiO_2$-$Na_2O \cdot Al_2O_3$.* J. Mater. Synth. Process., 1996. **4**(3): p. 181-187.

467. Korneev, V.I. and N.S. Mal'ts, *Phase correlations in the calcium silicate (Ca_2SiO_4)-sodium aluminate ($NaAlO_2$) system.* Tr. Vses. N.-i. i Proekt. In-t Alyumin., Magn. i Elektrod. Prom-sti, 1977(97): p. 12-17.

468. Druzhinina, N.K., P.D. Katsenelenbogen, and A.I. Egereva, *Influence of soda on interaction of dicalcium silicate with sodium aluminate.* Tr., Vses. Nauchn.-Issled. Alyumin.-Magnievyi Inst., 1960(46): p. 59-61.

469. Kukolev, G.V. and M.T. Mel'nik, *The problem of the stabilization of Ca_2SiO_4.* Dokl. Akad. Nauk SSSR, 1956. **109**: p. 1012-1014.

470. Khazanov, E.I., S.A. Stakheeva, and G.V. Kuz'mina, *Reaction of sodium aluminate with dicalcium silicate.* Zh. Prikl. Khim. (S.-Peterburg, Russ. Fed.), 1965. **38**(6): p. 1381-1383.

471. Druzhinina, N.K., et al., *Reaction of dicalcium silicate with sodium aluminate.* Tr., Vses. Nauchn.-Issled. Alyumin.-Magnievyi Inst., 1960(46): p. 40-50.

472. Hughes, H., *Formation of alkali silicates and aluminosilicates and their occurrence in blast furnaces.* Trans. Br. Ceram. Soc., 1966. **65**(12): p. 661-679.

473. Arroyabe, E., et al., *Does K_2CaSiO_4 exist? A phase-analytical study in the system K_2O-CaO-SiO_2 with implications for the characterization of residual materials.* J. Am. Ceram. Soc., 2011. **94**(8): p. 2652-2655.

474. Chen, M., et al., *Phase Equilibria Studies in the SiO_2-K_2O-CaO System.* Metall. Mater. Trans. B, 2016. **47**(3): p. 1690-1696.

475. Newman, E.S. and L.S. Wells, *Effect of Some Added Materials on Dicalcium Silicate.* J. Res. Nat. Bur. Stand., 1946. **36**(2): p. 137-158.

476. Arroyabe, E., et al., *$K_2Ca_6Si_4O_{15}$-structural and spectroscopical studies on a mixed tetrahedral-octahedral framework.* J. Solid State Chem., 2009. **182**(12): p. 3254-3261.

477. Ohsato, H., et al., *β-Wollastonite and para-wollastonite precipitated from the join potassium oxide-calcium silicate.* Nagoya Kogyo Daigaku Gakuho, 1980. **32**: p. 123-130.

478. Zhang, L., C. Schmetterer, and P.J. Masset, *Thermodynamic Modeling of the CaO-SiO_2-M_2O (M=K,Na) Systems.* High Temp. Mater. Processes (Berlin, Ger.), 2013. **32**(3): p. 223-228.

479. Brownmiller, L.T., *System lime-potash-alumina.* Am. J. Sci., 1935. **29 (5th ser)**: p. 261-277.

480. Van Hoek, J.A.M., F.J.J. Van Loo, and R. Metselaar, *Phase Relations in the Calcium Oxide-Potassium Oxide-Aluminum Oxide System.* Mater. Sci. Monogr., 1991. **66B**(Ceram. Today-Tomorrow's Ceram., Pt. B): p. 581-590.

481. Nurse, R.W. and H.G. Midgley, *Studies on the Melilite Solid Solutions.* J. Iron Steel Inst., London, 1953. **174**(2): p. 121-131.

482. Kushiro, I., *Wollastonite-Pseudowollastonite Inversion.* Carnegie Inst. Washington Yearb. (1964), 1964. **63**(10): p. 83-84.

483. Schairer, J.F. and N.L. Bowen, *The system anorthite-leucite-silica.* Bull. Soc. Geol. de Finlande, 1947. **20**(1): p. 67-87.

484. Gupta, A.K. and A.D. Edgar, *Phase relations in the system nepheline-leucite-anorthite at 1 atmosphere.* Can. Mineral., 1974: p. 354-356.

485. Nekvasil, H. and W.J. Carroll, *Experimental constraints on the high-temperature termination of the anhydrous 2 feldspar + L curve in the feldspar system at 11.3 kbar.* Am. Mineral., 1993. **78**(5-6): p. 601-606.

486. Eliezer, I., et al., *A four-component model for the vaporization of seeded slags - the system potassium oxide ($KO_{0.5}$)-calcium oxide-aluminum oxide ($AlO_{1.5}$)-silica.* Eng. Aspects Magnetohydrodyn., 1979. **18th**: p. C/4/1-C/4/7.

487. Hastie, J.W., et al., *Thermodynamic activity and vapor pressure models for silicate systems including coal slags.* NATO ASI Ser., Ser. C, 1984. **119**(Thermochem. Its Appl. Chem. Biochem. Syst.): p. 235-251.

488. Franco, R.R. and J.F. Schairer, *Liquidus temperatures in mixtures in the feldspars of soda, potash, and lime.* J. Geol., 1951. **59**: p. 259-266.

489. Seck, H.A., *Effect of pressure on the composition of coexisting alkali feldspars and plagioclases in the system $NaAlSi_3O_8$-$KAlSi_3O_8$-$CaAl_2Si_2O_8$-H_2O.* Contrib. Mineral. Petrol., 1971. **31**(1): p. 67-86.

490. Johannes, W., *Ternary feldspars: kinetics and possible equilibriums at 800°C.* Contrib. Mineral. Petrol., 1979. **68**(2): p. 221-230.

491. Barth, T.F.W., *Feldspar solid solutions.* Chem. Erde, 1962. **22**: p. 31-40.

492. Kroll, H. and H.U. Bambauer, *Displacive transformation of (potassium, sodium, calcium)-feldspars.* Neues Jahrb. Mineral., Monatsh., 1971. **[2]2**(9): p. 413-416.

493. Kroll, H. and H.U. Bambauer, *Diffusive and displacive transformation in plagioclase and ternary feldspar series.* Am. Mineral., 1981. **66**(7-8): p. 763-769.

494. Hovis, G.L., *Hydrofluoric acid solution calorimetric investigation of the effects of anorthite component on enthalpies of K-Na mixing in feldspars.* Am. Mineral., 1997. **82**(1-2): p. 149-152.

495. Schairer, J.F. and J.H.S. Yoder, *The Joins $Na_2O \cdot 5MgO \cdot 12SiO_2$-Sodium Disilicate and $2Na_2O \cdot 3MgO \cdot 5SiO_2$-Sodium Disilicate in the System Na_2O-MgO-SiO_2.* Carnegie Inst. Washington Yearb. (1969-1970), 1969: p. 157-160.

496. Bruckmann, P., et al., *An equation of state for roedderites, $(K, Na)_2Mg5[Si_{12}O_{30}]$, based on Knudsen cell mass spectrometry and synthesis of eifelite-roedderite crystalline solutions.* Phys. Chem. Miner., 1993. **20**(5): p. 362-368.

497. Botvinkin, O.K., T.A. Popova, and N.S. Manuilova, *System Na_2O-MgO-SiO_2.* Trans. 2nd Conf. Exper. Min., Acad. Sci. U. S. S. R., 1937: p. 87-101.

498. Cradwick, M.E. and H.F.W. Taylor, *Crystal structure of $Na_2Mg_2Si_6O_{15}$.* Acta Crystallogr., Sect. B, 1972. **29**(Pt. 12): p. 3583-3587.

499. Foris, C.M., F.C. Zumsteg, and R.D. Shannon, *Crystal data for sodium magnesium silicate, $Na_4Mg_2Si_3O_{10}$.* J. Appl. Crystallogr. (Journal of Applied Crystallography), 1979. **12**(4): p. 405-406.

500. Manuilova, N.S., *Crystalline phases in the system Na_2O-MgO-SiO_2.* Trans. 2nd Conf. Exper. Min., Acad. Sci. U. S. S. R., 1937: p. 96-101.

501. Shannon, R.D., *Ionic conductivity in sodium magnesium silicates.* Phys. Chem. Miner., 1979. **4**(2): p. 139-148.

502. Wu, P., et al., *Prediction of the Thermodynamic Properties and Phase Diagrams of Silicate Systems - Evaluation of the FeO-MgO-SiO_2 System.* ISIJ Int., 1993. **33**(1): p. 26-35.

503. Hausner, R. and M. Suppaner, *X-ray Powder Diffraction Data of a New Compound Sodium Calcium Magnesium Silicate ($Na_2Ca_4Mg_2Si_4O_{15}$).* Powder Diffr., 1992. **7**(1): p. 36-37.

504. Shahid, K.A. and F.P. Glasser, *Phase equilibriums in the glass forming region of the system sodium oxide-calcium oxide-magnesium oxide-silicon dioxide.* Phys. Chem. Glasses (Physics and Chemistry of Glasses), 1972. **13**(2): p. 27-42.

505. Silverman, W.B., *Effect of Alumina on Devitrification of Sodium Oxide-Dolomite Lime-Silica Glasses.* J. Am. Ceram. Soc., 1940. **23**(9): p. 274-281.

506. Simurka, P., M. Liska, and J. Antalik, *Liquidus Temperature and Structure of the Glass Melts in the 15 $Na_2O_{.10}$ (MgO, CaO, TiO_2, ZrO_2)$_{.75}$ SiO_2 System.* Ceram. Silik., 1995. **39**(1): p. 9-13.

507. Babcock, C.L., *Effect of substituting MgO for CaO on properties of typical soda-lime glasses.* J. Am. Ceram. Soc., 1944. **27**: p. 221-225.

508. Morey, G.W., *The Effect of Magnesia on the Devitrification of a Soda-Lime-Silica Glass.* J. Am. Ceram. Soc., 1930. **13**(10): p. 714-717.

509. Jones, S.P., *Structural interpretation of liquidus temperature measurements in the soda-lime-silica system.* Phys. Chem. Glasses, 1961. **2**(2): p. 55.

510. Lab., O.-I.G.C.G.R., *Effect of Substituting MgO for CaO on Properties of Typical Soda-Lime Glasses.* J. Am. Ceram. Soc., 1944. **27**(8): p. 221-225.

511. Swift, H.R., *Effect of magnesia and alumina on rate of crystal growth in some soda-lime-silica glasses.* J. Am. Ceram. Soc., 1947. **30**: p. 170-174.

512. Mathieu, R., et al., *Na_2O-solubility in CaO-MgO-SiO_2 melts.* Geochim. Cosmochim. Acta, 2010: p. 1-63.

513. Kim, W.-S., D.-H. Cho, and S.-K. Lim, *The activity of sodium oxide in molten float glass by EMF measurements.* Thermochim. Acta, 2004. **414**(2): p. 191-195.

514. Van Hoek, J.A.M., F.J.J. Van Loo, and R. Metselaar, *Phase diagrams of alumina-alkali oxide-alkaline earth oxide systems in relation to alkali corrosion.* Key Eng. Mater., 1991. **53-55(Austceram '90)**: p. 111-119.

515. Jung, I.-H., S.A. Decterov, and A.D. Pelton, *Critical Thermodynamic Evaluation and Optimization of the MgO-Al_2O_3, CaO-MgO-Al_2O_3 and MgO-Al_2O_3-SiO_2 Systems.* J. Phase Equilib., 2004. **25**(4): p. 329-345.

516. Schairer, J.F. and J.H.S. Yoder, *Crystallization in the System Nepheline-Fosterite-Silica at One Atmosphere Pressure.* Carnegie Inst. Washington Yearb. (1961), 1961. **60**: p. 141-144.

517. Schairer, J.F. and J.H.S. Yoder, *Ths system Albite-Fosterite-Silica.* Carnegie Inst. Washington Yearb. (1960), 1960. **Yb. 59**: p. 69-72.

518. Schairer, J.F. and H.S. Yoder, Jr., *Simple basalt systems. The system albite-forsterite-silica.* Year Book - Carnegie Inst. Washington, 1960. **59**: p. 67-70.

519. Yoder, H.S., Jr., *Genesis of principal basalt magmas.* Year Book - Carnegie Inst. Washington, 1964. **63**: p. 97-101.

520. Mao, H.-K. and J.F. Schairer, *Quenching Experiments in the Systems Jadeite ($NaAlSi_2O_6$)-Forsterite (Mg_2SiO_4) and Jadeite ($NaAlSi_2O_6$)-Anorthite ($CaAl_2Si_2O_8$).* Carnegie Inst. Washington Yearb. (1970), 1970: p. 221-222.

521. Schairer, J.F. and H.S. Yoder, Jr., *The quaternary system Na_2O-MgO-Al_2O_3-SiO_2.* Year Book - Carnegie Inst. Washington, 1958. **57**: p. 210-213.

522. Schairer, J.F., *The crystallization of rock-forming minerals from magmas and the nature of the residual liquid.* Carnegie Inst. Washington Yearb. (1957), 1957. **56**: p. 217-222.

523. Bowen, N.L., *Crystallization of haplobasaltic, haplodioritic and related magmas.* Am. J. Sci., 1915. **40**: p. 161-185.

524. Schairer, J.F. and J.H.S. Yoder, *Tha nature of residual liquids from crystallization, with data on the system nepheline-diopside-silica.* Am. J. Sci., 1960. **258A**(3): p. 273-283.

525. Murphy, W.M., *An experimental study of solid liquid equilibria in the albite-anorthite-diopside system*. 1977, University of Oregon: Eugene.

526. Kushiro, I. and J.F. Schairer, *Diopside solid solutions in the system diopside-anorthite-albite at 1 atm and at high pressures.* Carnegie Inst. Washington, Yearb., 1970: p. 222-226.

527. Schumoff-Deleano, V., *Einige Versuche uber das Zusammen-kristalisieren von Diopsid und Jadeit.* Centralbl. mineralogie, 1918: p. 227-230.

528. Kushiro, I., *The system diopside-anorthite-albite: determination of compositions of coexisting phases.* Carnegie Inst. Washington, Yearb., 1973. **72**: p. 502-507.

529. Schairer, J.F., *Melting Relations of the Common Rock-Forming Oxides.* J. Am. Ceram. Soc., 1957. **40**(7): p. 215-235.

530. Weill, D.F., R. Hon, and A. Navrotsky, *The igneous system calcium magnesium silicate ($CaMgSi_2O_6$)-calcium aluminum silicate ($CaAl_2Si_2O_8$)-sodium aluminum silicate ($NaAlSi_3O_8$) variations on a classic theme by Bowen.* Phys. Magmat. Processes, [Proc.] (Physics of Magmatic Processes. [Proceedings]), 1980: p. 49-92.

531. Schairer, J.F. and J.H.S. Yoder, *The System Albite-Anorthite-Forsterite at 1 Atmosphere.* Carnegie Inst. Washington Yearb. (1966), 1967. **65**(3): p. 204-209.

532. Schairer, J.F. and J.H.S. Yoder, *Join Albite-Anorthite-Akermanite.* Carnegie Inst. Washington Yearb. (1967-1968), 1967. **67**: p. 104-105.

533. Schairer, J.F. and J.H.S. Yoder, *Join Albite-Anorthite-Akermanite.* Carnegie Inst. Washington Yearb. (1969), 1969. **67**(8): p. 104-105.

534. Schairer, J.F. and H.S. Yoder, Jr., *The join akermanite ($Ca_2MgSi_2O_7$)-soda melilite ($NaCaAlSi_2O_7$).* Year Book - Carnegie Inst. Washington, 1964. **63**: p. 89-90.

535. Christie, O.H.J., *Subsolidus relations of silicates. IV. The systems akermanite-sodium gehlenite and gehlenite-sodium gehlenite.* Norske Geol. Tidsskr., 1962. **42**: p. 31-44.

536. Carstens, C.W. and K. Kristoffersen, *A study of the manganese-bearing slags.* Neues Jahrb. Mineral Geol., 1931. **62**(Abt. A, Beil.-Bd.): p. 163-196.

537. Bowen, N.L., J.F. Schairer, and E. Psnjak, *The System CaO-FeO-SiO_2.* Am. J. Sci., 1933. **26**: p. 193-284.

538. Harker, R.J. and O.F. Tuttle, *The lower limit of stability of akermanite ($Ca_2MgSi_2O_7$).* Am. J. Sci., 1956. **254**: p. 468-478.

539. Neuvonen, L.J., Bull Comm. Geol., Findlande, 1952. **158**: p. 50 pp.

540. Schairer, J.F. and J.H.S. Yoder, *Experimental Petrology. Crystal and Liquid Trends in Simplified Alkali Basalts.* Carnegie Inst. Washington Yearb. (1964), 1964. **63**(2): p. 64-74.

541. Onuma, K. and K. Yagi, *System diopside-akermanite-nepheline.* Am. Mineral., 1967. **52**(1-2): p. 227-43.

542. Osborn, E.F. and J.F. Schairer, *The Ternary System Pseudowollastonite-Alkermanite-Gehlenite.* Am. J. Sci., 4th Ser., 1941. **239**: p. 715-763.

543. Jung, I.-H., S.A. Decterov, and A.D. Pelton, *Critical Thermodynamic Evaluation and Optimization of the CaO-MgO-SiO_2 System.* J. Eur. Ceram. Soc., 2005. **25**(4): p. 313-333.

544. Bowen, N.L., *Genetic features of alnoitic rocks at Isle Cadieux, Quebec.* Am. J. Sci., 1922. **3**: p. 1-34.

545. Schairer, J.F., K. Yagi, and H.S. Yoder, *The System Nepheline-Diopside.* Carnegie Inst. Washington Yearb. (1962), 1962. **61**: p. 96-98.

546. Jung, I.-H., S.A. Decterov, and A.D. Pelton. *Critical Optimization of CaO-MgO-SiO_2 System*. in *KIMM Fall Meeting, Oct. 2001*. 2001. YeonSei University, Seoul, Korea.

547. Hytonen, K. and J.F. Schairer, *The system enstatite-anorthite-diopside.* Year Book - Carnegie Inst. Washington, 1960. **59**: p. 71-72.

548. Schairer, J.F., C.E. Tilley, and G.M. Brown, *The Join Nepheline-Diopside-Anorthite and its Relation to Alkali Basalt Formation.* Carnegie Inst. Washington Yearb. (1968), 1968. **66**: p. 467-471.

549. Rossi, G., et al., *Crystal chemistry and cation ordering in the system diopside-jadeite: a detailed study by crystal structure refinement.* Contrib. Mineral. Petrol., 1983. **83**(3-4): p. 247-58.

550. Newton, R.C., B.J. Wood, and O.J. Kleppa, *Thermochemistry of Silicate Solid Solutions.* Bull. Mineral., 1981. **104**(2-3): p. 162-171.

551. Holland, T.J.B., *The Experimental Determination of Activities in Disordered and Short-Range Ordered Jadeitic Pyroxenes.* Contrib. Mineral. Petrol., 1983. **82**(2-3): p. 214-220.

552. Gasparik, T., *Experimentally determined compositions of diopside-jadeite pyroxene in equilibrium with albite and quartz at 1200-1350°C and 15-34 kbar.* Geochim. Cosmochim. Acta, 1985. **49**(3): p. 865-870.

553. Vinograd, V.L., *Thermodynamics of Mixing and Ordering in the Diopside-Jadeite System: II. A Polynomial Fit to the CVM Results.* Mineral. Mag., 2002. **66**(4): p. 537-545.

554. Schairer, J.F. and N. Morimoto, *The system forsterite-diopside-silica-albite.* Year Book - Carnegie Inst. Washington, 1959. **58**: p. 113,115-118.

555. Dollase, W.A., *Transformations of the stuffed cristobalites, K_2MSiO_4, M = Mg, Zn, Co, Cd, with temperature and composition.* Phys. Chem. Miner., 1998. **25**(5): p. 389-392.

556. Schairer, J.F. *Phase equilibrium relations in the quaternary system K_2O-MgO-Al_2O_3-SiO_2.* in *Geol. Soc. America Meeting*. 1948. New York.

557. Seifert, F. and W. Schreyer, *Stability relations of $K_2Mg_5Si_{12}O_{30}$, an end member of the merrihueite-roedderite group of meteoritic minerals.* Beitr. Mineral. Petrol., 1969. **22**(3): p. 190-207.

558. Svanson, S.-E., E. Forslind, and J. Krogh-Moe, *Nuclear Magnetic Resonance Study of Boron Coordination in Potassium Borate Glasses.* J. Phys. Chem., 1962. **66**(1): p. 174-175.

559. Krogh-Moe, J., *Structure of vitreous and liquid boron oxide.* J. Non-Cryst. Solids, 1969. **1**(4): p. 269-84.

560. Strong, S.L. 1965-1966, MIT.

561. Jellison, G.E.J. and P.J. Bray, *A structural interpretation of ^{10}B and ^{11}B NMR spectra in sodium borate glasses.* J. Non-Cryst. Solids, 1978. **29**(2): p. 187-206.

562. Vedishcheva, N.M. and B.A. Shakhmatkin, *Influence of Fictive Temperature on the Structure of Borate Glasses: a Thermodynamic Prediction.* Phys. Chem. Glasses, 2000. **41**(5): p. 260-263.

563. Bray, P.J. and M.L. Lui. *NMR study of structure and bonding in glasses*. in *Struct. Bonding Noncryst. Solids, [Int. Symp.]*. 1986. Plenum, New York, N. Y.

564. Ostvold, T. and O.J. Kleppa, *Thermochemistry of Liquid Borates. II. Partial Enthalpies of Solution of Boric Oxide in Its Liquid Mixtures with Lithium, Sodium, and Potassium Oxides.* Inorg. Chem., 1970. **9**(6): p. 1395-1400.

565. Itoh, H., et al., *Electromotive-force Measurements of Molten Oxide Mixtures.* J. Chem. Soc., Faraday Trans. 1, 1984. **80**: p. 473-487.

566. Itoh, M., S. Sato, and T. Yokokawa, *E. M. F. Measurements of Molten Mixtures of Lithium Oxide +, Sodium Oxide +, and Potassium Oxide + Boron Oxide.* J. Chem. Thermodyn., 1976. **8**(4): p. 339-352.

567. Kuehne, K., *Development of electrochemical potentials on boundary faces between two glass systems.* Silikattechnik, 1964. **15**(5): p. 139-144.

568. Voronkova, Z.P. and O.M. Ivanova, *Electrochemical method for determining the homogeneity of borosilicate melts.* Tr. Gor'k. Politekh. Inst., 1969. **25**(14): p. 25-29.

569. Sato, S., et al., *Thermodynamic Activity of Sodium Oxide-Boron Oxide Melt. Use of Stabilized Zirconia as an Electrode Constituent.* J. Electrochem. Soc., 1972. **119**(11): p. 1524-1526.

570. Stegmaier, V.W. and A. Dietzel, *Tha Meaning of Basicity of Glass Melts and Attempt to Measure It.* Glastech. Ber., 1940. **18**(12): p. 353-362.

571. Shaw, R.R. and D.R. Uhlmann, *Subliquidus immiscibility in binary alkali borates.* J. Amer. Ceram. Soc., 1968. **51**(7): p. 377-382.

572. Thach Lan, T., *Investigations of phase segregation in certain glasses. I. The structure of Na borosilicate glasses.* Verres Refract., 1965. **19**(4): p. 416-428.

573. Galakhov, F.Y. and O.S. Alekseeva, *Metastable liquation region in ternary alkali metal borosilicate systems.* Likvatsionnye Yavleniya Steklakh, Tr. Vses. Simp., 1st, 1969: p. 80-83.

574. Rockett, T.J., W.R. Foster, and R.G.J. Ferguson, *Metastable Liquid Immiscibility in the System Silica-Sodium Tetraborate.* J. Am. Ceram. Soc., 1965. **48**(6): p. 329-331.

575. Haller, W., et al., *Metastable Immiscibility Surface in the System Na_2O-B_2O_3-SiO_2.* J. Am. Ceram. Soc., 1970. **53**(1): p. 34-39.

576. Morey, G.W. and H.E. Merwin, *Phase Equilibrium Relashionships in the Binary System, Sodium Oxide-Boric Oxide, with Some Measurements of the Optical Properties of the Glass.* J. Am. Chem. Soc., 1936. **58**(11): p. 2248-2254.

577. Jenckel, E., *Melting-point diagram of boric acid anhydride and sodium metaborate melts.* Z. Anorg. Allg. Chem., 1936. **227**: p. 214-220.

578. Milman, T. and R. Bouaziz, *Sodium borates.* Ann. Chim. (Paris), 1968. **3**(4): p. 311-321.

579. Kaplun, A.B. and A.B. Meshalkin, *Na_2O-B_2O_3 phase equilibria in the region from 48-84 mol% B_2O_3.* Zh. Neorg. Khim., 2003. **48**(10): p. 1704-1711.

580. Kaplun, A.B. and A.B. Meshalkin, *Oscillation methods in thermophysical and physicochemical investigations.* High Temp., 2010. **48**(4): p. 527-533.

581. Golubkov, V.V. and B.A. Shakhmatkin, *Specific Features of Temperature Dependences of the Intensity of Small-Angle X-ray Scattering in Oxide Systems at Liquidus Temperatures.* Glass Phys. Chem., 1999. **25**(4): p. 335-341.

582. Vartbaronov, O.R. and A.G. Bergman, *Sodium, potassium metaborate, tetraborate.* Russ. J. Inorg. Chem., 1967. **12**(11): p. 1688-1691.

583. Zintl, E. and W. Morawietz, *Ortho salts of oxygen acids.* Z. Anorg. Allg. Chem., 1938. **236**: p. 372-410.

584. Koenig, H. and R. Hoppe, *The knowledge of sodium borate.* Z. Anorg. Allg. Chem., 1977. **434**: p. 225-232.

585. Ritchie, C.F. and L.G. Black, *Method of producing caustic botate products*. 1939: USA.

586. Fang, S.-M., *The crystal structure of sodium metaborate, $Na_3(B_3O_6)$.* Z. Kristallogr., Kristallgeom., Kristallphys., Kristallchem., 1938. **99**: p. 1-8.

587. Marezio, M., H.A. Plettinger, and W.H. Zachariasen, *The bond lengths in the sodium metaborate structure.* Acta Cryst., 1963. **16**(7): p. 594-595.

588. Kaplun, A.B. and A.B. Meshalkin, *Na_2O-B_2O_3 phase equilibria in the region from 48-84 mol% B_2O_3.* Russ. J. Inorg. Chem., 2003. **48**(10): p. 1560-1565.

589. Liang, J.-K., *Formation and Crystallization Mechanism of Glasses in $NaBO_2$-B_2O_3 System.* Acta Phys. Sinica, 1990. **39**(1): p. 129-137.

590. Li, H. and J. Liang, *Dependence of crystallization behavior of sodium diborate ($Na_2O \cdot 2B_2O_3$) on its glass structure and the characteristics of phase transformation.* J. Am. Ceram. Soc., 1995. **78**(2): p. 470-478.

591. Krogh-Moe, J., *Crystal structure of α-sodium triborate, α-$Na_2O \cdot 3B_2O_3$.* Acta Crystallogr., Sect. B, 1974. **30**(3): p. 747-752.

592. Krogh-Moe, J., *Crystal structure of a sodium triborate modification, β-$Na_2O \cdot 3B_2O_3$.* Acta Crystallogr., Sect. B, 1972. **28**(Pt. 5): p. 1571-1576.

593. Ponomareff, J., *Acid sodium borates.* Z. Anorg. Chem., 1914. **89**: p. 383-392.

594. Penin, N., M. Touboul, and G. Nowogrocki, *Crystal Structure of a New Form of Sodium Octaborate β-$Na_2B_8O_{13}$.* J. Solid State Chem., 2002. **168**(1): p. 316-321.

595. Hyman, A., et al., *Crystal structure of sodium tetraborate.* Acta Crystallogr., 1967. **22**(6): p. 815-821.

596. Bubnova, R.S., et al., *Thermal behaviour of the rigid boron-oxygen groups in the α-$Na_2B_8O_{13}$ crystal structure.* Z. Kristallogr., 2002. **217**(9): p. 444-450.

597. Bouaziz, R., *Contribution a l'étude des borates de lithium et de sodium*. 1961, Paris University: Paris.

598. Vartbaronov, O.R. and A.G. Bergman, *Surface elements of prisms of the composition of the system Na,K‖CrO_4, BO_2, B_4O_7.* Trudy Rostovsk.-na-Donu Inst. Inzhener. Zelezno-Dorozhn. Transporta, 1959(28): p. 156-168.

599. Ota, R. and N. Soga, *Liquidus viscosities and glass-forming regions in the boron oxide-sodium oxide system.* Yogyo Kyokaishi, 1981. **89**(4): p. 218-220.

600. Ezikov, V.I. and S.V. Ezikova, *Low-temperature structural changes of oxide melts.* Vestn. Nats. Tekh. Univ. "KhPI", 2004(40): p. 111-114.

601. Vartbaronov, O.R. and A.G. Bergman, *Sodium, potassium metaborate, tetraborate.* Zh. Neorg. Khim., 1967. **12**(11): p. 3192-3198.

602. Meshalkin, A.B., *Study of phase equilibria and evaluation of thermodynamic properties of melts in binary borate systems.* Teplofiz. Aeromekh., 2005. **12**(4): p. 669-684.

603. Shvarts, E., V. Grundsteins, and A. Ievins, *Thermal decomposition of sodium monoborate.* Russ. J. Inorg. Chem., 1967. **12**(8): p. 1061-1062.

604. Wang, C., H. Yu, and Z.-p. Jin, *Applications of CALPHAD technique in the crystal growth of BBO.* Rengong Jingti Xuebao, 2001. **30**(3): p. 293-300.

605. Cooper, W.J. and D.A. Scarpiello, *Thermodynamic Properties of the Metal Bromides, Iodides, Sulfides, Sulfates, Chromates, Metaphosphates, Orthophosphates, Molybdates, Tungstates, Borates and Hydroxides*. 1964: U. S. Atomic Energy Comm. p. 58 pp.

606. Cole, S.S., S.R. Scholes, and C.R. Amberg, *The system Na_2O-B_2O_3. II. The system R_2O-B_2O_3. Properties of anhydrous and hydrated metaborates of sodium and potassium.* J. Am. Ceram. Soc., 1935. **18**: p. 58-61.

607. Rao, G.H., et al., *Optimization of the barium borate-sodium borate (BaB_2O_4-$Na_2B_2O_4$) and barium borate-potassium borate (BaB_2O_4-$K_2B_2O_4$) binary phase diagrams.* CALPHAD, 1989. **13**(2): p. 169-175.

608. Marinov, M.R., V. Boncheva-Chakurova, and M. Radenkova-Yaneva, *Phase Equilibrium in the $Na_2O \cdot 4B_2O_3$-$Li_2O \cdot SiO_2$ System.* Epitoanyag, 1972. **24**(6): p. 237-240.

609. Du, W.-F., et al., *Study of Phase Separation in Na_2O-B_2O_3 Glass System by Nuclear Magnetic Resonance.* J. Solid State Chem., 2000. **149**(2): p. 459-464.

610. Julsrud, S. and O.J. Kleppa, *Thermodynamics of the Ternary System Na_2O-P_2O_5-B_2O_3.* Zeitschrift fuer Naturforschung, A: Physical Sciences, 1987. **42**(5): p. 463-470.

611. Barin, I., O. Knacke, and Kubaschewski. Thermodynamic Properties of Inorganic Sunstances, Springer-Verlag, Berlin. Vol. 279 (10). 1977, Berlin: Springer-Verlag. 861pp.

612. Shul'ts, M.M., et al., *Calorimetric study of alkali borate glasses.* Fiz. Khim. Stekla, 1985. **11**(4): p. 472-479.

613. Shul'ts, M.M., et al., *Calorimetric study of vitreous and crystalline sodium borates.* Fiz. Khim. Stekla, 1979. **5**(1): p. 36-41.

614. Shul'ts, M.M., et al., *Thermodynamic characteristics of silicates and borates of alkali metals.* Szilikatip. Szilikattud. Konf., [Eloadasok], 13th, 1981. **1**: p. 189-193.

615. Vedishcheva, N.M. and B.A. Shakhmatkin, *Dissociation of alkali metal borates and acid-base interactions in oxide systems.* J. Therm. Anal., 1987. **32**(6): p. 1693-1696.

616. Vedishcheva, N.M., B.A. Shakhmatkin, and M.M. Shults, *Calorimetric study of vitreous and crystalline alkali metal borates.* J. Therm. Anal., 1988. **33**(3): p. 923-7.

617. Shartsis, L. and W. Capps, *Energy Relations in Binary Alkali Borates.* J. Am. Ceram. Soc., 1954. **37**(1): p. 27-32.

618. Shul'ts, M.M., et al., *Enthalpy of the Formation of Glassy and Crystalline Borates of Lithium, Sodium, and Potassium.* Stekloobraznoe Sostoyanie (1981) 7th, 1983: p. 75-82.

619. Yoshio, T. and K. Takahashi, *Energy Relations and Boron Coordination Number in Alkali Borates.* J. Ceram. Soc. Jpn., 1976. **84**(2): p. 62-70.

620. Smith, G.S. and G.E. Rindone, *High-Temperature Energy Relations in the Alkali Borates: Binary Alkali Borate Compounds and Their Glasses.* J. Am. Ceram. Soc., 1961. **44**(2): p. 72-78.

621. Grenier, G. and D. White, *The heat of solution of sodium metaborate at 0°C.* J. Phys. Chem., 1957. **61**: p. 1681-1682.

622. Adami, L.H. and J.C. J., *Heats of formation of four anhydrous sodium borates.* U. S. Bur. Mines, Rep. Invest., 1968(No. 7167): p. 9 pp.

623. Stewart, D.R., G.E. Rindone, and F. Dachille, *Heats of solution, density, and refractive index changes in sodium borate glasses subjected to high pressure.* J. Am. Ceram. Soc., 1967. **50**(9): p. 467-472.

624. Slough, W. and G.P. Jones, *Compilation of Thermodynamic Data for Borate Systems*. 1974. p. 21 pp.

625. Evans, A.G., *Preliminary Report on the Thermodynamic Properties of Selected Light-element and Some Related Compounds*. 1961.

626. Park, J.H. and D.J. Min, *Thermodynamic Behavior of Na_2O-B_2O_3 Melt.* Metall. Mater. Trans. B, 2001. **32B**(2): p. 297-303.

627. Park, J.H. and D.J. Min, *Thermodynamics of Na_2O-B_2O_3 slag.* Taehan Kumsok, Chaeryo Hakhoechi, 2000. **38**(3): p. 510-516.

628. Asai, K., T. Yokokawa, and T. Maekawa, *Thermodynamic Activity of Na_2O in Na_2O-B_2O_3-Al_2O_3 Melts.* The Chem. Soc. Jpn., 1982. **6**: p. 1005-1009.

629. Shakhmatkin, B.A. and M.M. Shul'ts, *Thermodynamic Functions of Vitreous Melts of the Sodium Oxide (Na_2O)-Boron Oxide (B_2O_3) System over a 700-1000°C Temperature Range.* Fiz. Khim. Stekla, 1978. **4**(3): p. 271-277.

630. Shakhmatkin, B.A. and M.M. Shul'ts, *Thermodynamic Properties and Structure of Alkali Borate Melts.* Fiz. Khim. Stekla, 1982. **8**(3): p. 270-276.

631. Shul'ts, M.M., V.L. Stolyarova, and G.A. Semenov, *Study of Thermodynamic Properties of $2NaBO_2$-B_2O_3 Melts by Mass Spectroscopy Method.* Fiz. Khim. Stekla, 1979. **5**(1): p. 42-51.

632. Greenblatt, S. and P.J. Bray, *A discussion of the fraction of four-coordinated boron atoms present in borate glasses.* Phys. Chem. Glasses, 1967. **8**(6): p. 213-217.

633. Zhong, J. and P.J. Bray, *Change in Boron Coordination in Alkali Borate Glasses, and Mixed Alkali Effects, as Elucidated by NMR.* J. Non-Cryst. Solids, 1989. **111**(1): p. 67-76.

634. Bray, P.J. and J.G. O'Keefe, *Nuclear Magnetic Resonance Investigations of the Structure of Alkali Borate Glasses.* Phys. Chem. Glasses, 1963. **4**(2): p. 37-46.

635. Tang, Y., Z. Jiang, and X. Song, *NMR, IR, and Raman spectra study of the structure of borate and borosilicate glasses.* J. Non-Cryst. Solids, 1989. **112**(1-3): p. 131-135.

636. Yano, T., et al., *Structural Investigation of Sodium Borate Glasses and Melts by Raman Spectroscopy. II. Conversion between BO_4 and BO_2O- Units at High Temperature.* J. Non-Cryst. Solids, 2003. **321**(3): p. 147-156.

637. Ring, P.J. 1964, Brown University: Providence, Rhode Island, USA.

638. Kobiashvili, Z. 1964, Brown University: Providence, Rhode Island, USA.

639. Silver, A.H. and P.J. Bray, *Nuclear magnetic resonance absorption in glass. I. Nuclear quadrupole effects in boron oxide, soda-boric oxide, and borosilicate glasses.* J. Chem. Phys., 1958. **29**: p. 984-990.

640. Westrum, E.F., Jr., *The low-temperature thermal and chemical thermodynamic properties of boron compounds.* Thermodyn. Transp. Prop. Gases, Liq., Solids, Pap. Symp. Therm. Prop., 1959: p. 275-281.

641. Grenier, G. and E.F.J. Westrum, *The Heat Capacity and Thermodynamic Functions of Sodium Metaborate from 5 to 350°K.* J. Am. Chem. Soc., 1956. **78**: p. 6226-6227.

642. Westrum, E.F.J. and G. Grenier, *Heat Capacities and Thermodynamic Properties of Crystalline and Vitreous Anhydrous Sodium Tetraborate from 6 to 350°K.* J. Am. Chem. Soc., 1957. **79**: p. 1799-1802.

643. Pankratz, L.B. and M.J. Ferrante, *Thermodynamic properties of four crystalline sodium borates*. 1971, Bur. Mines, Washington, DC, USA.: U. S. Nat. Tech. Inform. Serv., PB Rep. p. 1-8.

644. Van Klooster, H.S., *Mineralogisch-chemische Mitteilungen aus dem Institut für physikalische Chemie der Universität Gottingen. 5. Über die binaren systeme: Li_2O-SiO_2, Li_2SiO_3-$ZnSiO_3$, $ZnSiO_3$-$CdSiO_3$, Li_2SiO_3-$LiBO_2$, Na_2SiO_3-$NaBO_2$ und Na_2SiO_3-Na_2WO_4.* Z. Anorg. Chem, 1911. **69**: p. 135-157.

645. Morey, G.W., *The Ternary System Na_2O-B_2O_3-SiO_2.* J. Soc. Glass Technol., 1951. **35**(167): p. 270-283.

646. Ghanbari-Ahari, K. and A.M. Cameron, *Phase Diagram of Na_2O-B_2O_3-SiO_2 System.* J. Am. Ceram. Soc., 1993. **76**(8): p. 2017-2022.

647. Rockett, T.J. and W.R. Foster, *The High-Silica Liquidus Surface of the System Na_2O-B_2O_3-SiO_2.* Commun. Am. Ceram. Soc., 1981. **64**(11): p. C148-C149.

648. Rockett, T.J. and W.R. Foster, *Phase Relations in the System Boron Oxide-Silica.* J. Am. Ceram. Soc., 1965. **48**(2): p. 75-80.

649. Rockett, T.J. and W.R. Foster, *The System Silica-Sodium Tetraborate.* J. Am. Ceram. Soc., 1966. **49**(1): p. 30-33.

650. Appleman, D.E. and J.R. Clark, *Crystal structure of reedmergnerite, a boron albite, and its relation to feldspar crystal chemistry.* Am. Mineral., 1965. **50**(11-12): p. 1827-1850.

651. Scholes, S. and F.C.F. Wilkinson, *Glassy phase separation in sodium borosilicate glasses.* Discuss. Faraday Soc., 1970. **No. 50**: p. 175-181.

652. Polyakova, I.G., *Specific Features of Metastable Immiscibility in the Na_2O-B_2O_3-SiO_2 System According to Different Thermal Analysis Data.* Glass Phys. Chem., 1994. **20**(5): p. 386-391.

653. Polyakova, I.G. *The Regularities of Metastable Liquid Phase Separation of Sodium, Potassium and Rubidium Borosilicate Glasses: Lower Temperature Boundaries and Three-Phase Immiscibility*. in *Proc. 17th Int. Congress on Glass*. 1995. Beijing.

654. Polyakova, I.G., *The Regularities of Metastable Immiscibility in the Na_2O-B_2O_3-SiO_2 System: Lower- and Upper-Temperature Boundaries.* Glass Phys. Chem., 1997. **23**(1): p. 45-57.

655. Wakabayashi, H., et al., *Characterization of phase separation by measuring electrical conductivity of borosilicate glasses.* Yogyo Kyokaishi, 1987. **95**(3): p. 316-322.

656. Alekseeva, Z.D., et al., *More Precise Cupola Liquation in the Na_2O-B_2O_3-SiO_2 System.* Fiz. Khim. Stekla, 1977. **3**(2): p. 114-122.

657. Yun, Y.H. and P.J. Bray, *Nuclear Magnetic Resonance Studies of the Glassesin the System Na_2O-B_2O_3-SiO_2.* J. Non-Cryst. Solids, 1978. **27**(3): p. 363-380.

658. Galakhov, F.Y. and O.S. Alekseeva, *Metastable liquation in the sodium oxide-boron oxide-silicon dioxide system.* Dokl. Akad. Nauk SSSR, 1969. **184**(5): p. 1102-1104.

659. Pafomova, L.A., *Thermochemical investigation of sodium borosilicate glasses.* Structure of Glass, Proc. All-Union Conf. Glassy State, 3rd, Leningrad, 1960: p. 459-461.

660. Molchanova, O.S. and L.A. Pafomova, *Thermochemical investigation of the reaction of sodium borosilicate glass with hydrochloric acid.* Trudy Optichesk. Inst. im. Vavilova, 1953. **23**(141): p. 13-18.

661. Julsrud, S. and O.J. Kleppa, *A Thermochemical Study of the Liquid System Sodium Borate + Silica at 1394K.* Geochim. Cosmoshim. Acta, 1986. **50**(6): p. 1201-1204.

662. Navrotsky, A., *Thermochemistry of Borosilicate Melts and Glasses-From Pyrex to Pegmatites*, in *Boron. Mineralogy, Petrology and Geochemistry*, E.S. Grew, Anovitz, L. M., and P.H. Series Editor: Ribbe, Editors. 1996, Mineralogical Society of America, Washington, D. C. p. 165-180.

663. Hervig, R.L. and A. Navrotsky, *Thermochemistry of Sodium Borosilicate Glasses.* J. Am. Ceram. Soc., 1985. **68**(6): p. 314-319.

664. Navrotsky, A., et al., *Thermochyemical Studies of Silicate, Aluminosilicate, and Borosilicate Glasses.* High Temp. Sci., 1985. **19**(2): p. 133-150.

665. Asai, K. and T. Yokokawa, *Thermodynamic Activity of Na_2O in Na_2O-B_2O_3-SiO_2 Melt.* Trans. Jpn. Inst. Met., 1982. **23**(9): p. 571-577.

666. Toledano, P., *K and Rb borates.* Rev. Chim. Minerale, 1964. **1**(3): p. 353-413.

667. Polyakova, I.G. and E.V. Tokareva, *A study of phase equilibria in the potassium borate system: glass crystallization and solid state reaction.* Glass Phys. Chem. (Transl. of Fiz. Khim. Stekla), 1997. **23**(5): p. 354-367.

668. Rollet, A.P., *Potassium borates. System B_2O_3-K_2O.* Compt. rend., 1935. **200**: p. 1763-1765.

669. Rza-Zade, P.F. and E.D. Mamedova, *Reaction in the potassium oxide-boric oxide system.* Issled. Obl. Neorg. Fiz. Khim., 1971: p. 118-126.

670. Lehman, R.L., N.G. Glumac, and J.S. Gentry, *Thermal stability of potassium carbonate near its melting point.* Thermochim. Acta, 1998. **316**(1): p. 1-9.

671. Meshalkin, A.B., *Recalculation of the phase diagram of the potassium oxide-boron oxide system in the region of $K_2O \cdot 2B_2O_3$-$K_2O \cdot 5B_2O_3$ compositions.* Rasplavy, 2002(5): p. 77-82.

672. Kaplun, A.B. and A.B. Meshalkin, *Phase equilibria in K_2O-B_2O_3 system.* Zh. Neorg. Khim., 2002. **47**(7): p. 1167-1172.

673. Mamedova, Z.D., F.R. Samedov, and P.F. Rza-Zade, *Synthesis and study of $B_2O_3 \cdot K_2O$ and $2B_2O_3 \cdot K_2O$.* Azerb. Khim. Zh., 1969(3): p. 82-85.

674. Zachariasen, W.H., *The crystal structure of potassium metaborate, $K_3(B_3O_6)$.* J. Chem. Phys., 1937. **5**: p. 919-922.

675. Krogh-Moe, J., *Unit-cell data for some anhydrous K borates.* Acta Crystallogr., 1961. **14**: p. 68.

676. Krogh-Moe, J., *Crystal structure of pentapotassium enneakaidekaborate, $5K_2O \cdot 19B_2O_3$.* Acta Crystallogr., Sect. B, 1974. **30, Pt. 7**: p. 1827-1832.

677. Tokareva, E.V. and I.G. Polyakova. *Glass formation and phase equilibria in potassium borosilicate system*. in *Proc. 17th Int. Congress on Glass*. 1995. Beijing.

678. Vedishcheva, N.M., *Enthalpies of formation of alkali borate glasses and crystals*. 1988, Inst. Obshchei i neorg. khimii im. I. S. Kurnakova AN SSSR: Leningrad.

679. Ahoussou, A.P., J. Rogez, and A. Kone, *Calorimetric study of the dissolution of vitreous electrolytes of the system $0.67[xB_2O_3$-$(1-x)P_2O_5]$-$0.33K_2O$.* J. Soc. Ouest-Afr. Chim., 2006. **11**(22): p. 53-58.

680. Ahoussou, A.P., J. Rogez, and A. Kone, *Solution calorimetric study of mixing enthalpy in $0.8[xB_2O_3$-$(1-x)SiO_2]$-$0.2K_2O$ glasses at 298 K.* Mater. Res. Bull., 2007. **42**(8): p. 1577-1581.

681. Ahoussou, A.P., J. Rogez, and A. Kone, *Thermodynamical miscibility in $0.8[xB_2O_3$-$(1-x)P_2O_5]$-$0.2K_2O$ glasses.* J. Non-Cryst. Solids, 2007. **353**(3): p. 271-275.

682. Hattori, M. and A. Taniguchi, *Heats of solution of mixed alkali borate glasses.* Kogyo Kyokai Shi, 1977. **85**(4): p. 33-37.

683. Smith, G.S., *High Temperature Energy Relationships in the Alkali Borates*. 1959, Pennsylvania State University.

684. Paukov, I.E., L.M. Khriplovich, and A.P. Popov, *True specific heat at low temperatures, absolute entropy and enthalpy under standard conditions for KBO_2.* Zh. Fiz. Khim., 1970. **44**(2): p. 547.

685. Polyakova, I.G. and E.V. Tokareva. *Alkali Borosilicate Systems: Phase Diagrams and the Structure of Glass*. in *Proc. 2nd Int. Conf. Borate Glasses, Crystals and Melts, Abingdon (1996)*. 1996. Society of Glass and Technology, Sheffield.

686. Krzhizhanovskaya, M.G., et al., *A new borosilicate feldspar, $KBSi_3O_8$: synthesis, crystal structure and thermal behavior.* Z. Kristallogr. - Cryst. Mater., 2012. **227**(7): p. 446-451.

687. Kimata, M., *Crystal structure of $KBSi_3O_8$ isostructural with danburite.* Mineral. Mag., 1993. **57**(386): p. 157-164.

688. Taylor, P. and D.G. Owen, *Liquid Immiscibility in the System K_2O-B_2O_3-SiO_2.* Commun. Am. Ceram. Soc., 1981. **64**(11): p. C158-C-159.

689. Bergman, A.G. and O.R. Vartbaronov, *Irreversible reciprocal systems of chromates and metaborates of sodium and potassium.* Zh. Neorg. Khim., 1957. **2**: p. 2641-2648.

690. van Klooster, H.S., *Behavior of Metaboric and Metaphosphoric Acids in Fusions of.* Z. Anorg. Chem., 1911. **69**: p. 122-134.

691. Qiao, Z., G.H. Rao, and J.K. Liang, *Study of phase diagrams of some barium metaborate (BaB_2O_4) based systems.* Proc. - Electrochem. Soc., 1990. **90-17**(Proc. Int. Symp. Molten Salts, 7th, 1990): p. 179-184.

692. Bergman, A.G. and O.R. Bartbaronov, *Fusion Diagram for the System of the Chromates and Tetraborates of Sodium and Potassium.* Zh. Neorg. Khim., 1957. **2**(3): p. 648-654.

693. Georgievskaya, M., et al., *Thermal "order-disorder" behavior in $(Na_{1-x}K_x)_4B_8O_{14}$ solid solutions investigated by X-ray powder diffraction.* Cryst. Res. Technol., 2008. **43**(11): p. 1150-1160.

694. Bergman, A.G. and I.N. Nikonova, *Double decomposition in the absence of a solvent. LXI. Irreversibly reciprocal system: fluorides and tetraborates.* Zh. Obshch. Khim., 1942. **12**: p. 449-459.

695. Bubnova, R.S., et al., *Solid solutions $Na_{1-x}K_xB_3O_5$ ($0.5 < x \leq 1.0$).* Glass Phys. Chem., 2004. **30**(6): p. 551-557.

696. Kouyate, A., et al., *Influence of alkali mixed effect on the mixing enthalpy in $0.75B_2O_3$-$0.25[xNa_2O$-$(1-x)K_2O]$ glass system.* Chin. Chem. Lett., 2008. **19**(10): p. 1252-1255.

APPENDIX A OPTIMIZED PARAMETERS

Table A.1 Model parameters of Mullite solid solution in the Al_2O_3-SiO_2 system.

Parameter	**Value, J·mol^{-1}**
Compound Energy Formalism $(Al^{3+})(Al^{3+})[Al^{3+},Si^{4+}]^T[O^{2-},Va][O^{2-}]_4$	
$G(Al_2O_3(\text{corundum}))$, [123]	$-1703961.422+1099.9582T-155.019T\ln T+1930681.508T^{-1}$ $-3313.548T^{0.5}-68180607.70T^{-2}$, (298-2327K)
	$-1869396.264+1393.00T-192.464T\ln T$, (2327-3000K)
$G(Al_2SiO_5(\text{sillimanite}))$, [123]	$-2690896.89+1179.726T-183.87T\ln T+6180000T^{-1}$ $-267066667T^{-2}-0.009075T^2+3205.2\ln T$, (298-3000K)
$g°(Al_1Al_1Al_1O_1O_4^{1-})$, this work	$1.5G(Al_2O_3(\text{corundum}))+149008.976-8.368T$
$g°(Al_1Al_1Al_1Va_1O_4^{1+})$, this work	$1.5G(Al_2O_3(\text{corundum}))$
$g°(Al_1Al_1Si_1O_1O_4)$, this work	$G(Al_2SiO_5(\text{sillimanite}))+6604.444-2.094T$
$g°(Al_1Al_1Si_1Va_1O_4^{2+})$, this work	$G(Al_2SiO_5(\text{sillimanite}))-292880$

Table A.2 Model parameters of Mullite solid solution in the Al_2O_3-B_2O_3-SiO_2 system.

Parameter	**Value, J·mol^{-1}**
Compound Energy Formalism $(Al^{3+})(Al^{3+})[B^{3+},Al^{3+},Si^{4+}][O^{2-},Va][O^{2-}]_4$	
$G(Al_4B_2O_9)$, [16]	$-4679069.60+3724.42T-506.4862T\ln T+3861363T^{-1}$ $-16334.998T^{0.5}-166209346.67T^{-2}$, (298-1500K)
$g°(Al_1Al_1B_1O_1O_4^{1-})$, this work	$0.5G(Al_4B_2O_9)+162765.1312-0.27893T$
$g°(Al_1Al_1B_1Va_1O_4^{1+})$, this work	$0.5G(Al_4B_2O_9)-155030.5888-7.25227T$
$g^{00}_{Al/Al/Al,B/O}$, this work	-62760
$g^{00}_{Al/Al/Al,B/Va}$, this work	-62760
$g^{01}_{Al/Al/Al,B/O}$, this work	$-18250.608-25.104T$
$g^{01}_{Al/Al/Al,B/Va}$, this work	$-18250.608-25.104T$

Table A.3 Optimized properties of the compound phases in the Na_2O-SiO_2 system.

Compound	**$\Delta_f H°_{298.15}$, J·mol^{-1}**	**$S°_{298.15}$, J·mol^{-1}·K^{-1}**	**$C_P(T)$, J·mol^{-1}·K^{-1}**
$Na_{10}SiO_7$	−3179455	605	$194.9881-0.059584T+104296T^{-2}-7.27683\cdot10^{6}T^{2}+12.4856T^{0.5}$, (298-3000K)
$Na_4SiO_4(s_1)$	−2110400	195.81	$250.099-0.0074626T-2510842T^{-2}+1.060528\cdot10^{-6}T^{2}-644.7246T^{-0.5}$, (298-3000K)
$Na_4SiO_4(s_2)$	−2109900	196.22	$250.099-0.074626T-2510842T^{-2}+1.060528\cdot10^{-6}T^{2}-644.7246T^{-0.5}$, (298-3000K)
Na_2SiO_3	−1558350	115.15	$22.429-0.090292T-849713.67T^{-2}+4.7741345\cdot10^{-6}T^{2}+7.2317T^{0.5}$, (298-3000K)
$Na_6Si_2O_7$	−3612766	355.20	$602.25-0.040927T-1507296T^{-2}+5.397\cdot10^{-6}T^{2}-4842.824T^{-0.5}$, (298-3000K)
$Na_2Si_2O_5(s_1)$	−2470670	164.55	$386.7794-0.0384275T-969579T^{-2}+5.306755\cdot10^{-6}T^{2}-3577.436T^{-0.5}$, (298-3000K)
$Na_2Si_2O_5(s_2)$	−2470252	164.99	$386.7794-0.0384275T-969579T^{-2}+5.306755\cdot10^{-6}T^{2}-3577.436T^{-0.5}$, (298-3000K)
$Na_2Si_2O_5(s_3)$	−2469624	165.63	$386.7794-0.0384275T-969579T^{-2}+5.306755\cdot10^{-6}T^{2}-3577.436T^{-0.5}$, (298-3000K)
$Na_6Si_8O_{19}$	−9208406	602.71	$1216.046-0.08465T-10320398T^{-2}+1.194359\cdot10^{-5}T^{2}-8933.22T^{-0.5}$, (298-3000K)

Table A.4 Gibbs energy parameters of the liquid phase in the Na_2O-SiO_2 system.

Parameter	**Value, J·mol^{-1}**
Two-sublattice Quasichemical Formalism (Na, (Na_2), Si//O); Grouping: Na, (Na_2) in group 1; Si in group 2	
Coordination numbers: $Z^{Na}_{Na,Na//O,O}=0.68872188$, $Z^{Na_2}_{Na_2,Na_2//O,O}=1.37744375$, $Z^{Si}_{Si,Si//O,O}=2.7548875$, $Z^{O}_{Na,Na//O,O}=Z^{O}_{Na_2,Na_2//O,O}=Z^{O}_{Si,Si//O,O}=1.37744375$	
$g°(SiO_2)$	$-915415.777509442+562.199392079148T-83.513598136T\ln T+1227679.99104T^{-1}-1498.771995136T^{0.5}+46678699.0706667T^{-2}$, (298-1996K) $-952208.474882017+564.54913498152T-85.772T\ln T$, (1996-3000K)

Parameter	**Value, J·mol^{-1}**
g°(Na_2O)	−380898.281846976+340.194807097718T−66.216Tln$T$−0.021932551012T^2 +2.34791673093333·10$^{-6}T^3$+406685.0092T^{-1}, (298-1405K) −403977.403928942+608.846123951017T−104.6Tln$T$, (1405-1500K)
g°((Na_2)O)	g°(Na_2O)+2652.475+100.7894T
$g^{01}_{Na_2,Si}$	−593703−75.4123T
$g^{05}_{Na_2,Si}$	260616.9−99.282T
$g^{06}_{Na_2,Si}$	−10288.7+40.04182T
$\Delta g^{\circ}_{Na,Si}$	−314670+47.2792T
$g^{10}_{Na,Si}$	−75312
$g^{01}_{Na,Si}$	−170731
$g^{02}_{Na,Si}$	10999.52
$g^{03}_{Na,Si}$	90621.08
$g^{04}_{Na,Si}$	822.9528−5.07835T
$g^{05}_{Na,Si}$	−19711.9+109.6264T
$g^{07}_{Na,Si}$	114644.8−733.093T
$g^{08}_{Na,Si}$	2973.824+640.1397T

Table A.5 Optimized properties of the compound phases in the Na_2O-Al_2O_3 system

Phase	**$\Delta_f H°_{298.15}$, J·mol^{-1}**	**$S°_{298.15}$, J·mol^{-1}·K^{-1}**	**$C_P(T)$, J·mol^{-1}·K^{-1}**
$NaAlO_2(s_1)$	−1133190	70.40	89.148+0.0152925T−1.79326·10$^6T^{-2}$, (298-3000K)
$NaAlO_2(s_2)$	−1131893	72.15	89.148+0.0152925T−1.79326·10$^6T^{-2}$, (298-3000K)

Table A.6 Gibbs energy parameters of the solution phases in the Na_2O-Al_2O_3 system.

Parameter	**Value, J·mol^{-1}**
Liquid	
Two-sublattice Quasichemical Formalism (Na, (Na_2), Al, NaAl//O); Grouping: all species in group 1 Coordination numbers: $Z^{Na}_{Na,Na//O,O}$ = 0.68872188, $Z^{Na_2}_{Na_2,Na_2//O,O}$ = 1.37744375, $Z^{Al}_{Al,Al//O,O}$ = 2.06616563, $Z^{NaAl}_{NaAl,NaAl//O,O}$ = 2.7548875, $Z^{O}_{Na,Na//O,O} = Z^{O}_{Na_2,Na_2//O,O} = Z^{O}_{Al,Al//O,O} = Z^{O}_{NaAl,NaAl//O,O}$ = 1.37744375, $Z^{Na}_{Na,Al//O,O} = Z^{Al}_{Na,Al//O,O} = Z^{O}_{Na,Al//O,O}$ = 0.68872188, $Z^{Na}_{Na,NaAl//O,O} = Z^{NaAl}_{Na,NaAl//O,O}$ = 0.68872188, $Z^{O}_{Na,NaAl//O,O}$ = 0.5509775, $Z^{Al}_{Al,NaAl//O,O} = Z^{NaAl}_{Al,NaAl//O,O}$ = 2.06616563, $Z^{Al}_{Al,NaAl//O,O}$ = 1.18066607	
g°(Na_2O)	$-380898.281846976+340.194807097718T-66.216T\ln T-0.021932551012T^2$ $+2.34791673093333\cdot10^{-6}T^3+406685.0092T^{-1}$, (298-1405K) $-403977.403928942+608.846123951017T-104.6T\ln T$, (1405-1500K)
g°((Na_2)O)	g°(Na_2O)+2652.475+100.7894T
g°(Al_2O_3)	$-1615242.56879437+1240.32718657421T-179.3654901T\ln T+0.04596124T^2$ $-68180607.6986667T^{-2}-487670.49228T^{-1}-3313.54792064T^{0.5}$, (298-2327K) $-1750989.01540026+1342.116077338T-192.464T\ln T$, (2327-3000K)
g°($NaAlO_2$)	0.5 g°(Na_2O)+0.5 g°(Al_2O_3)−107747.52+26.2888T
$\Delta g^{\circ}_{Na,Al}$	$-39772.03377464-33.798190916T$
$g^{01}_{Na,Al}$	−50394.206828
$\Delta q^{\circ}_{Na,NaAl}$	−104600
$\Delta g^{\circ}_{Al,NaAl}$	−39293.11769568
$g^{30}_{Al,NaAl}$	28905.38127512
Beta-alumina	
Compound Energy Formalism $[Na^+,Va]_1^{BR}[Na^+,Va]_1^{aBR}[Al^{3+}]_2^{T}[O^{2-},Va]_1^{mO}Al_9^{other}O_{17}$	
$G(Na_4Al_{22}O_{35})$	$\frac{M\left(Na_4Al_{22}O_{35}\right)}{M\left(Na_2Al_{12}O_{19}\right)}G_{Na_2Al_{12}O_{19}}+96056.8-11.286T$

Parameter	Value, J·mol^{-1}
$G(NaAl_{11}O_{17})$	$\frac{M(NaAl_{11}O_{14})}{M(NaAl_9O_{14})}G_{NaAl_9O_{14}} - 47238.8 + 19.136T$
$G(Na_2Al_{12}O_{19})$	$-10884796.6973+6569.5933183378T^{-2}-953.391386T\ln T-0.01529252T^2$ $-340903038.3333T^{-2}+11446669.95T^{-1}-16567.7396T^{0.5}$, (298-3000K)
$G(NaAl_9O_{14})$	$-8004986.561353+4929.68845158T-709.22402T\ln T-0.00764626T^2$ $-272722430.667T^{-2}+8619357.24T^{-1}-13254.19168T^{0.5}$, (298-3000K)
Δ^2	41840
I^1	41840
I^2	−41840
Beta''-alumina	
Compound Energy Formalism $\left[Na^+,Va\right]_1^{BR}\left[Na^+,Va\right]_1^{aBR}\left[Al^{3+}\right]_2^{T}\left[O^{2-},Va\right]_1^{mO}Al_9^{other}O_{17}$	
$G(Na_4Al_{22}O_{35})$	$\frac{M(Na_4Al_{22}O_{35})}{M(Na_2Al_{12}O_{19})}G_{Na_2Al_{12}O_{19}} + 38414.9 + 8.368T$
$G(NaAl_{11}O_{17})$	$\frac{M(NaAl_{11}O_{14})}{M(NaAl_9O_{14})}G_{NaAl_9O_{14}} - 34727.2 + 20.92T$
$G(Na_2Al_{12}O_{19})$	$-10884796.6973+6569.5933183378T^{-2}-953.391386T\ln T-0.01529252T^2$ $-340903038.3333T^{-2}+11446669.95T^{-1}-16567.7396T^{0.5}$, (298-3000K)
$G(NaAl_9O_{14})$	$-8004986.561353+4929.68845158T-709.22402T\ln T-0.00764626T^2$ $-272722430.667T^{-2}+8619357.24T^{-1}-13254.19168T^{0.5}$, (298-3000K)
Δ^2	41840
I^1	41840
I^2	−41840

Table A.7 Optimized properties of the compound phases in the Na_2O-Al_2O_3-SiO_2 system.

Phase	$\Delta_f H°_{298.15}$, kJ·mol^{-1}	$S°_{298.15}$, J·mol^{-1}·K^{-1}	$C_P(T)$, J·mol^{-1}·K^{-1}
$NaAlSiO_4(s_1)$, δ-nepheline	−2102000	123.63	$493.076615+0.0939639776T-151815.863T^{-2}$ $+4.46154009\cdot10^{-6}T^2-4324.97775T^{-0.5}$

Phase	$\Delta_f H°_{298.15}$, kJ·mol^{-1}	$S°_{298.15}$, J·mol^{-1}·K^{-1}	$C_P(T)$, J·mol^{-1}·K^{-1}
			$-8.79158691T^{0.5}$, (298-3000K)
$NaAlSiO_4(s_2)$, β-nepheline	−2101000	125.79	$493.076615+0.0939639776T-151815.863T^{-2}$ $+4.46154009\cdot10^{-6}T^2-4324.97775T^{-0.5}$ $-8.79158691T^{0.5}$, (298-3000K)
$NaAlSiO_4(s_3)$, γ-nepheline	−2097800	128.58	$493.076615+0.0939639776T-151815.863T^{-2}$ $+4.46154009\cdot10^{-6}T^2-4324.97775T^{-0.5}$ $-8.79158691T^{0.5}$, (298-3000K)
$NaAlSiO_4(s_4)$, α-carnegieite	−2093933.3	126.97	$325.528705-0.0334952882T+1120441.76T^{-2}$ $+4.34757644\cdot10^{-6}T^2-3625.95672T^{-0.5}$, (298-3000K)
$NaAlSiO_4(s_4)$, β-carnegieite	−2102533	118.06	$325.528705-0.0334952882T+1120441.76T^{-2}$ $+4.34757644\cdot10^{-6}T^2-3625.95672T^{-0.5}$, (298-3000K)
$NaAlSi_2O_6$, jadeite	−3030000	138.07	$311.293-5.350264\cdot10^6T^{-2}-2005.1T^{-0.5}$ $+6.625669\cdot10^8T^{-1}$, (298-3000K)
$NaAlSi_3O_8(s_1)$, low albite	−3944000	207.49	$456.414581-0.0356270961T-299552.189T^{-2}$ $+2.88349378\cdot10^{-6}T^2-4370.00625T^{-0.5}$ $+0.981804374T^{0.5}$, (298-3000K)
$NaAlSi_3O_8(s_2)$, high albite	−3932300	219.89	$456.414581-0.0356270961T-299552.189T^{-2}$ $+2.88349378\cdot10^{-6}T^2-4370.00625T^{-0.5}$ $+0.981804374T^{0.5}$, (298-3000K)

Table A.8 Gibbs energy parameters of the solution phases in the Na_2O-Al_2O_3-SiO_2 system.

Parameter	Value, J·mol^{-1}
Liquid phase	
Two-sublattice Quasichemical Formalism (Na, (Na_2), Al, NaAl, Si//O); Grouping: Na, (Na_2), Al, NaAl in group 1; Si in group 2	
Coordination numbers: $Z^{Na}_{Na,Na//O,O} = 0.68872188$, $Z^{Na_2}_{Na_2,Na_2//O,O} = 1.37744375$, $Z^{Si}_{Si,Si//O,O} = 2.7548875$, $Z^{O}_{Na,Na//O,O} = Z^{O}_{Na_2,Na_2//O,O} = Z^{O}_{Si,Si//O,O} = 1.37744375$	

Parameter	**Value, J·mol^{-1}**
Grouping exceptions	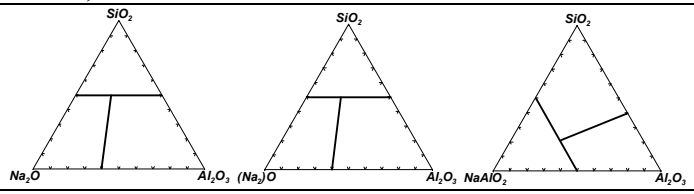
$\Delta q^{\circ}_{\mathrm{NaAl,Si}}$	$-56923.6970-1.5936T$
$q^{01}_{\mathrm{NaAl,Si}}$	−63782.7834
$q^{02}_{\mathrm{NaAl,Si}}$	27856.3270
$q^{001}_{\mathrm{Na,Si(NaAl)}}$	−45148.8762
$q^{011}_{\mathrm{Na,Si(NaAl)}}$	−35755.2530
$q^{021}_{\mathrm{Na,Si(NaAl)}}$	110174.2604
$q^{002}_{\mathrm{Na,Si(NaAl)}}$	10062.9237
$q^{012}_{\mathrm{Na,Si(NaAl)}}$	−2152.2007
$g^{001}_{\mathrm{Al,Si(NaAl)}}$	−33229.4551
$g^{021}_{\mathrm{Al,Si(NaAl)}}$	−97938.4804
$g^{001}_{\mathrm{NaAl,Si(Al)}}$	4923.4025
$q^{001}_{\mathrm{Na,Si(Al)}}$	21812.2453
$q^{101}_{\mathrm{Na,Si(Al)}}$	104841.147
Carnegieite solid solution	
Compound Energy Formalism $(NaAlSi,VaSi_2)_4O_{16}$	
$g^{\circ}(Na_4Al_4Si_4O_{16})$	$4\cdot G(\mathrm{Cg})$
$g^{\circ}(Va_4Si_8O_{16})$	$8\cdot G(\mathrm{Cri})+21365.111$
$G(\mathrm{Cg})$	$-2069159.1180132+2466.0868155T-325.528705T\ln T-560220.88T^{-1}$

Parameter	**Value, J·mol^{-1}**
	$-0.0167476444T^2-7.245960733\cdot10^{-7}T^3-14503.82688T^{0.5}$, (298-965.5K) $-6218990.09603468+11062.3187741194T-325.528705T\ln T-560220.88T^{-1}$ $-4.43495197196172T^2-7.245960733\cdot10^{-7}T^3-14503.82688T^{0.5}$, (965.5-966.5K) $-2060558.43435497+2457.1834163T-325.528705T\ln T-560220.88T^{-1}$ $-0.0167476444T^2-7.245960733\cdot10^{-7}T^3-14503.82688T^{0.5}$, (298-965.5K)
G(Cri)	$-924997.137509442+566.99969528T-83.513598136T\ln T+1227679.99T^{-1}$ $-46678699.0706667T^{-2}-1498.771995136T^{0.5}$, (298-1996K) $-961789.834882+569.34943818T-85.772T\ln T$, (1996-3000K)
${}^0L_{\mathrm{NaAlSi,VaSi_2}}$	−244663.9112
Nepheline solid solution	
Compound Energy Formalism $(\mathrm{NaAlSi, VaSi_2})_2(\mathrm{NaAlSi})_6\mathrm{O_{32}}$	
$g°(\mathrm{Na_2Na_6Al_8Si_8O_{32}})$	$8\cdot G$(Ne)
$g°(\mathrm{Va_2Na_6Al_6Si_{10}O_{32}})$	$6\cdot G(\mathrm{Ne})+4\cdot G(\mathrm{Tri})-36757.48-4.184T$
G(Ne)	$-2073105.93747905+3403.104836774T-493.076615T\ln T-0.0469819888T^2$ $+7.4359\cdot10^{-7}T^3-75907.9315T^{-1}+11.72211588T^{1.5}-17299.911T^{0.5}$, (298-462.5K) $-2304106.2535+4402.02512227T-493.076615T\ln T-1.1268958109612T^2$ $+7.43590015\cdot10^{-7}T^3-75907.9315T^{-1}+11.72211588T^{1.5}-17299.911T^{0.5}$, (462.5-463.5K) $-2072105.93727973+3400.945T-493.076615T\ln T-0.0469819888T^2$ $+7.43590015\cdot10^{-7}T^3-75907.9315T^{-1}+11.72211588T^{1.5}-17299.911T^{0.5}$, (463.5-1147.5K) $-3907306.21383229+6599.5511556T-493.076615T\ln T-1.4407101572T^2$ $+7.43590015\cdot10^{-7}T^3-75907.9315T^{-1}+11.722116T^{1.5}-17299.911T^{0.5}$, (1147.5-1148.5K) $-2068905.937405+3398.15755279283T-493.076615T\ln T-0.0469819888T^2$ $+7.43590015\cdot10^{-7}T^3-75907.9315T^{-1}+11.722116T^{1.5}-17299.911T^{0.5}$, (1147.5-3000K)
G(Tri)	$-944111.18439234+480.752826017315T-75.372668T\ln T$ $+2979047.5388T^{-1}-159707687.146667T^{-2}$, (298-1991K) $-961947.905277253+569.440180798T-85.772T\ln T$, (1991-3000K)

Parameter	**Value, J·mol^{-1}**
${}^{0}L_{\mathrm{NaAlSi,VaSi_2//NaAlSi}}$	−42653.5637
high-(Na,K)AlO_2	
One Sublattice ($NaAlO_2$, $VaSiO_2$)	
g°($NaAlO_2$)	G(high-$NaAlO_2$)
g°(SiO_2)	G(Cri)+8989.4650
G(high-$NaAlO_2$)	$-1165166.95547922+539.573969T-89.148488T\ln T-0.00764626T^{2}+896631.2T^{-1}$, (298-3000K)
G(Cri)	$-924997.137509442+566.999695279148T-83.513598136T\ln T$ $+1227679.99104T^{-1}-46678699.0706667T^{-2}-1498.771995136T^{0.5}$, (298-1996K) $-961789.834882017+569.34943818152T-85.772T\ln T$, (1996-3000K)
$q^{11}_{\mathrm{NaAlO_2,SiO_2}}$	$-80386.2033208-17.69397541808T$
$q^{21}_{\mathrm{NaAlO_2,SiO_2}}$	$-18.5172539016-17.69397541808T$
low-(Na,K)AlO_2	
One Sublattice ($NaAlO_2$, $VaSiO_2$)	
g°($NaAlO_2$)	G(low-$NaAlO_2$)
g°(SiO_2)	G(Tri)+8989.4650
G(low-$NaAlO_2$)	$-1166463.95547922+541.326671817318T-89.148488T\ln T$ $-0.00764626T^{2}+896631.2T^{-1}$, (298-3000K)
G(Tri)	$-944111.18439234+480.752826017315T-75.372668T\ln T$ $+2979047.5388T^{-1}-159707687.146667T^{-2}$, (298-1991K) $-961947.905277253+569.440180798T-85.772T\ln T$, (1991-3000K)
$q^{11}_{\mathrm{NaAlO_2,SiO_2}}$	$-80386.2033208-17.69397541808T$
$q^{21}_{\mathrm{NaAlO_2,SiO_2}}$	$-18.5172539016-17.69397541808T$

Table A.9 Optimized properties of the compound phases in the K_2O-SiO_2 system.

Phase	$\Delta_f H°_{298.15}$, **J·mol^{-1}**	$S°_{298.15}$,**J·mol^{-1}·K^{-1}**	$C_P(T)$, **J·mol^{-1}·K^{-1}**
K_4SiO_4	−2045900	245.47	$377.5780+0.080718T-252662T^{-2}-8.57340\cdot10^{-6}T^2$ $-3.69T^{0.5}-2436.45T^{-0.5}$, (298-3000K)
$K_{10}Si_3O_{11}$	−5659600	637.09	$-499.5366-0.498845T-7645648T^{-2}+2.13317T^2$ $+44.37T^{0.5}+8154.30T^{-0.5}$, (298-3000K)
$K_8Si_3O_{10}$	−5159000	537.77	$-1874.5412-0.957608T-17615664T^{-2}+4.52528T^2$ $+22855.79T^{-0.5}+84.43T^{0.5}$, (298-3000K)
K_2SiO_3	−1543600	146.15	$-504.5974-0.261292T-2838333T^{-2}+1.102578\cdot10^{-5}T^2$ $+23.74T^{0.5}+5570.60T^{-0.5}$, (298-3000K)
$K_2Si_2O_5(s_1)$	−2503700	190.58	$342.7178-0.030010T-1278812T^{-2}+4.163570\cdot10^{-6}T^2$ $-2760.94T^{-0.5}$, (298-3000K)
$K_2Si_2O_5(s_2)$	−2502487	192.96	$342.7178-0.030010T-1278812T^{-2}+4.163570\cdot10^{-6}T^2$ $-2760.94T^{-0.5}$, (298-3000K)
$K_2Si_2O_5(s_3)$	−2500897	194.79	$342.7178-0.030010T-1278812T^{-2}+4.163570\cdot10^{-6}T^2$ $-2760.94T^{-0.5}$, (298-3000K)
$K_2Si_4O_9(s_1)$	−4344929	265.68	$-6.9723-0.177124T-740777T^{-2}+2.016965\cdot10^{-6}T^2$ $+18.54T^{0.5}$, (298-3000K)
$K_2Si_4O_9(s_2)$	−4341717	269.39	$-6.9723-0.177124T-740777T^{-2}+2.016965\cdot10^{-6}T^2$ $+18.54T^{0.5}$, (298-3000K)

Table A.10 Gibbs energy parameters of the liquid phase in the K_2O-SiO_2 system.

Parameter	**Value, J·mol^{-1}**
Two-sublattice Quasichemical Formalism (K, (K_2), Si//O); Grouping: K, K_2 in group 1; Si in group 2	
Coordination numbers: $Z^{K}_{K,K//O,O}=0.68872188$, $Z^{K_2}_{K_2,K_2//O,O}=1.37744375$, $Z^{Si}_{Si,Si//O,O}=2.7548875$, $Z^{O}_{K,K//O,O}=Z^{O}_{K_2,K_2//O,O}=Z^{O}_{Si,Si//O,O}=1.37744375$	
$g°(K_2O)$	$-359688.062175177+388.245328T-75.947T\ln T$ $-0.008573T^2+295819.9922T^{-1}$, (298-1013K) $-381763.3563394+616.5487617T-107.0T\ln T$, (1013-1300K)

Parameter	Value, J·mol^{-1}
g°((K$_2$)O)	g°(K$_2$O)+119182.7+38.7395T
$g^{01}_{K_2,Si}$	−863253−7.59125T
$g^{06}_{K_2,Si}$	179976.9+1.97249T
$\Delta g^{\circ}_{K,Si}$	−336569+39.3296T
$g^{01}_{K,Si}$	−224359
$g^{02}_{K,Si}$	−38545.9
$g^{03}_{K,Si}$	5565.217
$g^{05}_{K,Si}$	−45919.4+33.88653T
$g^{07}_{K,Si}$	189554.1−45.5179T

Table A.11 Optimized properties of the compound phases in the K_2O-Al_2O_3 system.

Phase	$\Delta_f H°_{298.15}$, J·mol^{-1}	$S°_{298.15}$, J·mol^{-1}·K^{-1}	$C_P(T)$, J·mol^{-1}·K^{-1}
$KAlO_2(s_1)$	−1140546	85.55	2.17269−0.084748T−370521T^{-2}+5.446536·10$^{-6}T^2$ +5.97$T^{0.5}$, (298-3000K)
$KAlO_2(s_2)$	−1139251	87.15	2.17269−0.084748T−370521T^{-2}+5.446536·10$^{-6}T^2$ +5.97$T^{0.5}$, (298-3000K)

Table A.12 Gibbs energy parameters of the liquid phase in the K_2O-Al_2O_3 system.

Parameter	Value, J·mol^{-1}
Two-sublattice Quasichemical Formalism (K, (K$_2$), Al, KAl//O); Grouping: all species in group 1	
Coordination numbers: $Z^{K}_{K,K//O,O}$ = 0.68872188, $Z^{K_2}_{K_2,K_2//O,O}$ = 1.37744375, $Z^{Al}_{Al,Al//O,O}$ = 2.06616563, $Z^{KAl}_{KAl,KAl//O,O}$ = 2.7548875, $Z^{O}_{K,K//O,O} = Z^{O}_{K_2,K_2//O,O} = Z^{O}_{Al,Al//O,O} = Z^{O}_{KAl,KAl//O,O}$ = 1.37744375, $Z^{K}_{K,Al//O,O} = Z^{Al}_{K,Al//O,O} = Z^{O}_{K,Al//O,O}$ = 0.68872188, $Z^{K}_{K,KAl//O,O} = Z^{KAl}_{K,KAl//O,O}$ = 0.68872188, $Z^{O}_{K,KAl//O,O}$ = 0.5509775, $Z^{Al}_{Al,KAl//O,O} = Z^{KAl}_{Al,KAl//O,O}$ = 2.06616563, $Z^{Al}_{Al,KAl//O,O}$ = 1.18066607	
g°(K$_2$O)	−359688.062175177+388.2453279T−75.947Tln$T$−0.008573T^2

Parameter	Value, J·mol^{-1}
	$+295819.9922T^{-1}$, (298-1013K) $-381763.356339371+616.548761708T-107.0T\ln T$, (1013-1300K)
$g°(Al_2O_3)$	$-1615242.56879437+1240.32718657421T-179.3654901T\ln T+0.04596124T^2$ $-68180607.6986667T^{-2}-487670.49228T^{-1}-3313.54792064T^{0.5}$, (298-2327K) $-1750989.01540026+1342.116077338T-192.464T\ln T$, (2327-3000K)
$g°(KAlO_2)$	$0.5g°(K_2O)+0.5g°(Al_2O_3)-79715+1.79T$
$\Delta g^{\circ}_{K,Al}$	−275078.1862
$\Delta g^{\circ}_{K,KAl}$	−41840
$g^{01}_{KAl,Al}$	18645.0012
$g^{02}_{KAl,Al}$	−8725.3719

Table A.13 Optimized properties of the compound phases in the K_2O-Al_2O_3-SiO_2 system.

Phase	$\Delta_f H°_{298.15}$, J·mol^{-1}	$S°_{298.15}$, J·mol^{-1}·K^{-1}	$C_P(T)$, J·mol^{-1}·K^{-1}
$KAlSiO_4(s_1)$	−2123355	134.51	$184.290+9.8516\cdot10^{-3}T-1.31064\cdot10^{7}T^{-2}$ $-4.654035\cdot10^{-6}T^2+5.407401\cdot10^{-10}T^3+2.13893\cdot10^{9}T^{-3}$, (298-2100K)
$KAlSiO_4(s_2)$	−2122250	136.38	$178.030+2.68068\cdot10^{-2}T-1.31065\cdot10^{7}T^{-2}$ $-1.908168\cdot10^{-5}T^2+4.5061\cdot10^{-9}T^3+2.13893\cdot10^{9}T^{-3}$, (298-2100K)
$KAlSi_2O_6(s_1)$	−3061676	176.86	$92.9696194-0.144880712T-3655459.17T^{-2}$ $+1.11313225\cdot10^{-5}T^2+9.10974052T^{0.5}$, (298-3000K)
$KAlSi_2O_6(s_2)$	−3048456	192.73	$92.9696194-0.144880712T-3655459.17T^{-2}$ $+1.11313225\cdot10^{-5}T^2+9.10974052T^{0.5}$, (298-3000K)
$KAlSi_3O_8(s_1)$, microcline	−3969909	229.17	$101.953645-0.154738804T-4288457.84T^{-2}$ $+9.53756487\cdot10^{-6}T^2+11.4261484T^{0.5}$, (298-3000K)
$KAlSi_3O_8(s_2)$, sanidine	−3962001	239.40	$101.953645-0.154738804T-4288457.84T^{-2}$ $+9.53756487\cdot10^{-6}T^2+11.4261484T^{0.5}$, (298-3000K)

Table A.14 Gibbs energy parameters of the solution phases in the K_2O-Al_2O_3-SiO_2 system.

Parameter	**Value, J·mol^{-1}**
Liquid	
Two-sublattice Quasichemical Formalism (K, (K_2), Al, KAl, Si//O); Grouping: K, (K_2), Al, KAl in group 1; Si in group 2	
Grouping exceptions	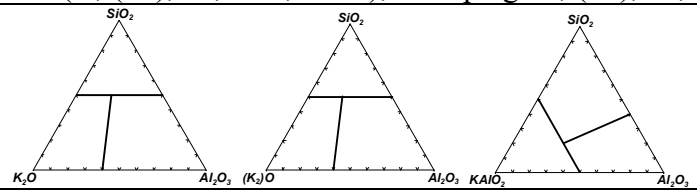
$\Delta g^{\circ}_{\mathrm{KAl,Si}}$	$-109103.5793592+6.73679362688T$
$g^{01}_{\mathrm{KAl,Si}}$	-54958.1198856
$g^{03}_{\mathrm{KAl,Si}}$	9852.53499792
$g^{001}_{\mathrm{K,Si(KAl)}}$	-77995.4728336
$g^{002}_{\mathrm{K,Si(KAl)}}$	1625.84650176
$g^{011}_{\mathrm{K,Si(KAl)}}$	72200.6591928
$g^{041}_{\mathrm{K,Si(KAl)}}$	41840
$g^{001}_{\mathrm{Al,Si(KAl)}}$	63746.0064608
$g^{011}_{\mathrm{Al,Si(KAl)}}$	-150169.4489848
$g^{011}_{\mathrm{KAl,Si(Al)}}$	20692.76708552
$g^{041}_{\mathrm{KAl,Si(Al)}}$	-65296.0776264
high-(Na,K)AlO_2	
Compound Energy Formalism (KAl, VaSi)O_2	
g°($KAlO_2$)	G(high-$KAlO_2$)
g°(SiO_2)	G(Cri)+8989.46504264
G(high-$KAlO_2$)	$-1165833.76022551+397.46483824688T-68.611499728T\ln T-0.0348505T^2$

Parameter	Value, J·mol^{-1}
	$+4.379283319\cdot10^{-6}T^{3}+486065.991T^{-1}$, (298-810K) $-1169279.832083+538.3971205T-91.97T\ln T-0.006T^{2}$, (810-2600K)
G(Cri)	$-924997.137509442+566.99969528T-83.513598136T\ln T+1227679.99T^{-1}$ $-46678699.0706667T^{-2}-1498.771995136T^{0.5}$, (298-1996K) $-961789.834882+569.34943818T-85.772T\ln T$, (1996-3000K)
$q^{11}_{KAlO_2,SiO_2}$	$-99411.84-2.5104T$
low-(Na,K)AlO_2	
One Sublattice ($KAlO_2$, $VaSiO_2$)	
g°($KAlO_2$)	$G_{low\text{-}KAlO_2}$
g°(SiO_2)	G(Tri)+8989.4650
G(low-$KAlO_2$)	$-1167128.76022551+399.0636037T-68.6115T\ln T-0.0348505T^{2}$ $+4.379283319\cdot10^{-6}T^{3}+486065.99104T^{-1}$, (298-810K) $-1170574.832083+539.9958859T-91.97T\ln T-0.006T^{2}$, (810-2600K)
G(Tri)	$-944111.18439234+480.752826017315T-75.372668T\ln T$ $+2979047.5388T^{-1}-159707687.146667T^{-2}$, (298-1991K) $-961947.905277253+569.440180798T-85.772T\ln T$, (1991-3000K)
$q^{11}_{KAlO_2,SiO_2}$	$-93303.2-2.5104T$
Nepheline	
Compound Energy Formalism (KAlSi, $VaSi_2)_2(KAlSi)_6O_{32}$	
g°($K_2K_6Al_8Si_8O_{32}$)	$8\cdot G$(Ks)
g°($Va_2K_6Al_6Si_{10}O_{32}$)	$6\cdot G$(Ne)$+4\cdot G$(Tri)$-6527.04-50.208T$
G(Ks)	$-2210626.994366+1149.333035T-184.2898924T\ln T-0.0049258016T^{2}$ $+7.75672484\cdot10^{-7}T^{3}+6553190.458775T^{-1}-4.506167565\cdot10^{-11}T^{4}$ $-356488327.2136T^{-2}$, (298-810K) $-2392185.685045+574.5318944T-0.5301675T^{2}$, (810-811K) $-2208290.417018+1109.99182858T-178.03014T\ln T-0.0134033937T^{2}$ $+3.180280448\cdot10^{-6}T^{3}+6553270.45756T^{-1}-3.7550839\cdot10^{-10}T^{4}$ $-356488327.063T^{-2}$, (811-2100K)
G(Tri)	$-944111.18439234+480.752826017315T-75.372668T\ln T$

Parameter	Value, J·mol^{-1}
	$+2979047.5388T^{-1}-159707687.146667T^{-2}$, (298-1991K) $-961947.905277253+569.440180798T-85.772T\ln T$, (1991-3000K)

Table A.15 Gibbs energy parameters of the solution phases in the K_2O-Na_2O-Al_2O_3-SiO_2 system.

Parameter	Value, J·mol^{-1}
Liquid	
Two-sublattice Quasichemical Formalism (Na, (Na_2), K, (K_2), Al, KAl, Si//O); Grouping:Na, (Na_2) K, (K_2), Al, NaAl, KAl in group 1; Si in group 2	
$g^{002}_{\mathrm{KAl,Si(NaAl)}}$	-4184
Carnegieite	
Compound Energy Formalism $(NaAlSi,VaSi_2,KAlSi)_4O_{32}$	
$g°(K_4Al_4Si_4O_{16})$	$4G(\mathrm{Ks})-2123354.988-134.520T$
G(Ks)	$-2210626.994366+1149.333035T-184.2898924T\ln T-0.0049258016T^2$ $+7.75672484\cdot10^{-7}T^3+6553190.458775T^{-1}-4.506167565\cdot10^{-11}T^4$ $-356488327.2136T^{-2}$, (298-810K) $-2392185.685045+574.5318944T-0.5301675T^2$, (810-811K) $-2208290.417018+1109.99182858T-178.03014T\ln T-0.0134033937T^2$ $+3.180280448\cdot10^{-6}T^3+6553270.45756T^{-1}-3.7550839\cdot10^{-10}T^4-356488327.063T^{-2}$, (811-2100K)
${}^0L_{\mathrm{NaAlSi,KAlSi}}$	-109989.1514
${}^1L_{\mathrm{NaAlSi,KAlSi}}$	52337.7079
Nepheline	
Compound Energy Formalism $(NaAlSi, VaSi_2, KaAlSi)_2(NaAlSi, KAlSi)_6O_{32}$	
$g°(K_2Na_6Al_8Si_8O_{32})$	$6G(\mathrm{Ne})+2G(\mathrm{Ks})-46024+38.4928T$
$g°(Na_2K_6Al_8Si_8O_{32})$	$2G(\mathrm{Ne})+6G(\mathrm{Ks})+100416$
G(Ne)	$-2073105.93747905+3403.104836774T-493.076615T\ln T-0.0469819888T^2$ $+7.4359\cdot10^{-7}T^3-75907.9315T^{-1}+11.72211588T^{1.5}-17299.911T^{0.5}$, (298-462.5K) $-2304106.2535+4402.02512227T-493.076615T\ln T-1.1268958109612T^2$ $+7.43590015\cdot10^{-7}T^3-75907.9315T^{-1}+11.72211588T^{1.5}-17299.911T^{0.5}$,

Parameter	Value, J·mol^{-1}
	(462.5-463.5K) $-2072105.93727973+3400.945T-493.076615T\ln T-0.0469819888T^2$ $+7.43590015\cdot10^{-7}T^3-75907.9315T^{-1}+11.72211588T^{1.5}-17299.911T^{0.5}$, (463.5-1147.5K) $-3907306.21383229+6599.5511556T-493.076615T\ln T-1.4407101572T^2$ $+7.43590015\cdot10^{-7}T^3-75907.9315T^{-1}+11.722116T^{1.5}-17299.911T^{0.5}$, (1147.5-1148.5K) $-2068905.937405+3398.15755279283T-493.076615T\ln T-0.0469819888T^2$ $+7.43590015\cdot10^{-7}T^3-75907.9315T^{-1}+11.722116T^{1.5}-17299.911T^{0.5}$, (1147.5-3000K)
G(Ks)	$-2210626.994366+1149.333035T-184.2898924T\ln T-0.0049258016T^2$ $+7.75672484\cdot10^{-7}T^3+6553190.458775T^{-1}-4.506167565\cdot10^{-11}T^4$ $-356488327.2136T^{-2}$, (298-810K) $-2392185.685045+574.5318944T-0.5301675T^2$, (810-811K) $-2208290.417018+1109.99182858T-178.03014T\ln T-0.0134033937T^2$ $+3.180280448\cdot10^{-6}T^3+6553270.45756T^{-1}-3.7550839\cdot10^{-10}T^4-356488327.063T^{-2}$, (811-2100K)
${}^0L_{\mathrm{KAlSi//NaAlSi,KAlSi}}$	104600
${}^0L_{\mathrm{VaAlSi//NaAlSi,KAlSi}}$	100416
${}^0L_{\mathrm{VaSi_2,KAlSi//NaAlSi}}$	−66944
${}^1L_{\mathrm{VaSi_2,KAlSi//NaAlSi,KAlSi}}$	−83680
Feldspar	
Modified Quasichemical Model (NaSi,KSi)$AlSi_2O_8$	
$G(NaAlSi_3O_8)$	$-3931982.36032337+3380.6552645543T-456.414581T\ln T+0.017813548T^2$ $-4.805823\cdot10^{-7}T^3+149776.0945T^{-1}-1.3090725T^{1.5}-17480.025T^{0.5}$, (298-1051K) $-10077408.7514725+15075.0917843T-456.41458T\ln T+5.545667194T^2$ $-4.805823\cdot10^{-7}T^3+149776.0946T^{-1}-1.3090725T^{1.5}-17480.025T^{0.5}$, (1051-1052K) $-3920282.36032284+3369.52830307T-456.414581T\ln T+0.017813548T^2$ $-4.805823\cdot10^{-7}T^3+149776.0945T^{-1}-1.3090725T^{1.5}-17480.025T^{0.5}$, (298-1051K)

Parameter	Value, J·mol^{-1}
$G(KAlSi_3O_8)$	$-4047081.44301101+826.569361295202T-101.953645T\ln T+0.077369402T^2$ $-1.589594145\cdot10^{-6}T^3+2144228.92T^{-1}-15.23486453T^{1.5}$, (298-772.5K) $-7099570.75440431+8729.45430988627T-101.953645T\ln T$ $-5.037766487056T^2-1.589594145\cdot10^{-6}T^3$ $+2144228.92T^{-1}-15.23486453T^{1.5}$, (772.5-773.5K) $-4039173.44292653+816.339089517093T-101.953645T\ln T$ $+0.077369402T^2-1.589594145\cdot10^{-6}T^3$ $+2144228.92T^{-1}-15.23486453T^{1.5}$, (773.5-3000K)
$q^{00}_{NaAl,KAl}$	$12133.6-1.2552T$
$q^{10}_{NaAl,KAl}$	6694.4
Leucite	
Compound Energy Formalism (Na,K)(Al)Si_2O_6	
g°($KAlSi_2O_6$)	$G(KAlSi_2O_6)$
g°($NaAlSi_2O_6$)	$G(NaAlSi_2O_6)+44350.4-37.656T$
$G(KAlSi_2O_6)$	$-3126554.845+738.1866T-92.97T\ln T+0.07244T^2-1.85522\cdot10^{-6}T^3$ $+1827729.585T^{-1}-12.146T^{1.5}$, (298-833K) $-8626076.931+13950.252T-92.97T\ln T-7.862734T^2-1.85522\cdot10^{-6}T^3$ $+1827729.585T^{-1}-12.146T^{1.5}$, (833-834K) $-3113334.845+722.3163T-92.97T\ln T+0.07244T^2-1.85522\cdot10^{-6}T^3$ $+1827729.585T^{-1}-12.146T^{1.5}$, (834-3000K)
$G(NaAlSi_2O_6)$	$-3067785.88286+2200.84973T-311.2930T\ln T+2675132.03T^{-1}-8020.404T^{0.5}$ $-110427816.89T^{-2}$, (298-1300K)

Table A.16 Optimized properties of the compound phases in the CaO-Na_2O-SiO_2 system.

Compound	$\Delta_f H°_{298.15}$, J·mol^{-1}	$S°_{298.15}$, J·mol^{-1}·K^{-1}	$C_P(T)$, J·mol^{-1}·K^{-1}
Na_2CaSiO_4 (NCS)	−2288459	110.65	$516.8534-0.060096T+4342260T^{-2}+7.576448\cdot10^{-6}T^2$ $-6916.03T^{-0.5}$, (298-3000K)
$Na_2Ca_2Si_2O_7$ (NC2S2)	−3864903	259.95	$530.2888-0.044635T-376045T^{-2}+5.836760\cdot10^{-6}T^2$ $-4747.45T^{-0.5}$, (298-3000K)

Compound	$\Delta_f H°_{298.15}$, J·mol^{-1}	$S°_{298.15}$, J·mol^{-1}·K^{-1}	$C_P(T)$, J·mol^{-1}·K^{-1}
$Na_8Ca_3Si_5O_{17}$ (N4C3S5)	−9172408	686.36	$1364.0553-0.091204T+36861T^{-2}+1.078035\cdot10^{-5}T^2-12359.95T^{-0.5}$, (298-3000K)
$Na_2CaSi_5O_{12}$ (NCS5)	−5924257	351.74	$781.7546-0.062473T-1904729T^{-2}+8.232823\cdot10^{-6}T^2-7118.43T^{-0.5}$, (298-3000K)
$Na_2Ca_3Si_6O_{16}$ (NC3S6)	−8394778	397.48	$1040.7508-0.084370T-2965977T^{-2}+1.120029\cdot10^{-5}T^2-9069.14T^{-0.5}$, (298-3000K)

Table A.17 Gibbs energy parameters of the solution phases in the CaO-Na_2O-SiO_2 system.

Parameter	Value, J·mol^{-1}
Liquid	
Two-sublattice Quasichemical Formalism (Na, (Na_2), Ca, Si//O); Grouping:Na, (Na_2), Ca in group 1; Si in group 2	
$g^{001}_{Na,Si(Ca)}$	26941.13
$g^{003}_{Na,Si(Ca)}$	−24167.9
$g^{011}_{Na,Si(Ca)}$	−131483
$g^{021}_{Na,Si(Ca)}$	−57805.3
Combeite	
Compound Energy Formalism $(Na_2, Ca)_2(Na_2,Ca)_3(Ca)_1Si_6O_{18}$	
g°(N2C3C1)	$2G(Na_2SiO_3)+4G(CaSiO_3)-41840+9.0189T$
g°(C2C3C1)	$6G(CaSiO_3)+92048-10.2506T$
g°(N2N3C1)	$5G(Na_2SiO_3)+G(CaSiO_3)+114892.6-83.68T$
g°(C2N3C1)	$3G(Na_2SiO_3)+3G(CaSiO_3)-85058+2.7355T$
$G(Na_2SiO_3)$	$-1554038.06796+1713.8563T-234.77T\ln T-8875.60T^{0.5}-2.255\cdot10^7T^{-2}$, (298-1363K) $-1639605.680+1121.5606T-177.31792T\ln T$, (1363-1450K)
$G(CaSiO_3)$	$-1664832.9406+1013.06077T-149.07266T\ln T+1.829674\cdot10^6T^{-1}-2761.18T^{0.5}-8.07249\cdot10^7T^{-2}$, (298-2000K) $-1719540.349+959.1093T-146.44T\ln T$, (2000-2002K)

Parameter	**Value, J·mol^{-1}**
${}^{0}L_{Ca//Na2,Ca//Ca}$	−154808
(2:1:3)	
Compound Energy Formalism $(Na_2,Ca)_1(Na_2,Ca)_1(Na)_6(Ca)_1Si_6O_{18}$	
g°(C1C1N3C1)	$3G(Na_2SiO_3)+3G(CaSiO_3)-47187.152-16.736T$
g°(N1C1N3C1)	$4G(Na_2SiO_3)+2G(CaSiO_3)-33488.736-25.9408T$
g°(C1N1N3C1)	$4G(Na_2SiO_3)+2G(CaSiO_3)-33489.1544-25.9408T$
g°(N1N1N3C1)	$5G(Na_2SiO_3)+G(CaSiO_3)+38526.6114-40.814T$
$G(Na_2SiO_3)$	$-1550958.06750207+1712.5563T-234.77T\ln T-22550000T^{-2}$ $-8875.6T^{0.5}$, (298-1363K) $-1636525.68110518+1120.26065T-177.31792T\ln T$, (1363-1450K)
$G(CaSiO_3)$	$-1664832.9406+1013.06077T-149.07266T\ln T+1.829674\cdot10^{6}T^{-1}$ $-2761.18T^{0.5}-8.07249\cdot10^{7}T^{-2}$, (298-2000K)
Pseudowollastonite	
Compound Energy Formalism $(Ca,Na_2)\{SiO_3\}$	
g°($CaSiO_3$)	$G(CaSiO_3)$
g°(Na_2SiO_3)	$G(Na_2SiO_3)+41840$
$G(CaSiO_3)$	$-1667538.64873175+927.913022T-141.15611T\ln T-156789158.86667T^{-2}$ $+2928797.4896T^{-1}-1668.927995T^{0.5}$, (298-1813K)
$G(Na_2SiO_3)$	$-1550958.0675+1712.5563T-234.77T\ln T-22550000T^{-2}$ $-8875.6T^{0.5}$, (298-1363K) $-1636525.6811+1120.2607T-177.31792T\ln T$, (1363-1450K)
$q^{11}_{CaSiO_3,Na_2SiO_3}$	−33472
α-C2S	
One Sublattice $(0.5Ca_2SiO_4,0.5K_4SiO_4)_2$	
g°(Ca_2SiO_4)	$G(Ca_2SiO_4)$
g°(Na_4SiO_4)	$G(Na_4SiO_4)+37656$
$G(Ca_2SiO_4)$	$-2241869.0653+947.1861T-160.4888T\ln T+3994699.9408T^{-1}$ $-216246658.6307T^{-2}-2807.6000T^{0.5}$, (298-5000K)
$G(Na_4SiO_4)$	$-2170301.03887+1565.46478T-250.0986T\ln T+0.003731T^{2}$

Parameter	Value, J·mol^{-1}
	$-1.76755\cdot10^{-7}T^{3}+1255421T^{-1}-2578.8984T^{0.5}$, (298-3000K)
α'-C2S	
One Sublattice $(0.5Ca_2SiO_4,0.5K_4SiO_4)_2$	
$g°(Ca_2SiO_4)$	$G(Ca_2SiO_4)$
$g°(Na_4SiO_4)$	$G(Na_4SiO_4)+37656$
$G(Ca_2SiO_4)$	$-2331645.8553+1371.8996T-210.4888T\ln T+3994699.9408T^{-1}$ $-216246658.6307T^{-2}-2807.6000T^{0.5}$, (298-1710K) $2246145.8610+949.6872T-160.4888T\ln T+3994699.9408T^{-1}$ $-216246658.6307T^{-2}-2807.6000T^{0.5}$, (1710-5000K)
$G(Na_4SiO_4)$	$-2170301.03887+1565.46478T-250.0986T\ln T+0.003731T^{2}$ $-1.76755\cdot10^{-7}T^{3}+1255421T^{-1}-2578.8984T^{0.5}$, (298-3000K)

Table A.18 Optimized properties of the compound phases in the CaO-Na_2O-Al_2O_3 system.

Compound	$\Delta_f H°_{298.15}$, J·mol^{-1}	$S°_{298.15}$, J·mol^{-1}·K^{-1}	$C_P(T)$, J·mol^{-1}·K^{-1}
$Na_2Ca_3Al_{16}O_{28}$	−16031527	690	$599.479116-0.46298107T-22342348.9T^{-2}+2.69437348\cdot10^{-5}T^{2}$ $+35.33722T^{0.5}$, (298-3000K)

Table A.19 Gibbs energy parameters of the solution phases in the CaO-Na_2O-Al_2O_3 system.

Parameter	Value, J·mol^{-1}
Liquid	
Two-sublattice Quasichemical Formalism (Na, (Na_2), Ca, Al, NaAl//O); Grouping: all species in group 1	
Coordination numbers: $Z^{Ca}_{Ca,Ca//O,O} = Z^{O}_{Ca,Ca//O,O} = 1.37744375$	
Grouping exceptions	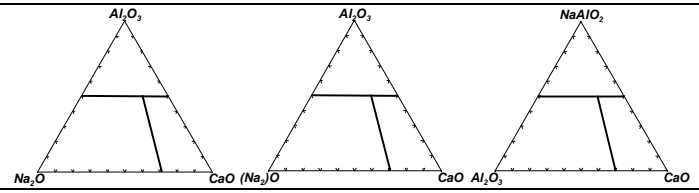
$\Delta\omega^{\circ}_{NaAl,Ca}$	−25104

Parameter	**Value, J·mol^{-1}**
$g^{001}_{\mathrm{Al,Ca(NaAl)}}$	−62760
$g^{001}_{\mathrm{NaAl,Al(Ca)}}$	50208
NCA2	
Compound Energy Formalism (Na_2, Ca){$Na_2Al_4O_8$}	
g°($Na_2CaAl_4O_8$)	G($CaAl_2O_4$)+2G($NaAlO_2$)+100416−83.68T
g°($Na_4Al_4O_8$)	4G($NaAlO_2$)+23012
G($CaAl_2O_4$)	−2336571.0998752+1603.120587T−227.04Tln$T$+14256666.897T^{-2} +280400.00664T^{-1}−6676.400$T^{0.5}$, (298-1877K)
G($NaAlO_2$)	−1166463.95548+541.326672T−89.148488Tln$T$+0.00764626T^2 +896631.2T^{-1}, (298-3000K)
C3A	
Compound Energy Formalism (Na_2,Ca){$Ca_8Al_6O_{18}$}	
g°($Ca_9Al_6O_{18}$)	3G(C3A)
g°($Na_2Ca_8Al_6O_{18}$)	G(NC8A3)+23012
G(C3A)	−3655463.30284+2119.246152T−321.58Tln$T$−110203331.3467T^{-2} +2890650.0788T^{-1}−5021.600$T^{0.5}$, (298-1814K)
G(NC8A3)	−11127559.8086313+6687.43234206T−1001.60201Tln$T$−0.02193255T^2 −341846873.581333T^{-2}+10787313.46228T^{-1}−14225.57175$T^{0.5}$ +2.34791673·10$^{-6}T^3$, (298-1405K) −11150638.9307+6956.0836589T−1039.986Tln$T$−341846873.5813T^{-2} +10380628.4531T^{-1}−14225.57175$T^{0.5}$, (1405-2327)

Table A.20 Optimized parameters of the solution phases in the Na_2O-CaO-Al_2O_3-SiO_2 system.

Parameter	**Value, J·mol^{-1}**
Liquid	
Two-sublattice Quasichemical Formalism (Na, (Na_2), Ca, Al, NaAl, Si//O); Grouping: Si in group 2, th remaining species in group 1	

Parameter	**Value, J·mol^{-1}**
Grouping exceptions	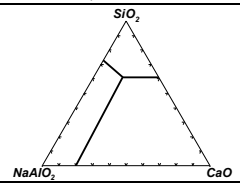
$q^{001}_{\mathrm{NaAl,Si(Ca)//O,O}}$	24548.0862
$q^{011}_{\mathrm{NaAl,Si(Ca)//O,O}}$	97307.5244
Feldspar	
Modified Quasichemical Model (NaSi,CaAl)$AlSi_2O_8$	
$G(NaAlSi_3O_8)$	$-3931982.36032337+3380.6552645543T-456.414581T\ln T+0.017813548T^2$ $-4.805823\cdot10^{-7}T^3+149776.0945T^{-1}-1.3090725T^{1.5}-17480.025T^{0.5}$, (298-1051K) $-10077408.7514725+15075.0917843T-456.41458T\ln T+5.545667194T^2$ $-4.805823\cdot10^{-7}T^3+149776.0946T^{-1}-1.3090725T^{1.5}-17480.025T^{0.5}$, (1051-1052K) $-3920282.36032284+3369.52830307T-456.414581T\ln T+0.017813548T^2$ $-4.805823\cdot10^{-7}T^3+149776.0945T^{-1}-1.3090725T^{1.5}-17480.025T^{0.5}$, (298-1051K)
$G(CaAl_2Si_2O_8)$	$-4235420.14289364+3179.0379419T-439.36937T\ln T$ $-14936.596T^{0.5}+52837204.68T^{-2}$, (298-1828K) $-4447513.480246+2505.38528956T-380.744T\ln T$, (1828-2500K)
$q^{01}_{\mathrm{NaSi,CaAl}}$	$55305.2851936-39.09622078952T$
$q^{02}_{\mathrm{NaSi,CaAl}}$	$-13660.98053864+22.9729806436T$
Nepheline	
Compound Energy Formalism (NaAlSi, $VaSi_2$, $CaAl_2)_2$(NaAlSi, $CaAl_2)_6O_{32}$	
g°($Ca_2Na_6Al_{10}Si_6O_{32}$)	$6G_{\mathrm{NaAlSiO_4}}+2G_{\mathrm{CaAl_2Si_2O_8}}+836800$
g°($Na_2Ca_6Al_{14}Si_2O_{32}$)	$2G_{\mathrm{NaAlSiO_4}}+6G_{\mathrm{CaAl_2Si_2O_8}}+58584.65$

Parameter	**Value, J·mol^{-1}**
g°($Va_2Ca_6Al_{12}Si_4O_{32}$)	$4G_{CaAl_2O_4}+2G_{CaAl_2Si_2O_8}+30008$
g°($Ca_2Ca_6Al_{16}O_{32}$)	$8G_{CaAl_2O_4}+3347200$
G(NaAlSiO$_4$)	$-2073105.93747905+3403.104836774T-493.076615T\ln T$ $-0.0469819888T^2+7.4359\cdot10^{-7}T^3-75907.9315T^{-1}+11.72211588T^{1.5}$ $-17299.911T^{0.5}$, (298-462.5K) $-2304106.2535+4402.02512227T-493.076615T\ln T-1.12689581096 12T^2$ $+7.43590015\cdot10^{-7}T^3-75907.9315T^{-1}+11.72211588T^{1.5}-17299.911T^{0.5}$, (462.5-463.5K) $-2072105.93727973+3400.945T-493.076615T\ln T-0.0469819888T^2$ $+7.43590015\cdot10^{-7}T^3-75907.9315T^{-1}+11.72211588T^{1.5}-17299.911T^{0.5}$, (463.5-1147.5K) $-3907306.21383229+6599.5511556T-493.076615T\ln T-1.4407101572T^2$ $+7.43590015\cdot10^{-7}T^3-75907.9315T^{-1}+11.722116T^{1.5}-17299.911T^{0.5}$, (1147.5-1148.5K) $-2068905.937405+3398.15755279283T-493.076615T\ln T-0.0469819888T^2$ $+7.43590015\cdot10^{-7}T^3-75907.9315T^{-1}+11.722116T^{1.5}-17299.911T^{0.5}$, (1147.5-3000K)
G($CaAl_2Si_2O_8$)	$-4235420.14289364+3179.0379419T-439.36937T\ln T$ $-14936.596T^{0.5}+52837204.68T^{-2}$, (298-1828K) $-4447513.480246+2505.38528956T-380.744T\ln T$, (1828-2500K)
G($CaAl_2O_4$)	$-2336571.09987519+1603.12058697T-227.04T\ln T+14256666.89733T^{-2}$ $+280400.00664T^{-1}-6676.4000T^{0.5}$, (298-1877K)
${}^1L_{VaSi_2//NaAlSi,CaAl_2}$	−501452.4
Carnegieite	
Compound Energy Formalism (NaAlSi,$VaSi_2$,$CaAl_2$)$_4$O$_{32}$	
g°($Ca_4Al_8O_{32}$)	$4G(CaAl_2O_4)+167360$
G($CaAl_2O_4$)	$-2336571.09987519+1603.12058697T-227.04T\ln T+14256666.89733T^{-2}$ $+280400.00664T^{-1}-6676.4000T^{0.5}$, (298-1877K)

Parameter	Value, J·mol^{-1}
${}^{0}L_{NaAlSi,CaAl_2}$	−104600
Melilite	
Compound Energy Formalism $(Ca,Na)_2(Al)(Al,Si)_2O_7$	
$G^{add}_{NaCaAlSi_2O_7}$	$-370515+299.9T$
$\Delta_{CN//A//AS}$	407046.9
Clinopyroxene	
Compound Energy Formalism $(Ca)(Al)(Al,Si)SiO_6$	
g°(NAS)	$G(NaAlSi_2O_6)$
g°(NAA$^-$)	$G(NaAlSi_2O_6)-G(CaFeSi_2O_6)-G(CaFeAlSiO_6)-\Delta_{NC//A//AS}$
$G(NaAlSi_2O_6)$	$-3067785.882865+2200.84973067T-311.292968T\ln T-110427816.8933T^{-2}$ $+2675132.0296T^{-1}-8020.4040T^{0.5}$, (298-1300K)
$G(CaFeSi_2O_6)$	$-2422037.816+2105.1353T-309.3T\ln T-0.007025T^2-15395000T^{-1}$ $+797666667T^{-2}-93220\ln T$, (298-3000K)
$G(CaFeAlSiO_6)$	$-2968263.1998+1666.1311T-4189837.9352T^{-1}-158617532T^{-2}$ $+4417.9539T^{0.5}$, (298-3000K)
$\Delta_{NC//A//AS}$	−8368

Table A.21 Optimized properties of the compound phases in the $CaO-K_2O-SiO_2$ system.

Phase	$\Delta_f H°_{298.15}$, J·mol^{-1}	$S°_{298.15}$, J·mol^{-1}·K^{-1}	$C_P(T)$, J·mol^{-1}·K^{-1}
K_2CaSiO_4 (KCS)	−2227000	184	$279.1355+0.339615T-2915947T^{-2}-10.59T^{0.5}$, (298-1500K) $-42.0322-0.160850T-0.00552T^{-2}+7.84789\cdot10^{-6}T^2$ $+13.20T^{0.5}$, (1500-3000K)
$K_4CaSi_6O_{15}$ (K2CS6)	−7592000	507	$-284.57-1.291283T-2.808319\cdot10^6T^{-2}+1.598825\cdot10^{-4}T^2$ $+65.927T^{0.5}$, (298-1500K) $415.077-0.17159T-0.116358T^{-2}+9.34212\cdot10^{-6}T^2$ $+13.1906T^{0.5}$, (1500-3000K)
$K_8CaSi_{10}O_{25}$ (K4CS10)	−12606000	888	$-516.850-22602T-4.294946\cdot10^6T^{-2}+2.80055\cdot10^{-4}T^2$ $+115.07T^{0.5}$, (298-1500K) $722.00-0.288661T-0.2300892T^{-2}+1.591969\cdot10^{-5}T^2$

Phase	$\Delta_f H°_{298.15}$, J·mol^{-1}	$S°_{298.15}$, J·mol^{-1}·K^{-1}	$C_P(T)$, J·mol^{-1}·K^{-1}
			$+21.9863T^{0.5}$, (1500-3000K)
$K_2Ca_2Si_2O_7$ (KC2S2)	−3900000	264	$281.501+0.19244T-3.96456\cdot10^6T^{-2}-4.0917\cdot10^{-5}T^2$ $-2.6089T^{0.5}$, (298-1500K) $23.4733-0.195574T-6.4613\cdot10^{-3}T^{-2}+9.49845\cdot10^{-6}T^2$ $+16.11T^{0.5}$, (1500-3000K)
$K_2Ca_2Si_6O_{15}$ (KC2S6)	−7632000	441	$-220.72164-1.1292T-3.3867\cdot10^6T^{-2}+1.395058\cdot10^{-4}T^2$ $+58.141T^{0.5}$, (298-1500K) $369.771-0.16758T-0.06212T^{-2}+8.81789\cdot10^{-6}T^2$ $+13.188T^{0.5}$, (1500-3000K)
$K_2Ca_2Si_9O_{21}$ (KC2S9)	−10370000	578	$-384.692-1.6547T-4.2059\cdot10^6T^{-2}+2.05586\cdot10^{-4}T^2$ $+84.564T^{0.5}$, (298-1500K) $497.72-0.22698T-0.067185T^{-2}+1.21599\cdot10^{-5}T^2$ $+17.647T^{0.5}$, (1500-3000K)
$K_2Ca_3Si_6O_{16}$ (KC3S6)	−8350000	476	$-163.70-1.101176T-4.162236\cdot10^6T^{-2}+1.35162\cdot10^{-4}T^2$ $+57.311T^{0.5}$, (298-1500K) $392.6273-0.182505T-0.0614T^{-2}+9.354459\cdot10^{-6}T^2$ $+14.61T^{0.5}$, (1500-3000K)
$K_2Ca_6Si_4O_{15}$ (KC6S4)	−8563000	499	$337.868-0.17536T-7.169675\cdot10^6T^{-2}+3.86726\cdot10^{-6}T^2$ $+17.157T^{0.5}$, (298-1500K) $233.999-0.281495T-8.5372\cdot10^{-3}T^{-2}+1.359139\cdot10^{-5}T^2$ $+23.30T^{0.5}$, (1500-3000K)

Table A.22 Gibbs energy parameters of the solution phases in the $CaO-K_2O-SiO_2$ system.

Parameter	Value, J·mol^{-1}
Liquid	
Two-sublattice Quasichemical Formalism (K, (K_2), Ca, Si//O); Grouping: K, (K_2), Ca in group 1; Si in group 2	
$g^{001}_{K,Si(Ca)}$	−41840
$g^{003}_{K,Si(Ca)}$	−54392

Parameter	**Value, J·mol^{-1}**
$g^{011}_{K,Si(Ca)}$	41840
$g^{021}_{K,Si(Ca)}$	−251040
(2:1:3)	
Compound Energy Formalism $(K_2,Ca)_1(K_2,Ca)_1(K)_6(Ca)_1Si_6O_{18}$	
g°(C1C1K3C1)	$3G(K_2SiO_3)+3G(CaSiO_3)$
g°(K1C1K3C1)	$4G(K_2SiO_3)+2G(CaSiO_3)-87864.42$
g°(C1K1K3C1)	$4G(K_2SiO_3)+2G(CaSiO_3)-87864$
g°(K1K1K3C1)	$5G(K_2SiO_3)+G(CaSiO_3)$
$G(CaSiO_3)$	$-1664832.94060224+1013.06076963769T-149.072660664T\ln T-80724903.56T^{-3}$ $+1829673.99472T^{-1}-2761.17992256T^{0.5}$, (298-2000K)
$G(K_2SiO_3)$	$-1585967.20823915+672.7176058T-118.900912T\ln T-0.024405272T^{2}$ $+707723.6T^{-1}$, (298-1249K)
α-C2S	
One Sublattice $(0.5Ca_2SiO_4,0.5K_4SiO_4)_2$	
g°(Ca_2SiO_4)	$G(\alpha\text{-}Ca_2SiO_4)$
g°(K_4SiO_4)	$G(K_4SiO_4)+20920$
$G(\alpha\text{-}Ca_2SiO_4)$	$-2241869.06531142+947.18610682T-160.4887674T\ln T-216246658.630667T^{-2}$ $+3994699.9408T^{-1}-2807.600T^{0.5}$, (298-5000K)
$G(K_4SiO_4)$	$-2121368.68357+1366.217889T-231.9060T\ln T-0.017146T^{2}-81928061.57333T^{-2}$ $+2364981.98384T^{-1}-961.1040T^{0.5}$, (298-1185K)
$q^{11}_{0.5Ca_2SiO_4,0.5K_4SiO_4}$	−15062.4
α'-C2S	
One Sublattice $(0.5Ca_2SiO_4,0.5K_4SiO_4)_2$	
g°(Ca_2SiO_4)	$G(\alpha'\text{-}Ca_2SiO_4)$
g°(K_4SiO_4)	$G(K_4SiO_4)+20920$
$G(\alpha'\text{-}Ca_2SiO_4)$	$-2331645.855265+1371.8995673T-210488764T\ln T-216246658.6307T^{-2}$ $+3994699.9408T^{-1}-2807.600T^{0.5}$, (298-1710K) $-2246145.861038+949.6871633T-160.4887674T\ln T-216246658.630667T^{-2}$ $+3994699.9408T^{-1}-2807.600T^{0.5}$, (1710-5000K)

Parameter	**Value, J·mol^{-1}**
$G(K_4SiO_4)$	$-2121368.68357164+1366.21788897T-231.9060T\ln T-0.017146T^2$ $-81928061.5733T^{-2}+2364981.98384T^{-1}-961.103995712T^{0.5}$, (298-1185K)
$q^{11}_{0.5Ca_2SiO_4,0.5K_4SiO_4}$	−15062.4

Table A.23 Optimized properties of the compound phases in the CaO-K_2O-Al_2O_3 system.

Compound	**$\Delta_f H°_{298.15}$, J·mol^{-1}**	**$S°_{298.15}$, J·mol^{-1}·K^{-1}**	**$C_P(T)$, J·mol^{-1}·K^{-1}**
$K_4Ca_3Al_{10}O_{20}$	−11700000	571.36	$257.5255-0.493266T-8203876T^{-2}+2.764377\cdot10^{-5}T^2$ $+37.38T^{0.5}$, (298-3000K)

Table A.24 Gibbs energy parameters of the solution phases in the CaO-K_2O-Al_2O_3 system.

Parameter	**Value,J·mol^{-1}**
Two-sublattice Quasichemical Formalism (K, (K_2), Al, KAl//O); Grouping: all species in group 1	
Grouping exceptions	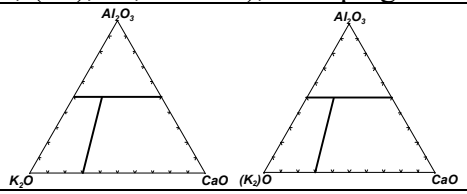
$g^{001}_{K,Al(Ca)}$	−16736
C3A	
One Sublattice ($K_2Ca_8Al_6O_{18}$,$CaCa_8Al_6O_{18}$)	
$g°(Ca_9Al_6O_{18})$	$3G$(C3A)
$g°(K_2Ca_8Al_6O_{18})$	G(KC8A3)+20920
G(C3A)	$-3655463.30284+2119.2461524T-321.5800T\ln T-110203331.34667T^{-2}$ $+2890650.0788T^{-1}-5021.600T^{0.5}$, (298-1814K)
G(KC8A3)	$-11037736.222+4254.976T-551.7867731T\ln T+0.23569662T^2-8.252173546\cdot10^{-6}T^3$ $+4134986.10^4T^{-1}-36.23313432T^{1.5}-10108.19416T^{0.5}$, (298-1500K) $-111041691.711+4728.255T-663.305713T\ln T+0.12176335T^2-2.501187\cdot10^{-6}T^3$ $+1919223.816T^{-1}-23.223378T^{1.5}-10108.19416T^{0.5}$, (1500-3000K)

Table A.25 Gibbs energy parameters of the solution phases in the Al_2O_3-CaO-K_2O-SiO_2 system.

Parameter	**Value, J·mol^{-1}**
Liquid	
Two-sublattice Quasichemical Formalism(K, (K_2), Ca, Al, KAl, Si//O);Grouping: K, (K_2), Ca, Al, KAl in group 1; Si in group 2	
$\omega^{001}_{\mathrm{KAl,Si(Ca)}}$	19246.4
$\omega^{031}_{\mathrm{KAl,Si(Ca)}}$	−33472
Feldspar	
Modified Quasichemical Model (KSi,CaAl)$AlSi_2O_8$	
$G(\mathrm{KAlSi_3O_8})$	$-4047081.44301101+826.569361295202T-101.953645T\ln T+0.077369402T^2-1.589594145\cdot10^{-6}T^3$ $+2144228.92T^{-1}-15.23486453T^{1.5}$, (298-772.5K) $-7099570.75440431+8729.45430988627T-101.953645T\ln T-5.037766487056T^2$ $-1.589594145\cdot10^{-6}T^3+2144228.92T^{-1}-15.23486453T^{1.5}$, (772.5-773.5K) $-4039173.44292653+816.339089517093T-101.953645T\ln T+0.077369402T^2-1.589594145\cdot10^{-6}T^3$ $+2144228.92T^{-1}-15.23486453T^{1.5}$, (773.5-3000K)
$G(\mathrm{CaAl_2Si_2O_8})$	$-4235420.14289364+3179.0379419T-439.36937T\ln T$ $-14936.596T^{0.5}+52837204.68T^{-2}$, (298-1828K) $-4447513.480246+2505.38528956T-380.744T\ln T$, (1828-2500K)
$q^{00}_{\mathrm{KSi,CaAl}}$	43932
Melilite	
Compound Energy Formalism $(Ca,K)_2(Al)(Al,Si)_2O_7$	
$G^{add}_{\mathrm{KCaAlSi_2O_7}}$	11718.9
$\Delta_{\mathrm{CK//A//AS}}$	−63670

Table A.26 Optimized properties of the compound phases in the MgO-Na_2O-SiO_2 system.

Phase	**$\Delta_f H°_{298.15}$, J·mol^{-1}**	**$S°_{298.15}$, J·mol^{-1}·K^{-1}**	**$C_P(T)$, J·mol^{-1}·K^{-1}**
Na_2MgSiO_4 (NMS)	−2184000	142.00	$246.0381-0.024179T-121578T^{-2}+6.963317\cdot10^{-7}T^2-2103.92T^{-0.5}$ $+1.90T^{0.5}$, (298-3000K)

Phase	$\Delta_f H°_{298.15}$, J·mol^{-1}	$S°_{298.15}$, J·mol^{-1}·K^{-1}	$C_P(T)$, J·mol^{-1}·K^{-1}
$Na_2Mg_2Si_2O_7$ (NM2S2)	−3754000	201.00	$565.4155+0.010233T+1111111T^{-2}-7.19946\cdot10^{-7}T^2-5560.84T^{-0.5}-1.84T^{0.5}$, (298-3000K)
$Na_2MgSi_3O_8$ (NMS3)	−4038000	223.00	$1447.8548+0.34617T+4220561T^{-2}-1.821973\cdot10^{-5}T^2-14440.21T^{-0.5}-30.36T^{0.5}$, (298-3000K)
$Na_4MgSi_3O_9$ (N2MS3)	−4693000	280.00	$561.2426+0.026946T-1073767T^{-2}-5.734023\cdot10^{-6}T^2+0.376T^{0.5}-4422.10T^{-0.5}$, (298-3000K)
$Na_4Mg_2Si_3O_{10}$ (N2M2S3)	−5314000	316.00	$706.1524-0.032162T+1203714T^{-2}+1.156342\cdot10^{-6}T^2-6873.88T^{-0.5}+1.51T^{0.5}$, (298-3000K)
$Na_4MgSi_4O_{10}$ (NMS4)	−4902300	320.00	$1007.3145+0.127475T+844247T^{-2}-5.92701\cdot10^{-6}T^2-12.89T^{0.5}-9500.53T^{-0.5}$, (298-3000K)
$Na_2Mg_2Si_4O_{11}$ (NM2S4)	−5602000	282.00	$1651.0776+0.35487T+3737621T^{-2}-1.831081\cdot10^{-5}T^2-31.193T^{0.5}-16311.79T^{-0.5}$, (298-3000K)
$Na_4Mg_3Si_5O_{15}$ (N2M3S5)	−7724000	500.00	$1301.814+0.053721T+4052024T^{-2}-2.755361\cdot10^{-6}T^2-6.98T^{0.5}-13550T^{-0.5}$, (298-3000K)
$Na_2Mg_2Si_6O_{15}$ (NM2S6)	−7364000	440.00	$1386.4314+0.158739T+288838T^{-2}-7.320454\cdot10^{-6}T^2-16.34T^{0.5}-12910.36T^{-0.5}$, (298-3000K)
$Na_2Mg_5Si_{12}O_{30}$ (NM5S12)	−14792000	740.00	$3493.634+0.341762T+11091535T^{-2}-3.698794\cdot10^{-6}T^2-45.71T^{0.5}-37315.14T^{-0.5}$, (298-3000K)

Table A.27 Gibbs energy parameters of the liquid phase in the MgO-Na_2O-SiO_2 system.

Parameter	Value, J·mol^{-1}
Two-sublattice Quasichemical Formalism (Na, (Na_2), Mg, Si//O); Grouping: Na, (Na_2), Mg in group 1; Si in group 2	
$g^{001}_{Na,Si(Mg)}$	55074.92
$g^{011}_{Na,Si(Mg)}$	−628736
$g^{012}_{Na,Si(Mg)}$	−78399.4
$g^{021}_{Na,Si(Mg)}$	1244195
$g^{031}_{Na,Si(Mg)}$	−905824

Table A.28 Thermodynamic properties of the compound phases in the MgO-Al_2O_3-Na_2O system.

Phase	**$\Delta_f H^\circ_{298.15}$, J·mol^{-1}**	**$S^\circ_{298.15}$, J·mol^{-1}·K^{-1}**	**$C_P(T)$, J·mol^{-1}·K^{-1}**
$Na_{11}Mg_{19}Al_{97}O_{170}$ (β''''-alumina)	−97200000	3471.71	$10049.751816772-0.193808195703T-74914909.46252T^{-2}$ $+2.07052057525\cdot10^{-5}T^2-66908.70809T^{-0.5}$ $+111047628.5168T^{-3}-111920.62255T^{-1}$, (298-3000K)
$Na_8Mg_{13}Al_{102}O_{170}$ (β'''-alumina)	−96620000	3302.09	$9939.638926344-0.204918819154T-78332224.44304T^{-2}$ $+2.2503371311\cdot10^{-5}T^2-68290.32476792T^{-0.5}$ $+75979956.3536T^{-3}-81396.8164T^{-1}$, (298-3000K)
$Na_{17}Mg_7Al_{103}O_{170}$ (β''-alumina)	−96370000	3570.71	$10166.952945916-0.2041252815T-65562205.56356T^{-2}$ $+2.089594693\cdot10^{-5}T^2-67144.8929T^{-0.5}$ $+40912284.1904T^{-3}-172968.23485T^{-1}$, (298-3000K)

Table A.29 Gibbs energy parameters of the solution phases in the MgO-Al_2O_3-Na_2O system

Parameter	**Value, J·mol^{-1}**
Liquid	
Two sublattice Quasichemical Formalism (Na, (Na_2), Mg, Al, NaAl//O); Grouping: Na, (Na_2), Mg, Al, NaAl in group 1; Si in group 2	
Grouping exceptions	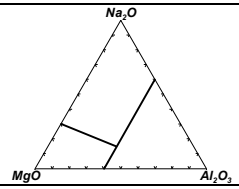
Beta	
Compound Energy Formalism $[Na^+,Va]_1^{BR}[Na^+,Va]_1^{aBR}[Al^{3+},Mg^{2+}]_2^{T}[O^{2-},Va]_1^{mO}Al_9^{other}O_{17}$	
$G^{add(Na-Mg)}$	−41840
Beta''	
Compound Energy Formalism $[Na^+,Va]_1^{BR}[Na^+,Va]_1^{aBR}[Al^{3+},Mg^{2+}]_2^{T}[O^{2-},Va]_1^{mO}Al_9^{other}O_{17}$	
$G^{add(Na-Mg)}$	−41840

Table A.30 Gibbs energy parameters of the liquid phase in the Na_2O-Al_2O_3-MgO-SiO_2 system.

Parameter	**Value, J·mol^{-1}**
Two sublattice Quasichemical Formalism (Na, (Na_2), Mg, Al, NaAl, Si//O); Grouping: Na, (Na_2), Mg, Al, NaAl in group 1; Si in group 2	
$\omega^{001}_{\mathrm{NaAl,Si(Mg)}}$	87864
$\omega^{003}_{\mathrm{NaAl,Si(Mg)}}$	19219.3
$\omega^{011}_{\mathrm{NaAl,Si(Mg)}}$	−77545.4

Table A.31 Gibbs energy parameters of the solution phases in the Al_2O_3-CaO-MgO-Na_2O-SiO_2 system.

Parameter	**Value, J·mol^{-1}**
Liquid	
Two-sublattice Quasichemical Formalism (Na, (Na_2), Ca, Mg, Al, NaAl, Si//O); Grouping: Na, (Na_2), Ca, Mg, Al, NaAl in group 1; Si in group 2	
$q^{001}_{\mathrm{Mg,NaAl(Ca)}}$	−502080
Melilite	
Compound Energy Formalism $(Ca,Na)_2(Mg,Al)(Al,Si)_2O_7$	
$\Delta_{\mathrm{CN//AM//S}}$	210047

Table A.32 Optimized properties of the compound phases in the K_2O-MgO-SiO_2 system.

Phase	**$\Delta_f H°_{298.15}$, J·mol^{-1}**	**$S°_{298.15}$, J·mol^{-1}·K^{-1}**	**$C_P(T)$, J·mol^{-1}·K^{-1}**
$K_2MgSiO_4(s_1)$ (KMS)	−2173000	173.00	$169.6445+0.094581T-2180454T^{-2}-1.282961\cdot10^{-5}T^2-0.9931T^{0.5}$, (298-3000K)
$K_2MgSiO_4(s_2)$ (KMS)	−2171030	175.52	$169.6445+0.094581T-2180454T^{-2}-1.282961\cdot10^{-5}T^2-0.9931T^{0.5}$, (298-3000K)
$K_2MgSi_2O_6$ (KMS2)	−3056220	205.00	$81.9754-0.066282T-1621362T^{-2}-1.29535\cdot10^{-6}T^2+8.86T^{0.5}$, (298-3000K)
$K_2MgSi_3O_8$ (KMS3)	−4105000	250.00	$113.1862-0.21083T-5022077T^{-2}+1.566134\cdot10^{-5}T^2+13.94T^{0.5}$, (298-3000K)
$K_2MgSi_5O_{12}$ (KMS5)	−5935000	341.00	$112.2018-0.361435T-6980408T^{-2}+2.7561\cdot10^{-5}T^2+22.87T^{0.5}$, (298-3000K)
$K_2Mg_5Si_{12}O_{30}$ (KM5S12)	−14910000	716.00	$310.4054-0.71603T-17189889T^{-2}+4.942431\cdot10^{-5}T^2+49.91T^{0.5}$, (298-3000K)
$K_4Mg_2Si_5O_{14}$ (K2M2S5)	−7256000	474.00	$308.9543-0.27246T-10561357T^{-2}+1.92580\cdot10^{-5}T^2+18.36T^{0.5}$, (298-3000K)
$K_{10}Mg_5Si_{11}O_{32}$ (K5M5S11)	−16800000	1070.00	$540.911-0.33902T-13151717T^{-2}-7.49564\cdot10^{-7}T^2+42.28T^{0.5}$, (298-3000K)

Table A.33 Gibbs energy parameters of the solution phases in the K_2O-MgO-SiO_2 system.

Parameter	**Value, J·mol^{-1}**
Liquid	
Two-sublattice Quasichemical Formalism (K, (K_2), Mg, Si//O); Grouping: K, (K_2), Mg in group 1; Si in group 2	
$q^{001}_{(K,Si)Mg}$	11851.06
$q^{011}_{(K,Si)Mg}$	−119517
$q^{041}_{(K,Si)Mg}$	−130913
$q^{013}_{(K,Si)Mg}$	−97450.4

Parameter	**Value, J·mol^{-1}**
Nepheline	
Compound Energy Formalism ($VaSi_2$, $0.5K_2MgSi_3)_2(0.5K_2MgSi_3)_6O_{32}$	
g°($K_8Mg_4Si_{12}O_{32}$)	$4G(K_2MgSi_3O_8)$
g°($K_6Mg_3Si_{13}O_{32}$)	$3G(K_2MgSi_3O_8)+4G(\text{Tri})$
$G(K_2MgSi_3O_8)$	$-4150209.2394989+925.63917458T-113.18615T\ln T+0.105414948T^2-2.61022308\cdot10^{-6}T^3$ $+2511038.35T^{-1}-18.5895448T^{1.5}$, (298-3000K)
$G(\text{Tri})$	$-944111.18439234+480.752826T-75.372668T\ln T+297904753 88T^{-1}$ $-159707687.146667T^{-2}$, (298-1991K) $-961947.905277+569.440180798T-85.772T\ln T$, (1991-3000K)
high-(Na,K)AlO_2	
Compound Energy Formalism ($0.5K_2MgSiO_4$, SiO_2)	
g°(K_2MgSiO_4)	$G(K_2MgSiO_4)$
g°(SiO_2)	$G(\text{Cri})+8989.465$
$G(K_2MgSiO_4)$	$-2229074.96733319+968.809739856062T-169.644531T\ln T-0.04729039275T^2$ $+2.1382676\cdot10^{-6}T^3+1090226.86T^{-1}+1.3240797267T^{1.5}$, (298-3000K)
$G(\text{Cri})$	$-924997.137509442+566.99969528T-83.513598136T\ln T+1227679.99T^{-1}$ $-46678699.0706667T^{-2}-1498.771995136T^{0.5}$, (298-1996K) $-961789.834882+569.34943818T-85.772T\ln T$, (1996-3000K)
$q^{11}_{SiO_2,0.5K_2MgSiO_4}$	-62760
$q^{21}_{SiO_2,0.5K_2MgSiO_4}$	-20920
low-(Na,K)AlO_2	
Compound Energy Formalism ($0.5K_2MgSiO_4$, SiO_2)	
g°(K_2MgSiO_4)	$G(K_2MgSiO_4)$
g°(SiO_2)	$G(\text{Tri})+8989.465$
$G(K_2MgSiO_4)$	$-2227104.96733319+966.287332685767T-169.644531T\ln T-0.04729039275T^2$ $+2.1382676167\cdot10^{-6}T^3+1090226.86T^{-1}+1.3240797267T^{1.5}$, (298-3000K)
$G(\text{Tri})$	$-944111.18439234+480.752826017315T-75.372668T\ln T$ $+2979047.5388T^{-1}-159707687.146667T^{-2}$, (298-1991K) $-961947.905277253+569.440180798T-85.772T\ln T$, (1991-3000K)

Parameter	Value, J·mol^{-1}
$q^{11}_{SiO_2,0.5K_2MgSiO_4}$	−62760
$q^{21}_{SiO_2,0.5K_2MgSiO_4}$	−20920

Table A.34 Optimized properties of the compound phases in the Na_2O-B_2O_3 system.

Compound	$\Delta_f H°_{298.15}$, J·mol^{-1}	$S°_{298.15}$, J·mol^{-1}·K^{-1}	$C_P(T)$, J·mol^{-1}·K^{-1}
Na_3BO_3	−1540000	148.60	$207.734677+0.0281676712T+3353459.71T^{-2}-5.02892587\cdot10^{-6}T^2-35072.9097T^{-1}$, (298-3000K)
$Na_4B_2O_5$	−2521000	222.00	$296.337139+0.0588632256T+3883873.56T^{-2}-9.80283616\cdot10^{-6}T^2-46193.7908T^{-1}$, (298-3000K)
$NaBO_2(s_1)$	−975000	73.53	$85.1787882+0.032253T+150450.836T^{-2}-4.70704281\cdot10^{-6}T^2-9014.685T^{-1}$, (298-3000K)
$NaBO_2(s_2)$	−972000	76.52	$85.1787882+0.032253T+150450.836T^{-2}-4.70704281\cdot10^{-6}T^2-9014.685T^{-1}$, (298-3000K)
$Na_2B_4O_7(s_1)$	−3285000	189.52	$260.308976+0.119986207T+257224.416T^{-2}-1.51860803\cdot10^{-5}T^2-33238.6986T^{-1}$, (298-3000K)
$Na_2B_4O_7(s_2)$	−3281000	194.26	$260.308976+0.119986207T+257224.416T^{-2}-1.51860803\cdot10^{-5}T^2-33238.6986T^{-1}$, (298-3000K)
$Na_2B_4O_7(s_3)$	−3284000	189.52	$260.308976+0.119986207T+257224.416T^{-2}-1.51860803\cdot10^{-5}T^2-33238.6986T^{-1}$, (298-3000K)
$NaB_3O_5(s_1)$	−2299495	121.34	$231.085428+0.0365356492T+2647652.43T^{-2}-5.78970138\cdot10^{-6}T^2-44668.3774T^{-1}$, (298-3000K)
$NaB_3O_5(s_2)$	−2297700	121.34	$231.085428+0.0365356492T+2647652.43T^{-2}-5.78970138\cdot10^{-6}T^2-44668.3774T^{-1}$, (298-3000K)
$NaB_3O_5(s_3)$	−2296700	121.34	$231.085428+0.0365356492T+2647652.43T^{-2}-5.78970138\cdot10^{-6}T^2-44668.3774T^{-1}$, (298-3000K)
$Na_2B_8O_{13}(s_1)$	−5900726	297.06	$808.746982-0.0717848964T+24214176T^{-2}+9.89975497\cdot10^{-6}T^2-224257.767T^{-1}$, (298-3000K)
$Na_2B_8O_{13}(s_2)$	−5898000	297.06	$808.746982-0.0717848964T+24214176T^{-2}+9.89975497\cdot10^{-6}T^2$

Compound	$\Delta_f H°_{298.15}$, J·mol^{-1}	$S°_{298.15}$, J·mol^{-1}·K^{-1}	$C_P(T)$, J·mol^{-1}·K^{-1}
			$-224257.767T^{-1}$, (298-3000K)
$NaB_5O_8(s_1)$	−3581682	188.00	$501.959316-0.0471588596T+16058880.8T^{-2}+6.55692281\cdot10^{-6}T^2$ $-143902.757T^{-1}$, (298-3000K)
$NaB_5O_8(s_2)$	−3580682	189.01	$501.959316-0.0471588596T+16058880.8T^{-2}+6.55692281\cdot10^{-6}T^2$ $-143902.757T^{-1}$, (298-3000K)
$NaB_5O_8(s_3)$	−3579682	189.97	$501.959316-0.0471588596T+16058880.8T^{-2}+6.55692281\cdot10^{-6}T^2$ $-143902.757T^{-1}$, (298-3000K)
$NaB_9O_{14}(s_1)$	−6103200	340.00	$733.364943+0.0219247083T+19781976.3T^{-2}-5.58237055\cdot10^{-6}T^2$ $-193788.391T^{-1}$, (298-3000K)
$NaB_9O_{14}(s_2)$	−6102200	341.67	$733.364943+0.0219247083T+19781976.3T^{-2}-5.58237055\cdot10^{-6}T^2$ $-193788.391T^{-1}$, (298-3000K)
$NaB_9O_{14}(s_3)$	−6101200	342.76	$733.364943+0.0219247083T+19781976.3T^{-2}-5.58237055\cdot10^{-6}T^2$ $-193788.391T^{-1}$, (298-3000K)

Table A.35 Gibbs energy parameters of the liquid phase in the Na_2O-B_2O_3 system.

Parameter	Value, J·mol^{-1}
Two-sublattice Quasichemical Formalism (Na, (Na_2), B, NaB//O); Grouping: Na, (Na_2) in group 1; B, NaB in group 2	
Coordination numbers: $Z^{Na}_{Na,Na//O,O}$ = 0.68872188, $Z^{Na_2}_{Na_2,Na_2//O,O}$ = 1.37744375, $Z^{B}_{B,B//O,O}$ = 2.0661656, $Z^{NaB}_{NaB,NaB//O,O}$ = 2.7548875, $Z^{O}_{Na,Na//O,O} = Z^{O}_{Na_2,Na_2//O,O} = Z^{O}_{B,B//O,O} = Z^{O}_{NaB,NaB//O,O} = Z^{O}_{Na,B//O,O} = Z^{O}_{Na,NaB//O,O}$ = 1.37744375, $Z^{B}_{NaB,B//O,O}$ = 3.5, $Z^{NaB}_{NaB,B//O,O}$ = 10.5, $Z^{O}_{NaB,B//O,O}$ = 3.23076923	
Grouping exceptions	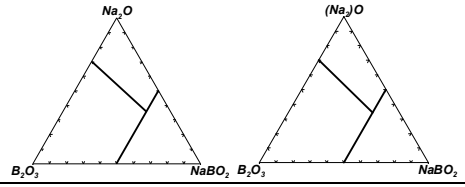

Parameter	Value, J·mol^{-1}
$\Delta g^{\circ}_{Na,B}$	−324177+33.472T
$g^{10}_{Na,B}$	−62760
$g^{01}_{Na,B}$	−37417.8
$\Delta g^{\circ}_{Na,NaB}$	−37656
$\Delta g^{\circ}_{NaB,B}$	−41674.4+6.901561T
$g^{10}_{NaB,B}$	−174874−28.9065T
$g^{01}_{NaB,B}$	8522.804−1.40286T
$g^{02}_{NaB,B}$	−4868.94+4.99214T

Table A.36 Optimized properties of the compound phases in the Na_2O-B_2O_3-SiO_2 system.

Compound	$\Delta_f H^{\circ}_{298.15}$, J·mol^{-1}	$S^{\circ}_{298.15}$, J·mol^{-1}·K^{-1}	$C_P(T)$, J·mol^{-1}·K^{-1}
$NaBSiO_4$	−1896000	119.05	197.8956+0.014551T−5958095T^{-2}+958246123T^{-3} −1052.71$T^{-0.5}$, (298-1500K) 192.5414−5958095T^{-2}+95826123T^{-1}, (1500-2000K)

Table A.37 Gibbs energy parameters of the liquid phase in the Na_2O-B_2O_3-SiO_2 system.

Parameter	Value, J·mol^{-1}
Two-sublattice Quasichemical Formalism (Na, (Na_2), B, NaB, Si//O); Grouping: Na, (Na_2) in group 1; B, NaB, Si in group 2	
Grouping exceptions	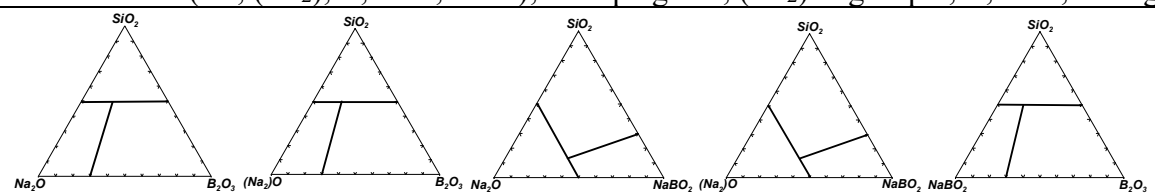

Parameter	Value, J·mol^{-1}
$q^{001}_{\mathrm{Na,Si(NaB)}}$	−13388.8
$q^{002}_{\mathrm{NaB,Si(Na)}}$	376560
$q^{001}_{\mathrm{Na_2,Si(B)}}$	−41840
$q^{101}_{\mathrm{Na,Si(B)}}$	−41840
$\Delta g^{\circ}_{\mathrm{NaB,Si}}$	−88858.7
$g^{101}_{\mathrm{B,Si(NaB)}}$	8368

Table A.38 Optimized properties of the compound phases in the K_2O-B_2O_3 system.

Compound	$\Delta_f H°_{298.15}$, J·mol^{-1}	$S°_{298.15}$, J·mol^{-1}·K^{-1}	$C_P(T)$, J·mol^{-1}·K^{-1}
K_3BO_3	−1488500	180	$178.928+0.0432324T+4.38622\cdot10^5T^{-2}-7.561286\cdot10^{-6}T^2$ $-16107.35T^{-1}$, (298-3000K)
KBO_2	−999897	80	$106.53-7.6108\cdot103T+4.27454\cdot10^5T^{-2}+1.273816\cdot10^{-6}T^2$ $-12453.85T^{-1}$, (298-3000K)
$K_2B_4O_7$	−3399000	209.9	$328.68-0.02699T-7.61074\cdot10^5T^{-2}+4.612434\cdot10^{-6}T^2$ $-40451.69T^{-1}$, (298-3000K)
$KB_3O_5(s_1)$	−2373000	131.925	$274.013-0.033383T+1.808916\cdot10^6T^{-2}+5.626729\cdot10^{-6}T^2$ $-53050.93T^{-1}$, (298-3000K)
$KB_3O_5(s_2)$	−2367000	131.925	$274.013-0.033383T+1.808916\cdot10^6T^{-2}+5.626729\cdot10^{-6}T^2$ $-53050.93T^{-1}$, (298-3000K)
$K_{10}B_{38}O_{62}$	−29012714	1535.05	$4106.015-0.583939T+5.398407\cdot10^7T^{-2}+9.726733\cdot10^{-5}T^2$ $-9.741885\cdot10^5T^{-1}$, (298-3000K)
KB_5O_8	−3682600	185.9	$470.075-0.060309T+4370507T^{-2}+1.009499\cdot10^{-5}T^2$ $-98668.5T^{-1}$, (298-3000K)

Compound	$\Delta_f H°_{298.15}$, J·mol^{-1}	$S°_{298.15}$, J·mol^{-1}·K^{-1}	$C_P(T)$, J·mol^{-1}·K^{-1}
KB_9O_{14}	−6223500	293.8	$707.968-0.067972T+258907T^{-2}+1.1568\cdot10^{-5}T^2$ $-103667.3T^{-1}$, (298-3000K)

Table A.39 Gibbs energy parameters of the liquid phase in the K_2O-B_2O_3 system.

Parameter	Value, J·mol^{-1}
Two-sublattice Quasichemical Formalism (K, (K_2), B, KB//O); Grouping: K, (K_2) in group 1; B, KB in group 2	
Coordination numbers: $Z^{K}_{K,K//O,O}$ = 0.68872188, $Z^{K_2}_{K_2,K_2//O,O}$ = 1.37744375, $Z^{B}_{B,B//O,O}$ = 2.0661656, $Z^{KB}_{KB,KB//O,O}$ = 2.7548875, $Z^{O}_{K,K//O,O} = Z^{O}_{K_2,K_2//O,O} = Z^{O}_{B,B//O,O} = Z^{O}_{KB,KB//O,O} = Z^{O}_{K,B//O,O} = Z^{O}_{K,KB//O,O}$ = 1.37744375, $Z^{B}_{KB,B//O,O}$ = 3.33333333, $Z^{KB}_{KB,B//O,O}$ = 10.0, $Z^{O}_{KB,B//O,O}$ = 3.07692308	
Grouping exceptions	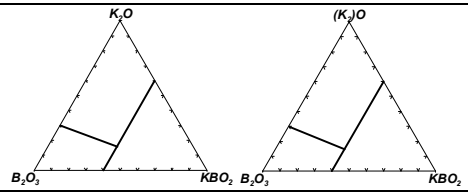
$\Delta g^{\circ}_{K,B}$	−292880
$g^{10}_{K,B}$	−41840
$g^{01}_{K,B}$	−38122.9
$\Delta g^{\circ}_{K,KB}$	−83680
$g^{01}_{K,KB}$	−83680
$\Delta g^{\circ}_{KB,B}$	−33165.6
$g^{10}_{KB,B}$	−58930.7
$g^{01}_{KB,B}$	7112.8
$g^{001}_{K,B(KB)}$	−83680

Table A.40 Optimized properties of the compound phases in the K_2O-B_2O_3-SiO_2 system.

Compound	**$\Delta_f H°_{298.15}$, J·mol^{-1}**	**$S°_{298.15}$, J·mol^{-1}·K^{-1}**	**$C_P(T)$, J·mol^{-1}·K^{-1}**
$KBSi_2O_6$	−2999000	100.00	$-2.782-0.357966T-118697T^{-2}+4.53272\cdot10^{-5}T^2+17.62T^{0.5}$ $-12453.85T^{-1}$, (298-1500K) $11.8305-0.047211T+427454T^{-2}+3.5018\cdot10^{-6}T^2+2.97T^{0.5}$ $-12453.85T^{-1}$, (1500-3000K)
KBS_3O_8	−3911300	140	$-3809643.7687+5587.774T-784.056682T\ln T-0.048281334T^2$ $+4.1004482\cdot10^{-7}T^3-801532.252T^{-1}+14.76909T^{1.5}$ $-27543.3942T^{0.5}-12453.8506\ln T$, (298-3000K)

Table A.41 Gibbs energy parameters of the liquid phase in the K_2O-B_2O_3-SiO_2 system.

Parameter	**Value, J·mol^{-1}**
Two-sublattice Quasichemical Formalism (K, (K_2), B, KB, Si//O); Grouping: K, (K_2) in group 1; Si, B, KB in group 2	
Grouping exceptions	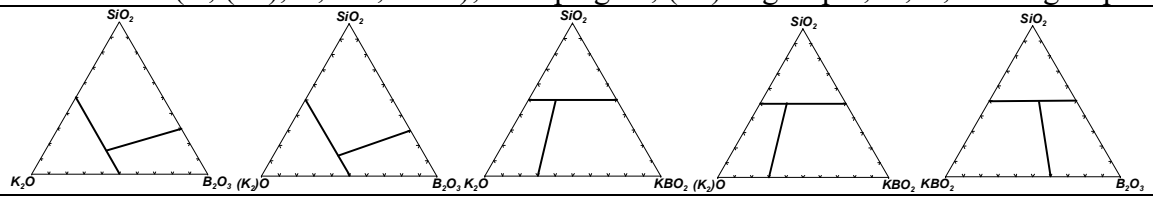
$\Delta g^{\circ}_{KB,Si}$	−63841.6
$g^{01}_{KB,Si}$	−9782.42
$g^{021}_{K,Si(KB)}$	22660
$g^{101}_{K,Si(KB)}$	112968
$g^{001}_{K,Si(KB)}$	−89757.6
$g^{001}_{Si,KB(B)}$	−6694.4
$g^{001}_{KB,B(Si)}$	−2566.62
$g^{002}_{KB,B(Si)}$	408.6354

Table A.42 Gibbs energy parameters of the solution phases in the K_2O-Na_2O-B_2O_3 system.

Parameter	**Value, J·mol^{-1}**
Liquid	
Two-sublattice Quasichemical Formalism (Na, (Na_2), NaB, K, (K_2), B, KB, Si//O); Grouping: Na, (Na_2), K, (K_2) in group 1; Si, B, NaB, KB in group 2	
Grouping exceptions	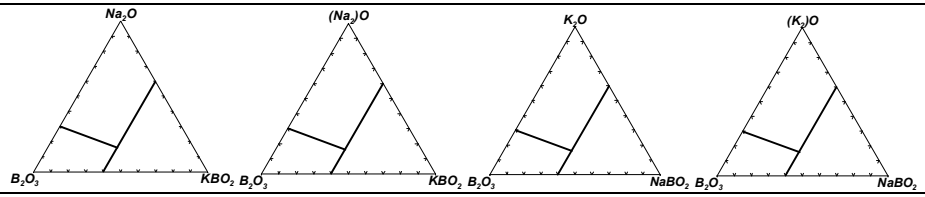
$\Delta g^{\circ}_{\mathrm{NaB,KB}}$	−125520
$g^{101}_{\mathrm{B,KB(NaB)}}$	−16736
Monoborate	
Compound Energy Formalism (Na^+,K^+){BO_2^-}	
g°($NaBO_2$)	G($NaBO_2$)
g°(KBO_2)	G(KBO_2)
G($NaBO_2$)	$-958938.0418+535.75935T-85.1787882T\ln T-0.0161265T^2+7.84507135\cdot10^{-7}T^3$ $-75225.418T^{-1}-9014.685\ln T$, (298-1002.5K) $-2461937.4513+3534.2619T-85.1788T\ln T-1.51164T^2+7.84507135\cdot10^{-7}T^3$ $-75225.418T^{-1}-9014.68499\ln T$, (1002.4-1003.5K) $-955938.0437+532.768T-85.17879T\ln T-0.0161265T^2+7.8451\cdot10^{-7}T^3$ $-75225.418T^{-1}-9014.685\ln T$, (1003.5-3000K)
G(KBO_2)	$-971395.50+670.658780T-106.531528T\ln T+0.0038054T^2-2.123027\cdot10^{-7}T^3$ $-213727.099T^{-1}-12453.8506\ln T$, (298-3000K)
$q^{11}_{\mathrm{NaBO_2,KBO_2}}$	−22593.6
$q^{21}_{\mathrm{NaBO_2,KBO_2}}$	−20920
Diborate	
Compound Energy Formalism (Na^+,K^+)$_2$ {$B_4O_7^{2-}$}	

Parameter	**Value, J·mol^{-1}**
g°($Na_2B_4O_7$)	G($Na_2B_4O_7$)
g°($K_2B_4O_7$)	G($K_2B_4O_7$)
G($Na_2B_4O_7$)	$-3210807.2154+1699.05979T-260.308976T\ln T-0.059993T^2$ $+2.53101338\cdot10^{-6}T^3-128612.208T^{-1}-33238.6986\ln T$, (298-843.5K) $-4896735.69811+5696.51914T-260.308976T\ln T-2.42956T^2+2.53101338\cdot10^{-6}T^3$ $-1286.12.208T^{-1}-33238.6986\ln T$, (298-843.5K) $-3206807.3865+1694.320653T-260.308976T\ln T-0.059993T^2+2.53101338\cdot10^{-6}T^3$ $-128612.208T^{-1}-33238.6986\ln T$, (844.5-3000K)
G($K_2B_4O_7$)	$-3308364.91464+2123.603T-328.683459T\ln T-7.6873903\cdot10^{-7}T^3+380536.934T^{-1}$ $-40451.6938\ln T$, (298-3000K)
$q^{11}_{NaB_2O_{3.5},KB_2O_{3.5}}$	−4184
Triborate	
Compound Energy Formalism (Na^+,K^+){$B_3O_5^-$}	
g°(NaB_3O_5)	G(NaB_3O_5)
g°(KB_3O_5)	G(KB_3O_5)
G(NaB_3O_5)	$-2151251.5678+1571.94296T-231.085428T\ln T-0.018267825T^2+9.6495023\cdot10^{-7}T^3$ $-1323826.215T^{-1}-44668.3774\ln T$, (298-3000K)
G(KB_3O_5)	$-2197983.8386+1861.35764T-274.012728T\ln T+0.01669166T^2-9.377882\cdot10^{-7}T^3$ $-904457.815T^{-1}-53050.9256\ln T$, (298-3000K)
$q^{11}_{NaB_3O_5,KB_3O_5}$	10460